

AD A 039081

AD

R-TR-77-008

PROCEEDINGS, FIRST CONFERENCE ON:

**DYNAMICS
OF
PRECISION GUN WEAPONS**

12

HELD AT
ROCK ISLAND, ILLINOIS
JANUARY 26-27, 1977

DDC
RECEIVED
MAY 5 1977
D

DISTRIBUTION STATEMENT A

Approved for public release;
Distribution Unlimited

UNDER THE AUSPICES OF:

US ARMY ARMAMENT RESEARCH AND DEVELOPMENT COMMAND

DOVER, NEW JERSEY

PROCEEDINGS, FIRST CONFERENCE

DDC FILE COPY

UNCLASSIFIED

SECURITY CLASSIFICATION OF THIS PAGE (When Data Entered)

REPORT DOCUMENTATION PAGE		READ INSTRUCTIONS BEFORE COMPLETING FORM
1. REPORT NUMBER R-TR-77-008	2. GOVT ACCESSION NO.	3. RECIPIENT'S CATALOG NUMBER (9)
4. TITLE (and Subtitle) Dynamics of Precision Gun Weapons		5. TYPE OF REPORT & PERIOD COVERED Final report
7. AUTHOR(s) Individual papers		6. PERFORMING ORG. REPORT NUMBER
9. PERFORMING ORGANIZATION NAME AND ADDRESS US Army Armament Materiel Readiness Cmd Rock Island, IL		8. CONTRACT OR GRANT NUMBER(s)
11. CONTROLLING OFFICE NAME AND ADDRESS US Army Armament Materiel Readiness Cmd R&D Rock Island, IL		10. PROGRAM ELEMENT, PROJECT, TASK AREA & WORK UNIT NUMBERS
14. MONITORING AGENCY NAME & ADDRESS (if different from Controlling Office)		12. REPORT DATE January 1977
		13. NUMBER OF PAGES 713
		15. SECURITY CLASS. (of this report) Unclassified
16. DISTRIBUTION STATEMENT (of this Report) No restrictions		15a. DECLASSIFICATION/DOWNGRADING SCHEDULE
<div style="border: 1px solid black; padding: 5px; text-align: center;"> DISTRIBUTION STATEMENT A Approved for public release; Distribution Unlimited </div>		
17. DISTRIBUTION STATEMENT (of the abstract entered in Block 20, if different from Report)		
18. SUPPLEMENTARY NOTES Papers presented at conference on Dynamics of Precision Gun Weapons		
19. KEY WORDS (Continue on reverse side if necessary and identify by block number) Ballistics, Precision, Target acquisition, Stabilization, Dynamics, barrel vibration.		
20. ABSTRACT (Continue on reverse side if necessary and identify by block number) Twenty-two papers are presented by authors from five defense laboratories, three industrial concerns and five universities. Purpose of papers was to disseminate information on the dynamics of precision gun weapons.		

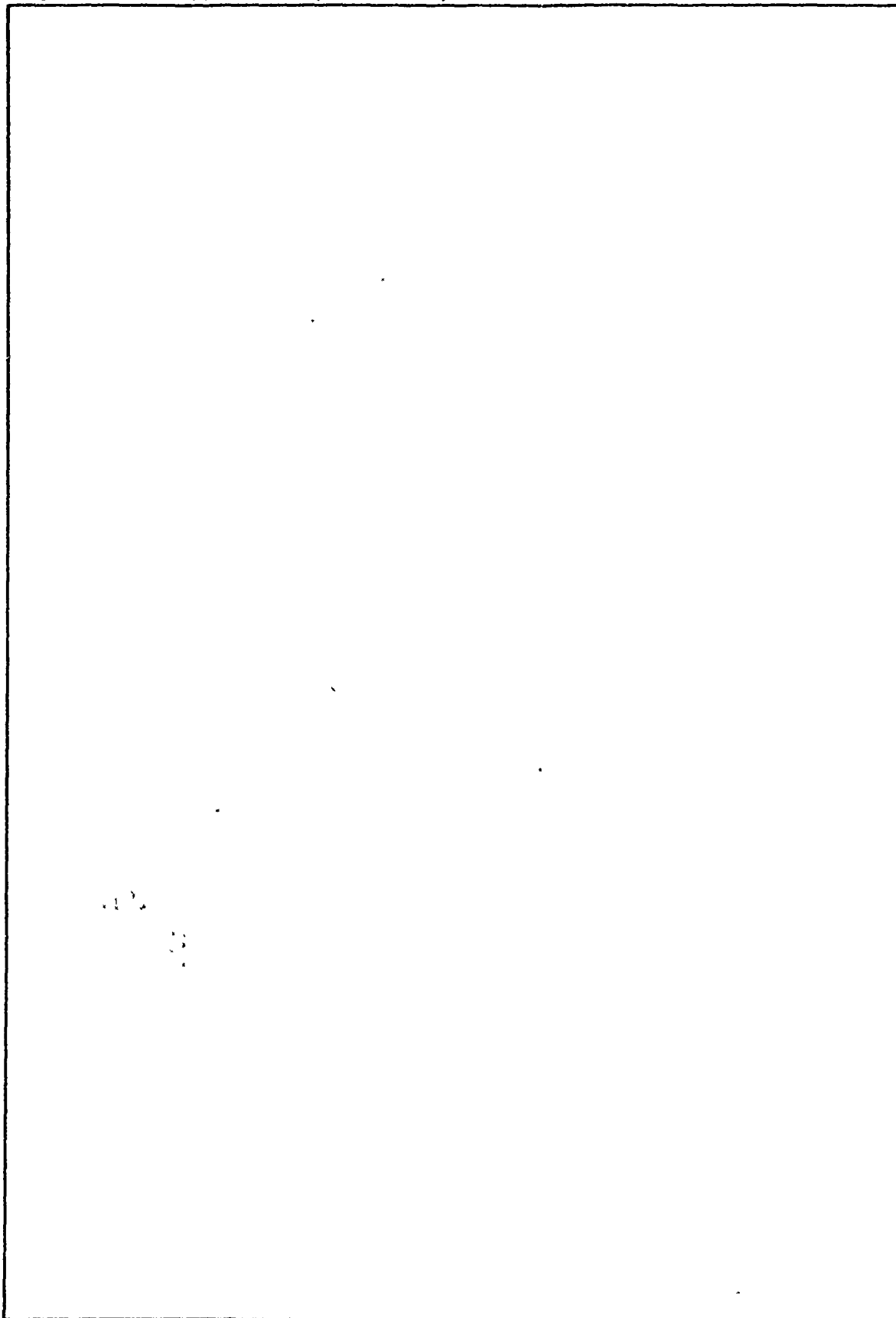
DD FORM 1 JAN 73 1473

EDITION OF 1 NOV 65 IS OBSOLETE

UNCLASSIFIED

SECURITY CLASSIFICATION OF THIS PAGE (When Data Entered)

SECURITY CLASSIFICATION OF THIS PAGE(When Data Entered)



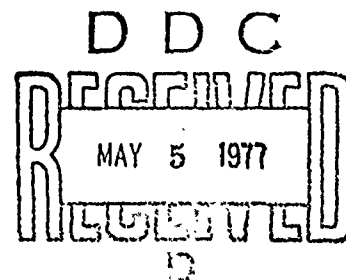
SECURITY CLASSIFICATION OF THIS PAGE(When Data Entered)

ACCESSION NO.	
NTIS	Write Section <input checked="" type="checkbox"/>
EDC	Duty Section <input type="checkbox"/>
UNANNOUNCED <input type="checkbox"/>	
JUSTIFICATION	
BY	
DISTRIBUTION/AVAILABILITY CODES	
Dist.	AVAIL. and/or SPECIAL
A	

Proceedings, First Conference on:

D Y N A M I C S
O F
P R E C I S I O N G U N W E A P O N S

Held At
Rock Island, Illinois
January 26-27, 1977



Sponsored and Organized by:

ROYCE BECKETT, Director, Rodman Laboratory
MICHAEL HALTER, ARMCOM, Rock Island, Illinois
EDWARD HAUG, Professor, University of Iowa
VADTM KOMKOV, Professor, Texas Tech University

<p style="text-align: center;">DISTRIBUTION STATEMENT A</p> <p style="text-align: center;">Approved for public release Distribution Unlimited</p>
--

Edited by E J. Haug, February 18, 1977

FORWARD

The accuracy of a ballistic projectile is dependent upon the precision with which a gun can be pointed and upon the dynamics of the barrel and projectile during launch. Advances in target acquisition and in stabilization and control technology yield great potential for finding a target and then aiming a gun with high accuracy. Less attention has been given to the dynamics of the gun and projectile and how it effects accuracy. Those factors of gun and projectile dynamics that contribute to errors are:

- (a) The effect of the droop and related dynamic behavior of a bent gun tube projectile interaction.
- (b) Balloting, or tube projectile interaction for projectiles with rapid spin.
- (c) Effects of barrel vibration and vibration of the supporting structure or vehicle, which is transmitted to the gun barrel.
- (d) Response produced by weapon mechanism motion.

The purpose of the conference was to:

- (a) Present the work of specialists who are addressing problems of gun precision, and to
- (b) Afford an opportunity for discussion and coordination of methods and approaches to evaluating precision.

The conference was held in the Sheraton Hotel, Rock Island, Illinois, January 26-27, 1977. Twenty-two papers were presented, with authors distributed among:

- (a) Five Defense Laboratories,
- (b) Three industrial concerns,
- (c) Five universities.

It is, further, interesting to note that four of the papers were co-authored by individuals from various permutations of these organizations. Finally, the distribution of participants included:

- (a) Fifteen U.S. defense laboratories,
- (b) One U.K. defense laboratory,
- (c) Three military field organizations,
- (d) Nine industrial concerns,
- (e) Eight universities.

Based on the intensity of discussion and interaction among the diverse groups of participants, we feel that the goal of dissemination of information was met.

CONFERENCE PARTICIPANTS

Dr. Martin Soifer	S & D Dynamics Inc., Long Island
Alexander S. Elder	BRL, Aberdeen, Maryland
C.L. Henry	BRL, Aberdeen, Maryland
B.T. Haug	BRL, Aberdeen, Maryland
R.K. Loder	BRL, Aberdeen, Maryland
Robert H. Whyte	G.E., Burlington, Vermont
Roger H. Lapp	APL, Johns Hopkins University
Dean S. Williams	Aeronutronic Ford, California
Leland A. Watermeier	BRL, Aberdeen, Maryland
Prof. Ben Noble	University of Wisconsin
Prof. A.P. Boresi	University of Illinois
H.L. Langhaar	University of Illinois
R.E. Miller	University of Illinois
T.T. Feng	Ebasco, New York
B.L. Stearns	G.E., Burlington, Vermont
William L. Andre	Air Mobility Lab, Moffett Field, California
Clive N. Bowden	RARDE, England
S.B. Kramer	Hughes Helicopter, California
Harry J. Davis	Harry Diamond Laboratory
John C. Houston	ARES Inc., Ohio
James E. Wildman	ARES Inc., Ohio
Edward J. Haug	University of Iowa
Dr. William Holm	Georgia Tech.
Arthur Akers	Iowa State University
Steven Newell	Battelle, Columbus, Ohio
Thomas Lewis	General Dynamics, Pomona
Dr. Norman Wykoff	Jefferson Proving Ground
Dan Sabo	AVSCOM, St. Louis
Victor Lindner	Picatinny Arsenal
Charles Christensen	Naval Ordnance, Maryland
George Reis	Sandia Lab
William Pryor	Picatinny Arsenal
Howard Brunvoll	Picatinny Arsenal
John Masly	Picatinny Arsenal
Grant Manning	Picatinny Arsenal
J. Domen	Picatinny Arsenal
Dr. Charles Murphy	Picatinny Arsenal
CWO D. Luke	BRL, Aberdeen, Vermont
CW3 N. Goddard	MCDEC, Quantico
SSGT. G. Gregory	MCDEC, Quantico
Jim Heater	MCDEC, Quantico
Kevin Fansler	Picatinny Arsenal
Edward Schmidt	BRL, Aberdeen, Maryland
Dr. Thomas Simpkins	BRL, Aberdeen, Maryland
Robert Ryan	Watervliet Arsenal
	Watervliet Arsenal

George Pflegl
 P.A. Cox
 George Soo Hoo
 William Rodgers
 Harry Reed
 Paul Boggs
 Joe Schmitz
 Robert Trisiletti
 Anthony Suchacki
 T. Tsui
 Andrew Hauser
 James Brown
 Bill Frazier
 Vadin Komkov
 Michael Bawaren
 Willie Hall
 Forbes Brown
 CPT Michael Halter
 John Brinkman
 Gary Fischer
 George Balunis
 Dr. Royce Beckett
 Harvey Garver
 Edward Larrison
 Dr. Ko Chang Pan
 Dr. Shih Chi Chu
 Robert Radkiewicz
 Verlin Baumgarth
 Robert Kasten
 Wayne Piehl
 Thomas Hutchings

Watervliet Arsenal
 Southwest Research Inst., San Antonio
 Dept. of the Navy
 Naval Ordnance, Alexandria, Virginia
 BRL, Aberdeen, Maryland
 ARO, Durham, North Carolina
 Frankford Arsenal
 Frankford Arsenal
 Chrysler Defense, Michigan
 AMMRC, Lexington, Massachusetts
 University of Iowa
 Armor & Engr. Board, Fort Knox
 Armor & Engr. Board, Fort Knox
 Texas Tech
 Frankford Arsenal
 Quantico, Virginia
 Lehigh University
 ARMCOM, Rock Island, Illinois
 ARMCOM, Rock Island, Illinois
 ARMCOM, Rock Island, Illinois
 ARMCOM, Rock Island, Illinois
 Rodman Laboratory, Rock Island
 Rodman Laboratory, Rock Island
 Rodman Laboratory, Rock Island
 Rodman Laboratory, Rock Island
 Rodman Laboratory, Rock Island
 Rodman Laboratory, Rock Island
 Rodman Laboratory, Rock Island
 Rodman Laboratory, Rock Island
 Rodman Laboratory, Rock Island
 Rodman Laboratory, Rock Island

TABLE OF CONTENTS

	<u>Page</u>
 SESSION 1: MECHANICS OF WEAPONS	
Chairman: Mr. Victor Linder Picatinny Arsenal	
"Historical Review and Survey of Current Problems in Weapon Dynamics". A.S. Elder, Ballistics Research Laboratory, Aberdeen, Maryland.	1
"Fundamentals of Weapon Dynamic Effects on Precision". V. Komkov, Texas Tech University, Lubbock, Texas.	27
"A Theoretical Model for In-Bore Projectile Balloting/Barrel Motion". G.S. Hoo, U.S. Naval Surface Weapons Center Dahlgren, Virginia.	46
"Parametric Resonance in Gun Tubes". T.E. Simkins, Watervliet Arsenal, Watervliet, New York.	81
"Balloting-Energy Growth Possibilities". K.S. Fansler, Ballistics Research Laboratory, Aberdeen, Maryland.	147
"Transverse Dynamic Response of Gun Barrel with Time Varying Supports". T.T. Feng, Ebasco Services Inc., New York, New York. T. Hung, U.S. Army Armament Command, Rock Island, Illinois.	179
"Aerodynamic Interference during Sabot Discard". E.M. Schmidt, Ballistics Research Laboratory, Aberdeen, Maryland.	199
 SESSION 2: NUMERICAL METHODS AND APPROXIMATION TECHNIQUES	
Chairman: Mr. John Brinkman U.S. Army Armament Command	
"A State Space Method for Optimization of Weapon System Dynamics". E.J. Haug and J.S. Arora, University of Iowa Iowa City, Iowa.	217
"Sensitivity Analysis and Optimal Design of the 75mm Automatic Cannon Mechanism". R.C. Huang, E.J. Haug and J.G. Andrews, University of Iowa, Iowa City, Iowa.	258

	<u>Page</u>
"A Finite Element Method of Optimizing Precision of a Vibrating Weapon". J.S. Arora and E.J. Haug, University of Iowa, Iowa City, Iowa. T.T. Feng, Ebasco Service Inc., New York, New York.	305
"A Report of the Finite Element Method (FEM) Analysis of the Medium Caliber, Anti-Armor Automatic Cannon". G.A. Pflcgl, Watervliet Arsenal, Watervliet, New York.	340
"Radial and Transverse Response of Gun Tubes by Finite Element Methods". T.E. Simkins, Watervliet Arsenal, Watervliet, New York.	373
"Investigation of Causes of Dispersion in Low-Dispersion Automatic Cannon System (LODACS) Concept". R.S. Newell, Battelle Memorial Institute, Columbus, Ohio.	470
SESSION 3: INSTRUMENTATION AND EXPERIMENTAL TECHNIQUES	
Chairman: Mr. Harvey Garver Rock Island Arsenal	
"Application of Accelerometers for the Measurement of Gun Tube Motion". J.O. Pilcher, C.L. Henry and R.B. Murray, Ballistics Research Laboratory, Aberdeen, Maryland.	497
"Deflecting Penetrator Simulation". W.H. Hathaway, B.K. Stearns and R.H. Whyte, General Electric Company, Burlington, Vermont.	514
"The Experimental Verification of Buffer Discharge Coefficients". A. Akers, Iowa State University, Ames, Iowa.	528
"Precision Pointing and Stabilization of a Low Dispersion Automatic Cannon System". R.E. Kasten, Rock Island Arsenal Rock, Island, Illinois. N. Loh, University of Iowa, Iowa City, Iowa.	546
"On the Gun Pointing Accuracy of an Anti-Armor Automatic Cannon". A.P. Boresi, H.L. Langhaar and R.E. Miller, University of Illinois, Urbana, Illinois S.C. Chu, Rock Island Arsenal, Rock Island, Illinois.	577

	<u>Page</u>
"Electromagnetic Pulse Instrumentation and Measurement Technique for the Determination of Projectile Velocity, Spin, Precession and Nutation". R.K. Loder, E.M. Wineholt, J.O. Pilcher, J.R. Gramling and J.Q. Schmidt, Ballistics Research Laboratory, Aberdeen, Maryland.	603
"Effects of Eccentric Firing". B.K. Stearns, General Electric Company, Burlington, Vermont.	642
"Optical Device for Determining Small Angular Motion". B.T. Haug, Ballistics Research Laboratory, Aberdeen, Maryland.	659
"Stochastic Optimal Control of a Helicopter Gun Turret". F.T. Brown and S.H. Johnson, Lehigh University, Bethlehem, Pennsylvania.	674

HISTORICAL REVIEW AND SURVEY OF CURRENT PROBLEMS
IN WEAPON DYNAMICS

A. S. ELDER
Ballistics Research Laboratory
Aberdeen, Maryland

TABLE OF CONTENTS

	<u>Page</u>
I. INTRODUCTION	2
II. CAUSES AND CONSEQUENCES OF TUBE VIBRATION	3
III. REVIEW OF WORK COMPLETED BEFORE 1957	7
IV. SUMMARY OF TUBE VIBRATION AND ACCURACY STUDIES AT THE BALLISTIC RESEARCH LABORATORY	10
V. CURRENT THEORETICAL AND EXPERIMENTAL PROGRAMS	16
VI. MODELING THEORY	19
VII. MECHANICAL ASPECTS OF VARIABLE BIAS	25
VIII. CONCLUSIONS	26

I. INTRODUCTION

Tank guns must have a high probability of hitting the target with the first round of an engagement in order to survive. Vibrations of the gun tube while the projectile is in the bore have long been recognized as an important source of error. The forces which occur as the projectile emerges from the muzzle, but is still in contact with the tube, are very large but of short duration. These forces produce impulsive changes in the vector velocity of the projectile and are about as important as tube vibrations as a source of error. Errors due to transient aerodynamic forces while the projectile is in the transitional ballistic regime are relatively minor and will not be considered in this report. In the error budget for tank guns, only a small proportion is allotted to tube motion and other mechanical causes; the major allotments in the error budget are assigned to fire control and target acquisition. The emphasis on reducing the gun contribution to the error budget has been the major driving force for research in gun tube vibrations.

Gun tubes for rapid fire guns must absorb large amounts of heat. In meeting this requirement, the gun tubes are overdesigned structurally and are relatively stiffer than tubes for tank guns. The gun tube vibration problem is much less severe. However, these rapid fire guns

are generally mounted on vehicles or aircraft with considerable structural flexibility. The various modes of vibration are readily excited by successive rounds. Consequently the gun, mount, and supporting structure must be considered as a single system in the analysis of vibratory motion. On the other hand, the structural elements supporting the trunnions in a tank are very stiff, so the motion of the trunnions is negligible while the projectile is in the bore.

In conventional artillery, errors associated with indirect fire, variable drag, and the meteorological message tend to dominate the error budget. These errors may be considerable, especially at extended ranges, so firing for registration is practiced whenever the tactical situation permits. The errors due to gun motion, transverse muzzle forces, and transitional aerodynamic forces are lumped together as jump. A jump correction is determined during firing trials and posted in the firing tables. Experience has shown the jump correction for artillery is reasonably constant during the life of the gun.

In this report we will consider mainly tank guns in the 90mm-120mm range. First we will summarize the known causes of tube vibration and the mechanical aspects of variable bias. Second, we will review work prior to 1957 in a cursory manner and, third, the work performed during the following decade at the USA Ballistic Research Laboratory and elsewhere. Finally, we will review the current state-of-the-art, delineate pacing problems as we see them, and indicate direction and technical level of future investigations.

II. CAUSES AND CONSEQUENCES OF TUBE VIBRATION

Several types of vibratory and rigid body motion occur during the firing cycle of a conventional tank gun. During recoil the gun rotates

slightly about the trunnions, due partly to clearances and partly to elasticity of the elevating mechanism. The trunnions are subject to large recoil forces and, consequently, the supporting structure deforms slightly, permitting the trunnions to move perceptibly. Vibratory motion falls into three general categories: large amplitude, low frequency vibrations which have a major effect on accuracy; high frequency, small amplitude vibrations which may affect the structural integrity of fuzes and other components; and traveling stress waves arising from impact loads.

The major contribution to large amplitude vibrations is due to unbalanced recoiling parts. If the center of gravity does not lie on the axis of the bore, a large turning moment is produced by the acceleration of the gun tube. The component of unbalance which lies in the vertical plane will cause the gun to rotate slightly in the trunnions and also cause low frequency tube vibration of significant amplitude. In theory, the combined rigid body and vibratory motion should contribute a consistent bias to the point of impact for a given round. In practice, bias in tank guns is more variable than in artillery. In addition, a worn concentric recoil mechanism will produce excessive dispersion in tank guns.

Rifling torque produces rather large torsional vibrations, especially near the muzzle. The tube acts like a torsion bar, twisting mainly in one direction while the projectile is in the bore, and then oscillating severely after the projectile emerges. The effects on accuracy are minor in a straight tube. However, if the tube is bent or droops naturally, the torsional vibrations become coupled with other types of motion resulting in increased dispersion. If points along the outside of the tube are used to measure displacement of the boreline during firing, then the experimental

results should be corrected for twist of the tube. The most obvious method is to make measurements on opposite sides of the tube so that the effect of torsion can be averaged out.

The powder pressure and recoil forces produce axial vibrations which can be detected with strain gages. The effects on accuracy are negligible; however, stress waves must be considered under some circumstances. L. H. Thomas proved that axial stress waves reflected by the muzzle were one cause of failure in the 90mm tank gun.¹ The tubes failed near the junction of the tube and breech ring.

Unbalanced projectiles produce large centrifugal forces which cause vibrations of moderate frequency. These vibrations are small during the early part of the interior ballistic cycle, but reach considerable amplitude near the muzzle. High explosive shells are the major cause of these vibrations as shells are generally not balanced during production. Kinetic energy rounds are machined to close tolerances and measurements of typical samples have shown the unbalance to be negligible. Thus we should not anticipate significant tube vibrations from centrifugal loading when kinetic energy rounds are fired.

Radial vibrations have been observed by Cranz in his pioneering studies. As these vibrations are symmetric, there should be no affect on accuracy.

Two effects related to the droop of the tube have been studied. Finston, at Brown University, considered the reaction of the projectile against a slightly drooped tube. Inertia of both the tube and projectile

¹ *Personal communication, B. I. Hart, formerly Mathematician at the USA Ballistic Research Laboratories. L. H. Thomas performed the work for the Ordnance Corp around 1947-1950.*

were considered. Simkins, at Watervliet Arsenal, has considered the Bourdon effect, in which gas pressure tends to straighten the tube. Both problems require advanced nonlinear analysis.

Balloting in the bore causes high frequency vibrations in the projectile. These vibrations may be severe enough to damage the fuze or other sensitive components. Stress waves of small amplitude will be propagated in the tube. It seems probable that the energy transmitted to the tube by impact is too small to set up standing waves. Tube motion produced by these impacts should have little effect on accuracy.

Artillery with bag type charges is subject to problems arising from gravity effects and improper seating of the projectile. If the projectile is slightly cocked during ramming, eccentric engraving of the rotating band will result, leading to static unbalance. Gravity alone may be sufficient to tilt a projectile loaded by hand. The resulting loss of symmetry in loading conditions is a cause of yawing in the bore, which is considered to be a major cause of preferential wear that has been observed from time to time. Wear at the muzzle may be important in large caliber, high velocity guns, and will cause a loss of accuracy. It is believed the cause is mainly mechanical, due to high sliding velocities and large centrifugal forces at the muzzle.²

This catalog of interrelated phenomena shows why progress has been slow and sporadic. A truly scientific experiment in which the various causes of tube vibration and their effects are isolated and studied

² Lloyd E. Line, Jr., "Erosion of Guns at the Muzzle," OSRD Report No. 6322, August 1945. Also filed as NDRC Report A-357.

one at a time is far too costly in practice. Low frequency vibrations affecting accuracy have received the most attention and are reasonably well understood at the present time. The analysis of these vibrations follows the usual strength of materials formulations. The greatest present uncertainty lies in formulating effective boundary conditions at the interface of the gun tube and recoil mechanism. High frequency vibrations due to an unbalanced projectile and balloting are more random in nature, and correlation between theory and experiment is unsatisfactory.

III. REVIEW OF WORK COMPLETED BEFORE 1957

Only a cursory review will be given here in view of an earlier report by the author.³ The major objectives were to determine average jump for firing tables and to delineate causes of dispersion. The recorded progress is remarkable considering two important experimental variables were neglected and the engineering calculations indicated by the theory pressed the available means of computation to the limit. It is now recognized that solar radiation produces curvature in the tube which affects the point of impact. Sissom and others recognized its importance but the results of most experimental work did not include the necessary corrections. The second source of errors is associated with laying the gun. Generally a correction for the difference between the alignment of the gunner's quadrant and boresight line was included. However, careful experimental work must be based on the inclination and transverse velocity of the muzzle at shot ejection. These quantities are not correlated exactly

³ A. S. Elder, *"A Review of the Literature to the Bias in the Point of Impact Associated with the Lateral Motion of a Gun During Firing,"*

BRL Memo Report No. 1157, July 1958. AD No. 302698.

with the boresight axis obtained under static conditions due to the various types of gun tube vibration previously described. Finally, computational difficulties led to oversimplified mathematical models which did not correspond sufficiently to the system under consideration.

C. Cranz identified radial vibrations, longitudinal vibrations, torsional vibrations, and transverse vibrations in experimental studies with a rifle barrel. These are the most important types of vibration for guns of any caliber. All other possible modes of vibration should be highly localized and have little effect on accuracy or structural integrity.

F. L. Uffleemann carried out a series of instrumented firing tests with the 17 pdr and 75mm guns. The experiments showed unexplained high frequency components in addition to the displacement due to bending. He also showed that apparent changes in jump of the 75mm gun mounted on the Sherman tank were due to errors in laying.

E. Harrison and others showed a significant correlation between vertical jump and curvature of the barrel in the vertical plane. This should be expected in view of Finston's work on tube droop mentioned previously.

B. D. Sissom showed that jump associated with a given gun changed over an extended period of time and was larger than differences in jump produced by a change of ammunition. He supervised significant work on thermal bending and was among the first to emphasize correct muzzle conditions in experimental studies.

J. A. Mahoney obtained a strong correlation between the static unbalance in a T-154 cartridge and the point of impact.

E. H. Lee performed the most important theoretical work of this period in connection with the instrumented firing tests conducted by Ufflemann. He analyzed the low frequency vibrations due to static unbalance of the recoiling parts. The flexible barrel and rigid tipping parts were considered separately; the conditions at the interface were then matched by successive approximations. The results did not agree completely with the results of the instrumented firing tests.

J. C. P. Miller considered the 17 pdr as a single elastic system and obtained normal modes in accord with this concept. The matching procedure used by Lee was avoided. Essentially, Miller's analysis is equivalent to a solution in terms of normal coordinates of Lagrange. He calculated the normal modes by an iterative procedure.

J. L. Lubkin showed specifically that the transverse linear velocity of the muzzle, as well as the direction of the bore axis at the muzzle must be considered in both theoretical and experimental studies. He was among the first to consider wave propagation methods as well as normal mode analysis in studying torsional vibrations due to the rifling torque.

The work of Darpas⁴ was cited in the preceding reference, but was not given the attention it deserves. Darpas considered the gyroscopic motion of an unbalanced projectile in the tube and the yawing motion which results. The effects of yaw on the trajectory and point of impact

⁴ J. G. Darpas, "Transverse Forces on a Projectile Which Rotates in the Barrel," *Memorial de l'artillerie francaise*, 31, 19 (No. 1, 1957). English translation by H. P. Hitchcock, BRL Memo Report No. 1204, March 1959. AD No. 217015.

were also considered. He showed that the centrifugal force near the muzzle produced very large transverse forces, accounting for abnormal wear in certain 152mm gun tubes. He did not consider the transverse vibrations which would be caused by these forces. This work emphasized the importance of unbalanced projectiles as a major source of yawing motion in bore and gave the forcing function required for an analysis of vibrations due to the centrifugal force.

Both Lee and Darpas considered the limitations of the Bernoulli-Euler equation for transverse vibrations. Lee showed that shearing strains were important early in the interior ballistic cycle and, consequently, the Timoshenko equation was to be preferred. Darpas noted that the Bernoulli-Euler equation could not predict traveling bending waves as it was dispersive in nature. Standing waves, of course, are readily obtained by separation of variables.

The work of L. H. Thomas on longitudinal waves should be mentioned again in passing. The work reviewed in this section formed the basis of an extensive program by Gay, Elder and Sissom in the late Fifties.

IV. SUMMARY OF TUBE VIBRATION AND ACCURACY STUDIES AT THE BALLISTIC RESEARCH LABORATORY

A major study of tank gun accuracy was carried out by Gay, Elder and Sissom during the late Fifties.⁵ The investigation was divided into four parts, as shown below:

⁵ H. P. Gay and A. S. Elder, *"The Lateral Motion of a Tank Gun and Its Effect on the Accuracy of Fire,"* BRL Report No. 1070, March 1959.
AD No. 217657.

"(1) A theoretical study by BRL. The purpose of this study was to devise methods of calculating motion of the weapon, thus establishing the importance of the various factors contributing to its motion. The 90mm Tank Gun, T-139, was used to illustrate the effects in a typical weapon. To conserve time and funds, only motion in the vertical plane was to be considered.

"(2) Development of apparatus by BRL. Since the motion of the T-139 Gun is very small prior to shot ejection, new techniques and methods were required to measure it.

"(3) Development of apparatus by D&PS. This portion of the program includes the development of very accurate sights for laying the weapon and instrumentation for measuring the curvature of the center line of the tube. Measurements of weights, centers of gravity, and moments of inertia required for the calculations are also included in this portion.

"(4) Firing Program by D&PS. The purpose of these tests was to measure the motion of the weapon and the point of impact of the projectile, thus providing data for comparing theory and experiment and also providing a basis for evaluating the importance of various factors."

The conclusions of this study still appear reasonably valid and are given below:

"A series of theoretical and experimental investigations were conducted to determine the effects of droop and gun vibration on the accuracy of tank guns. Tests of the 90mm Gun, T-139, indicate that, in general, only a part of the observed difference between the point of aim and the point of impact on the target can be ascribed to motion of the weapon at the instant of shot ejection. Measurements of the yawing motion of the projectile in free flight indicate that the remainder cannot be definitely attributed only to aerodynamic jump. It is evident from records of bending strain in the tube that theoretical analysis of the lateral motion of the tube associated with a projectile whose center of gravity does not coincide with the axis of the tube indicates that this condition may produce large lateral forces. Since these lateral forces affect the motion of the projectile during its emergence to determine the source of a few mils difference between the point of aim and the point of impact, it is necessary to measure accurately the yawing motion of the projectile in the bore, during launching, and during the blast regime."

In retrospect, the achievements and shortcomings of this program can be considered with greater detachment than during the period the program was in progress. The experiments were conducted at night, so bending of the tube due to solar heating was avoided completely. Mr. Sisson personally layed the gun with great care before each round, using a muzzle sight. Thus, major sources of error which had affected other programs were eliminated altogether. Considerable aerodynamic data was also obtained as these rounds were fired at the Transonic Range.

The experiments and analysis were conducted within the framework given by Ufflemann, Lee and Sneddon. Vibrations due to the unbalanced recoiling mass, unbalanced projectile, and rifling torque were taken into account. The Benoulli-Euler equation was used for bending.

Numerical techniques were based on Myklestad's method of calculating normal modes. This method is now standard and is imbedded in such general purpose codes as NASTRAN. Langer's asymptotic method⁶ was used to estimate the higher frequencies, thus greatly reducing the number of iterations required to obtain a given frequency and the corresponding model shapes. Both Lee's and Miller's method of analyzing the motion due to unbalanced recoiling parts were used. In addition to different methods of analysis, different mathematical modeling of the tube was used in the two approaches. In Lee's method, the rear portion of the tube was considered to be rigid, while in Miller's method the entire length of the tube was considered to be elastic, and the stiffness was calculated by the usual methods. The

⁶ A. S. Elder, "Numerical and Asymptotic Methods of Integrating the Bernoulli-Euler Equation," BRL Technical Note No. 1422, August 1961. AD No. 266692.

model used in Miller's method indicated that the elasticity of the rear portion of the tube should be taken into account, as the deformation curves differed significantly. However, the slope of the muzzle, which affects accuracy, did not differ very much in the two sets of calculations. Reasonable agreement was obtained between calculations and the observed motion, but the correlation fell short of expectations.

On the other hand, predictions of motion for the unbalanced projectile were not confirmed experimentally. Later work, described below, showed that yawing motion in the bore was more erratic than predicted and not in accord with the model used by Lee and Sneddon.

In addition, marked local bending was observed in the vicinity of the projectile. We examined many photographic plates under the comparator before we were convinced that our observations were valid. These deflections are not predicted by the Bernoulli-Euler theory, which was the basis of our structural analysis, but have been analyzed in the two-dimensional theory of elastic beams.⁷ The local bending of a hollow cylinder is now being studied in detail, using Fourier analysis and the three-dimensional equations of elasticity.

Calculations for bending vibrations of a 175mm gun tube were also carried out in an attempt to find the cause of abnormal dispersion.⁸

⁷ S. Timoshenko and J. N. Geodier, Theory of Elasticity, McGraw Hill Book Company, 1951, pages 102-107.

⁸ A. S. Elder, "The Lateral Motion of a 175mm Gun Tube Produced by an Eccentric Projectile," BRL Memo Report No 1318, July 1962. AD No. 286860.

Calculations showed that tube vibrations produced by an eccentric projectile could not account for the observed dispersion. During the course of the calculations for the lateral velocity and displacement of the tube, it was found that the interior ballistic calculations of travel, velocity and acceleration of the projectile as functions of time were internally inconsistent. Finally, a new time base was obtained from the velocity and travel curves by integration, and the original time scale discarded as redundant. The tube vibration calculations then proceeded without further difficulty.

H. P. Gay was finally able to obtain a correlation between the orientation of the center of gravity of a proof slug and the point of impact.⁹ The unbalance was sufficient to override other effects. The equations of motion of an unstable pendulum were used to calculate deviations of the trajectory and vector velocity of the projectile at the muzzle. As the 37mm gun tube used in these experiments was quite stiff, it seems probable that vibrations of the muzzle did not play a significant role in determining the point of impact.

In another test,¹⁰ a mirror was attached to the nose of a projectile and the angular motion recorded photographically. The angular motion showed a zig-zag pattern, indicating severe balloting, and did not conform to the smooth spiraling motion we anticipated in calculating the motion of the tube due to an unbalanced projectile.

⁹ H. P. Gay, *"On the Motion of a Projectile as it Leaves the Muzzle,"*
BRL Technical Note No. 1425, August 1961. AD No. 301974.

¹⁰ R. D. Kirkendall, *"The Yawing Motion of Projectiles in the Bore,"*
BRL Technical Note No. 1729, September 1970, AD No. 878327L.

In view of the preceding tests, it was evident that research on muzzle vibrations and in-bore projectile motion should be carried out concurrently. Current work at the Ballistic Research Laboratory is being organized in this manner.

V. CURRENT THEORETICAL AND EXPERIMENTAL PROGRAMS

During the last several years Dr. T. Simkins and his associates have been carrying out a fundamental program at Watervliet Arsenal with special emphasis on secondary effects. The NASTRAN Code was used as the main computation tool in calculating transient motion of the M113 gun tube.¹¹ Tube droop and gas pressure were the primary causes of excitation considered. The axial tension resulting from the rearward acceleration of the tube was also considered. (This effect is considerable at higher zones in the vicinity of the breech and must be considered in the reduction of strain gage records.) The local stresses caused by the rotating band were not calculated. The vibrational response for the traveling pressure was calculated for several stations and compared with experimental data obtained at the Ballistic Research Laboratory.

The Bourdon effect was the only secondary source of excitation considered in this report. If a curved tube is pressurized internally, it will tend to straighten; this effect is the basis of the Bourdon pressure gage. The bending moment is proportional to the product of the curvature and internal pressure assuming the external pressure is negligible.

¹¹ T. Simkins, G. Pflegl, R. Scanlon, "Dynamic Response of the M113 Gun Tube to Traveling Ballistic Pressure and Data Smoothing as Applied to XM150 Acceleration Data," Report No. WVLT-TR-75015, Watervliet Arsenal, Watervliet, NY, April 1975.

The secondary effects of a moving mass have been considered more recently.¹² In all the work at the Ballistic Research Laboratory and most of the work elsewhere, the mass of the projectile has been replaced by a moving force which appears on the right hand side of the equations of motion. This formulation is linear and is readily solved by modal analysis. On the other hand, the correct formulation in terms of a moving mass is nonlinear and must be solved by numerical methods, perhaps by perturbation theory. The difference in the two solutions is significant but not overwhelming and is less than the error incurred by neglecting balloting motion.

Parasitic resonance caused by periodic heating and cooling in a rapid-fire gun is one item of current interest at Watervliet. The governing equation has a periodic coefficient for the stiffness term and thus is closely related to Hill's equation. Axial stress waves produced by rapid radial expansion of the tube are also under consideration. The axial waves are caused by the combined effects of longitudinal inertia which restrains the tube and the Poisson effect which tends to contract it locally in the axial direction. This tensile load must be added to the tensile load produced by the rearward acceleration of the tube during firing.

Research on gun tube vibration and accuracy have recently been resumed at the Ballistic Research Laboratory after an interval of several years. In-bore motion and muzzle conditions are being studied concurrently as

¹² T. E. Simkins, "Structural Response to Moving Projectile Mass by the Finite Element Method," Report No. WVLT-TR-75044, Watervliet Arsenal, Watervliet, NY, July 1975.

part of an overall program on the dynamics and interaction of the gun tube and projectile. A rigid firing mount, especially designed for accuracy studies, has been installed and is now being used for 105mm instrumented firing tests. At present, programs involving the M392 and XM735 105mm kinetic energy rounds are in the early stages and will be continued as circumstances permit. The new instrumentation being developed for these programs is described in other papers.

The parameters for this gun-mount system have recently been measured for incorporation into computer programs being developed by the Southwest Research Institute. In addition to standard normal mode analysis, the equations of motion can be integrated numerically in space and time. In this manner the variable length of the vibrating part of the tube, due to recoil, has been taken into account, together with the nonlinear constraints the recoil mechanism imposes on the rotation of the gun about its trunnions. The overturning moment produced by the powder pressure couple has been measured directly with a weigh bar which replaced the hydraulic strut normally used to elevate and depress the gun when mounted in a tank.

The nonlinear coupling between torsional vibrations and tube droop, mentioned previously, is also being analyzed at the Southwest Research Institute.

A research program concerned with gun tube vibrations and related problems is continuing at the Ballistic Research Laboratory. As mentioned previously, local bending produced by an unbalanced projectile is being analyzed by Fourier methods using the exact equations of elasticity. This

work is an outgrowth of our program on symmetric stresses due to gas pressure and rotating band pressure and uses similar techniques.

We wish to replace Myklestad's method for a vibrating tube with a more accurate program using exact solutions for the various segments. A tube can be modeled as a few lumped constants, cylindrical sections, and segments in which the outer surface is conical. Only four or five segments should generally be required. The solution for the segment formed by a conical surface has recently been derived and will be combined with the known solutions for the cylindrical sections. The various segments will be combined by matching the displacement, slope, moment, and shear at each junction.

Our program will continue in collaboration with other agencies whenever topics of mutual interest arise.

VI. MODELING THEORY

The formulation of the field equations and boundary conditions should be sufficiently realistic to yield results of sufficient accuracy and yet not too complex or cumbersome for detailed analysis and computation. Equations for large systems are generally put together from a number of simple models; on the other hand, if only a single aspect or component of the system is under consideration, a more detailed model is frequently in order.

Finite element formulations and large codes such as NASTRAN are used universally to analyze the gross response of a large system, provided the system is elastic and the instantaneous response and wave analysis are not required. Beams, rods, plates, ring elements, and a variety of other

configurations are used as subelements. The stresses may be calculated by finite elements or from a strength of materials formula.

The Bernoulli-Euler equation for vibrating beams is satisfactory for periodic vibrations of moderate frequency and for transient vibrations, but is not satisfactory for shock conditions or the propagation of flexural waves. In addition to separable solutions, there is a source function due to Fourier¹³ which is useful for short intervals of time just after impact. The source function for the one-dimensional equation for the conduction of heat in a solid is used as the basis for the following analysis. This equation for heat conduction is

$$k \frac{\partial^2 v}{\partial x^2} = \frac{\partial v}{\partial t}. \quad (1)$$

The corresponding one-dimensional source function is

$$u = t^{-1/2} \exp(-x^2/4kt). \quad (2)$$

To derive the Bernoulli-Euler equation from (1), differentiate once with respect to t :

$$k \frac{\partial^3 v}{\partial x^2 \partial t} = \frac{\partial^2 v}{\partial t^2}. \quad (3)$$

Now differentiate (1) twice with respect to x :

$$k \frac{\partial^4 v}{\partial x^4} = \frac{\partial^3 v}{\partial x^2 \partial t}. \quad (4)$$

¹³ *Secondary Source: Rayleigh (Baron), Theory of Sound, Dover Publications, New York, 1945. Vol 1, pp 302-304, contains a digest of Fourier's analysis.*

On eliminating $\frac{\partial^3 v}{\partial x^2 \partial t}$ from the last two equations, we find

$$k^2 \frac{\partial^4 v}{\partial x^4} = \frac{\partial^2 v}{\partial t^2} . \quad (5)$$

The Bernoulli-Euler equation can be written in the form

$$\frac{\partial^4 v}{\partial x^4} = -a^{1/2} \frac{\partial^2 v}{\partial t^2} . \quad (6)$$

Equations (5) and (6) are equivalent if

$$a^2 = -1/k^2, \quad a = \pm i/k.$$

Hence equation (6) has the source functions

$$u_1 = t^{-1/2} \sin(ax^2/4t) \quad (7)$$

$$u_2 = t^{-1/2} \cos(ax^2/4t). \quad (8)$$

These equations indicate that an impulse applied at one point on a long bar will cause an instantaneous response over the entire length of the bar. Both experiments and the equations of motion in the theory of elasticity show that an instantaneous response for distant points along the bar is impossible. An initial disturbance causes a wave which travels with constant, finite velocity.

The Timoshenko equation is the simplest equation which will predict flexural waves.¹⁴ This equation, which is quite complicated, has the general form

$$A \frac{\partial^4 y}{\partial x^4} + B \frac{\partial^2 y}{\partial t^2} + C \frac{\partial^4 y}{\partial x^2 \partial t^2} + D \frac{\partial^4 y}{\partial t^4} = 0. \quad (9)$$

¹⁴ S. Timoshenko, *Vibration Problems in Engineering*, 2d Edition, D. Van Nostrand Company, New York, 1927, pp 337-342.

The constants A, B, C, and D depend on the moduli and section properties of the bar.

Both the Bernoulli-Euler and Timoshenko equations give the axial stress and transverse deflection with reasonable accuracy, especially for the lower modes of vibration. The remaining stresses are approximate, as we are applying a single equation of motion to bars with geometrically different cross sections.

Finally, we consider the Pochhammer-Chree theory for an infinite circular cylinder. The exact equations of motion from the linear theory of elasticity are used to investigate longitudinal, torsional, and bending vibrations. One can satisfy exactly the boundary conditions on the cylindrical surfaces, but can only satisfy end conditions on a finite bar in an approximate manner. The investigation of the "trapped end modes" required to satisfy end conditions exactly requires advanced mathematical analysis which will not be considered here.

We can use the Pochhammer-Chree theory in technical problems if we are content with the approximate description of end conditions, as indicated by Love.¹⁵ A two-fold eigenvalue problem is involved, the first to determine wave length as a function of frequency in an infinite cylinder, the second to combine four solutions of this type in such a way that the end conditions are satisfied approximately. The following analysis is an elaboration of very condensed remarks by Love and Herrmann.

¹⁵ A. E. H. Love, *A Treatise on the Mathematical Theory of Elasticity*, Dover Publications, New York, 1944. See page 292.

Sinusoidal vibrations in an infinite hollow cylinder have been studied in detail, both theoretically and numerically.¹⁶ In summary, Herrmann, et al, assume displacements of the form

$$U_r = \cos \theta \cos (\omega t + \alpha z) \sum_{j=1}^4 a_j f_j(r)$$

$$U_\theta = \cos \theta \cos (\omega t + \alpha z) \sum_{j=1}^4 b_j g_j(r)$$

$$U_z = \cos \theta \sin (\omega t + \alpha z) \sum_{j=1}^4 c_j h_j(r)$$

Where the f , g , and h functions are specific combinations of Bessel functions required to satisfy the equation of elasticity and are appropriate for bending; the stresses are calculated from the displacements; then, the conditions for stress free cylindrical surfaces are set forth. This frequency equation amounts to an implicit functional relation between ω and α which is tabulated in scaled form.

We require four linearly independent solutions for the finite bar. A second set is obtained by substituting $\sin (\omega t + \alpha z)$, and $-\cos (\omega t + \alpha z)$ for the corresponding factors in the above equations. Solutions which increase or decay experimentally along the length of the bar are found by setting

$$V_r = \cos \theta \cos (\omega t + i\beta z) \sum_{j=5}^9 a_j f_j(r)$$

$$V_\theta = \cos \theta \cos (\omega t + i\beta z) \sum_{j=5}^9 b_j g_j(r)$$

$$V_z = \cos \theta \sin (\omega t + i\beta z) \sum_{j=5}^9 c_j h_j(r)$$

¹⁶ A. E. Armenakas, D. C. Gazis, A. Herrmann, *Free Vibrations of Circular Cylindrical Shells*, Pergamon Press, New York, 1969.

and calculating β as a function of ω by solving the appropriate frequency equation. Finally, a fourth set of solutions can be found by interchanging sines and cosines as indicated above.

These four solutions can be combined to satisfy certain combinations of boundary conditions at the ends. We finally should obtain a specific set of circular frequencies $\omega_1, \omega_2, \omega_3 \dots$ with the corresponding values of α and β . The analysis would give us very accurate theoretical results to compare with experiments on circular portions of the gun tube which are not too close to the ends.

The imposition of reasonably correct boundary conditions is frequently more difficult than solution of the field equations and generally requires more engineering judgment. In formulas relating to the stresses in cylinders and bars, we assume that the loads are applied at the ends. However, in practice, the loads are generally applied at the lateral surfaces along the major dimension. The elementary formulas are still valid a reasonable distance from the load by St. Venant's principle; however, local disturbances to the nominal stress distribution occur in the vicinity of the load. These disturbances are of secondary importance in analyzing the gross structural behavior of an entire system, but are important in interpreting strains in the vicinity of the load. External tube strains due to gas and band pressure are an example of local strains which have yielded considerable information concerning the stresses imposed by the interior ballistic cycle.

On more philosophical grounds, one must be cautious about using redundant information which will almost certainly be internally inconsistent. This redundancy affected the interior ballistic calculations mentioned

previously. Only the minimum data should be used and all possible variables obtained by calculations. In this way, the final calculations should be internally consistent, although not necessarily more compatible with observations.

VII. MECHANICAL ASPECTS OF VARIABLE BIAS

Nowhere is adequate modeling more important than in the analysis of variable bias in tank guns. In preparation for this paper, the author discussed accuracy problems at considerable length with Dr. Serge Zarodney. Tank guns experience an occasion-to-occasion shift in the center of impact which is unusual in artillery. The portion due to solar radiation and the resulting bending of the tube is well understood and can be greatly reduced by a thermal jacket. After thermal corrections have been made a small residual bias remains which is due to a variety of mechanical causes. Dr. Zarodney¹⁷ believes that the recoil spring in a worn recoil mechanism may rotate and thus affect the unsymmetrical component of the recoil force. He has some statistical data to support his contention. In a recent conversation, Mr. Ruff of MTD indicated that new or fully reconditioned recoil mechanisms gave excellent accuracy, but dispersion increased noticeably with worn mechanisms. Moreover, our difficulty in predicting gross vibratory motion of the tube appears in part due to uncertainties in modeling interface conditions between the gun tube and recoil mechanism. This area requires engineering analysis and experiment to determine the actual motion of a worn recoil spring and the effective boundary conditions for our accuracy and vibrations studies. We are no longer restricted to modal analysis, but

¹⁷ Dr. S. Zarodney, *Official Suggestion*, submitted to BRL.

may now integrate the equations of motion step-by-step and account for time dependent, nonlinear boundary conditions at each state of the calculation.

VIII. CONCLUSIONS

New instrumentation, improved computers, and more direct methods of integrating the equations of motion should now enable us to perform engineering and mathematical analysis with greater realism than was possible a few years ago. Moreover, high first round hit probability is still essential for tanks. The difficulties and uncertainties outlined in this paper should point the way toward future investigations.

FUNDAMENTALS OF WEAPON
DYNAMIC EFFECTS ON PRECISION

V. KOMKOV
Texas Technical University
Lubbock, Texas

TABLE OF CONTENTS

	<u>Page</u>
I. INTRODUCTORY REMARKS	28
II. ACCURACY	28
III. SOME ASSUMPTIONS AND CORRESPONDING VARIATIONAL PRINCIPLES	31
IV. THE "BOOTSTRAPPING" TECHNIQUE	33
V. AN EXAMPLE OF A REALISTIC MODELLING OF TRANSIENT BOUNDARY CONDITIONS	33
VI. A POSSIBLE APPROACH TO THE MATHEMATICAL MODELLING	36
VII. COMPUTATIONAL ASPECTS	39
VIII. EFFECTS OF PROJECTILE-BARREL INTERACTION, BOURDEN TUBE EFFECT AND MORE DETAILED ANALYSIS	43
REFERENCES	44

1. Introductory Remarks.

In recent years, spectacular advances have been made in weapon technology regarding location and identification of targets and guidance of projectiles to the target. It is a fact that most weapons used now and probably in the near future will be conventional, That majority of the projectiles are not guided and that conventional fire power remains the main factor in the arsenal of any army. While great strides have been made in target location and identification, very little progress has been made eliminating a basic source of inaccuracy.

2. Accuracy.

A considerable literature exists regarding the dynamics of conventional weapon systems. Leonardo da Vinci, Descartes, and Cauchy all devoted considerable effort to the study of guns and their dynamic behavior. More recently, Hardy, Littlewood, Krylov, and Sneddon are names which easily come to mind when internal ballistics and related dynamic phenomena are discussed. (See [6] and [7]) Historical notes on some aspects of internal ballistic phenomena are given in Cranz's classic textbook on this subject [5]. The problems of weapon response and accuracy criteria are complex and despite the existence of extensive theoretical literature, in all known weapon design procedures, the practical trial and error experimental techniques are still being pursued.

Most of the existing literature on the dynamic behavior of conventional weapon systems consists of discussing "one problem at a time". Some cause of inaccuracy or poor performance is isolated, then a mathematical model is suggested, and solutions of the corresponding differential equations of motion are discussed. Typical attempts at isolating and discussing the effects of "one problem at a time" are the papers of D. Hardison [1], A. S. Elder [2], D. E. Wente [3], and J. G. Darpas [4].

The main causes of conventional weapon inaccuracy can be identified in the literature referring to test results as:

- a) The uneven ammunition and internal ballistic variations.
- b) The effects of the droop or of the static deflection,
- c) Balloting of the round and other projectile-barrel interactions.
- d) Mechanical vibrations of the gun barrel caused either by the recoiling mass or by the forces applied from the supporting structure.
- e) External causes due to motion of the mount, or other external disturbances.

In the analysis carried out in the past, "one cause at a time was considered. For example, the effect of balloting would be considered, while transverse vibration and "whip effects" due to the droop are ignored. Or, the vibration of the barrel would be analysed while balloting and droop effects are ignored.

Such analysis is not even helpful in understanding the problem if the effects discussed are not independent of each other. The effect of torsional vibrations on transverse motion of the barrel can not be ignored if the center of

gravity of the transversely vibrating system does not coincide with the center of torsion, and the two modes of vibration are then coupled. Similarly, the Borden tube effects and the projectile tube interaction, affect the transverse vibration and should not be studied as separate phenomena.

The main objection to such study was the theoretical difficulty in setting up of the appropriate equations of motion, and of realistic boundary conditions. This last remark will be discussed in greater detail in part B of this proposal.

The mathematical problem of defining the accuracy of a gun can be approached from the practical point of view of "what is it that we wish to minimize?" A closer look at the problem reveals that the position, angle and velocity of the barrel at the time when the projectile leaves the barrel are the most important parameters determining the accuracy of the weapon. Let $u(x,t)$ denote the displacement of the gun barrel $x \in [0, l]$, $t \geq 0$, where x denotes the position along the gun barrel and t is time. If $x=0$ is the muzzle, we wish to minimize

$$\left\{ \alpha \left\| \frac{\partial u}{\partial x} \right\|^2 + \beta \left\| \frac{\partial u}{\partial t} \right\|^2 \right\} \quad \begin{cases} x=0 \\ t=T \end{cases}$$

Where T is the predicted time of projectile leaving the muzzle. Since T can be predicted only with some probability p , we can introduce a Gaussian distribution $\psi(t)$ centered at $t=T$ and suggest a Sobol'ev norm

$$\|u\|_{\alpha\beta}^2 = \int_{x=0}^{x=B} \int_{T-\epsilon}^{T+\epsilon} \psi(t) [\alpha (u_x(x,t))^2 + \beta (u_t(x,t))^2] dx dt,$$

where $0 < \beta < l$ is determined from data. Alternately, a weight function $\eta(x)$ can be introduced

$$\int_{x=0}^{x=l} \eta(x) dx = 1, \quad \text{and} \quad \eta(x) > 0,$$

attaining a maximum at $x=0$.

$$\|u\|_{acc.}^2 = \int_0^l \eta(x) \int_{T-\epsilon}^{T+\epsilon} \psi(t) [\alpha u_x^2 + \beta u_t^2] dt dx$$

The problem of predicting and improving accuracy can be reduced to the problem of finding a constrained minimum of $\|u\|_{acc}$ in the Sobolev space H^2 .

This concept of accuracy is not necessarily the last word in mathematical modelling of weapon systems and certainly the bootstrap techniques described in part "B" can be applied in effort to find α, β or to even revise the whole concept of what is an accuracy, and how to represent it by a norm in a Hilbert space or perhaps only in a normed space, or by an entirely different mathematical formulation. Instead of assuming a specific set of differential equations of motion and a time-independent set of boundary conditions, the investigation should rely on energy techniques, using some recent results ([10], [11]).

3. Some Assumptions and Corresponding Variational Principles.

If one assumes the Euler-Lagrange (linear) beam theory and Voigt-type dissipation, the Kinetic and Potential energy are easily identified. To represent the equations of motion and the adjoint equations the following bilinear products are introduced

$$T(u,v) = \frac{1}{2} \int_0^{l(t)} \left[\rho A(x) \frac{\partial u}{\partial t} \frac{\partial v}{\partial t} \right] dx \quad (3.1)$$

$$V(u,v) = \frac{1}{2} \int_0^{l(t)} \left(EI(x) \frac{\partial^2 u}{\partial x^2} \frac{\partial^2 v}{\partial x^2} \right) dx \quad (3.2)$$

$$D(u,v) = \frac{1}{2} \int_0^{l(t)} E^* I(x) \left[\frac{\partial}{\partial t} \left(\frac{\partial^2 u}{\partial x^2} \right) \cdot \frac{\partial^2 v}{\partial x^2} - \frac{\partial}{\partial t} \left(\frac{\partial^2 v}{\partial x^2} \right) \cdot \frac{\partial^2 u}{\partial x^2} \right] dx \quad (3.3)$$

Additional energy terms involving effects of the projectile, for example

$$\int_{x=a_0+l_0}^{x=a_0+l_0(t)} \eta(x) \frac{\partial u}{\partial t} \frac{\partial v}{\partial t} dx, \quad l_0 \rightarrow l_0(t) \quad (3.4)$$

describing the motion of the projectile, etc. can be added to Kinetic potential or dissipation terms in formulation of the Lagrangian functional

$$L_{1,2}(u,v) = T(u,v) - (V(u,v) + D(u,v)) \quad (3.5)$$

The variational principles described subsequently here can be directly applied to derive the equations of motion. The details of corresponding numerical technique will not be discussed in detail here. Primary method will consist of a direct application of the Galerkin approach. The results obtained can be checked numerically against expected equations of motion. That is at times when no projectile is present in the tube, the numerical solution of the problem should approximate either Timoshenko's, or perhaps the Euler-Lagrange equation of beam motion. Checks should be performed against experimental data to confirm or to deny the validity of the basic equations of motion.

4. The "bootstrapping" technique

Before formulating a mathematical theory which models the physical behavior of any weapon, it is advisable to have a careful experimental check on reliability of the mathematical model.

To make a point let us consider a deceptively simple model of vibration of a gun barrel.

Instinctively some people assume the Lagrange equations for a vibrating beam to be a close approximation, and in the absence of an intermediate support, the following system is regarded as a mathematical model.

$$\frac{\partial^2}{\partial x^2} (EI(x) \frac{\partial^2 w}{\partial x^2}) + \rho A \frac{\partial^2 w}{\partial t^2} = q(x_0, t) \quad (4.1)$$

$$\left. \begin{array}{l} w(l, t) \equiv 0 \\ \frac{\partial^2 w}{\partial x^2}(0, t) \equiv 0 \end{array} \right\} \quad (4.2a)$$

$$\left. \begin{array}{l} \frac{\partial w}{\partial x}(l, t) \equiv 0 \\ \frac{\partial}{\partial x} (EI(x) \frac{\partial^2 w}{\partial x^2}(0, t)) \equiv 0 \end{array} \right\} \quad (4.2b)$$

$$\forall t \in [0, \infty).$$

Of course it is hard to find a weapon which satisfies such equation of motion, and almost impossible to find one satisfying the above boundary conditions (catelevered - free).

A check on solutions and introduction of more complex equations and boundary terms in subsequent computation is referred to as the "bootstrap method".

An "intermediate" modelling of the weapon behaviour is discussed in the next sections.

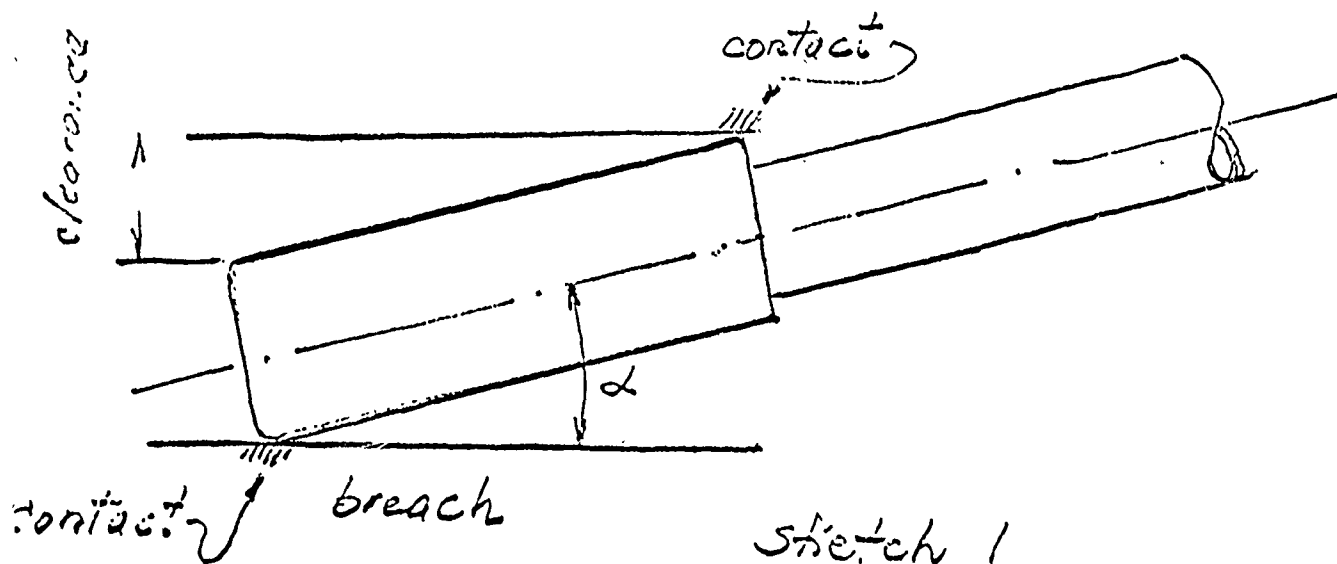
5. An example of a realistic modelling of transient boundary conditions.

The cantilever condition at the breach of a gun represented by

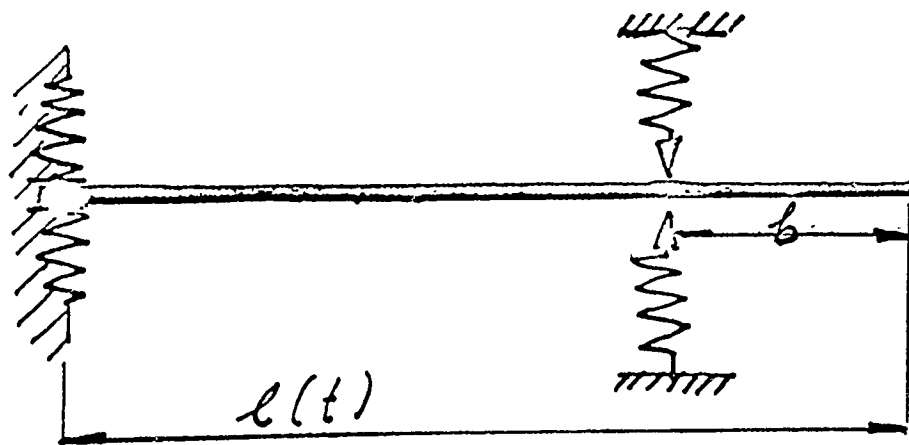
$$\left. \begin{aligned} w(l, t) &\equiv 0 \\ \frac{\partial w(l, t)}{\partial x} &\equiv 0 \end{aligned} \right\}$$

is clearly unrealistic, and in case of each individual weapon design a more complex boundary condition has to be established.

For example, an automatically firing weapon may have a large clearance at the breach during the first round (.012", for example, for the Rarden gun) so that the original motion of the gun barrel is a "free-free" beam motion. Then, the breach clearance is replaced by contact stress support at opposite ends, as roughly shown by the sketch (exaggerated).



The motion becomes roughly a vibration of a beam cantilevered from a (nonlinearly) elastic wall. Now an intermediate support pad may make contact providing an elastic support. Diagrammatically, we could regard this as a motion of a beam supported as follows.



sketch 2

Due to simultaneous recoil motion, the length b_0 , as well as the total length, are functions of time, making this a very complex dynamic motion with complex time-dependent boundary conditions.

(Observe that the torsional vibration and the corresponding boundary conditions have not been even mentioned in this model.)

The clearances and the boundary conditions described here will change with the subsequent rounds because of the heating of the barrel. The above example was given only to illustrate the degree of difficulty encountered in attempting to produce a physically sensible version of a mathematical model for an automatically fired conventional weapon.

We could assume the Voigt type dissipation arriving at the equation:

$$\frac{\partial^2}{\partial x^2} (EI(x) \frac{\partial^2 u}{\partial x^2}) + \frac{\partial}{\partial t} \left[\frac{\partial^2}{\partial x^2} (E^* I(x) \frac{\partial^2 u}{\partial x^2}) \right] + A(x) \rho \frac{\partial^2 u}{\partial t^2} = f_p(x, t) \quad (5.1a)$$

with u satisfying the conditions

$$u - \frac{\partial u}{\partial t} = 0 \text{ at } x = l(t) \text{ for all } t > 0,$$

$$\frac{\partial^3 u}{\partial x^3} = \frac{\partial^2 u}{\partial x^2} = 0 \text{ at } x = 0,$$

The problem of simultaneous minimization of a given functioned $J(z(\cdot))$ and compliance with the differential equations (5.1) can be restated with the use of Lagrangian multipliers, provided we have sufficient information concerning second derivatives of the Hamiltonian function $H(u,v)$ defined in section 6.

6. A Possible Approach to the Mathematical Modelling.

If the torsional effects are neglected, the equations of motion are closely related to the properties of following inner product defined on $\Omega = (0, l(t))$.

$$\tilde{H}_{\Omega}(u,v) = T(u,v) + V(u,v) + D(u,v). \quad (6.1)$$

Assuming that u, v are elements of the Sobolëv space $H_0^2(\Omega)$, the functionals T, V, D are defined as:

$$T(u,v) = \frac{1}{2} \int_0^{l(t)} [\rho A(x) (\frac{\partial u}{\partial t} \frac{\partial v}{\partial t})] dx \quad (6.2a)$$

$$V(u,v) = \frac{1}{2} \int_0^{l(t)} [EI(x) (\frac{\partial^2 u}{\partial x^2} \frac{\partial^2 v}{\partial x^2})] dx \quad (6.2b)$$

and

$$D(u,v) = \frac{1}{4} \int_0^{l(t)} [E^* I(x) (\frac{\partial}{\partial t} (\frac{\partial^2 u}{\partial x^2}) \frac{\partial^2 v}{\partial x^2} - \frac{\partial^2 u}{\partial x^2} \frac{\partial}{\partial t} (\frac{\partial^2 v}{\partial x^2}))] dx. \quad (6.2c)$$

The functional $\tilde{H}_{\Omega}(u,v)$ will be called the formal Hamiltonian of the system.

We also introduce the boundary product

$$\tilde{H}_{\partial\Omega}(u,v) = \{ [\frac{\partial}{\partial x} (EI(x) \frac{\partial^2 u}{\partial x^2}) + \frac{\partial^2}{\partial t \partial x} (E^* I(x) \frac{\partial^2 v}{\partial x^2}) \} \cdot v$$

$$\begin{aligned}
& + \left[EI(x) \frac{\partial^2 u}{\partial x^2} + \frac{\partial}{\partial t} (E^* I(x) \frac{\partial^2 u}{\partial x^2}) \right] \frac{\partial v}{\partial x} \Big|_0^{l(t)} \\
& + \left[\frac{\partial}{\partial x} (EI(x) \frac{\partial^2 v}{\partial x^2}) - \frac{\partial^2}{\partial t \partial x} (E^* I(x) \frac{\partial^2 v}{\partial x^2}) \right] \cdot u \\
& + \left[EI(x) \frac{\partial^2 v}{\partial x^2} - \frac{\partial}{\partial t} (E^* I(x) \frac{\partial^2 v}{\partial x^2}) \right] \frac{\partial u}{\partial x} \Big|_0^{l(t)}. \quad (6.3)
\end{aligned}$$

The "Hamiltonian" $H(u, v)$ is defined by

$$H(u, v) = \tilde{H}_\Omega(u, v) + \tilde{H}_{\partial\Omega}(u, v), \quad (6.4)$$

for all functions continuous on $\Omega \cup \partial\Omega$ and of the Sobol'ev class $H_0^2(\Omega)$.

The corresponding Lagrangian can be defined simply as

$$L = T - (V + D) \quad (6.5)$$

provided $\tilde{H}_{\partial\Omega}(u, v) \equiv 0$. (6.5a)

For the sake of greater generality we shall consider a more abstract formulation of this problem.

Let us denote by

$$p_u = \sqrt{\rho A(x)} \frac{\partial u}{\partial t} \quad (6.6a)$$

$$p_v = \sqrt{\rho A(x)} \frac{\partial v}{\partial t} \quad (6.6b)$$

i.e. p_u (p_v) is the (linear) momentum density function corresponding to the displacements $u(x, t)$ ($v(x, t)$ respectively).

$$p_u = Au, \quad A = \sqrt{\rho A(x)} \frac{\partial}{\partial t} : \quad (6.6c)$$

$$\rightarrow H_0^2(\Omega).$$

$$M_u = \sqrt{EI(x)} \frac{\partial^2 u}{\partial x^2}, \quad (6.6d)$$

$$M_v = \sqrt{EI(x)} \frac{\partial^2 v}{\partial x^2}, \quad (6.6e)$$

$$M_u = BU,$$

$$B: H_0^2(\Omega) \rightarrow L_2(\Omega).$$

$$M_u^* = \sqrt{E^*I(x)} \frac{\partial^2 u}{\partial x^2} \quad (6.6f)$$

$$M_v^* = \sqrt{E^*I(x)} \frac{\partial^2 v}{\partial x^2} \quad (6.6g)$$

$$Cu = \frac{\partial}{\partial t} M_u^* \quad (6.6h)$$

$$C: L_2(\Omega) \rightarrow L_2(\Omega)$$

the formal adjoint of C is defined by

$$C^* = - \frac{\partial}{\partial t} \sqrt{E^*I(x)} \frac{\partial^2}{\partial x^2} \quad (6.6i)$$

$$C^*: L_2(\Omega) \rightarrow L_2(\Omega).$$

The Hamiltonian $H(u,v)$ can be rewritten as:

$$H(u,v) = \frac{1}{2} \langle p_u, p_v \rangle_{\Omega} + \frac{1}{2} \langle M_u, M_v \rangle_{\Omega} + \frac{1}{4} (\langle Cu, v \rangle_{\Omega} + \langle u, C^*v \rangle_{\Omega}) + \tilde{H}_{\partial\Omega}(u,v), \quad (6.7)$$

$\langle f \cdot g \rangle_{\Omega} \stackrel{\text{def}}{=} \int_{\Omega} (f \cdot g) dx$. The Lagrangian $L(u,v)$ is given by

$$L(u,v) = \langle p_u, p_v \rangle_{\Omega} - H(u,v) - \langle \tilde{f}_p, v \rangle_{\Omega} \quad (6.8)$$

Performing Frechet differentiation of $L(u,v)$ with respect to v we recover the equation (5.1) and the boundary conditions (5.1b). The condition (5b) is so far ignored.

Differentiating (in the sense of Fréchet) with respect to u we obtain the adjoint homogeneous differential equation

$$\frac{\partial^2}{\partial x^2} [EI(x) \frac{\partial^2 v}{\partial x^2}] - \frac{\partial}{\partial t} [\frac{\partial^2}{\partial x^2} E^* I(x) \frac{\partial^2 v}{\partial x^2}] + \rho A(x) \frac{\partial^2 v}{\partial t^2} = 0, \quad (6.9)$$

with the "adjoint" boundary conditions

$$\begin{aligned} \frac{\partial^2 v}{\partial x^2} = \frac{\partial^3 v}{\partial x^3} &\equiv 0 & \text{at } x = l(t), \\ v = \frac{\partial v}{\partial x} &\equiv 0 & \text{at } x = 0. \end{aligned} \quad (6.10)$$

7. Computational Aspects.

We wish to minimize

$$J = A\|u\|_p^2 + B\|u_t\|_p^2 + \int_{t_0}^{t_0+p} L(u,v) dt + \int_{t_0}^{t_0+p} \frac{(u(b(t)))^2}{\epsilon_n} dt, \quad (7.1)$$

by choosing the design $D(x)$. ϵ_n is a sufficiently small constant acting as a penalty. This is a restatement of the Lagrangian multiplier problem posed in (5.2).

Before attempting to minimize J (or J_p subject to constraints) we establish a Galerkin-type approximation to the equations of motion of the system.

The search for natural modes of vibration.

We shall assume that the deflection functions $u(x,t)$, $v(x,t)$ which solve equations (5.1), (6.9) respectively are of the form

$$u(x,t) = \sum_{n=1}^{\infty} u_n(x, \ell(t)) \phi_n(t) \quad (7.1)$$

$$v(x,t) = \sum_{n=1}^{\infty} v_n(x, \ell(t)) \psi_n(t) \quad (7.2)$$

As a first approximation, the firing period is subdivided $t_0, t_1, \dots, t_m = t_0+p$, with $t_{i+1} - t_i = \Delta t_i = \text{constant}$. On each subinterval $[t_i, t_{i+1}]$ $\ell(t)$ is regarded as constant. The average value of $\ell(t)$ denoted by $\ell_i(t)$ being taken from a graph.

The approximate solutions on each subinterval are denoted by $u_j(x,t)$, $v_j(x,t)$, and

$$u_j(x,t) = \sum_n u_{n,j}(x, \ell_j) \phi_{n,j}(t) \quad (7.3a)$$

$$v_j(x,t) = \sum_n v_{n,j}(x, l_j) \psi_{n,j}(t) \quad (7.3b)$$

The functionals T, V, D are recomputed

$$T_j(u,v) = \frac{2}{2} \sum_n \left(\frac{\partial \varphi_{n,j}(t)}{\partial t} \frac{\partial \psi_{n,j}(t)}{\partial t} \int_0^{l(t)} [A(x) u_{n,j}(x, l_j) v_{n,j}(x, l_j)] dx \right) \quad (7.4)$$

$$V_j(u,v) = \frac{E}{2} \sum_n (\varphi_{n,j}(t) \psi_{n,j}(t) \int_0^{l(t)} [I(x) \frac{\partial^2 u_{n,j}(x, l_j)}{\partial x^2} \frac{\partial^2 v_{n,j}(x, l_j)}{\partial x^2}] dx) . \quad (7.5)$$

$$D_j(u,v) = \frac{E^*}{4} \sum_n \left(\frac{\partial \varphi_{n,j}(t)}{\partial t} \psi_{n,j} \int_0^{l(t)} \left[I \frac{\partial^2 u_{n,j}}{\partial x^2} \frac{\partial^2 v_{n,j}}{\partial x^2} \right] dx \right. \\ \left. - \varphi_{n,j} \frac{\partial \psi_{n,j}}{\partial t} \int_0^{l(t)} \left[I \frac{\partial^2 u_{n,j}}{\partial x^2} \frac{\partial^2 v_{n,j}}{\partial x^2} \right] dx \right) . \quad (7.6)$$

If sufficient smoothness of solutions is assumed, then the equations of motion are the usual Euler-Lagrange equations, associated with the action integral: $\int_{t_0}^{t_0+p} L dt$.

$$\sum_n \left(\frac{\partial}{\partial t} \left(\frac{\partial L}{\partial \dot{\varphi}_{n,j}} \right) - \frac{\partial L}{\partial \varphi_{n,j}} \right) = 0 \quad (7.7)$$

$$\sum_n \left(\frac{\partial}{\partial t} \left(\frac{\partial L}{\partial \dot{\psi}_{n,j}} \right) - \frac{\partial L}{\partial \psi_{n,j}} \right) = f_p(x,t) \quad (7.8)$$

Written out in full, we have the following system of ordinary differential equations (in the variable t).

$$\sum_n (\ddot{\psi}_{n,j} \int_0^{l_j} [A(x) u_{n,j}(x, l_j) v_{n,j}(x, l_j)] dx - \frac{E^*}{4} \dot{\psi}_{n,j} \int_0^{l_j} [\frac{\partial^2 u_{n,j}}{\partial x^2} \frac{\partial^2 v_{n,j}}{\partial x^2}] dx + \frac{E}{2} \psi_{n,j} \int_0^{l_j} [I(x) \frac{\partial^2 u_{n,j}}{\partial x^2} \frac{\partial^2 v_{n,j}}{\partial x^2}] dx) = 0. \quad (7.9)$$

$$\sum_n \ddot{\psi}_{n,j} \int_0^{l_j} [A(x) u_{n,j} v_{n,j}] dx + \frac{E^*}{4} \dot{\psi}_{n,j} \int_0^{l_j} [\frac{\partial^2 u_{n,j}}{\partial x^2} \frac{\partial^2 v_{n,j}}{\partial x^2}] dx + \frac{E}{2} \psi_{n,j} \int_0^{l_j} [I(x) \frac{\partial^2 u_{n,j}}{\partial x^2} \frac{\partial^2 v_{n,j}}{\partial x^2}] dx = f_p(x, t). \quad (7.10)$$

A homogeneous version of 7.10 (with $f_p(x, t) \equiv 0$) will be denoted by (7.10^H) .

This is a system of ordinary differential equations with constant coefficients. Hence the solutions are of the form

$$\phi_{n,j} = a_{n,j} e^{\lambda_{n,j} t} + \psi_{p,n,j}(t), \quad (7.11)$$

where $\psi_{p,n,j}(t)$ is a particular solution of the equation (7.10).

In this case (since $f_p(x, t)$ is a Dirac delta) a particular solution is easy to find provided the solution of the homogeneous system (7.10^H) is known.

8. Effects of Projectile - Barrel Interaction, Bourden Tube Effect and More Detailed Analysis

Once the basic idea of the generalized Lagrangian is considered, additional complications are taken care of by including more terms in the total Kinetic energy product $T(u,v)$, the total potential energy product $V(u,v)$ and the dissipation product $D(u,v)$.

For example the effect of the projectile-tube interaction can be approximated by adding to the term $\frac{1}{2} \int_0^{l(t)} [\rho A(x) \frac{\partial u}{\partial t} \frac{\partial v}{\partial t}] dx$

$$\frac{1}{2} m \left(\frac{\partial u}{\partial t} \frac{\partial v}{\partial t} \right) \Big|_{X(t)} \quad (8.1)$$

where $X(t)$ is the predicted position of the projectile, during the interaction period. The extra term (8.1) is set equal to zero otherwise.

The Bourden tube effect can be approximated by considering the following energy term:

$$V_{B+d} = \frac{1}{\pi} \int_0^{l(t)} \left| \frac{\partial^2 u}{\partial x^2} \cdot v \right| p \frac{d_i^2}{4} dx$$

where p is the internal pressure $p = p(t)$ and d_i is the internal diameter (the caliber).

Other effects which seriously affect the behavior of the system (for example the rate of spin of the projectile) are added when the discrepancy between the test data and the computer prediction based on the mathematical model becomes too large to ignore.

References

- [1] D. Hardison, "An analysis of tank posture in a simulated firing position", BRL report #749 (1954) Aberdeen, Md. (classified).
- [2] A. S. Elder, Stresses in a gun tube produced by internal pressure and shear, JANNAF Symposium, Las Vegas, Nevada, 1973.
- [3] D. E. Wente, An investigation of the effects of natural frequency of vibration of the barrel on the dispersion of an automatic weapon, Report # 311, U. S. Army Ordnance Corps, Purdue Univ. Experimental Station, April 1955.
- [4] J. G. Darvas, Efforts transverse aux sur les projectiles, Memoire d'Artillerie Francaise, T. 31, 1957.
- [5] C. Cranz, Cranz's Textbook of Ballistics, (Translated by C. C. Bramble et al), #III, 2nd ed., 1972, National Defence Research Committee.
- [6] E. H. Lee, Theoretical investigation of barrel vibrations and their influence on jump and dispersion, Ministry of Supply, Theoret. Res. Report #9/45, Part I, London, (1945).
- [7] E. H. Lee, I. N. Sneddon and H. W. Parsons, Theoretical investigation of barrel vibrations and their influence on jump and dispersion, Theoret. Res. Report #9/45, Part II, Ministry of Supply, London (1945).
- [8] B. D. Sissom, First report on evaluation of jump in tank guns, Aberdeen Proving Ground, D&PS (1955).
NOTE: [8] is classified "confidential".
- [9] S. C. Chu, and K. C. Pan, Dynamic behavior of elastic slide crank and recoil mechanism, ASME mechanisms conference, New York, 1967.

10. A. M. Arthurs, Complimentary Variational Principles, Clarendon Press, Oxford University, 1975.
11. V. Komkov, Another Look at Variational Principles, Journal of Math. Anal. Applic, to appear in 1977.
12. H. P. Gay and A. S. Elder, The lateral motion of a tank gun, and its effect on the accuracy of fire B.R.L. technical report #1070, (March 1959).
13. V. Komkov, Weapon Accuracy Project, Report #1, Texas Tech and U. S. Army Armcom, October 1976.
14. S. Bodner and P.S. Symonds, "Experimental and theoretical investigation of cantilever beams subjected to impulsive loading", Journ. Appl. Mechanics, 29 Series E (1962) p. 719.
15. G. S. Pisarenko, "Vibrations of elastic systems taking into account the energy dissipation in metals" Dokl. Akad. Nauk U.S.S.R. (1955).
16. W. E. Baker, W. E. Woolam and D. Young, Air and internal damping of thin cantilever beams, Int. J. Mech. Sci., Vol. 9, (1967) p. 743-766.
17. C. Zener, Elasticity and anelasticity in metals, Univ. of Chicago Press, 1948.
18. V. Komkov, On lower bounds on the natural frequencies of inhomogeneous plates. Quarterly of Applied Mathematics, #1 (1974) pp. 395-401.

A THEORETICAL MODEL FOR IN-BORE
PROJECTILE BALLOTING AND BARREL MOTION

G.S. HOO
U.S. Naval Surface Weapons Center
Dahlgren, Virginia

TABLE OF CONTENTS

	<u>Page</u>
ABSTRACT	47
I. INTRODUCTION	48
II. THEORY	49
A. COORDINATE SYSTEMS	50
B. EQUATIONS OF MOTION FOR THE PROJECTILE	54
C. FORCES AND MOMENTS ACTING ON THE PROJECTILE	55
D. EQUATION OF MOTION FOR THE GUN TUBE	63
III. RESULTS	64
A. PROJECTILE BALLOTING MODEL	64
B. GUN TUBE MOTION MODEL	76
IV. FUTURE WORK	76
V. REFERENCES	80

ABSTRACT

An in-bore dynamics model is currently under development at the Naval Surface Weapons Center, Dahlgren Laboratory. During the initial phase of the model formulation, two separate computer codes have been generated. One of the programs is a six degree of freedom dynamics model for simulating projectile balloting. The other is a finite difference model of gun barrel motion and vibration. At the present time, the two codes have only been run independently of one another. The programs can be used for investigating in detail the ballistic process. The effects upon the projectile and barrel dynamics of factors such as manufacturing tolerances for projectiles and barrels, projectile unbalances, barrel wear, barrel stiffness, etc. can be examined. Balloting affects the initial yaw and yaw rate of the projectile as it exits the gun barrel. These latter two parameters in turn govern the accuracy and dispersion of the round.

This paper describes the two models that have been developed. The results of several sample calculations carried out for a 76mm projectile are presented.

I. INTRODUCTION

A mathematical model for simulating the in-bore dynamics of projectile balloting and gun tube motion is being developed at the Naval Surface Weapons Center, Dahlgren Laboratory. Two computer codes have been generated in the initial phase of the model formulation. One of the programs is a six degree-of-freedom dynamics model for simulating projectile balloting; the other is a model of gun barrel motion and vibration. At the present time, the two codes have only been run independently of one another. Eventually, the two will be coupled to permit them to run concurrently. It will then be possible to determine the combined effects of barrel motion and vibration upon projectile balloting, and conversely, the effects of balloting upon the barrel dynamics. The essential variables to be obtained from this simultaneous analysis are the initial maximum yaw and yaw rate of the projectile after it exits the muzzle. These initial values can then be combined with already existing exterior ballistics codes to provide gun performance parameters such as accuracy and dispersion of the shot down-range.

The basic premise for developing a projectile-barrel interaction model is to be able to provide an analytical tool for examining problems which may arise in the development of new and in some cases existing armament. For example, while setback forces and accelerations can easily be obtained from interior ballistics calculations, similar quantities for the projectile sideslap are not readily available. A balloting model could provide the magnitudes of these unknowns. This is important for fuze designers and would ensure at least that their products have been adequately designed to

survive the in-bore launch environment. Similarly, this has bearing upon the sophisticated projectiles being developed at the present time with increasing amounts of electronics and mechanical hardware mounted on board. Another possible application would be towards the new lightweight, high rate of fire gun systems being developed to combat more maneuverable and mobile enemy targets. By necessity, the systems require lightweight barrels which are less stiff and which consequently may introduce more droop and vibration than barrels employed in the past. The high rate of fire places a requirement for improving heat transfer from the gun tube and may even result in ribbed barrels. A mathematical model could be used to examine the influences of barrel droop, varying barrel stiffness and cross-sectional areas, etc., upon the balloting motion.

With the model in its current status it is possible to relate the extent to which changes in various physical and geometrical parameters for the projectile and barrel can influence balloting. The in-bore motion will in turn govern the projectile yaw and yaw rate outside the muzzle. The model permits examination of factors such as clearance between projectile bourrelet and gun bore, projectile machining tolerances, projectile unbalances, barrel wear, barrel stiffness, etc.

The following section describes the analytical treatment of the balloting and barrel motion models that were developed. The results of several sample calculations are presented afterwards to demonstrate the present capabilities of the two computer codes.

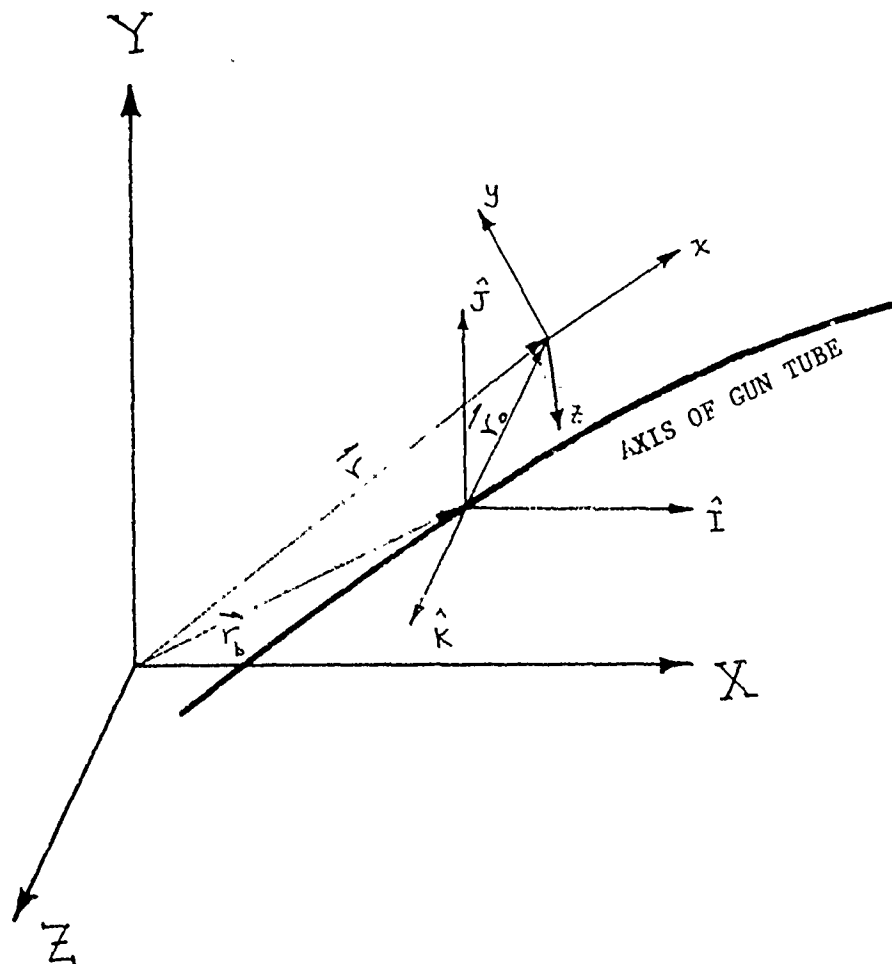
II. THEORY

Recent work being conducted in the field of modeling of the in-bore projectile dynamics include investigations by F. J. Perdreauxville (References 1-3) at Sandia Laboratories and S. H. Chu (References 4, 5) at Picatinny

Arsenal. Chu derives the differential equations of motion using Euler's approach. Perdreauxville, on the other hand, applies Lagrangian dynamics to obtain the equations of motion. The model that has been developed at the Naval Surface Weapons Center, Dahlgren Laboratory, also uses Lagrange's method. Many of the assumptions being employed in the differing model formulations are common to one another. A brief description of the theoretical treatment of the NSWC/DL model follows. Emphasis is placed upon the coordinate systems, the equations of motion for both the projectile and barrel, and the forces and moments involved in the in-bore dynamics.

A. Coordinate Systems

Fig. 1 illustrates the various coordinate systems being utilized in the modeling procedure. The inertial XYZ reference frame is established at the initial rammed position of the projectile within the gun tube. The origin of the system lies in the plane of the rotating band. The X axis is assumed to coincide with the bore centerline of a straight, rigid gun tube at 0° quadrant elevation. The Y axis is taken to be positive in the vertical direction; the Z axis is located in the horizontal plane as determined by applying the right hand rule. The vector, \bar{r} , locates the instantaneous position of the origin of the body fixed xyz coordinate system with respect to the inertial axes. The xyz origin also lies in the plane of the rotating band with the x axis coincident with the projectile axis. An additional IJK coordinate system, whose directions are parallel to the inertial directions, is also utilized. The origin of the IJK system lies on the axis of the gun tube and in the yz plane of the rotating band. The IJK origin is located with respect to the inertial reference frame by the position vector \bar{r}_b .



$$\ddot{\vec{r}} = \ddot{\vec{r}}_b + \ddot{\vec{r}}_o$$

$$\ddot{\vec{r}}_b = \left(\frac{\partial \vec{r}_b}{\partial s} \right) \ddot{s} + \left(\frac{\partial^2 \vec{r}_b}{\partial s^2} \right) (\dot{s})^2 + 2 \left(\frac{\partial^2 \vec{r}_b}{\partial s \partial t} \right) \dot{s} + \frac{\partial^2 \vec{r}_b}{\partial t^2}$$

COORDINATES

Figure 1

The vector \bar{r}_0 locates the body fixed xyz axes with respect to the IJK system. The position vector, \bar{r} , can then be expressed by

$$\bar{r} = \bar{r}_b + \bar{r}_0.$$

Differentiating with respect to time twice, the acceleration vector, $\ddot{\bar{r}}$, becomes

$$\ddot{\bar{r}} = \ddot{\bar{r}}_b + \ddot{\bar{r}}_0.$$

The effects of the barrel upon the projectile balloting can be accounted for by the acceleration vector, $\ddot{\bar{r}}_b$. Assuming \bar{r}_b to be a function of displacement along the gun tube (represented as the path s), and also a function of time t , (i.e., $\bar{r}_b = f(s, t)$), the acceleration vector, $\ddot{\bar{r}}_b$, can be written as

$$\ddot{\bar{r}}_b = \left(\frac{\partial \bar{r}_b}{\partial s} \right) \ddot{s} + \left(\frac{\partial^2 \bar{r}_b}{\partial s^2} \right) (\dot{s})^2 + 2 \left(\frac{\partial^2 \bar{r}_b}{\partial s \partial t} \right) \dot{s} + \frac{\partial^2 \bar{r}_b}{\partial t^2}$$

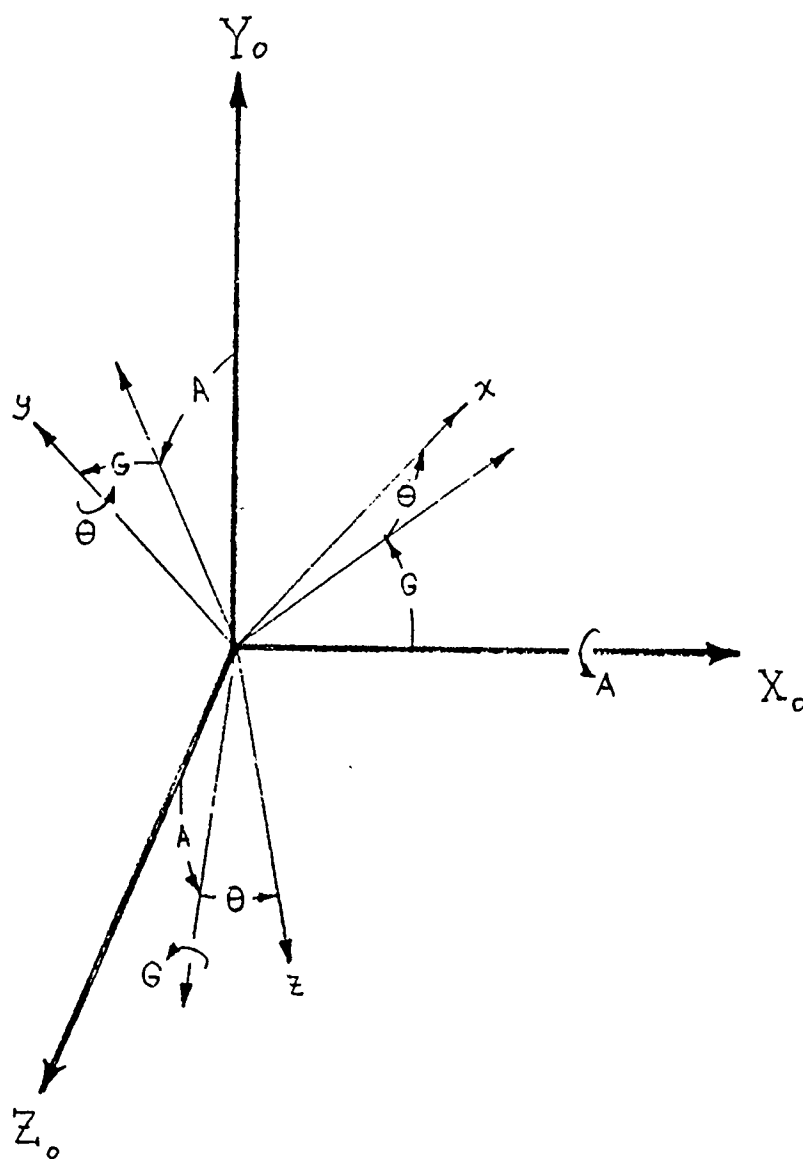
where

\dot{s} = velocity along the path, and

\ddot{s} = acceleration along the path.

The projectile velocity, \dot{s} , and acceleration, \ddot{s} , can be obtained from interior ballistics calculations, while the partial derivatives can be obtained from the barrel motion model to be described later.

With the location of the projectile with respect to the inertial reference frame specified, there remains the establishment of the relationship between the orientation of the body fixed xyz system and the inertial directions. The projectile orientation can be described in terms of the Euler angles shown in Fig. 2. The origin of the $X_0Y_0Z_0$ coordinate system illustrated coincides with the origin of the body fixed xyz system. The directions of the $X_0Y_0Z_0$ system are parallel to the inertial directions.



EULER ANGLES

Figure 2

The transformation from the inertial directions to the body fixed directions can be achieved first by a rotation through an angle A about the X_0 axis, next by a rotation G about the new Z_0 axis (or line of nodes), and finally by a rotation Θ about the body y axis.

B. Equations of Motion for the Projectile

The equations of motion for the projectile are derived using Lagrange's equation. The shell is considered to be a free rigid body whose kinetic energy, T , is given by (see Reference 6)

$$T = \frac{1}{2} m v_0^2 + \frac{1}{2} (I_x \omega_x^2 + I_y \omega_y^2 + I_z \omega_z^2 - 2I_{xy} \omega_x \omega_y - 2I_{xz} \omega_x \omega_z - 2I_{yz} \omega_y \omega_z) + m [v_{0x} (\omega_y \bar{z} - \omega_z \bar{y}) + v_{0y} (\omega_z \bar{x} - \omega_x \bar{z}) + v_{0z} (\omega_x \bar{y} - \omega_y \bar{x})]$$

where

m = mass of the projectile,

v_0 = inertial space velocity of rotating band center,

v_{0x} , v_{0y} , v_{0z} = components of v_0 in the body fixed directions,

I_x , I_y , I_z , I_{xy} , I_{xz} , I_{yz} = moments and products of inertia

ω_x , ω_y , ω_z = components of the inertial space angular velocity about the body fixed directions, and

\bar{x} , \bar{y} , \bar{z} = coordinates of the center of mass in the body fixed coordinate system.

The linear inertial space velocity components, v_{0x} , v_{0y} , and v_{0z} , can be expressed in terms of the inertial XYZ directions. The angular velocities, ω_x , ω_y , and ω_z , can be expressed in terms of the Euler angles, A , G , and Θ .

Application of Lagrange's equation

$$\frac{d}{dt} \left(\frac{\partial T}{\partial \dot{q}_r} \right) - \frac{\partial T}{\partial q_r} = F_{q_r}$$

where

q_r = generalized coordinates (such as X,Y,Z,A,G, and θ), and

F_{q_r} = applied forces or moments in the directions of the generalized coordinates,

yields six coupled partial differential equations of motion - three of which are the force equations in the inertial X, Y, and Z directions and the other three of which are moment equations in the Euler angle directions. Writing the equations in matrix notation, the accelerations, $\ddot{X}, \ddot{Y}, \ddot{Z}, \ddot{A}, \ddot{G}$, and $\ddot{\theta}$, can then be solved for by inversion. At NSWC/DL, a simulation language, CSSL3 (Continuous System Simulation Language III, see Reference 7), is utilized to integrate the accelerations to obtain velocities and displacements. The integration technique currently being employed is a self starting, variable time step, Runge-Kutta/Moulton scheme. The step size is adjusted as the computations proceed in an effort to control the amount of integration error.

C. Forces and Moments Acting on the Projectile

The applied forces and moments appearing in the equation of motion for the projectile need to be specified. All the forces acting on the shell must be given in terms of the inertial directions. Moments must be expressed in terms of the Euler angle directions to be compatible with the forms of the derived equations.

1. Forces and Moments Due to Gravity

The weight of the projectile is considered to act at the center of mass in the negative inertial Y direction. The origin of the body fixed coordinate system is located in the plane of the rotating band. The

gravitational force will therefore introduce a torque about the origin which needs to be included as part of the moment system being applied to the projectile.

2. Force Acting at the Base

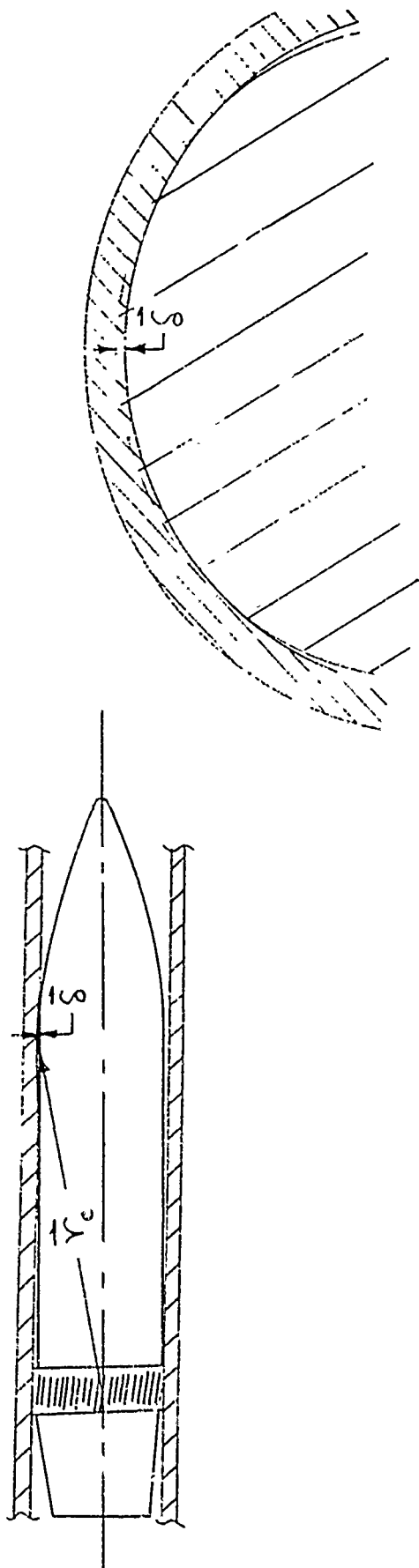
The force acting on the base of the projectile is obtained from theoretical interior ballistics computations. These calculations usually provide base pressure as a function of time which can easily be converted to a driving force acting on the base. The force is assumed to act in the positive inertial X direction. A shot start pressure can also be taken into account. In this situation, the driving force on the base is not included in the solution of the problem until the base pressure exceeds the shot start pressure.

3. Rifling Torque

For a rifled gun barrel, the driving force acting on the base of the projectile will impart a torque. The moment is considered to act in the direction of the bore centerline. Its magnitude is determined as a function of the rifling twist (e.g., expressed in turns per caliber) and of the axial acceleration of the projectile along the path of the bore centerline.

4. Forces and Moments Due to Bourrelet Contact

When the projectile contacts the gun tube, the rebound force at the bourrelet is accounted for by a simple spring deflection model as illustrated in Fig. 3. The orientation of the shell as it travels down the barrel is not restricted solely to within the confines of the gun bore. Under the model formulation, elastic behavior of the projectile and barrel are assumed. The displacement, $\bar{\delta}$, of the projectile into the bore determines the magnitude of the rebound force. An appropriate value for the spring



$$\vec{F}_b = k_b \vec{s} \quad \vec{F}_f = \mu k_b |\vec{s}| \frac{\vec{V}_s}{|\vec{V}_s|}$$

$$\vec{M}_b = \vec{r}_c \times \vec{F}_b \quad \vec{M}_f = \vec{r}_c \times \vec{F}_f$$

$$(\vec{M}_b)_{AG\dot{\theta}} = \vec{Q} \cdot \vec{M}_b \quad (\vec{M}_f)_{AG\dot{\theta}} = \vec{Q} \cdot \vec{M}_f$$

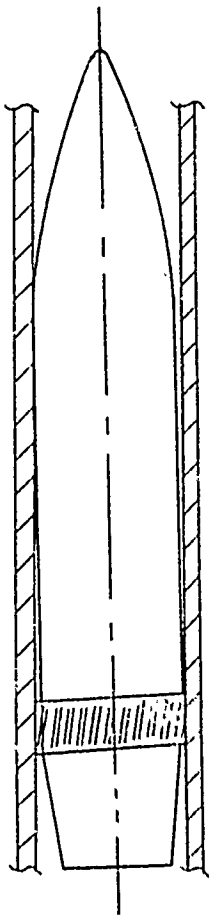
FORCES AND MOMENTS DUE TO
BOURRELET CONTACT

Figure 3

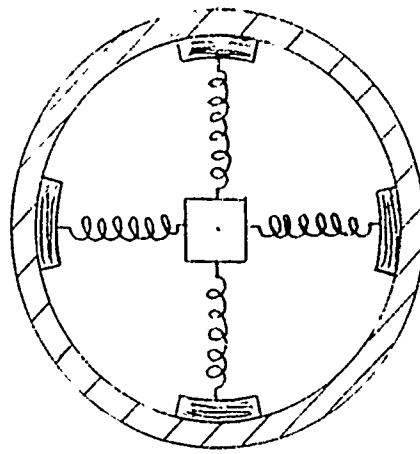
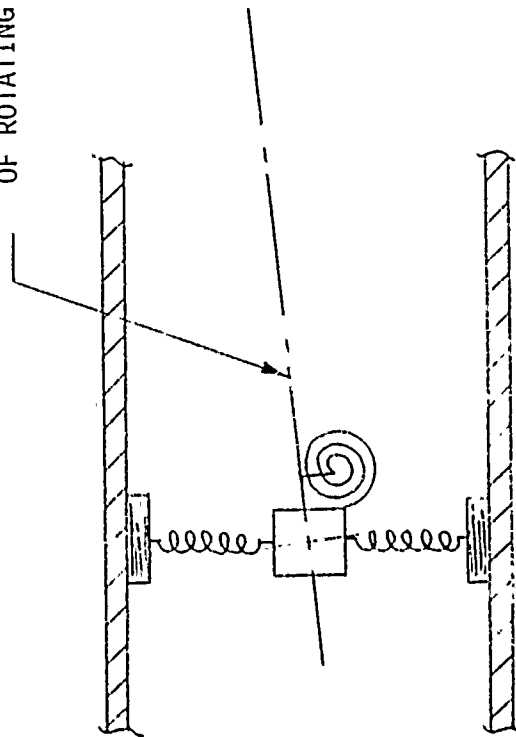
stiffness, k_b , must be obtained from strength of material considerations or from experimental procedures. The balloting force acts normal to the projectile centerline and also produces a moment about the origin of the body fixed coordinates. The contact force also contributes a friction force since the projectile is sliding on the walls of the gun tube. The direction of the friction force is opposite to the sliding velocity vector at the contact point. This velocity vector is composed of the velocity of the shell in the direction of the gun axis centerline as well as the velocity due to the rifling spin. An appropriate value for the coefficient of sliding friction must be selected. Again, since the friction force acts at the bourrelet, the torque that it produces about the origin must be taken into consideration.

5. Forces at the Rotating Band

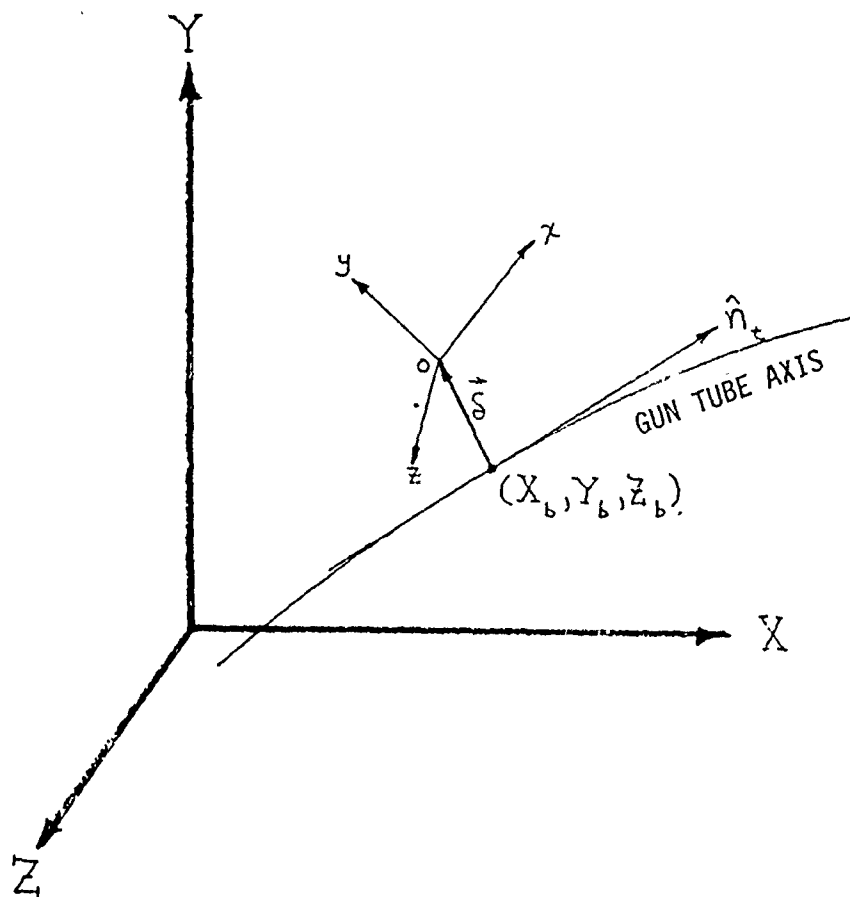
A rotating band model is incorporated into the balloting formulation. Both torsional and transverse springs are included as shown in the schematic diagram of Fig. 4. The springs act in the plane of the rotating band and simulate the properties inherent to the band. The transverse springs permit the origin of the body fixed coordinate system, which in essence represents the projectile, to move about but not strictly along the gun tube axis as shown in Fig. 5. An appropriate value for the spring stiffness, k , must be determined analytically or experimentally. When the projectile is engraved symmetrically, the transverse springs act to restore the projectile origin towards the bore centerline. In the case of an unsymmetrically engraved band, the springs act to restore the projectile origin to the eccentric position. For the torsional spring, a projectile plane of yaw is



NORMAL TO PLANE
OF ROTATING BAND



ROTATING BAND MODEL
Figure 4



$$\vec{F}_R = k \vec{\delta}$$

$$\vec{\delta} = [(X_o - X_b)\hat{i} + (Y_o - Y_b)\hat{j} + (Z_o - Z_b)\hat{k}]$$

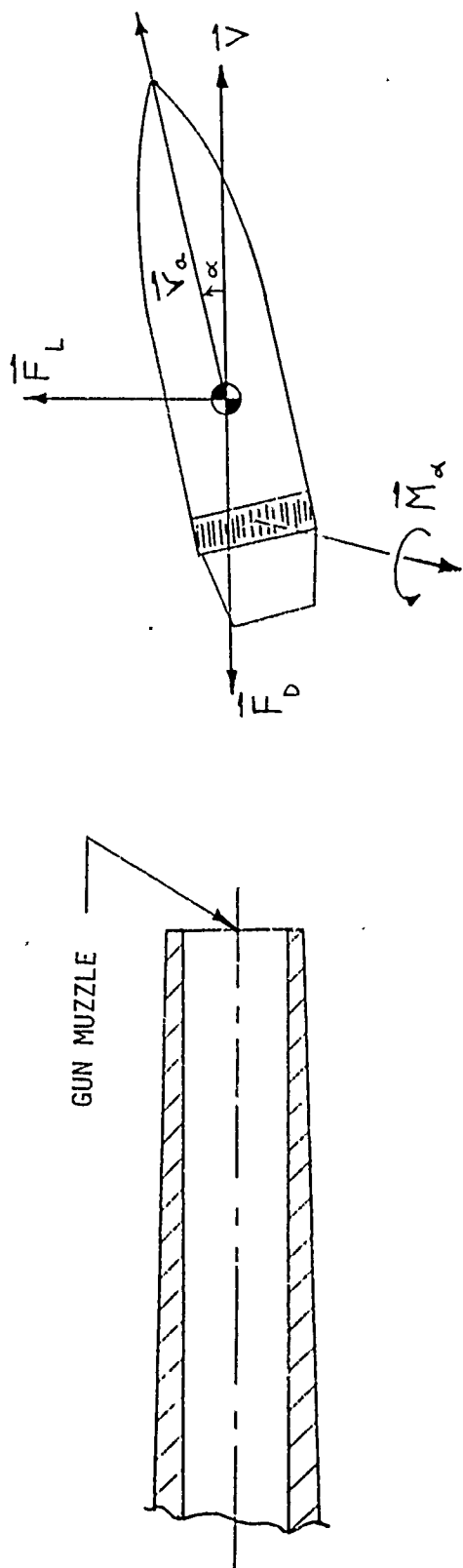
NORMAL FORCE AT ROTATING BAND

Figure 5

assumed which contains both the positions of the gun tube and projectile axes at the time of engraving. As the projectile travels down a rifled barrel, this plane of yaw will rotate. The restoring torque will always act in a direction perpendicular to the plane such that the initial orientation of the projectile is attained. The magnitude of the moment is calculated based upon the difference between the angle of the initial projectile orientation and the instantaneous yaw. The value of the torsional spring stiffness must also be determined analytically or experimentally.

6. Aerodynamic Forces and Moments

Once the projectile exits the muzzle, the forces and moments due to the sources mentioned above all vanish except for those due to gravity. To provide for a more realistic treatment of the exterior ballistics (in order to determine more accurately quantities such as the initial maximum projectile yaw and yaw rate), some aerodynamic forces and moments are taken into consideration in the solution of the equations of motion. Lift and drag forces, as well as a pitching moment, are calculated as delineated in Fig. 6. It is assumed that values for C_L , C_D , and $C_{m\alpha}$, representing the lift, drag, and pitching moment coefficients respectively, are available. Upon muzzle exit, the projectile velocity is represented by the vector \bar{V} of Fig. 6. The lift acts in the direction of the projectile yaw, and consequently in the plane of yaw, perpendicular to the velocity vector. The drag is taken to act in the direction opposite to the velocity vector. Both of these forces act at the center of mass and produce moments about the origin of the body fixed coordinates. The pitching moment is perpendicular to the projectile plane of yaw and creates a torque in the direction of the projectile yaw.



$$\vec{F}_L = C_L \frac{\rho V^2}{2} A \frac{(\vec{V} \times \vec{r}_a) \times \vec{V}}{|(\vec{V} \times \vec{r}_a) \times \vec{V}|}$$

$$\vec{F}_D = -C_D \frac{\rho V^2}{2} A \frac{\vec{V}}{|\vec{V}|}$$

$$(\vec{M}_\alpha)_{AG\dot{\theta}} = \vec{Q} \cdot \left[C_{m\alpha} \frac{\rho V^2}{2} A l \frac{(\vec{V} \times \vec{r}_a)}{|\vec{V} \times \vec{r}_a|} \right]$$

AERODYNAMIC FORCES AND MOMENTS

Figure 6

D. Equation of Motion for the Gun Tube

The gun barrel is considered to be a cantilever beam, clamped at the breech end and free at the muzzle end. The differential equation of motion for the transverse vibration of a beam is given by

$$\frac{\partial^2}{\partial X^2} \left[EI(X) \frac{\partial^2 \bar{W}}{\partial X^2} \right] - \frac{\partial}{\partial X} \left[P(X,t) \frac{\partial \bar{W}}{\partial X} \right] + M(X) \frac{\partial^2 \bar{W}}{\partial t^2} + C \frac{\partial \bar{W}}{\partial t} = \bar{F}(X,t).$$

where

E = modulus of elasticity,

C = coefficient of damping,

$I(X)$ = mass moment of inertia per unit length,

$M(X)$ = mass per unit length,

$P(X,t)$ = axial load per unit length,

$\bar{F}(X,t)$ = transverse load per unit length, and

\bar{W} = transverse displacement vector.

Two separate equations of motion are actually represented in the above expression since the displacement vector can be written as

$$\bar{W} = Y(X,t) \hat{j} + Z(X,t) \hat{k}.$$

The \hat{j} component accounts for motion in the vertical YZ inertial plane, the \hat{k} component for motion in the horizontal XZ inertial plane. Reference 8 has shown that the effects of torsion upon the cross motion of the barrel are small. The torsional effects have, therefore, been neglected in this formulation. The barrel can be considered as a tapered hollow cylinder with variable cross sectional areas, variable mass, and variable moments of inertia, all as functions of position along the length of the tube. The axial loading, $P(X,t)$, and the transverse loading, $\bar{F}(X,t)$, are functions of both distance along the gun tube and time. The axial loading on the barrel may come in the

form of recoil or of friction between the projectile and gun bore. The transverse loadings may be obtained from the previous balloting considerations wherein forces equal and opposite to those acting on the projectile at the bourrelet and rotating band are taken to act upon the gun tube. A moving load consisting of the weight of the projectile is also considered. The equation of motion for each of the horizontal and vertical directions is solved independently of the other by means of finite differences. The gun barrel can be modeled by any number of discrete node points. Each node will possess its own mass and moment of inertia. The motion of each point is monitored throughout the duration of a calculation. The two independent solutions can then be superimposed to yield the total gun barrel motion.

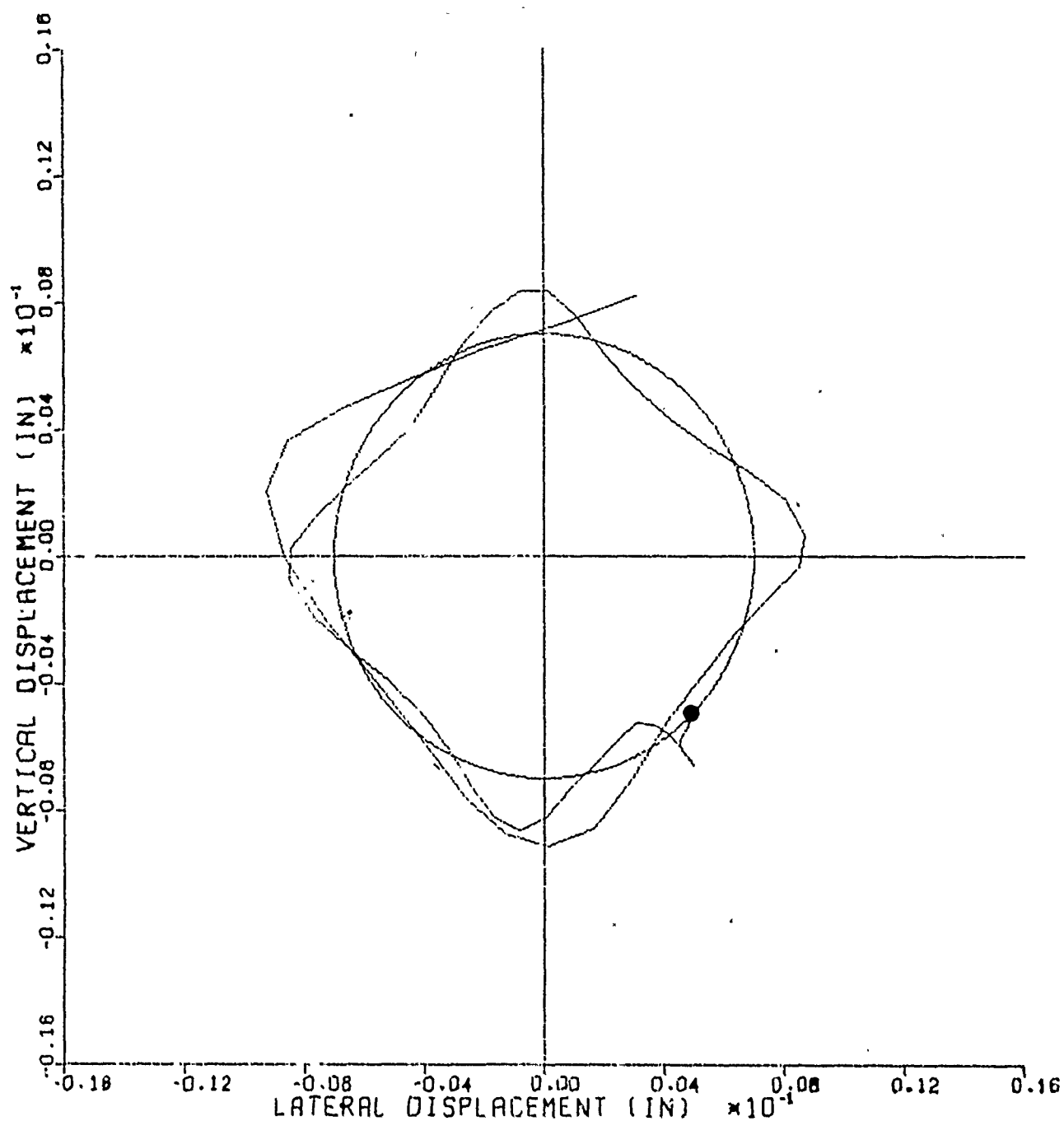
III. RESULTS

A. Projectile Balloting Model

The balloting model has been utilized to simulate the dynamics of a 76mm projectile. The results of several sample calculations are provided in the following paragraphs.

1. Dynamically Balanced Projectile

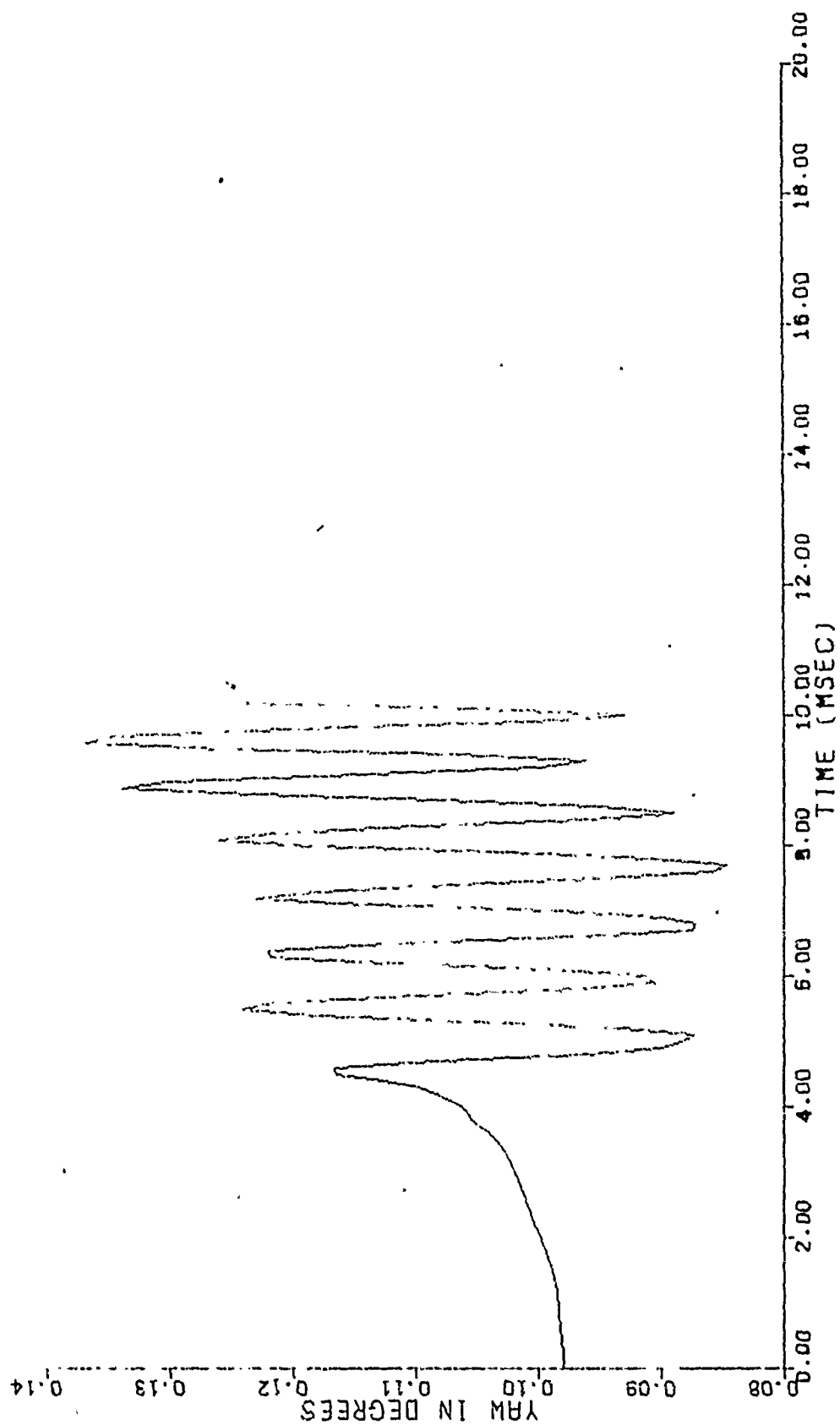
The first computer run to be reviewed is for a dynamically balanced projectile; hereafter this problem is denoted as Case 76.012. The gun tube is assumed to be straight and rigid as will be the case in all succeeding balloting runs to be presented here. The rotating band is considered to be engraved symmetrically. Fig. 7 depicts the transverse projectile motion at the bourrelet during the in-bore period. The trace corresponds to the point on the projectile axis in the plane of the bourrelet. The circle of diameter 0.014 in. (0.356mm) therefore represents



DISPLACEMENTS AT BOURRELET
CASE 76.012 INTERMEDIATE CLEARANCE

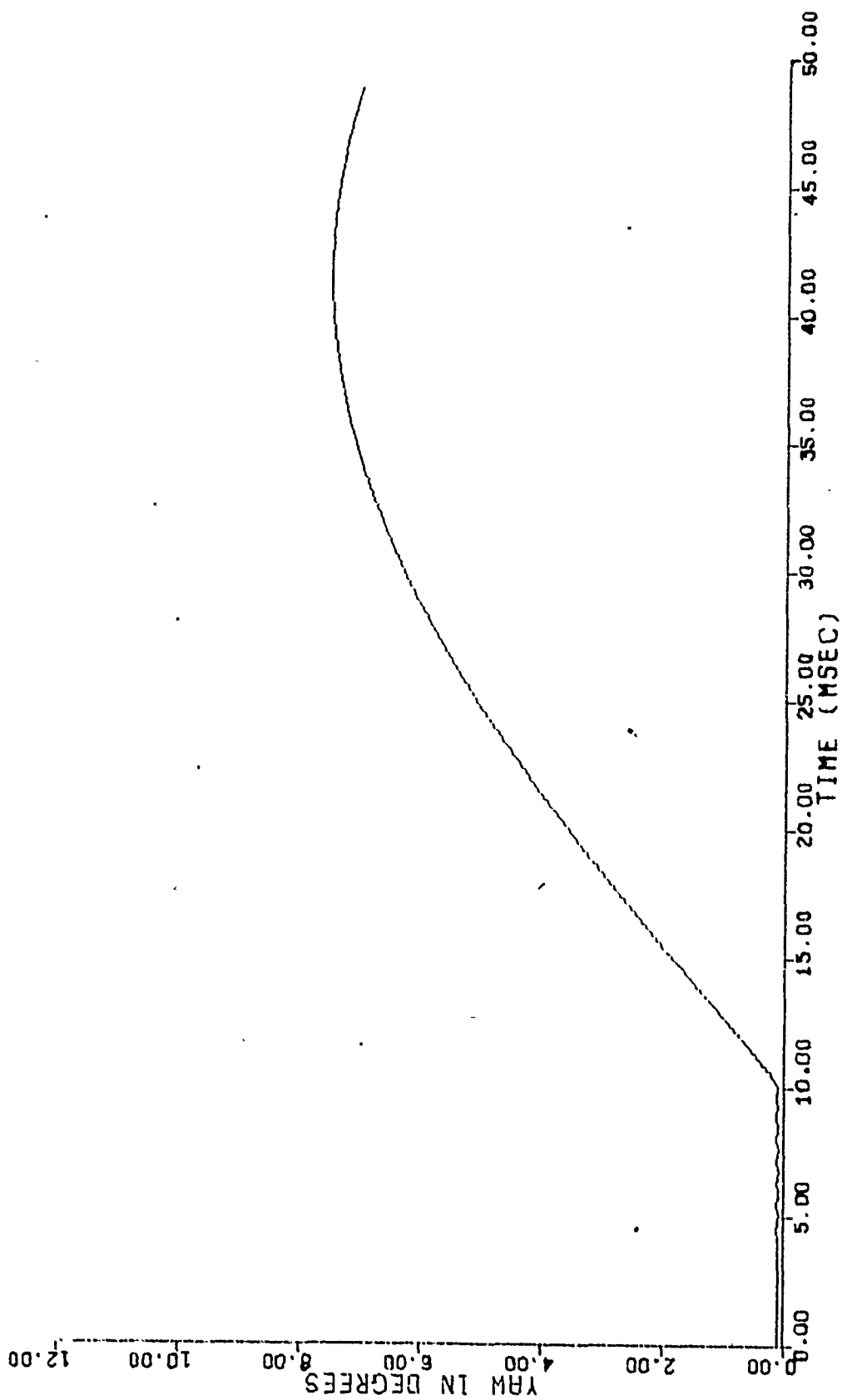
Figure 7

the locus of this bourrelet point should the projectile just slide along the bore surface. The dot on the circumference indicates the initial projectile orientation inside the gun tube at the time of ramming. As can be seen, the projectile is taken to be in contact with the bore initially. The view illustrated is seen from the base of the projectile. The rifling twist is clockwise. The model shows the projectile to ballot and precess in the direction of the rifling. Fig. 8 depicts the in-bore yaw versus time. The in-bore period is approximately 10 msec. The motion for the most part oscillates about the limit set by the clearance between the projectile and gun bore. A certain degree of elastic behavior is permitted in the bourrelet and gun bore interaction and accounts for yaw angles greater than that which can be attributed to clearance alone. Upon muzzle ejection, aerodynamic lift and drag forces are taken to act upon the projectile in addition to the gravity force. An aerodynamic pitching moment is also considered. The effects of muzzle blast during the transition ballistics regime are neglected. Fig. 9 shows the first maximum yaw outside the muzzle to be about 7.52 degrees (0.131 rad). The calculated yaw outside the muzzle will in general be sinusoidal with the minimum value being that which occurred at muzzle ejection. Fig. 10 shows yaw rate versus time for the 76mm. First maximum yaw rate occurs slightly after muzzle release and is about 367 degrees per second (6.41 rad per second). The calculated yaw rate will also be sinusoidal with a minimum value corresponding to the negative of the first maximum. From the magnitudes of these last two parameters, it should be possible to obtain accuracy and dispersion of the round downrange by use of presently existing exterior ballistics codes. The contact forces calculated at the bourrelet are shown in Fig. 11. The top



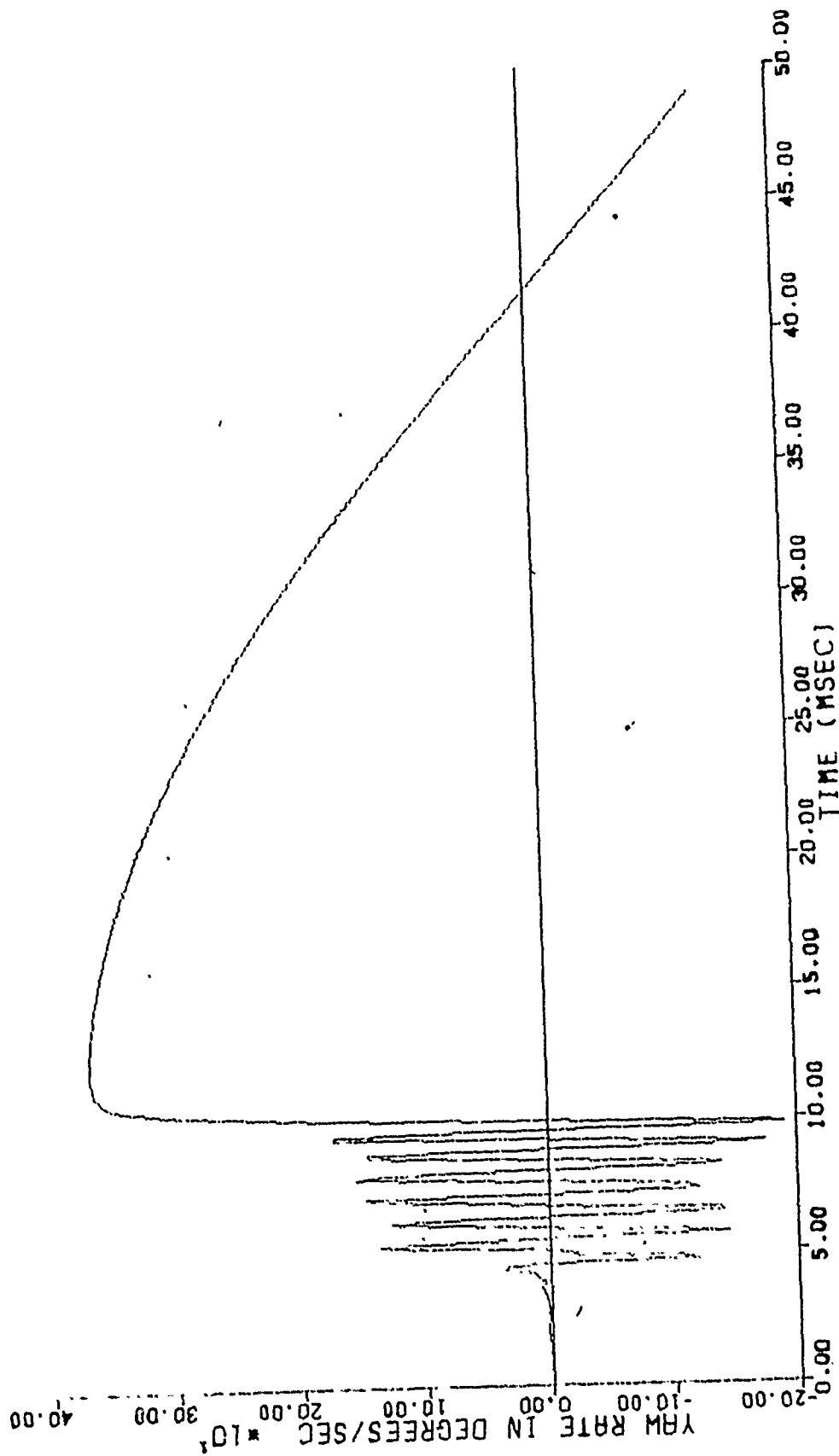
CASE 76.012 INTERMEDIATE CLEARANCE

Figure 8. In-bore Yaw Versus Time



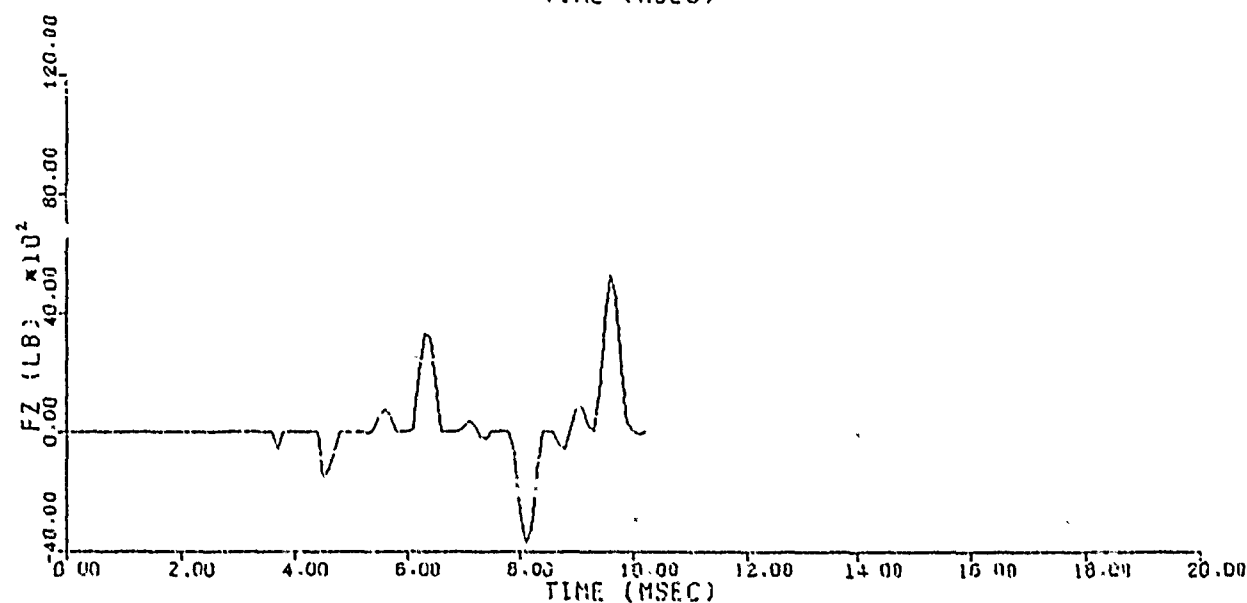
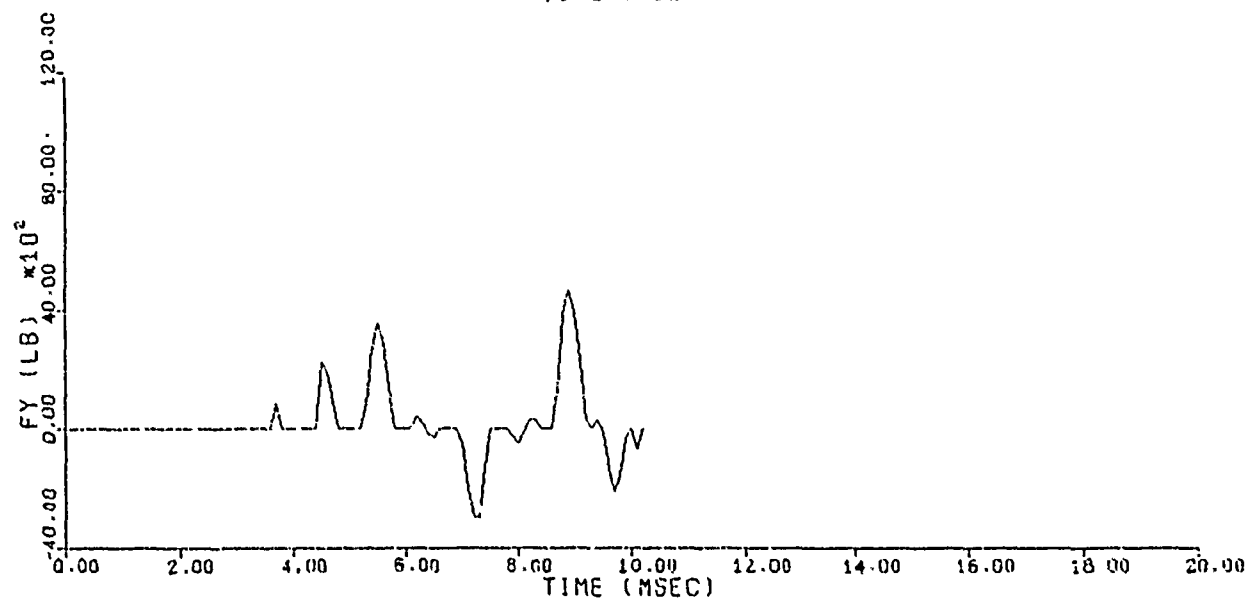
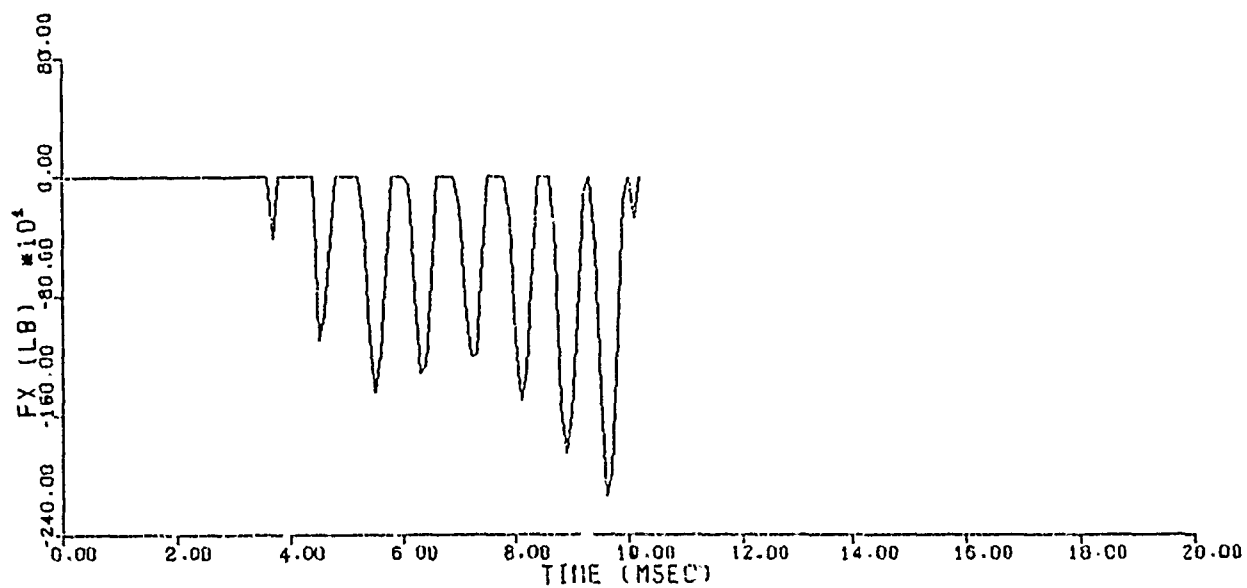
CASE 76.012 INTERMEDIATE CLEARANCE

Figure 9. Yaw Versus Time



CASE 76.012 INTERMEDIATE CLEARANCE

Figure 10. Yaw Rate Versus Time



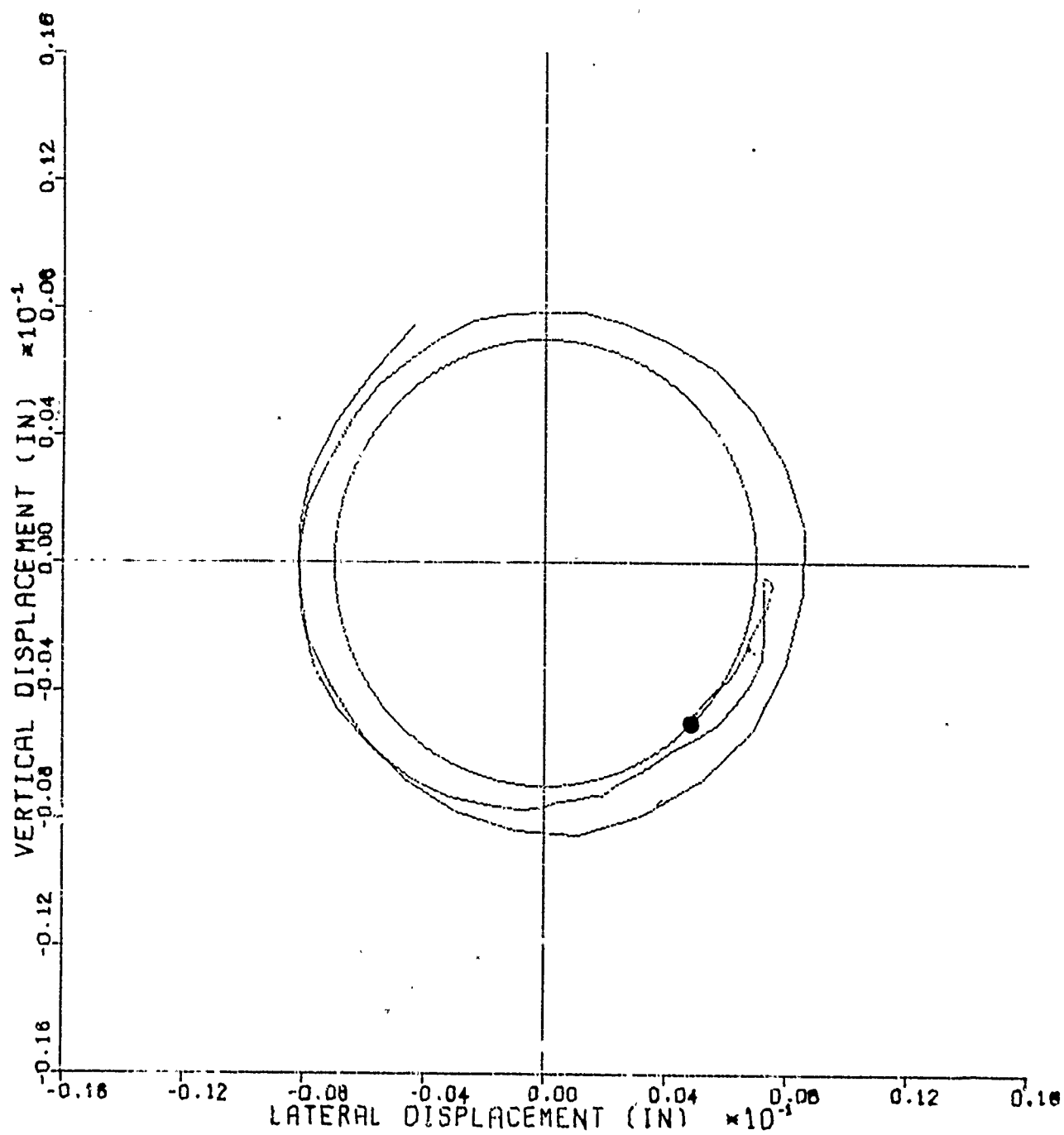
FORCES AT THE BOURRELET
CASE 76.012 INTERMEDIATE CLEARANCE

Figure 11

diagram shows the friction force during contact. The force acts intermittently, returning to zero whenever contact between the projectile and bore is lost. A constant coefficient of friction of $\mu=0.4$ was assumed so that the normal force has the same appearance as this first figure except for proportionately larger magnitudes. The latter two diagrams show the decomposition of the contact force in each of the lateral directions.

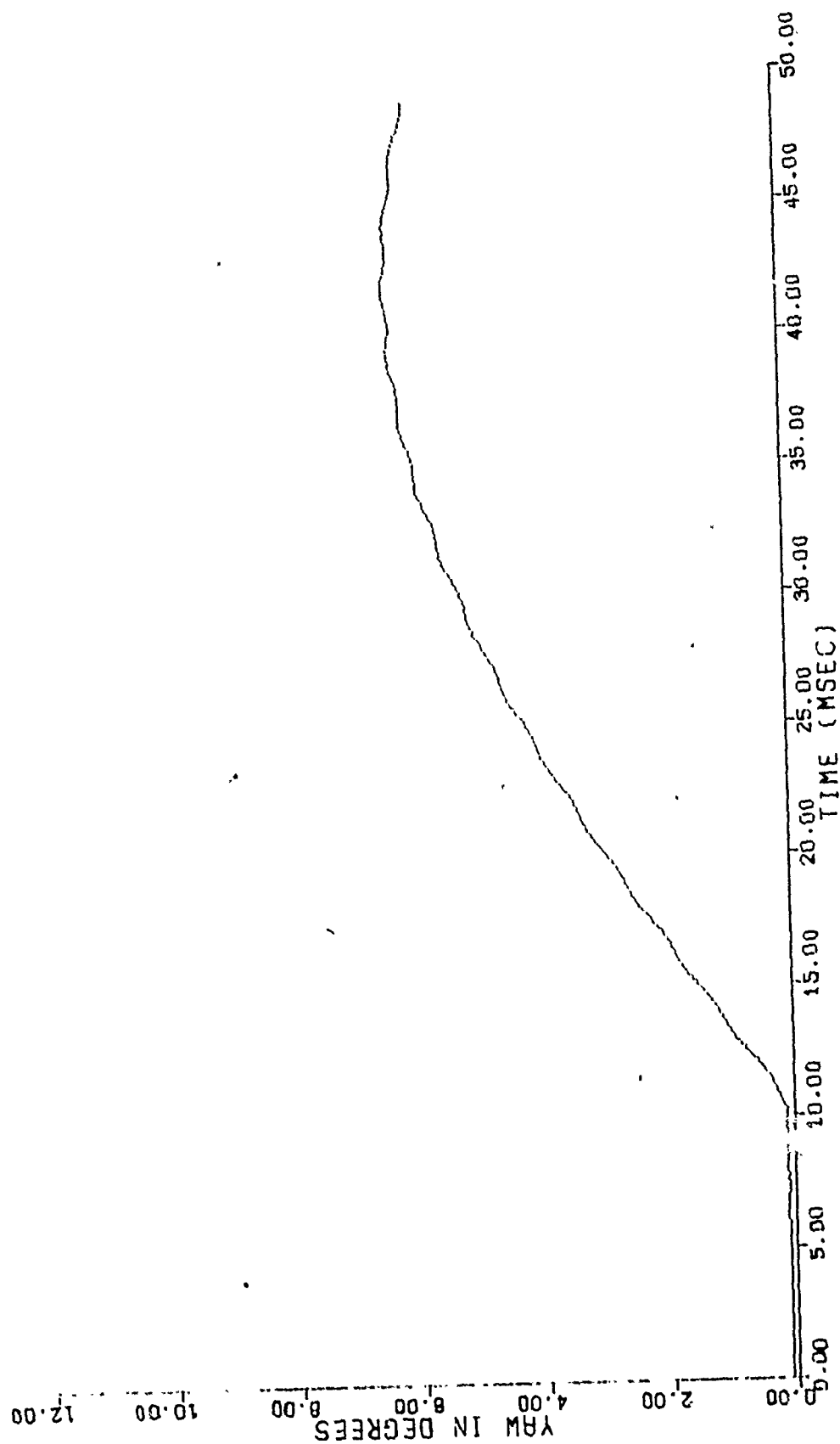
2. Small Projectile Unbalance

The second sample calculation to be presented here, Case 76.212T, represents a projectile with 0.01 in. (0.254mm) center of mass offset. The projectile is initially in contact with the bore in the lower right quadrant as shown in Fig. 12. The unbalance itself is taken to be in the twelve o'clock position. The projectile is seen to lift slightly from the bore surface during the initial stages of motion. However, the unbalance eventually takes effect and causes the projectile bourrelet to essentially trace the gun bore circumference down the length of the tube. The corresponding yaw versus time for this case is shown in Fig. 13. Projectile ejection takes place shortly after 10 msec. The yaw outside the muzzle reaches a maximum of about 6.38 degrees (0.111 rad). The yaw rate versus time, illustrated in Fig. 14, shows the maximum to be approximately 358 degrees per second (6.24 rad per second). Fig. 15 depicts the balloting force versus time curves in the three inertial directions. The bourrelet retains sliding contact with the bore for the majority of the in-bore ride, and consequently no repetitive impacts are noted in these curves compared to those of Fig. 11. A comparison of the yaw, yaw rate, and bourrelet contact forces, shows the slightly out-of-balance round to have a somewhat beneficial effect upon the projectile performance over that of a balanced round. However, the continual contact may adversely contribute to barrel wear.



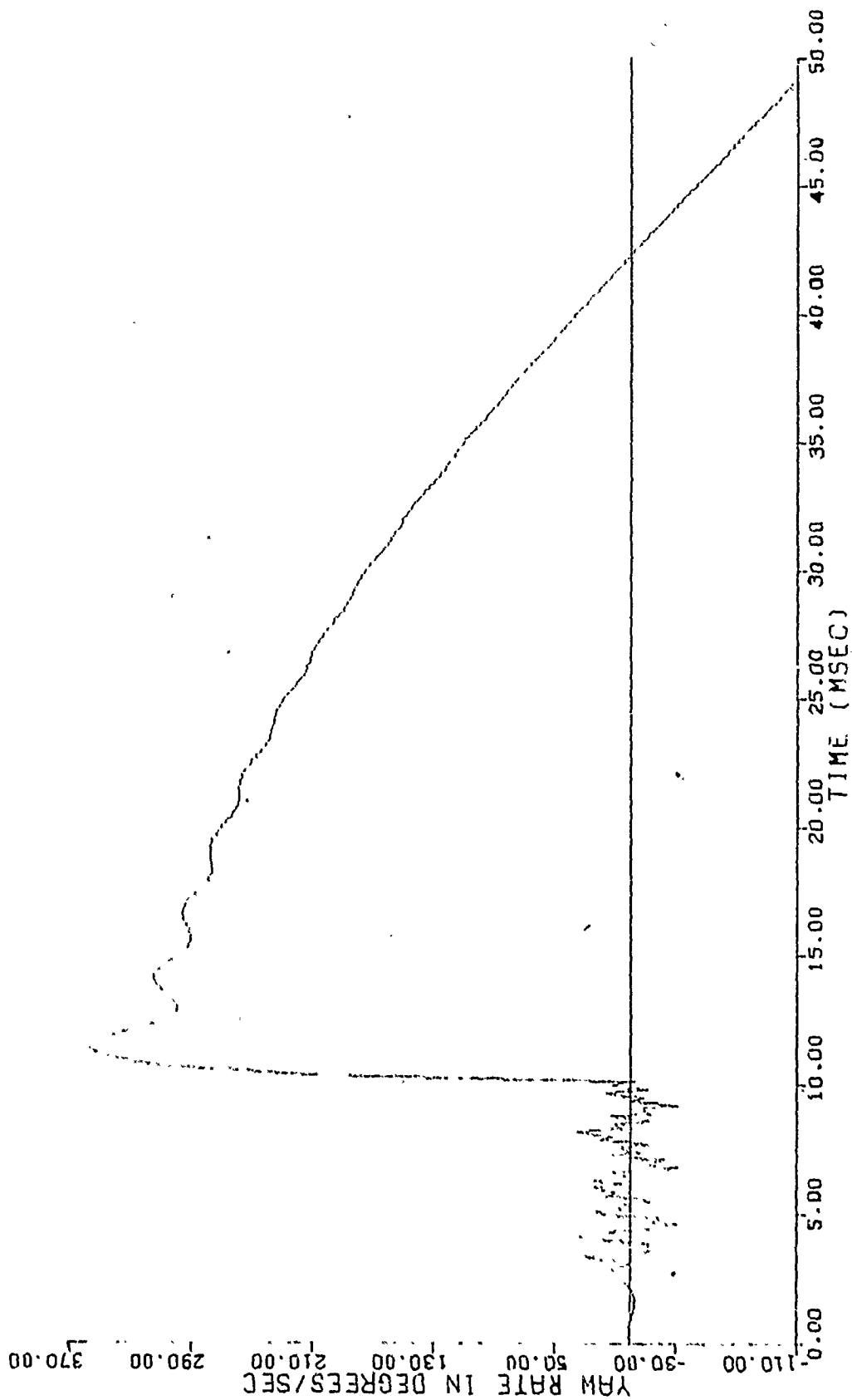
DISPLACEMENTS AT BOURRELET
CASE 76.212T INTERMEDIATE CLEARANCE

Figure 12



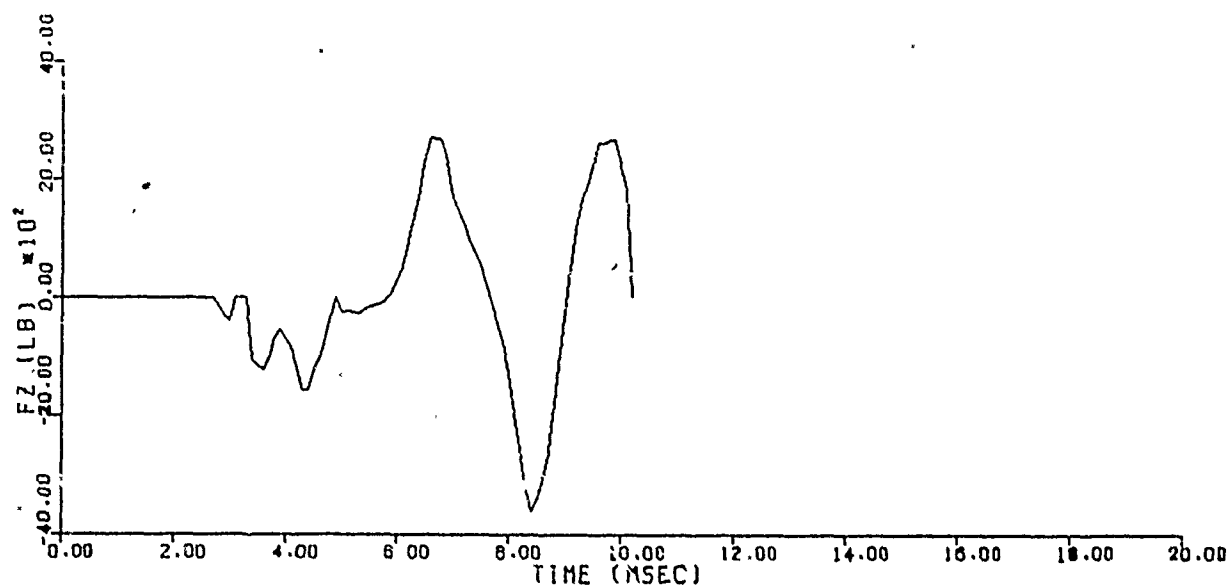
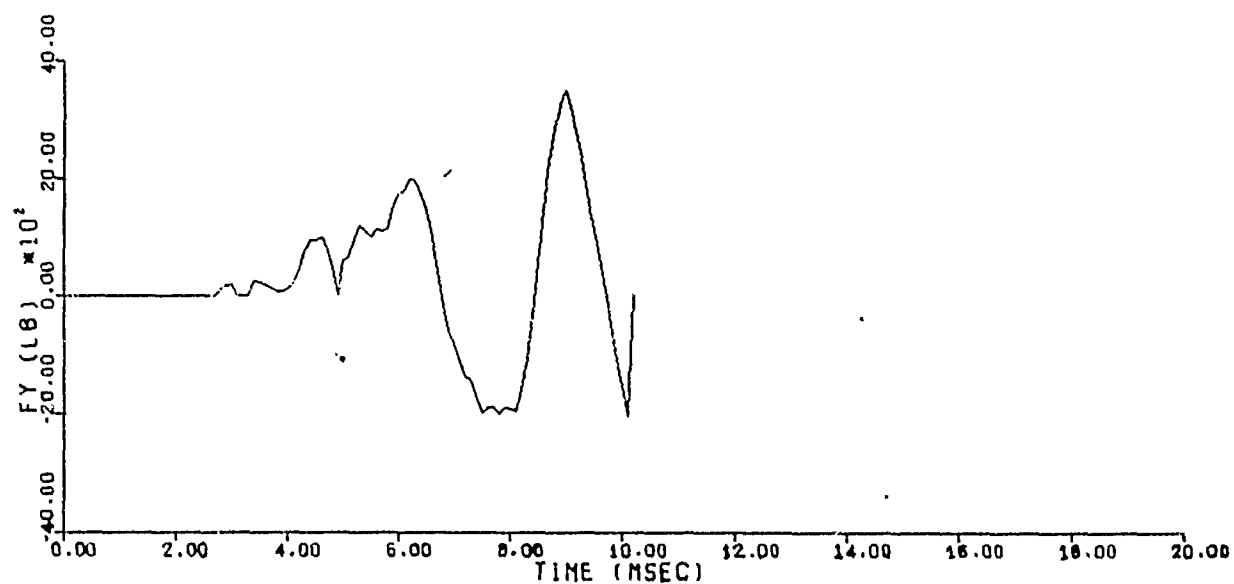
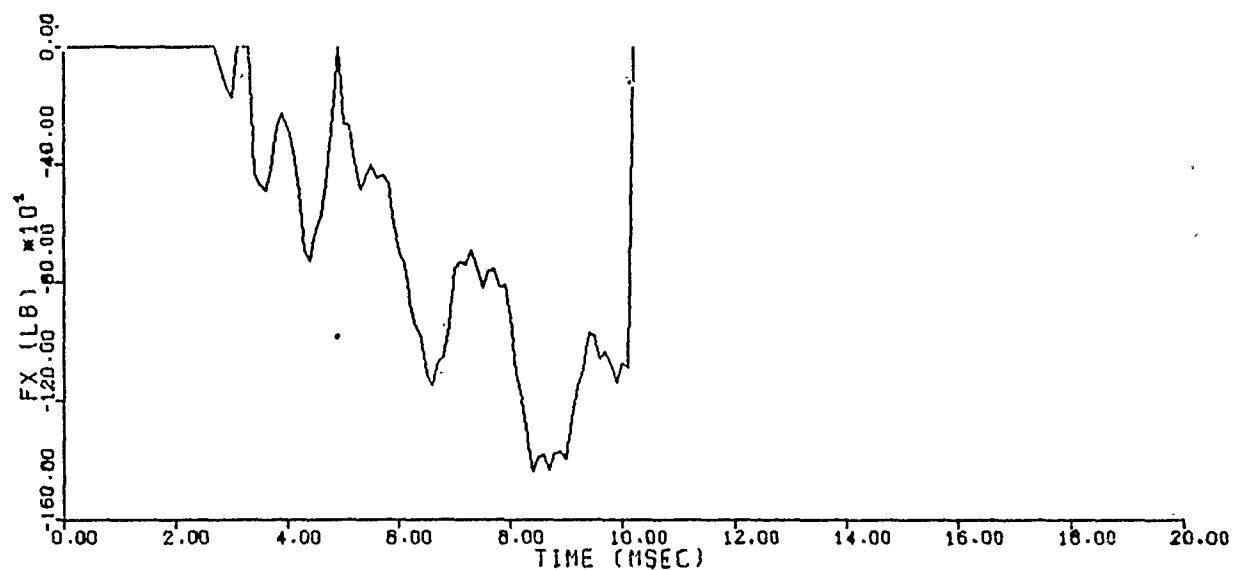
CASE 76.212T INTERMEDIATE CLEARANCE

Figure 13. Yaw Versus Time



CASE 76.212T INTERMEDIATE CLEARANCE

Figure 14. Yaw Rate Versus Time



FORCES AT THE BOURRELET
CASE 76.212T INTERMEDIATE CLEARANCE

Figure 15

B. Gun Tube Motion Model

The geometry of a 76mm/62 OT0 MELARA barrel is illustrated in the cross-sectional view of Fig. 16. The barrel has a somewhat complex geometry consisting of several tapered sections.

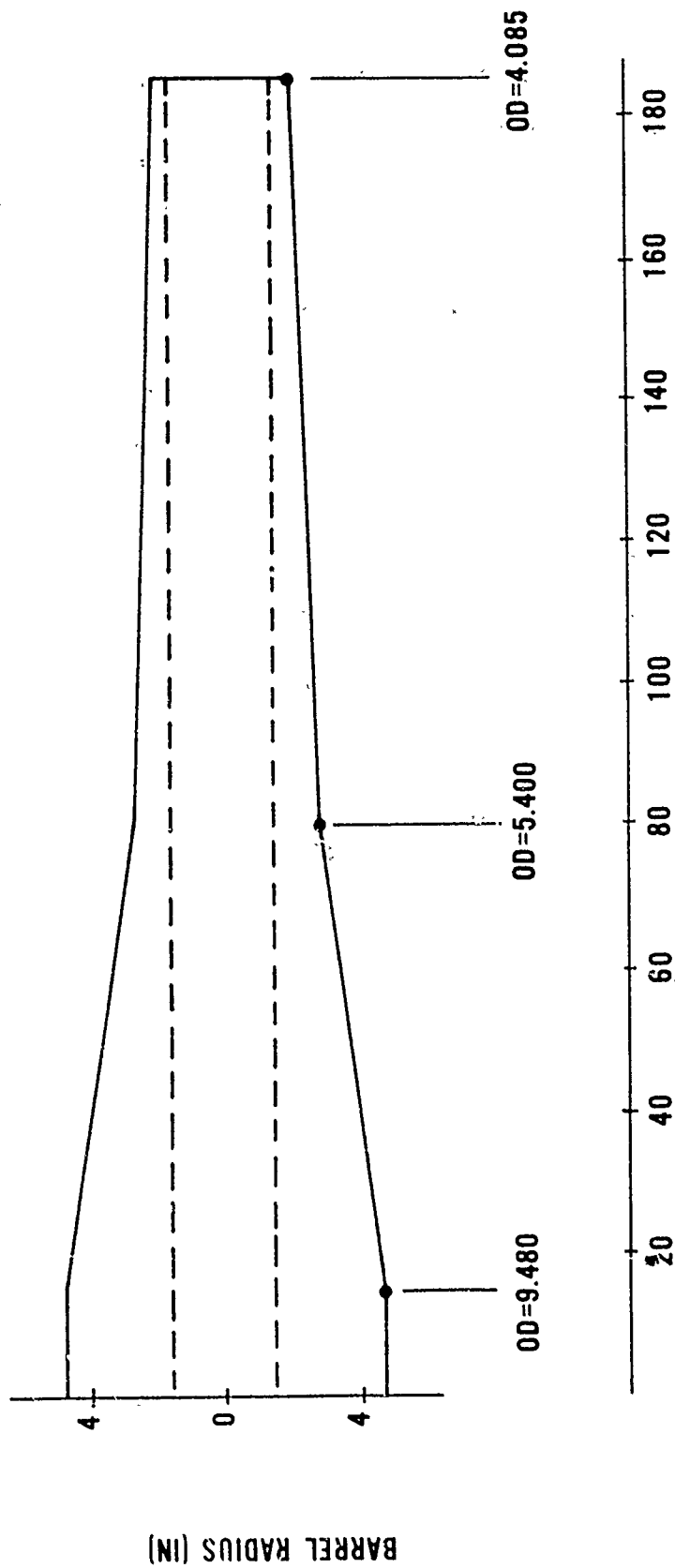
The results of the sample calculation of the barrel motion model outlined here corresponds to Case 76.012 of the previous balloting runs. The negative of the transverse loadings at the bourrelet from Fig. 11 coupled with the 76mm in-bore displacement-time curve were input as the forcing function in the solution of the equations of motion for the barrel. The transverse tube motion at the muzzle is illustrated in Fig. 17. The barrel is initially drooped under its own weight - the muzzle deflection from the horizontal being about 0.0111 in. (0.281mm). The dot on the displacement curve corresponds to the projectile ejection time of 10.2 msec. At this instant, the muzzle jump is 0.0015 in. (0.0381mm) but is on the decline. The muzzle deflection in the horizontal plane is 0.00527 in. (0.134mm) in the negative Z direction at the time of muzzle release. The results of this computation show very little muzzle deflection during the in-bore projectile travel. Much larger motions are exhibited after projectile ejection.

IV. FUTURE WORK

Some of the capabilities of the projectile balloting and barrel motion models have been demonstrated in the examples of the previous sections. It would be desirable to investigate the effects of other parameter variations, such as clearances and stiffnesses, and to correlate the results. A non-dimensional approach may be undertaken in order to

CONFIGURATION FOR BARREL NO.1

NATURAL FREQUENCY=12.7 HZ
INNER=3.0 IN



DISTANCE FROM THE BREECH (IN)

Figure 16. Schematic for 76mm/62 OTO MELARA Barrel

BARREL DEFLECTION PATTERN
DISTANCE FROM THE MUZZLE = 0. INCH

0 = INITIAL STATIC DROOP

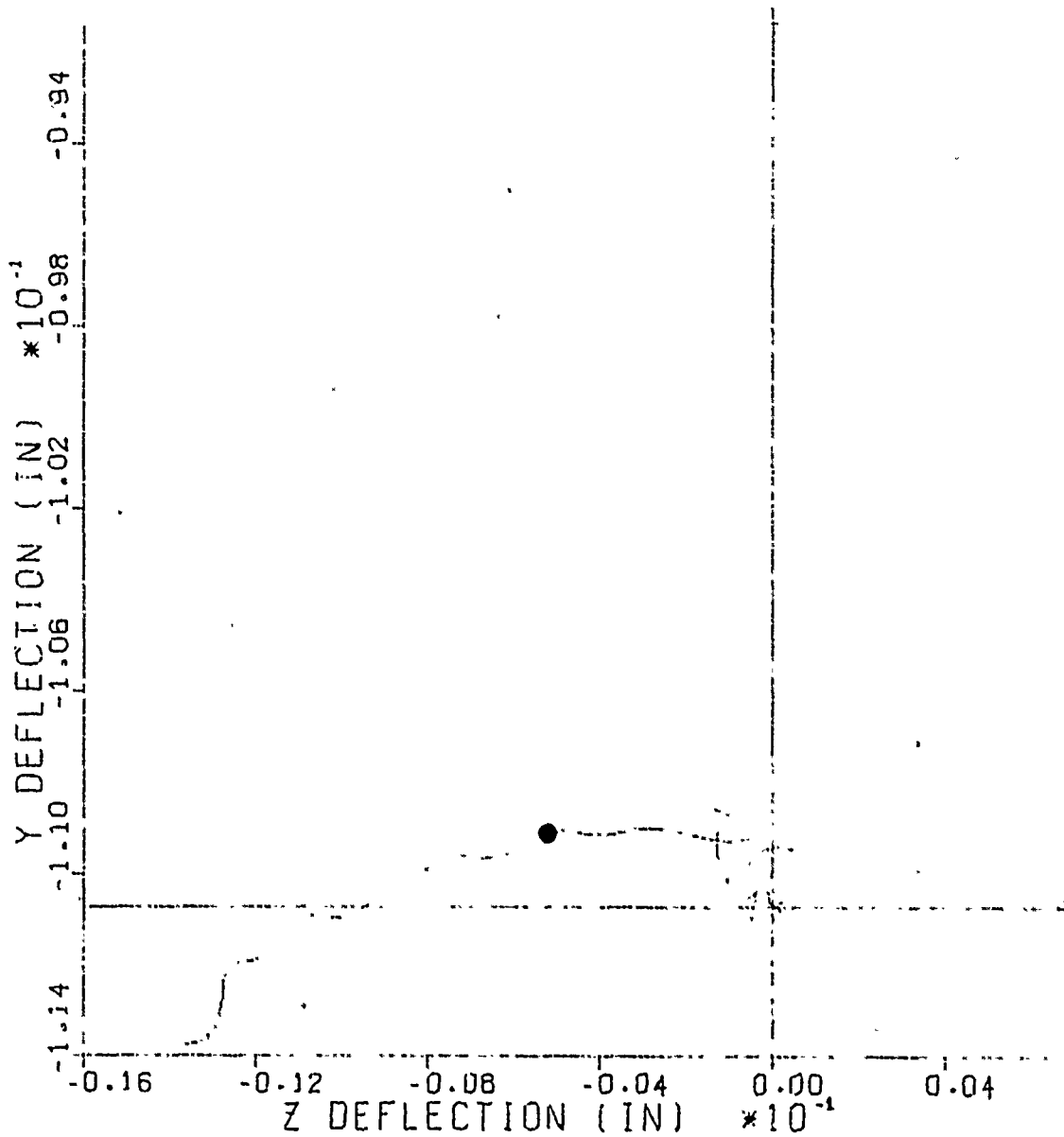


Figure 17. Transverse Muzzle Deflection for
a Balanced 76mm Projectile

generalize the results as much as possible to enable their application to a wide variety of gun systems. The coupling of the two codes remains to be concluded in the future. Once this is achieved, the total projectile barrel interaction dynamics will be described in detail. Experimental confirmation of the codes is also required. Techniques for measuring projectile balloting and barrel motion were developed at NSWC/DL during FY 75. Correlation of the experimental data with the numerical solution would immensely increase user confidence in the program predictions.

V. REFERENCES

1. Perdreauxville, F. J., *Analysis of the Lateral Motion of a Projectile in the Gun Tube*, Research Report SC-RR-710071, Sandia Laboratories, Albuquerque, New Mexico, April 1971.
2. Perdreauxville, F. J., *Analysis of the Lateral Motion of an Unbalanced Projectile in a Rigid Gun Tube*, Report SAND 74-0361, Sandia Laboratories, Albuquerque, New Mexico, December 1974.
3. Perdreauxville, F. J., *Analysis of the Lateral Motion of an Unbalanced Projectile in an Elastic Gun Tube*, Report SAND 74-0362, Sandia Laboratories, Albuquerque, New Mexico, December 1974.
4. Chu, S. H., and Soechting, F. K., *Transverse Motion of an Accelerating Shell*, Technical Report 4314, Picatinny Arsenal, Dover, New Jersey, June 1972.
5. Chu, S. H., *Transverse Motion of Eight-Inch Projectile XM-753 in Gun Tube XM201*, Technical Report 4918, Picatinny Arsenal, Dover, New Jersey, December 1975.
6. Wells, D. A., *Theory and Problems of Lagrangian Dynamics*, Schaum Publishing Company, New York, 1967.
7. *Continuous System Simulation Language III (CSSL3)*, Control Data Corporation, Sunnyvale, California, 1974.
8. Haden, H. G., *Some Theoretical Studies of Gun Barrel Vibration*, Royal Armament Research and Development Establishment Memorandum (P) 45/63, August 1963.

PARAMETRIC RESONANCE IN GUN TUBES

T.E. SIMKINS

T.E. SIMKINS

Watervliet Arsenal

Watervliet, New York

TABLE OF CONTENTS

	<u>Page</u>
ABSTRACT	82
INTRODUCTION AND BACKGROUND	84
EFFECT OF LINEAR DAMPING	86
TWO EXAMPLES OF HILL'S EQUATION	87
PARAMETRIC EXCITATION - ARMAMENT	90
EVIDENCE OF PARAMETRIC RESONANCE IN GUN TUBES	92
EQUATIONS OF MOTION	93
EXAMPLE I - THE MCAAC GUN TUBE	99
MULTIPLE ROUND PARAMETRIC RESONANCE - IMPULSE EXCITATION	103
STABILITY ANALYSIS	106
THE CHARACTERISTIC EXPONENT - MAXIMUM VALUE	109
EXAMPLE II - M139 AUTOMATIC WEAPON	112
DISCUSSION	115
APPENDIX A	117
REFERENCES	123

ABSTRACT

This work examines the likelihood of encountering parametric resonance in gun tubes. The resonance is induced conceptually by the periodic changes in transverse stiffness induced by

- (i) the axial vibrations resulting from a single application of ballistic pressure - "single round parametric resonance".
- (ii) the periodic applications of ballistic pressure such as encountered in an automatic weapon - "multiple round parametric resonance".

Results show that ballistic cycles currently employed in the 60mm MCAAAC semi automatic cannon are not likely to excite single round resonance. Unusually brief cycles, however, are shown to be capable of producing resonance amplifications of three orders of magnitude in less than twenty cycles of axial vibration. By proper design of the pressure cycle and/or the fundamental axial frequency of the tube, this type of resonance is rather easily avoided.

Further results show that for the 20mm M139 machine gun, amplifications in excess of fifty can be reached in under five seconds of continuous firing. A special application of the work of Krajcinovic and Herrmann leads to a set of instability contours from which the growth (characteristic) exponent can be determined as a function of the ratio of natural and excitation frequencies and the product of the ballistic impulse and the tube slenderness ratio. Control or elimination of multi-round resonance can be maintained either through

control of the initial conditions or by designing for mismatch between the transverse frequencies and integral multiples of one-half the excitation frequency, i.e., the firing rate.

INTRODUCTION AND BACKGROUND

Forced vibrations of undamped linear systems are characterized by the differential equation:

$$\ddot{x} + \omega^2 x = f ; \quad \omega^2 = k/m \quad (1)$$

where m and k are the inertia and stiffness parameters of the system and x represents the system displacement. Conventionally m and k are constants and f is a time-variant force which causes resonance if it contains a component having the system period $2\pi/\sqrt{k/m}$. The resonant term is linear in the time variable t and is a particular solution of (1).

If ω is time dependent the solution of equation (1) is much more complicated and in most cases has only been achieved through approximate methods or numerical quadrature. An important subclass of problems exists, however, for which a good deal of theoretical progress has been made. These are problems in which the variation of ω is periodic and f is identically zero. Such cases are represented by the homogeneous linear differential equation:

$$\ddot{x} + \omega^2(t)x = 0 \quad (2)$$

where $\omega^2 = \omega_0^2(1 - \epsilon\phi(t))$

and ϕ is periodic in time. Since this equation is homogeneous it admits a general solution of the form:

$$x = Ax_1(t) + Bx_2(t) \quad (2a)$$

where A and B depend only on the initial conditions of the problem.

Floquet's theorem¹ allows for two solutions of the form:

¹Morse, P. M. and Feshbach, H., Methods of Theoretical Physics, McGraw Hill, 1953, 557.

$$\begin{aligned} x_1(t) &\doteq \phi_1 e^{\gamma t} \\ x_2(t) &= \phi_2 e^{-\gamma t} \end{aligned} \quad (3)$$

Historically, equation (2) is known as Hill's Equation and (3) are its Floquet solutions. (See Appendix A.) The $\phi_i(t)$ have the same periodicity as the 'excitation' function $\Phi(t)$. Thus if γ has a non-zero real part, one of these solutions is unstable and the general solution exhibits exponential growth provided that the initial conditions are not those which would cause the corresponding coefficient of the growth term to vanish. Theoretically it has been shown² that unstable solutions can result whenever the ratio of a system natural frequency to the frequency of excitation takes on values in the neighborhoods of integral multiples of one-half (cf Fig. 1). Thus the primary instability, for example, will be encountered when the excitation frequency approaches twice a natural frequency of the system. We therefore have three fundamental differences between conventional forced-resonance and that induced parametrically:

(a) Forced resonance is independent of the initial conditions whereas parametric resonance is not. Given a force component operating at a natural frequency of a system, resonance must occur whereas a parameter (stiffness, mass) varying periodically at $2/n$ times the system frequency (n an integer) need not produce resonance

²Bolotin, V. V., The Dynamic Stability of Elastic Systems, Holden-Day, 1964, 22-23.

if the initial conditions can be controlled. This is especially significant when the short term response of a system is of interest for there is a wide choice of initial conditions for which the early response will have decreasing amplitude.

(b) Forced resonance consists of oscillations whose amplitude increases linearly with time whereas parametric resonance produces exponential growth.

(c) Forced resonance occurs if and only if the forcing frequency exactly equals a natural frequency of the system. In contrast parametric resonance can occur whenever an integral multiple of the excitation frequency approaches twice the value of a natural frequency. That is, parametric resonance - unlike forced resonance - is not a singular phenomenon but occurs throughout the neighborhood regions of a countable infinity of critical frequency ratios. It is therefore a regional phenomenon. An infinity of unstable regions exist, the most important of which is the primary region of instability.

Effect of Linear Damping

The addition of the linear damping term, $2c\dot{x}$, into equation (2) creates no complication since a transformation $x = vw$ can always be found (even when c is time dependent) - such that $w = e^{-\int c dt}$ and v solves the differential equation:

$$\ddot{v} - [c^2 + \dot{c} - \omega^2(1 - \epsilon\phi(t))]\dot{v} = 0$$

which has the form of equation (2) and therefore possesses solutions

(3). Thus

$$x = vw = A\phi_2(t)e^{[\gamma t - \int c dt]} + B\phi_2(t)e^{-[\gamma t - \int c dt]}$$

i.e., the inclusion of a linear damping term results in a simple subtraction from γ .

Two Examples of Hill's Equation

Several examples of Hill's equation are given in the literature^{2,3}. The one most often cited pertains to a beam column subjected to a periodically varying axial compressive load $P(t)$ such as depicted in figure a below:

Figure (a) - Classical Beam Problem Governed by Hill's Equation

The governing differential equation from Euler-Bernoulli beam theory is:

$$EI \frac{\partial^4 u}{\partial x^4} + P(t) \frac{\partial^2 u}{\partial x^2} + \rho \frac{\partial^2 u}{\partial t^2} = 0 \quad (4)$$

As Krajcinovic and Hermann⁵ have pointed out, an attempt to separate variables through the substitution $u(x,t) = X(t)f(t)$ will result in the ordinary differential equation:

²Bolotin, V. V., The Dynamic Stability of Elastic Systems, Holden-Day, 1964, 22-23.

³Den Hartog, J. P., Mechanical Vibrations, McGraw Hill, 1940, 378.

⁵Krajcinovic, P. P. and Hermann, G., Stability of Straight Bars Subjected to Repeated Impulsive Compression, AIAA Journal, Oct 68, 2025-2027.

$$\frac{EI}{\rho} \frac{X^{iv}}{X} + \frac{P(t)}{\rho} \frac{X''}{X} = -\frac{\ddot{f}}{f}$$

Since the right hand side of this equation is independent of x :

$$\frac{EIX^{iv}}{\rho X} = \text{const} = \alpha$$

and

$$\frac{X''}{\rho X} = \text{const} = \alpha\beta$$

$$\text{Thus} \quad \ddot{f} + \alpha[1 - \beta P(t)]f = 0 \quad (5a)$$

$$\text{and} \quad EIX^{iv} - \alpha\rho X = 0 \quad (5b)$$

$$\text{and} \quad EIX^{iv} + \frac{1}{\beta} X'' = 0 \quad (5c)$$

While equation (5a) is the desired Hill's equation for the system, the separation of variables approach is only valid when $X(x)$ also satisfies equations (5b) and (5c); i.e., the modes of free vibration which solve (5b), must be identical to the buckling modes which solve (5c). The case depicted in figure (a) - a hinged-hinged support system - does in fact satisfy both of these conditions. In most cases, however, the boundary conditions lead to modes which do not satisfy both (5b) and (5c). In such cases an approximate Hill's equation can be obtained through a variational procedure, such as that due to Galerkin. In either case, therefore, the problem is reduced to the analysis of equation (5a) where α and β derive from an analysis which is either exact or approximate.

Another example - one which more directly leads to Hill's equation - considers a system with time-variant inertia, such as a child pumping a swing (figure b). Essentially a concentrated mass is raised and lowered periodically along a relatively massless rod

(or chain, etc.) which pivots at 0. The rotational inertia of the pendulum thus varies periodically in time. The example is one where the path taken by the mass through the gravitational field results in a net amount of work per cycle of the motion.

The equation of motion:

$$\begin{aligned} -\ell(t)mg \sin\theta &= \frac{d}{dt} (m\ell^2(t)\dot{\theta}) \\ &= 2m\ell \frac{d\ell}{dt} \frac{d\theta}{dt} + m\ell^2 \frac{d^2\theta}{dt^2} \quad (6) \end{aligned}$$

Approximating: $\sin \theta \sim \theta$,

$$\ell(t) \frac{d^2\theta}{dt^2} + 2 \frac{d\ell}{dt} \frac{d\theta}{dt} + g\theta = 0$$

Figure (b) - Swing Problem Leading to Hill's Equation

Defining $\ell = \ell_0 + h(t)$, $\tau = \omega t$, and $\omega^2 = g/\ell_0$ leads to the nondimensional equivalent of equation (6):

$$\left(1 + \frac{h(\tau)}{\ell_0}\right) \ddot{\theta} + 2 \frac{\dot{h}}{\ell_0} \dot{\theta} + \theta = 0 \quad ; \quad (\dot{}) = d/d\tau$$

If $h(\tau) = \ell_0 \epsilon \cos 2\tau$ and only first order terms in ϵ are retained:

$$\ddot{\theta} - 4\epsilon \sin 2\tau \dot{\theta} + (1 - \epsilon \cos 2\tau)\theta = 0 \quad (7)$$

Through the afore-mentioned transformation $\theta = vw$, the equation for v and w are:

$$\ddot{v} + (1 + 3\epsilon \cos 2\tau)v = 0 \quad (\text{Hill's Equation})$$

and

$$w = e^{-\epsilon \cos 2\tau}$$

A great amount of consideration has been given⁶ to cases where the 'characteristic exponent' γ , is purely imaginary and the periodic excitation $\Phi(t)$ is sinusoidal. Equation (2) then reads:

$$\ddot{x} + (a - 2q \cos 2\tau)x = 0 \quad (8)$$

This equation - a special case of Hill's equation - is called Mathieu's Equation (canonical form). As with any Hill's equation, Mathieu's equation yields periodic solutions (called Mathieu functions) corresponding to purely imaginary, rational values of the characteristic exponent γ . With a view toward special armament applications, however, this report will deal only with the unstable solutions of Hill's equation, i.e., those cases in which γ is real.

PARAMETRIC EXCITATION - ARMAMENT

There are at least two possible sources of parametric excitation in gun tubes - that is, two ways in which periodic coefficients can be introduced into the beam equations of motion. The most obvious can be called 'multiple round excitation' and derives from the periodicity present in automatic weapons in which several time-variant forces operate at the firing rate of the weapon. A reasonably comprehensive

⁶McLachlan, N. W., Theory and Application of Mathieu Functions, Oxford Clarendon Press, 1947.

differential equation including these forces was derived in a previous report⁷. Figure (2) shows a cantilevered beam model of a gun tube acted upon by several curvature-induced loads (constant projectile velocity is assumed for simplicity). In general one observes several time dependent coefficients multiplying the various displacement derivatives. In automatic weapons, these coefficients are reproduced periodically according to the firing rate and will appear in the Hill's equation obtained upon integration of the space variable. In this report the effects of only one such term will be investigated - namely, that corresponding to the periodic ballistic pressure applied axially at the breech.

A second and less obvious cause of parametric excitation derives from the coupling between axial and transverse tube vibrations. The simplest equation incorporating the necessary nonlinear coupling terms was derived by McIvor and Bernard⁸ in 1973. Essentially the idea is that a single impulsively applied load will set a column ringing with free axial vibrations. Nonlinear terms - oscillating at the frequency of these vibrations, couple with the transverse displacement variables through the stiffness coefficients. We can call this 'single round excitation'. Thus kinetic energy from the axial vibrations can feed transverse modes and lead to parametric resonance. The governing

⁷Simkins, T., Pflegl, G., Scanlon, R., Dynamic Response of the M113 Gun Tube to Travelling Ballistic Pressure and Data Smoothing as Applied to XM150 Acceleration Data, WVT-TR-75015.

⁸McIvor, J. K., and Bernard, J. E., The Dynamic Response of Columns Under Short Duration Axial Loads, Trans ASME, September 1973, 688.

differential equations were solved by the authors through a Galerkin procedure for the special case of a simply supported beam subjected to an axial end load of short duration. [It should be noted, however, that there is no guarantee that the variational quantity employed will indeed admit an extremum when the associated differential operator is nonlinear.] Since a good deal of energy is apt to be consumed in rigid body recoil in armament applications, fixed supports are to be avoided. Consequently a tube (beam) cantilevered from end supports which allow axial movement (figure 5) was chosen as the subject of analysis for this report. (Relative motion of the support is ignored.)

Evidence of Parametric Resonance in Gun Tubes

In order to minimize shot dispersion in automatic weapons the current design handbook⁹ dealing with gun tube design advises that the ratio of the fundamental transverse frequency of the tube to the firing rate be kept greater than 3.5. The basis for this value is a plot of shot dispersion vs. frequency ratio R_f appearing in the handbook and reproduced as figure 3 of this report. Referring to this figure three very prominent maxima are observed at successive integral values of $R_f = 1, 2$ and 3 . The reference cited in connection with this plot is a 1955 report by Wente, Schoenberger and Quinn of Purdue University¹⁰. Their results, shown in figure 4, are in marked contrast to those of figure 3, however. Absent is the maximum at $R_f = 3.0$ shown in figure 3.

⁹AMCP 706-252, Engineering Design Handbook, Gun Series, Gun Tubes, February 1964.

¹⁰Wente, B. E., Schoenberger, R. L., and Quinn, B. E., An Investigation of the Effect of the Natural Frequency of Vibration of the Barrel Upon the Dispersion of an Automatic Weapon, Purdue U., 1955, AD64132.

It is also noted that figure 4 contains no information below the value $R_f = 1.0$. Thus the only features common to both figures are apparently the maxima at $R_f = 1.0$ and $R_f = 2.0$. Accepting these maxima as the only credible information to be gleaned from the reference publications one searches for an explanation as to their cause. While the maximum at $R_f = 1.0$ may be attributed either to parametric or to ordinary (forced) resonance, that at $R_f = 2.0$ cannot be due to ordinary resonance and may be evidence of parametric resonance - which, as previously discussed, can be expected to occur near nominal values of $R_f = 1/2, 1, 3/2, \dots, n/2, \dots$. Though parametric resonance should also produce a dispersion maximum at $R_f = 1.5$ in Wente's plot, it may be that it has been missed due to the paucity of data points.

Equations of Motion

The model chosen to represent armament applications is shown in figure 5. The equations of motion which include coupling between transverse and axial displacements are those of McIvor and Bernard⁸. Eliminating their dissipation parameter for simplicity, these are:

$$\ddot{u} - [u' + \frac{1}{2} v'^2]' = 0 \quad (9a)$$

$$\ddot{v} + \alpha^2 v'' - (u'v')' = 0 \quad (9b)$$

Boundary Conditions

$$P(\tau)/EA = \epsilon_a(0, \tau) = [\frac{\partial u}{\partial s} + \frac{1}{2} (\frac{\partial v}{\partial s})^2]_{0, \tau} \quad a$$

$$0 = \epsilon_a(1, \tau) = [\frac{\partial u}{\partial s} + \frac{1}{2} (\frac{\partial v}{\partial s})^2]_{1, \tau} \quad b$$

⁸McIvor, J. K., and Bernard, J. E., The Dynamic Response of Columns Under Short Duration Axial Loads, Trans ASME, September 1973, 688.

$$0 = v(0, \tau) \quad c$$

$$0 = v''(1, \tau) \quad d$$

$$0 = v'(0, \tau) \quad e$$

$$0 = v'''(0, \tau) \quad f$$

where: $u = \eta/L$ = dimensionless axial displacement
 $v = \xi/L$ = dimensionless transverse displacement
 $s = x/L$ = dimensionless coordinate
 $\alpha^2 = I/AL^2$ = square of the reciprocal of the slenderness ratio
 $\tau = at/L$ = dimensionless time variable
 $a = (EA/\rho)^{1/2}$ = extensional wave speed
 E = Young's Modulus of Elasticity
 A = Beam Cross sectional area
 ρ = mass per unit length
 I = area moment of inertia
 $P(\tau)$ = end loading, a ballistic pressure function of duration τ_0
 ϵ_a = axial strain including lowest ordered nonlinearity

Multiplying (9a) and (9b) by δu and δv respectively and integrating over the length of the beam:

$$\int_0^1 (\ddot{u} \delta u - [u' + \frac{1}{2} v'^2]' \delta u) ds = 0 \quad (10a)$$

$$\int_0^1 (\ddot{v} \delta v - [u' v']' \delta v + \alpha^2 v' \delta v) ds = 0 \quad (10b)$$

Using boundary conditions a and b together with an integration by parts, (10a) becomes:

$$\int_0^1 \{ \ddot{u} \delta u + [u' + \frac{1}{2} v'^2] \delta u' \} ds + \frac{P(\tau)}{EA} \delta u(0, \tau) = 0 \quad (11a)$$

Similarly, boundary conditions b through f applied to (10b) yield:

$$\int_0^1 (\ddot{v} \delta v + u' v' \delta v' + \alpha^2 v'' \delta v'') ds + \frac{1}{2} v'(1, \tau)^3 \delta v(1, \tau) = 0 \quad (11b)$$

The last term in (11b) is an order higher than those retained and is therefore ignored. Except for the boundary terms, equations (11) are identical to those obtained by McIvor and Bernard for the case of a simply supported beam under end loading. Our boundary conditions, however, dictate a choice of completely different approximating functions in the Galerkin approach to solution. Since both ends of the beam in our problem are free to move axially, we must choose functions which do not constrain the function u at the end points $(0,1)$, i.e., there are no geometric constraints such as are present in the problem solved by McIvor and Bernard. A set of functions which appear to satisfy these requirements:

$$u = \sum_j q_j(\tau) \cos j\pi s \quad ; \quad j = 0, 1, 2, \dots \quad (12)$$

For the transverse motion, the eigenfunctions of a cantilevered beam satisfy the conditions c thru f. Hence:

$$v = \sum_m T_m(\tau) W_m(s) \quad ; \quad m = 1, 2, 3, \dots \quad (13)$$

where

$$W_m(s) = \cosh \beta_m s - \cos \beta_m s - \frac{\cosh \beta_m + \cos \beta_m}{\sinh \beta_m + \sin \beta_m} (\sinh \beta_m s - \sin \beta_m s)$$

and the β_m have values 1.875, 4.694, 7.855, etc.; further values can be found in any standard vibrations textbook (cf ref 11).

Substitution of (12) and (13) into equations (11) and making use of the orthogonality of the trial functions and the independence of the variational quantities δq_j and δT_m leads to the following sets of nonlinearly coupled, ordinary differential equations:

$$j = 0 : \quad \ddot{q}_0 = -P(\tau)/EA \quad (14)$$

$$j = 1, 2, \dots \quad \ddot{q}_j + (j\pi)^2 q_j + \sum_{m,n} A_{jmn} T_m T_n = -2P(\tau)/EA \quad (15a)$$

$$m = 1, 2, \dots \quad \ddot{T}_m + \alpha^2 \beta_m^4 T_m + \sum_{j,n} A_{jmn} q_j T_n = 0 \quad (15b)$$

where the A_{jmn} are defined from the integration:

$$\int_0^1 v'^2 \delta u' ds = -\pi \int_0^1 \sum_m T_m W_m' \sum_n T_n W_n' \sum_{j=1,2,\dots} j \delta q_j \sin j \pi s ds \equiv \sum_{j,m,n} A_{jmn} T_m T_n \delta q_j$$

Table I gives the values of these coupling coefficients through A_{666} . Equation (14) is decoupled from the others and being representative of rigid body motion is of no further interest. Equations (15) can be solved numerically by any of several numerical integration programs¹² once α has been specified along with the nondimensional load function $P(\tau)/EA$.

¹¹ Nowacki, W., Dynamics of Elastic Systems, Chapman and Hall, 1963, 122.

¹² Ralston and Wilt, Mathematical Methods for Digital Computations, Wiley, 1960, 95-109.

RESONANCE

During parametric resonance certain transverse coordinates $T_m(\tau)$ become much larger than the rest. Thus the quadratic coupling terms can be ignored except those expected to resonate. In single round resonance it is expected that the response to $P(\tau)$ will mainly occur in the $q_1(\tau)$ variable (i.e., the fundamental axial mode) and therefore only one such term need be considered. If $m = M$ represents the particular transverse mode such that $\alpha\beta_M^2 = \pi/2$, primary parametric resonance will result. That is, the natural frequency $\alpha\beta_M^2$ is half the frequency of the exciting variable $q_1 = A \sin \pi \tau$, $\tau \leq \tau_0$, where τ_0 is the duration of the load pulse $P(\tau)$.

For the study of single round parametric resonance therefore, equations (15) reduce to:

$$\ddot{q}_1 + \pi^2 q_1 = -2P(\tau)/EA \equiv -2P^*(\tau) ; \quad \tau \leq \tau_0 \quad (16a)$$

$$\ddot{T}_M + (\alpha^2 \beta_M^4 + A_{1MM} q_1(\tau)) T_M = 0 \quad (16b)$$

In multiple round resonance, transient axial vibrations are ignored and the $q_j(\tau)$ are assumed to follow periodic applications of the load function quasi-statically. In this case, if the firing rate is twice the M th transverse frequency, parametric resonance will result. Since all of the $q_j(\tau)$ are periodic according to the firing rate, it is not acceptable to retain only the term in q_1 as in the case of single round resonance. However, the amplitudes of these quasi-static responses attenuate as $1/j^2$ (neglecting the quadratic term in 15a) and only a few need be retained for accuracy. In place of

equations (15) we therefore have:

$$\ddot{q}_j + (j\pi)^2 q_j = -2P(\tau)/EA \equiv -2P^*(\tau) \quad (17a)$$

$$\ddot{T}_M + (\alpha^2 \beta_M^4 + \sum_j A_{jMM} q_j(\tau)) T_M = 0 \quad (17b)$$

where $\frac{\alpha \beta_M^2}{2\pi} \doteq (\text{weapon firing rate})/2$

The periodic character of the q_j in either (16b) or (17b) qualifies these as Hill's equations. As earlier indicated, the general solution to Hill's equation can be written as:

$$T_M(\tau) = a\phi_1(\tau)e^{\gamma\tau} + b\phi_2(\tau)e^{-\gamma\tau} \quad (18)$$

where the ϕ_i are periodic functions having the period of q_j .

It should be mentioned in passing that when γ is real, a plot of the solution (18) will always show oscillations near the natural frequency $\alpha\beta_M^2$ even though the ϕ_i have the same period as q , i.e., approximately half the natural period $\frac{2\pi}{\alpha\beta_M^2}$. That is, the periodicity is not representative of the oscillatory appearance of the response.

It can be shown (see Appendix A) that once a solution for Hill's equation is obtained over one period of the excitation, it can be extended analytically for all time by means of Floquet's theorem. Further, in the case of Mathieu's equation, analytical methods have been developed leading to the direct determination of γ , the characteristic exponent. A detailed series of curves for this purpose were developed by S. J. Zaroodny¹³ in 1955.

¹³Zaroodny, S. J., An Elementary Review of the Mathieu-Hill Equation of a Real Variable Based on Numerical Solutions, Ballistic Research Laboratory Memo. Report 878, Aberdeen Proving Ground, MD, 1955.

EXAMPLE I - THE MCAAAC GUN TUBE

It is of interest to assess the likelihood of encountering single round parametric resonance in the particularly long and slender tube planned for the Medium Caliber Anti-Armor Automatic Cannon* currently in the design stage. To this end equations (16) will be employed after first establishing the magnitude of $P^*(\tau)$ and the mode M in which resonance might be expected.

Equation (16b) always possess the (trivial) solution $T_M = 0$. This solution only applies when the 'initial' conditions of displacement and velocity following the application of the load $P(\tau)$ are identically zero in which case the response T_M will be null no matter how intense the 'excitation' $q_j(\tau)$. This is of little concern in armament applications since a good deal of transverse motion is certain to be excited by the firing of a round. For example the recoil of a slightly curved gun tube or the motion of the projectile therein will always excite some non-zero 'initial' motion. The axial vibration $q_1(\tau)$ in response to the ballistic pressure pulse will generally result in amplification of these initial motions by its appearance in equation (16) if the parameter α happens to be 'tuned' for parametric resonance.

According to results from the latest finite element (NASTRAN) model of the MCAAAC tube (see Table II), the fundamental axial frequency is very close to being twice the frequency of the fifth transverse mode -

* The MCAAAC concept plans for a two or three round 'burst' and is therefore not an automatic weapon in the same sense as a conventional machine gun. Thus multi-round resonance is thought not to apply and the investigation is confined to that of resonance which might be induced from the firing of a single round.

making primary parametric resonance of this mode a possibility if enough axial excitation is produced from the application of ballistic pressure to the breech. The parameters for a uniform beam model of this tube were chosen, therefore, so that the fundamental axial frequency of 580 hz corresponds to π in equation (16a) and exactly half this value corresponds to $\alpha\beta_5^2$ of equation (16b). A summary of the pertinent parameters implied by these assumptions appears in Table III. The load function is approximated by a haversine shape. Thus (16a) reads:

$$\ddot{q}_1 + \pi^2 q_1 = -P_0^* (1 - \cos \frac{2\pi\tau}{\tau_0}) ; \quad \tau \leq \tau_0$$

The response following the termination of ballistic pressure is sinusoidal with amplitude:

$$q_1(\max) = \left| 2P_0^* \left(\frac{\sin \pi\tau_0/2}{1 - (\frac{\tau_0}{2})^2} \right) \right|$$

Assuming negligible response from the other axial modes, equation (16) becomes (for suitable choice of 'initial' time zero):

$$\ddot{T}_5 + \alpha^2 \beta_5^4 (1 + \epsilon \cos \pi\tau) T_5 = 0$$

$$\text{where } \epsilon = A_{155} q_1(\max) / \alpha^2 \beta_5^4$$

Using values from Tables I and III, ϵ is evaluated at 2.07×10^{-2} . The solution for T_5 is given by expression (18). In view of the smallness of ϵ and the precise state of tuning assumed, a very good approximation for γ can be obtained by the method of strained parameters¹⁴. The result is:

$$\gamma \doteq \pi\epsilon/8$$

¹⁴Nayfeh, A. H., Perturbation Methods, John Wiley, 1973, 63.

In real time the magnitude of this exponent (see Table III) becomes:

$$\frac{\pi E}{8} \times 1160 \doteq 9.44$$

In general the coefficient of the growth term in (18) depends on both the initial displacement and velocity of the Mth transverse mode at 'time zero'. It is this quantity which is amplified, the remaining term of (18) becoming less important as time moves on. As a specific example it is notable that for certain initial conditions (see Appendix A), the general solution (18) degenerates to:

$$T_M(\tau) = C\phi_1(\tau)e^{\gamma\tau} ; \gamma > 0$$

In this case any transverse initial displacement $T_5(0)$ is amplified according to the multiplier $e^{\gamma\tau}$. The real time computed value of 9.44 implies an amplification factor of nearly three orders of magnitude only 3/4 seconds after excitation. In practice, however, this build-up is unlikely owing to the attenuating effect of damping and the improbable state of tuning and initial conditions necessary for maximum γ .

The probability of experiencing single round parametric resonance can be significantly increased if the duration of the ballistic cycle becomes briefer than that assumed. Actually, it is the ratio of the period of the ballistic pulse - whatever its shape - to the fundamental axial period which is of importance. Figure 6¹⁵ shows the

¹⁵Harris, C. M., and Crede, C. E., Shock and Vibration Handbook, Vol. I - Basic Theory and Measurements, McGraw-Hill, 1961, 8-24.

enormous influence of this ratio on the value of γ . For example, a haversine pulse of ratio 0.8 will solicit an axial response $[q_1(\max)]$ which is about twenty-five times greater than the previous case (where the ratio was approximately 3.5). Since γ directly depends on $q_1(\max)$, an amplification of three orders of magnitude is realized in less than seventeen cycles of axial vibration (about 30 milliseconds). In view of this potential for large γ it is therefore important that the design of a weapon be such that axial vibration magnitudes be kept small - principally by creating intentional mismatch between the fundamental axial period and the period of the ballistic cycle. Referring again to figure 6, a haversine ballistic period should be at least twice the fundamental axial period. For ballistic pulse shapes which deviate considerably from a haversine, a response spectrum similar to that of figure 6 can be easily derived via computer.

Before moving on to a specific example in multiple round resonance, some consideration should be given to the manner in which the excitation differs from that considered in the single round situation. As previously stated it is not the free axial vibrations but rather the quasi-static responses of the axial modes which serve as excitation of transverse vibrations. For example if $P^*(\tau)$ is a single haversine pulse of duration τ_0 :

$$\text{i.e. } P^*(\tau) = P_0^*/2(1 - \cos 2\pi\tau/\tau_0)$$

then the solution to (17a) is:

$$q_j(\tau) = \frac{-p_0^*}{(j\pi)^2} \left[1 - \frac{\tau_0^2}{\tau_0^2 - (\frac{2}{j})^2} \cos \frac{2\pi\tau}{\tau_0} + \frac{(\frac{2}{j})^2}{\tau_0^2 - (\frac{2}{j})^2} \cos j\pi\tau \right] \quad (19)$$

If $\tau_0 \gg 2/j$, the natural period, then

$$q_j \doteq -2p^*(\tau)/(j\pi)^2 \quad (20)$$

that is, the response is quasi-static. In all weapons of short tube length - typically automatic small arms - the ballistic period is much longer than the fundamental natural period of axial vibration and the assumption, $\tau_0 \gg 2/j$ is justified. Thus the oscillatory terms in the solution (19) can be neglected with little sacrifice to accuracy. On the other hand while τ_0 may be long compared to the fundamental axial period, it is very short when compared to the periods of the first few transverse modes. It is tempting, therefore, to consider replacing the $q_j(\tau)$ - as they appear in (17b) - by impulsive type terms. It will be shown that such a replacement sacrifices little in the way of accuracy and leads to a very convenient consolidation of results.

Multiple Round Parametric Resonance - Impulse Excitation

In 1968, D. P. Krajcinovic and G. Herrmann published work⁵ dealing with the parametric resonance of bars subjected to repeated impulsive compression. The equation studied by the authors can be obtained by substituting the quasi-static solutions of (17a) into (17b):

$$\ddot{T}_M + \Omega_M^2 [1 - \nu_M p^*(\tau)] T_M = 0 \quad (21)$$

⁵Krajcinovic, P. P. and Herrmann, G., Stability of Straight Bars Subjected to Repeated Impulsive Compression, AIAA Journal, Oct. 68, 2025-2027.

where

$$\Omega_M^2 = \alpha^2 \beta_M^4 \quad \text{and} \quad v_M = \sum_j 2A_{jMM} / (j\pi\Omega_M)^2$$

The load function considered by Krajcinovic and Herrmann:

$$P^*(\tau) = P_1^* + P_0^* \sum_{k=-\infty}^{k=\infty} \delta(\theta\tau - k\theta\bar{\tau}) \quad (22)$$

where $\bar{\tau}$ is the period of $P^*(\tau)$. Physically, (22) represents an infinite series of impulsively applied compressive loads superposed upon a steady load of magnitude P_1^* . $\delta(z)$ represents the Dirac function and θ is a parameter having the dimensions of frequency. In practice the authors did not have to deal with the full load expression (22) but only one cycle thereof, for example - a single impulse applied at $\tau = \bar{\tau}$. This is possible because Floquet theory (see Appendix A) enables the solution over one period of the excitation to be extended indefinitely in time. Furthermore, questions of stability can be answered by considering whether the motion grows or decays as a result of a single load application. Thus the load function actually used for analysis was equivalent to:

$$P^*(\tau) = P_0^* \delta[\theta(\tau - \bar{\tau})] \quad (23)$$

that is, a single impulsively applied load at $\tau = \bar{\tau}$.

Defining $v_M P_0^* = \mu_M$, equation (21) becomes:

$$\ddot{T} + \Omega^2 [1 - \mu \delta(\theta(\tau - \bar{\tau}))] T = 0 \quad (24)$$

(The subscript M is implied throughout.)

Now two linearly independent solutions to equation (24) which satisfy the unitary initial conditions (26) are:

$$\begin{aligned} T_1(\tau) &= \cos \Omega \tau \\ T_2(\tau) &= \frac{1}{\Omega} \sin \Omega \tau \end{aligned} \quad (28)$$

$$\dots \tau \leq \bar{\tau}$$

In order to use the inequality (27), the values of $T_1(\bar{\tau}^+)$ and $\dot{T}_2(\bar{\tau}^+)$ are required. While the functions themselves are continuous at $\tau = \bar{\tau}$, their derivatives are not - owing to the application of the impulse at this instant. Thus the derivative, $\dot{T}_2(\bar{\tau})$ cannot be obtained by simply substituting into the derivative expression for T_2 . The step change in the derivative, however, can be computed by a direct integration of equation (24) over a short time interval containing the point $\tau = \bar{\tau}$.

$$\text{i.e.} \quad \left[\dot{T} \right]_{\bar{\tau}-\epsilon}^{\bar{\tau}+\epsilon} = \int_{\bar{\tau}-\epsilon}^{\bar{\tau}+\epsilon} \Omega^2 [\mu \delta(\theta(\tau - \bar{\tau}) - 1)] T(\tau) d\tau$$

Since $T(\tau)$ is continuous at $\bar{\tau}$, the term $\Omega^2 T$ contributes nothing to the integral as ϵ is made vanishingly small. Thus

$$\left[\dot{T} \right]_{\bar{\tau}-\epsilon}^{\bar{\tau}+\epsilon} = \frac{\Omega^2 \mu T(\bar{\tau})}{|\theta|} \quad (\epsilon \rightarrow 0) \quad (29)$$

The right hand side of (29) derives from the relation:

$$\int_{-\infty}^{\infty} \delta(az) \phi(z) dz = \frac{1}{|a|} \int_{-\infty}^{\infty} \delta(z) \phi\left(\frac{z}{a}\right) dz = \frac{1}{|a|} \phi(0)$$

where $\phi(z)$ is a test function. Since θ is arbitrary it can always be chosen as positive and the absolute signs omitted accordingly.

Stability Analysis

Floquet's theorem¹⁶ guarantees the existence of particular solutions $T(\tau)$, to equation (24) such that

$$T(\tau + \bar{\tau}) = \rho T(\tau) \quad (25)$$

where $\bar{\tau}$ is the period of the applied load. We are interested in determining the conditions under which ρ may be real and have an absolute value greater than unity indicating a growth of the response amplitude after one period of the excitation. Bolotin¹⁷ has shown that if two linearly independent solutions $T_1(\tau)$ and $T_2(\tau)$ are chosen which satisfy the so-called 'unitary conditions':

$$\begin{aligned} T_1(0) &= 1 & \dot{T}_1(0) &= 0 \\ T_2(0) &= 0 & \dot{T}_2(0) &= 1 \end{aligned} \quad (26)$$

then the equation for ρ becomes simply:

$$\rho^2 - 2A\rho + 1 = 0$$

where

$$A = \frac{1}{2}[T_1(\bar{\tau}^+) + \dot{T}_2(\bar{\tau}^+)]$$

The condition that a value of ρ exists with $|\rho| > 1$, therefore amounts to:

$$|A| > 1 \quad (27)$$

It is also apparent that the two roots of the quadratic equation are reciprocal - i.e., $\rho_1\rho_2 = 1$.

¹⁶Meirovitch, L., Methods of Analytical Dynamics, McGraw-Hill, 1970, 264.

¹⁷Bolotin, V. V., The Dynamic Stability of Elastic Systems, Holden-Day, 1964, 14.

Thus, from (29):

$$\dot{T}_2(\bar{\tau}^+) = \frac{\Omega^2 \mu}{\theta} T_2(\bar{\tau}) + \dot{T}_2(\bar{\tau}^-) = \frac{\Omega^2 \mu}{\theta} T_2(\bar{\tau}) + \cos \Omega \bar{\tau}$$

hence

$$|A| = \frac{1}{2} \left| 2 \cos \Omega \bar{\tau} + \frac{\Omega \mu}{\theta} \sin \Omega \bar{\tau} \right|$$

Thus the instability condition (27) becomes:

$$|A| = \left| \frac{\Omega \mu}{2\theta} \sin \Omega \bar{\tau} + \cos \Omega \bar{\tau} \right| > 1 \quad (30)$$

In the work performed by Krajcinovic and Herrmann, θ is defined as being inversely proportional to $\bar{\tau}$ ($\theta = \frac{2\pi}{\bar{\tau}}$) which is the customary definition when treating continuous excitation functions. Adhering to this definition in the case of repetitive, discontinuous loads, however, leads to a load function which is physically improbable.

For the load function (23):

$$\text{i.e.} \quad P^*(\tau) = P_0^* \delta[\theta(\tau - \bar{\tau})]$$

the impulse of this load under the above definition of θ becomes:

$$P_0^* \int_{-\infty}^{\infty} \delta[\theta(\tau - \bar{\tau})] d\tau = \frac{P_0^*}{\theta} = \frac{P_0^* \bar{\tau}}{2\pi} \quad (31)$$

that is, the impulse strength is seen to depend on $\bar{\tau}$, the period of time between impulses. This is not the physical situation of interest in armament - and many other - applications which imply a sequence of equally strong impulses independent of their spacing in time.

Fortunately, these cases can be handled merely by redefining θ , i.e.,

let $\theta = \frac{1}{\tau_0}$, where τ_0 represents the duration of the ballistic load function as shown in figure c.

Figure (c) - Periodic Ballistic Pressure Function.

Under this definition of θ , the impulse (31) becomes:

$$\frac{P_0^*}{\theta} = P_0^* \tau_0 \equiv I_0$$

I_0 is defined as an impulse conveyed by a load of average value P_0^* and duration τ_0 . In practice $P^*(\tau)$ in equation (21) is to be replaced by the load function $P_0^* \delta[\theta(\tau - \bar{\tau})]$ which has the same impulse as $P^*(\tau)$. Thus P_0^* must represent the nondimensional time average axial load on the breech due to ballistic pressure.

The result of redefining θ on the instability condition (30) is considerable. Whereas the expression for A in (30) is purely a function of μ and the ratio of the natural frequency to that of the excitation, this is not the case when the meaning of θ is changed. Substituting $\theta = 1/\tau_0$ into (30) the condition for instability becomes:

$$|A| = \left| \frac{\Omega_M \tau_0}{2} \sin \Omega_M \bar{\tau} + \cos \Omega_M \bar{\tau} \right| > 1 \quad (32)$$

Thus for the Mth equation (17b) we have $\mu = \mu_M$ and $\Omega = \Omega_M$ as previously defined so that (32) becomes finally,

$$\begin{aligned} |A_M| &= \left| \sum_j \frac{A_{jMM}}{(j\pi\beta_M)^2} \frac{I_0}{\alpha} \sin \Omega_M \bar{\tau} + \cos \Omega_M \bar{\tau} \right| \equiv \\ &\equiv \left| \frac{C_M I_0}{\alpha} \sin 2\pi \frac{\Omega_M}{\omega_e} + \cos 2\pi \frac{\Omega_M}{\omega_e} \right| \end{aligned} \quad (33)$$

where definitions for C_M and ω_e are inferred. ω_e now represents the frequency of the impulse excitation instead of θ . A_M is seen to depend on I_0/α - the product of the impulse and the slenderness ratio - and the ratio of the unperturbed natural frequency to that of the excitation. It is also apparent that in contrast to (30), A_M is now periodic in the frequency ratio implying equal stability criteria for all 'zones' of instability $\frac{\Omega_M}{\omega_e} = 1/2, 1, 3/2, \dots, n/2, \dots$

The Characteristic Exponent - Maximum Value

The general solution to Hill's equation (17b) is given by (18). This solution, having property (25), implies the following definition for γ , the characteristic, or 'growth', exponent:

$$\gamma = \frac{\ln |\rho|}{\bar{\tau}} ; \quad \gamma \text{ real}$$

For a given excitation frequency ω_e , $\bar{\tau}$ is a specified quantity and maximum values of $|\rho|$ determine maximum γ . In calculating the particular frequency ratio for which $|\rho|$ will be maximum, we first let

$$\Omega_M/\omega_e = n/2 + \delta$$

n designates the zone of instability while δ a local coordinate to be varied in searching for a maximum value of $|\rho|$. Substituting in (33):

$$A_M = \left[\frac{C_M I_0}{\alpha} \sin 2\pi\delta + \cos 2\pi\delta \right] (-1)^n$$

$$\frac{\partial A_M}{\partial \delta} = 0 = (-1)^n [C_M I_0 / \alpha \cos 2\pi\delta - \sin 2\pi\delta]$$

so that $\frac{1}{2\pi} \tan^{-1} \frac{C_M I_0}{\alpha} = \delta_1$, a value of δ for which A_M is extreme.

From (26b):

$$\rho = A_M \pm \sqrt{A_M^2 - 1}$$

For extreme values of ρ :

$$\frac{\partial \rho}{\partial \delta} = \frac{\partial A_M}{\partial \delta} (1 \pm A_M (A_M^2 - 1)^{-1/2}) = 0$$

Thus when $\delta = \delta_1$, ρ will also be extreme. Substituting:

$$|\rho|_{\text{ext}} = \left| \frac{1}{\cos 2\pi\delta_1} \pm \sqrt{\frac{1}{\cos^2 2\pi\delta_1} - 1} \right|$$

hence

$$|\rho|_{\text{max}} = \left| \frac{1 \pm \sin 2\pi\delta_1}{\cos 2\pi\delta_1} \right| \quad (34)$$

where the sign is chosen to agree with that of δ_1 . Note that $|\rho|_{\text{max}}$ is confirmed in (34) to be completely independent of the zone number n. For practical ranges of $\frac{C_M I_0}{\alpha}$, δ_1 is small and can be considered a linear function of this parameter.

$$\text{i.e. } 2\pi\delta_1 = C_M I_0 / \alpha$$

$$\text{and (34) gives: } |\rho|_{\text{max}} = 1 + \left| \frac{C_M I_0}{\alpha} \right|$$

$$\text{or } -\ln |\rho|_{\text{max}} = C_M I_0 / \alpha, \text{ to a high degree of accuracy.} \quad (35)$$

Figure 7 is a contour plot applicable to all instability zones. The contours are curves $\ln|\rho| = \text{constant}$. The plot shows that the instability becomes broader in band and that for larger values of the parameter $R = C_M I_0 / \alpha$ the values of $\ln|\rho|$ become less sensitive to variations in δ , i.e., the contour slopes $\frac{dR}{d\delta}$ become flatter.

It still remains to determine the conditions under which a repetitive load function can be justifiably replaced in Hill's equation by a repetitive series of impulses. It is expected that these conditions will not strongly depend on the particular shape of the function involved but rather its duration, τ_0 and the frequency, Ω , of the system on which it acts. For the sake of argument, therefore, a sequence of rectangular pulses $\Phi(\tau)$ is chosen as excitation to Hill's equation:

$$\ddot{f} + \Omega^2 (1 - \mu\Phi(\tau))f = 0$$

where

$$\begin{aligned}\Phi(\tau) &= 1, \quad 0 < \tau \leq \tau_0 \\ &= 0, \quad \tau_0 < \tau \leq \bar{\tau}\end{aligned}$$

and

$$\Phi(\tau + \bar{\tau}) = \Phi(\tau)$$

The corresponding expression for A in this case turns out to be¹⁸:

$$\begin{aligned}A &= (\sin \Omega\tau_0 \cos p_1\tau_0 - \frac{(p_1^2 + \Omega^2)}{2\Omega p_1} \cos \Omega\tau_0 \sin p_1\tau_0) \sin \Omega\bar{\tau} + \\ &+ (\cos p_1\tau_0 \cos \Omega\tau_0 + \frac{(p_1^2 + \Omega^2)}{2\Omega p_1} \sin p_1\tau_0 \sin \Omega\tau_0) \cos \Omega\bar{\tau}\end{aligned} \quad (36)$$

where $p_1 = \Omega\sqrt{1-\mu}$

¹⁸Boltin, V. V., The Dynamic Stability of Elastic Systems, Holden-Day, 1964, 18.

It is easily verified that for small values of the quantity $\Omega\tau_0$, the expression for A above reduces to that in (32). Expanding the transcendental terms containing the parameter $\Omega\tau_0$, and retaining up to third order terms in this parameter, (36) becomes:

$$\begin{aligned} A &= \Omega\mu\tau_0/2 (1 + \Omega^2\mu\tau_0/6) \sin\Omega\bar{\tau} + \cos\Omega\bar{\tau} \\ &= \frac{C_M I_0}{\alpha} (1 + \frac{C_M I_0}{\alpha} \frac{\Omega\tau_0}{3}) \sin\Omega\bar{\tau} + \cos\Omega\bar{\tau} \end{aligned}$$

It is therefore concluded that if

$$\Omega\tau_0 \ll \frac{3\alpha}{C_M I_0} \quad (37)$$

the approximation (33) will be good.

EXAMPLE II - M139 AUTOMATIC WEAPON

The 20mm M139 at first glance (figure 8) would appear to be vulnerable to transverse vibration excitation. It has the appearance of a long and slender tube - as compared with, say, a typical .30 caliber gun such as illustrated in reference (9). Actually the slenderness ratio of the two are nearly equal having values of approximately 103 and 92 respectively. In spite of this our intuition is not in error. As previously demonstrated, it is not the slenderness ratio alone, but its product with the non-dimensional ballistic impulse which determines the strength of the exponential growth in parametric resonance. As it turns out, this impulse (I_0) for the 20mm round is nearly three times larger than that computed for the .30 cal weapon.

A complete set of calculations follow - leading to the evaluation of the parameters C_M and I_0/α . The possible values of the growth

exponent γ are then determinable from figure (7).

A uniform tube approximation is assumed:

$D_o = 1.5$ in - tube outer diameter

$D_i = 0.79$ in - tube inner diameter

$L = 72$ in - overall tube length

$P_{AV} = 40,000$ psi - time-average ballistic pressure

$t_o = .0015$ sec - effective duration time of ballistic pressure

function

$a = 2.02 \times 10^5$ in/sec - extensional wave speed

$E = 30 \times 10^6$ psi - Young's Modulus of Elasticity

If the ratio of the unperturbed natural frequency Ω_M to the excitation frequency ω_e is nearly an integral multiple of $1/2$, parametric resonance is possible.

$$\text{i.e., } \frac{\Omega_M}{\omega_e} \equiv \frac{\alpha \beta_M^2}{2\pi/\bar{\tau}} \doteq n/2 \quad n = 1, 2, 3, \dots$$

$$\text{or } \bar{\tau} = \frac{n\pi}{\alpha \beta_M^2}$$

$\bar{\tau}$ is the time between rounds. In real time, $t = \bar{\tau}L/a$, corresponding to a firing rate of 915 rounds per minute - a reasonable value in practice. From the previously assigned values:

$$\frac{1}{\alpha} = L\sqrt{A/T} = 103.3 \quad - \text{the slenderness ratio}$$

If we choose $M = 1$, that is, parametric resonance of the fundamental transverse mode of vibration, then for $n = 2$,

$$\bar{\tau} = \frac{2\pi}{\alpha \beta_1^2} \doteq 184 \quad \text{and} \quad \bar{t} \doteq .066 \text{ sec}$$

where we have used the value $\beta_1 = 1.875$ - corresponding to the fundamental mode of a cantilevered beam.

The nondimensional axial load (average)*:

$$P_0^* = \frac{\pi P_{AV} D_i^2}{4 EA} = 5.12 \times 10^{-4}$$

The duration of this load in nondimensional time:

$$\tau_0 = \frac{a}{L} t_0 = 4.21$$

Thus the nondimensional impulse is:

$$I_0 = P_0^* \tau_0 = 21.58 \times 10^{-4}$$

Recalling the definition of C_M :

$$C_M = \sum_j \frac{A_{jMM}}{(j\pi\beta_M)^2}$$

For $M = 1$, therefore:

$$C_1 = \sum_j \frac{A_{j11}}{[j\pi(1.875)]^2} \doteq .234$$

The parameter $\Omega_1 \tau_0$ must satisfy the smallness criterion (38); i.e.,

$$\Omega_1 \tau_0 \ll \frac{3\alpha}{C_1 I_0}$$

Substituting values for the parameters:

$$.0956 \ll 57.5$$

which would appear to be satisfactory.

*Note that the real quantity of interest is the nondimensional impulse, I_0 . If ballistic curves are available this quantity can be determined directly by a simple integration.

Expression (36), or equivalently figure (7) shows that the greatest value for $\ln|\rho|_{\max}$ is .052. The corresponding growth coefficient:

$$\gamma_{\max} = \frac{\ln|\rho|_{\max}}{\bar{t}} = \frac{.052}{.066} = .786$$

This value of γ can produce a vibration amplification of over 50 in 5 seconds of repeated firing. In other words if at any time during firing the deflection of, say, the muzzle is a given amount then 5 sec later this deflection can be over 50 times greater.

It is not likely that the exact state of tuning will exist such that the maximum amplification will be realized. Furthermore, as previously shown, damping will reduce the amplification. On the other-hand there are other loads which have not been considered and which may be non-mitigating. Reactions from the moving projectile and the travelling propellant pressure as well as the relative movements of supports are synchronous with the load considered in this report and may add to its effect - possibly more than offsetting the reduction caused by damping. Again it is mentioned in connection with figure (7) that the state of tuning leading to large amplifications need not be as precise when larger values of the abscissa are encountered.

Discussion

The models assumed in this report are of course, somewhat idealized. It is always a question as to when more detail should be included. How much is gained, for example, by including the geometry of a variable cross sectional area when knowledge of the support

conditions is always so imprecise? Further, it is almost certain that the general character of the results shown in figure 7 will prevail regardless of the detail incorporated in the modeling effort. That is, no matter how detailed the model, parametric resonance will probably be confined to a narrow band of frequencies for the tensile loads likely to be induced on the tube through firing. The frequency is going to have to be 'just right' for it to occur. But given the proper frequency ratio our preceding analysis definitely suggests that ballistic forces are sufficient to create significant exponential growth. It is doubtful if any higher degree of confidence in these general findings could be obtained through the use of more refined models. On the other hand, the frequencies and even the particular mode which may resonate cannot be predicted with confidence unless an extremely detailed model is employed. Even then, in cases where parametric resonance is suspect, field measurements should be made to determine precisely the frequencies of free vibration and excitation. As mentioned earlier in this report, there exists certain inconclusive evidence^{9,10} that dispersion maxima observed in tests with certain automatic weapons may be caused by parametric resonance. On the basis of the feasibility demonstrated herein, it is advisable that such experiments be repeated in a more tightly controlled manner so that a conclusion may finally be drawn.

⁹AMCP 706-252, Engineering Design Handbook, Gun Series, Gun Tubes, February 1964.

¹⁰Wente, D. E., Schoenberger, R. L., and Quinn, B. E., An Investigation of the Effect of the Natural Frequency of Vibration of the Barrel Upon the Dispersions of an Automatic Weapon, Purdue U., 1955, AD 64132.

APPENDIX A

HILL'S EQUATION - FLOQUET SOLUTIONS

The general differential equation of interest (Hill's Equation) is:

$$Y'' + \Omega^2 [1 - \epsilon\phi(t)]Y = 0 \quad (A1)$$

where

$$\phi(t + T) = \phi(t)$$

Since equation A1 is a second order linear, ordinary and homogeneous differential equation, its general solution can be written in terms of any two solutions $f_1(t)$ and $f_2(t)$ which are known to be linearly independent.

$$\text{i.e.} \quad Y(t) = Af_1(t) + Bf_2(t) \quad (A2)$$

where the constants A and B are determined by the initial conditions.

Because equation A1 is unchanged if T is added to t, $f_1(t+T)$ and $f_2(t+T)$ must also be solutions. But from the fundamental theory of linear, homogeneous differential equations, any other solutions to A1 must be expressible as a linear combination of the linearly independent solutions $f_1(t)$ and $f_2(t)$;

$$\begin{aligned} \text{i.e.} \quad f_1(t+T) &= a_{11}f_1(t) + a_{12}f_2(t) \\ f_2(t+T) &= a_{21}f_1(t) + a_{22}f_2(t) \end{aligned} \quad (A3)$$

There are many choices for $f_1(t)$ and $f_2(t)$ and with each choice one can expect different coefficients a_{ij} . Floquet (2) has shown that among the choices for these solutions there exist those such that:

$$Y(t+T) = \rho Y(t) \quad (A4)$$

that is, the solution one period of the excitation later, is a constant multiple of the solution at time t.

Substituting into A2:

$$Af_1(t+T) + Bf_2(t+T) = \rho[Af_1(t) + Bf_2(t)]$$

Using A3:

$$\sum_{j=1}^2 \{Aa_{1j}f_j(t) + Ba_{2j}f_j(t)\} = \rho[Af_1(t) + Bf_2(t)]$$

Since f_1 and f_2 are independent:

$$\begin{aligned} Aa_{11} + Ba_{21} &= A\rho \\ Aa_{12} + Ba_{22} &= B\rho \end{aligned} \quad (A5)$$

A5 only has nontrivial solutions if the determinant of the coefficients of A and B vanish:

$$\text{i.e.,} \quad \begin{vmatrix} a_{11} - \rho & a_{21} \\ a_{12} & a_{22} - \rho \end{vmatrix} = 0 \quad (A6)$$

Substituting into either of the equations A5, each root ρ_j gives a ratio B/A such that the solution will satisfy the condition A4.

$$\left(\frac{B}{A}\right)_j = \frac{\rho_j - a_{11}}{a_{21}} \quad (A7)$$

In particular, if $f_1(t)$ and $f_2(t)$ are chosen to satisfy the so called 'unitary initial conditions':

$$\begin{aligned} f_1(0) &= 1 & f_2(0) &= 0 \\ f_1'(0) &= 0 & f_2'(0) &= 1 \end{aligned}$$

then, from A2:

$$A = Y(0)$$

$$B = Y'(0)$$

and hence the ratio B/A is the ratio of initial conditions such that A_4 is satisfied. Further, from A_3 , definitions are given to the a_{ij} :

$$a_{11} = f_1(T)$$

hence

$$a_{21} = f_2(T)$$

$$a_{12} = f_1'(T)$$

$$a_{22} = f_2'(T)$$

$$\text{and } [Y'(0)/Y(0)]_j = \frac{\rho_j - f_1(T)}{f_2(T)} \quad (A8)$$

The quadratic equation for ρ (A_6) becomes:

$$\rho^2 - 2A\rho + B = 0$$

where**

$$A = \frac{1}{2} [f_1(T) + f_2'(T)]$$

$$B = f_1(T)f_2'(T) - f_2(T)f_1'(T) \quad (A9)$$

Multiplying the first of these equations by f_2 and the second by f_1 and subtracting:

$$f_1 f_2'' - f_2 f_1'' = 0^* \quad (19)$$

Integrating:

$$B = f_1(t)f_2'(t) - f_2(t)f_1'(t) = \text{const}$$

The constant has unit value in view of the unitary initial conditions employed.

19Boyce, W. E. and DiPrima, R. C., Elementary Differential Equations and Boundary Value Problems, John Wiley, 1966, 89.

*Note that this equation can be written $W'_{12} = 0$, where W_{12} is the Wronskian of $f_1(t)$ and $f_2(t)$.

**If any of the f_i have jump discontinuities at $t = T$, then $A = A(\tau^+)$ is implied.

Thus equation A6 becomes:

$$\rho^2 - 2A\rho + 1 = 0 \quad (A10)$$

whereupon

$$\rho = A \pm \sqrt{A^2 - 1}$$

Note that the two roots of this equation are reciprocal, i.e. $\rho_1 \rho_2 = 1$

Thus corresponding to real roots, A4 represents a solution which grows or diminishes (according to the choice of ρ) following each period of the excitation, T. The ratio of initial conditions which will lead to either of these solutions alone is given by A8.

EXAMPLE - Delta Function Excitation

$$\text{Let } \Phi(t) = \sum_{k=1}^{\infty} \delta(t-kT)$$

From A10, the roots ρ_j depend entirely on the quantity

$$A = \frac{1}{2} [f_1(T) + f_2'(T)]$$

where $f_1(t)$ and $f_2(t)$ are linearly independent solutions of Hill's Equation (A1) satisfying unitary initial conditions. These can be chosen as:

$$\begin{aligned} f_1(t) &= \cos \Omega t \\ f_2(t) &= \frac{1}{\Omega} \sin \Omega t \end{aligned} \quad (A11)$$

Thus $f_1(T) = \cos \Omega T$

The expression obtained by a formal differentiation of $f_2(t)$ above, is valid up to but not including time $t = T$ since the application of the first 'impulse' will cause $f_2'(T)$ to be discontinuous. This jump discontinuity can be evaluated by an integration of Hill's Equation (A1):

$$f_2'(T) - f_2'(T^-) = \lim_{\Delta t \rightarrow 0} \int_{T-\Delta t}^{T+\Delta t} \Omega^2 [\epsilon \delta(t-T) - 1] f_2(t) dt = \epsilon \Omega^2 f_2(T)$$

Thus

$$f_2'(T) = \epsilon \Omega \sin \Omega T + \cos \Omega T$$

and

$$A = \frac{\epsilon \Omega}{2} \sin \Omega T + \cos \Omega T$$

whereupon the roots ρ_1, ρ_2 may be evaluated.

For any given finite value of ϵ , intervals of the parameter ΩT exist such that these roots will be real and since their product must be unity, the following possibilities arise:

$$(i) \quad \rho_1 = \rho_2 = \pm 1$$

$$(ii) \quad \rho_1 > 1, \rho_2 < 1$$

Case (i) represent borderline situations, that is, the solutions A4 neither grow or decay with each period T of the excitation. Case (ii), on the other hand, produces one solution of the form A4 which grows in amplitude by a factor $\rho_1 > 1$ and another which decays by the factor $\rho_2 < 1$, each period of the excitation. The initial conditions which produce either of these solutions must only satisfy A8,

$$\text{i.e.} \quad \frac{Y'(0)}{Y(0)} = \frac{\rho_i - f_1(T)}{f_2(T)} = [\rho_i - \cos \Omega T] \Omega / \sin \Omega T$$

Figure A1(a,b) shows the solution when this ratio is enforced. In general, however, the solution for arbitrary initial conditions is a linear combination of these special solutions of pure growth and decay. Figure A1(c) shows one such solution exhibiting early decay eventually to be overpowered by the growing solution.

The solutions of pure growth or pure decay can be represented as:¹⁷

$$f_j(t) = \psi_j(t) e^{\frac{t}{T} \ln \rho_j} \quad (A12)$$

where

$$\psi_j(t+T) = \psi_j(t)$$

so that indeed,

$$f_j(t+T) = \psi_j(t) e^{(\frac{t}{T} + 1) \ln \rho_j} = \rho_j f_j(t)$$

as required. In general ρ is complex

hence

$$\ln \rho_j = \ln |\rho_j| + i \arg(\rho_j)$$

Thus

$$f_j(t) = \phi_j(t) e^{\frac{t}{T} \ln |\rho_j|}$$

where

$$\phi_j(t) = \psi_j(t) e^{\frac{it}{T} \arg \rho_j} \quad (A13)$$

When the ρ_j are real, $\phi_j(t) = \psi_j(t)$ and are periodic in T . Thus the general solution to Hill's equation may be written

$$Y(t) = C_1 \phi_1(t) e^{\frac{t}{T} \ln |\rho_1|} + C_2 \phi_2(t) e^{\frac{t}{T} \ln |\rho_2|}$$

or, enforcing the relation $\rho_1 \rho_2 = 1$:

$$Y(t) = C_1 \phi_1(t) e^{\frac{t}{T} \ln |\rho_1|} + C_2 \phi_2(t) e^{-\frac{t}{T} \ln |\rho_1|}$$

¹⁷Bolotin, V. V., The Dynamic Stability of Elastic Systems, Holden-Day, 1964, 14.

REFERENCES

1. Morse, P. M. and Feshbach, H., Methods of Theoretical Physics, McGraw Hill, 1953, 557.
2. Bolotin, V. V., The Dynamic Stability of Elastic Systems, Holden-Day, 1964, 22-23.
3. Den Hartog, J. P., Mechanical Vibrations, McGraw Hill, 1940, 378.
4. Tong, K., Theory of Mechanical Vibrations, J. Wiley and Sons, 1960.
5. Krajcinovic, D. P. and Herrmann, G., Stability of Straight Bars Subjected to Repeated Impulsive Compression, AIAA Journal, Oct 68, 2025-2027.
6. McLachlan, N. W., Theory and Application of Mathieu Functions, Oxford Clarendon Press, 1946.
7. Simkins, T., Pflegl, G., Scanlon, R., Dynamic Response of the M113 Gun Tube to Travelling Ballistic Pressure and Data Smoothing as Applied to XM150 Acceleration Data, WVT-TR-75015.
8. McIvor, J. K., and Bernard, J. E., The Dynamic Response of Columns Under Short Duration Axial Loads, Trans ASME, Sept 1973, 688.
9. AMCP 706-252, Engineering Design Handbook, Gun Series, Gun Tubes, Feb 1964.
10. Wente, D. E., Schoenberger, R. L., and Quinn, B. E., An Investigation of the Effect of the Natural Frequency of Vibration of the Barrel Upon the Dispersion of an Automatic Weapon, Purdue U., 1955, AD 64132.

11. Nowacki, W., Dynamics of Elastic Systems, Chapman and Hall, 1963, 122.
12. Ralston and Wilt, Mathematical Methods for Digital Computation, Wiley, 1960, 95-109.
13. Jaroodny, S. J., An Elementary Review of the Mathieu-Hill Equation of a Real Variable Based on Numerical Solutions, Ballistic Research Laboratory Memo., Report 878, Aberdeen Proving Ground, MD, 1955.
14. Nayfeh, A. H., Perturbation Methods, John Wiley, 1973, 63.
15. Harris, C. M., and Crede, C. E., Shock and Vibration Handbook, Vol I - Basic Theory and Measurements , McGraw Hill, 1961, 8-24.
16. Meirovitch, L., Methods of Analytical Dynamics, McGraw Hill, 1970, 264.
17. Bolotin, V. V., The Dynamic Stability of Elastic Systems, Holden-Day, 1964, 14.
18. Bolotin, V. V., The Dynamic Stability of Elastic Systems, Holden-Day, 1964, 18.
19. Boyce, W. E. and DiPrima, R. C., Elementary Differential Equations and Boundary Value Problems, John Wiley, 1966, 89.

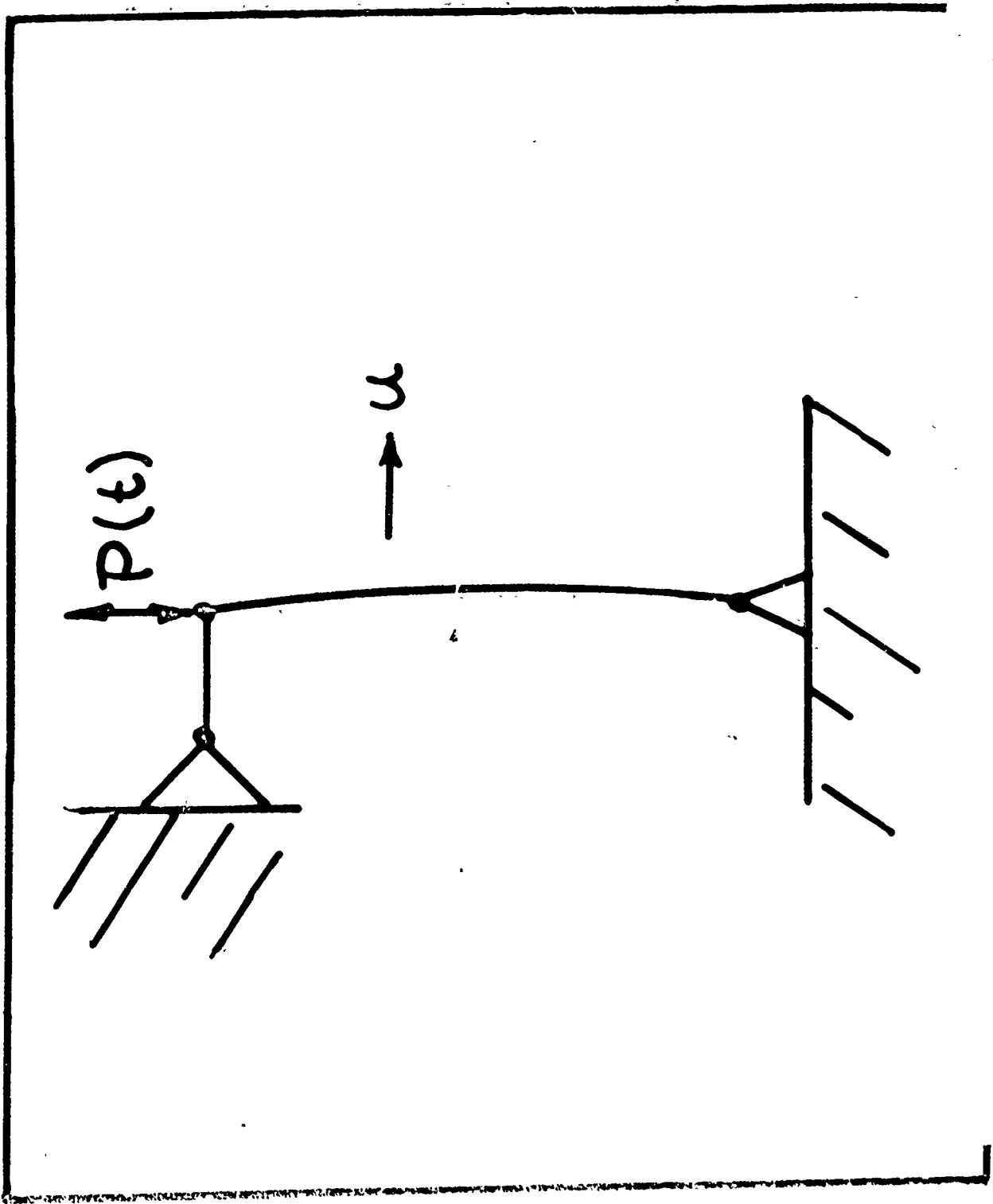


Figure (a) - Classical Beam Problem Governed by Hill's Equation

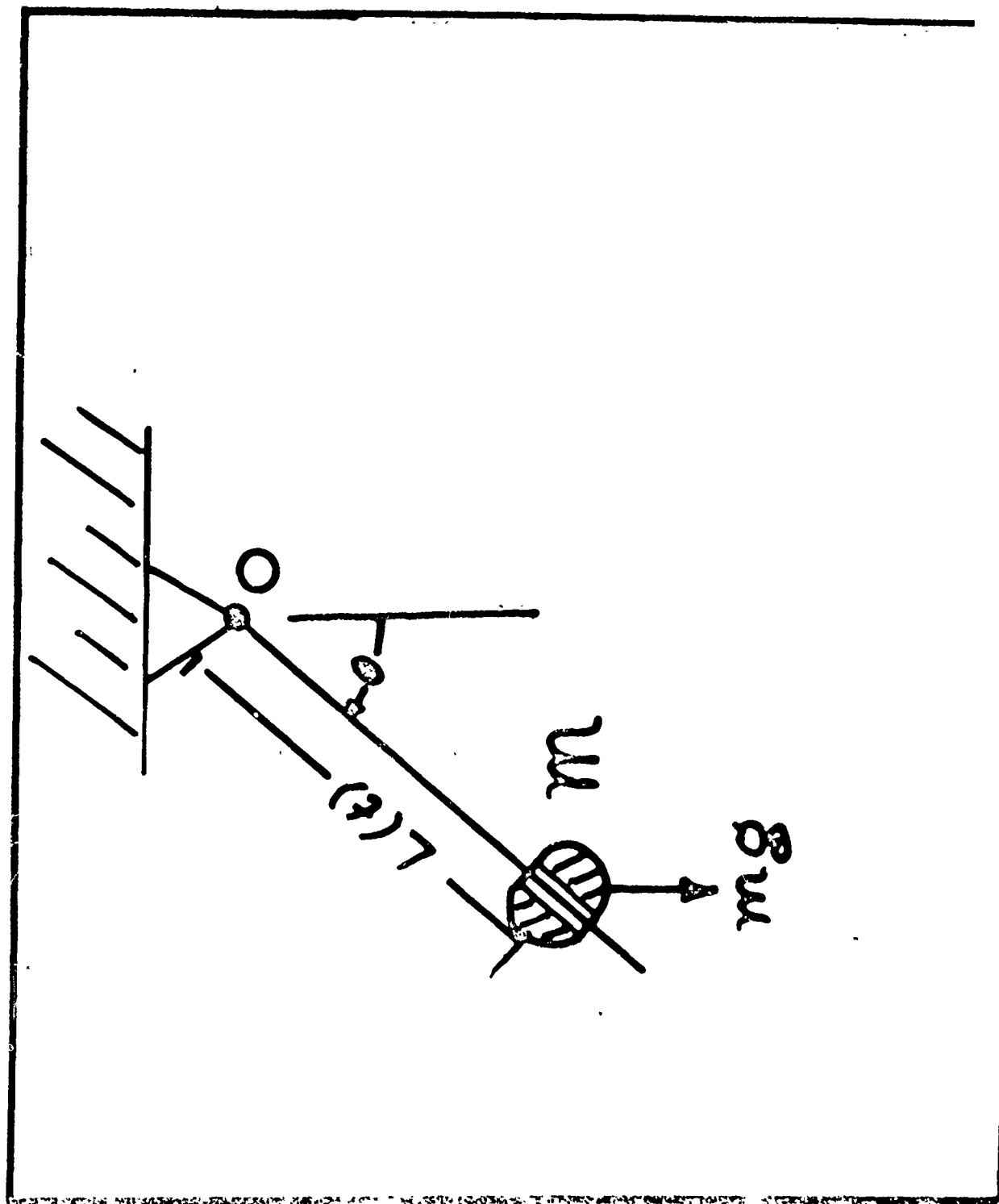


Figure (b) - Swing Problem Leading to Hill's Equation

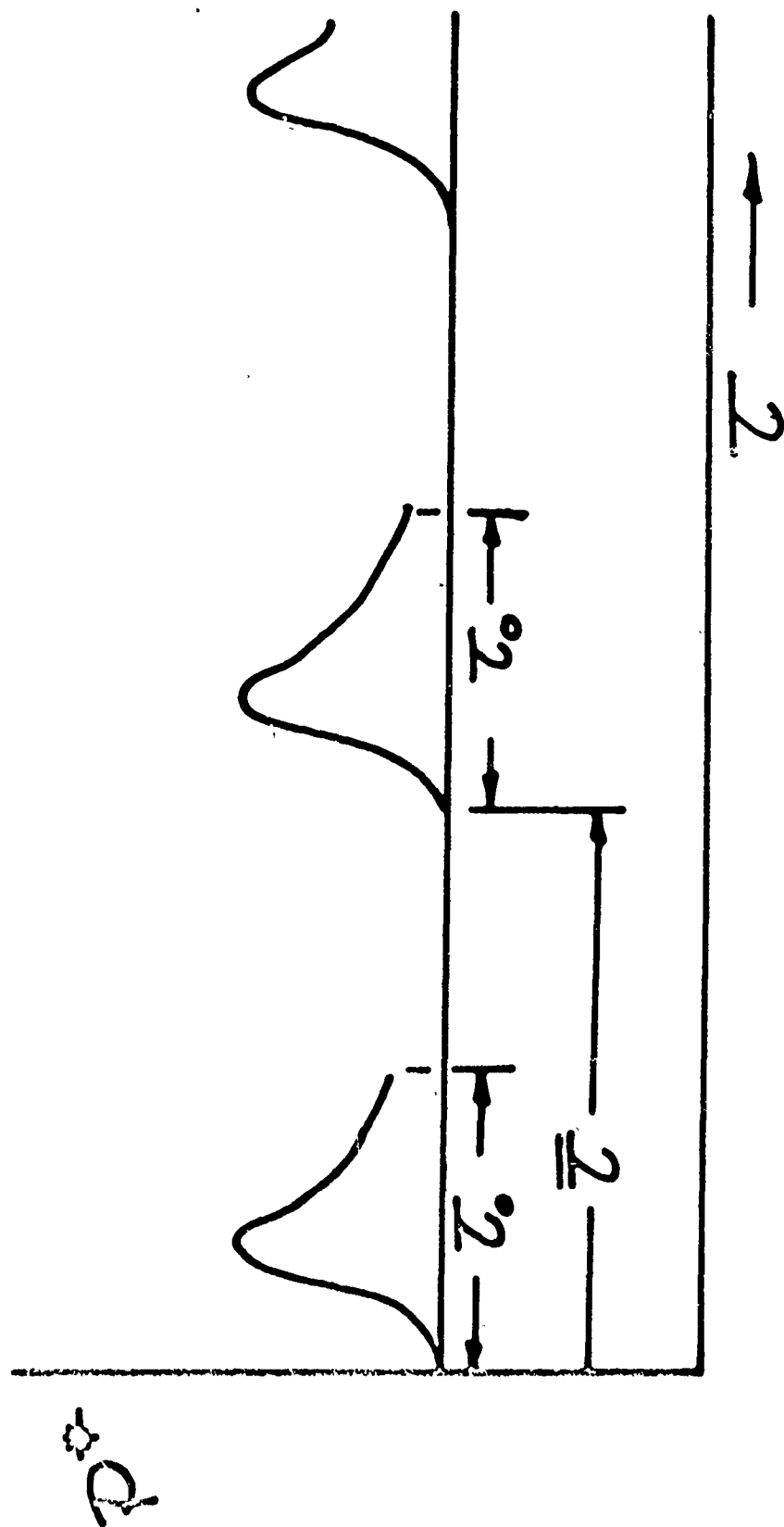


Figure (c) - Periodic Ballistic Pressure Function

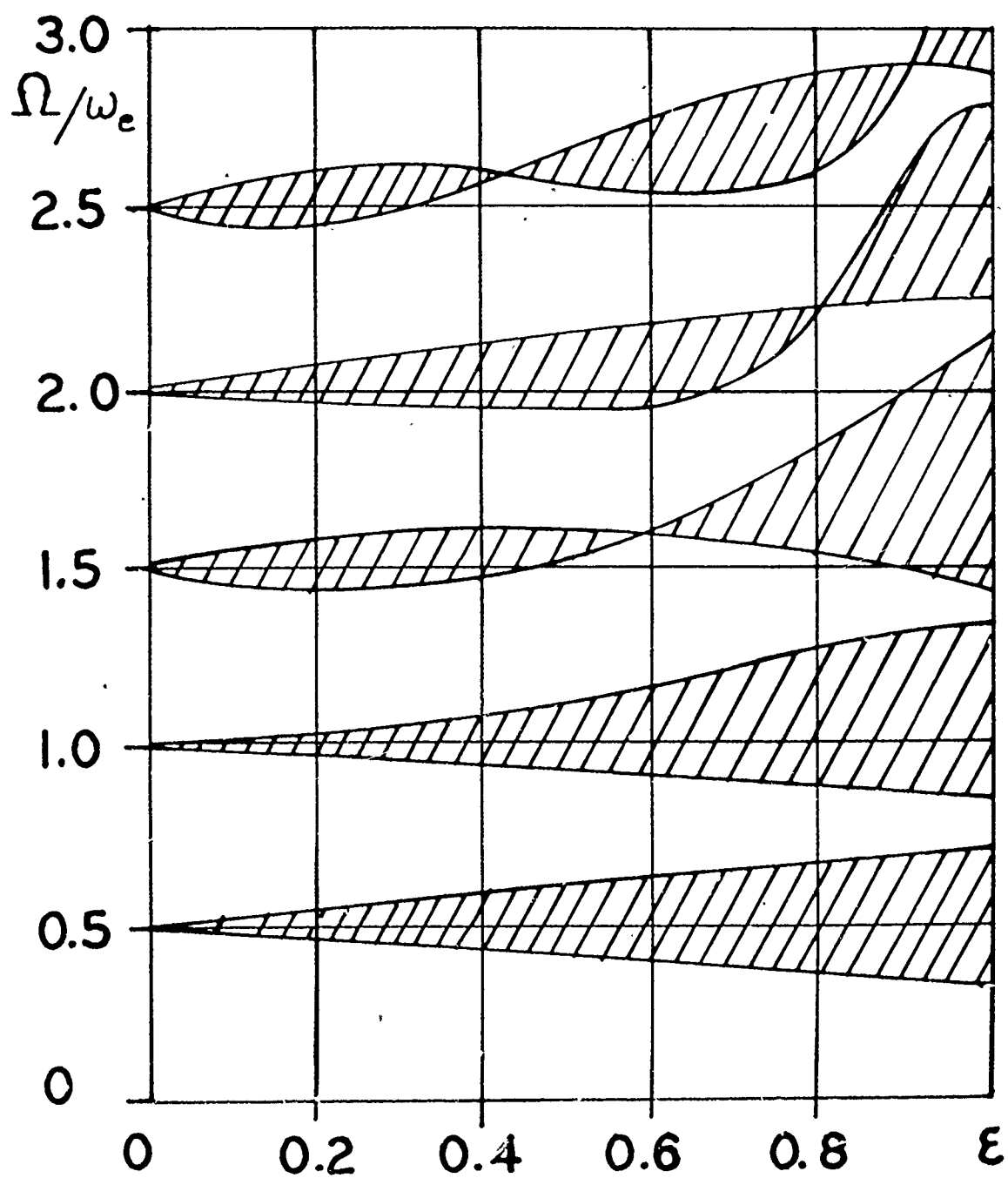
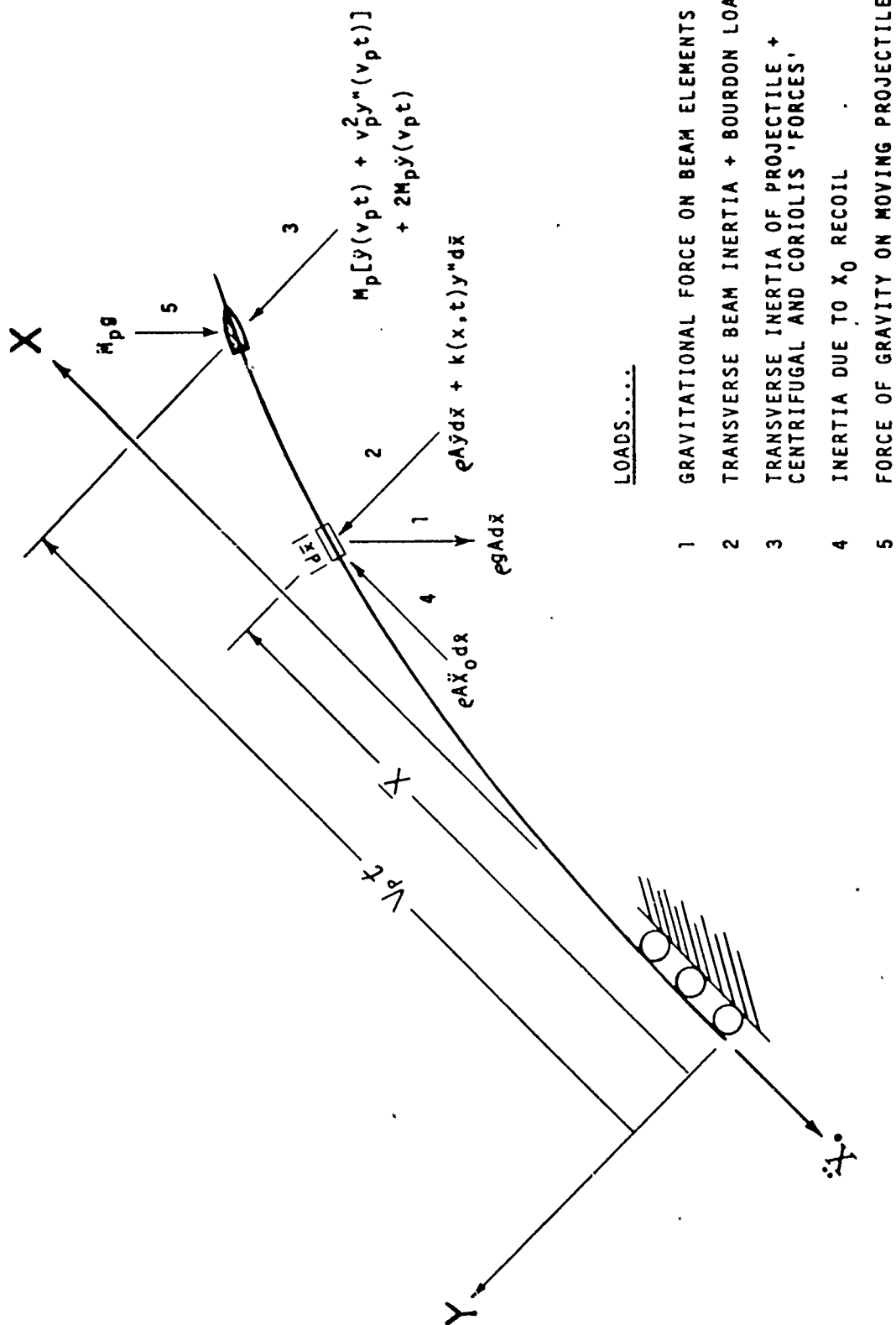


Figure 1 - Instability Zones. Excitation in Hill's Equation is a Rectangular Ripple Function. (cf ref (2), p. 18, fig. 4).



LOADS.....

- 1 GRAVITATIONAL FORCE ON BEAM ELEMENTS
- 2 TRANSVERSE BEAM INERTIA + BOURDON LOADING
- 3 TRANSVERSE INERTIA OF PROJECTILE + CENTRIFUGAL AND CORIOLIS 'FORCES'
- 4 INERTIA DUE TO x_0 RECOIL
- 5 FORCE OF GRAVITY ON MOVING PROJECTILE

Figure 2 - Curvature Induced Loads - From Reference (7).

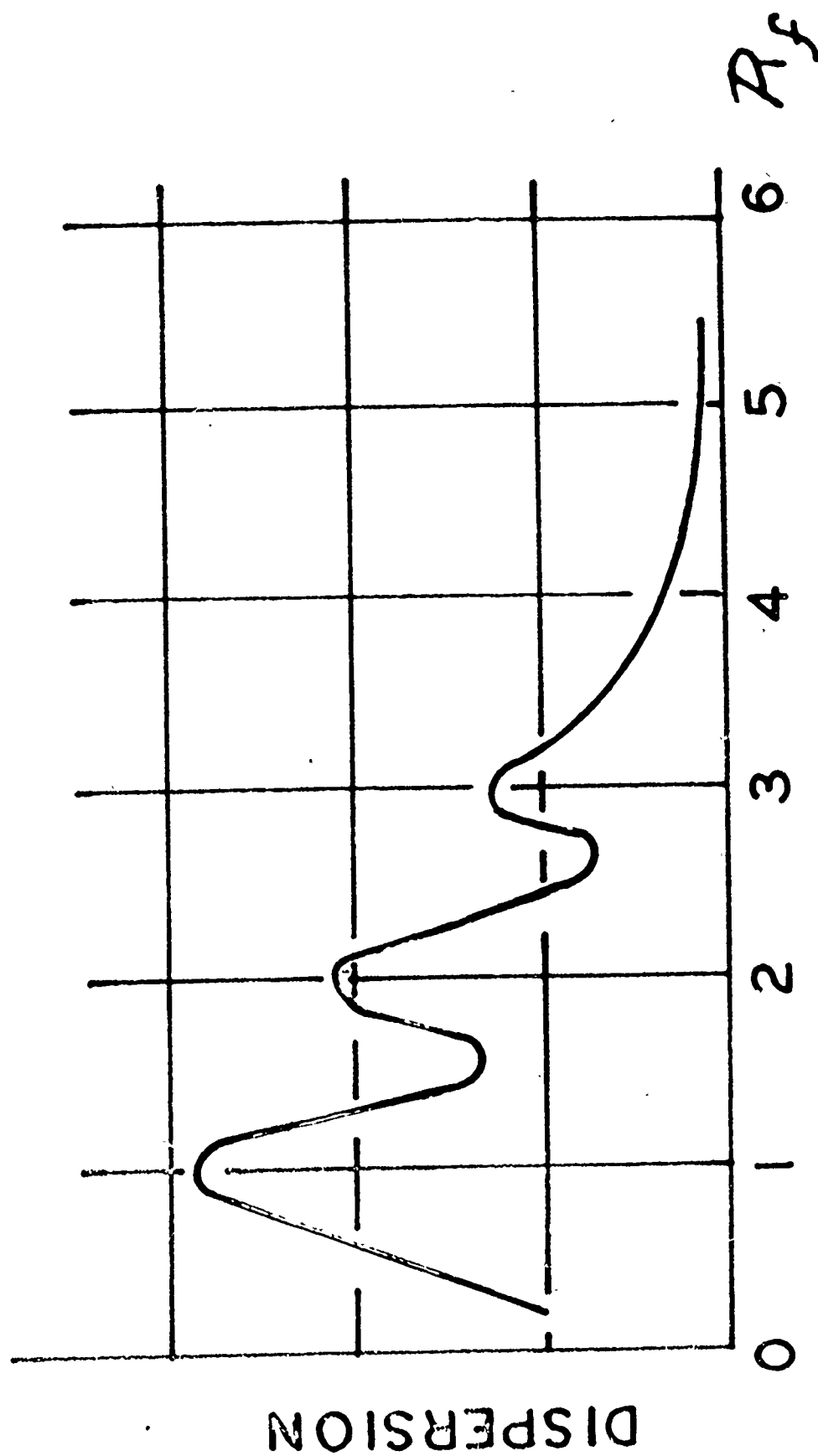


Figure 3 - Dispersion of Shot vs. Frequency Ratio (R_f = nat. frequency/firing rate) as reported in reference (9).

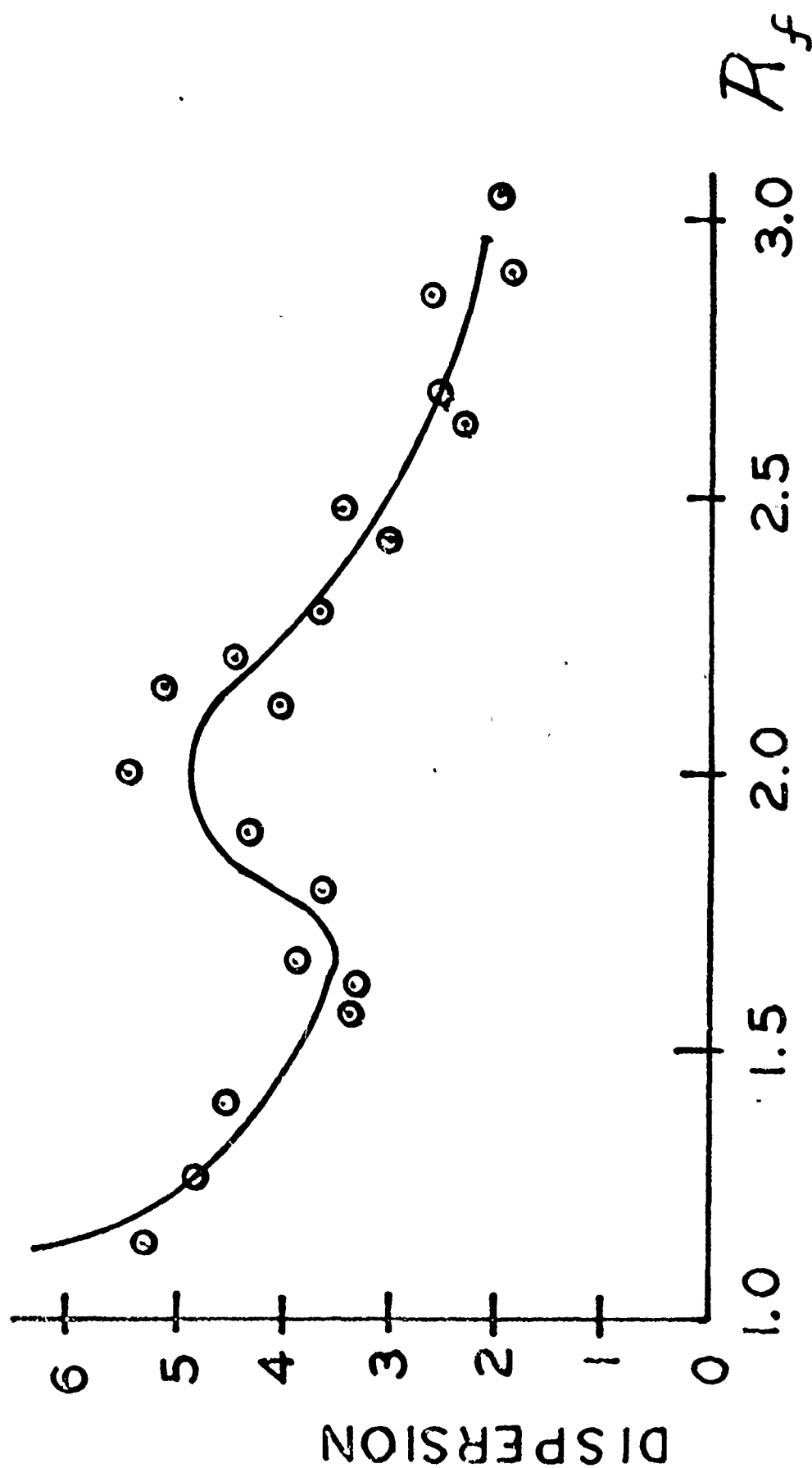


Figure 4 - Dispersion of Shot vs. Frequency Ratio - as reported in reference (10).

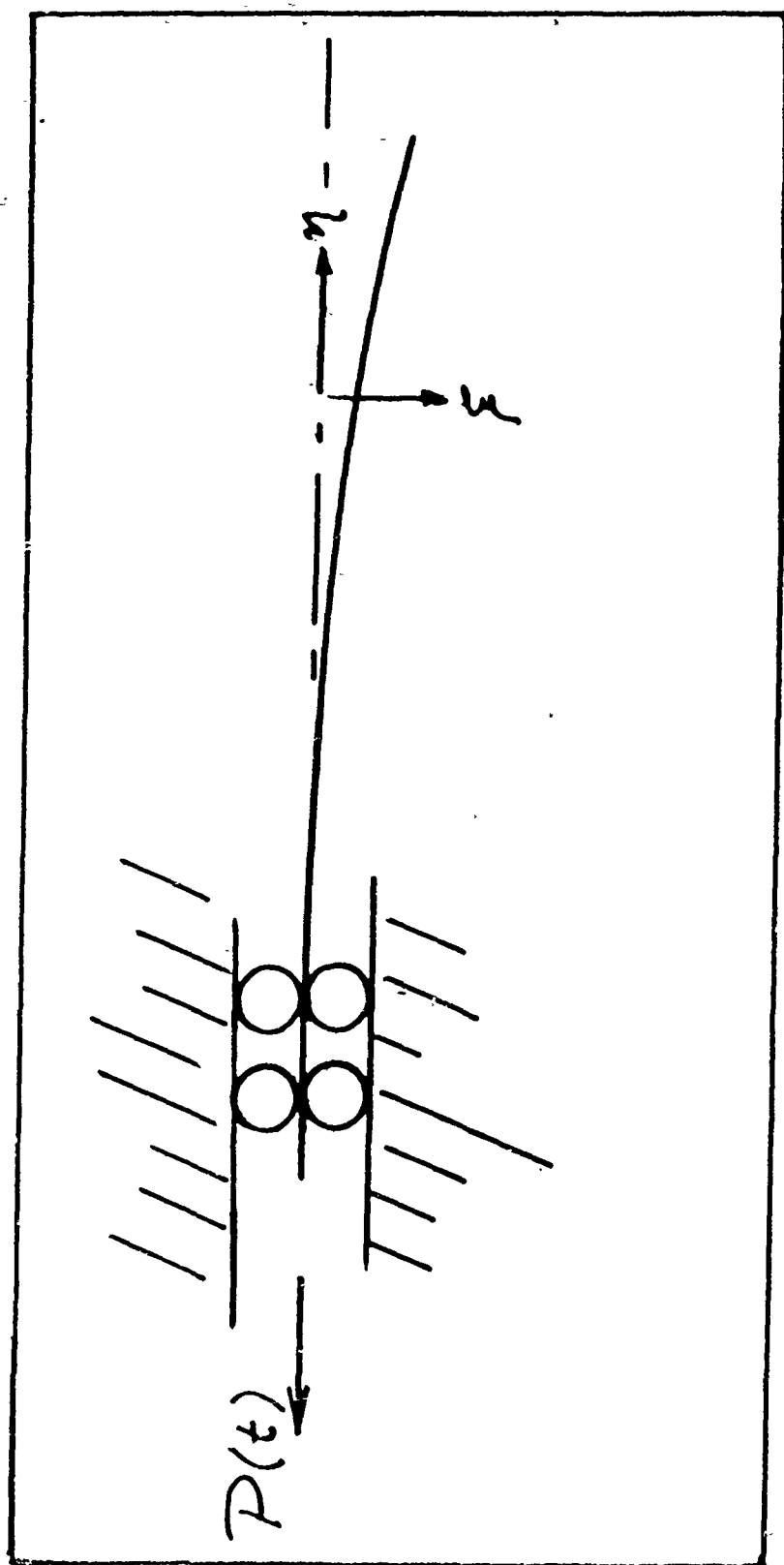


Figure 5 - Gun Tube Model - An Axially Free Cantilevered Beam

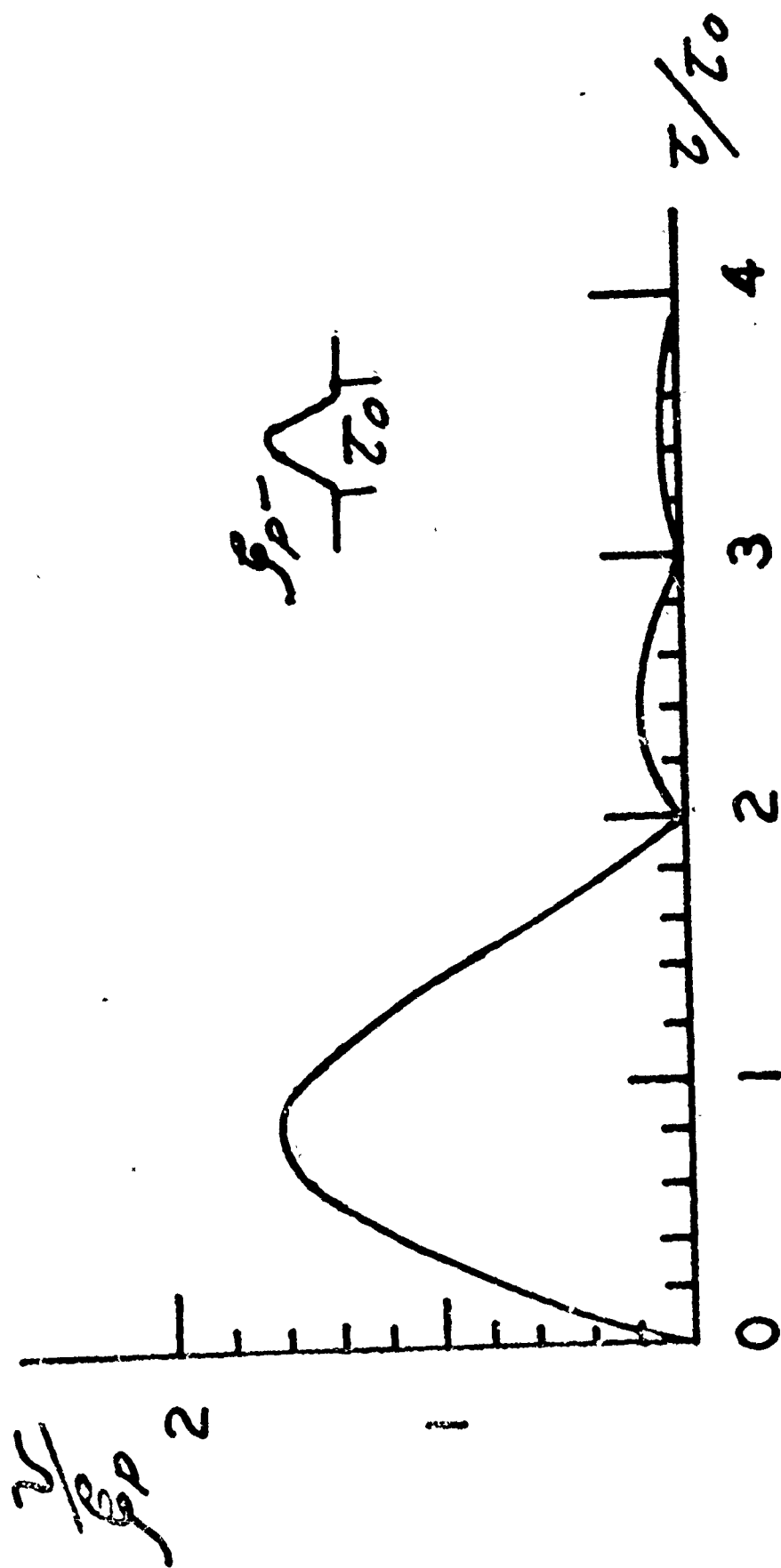


Figure 6 - Residual Response Spectra, Haversine Excitation; from Reference (15).

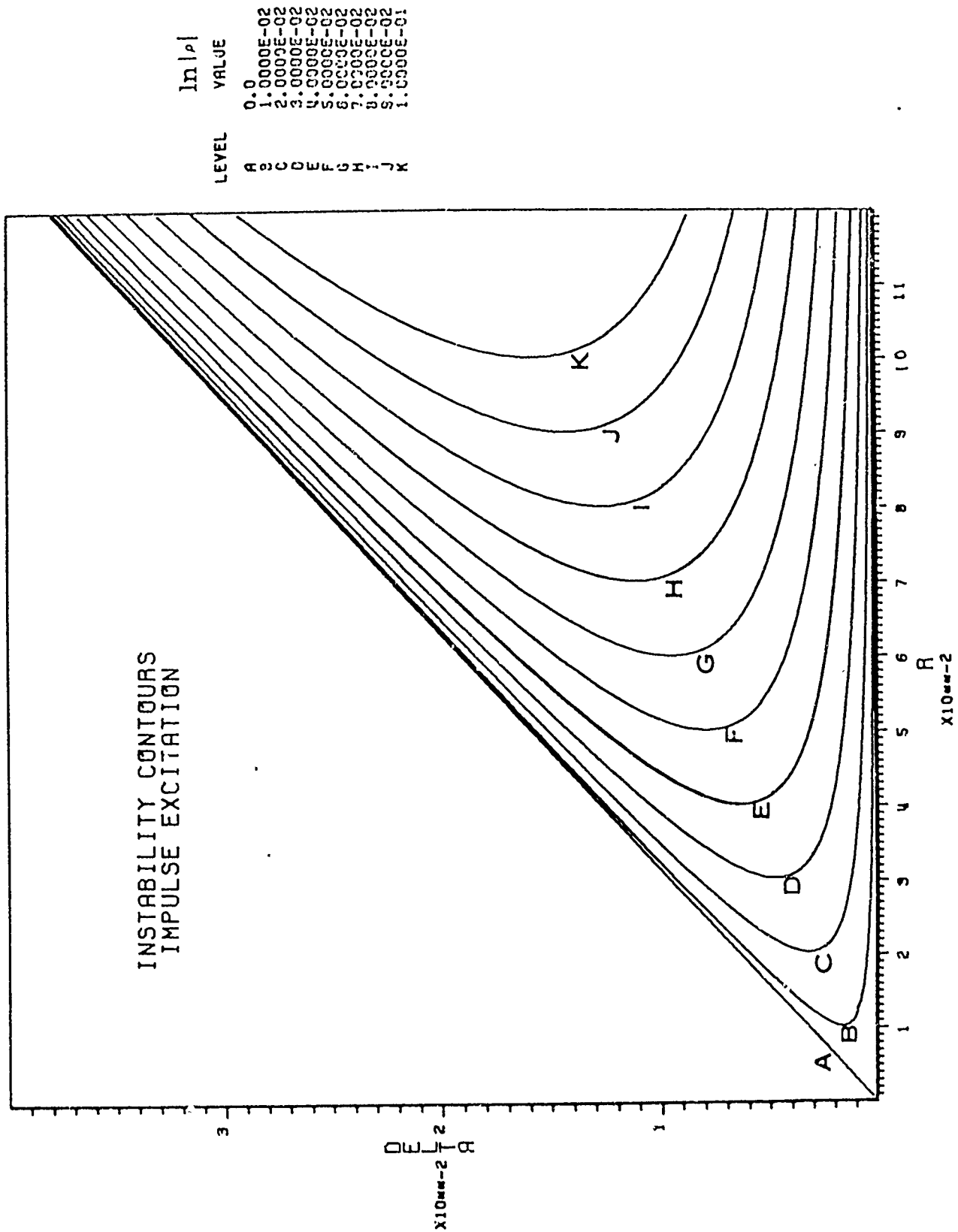
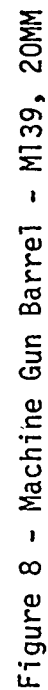


Figure 7 - Instability Contours - $R = C_M I_0 / \alpha$;
 $\alpha / n/2 + \delta$ (see text).



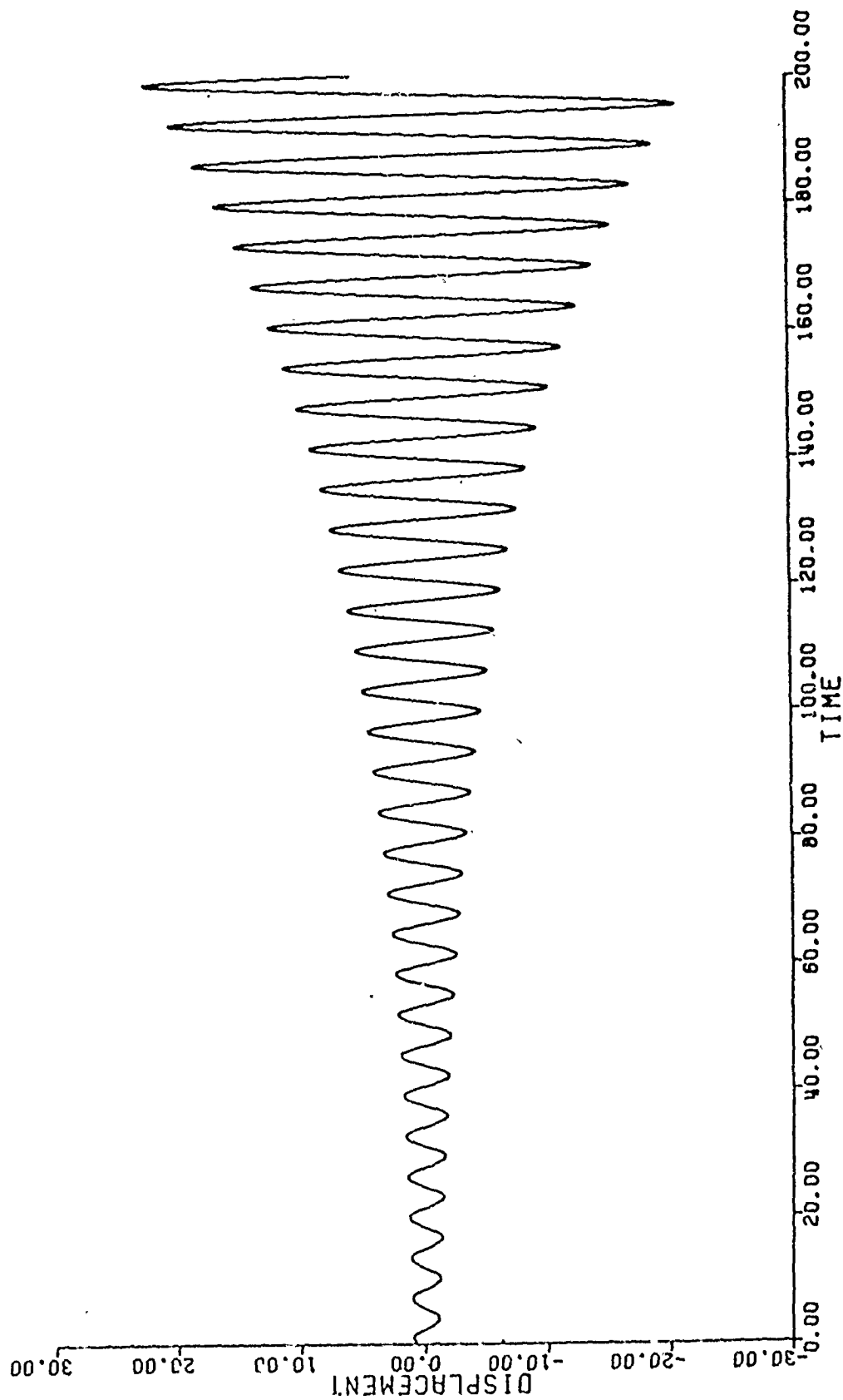


Figure A1 (a) - Pure Growth: $y = c_1 Q_{1e}^{Yt}$. Initial conditions: $y(0) = .6892237$
 $\dot{y}(0) = .7245468$

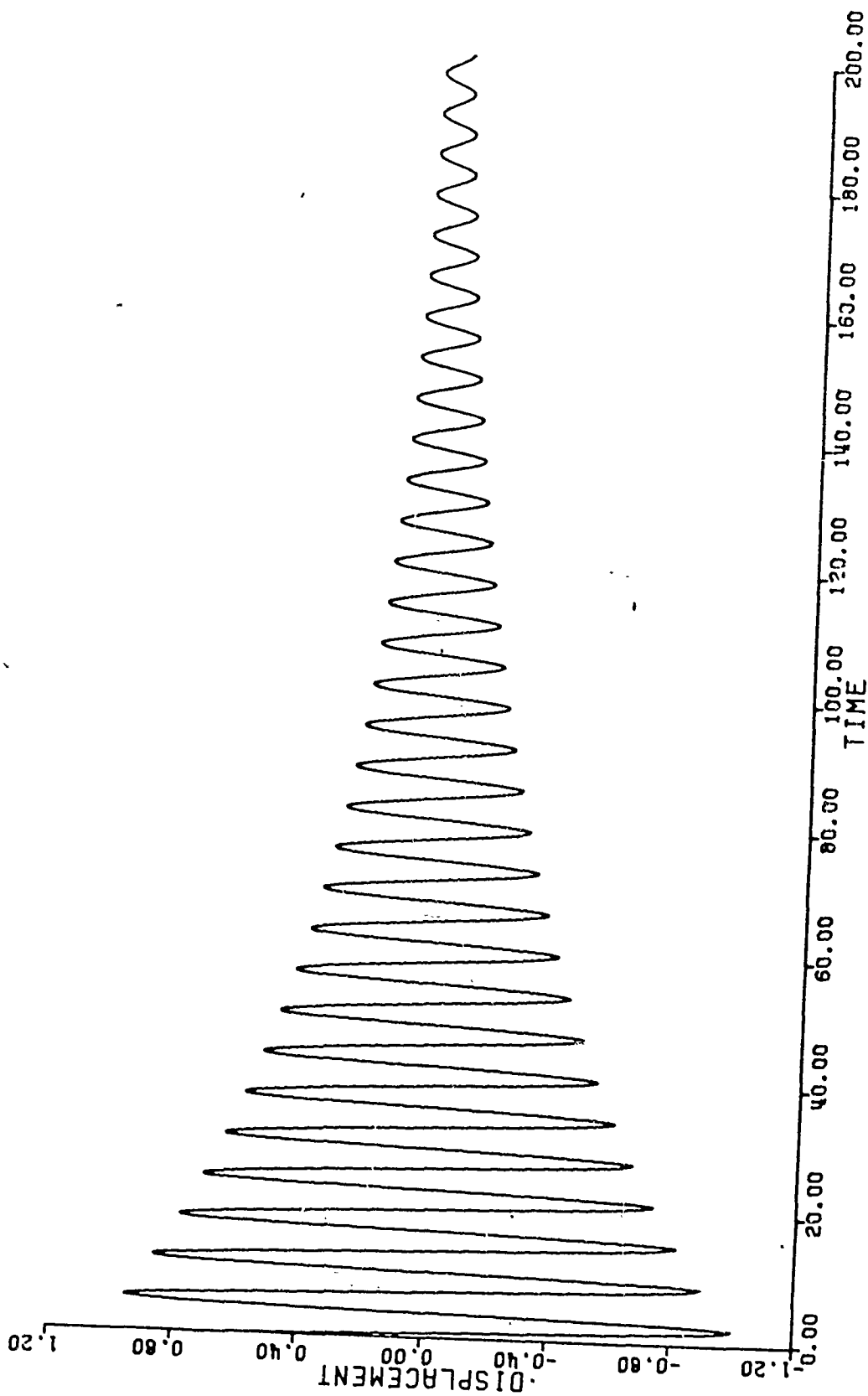


Figure A1 (b) - Pure Decay: $y = c_2 e^{-\lambda t}$. Initial Conditions: $y(0) = .7245462$
 $\dot{y}(0) = -.6892250$

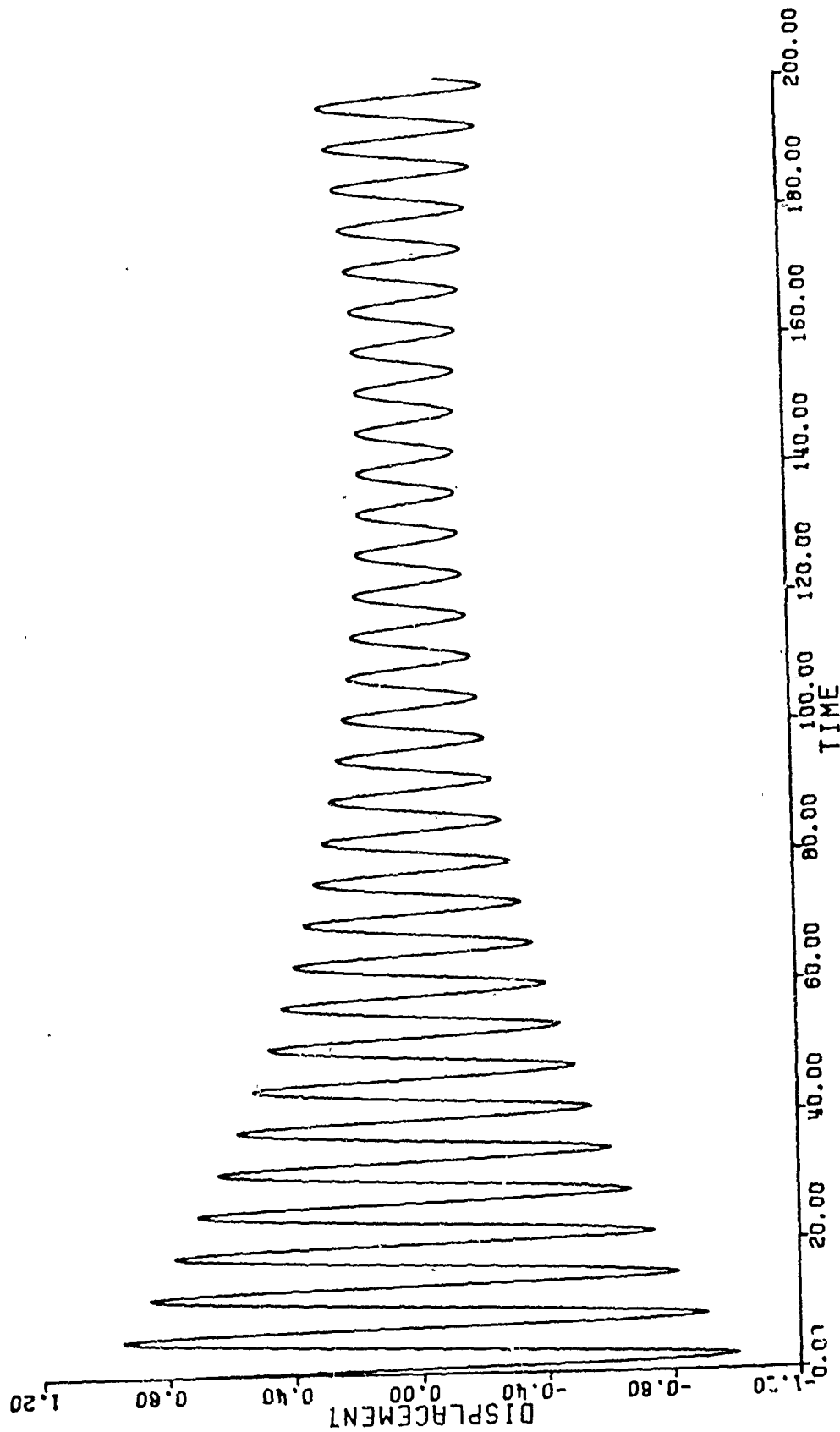


Figure A1 (c) - General Case: $y = a\phi_1 e^{\gamma t} + b\phi_2 e^{-\gamma t}$. Initial conditions:
 $y(0) = .7239993$ $\dot{y}(0) = -.6889993$

TABLE I*- COUPLING COEFFICIENTS A_{jmn}

$A_{111} = -9.83$	$A_{121} = 11.1$
$A_{112} = 11.1$	$A_{122} = -50.1$
$A_{113} = 7.71$	$A_{123} = 16.4$
$A_{114} = 1.91$	$A_{124} = 30.3$
$A_{115} = 1.68$	$A_{125} = 6.93$
$A_{116} = .819$	$A_{126} = 7.54$
$A_{131} = 7.71$	$A_{141} = 1.91$
$A_{132} = 16.4$	$A_{142} = 30.3$
$A_{133} = -128.$	$A_{143} = 18.4$
$A_{134} = 18.4$	$A_{144} = -247.$
$A_{135} = 69.6$	$A_{145} = 18.9$
$A_{136} = 11.3$	$A_{146} = 122.$
$A_{151} = 1.68$	$A_{161} = .819$
$A_{152} = 6.93$	$A_{162} = 7.54$
$A_{153} = 69.6$	$A_{163} = 11.3$
$A_{154} = 19.0$	$A_{164} = 122.$
$A_{155} = -404.$	$A_{165} = 19.3$
$A_{156} = 19.3$	$A_{166} = -601.$

*Certain symmetries are evident throughout the Table. No attempt has been made to make use of symmetry properties in order to shorten the tabulation.

$$A_{211} = 9.78$$

$$A_{212} = -48.6$$

$$A_{213} = 26.3$$

$$A_{214} = 25.4$$

$$A_{215} = 3.35$$

$$A_{216} = 5.94$$

$$A_{231} = 26.3$$

$$A_{232} = -115.$$

$$A_{233} = 94.5$$

$$A_{234} = -247.$$

$$A_{235} = 61.6$$

$$A_{236} = 201.$$

$$A_{251} = 3.35$$

$$A_{252} = 92.8$$

$$A_{253} = 61.6$$

$$A_{254} = -433.$$

$$A_{255} = 85.9$$

$$A_{256} = -670.$$

$$A_{221} = -48.6$$

$$A_{222} = 84.5$$

$$A_{223} = -115.$$

$$A_{224} = 45.7$$

$$A_{225} = 92.8$$

$$A_{226} = 18.4$$

$$A_{241} = 25.4$$

$$A_{242} = 45.7$$

$$A_{243} = -247.$$

$$A_{244} = 89.5$$

$$A_{245} = -433.$$

$$A_{246} = 68.9$$

$$A_{261} = 5.94$$

$$A_{262} = 18.4$$

$$A_{263} = 201.$$

$$A_{264} = 68.8$$

$$A_{265} = -670.$$

$$A_{266} = 93.4$$

$$A_{311} = -6.53$$

$$A_{312} = 33.8$$

$$A_{313} = -112.$$

$$A_{314} = 45.5$$

$$A_{315} = 53.4$$

$$A_{316} = 2.50$$

$$A_{331} = -112.$$

$$A_{332} = 164.$$

$$A_{333} = -156.$$

$$A_{334} = 196.$$

$$A_{335} = -434.$$

$$A_{336} = 111.$$

$$A_{351} = 53.4$$

$$A_{352} = 73.1$$

$$A_{353} = -434.$$

$$A_{354} = 197.$$

$$A_{355} = -440.$$

$$A_{356} = 194.$$

$$A_{321} = 33.8$$

$$A_{322} = -174.$$

$$A_{323} = 164.$$

$$A_{324} = -216.$$

$$A_{325} = 73.1$$

$$A_{326} = 183.$$

$$A_{341} = 45.5$$

$$A_{342} = -216.$$

$$A_{343} = 196.$$

$$A_{344} = -279.$$

$$A_{345} = 197.$$

$$A_{346} = -722.$$

$$A_{361} = 2.50$$

$$A_{362} = 183.$$

$$A_{363} = 111.$$

$$A_{364} = -722.$$

$$A_{365} = 194.$$

$$A_{366} = -639.$$

$$A_{411} = 8.19$$

$$A_{412} = -23.1$$

$$A_{413} = 62.5$$

$$A_{414} = -201.$$

$$A_{415} = 68.8$$

$$A_{416} = 91.8$$

$$A_{431} = 62.5$$

$$A_{432} = -351.$$

$$A_{433} = 273.$$

$$A_{434} = -237.$$

$$A_{435} = 303.$$

$$A_{436} = -674.$$

$$A_{451} = 68.8$$

$$A_{452} = -349.$$

$$A_{453} = 303.$$

$$A_{454} = -394.$$

$$A_{455} = 381.$$

$$A_{456} = -588.$$

$$A_{421} = -23.1$$

$$A_{422} = 108.$$

$$A_{423} = -351.$$

$$A_{424} = 266.$$

$$A_{425} = -349.$$

$$A_{426} = 98.3$$

$$A_{441} = -201.$$

$$A_{442} = 266.$$

$$A_{443} = -237.$$

$$A_{444} = 366.$$

$$A_{445} = -394.$$

$$A_{446} = 316.$$

$$A_{461} = 91.8$$

$$A_{462} = 98.3$$

$$A_{463} = -674.$$

$$A_{464} = 316.$$

$$A_{465} = -588.$$

$$A_{466} = 375.$$

$$A_{511} = -7.19$$

$$A_{512} = 28.9$$

$$A_{513} = -38.5$$

$$A_{514} = 98.5$$

$$A_{515} = -316.$$

$$A_{516} = 96.6$$

$$A_{531} = -38.5$$

$$A_{532} = 183.$$

$$A_{533} = -66.9$$

$$A_{534} = 401.$$

$$A_{535} = -339.$$

$$A_{536} = 420.$$

$$A_{551} = -316.$$

$$A_{552} = 390.$$

$$A_{553} = -339.$$

$$A_{554} = 535.$$

$$A_{555} = -494.$$

$$A_{556} = 575.$$

$$A_{521} = 28.9$$

$$A_{522} = -80.1$$

$$A_{523} = 183.$$

$$A_{524} = -586.$$

$$A_{525} = 390.$$

$$A_{526} = -512.$$

$$A_{541} = 98.5$$

$$A_{542} = -586.$$

$$A_{543} = 401.$$

$$A_{544} = -324.$$

$$A_{545} = 535.$$

$$A_{546} = -542.$$

$$A_{561} = 96.6$$

$$A_{562} = -512.$$

$$A_{563} = 420.$$

$$A_{564} = -542.$$

$$A_{565} = 575.$$

$$A_{566} = -698.$$

$$A_{611} = 7.85$$

$$A_{612} = -24.7$$

$$A_{613} = 49.3$$

$$A_{614} = -56.3$$

$$A_{615} = 142.$$

$$A_{616} = -456.$$

$$A_{631} = 49.3$$

$$A_{632} = -130.$$

$$A_{633} = 296.$$

$$A_{634} = -1078.$$

$$A_{635} = 552.$$

$$A_{636} = -459.$$

$$A_{651} = 142.$$

$$A_{652} = -878.$$

$$A_{653} = 552.$$

$$A_{654} = -432.$$

$$A_{655} = 750.$$

$$A_{656} = -632.$$

$$A_{621} = -24.7$$

$$A_{622} = 101.$$

$$A_{623} = -130.$$

$$A_{624} = 270.$$

$$A_{625} = -878.$$

$$A_{626} = 539.$$

$$A_{641} = -56.3$$

$$A_{642} = 271.$$

$$A_{643} = -1078.$$

$$A_{644} = 556.$$

$$A_{645} = -432.$$

$$A_{646} = 716.$$

$$A_{661} = -456.$$

$$A_{662} = 539.$$

$$A_{663} = -459.$$

$$A_{664} = 716.$$

$$A_{665} = -632.$$

$$A_{666} = 836.$$

TABLE II - EIGENVALUE ANALYSIS (NASTRAN) - MCAAAC, 60MM
(Trussed Configuration)

<u>Mode Type</u>		<u>Frequency (hz)</u>
Recoil mode		1.81
Fundamental	Transverse mode	79.5
2nd	Transverse mode	100.5
3rd	Transverse mode	125.6
4th	Transverse mode	218.7
5th	Transverse mode	296.2
6th	Transverse mode	412.7
7th	Transverse mode	525.9
Fundamental	Axial mode	580.1
2nd	Axial mode	1189.2
3rd	Axial mode	1898.4
4th	Axial mode	2496.2

TABLE III - PARAMETRIC VALUES, MCAAAC TUBE

The parametric values listed below are based on the material constants E_p for steel, a peak ballistic pressure of 75,500 psi, and the NASTRAN-predicted frequencies for the fundamental axial vibration and the fifth transverse vibration modes.

$$\begin{aligned}\alpha^2 &= 6.44 \times 10^{-5} \\ \tau/t &= 1160 \\ \frac{P(\tau)}{EA} &= \frac{P_0^*}{2} \left(1 - \cos \frac{2\pi\tau}{\tau_0} \right) \\ P_0^* &= 7.03 \times 10^{-4} \\ \tau_0 &= 6.96\end{aligned}$$

BALLOTING-ENERGY GROWTH POSSIBILITIES

K.S. FANSLER

Ballistics Research Laboratory
Aberdeen, Maryland

TABLE OF CONTENTS

	<u>Page</u>
ABSTRACT	148
I. INTRODUCTION	149
II. THE DIFFERENTIAL EQUATION OF MOTION	151
III. FRICTION COEFFICIENTS	158
IV. BALLOTING-ENERGY ANALYSIS	164
V. SUMMARY AND CONCLUSIONS	174
REFERENCES	177

ABSTRACT

The possibility for balloting-energy growth is examined. The basic equations are developed and the important parameters for balloting motion are obtained and discussed. It is concluded from the analysis that balloting-energy growth can not occur for conventionally designed projectiles.

I. Introduction

The energy contained in the shell's transverse motion directed toward a bore surface has supposedly become large enough on certain occasions to damage both shell and the gun tube. As Gay [1] has shown, the theories of Reno [2] and Thomas [3] do not predict that such large balloting energies may develop. Reno does not consider sliding friction but assumes that the plane of yaw rotates with the shell. Thomas [2] does not use this constraint but assumes that there exists sliding friction between bourrelet and bore. Chu and Soechting [4] extends Thomas' [2] theory to assume sliding friction between rotating band and bore and also assumes that the shell may have an eccentricity in its center of gravity; here the balloting energy should also decrease with time.

More recently, Walker [5] has developed a theory which predicts that growth in balloting energy may occur. His theory extends Thomas' theory by further assuming friction between the bore and rotating band. According to Walker, the impact impulse generated by the bourrelet hitting a land is followed (due to the finite speed of the elastic wave) by a reaction impulse which occurs on the opposite side of the shell at the rotating band. This causes an added frictional force on this part of the rotating band and results in an impulse of torque that will possibly increase the total transverse angular momentum possessed by the shell. The magnitude of this added angular momentum is proportional to the effective coefficient of friction for the rotating band. The resulting theory is used to explain the breakup of the 8" XM 201 shell in the M110E2 gun tube [5, 6].

Originally, it was desired to apply Walker's [5] theory of balloting to Chu and Soechting's [4] computer description of in-bore motion. In studying Walker's theory, however, it appears that the theory is formulated

incorrectly. Also the values used for the coefficients of friction are thought to be in error by an order of magnitude. The revised theory together with more realistic values of the coefficients of friction result in a completely different picture of balloting-energy growth and decay. It is the purpose of this report to present this more accurate picture and to establish upper-bound limits on the energy growth rate or decay that may be expected.

One apparent error in the formulation of the theory concerns the magnitude of the reaction impulse at the rotating band. Walker claims that the reaction force at the rotating band is equal and opposite to the impact force on the bourrelet. Walker deduces this from his following statement: "The force component Y' is given by the requirement that the sum of the forces acting in the y direction is zero." Here Y' is the normal reaction force at the rotating band. If this were a statics problem, his approach might be valid. Nevertheless, this is a dynamics problem, we must replace his requirement from statics with requirements about how the projectile is constrained to move. If this is done, it is found that the value of the reaction force depends upon the values for the shell of the location of the center of gravity, the distance between the rotating band and bourrelet and the radius of gyration.

According to Walker's [5] theory, since the growth rate of balloting energy is a strong function of the value of the coefficient of friction at the rotating band, it is an important parameter. Walker used a rotating-band coefficient of friction of 0.55, a value that might be expected for slow sliding velocities under small normal pressures. In order to arrive at reasonable values for these coefficients of friction, both

the theory and experiment were investigated. According to a report [7] summarizing the Franklin Institute's experiments, the coefficient of friction decreases for both increasing values of sliding velocities and values of normal pressures. Herzfeld and Kosson [8] postulated that a hydrodynamic film exists between the rotating band and bore at the higher speeds; they found agreement with much of the experimental data available at the time. Bowden [9], however, describes an experiment that shows no hydrodynamic film being generated at typical in-bore projectile velocities. Nevertheless, the normal pressures for this experiment were much less than found at the rotating band and bore interface. Thus, although Herzfeld and Kosson's [8] theory agrees with experiment and appears plausible, the theory is not completely confirmed.

II. The Differential Equations of Motion

In this section, the differential equations of motion obtained by Walker are developed to prepare the way for a discussion of balloting-energy growth or decay. The development is repeated here also for the sake of clarity.

Following Walker, we will utilize Thomas' assumptions and in addition we will assume that friction exists between the rotating band and bore due to the reaction forces. The description of the motion will be given in Eulerian angles. The rotations defining the Eulerian angles are given according to Goldstein [10] in Figure 1. For more clarity, Figure 2 gives some of the axes in terms of the gun-projectile system. The kinetic energy of an axially symmetric shell with respect to the point C is

$$T = \frac{1}{2} I (\omega_y^2 + \omega_x^2) + \frac{1}{2} A \omega_z^2 \quad (1)$$

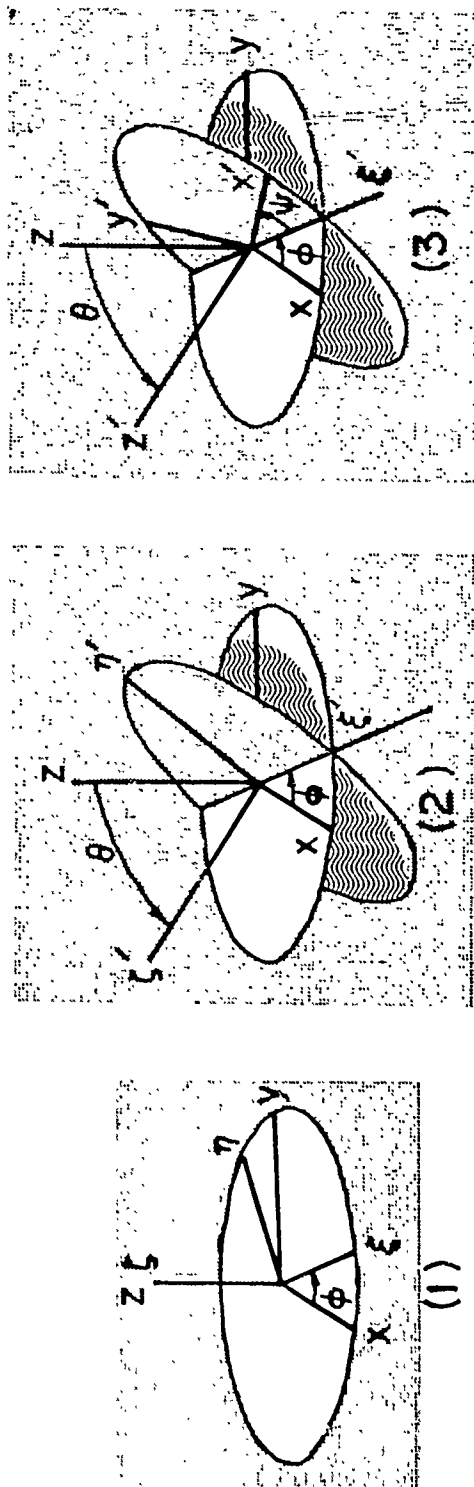


Figure 1. The coordinate axes and rotations defining the Euler angles.

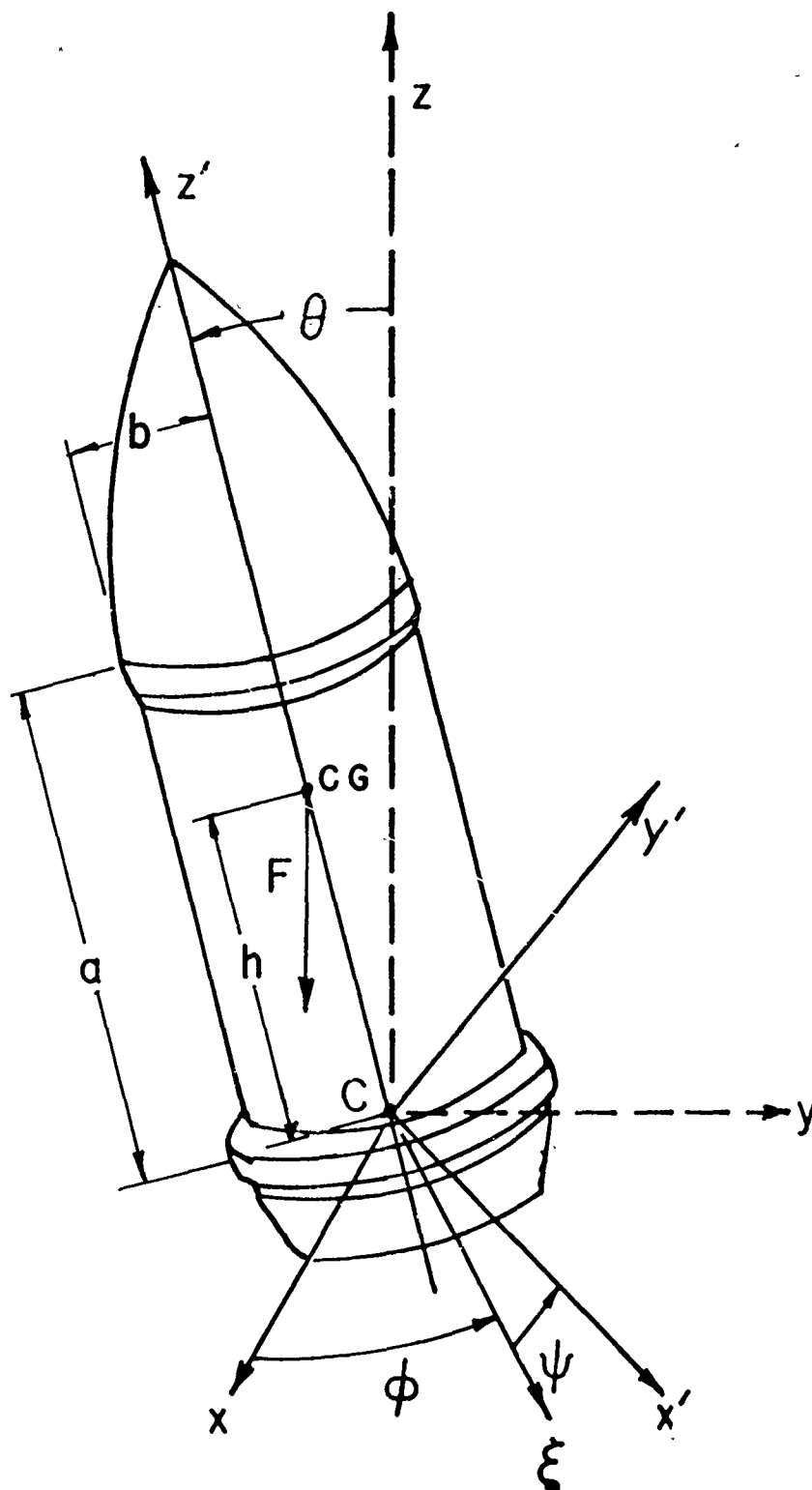


Figure 2. Description of projectile's orientation given in terms of Euler angles. The amount of yaw about the point C is given in terms of θ and the plane of yaw is given by the angle between the line of nodes ξ and x . The inertial force F along the bore line z is also given. Also shown is the distance between the rotating band and bourrelet a , the distance from C to the center of gravity CG and the radius of the bourrelet b .

where ω_i is the angular velocity about the i 'th axis and A is the axial moment of inertia about the line of axial symmetry. The transverse moment of inertia I about C is given as

$$I = B + m h^2 \quad (2)$$

Where B is the transverse moment of inertia about the c.g., m is the mass of the shell, and h is the distance from the point C to the c.g. of the shell.

Transforming to the Eulerian angle description, it is obtained that

$$T = \frac{1}{2} I (\dot{\theta}^2 + \dot{\phi}^2 \sin^2 \theta) + \frac{1}{2} A (\dot{\psi} + \dot{\phi} \cos \theta)^2 \quad (3)$$

For the projectile having the acceleration \ddot{s} , the potential energy is

$$V = m \ddot{s} h \cos \theta \quad (4)$$

Following Walker now, except to vary the presentation for clarification purposes, we have that the Lagrangian is

$$L = T - V$$

The Lagrangian equations are

$$\frac{d}{dt} \frac{\partial L}{\partial \dot{q}_i} - \frac{\partial L}{\partial q_i} = Q_i \quad (5)$$

where

$$q_1 = \theta ; \quad q_2 = \phi ; \quad q_3 = \psi \quad (6)$$

and the Q_i are the generalized constraint forces imposed upon the projectile by the gun tube. The generalized force Q_1 in the θ direction is simply the torque about the line of nodes given by the ξ axis in Figure 1. The

expression for Q_1 would be

$$Q_1 = -z \tilde{\eta} + \eta \tilde{z} - z_b \tilde{\eta} + \eta_b \tilde{z}_b \quad (7)$$

where $\tilde{\eta}$ and \tilde{z} are the forces on the bourrelet along η and z respectively.

The subscript b refers to the quantities at the rotating band. These forces would be positive when they are pointing in the direction of increasing coordinate values. From the geometry of Figure 2 we have that

$$z = a \cos \theta - b \sin \theta \quad (8a)$$

$$\eta = -b \cos \theta - a \sin \theta \quad (8b)$$

$$\eta_b = r \quad (8c)$$

$$z_b = 0 \quad (8d)$$

Thus

$$Q_1 = -(a \cos \theta - b \sin \theta) \tilde{\eta} - (b \cos \theta - a \sin \theta) + r \tilde{z}_b \quad (9)$$

For the ϕ coordinate, the torque would be along the z direction

$$Q_2 = -\eta \tilde{\xi} - \eta_b \tilde{\xi}_b + N_a \cos \theta \quad (10)$$

Here N_a is the torque on the projectile transmitted through the rotating band.

From Eqs. (8b) and (8c), we have that

$$Q_2 = (b \cos \theta + a \sin \theta) \tilde{\xi} - r \tilde{\xi}_b + N_a \cos \theta \quad (11)$$

Here it is assumed that the rotating band does deform into a section of a sphere of radius r . Otherwise the expression would be somewhat more complex.

For the ψ coordinate, the torque along the z' direction would be

$$Q_3 = -\eta' \tilde{\xi}' - \eta'_b \tilde{\xi}'_b + N_a \quad (12)$$

Here we have that $\eta' = b$, $\eta'_b = r$, $\tilde{\xi}' = \tilde{\xi}$, and $\tilde{\xi}_b = \tilde{\xi}_b$. Thus we have that

$$Q_3 = -b \tilde{\xi} - r \tilde{\xi}_b + N_a \quad (13)$$

The Lagrange equations in Eulerian coordinates become, from Eqs. (3) through (13)

$$I\ddot{\theta} - I\dot{\phi}^2 \sin\theta \cos\theta + A(\dot{\psi} + \dot{\phi} \cos\theta)\dot{\phi} \sin\theta - m\dot{s}h \sin\theta = - (a \cos\theta - b \sin\theta)\tilde{\eta} - (b \cos\theta - a \sin\theta)\tilde{z} + r \tilde{\xi}_b \quad (14)$$

$$\frac{d}{dt}[I\dot{\phi} \sin^2\theta + A(\dot{\psi} + \dot{\phi} \cos\theta) \cos\theta] = (b \cos\theta + a \sin\theta)\tilde{\xi} - r \tilde{\xi}_b + N_a \cos\theta \quad (15)$$

$$\frac{d}{dt}[A(\dot{\psi} + \dot{\phi} \cos\theta)] = -b \tilde{\xi} - r \tilde{\xi}_b + N_a \quad (16)$$

These are essentially the equations that Walker [5] obtained also.

We can now examine the generalized forces in greater detail. The forces $\tilde{\eta}$, \tilde{z} and $\tilde{\xi}$ act on the projectile during the impact of the bourrelet. The details of the $\tilde{\eta}$ force during impact will be discussed later. The \tilde{z} and $\tilde{\xi}$ forces are caused by the presence of friction during impact and adopting Thomas' assumption,

$$\tilde{\xi}^2 + \tilde{z}^2 = \mu^2 \tilde{\eta}^2 \quad (17)$$

The direction of the $\tilde{\xi}$ force will be opposite to the direction of the ξ component of velocity at the bourrelet's point of contact. Since the motion of the shell is in the positive z direction and \tilde{z} is a frictional component of force, the direction of \tilde{z} is in the negative z direction and \tilde{z} is a negative quantity. Thus, according to Thomas:

$$\frac{\tilde{\xi}}{b(\dot{\psi} + \dot{\phi} \cos\theta) + a\dot{\phi} \sin\theta} = -\frac{\tilde{z}}{\dot{z}} \quad (18)$$

(18)

The sign of the $\tilde{\xi}$ may now be investigated. The quantity $\psi + \phi \cos \theta$ is simply the angular velocity about the body symmetric axis $\dot{\alpha}$ and is a known quantity from the relationship

$$\dot{\alpha} = \pi \dot{z} / (r n) \quad (19)$$

Here n is the number of calibers traveled for the projectile to perform one revolution. Since $\sin \theta$ is a small quantity and it is expected that $\dot{\phi}$ might be similar in magnitude to $\dot{\alpha}$, using Eq. (19) we can approximate Eq. (18) by

$$\tilde{\xi} = \pi \tilde{z} / n \quad (20)$$

Since \tilde{z} is a negative quantity, $\tilde{\xi}$ is also a negative quantity from Eq. (20). Substituting Eq. (20) into Eq. (17) we obtain that

$$\tilde{z} = \mu \tilde{\eta} / (1 + \pi^2 / n^2)^{1/2} \quad (21)$$

Now by similar reasoning as was applied before to find the frictional force relationships between the force components at the bourrelet, the force relationships at the rotating band are found to be

$$\tilde{\xi}_b = \pi \tilde{z}_b / n \quad (22)$$

$$\tilde{z}_b = \mu \tilde{\eta}_b / (1 + \pi^2 / n^2)^{1/2} \quad (23)$$

III. Friction Coefficients

Since the band coefficient of friction is found to be an important parameter for describing balloting motion, it will be discussed in more detail. Besides the experiments conducted at the Franklin Institute [7, 11] and results reported by Bowden [9], friction coefficients were obtained by Sauer [12] using a rocket sled. The pressures, though high, were much less than experienced by a rotating band in-bore. Nevertheless, he obtained evidence that a molten metal film existed at least for their higher pressures. In addition, he developed a theory for wear and friction assuming molten metal at the interface [13]. In the present paper, it will be assumed that a molten-metal film exists at the rubbing interfaces.

As mentioned earlier, experiments show that the coefficient of friction decreases for increasing values of both sliding velocities and normal loadings [7, 11]. With these data and in addition some data obtained for higher pressures by using a shell pusher, Pilcher and Wineholt [14], in a correlation study, have obtained the coefficient of friction as a function of velocity and pressure. These data were obtained for a steady-state process; i.e., the temperature profile through the thickness of the traveling block changes rapidly shortly after initiation of the friction process and thereafter approaches a steady-state profile. Since the shell's travel through the length of the gun-tube is a transient process, there exists the possibility that steady-state conditions would not be approximated. Nevertheless, the application of an equation developed by H. G. Landau [15] shows that steady-state conditions will be approximated for most of the projectile's travel in-bore. The application of Herzfeld and Kosson's [8]

theory confirms the results obtained by Landau's [15] equation.

The values of the band-friction coefficient for a large-caliber projectile may be obtained by using Pilcher and Wineholt's [14] formulation. Friction-coefficient values are calculated for the 8" XM 201 projectile that broke up in-bore. Figure 3 gives these values as a function of shell velocity. Here it is seen that the coefficient of friction decreases with the distance that the shell has traveled in-bore. For most of the distance traveled, the friction coefficient is an order of magnitude lower than common handbook values.

The friction coefficient values obtained are for steady pressures of the band on the bore surfaces. There exists the possibility that during the reaction impulse, the liquid metal film could become much reduced in thickness and essentially solid to solid contact could be made. This form of contact would tend to raise the effective coefficient of friction. Herzfeld and Kosson's theory will be used to investigate this possibility since the formulation is simple and there is some agreement with experiment.

To investigate the extent of film thinning due to the impulse, consider a block of mass M_0 with a liquid film separating the block from a plane surface. The geometry is exhibited in Figure 4. The initial thickness of this liquid film is δ_0 . The width of this block is $2a_1$. If the block is given an initial velocity V_0 , at some later time the velocity of the block will be V_1 and the thickness of the film will be δ . A coordinate system may be constructed as shown with the origin of the coordinate system placed halfway between the plane surface and the surface of the block. The length of the block z_0 is assumed large enough

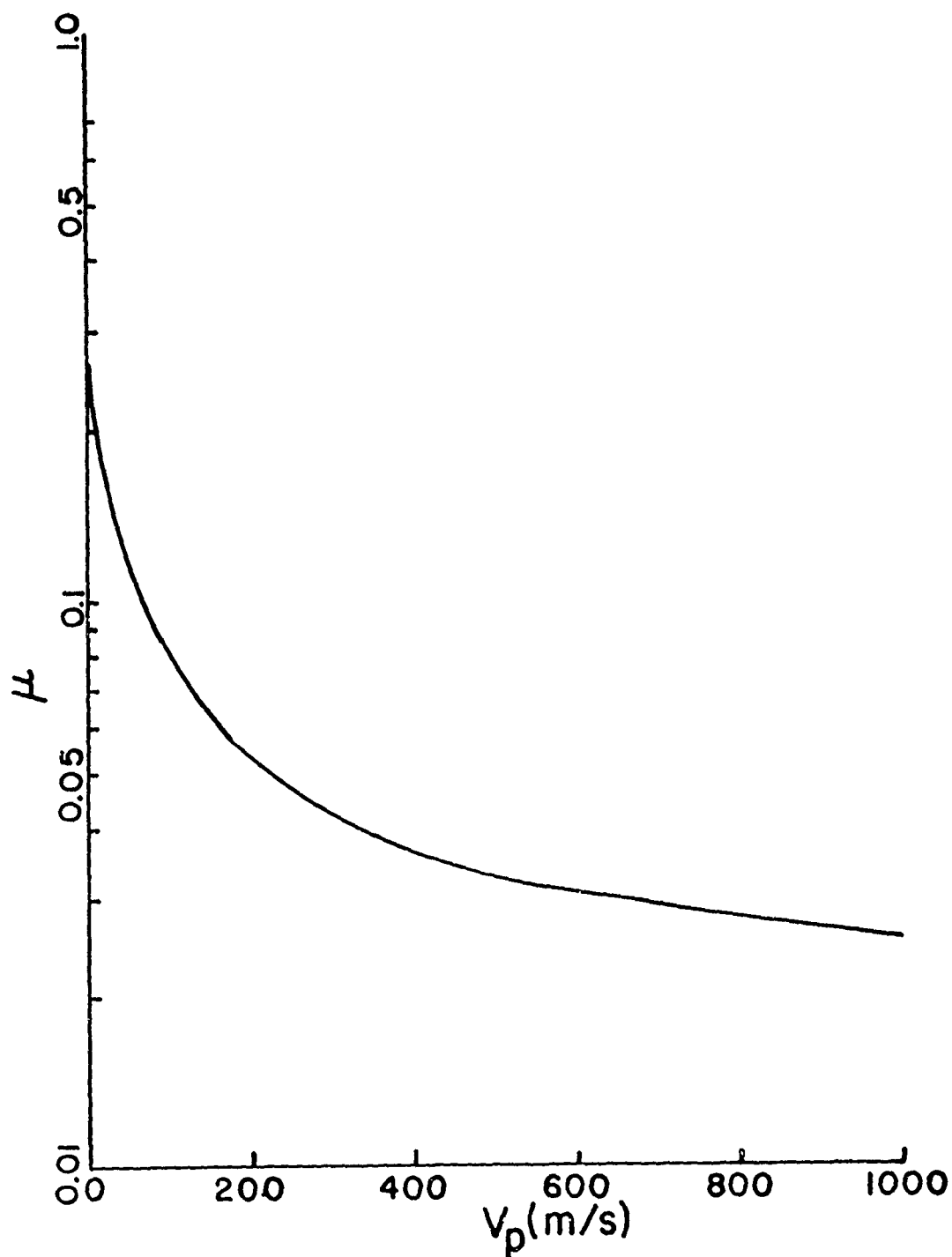


Figure 3. Rotating-band friction coefficient of 8" XM201 projectile as a function of projectile velocity. The pressure at the rotating-band is estimated as $3.1 \cdot 10^8$ Pa.

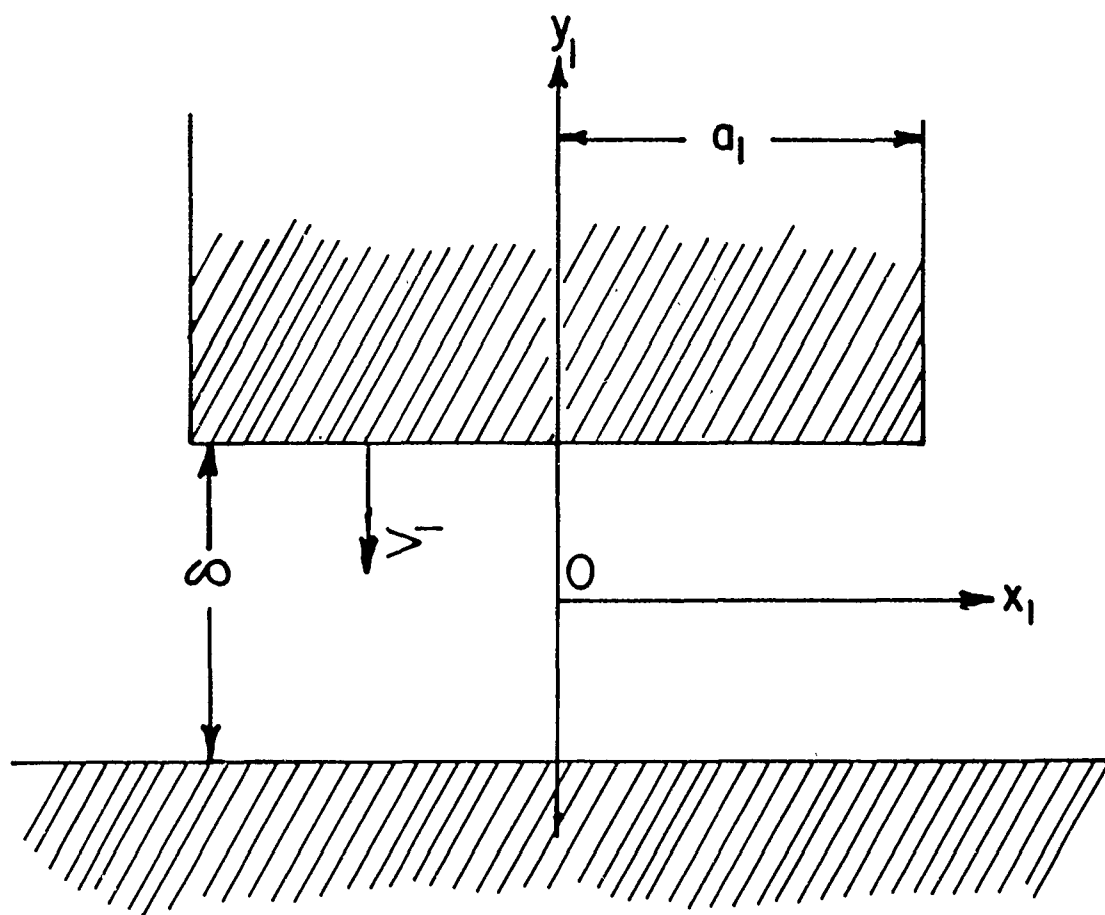


Figure 4. Collision of flat parallel surfaces separated by a molten metal film of thickness δ .

so that fluid outflow travels essentially in a line parallel to the X_1 coordinate. The thickness of the film is assumed small enough so that the Navier-Stokes equations may be approximated with

$$\frac{\partial^2 u_1}{\partial y_1^2} = \frac{1}{\gamma} \frac{dp}{dx_1} \quad (24)$$

with boundary conditions

$$u_1 = 0, y_1 = \pm \delta/2; p = 0, x_1 = \pm a_1$$

Here u_1 is the component of fluid velocity in the direction X_1 , p is the pressure which varies only in the X_1 direction and γ is the viscosity coefficient. The part of the solution of interest here is for p :

$$p = \frac{6\gamma V_1}{\delta^3} (a_1^2 - x_1^2) \quad (25)$$

Now the block loses kinetic energy according to

$$M_e V_1 dV_1 = -F d\delta \quad (26)$$

where

$$F = 2z_0 \int_0^{a_1} p dx_1 \quad (27)$$

Integrating Eq. (27), substituting the resulting expression for F into Eq. (26) and integrating, it is obtained that

$$V_1 = V_0 - \frac{16z_0\gamma a_1^3}{M_e} \left(\frac{1}{\delta^2} - \frac{1}{\delta_0^2} \right) \quad (28)$$

The final value of film thickness δ_t is found when $V_1 = 0$. Preliminary investigations showed that δ_t was near in value to δ_0 . Thus, one may

obtain the expression:

$$\frac{\delta_o - \delta_t}{\delta_o} = \frac{V_o M_e \delta_o^2}{32 z_o \gamma a_1^3} \quad (29)$$

The expression for δ_o may be obtained from Herzfeld and Kosson's report. When the projectile is somewhat away from the breech, the value of δ_o may be approximated as

$$\delta_o = \frac{\gamma V_p^{3/2}}{2 (\rho_T c_T)^{1/2} T_b} \left(\frac{2 \pi a_1}{k_T} \right)^{1/2} \quad (30)$$

Here ρ_T is the density of the tube material, c_T is the heat capacity of the tube material, T_b is the melting point for the band material and k_T is the thermal conductivity of the gun tube material. Now equating $M_e V_o$ with the expression for the reaction impulse given the rotating band at or after impact, rearranging the expression so it may be given in terms of the balloting energy ϵ_o and substituting into Eq. (29), it is obtained that

$$\frac{\delta_o - \delta_t}{\delta_o} = \frac{(2 I \epsilon_o)^{1/2} (1+e) |R| \delta_o^2}{32 z_o \gamma a a_1^3}, \quad (31)$$

Here z_o would be of the order of the radius of the projectile.

The values for δ_o and $(\delta_o - \delta_t)/\delta_o$ may be readily calculated. An initial value of $\epsilon_o \approx 5$ joules was used by Walker. The other data would be as follows

$$\begin{aligned} a &= 23.06 \text{ cm} \\ a_1 &= 2.5 \text{ cm} \\ I &= 6.171 \cdot 10^7 \text{ gm cm}^2 \\ z_o &= 10 \text{ cm} \\ \rho_T c_T &= 1.053 \text{ cal/cm}^3/\text{k} \end{aligned}$$

$$\begin{aligned}
T_b &\doteq 1000 \text{ K} \\
V_p &= 8 \cdot 10^4 \text{ cm/s} \\
k_T &= 0.105 \text{ cal/cm/s/K} \\
\gamma &= 0.035 \text{ poise} \\
|R| &\doteq 0.5
\end{aligned}$$

Substituting into Eq. (30) with the suitable value, it is obtained that $\delta_o \doteq 7 \cdot 10^{-4} \text{ cm}$. Substituting data into Eq. (31), it is obtained that $(\delta_o - \delta_t)/\delta_o \doteq 0.012$. Thus it is seen that the liquid layer would be thinned only an insignificant amount. The effective coefficient of friction for the reaction impulse would be expected to approximate values obtained for land-friction coefficients.

IV. Balloting-Energy Analysis

If the θ component of momentum can grow, the impacts of the bourrelet on the gun-bore surface could possibly cause extensive damage. It is of interest then to closely examine Walker's [5] mechanism for energy growth as discussed earlier. It is also desired to obtain a closed form expression for the balloting energy if possible.

The presence of axial torque due to gun-bore rifling makes the last objective more difficult. As will be seen, however, a measure of the balloting-energy growth can still be obtained. When the projectile is not making contact with the bourrelet and if there were no axial torque, Eq. (5-53) in Goldstein [10] shows that $|\dot{\theta}|$ depends only on θ . Thus the balloting energy immediately after impact would equal the balloting energy immediately before the subsequent impact. With the presence of an axial torque, whether $|\dot{\theta}|$ increases or decreases for subsequent equal values of θ may be examined by assuming the following relationship:

$$A \omega_{\dot{\theta}} = A \omega_{\dot{\theta}_0} + N_a t \quad (32)$$

where T is assumed constant. Here t is the elapsed time since immediately after impact. The quantity $a_{z'}'$ in the value of $a_{z'}$ at the initial time. Likewise Eq. (15) may be integrated in the same way and with some substitutions between the resulting equation and Eq. (25), one can obtain that

$$\dot{\phi} = \dot{\phi}_0 \frac{\sin^2 \theta_0}{\sin^2 \theta} + \frac{N_a}{I \sin^2 \theta} (\int \cos \theta dt - t \cos \theta) \quad (33)$$

Substituting Eq. (32) and (33) into Eq. (14), it may be obtained that

$$\begin{aligned} I \ddot{\theta} - \frac{I \dot{\phi}_0 \sin^4 \theta_0 \cos \theta}{\sin^3 \theta} + A \omega_{z'} \dot{\phi}_0 \frac{\sin^2 \theta_0}{\sin \theta} - m \dot{s} h \sin \theta = \quad (34) \\ \frac{N_a \dot{\phi}_0 \sin^2 \theta_0}{\sin \theta} \left[\frac{2 \cos \theta}{\sin^2 \theta} (\int \cos \theta dt - t \cos \theta) - t \right] \\ - \frac{N_a A \omega_{z'}}{I \sin \theta} (\int \cos \theta dt - t \cos \theta) \\ + \frac{N_a^2 (\int \cos \theta dt - t \cos \theta)}{I \sin \theta} \left[\frac{\cos \theta}{\sin^2 \theta} (\int \cos \theta dt - t \cos \theta) - t \right] \end{aligned}$$

Now consider when $\theta = \theta_0$ at a later time (but before the next impact). The first two terms on the right hand side may be added together to obtain a negative quantity; similarly the last two terms on the right hand side may be added together to obtain a negative quantity. The sum of the terms on the right hand side of the equation is always negative.

Compared to θ_0 , $\theta(t)$ is seen to be a smaller quantity. The torque then tends to align the axis of the projectile up with the gun-bore axis and results in softened subsequent impacts. In this analysis axial torque will be neglected. By neglecting the torque, an upper bound value for balloting-energy growth rate will be sought and the analysis becomes much simpler.

As discussed earlier in the Introduction, Harris Walker obtained the reaction forces at the rotating band in terms of the impact forces on the bourrelet; he asserts that there is a time lag τ_e between the application of the force $\tilde{\eta}$ and the equal and opposite force η_b to the shell. Walker asserts that the time lag occurs because the stress wave must travel from the bourrelet to the rotating band. Thus

$$\tilde{\eta}_b(t) = -\tilde{\eta}(t - \tau_e)$$

The amount of time lag is important in determining the amount of balloting energy added. Certainly, if the reaction impulse occurred immediately before the next impact, the balloting energy could be decreased by the overturning moment caused by friction. Additional insight may be obtained from the following equation:

$$\Delta T = \int N_{fi} \omega_i dt \quad (35)$$

Here ΔT is the increment of kinetic energy gained or lost by the shell due to the torque impulse. The vector N_{fi} is the torque applied about the center of the rotating band during the reaction impulse and is caused by the presence of friction, ω_i is the angular velocity of the shell. The reaction torque is assumed to occur after the impacting process. Here the integrand is integrated over the duration of the torque. At bourrelet-bore impact the corresponding impulse will be in a direction approximately parallel to the line of nodes if the friction coefficient at the bourrelet is small. According to a report of Gay [1] which gives a representative motion of the figure-axis of a shell, the angle between ω_i and N_{fi} would increase with time after impact so that the dot product of the two vectors

would decrease. Furthermore, the magnitude of ω_1 will be smaller with smaller values of θ . Thus, the largest increment of energy given to the total energy would occur if the reactive impulse occurred immediately after impact of the bourrelet.

Guided by these arguments and seeking an upper bound for the energy growth rate, a tentative hypothesis is made that the reaction impulse occurs immediately after the impact impulse occurs. A rigid-body model consistent with this time-lag hypothesis may be easily constructed and treated. In this model, the bourrelet impacts against the bore and the rotating band is assumed to be free of any constraining influences. Immediately after this impact process, the reaction impulse is applied to the rotating band and the bourrelet is assumed to be free of any constraining influences. In this rigid-body approximation, the constraint that the axis of rotation must be in the plane of the rotating band determines the value of the reaction impulse.

It is convenient for the analysis of the model to express the kinetic energy in coordinates about the center of mass of the projectile.

This expression would be

$$T = \frac{m}{2} (\dot{\eta}_{cg}^2 + \dot{z}_{cg}^2 + \dot{y}_{cg}^2) + \frac{m}{2} k^2 (\dot{\theta}^2 + \dot{\phi}^2 \sin^2 \theta) + \frac{A}{2} (\dot{\psi} + \dot{\phi} \cos \theta)^2 \quad (36)$$

The subscript cg denotes the values for the center of mass for the projectile and k is the transverse radius of gyration for the projectile. By the assumptions used to seek an upper-bound value for balloting energy growth and since the impact and reaction forces are of short duration, it is sufficient for the analysis to use the impulsive equations of motion and

focus upon the motions immediately after an impulse occurs. For impulsive forces, it can be shown that

$$\left(\frac{\partial T}{\partial q_i}\right)_1 - \left(\frac{\partial T}{\partial q_i}\right)_0 = P_{q_i} \quad (37)$$

Here p_{q_i} is the generalized impulsive force for the q_i coordinate. The first term on the left is for the value immediately after the impulsive force has acted and the term with the subscript 0 is for the value immediately before the force has acted.

From Eqs. (36) and (37), the transverse momentum given by the bourrelet impact is

$$m(\dot{\eta}_{cg})_1 - m(\dot{\eta}_{cg})_0 = P_{\eta} \quad (38)$$

Where P_{η} is the impact impulse. Additionally, using Eq. (21), the impulsive torque about the center of gravity may be obtained:

$$mk^2\dot{\theta}_1 - mk^2\dot{\theta}_0 = -(a-h)P_{\eta} + \frac{b\mu P_{\eta}}{(1+\pi^2/m^2)^{1/2}} \quad (39)$$

The other impulsive equations of motion obtained from Eq. (36) are not pertinent to the analysis. The initial conditions are given as

$$(\dot{\eta}_{cg})_0 = -h\omega \quad (40)$$

$$\dot{\theta}_0 = \omega \quad (41)$$

In addition, it is postulated that the coefficient of restitution is known or can be estimated so that

$$(\dot{\eta}_{cg})_1 = eh\omega \quad (42)$$

where e is the coefficient of restitution. Immediately it is seen from Eqs. (38), (40), and (42) that

$$p_{\eta} = m h \omega (e+1) \quad (43)$$

Then substituting Eqs. (43) and (41) into Eq. (39), the following equation may be obtained:

$$\dot{\theta}_1 = -\frac{\omega}{k^2} \{ h(a-h-b\mu G)(e+1) - k^2 \} \quad (44)$$

where

$$G = 1 / (1 + \pi^2 / m^2)^{1/2}$$

Now the reaction impulse process may be examined. From Eqs. (36) and (37), the transverse momentum given by the reaction impulse at the rotating band is

$$m(\dot{\eta}_{cg})_2 - m(\dot{\eta}_{cg})_1 = (p_{\eta})_b \quad (45)$$

The impulsive torque is given as

$$m k^2 \dot{\theta}_2 - m k^2 \dot{\theta}_1 = h(p_{\eta})_b + b G v (p_{\eta})_b \quad (46)$$

In addition, the condition that the rotating band must be the axis of rotation is given by

$$\eta_{cg} = -h \theta_2 \quad (47)$$

Eliminating $(p_{\eta})_b$ between Eqs. (45) and (46) and then using Eqs. (45) and (47), one can obtain that

$$\dot{\theta}_2 = -\frac{\omega [e h G v b - h^2 + h(a - G b \mu)(e+1) - k^2]}{[h(h + G v b) + k^2]} \quad (48)$$

(48)

The value of $(p_n)_b$ may be found by substituting Eqs. (42), (47) and (48) into Eq. (45):

$$(p_n)_b = \frac{mhw(e+1)[h(a-h-Gb\mu) - k^2]}{h(h+Gvb) + k^2} \quad (49)$$

Utilizing Eqs. (43) and (49), the following ratio can be obtained:

$$R \equiv (p_n)_b / p_n = \frac{h(a-h-Gb\mu) - k^2}{h(h+Gvb) + k^2} \quad (50)$$

With the rebound angular velocity $\dot{\theta}_2$ obtained, the effective coefficient of elasticity may be obtained. From Eq. (48) it is seen that the effective coefficient of restitution is

$$e_e = \frac{[ehGvb - h^2 + h(a-Gb\mu)(e+1) - k^2]}{h(h+Gvb) + k^2} \quad (51)$$

The quantities A , h , k and b may be nondimensionalized by the quantity $2b$ to obtain these quantities in calibers. One then obtains that

$$e_e = \frac{[eh'Gv + h'(2a' - G\mu)(e+1) - 2h'^2 - 2k'^2]}{[h'(2h' + Gv) + 2k'^2]} \quad (52)$$

From Eq. (52), it is seen that values for μ and v of the order 0.05 will change the value of e_e little from the value of e_e if the friction coefficients were assumed to be zero. Assuming the friction coefficients to be zero, a calculation of e_e may be easily made for the 8" projectile that was of interest to Walker. Here

$$a = 1.135 \text{ calibers, } h = 0.71 \text{ cal.,}$$

$$k = 1.066 \text{ cal., } e = 0.7$$

and

the twist is $n = 20$ cal/revolution. Plugging these values into Eq. (52), it is obtained that $e_e = -0.165$. Since e_e is negative, this means that the resulting movement of the bourrelet is toward the bourrelet and not away from the bourrelet as might be expected. Here, with this simple model, the impacting process continues after the first reaction impulse. Thus, the hypothesis that the impacting process is completed before the reaction process is started is seen to be contradicted by the results from a model suggested by the hypothesis. Friction effects can not rescue the hypothesis from contradiction either since if $\mu \geq \nu$ (as one would expect it to be), then e_e becomes a greater quantity in the negative sense.

Certainly, these results do not rule out that part of the reaction process occurs after the impacting process is completed. Thus, there still exists the possibility that the presence of band friction might increase the effective coefficient of restitution.

If the impact forces and reaction forces overlap in time, another simple model is suggested. Let us consider that the impact and reaction forces occur simultaneously. The impulsive Lagrange equations for this case are

$$m(\dot{\eta}_{cg})_1 - m(\dot{\eta}_{cg})_0 = P_\eta + (P_\eta)_b \quad (53)$$

$$mk^2\dot{\theta}_1 - mk^2\dot{\theta}_0 = -(a-h)P_\eta + Gb\mu P_\eta + h(P_\eta)_b + Gb\nu(P_\eta)_b \quad (54)$$

In a similar way as before it is obtained that

$$P_\eta = m\omega(1+e) \frac{[h(h+Gb\nu) + k^2]}{[a + Gb(\nu - \mu)]} \quad (55)$$

$$(p_{\eta})_b = m \omega (1+e) \frac{[h(a-h-Gb\mu) - k^2]}{[a + Gb(\nu - \mu)]} \quad (56)$$

The ratio of $(p_{\eta})_b$ to p_{η} , R , is seen to be that obtained earlier and given by Eq. (50). The value of R does not depend on the details of the impact and reaction processes; rather, it is determined only by the requirement that rotation must occur around an axis in the plane of the rotating band. Here the effective coefficient of restitution e_e is simply e and no increment in balloting energy can be obtained from the effects of either band friction or bourrelet friction. Even though no possibility exists for balloting energy amplification, it would be desirable to minimize the magnitude of the impact impulse. Thus, according to Eq. (56), the distance from rotating band to bourrelet a should be as large as possible.

It appears from the above results that e_e might possibly be less than e for overlapping impact and reaction forces. The present author cannot prove this, however; instead an upper bound value for e_e will be obtained. Since large balloting energies may be possible according to some evidence, it is an attempt to explore these possibilities even though the dynamics of the motion may be complicated. The maximum $(p_{\eta})_b$ that might occur is given by Eq. (56), which is valid for simultaneous impulses. Now suppose that by some mechanism unknown to the author, the friction force were applied at the rotating band after the impact and reaction processes had occurred. The value of e_e would then be greater than e . The expression for the maximum angular momentum due to this application of frictional force on the rotating band is

$$I \Delta \dot{\theta} = b G (p_{\eta})_b \nu \quad (57)$$

where it is assumed that $v = 0$ in the expression for $(p_n)_b$.

The expression for e_e is

$$e_e = - \frac{\dot{\theta}_2}{\omega} = \frac{-\dot{\theta}_1 - \Delta \dot{\theta}}{\omega} \quad (58)$$

$$e_e = \frac{e\omega - \Delta \dot{\theta}}{\omega}$$

Substituting Eqs. (56) and (57) into Eq. (58) and since $I = m(h^2 + k^2)$

$$e_e = e - \frac{(1+e)GvR}{2a' - G\mu} \quad (59)$$

where R is expressed by Eq. (50) and a' is the value of a in calibers.

First, consider what e_e would be for accepted parameter values.

If it is assumed that $e = 0.7$, $\mu = 0.2$ from the results of Bowden, $v = 0.05$ and the values of a' , h' , and k' are as given earlier for the 8" projectile, it can be calculated that $e_e = 0.75$. If Walker's values of $\mu = 0.5$ and $v = 0.55$ are used, $e_e = 1.59$. The balloting-energy growth would then be rapid as Walker predicted.

With the assumptions made in this paper, an upper bound value for energy growth rate can be obtained in terms of e_e . Neglecting torque, after n impacts θ would be

$$\dot{\theta} = \omega e_e^n \quad (60)$$

where

$$\dot{\theta} \equiv |\dot{\theta}|$$

Now treating n as a continuous variable, n can be expressed as $n = \theta/(2\Delta)$

where $\Delta = c/a$. The quantity c is the clearance between the bore and

bourrelet when the shell is centered in the bore. Substituting the

expression for n into Eq. (60) and integrating, the following expression

can be obtained:

$$t = \frac{2\Delta (1 - e^{-\Theta/(2\Delta)})}{\omega_0 \ln e_e} \quad (61)$$

Since the balloting energy ϵ is $\epsilon = \frac{1}{2} I \dot{\theta}^2$, manipulation of Eqs. (60), (61) and the expression for n show that

$$\epsilon = \epsilon_0 / [1 - (\epsilon_0/2I)^{1/2} \gamma t]^2 \quad (62)$$

where

$$\gamma = (\ln e_e) / \Delta$$

Equation (62) is the expression that Walker also obtained although the expression for γ obtained here is completely different than what Walker obtained for γ .

Summary and Conclusions

Since errors were discovered in Walker's report concerning the balloting motion of a projectile in-bore, it was decided to attempt a correct development but using the same general approach. That is the projectile is treated primarily as a rigid body. The elastic character of the projectile was taken into account by Walker by assuming a time lag between the impact forces at the bourrelet and the reaction forces at the rotating band. Initially, a time lag between the application of the two impulses was hypothesized in this paper. To avoid numerical integration of the differential equations of motion and obtain an upper bound to energy growth rate, it is postulated that the reaction forces occur immediately after the impact forces.

The impulsive Lagrange equations of motion may then be used. Determination of the reaction impulsive force and the final motion is obtained by the requirement that the projectile must rotate about an axis in the plane of the rotating band. For the 8" XM201 shell and many other shells, the resulting calculations show that the final motion is toward the bore surface and not away from the bore surface as one might expect. Thus a model suggested by the hypothesis contradicts the hypothesis since the bourrelet contacts the bore after the reaction impulse. From these results, it appears that the impact and reaction forces are occurring with considerable overlap; i.e., part of the impact forces are occurring when the reaction forces are occurring.

These results suggest investigating a projectile having impact and reaction impulses occurring simultaneously. It is interesting to examine the resulting expression for the impact impulse, Eq. (55), more closely for the possibility of obtaining large impact impulses. For conventionally designed projectiles the first term of the denominator is much larger than the magnitude of the second term. The second term will be negative since the band-friction coefficient might be expected to be of the order 0.05 while the bourrelet friction coefficient might be expected to be of order 0.2. Now, suppose by some accident or design flaw, the effective value of μ might be decreased considerably, even to the point that the magnitude of the first term would be comparable to the magnitude of the second term. Thus, the value of the impact impulse could possibly become large enough to damage the gun-bore surface even though the balloting energy might be small.

With these dynamic models, it is still not clear if balloting energy amplification could occur. However, it does appear that the simultaneous impulse model would give the maximum reaction impulse for a given balloting energy. An upper-bound value for the effective coefficient of restitution should then be obtained by utilizing the simultaneous impulse model together with the assumption that the resultant torque impulse due to band friction is applied immediately after the reaction impulse. If the more correct values of bore friction are used, it appears that the effective coefficient of restitution would be only about 0.05 greater than the coefficient of elasticity. The effective coefficient of restitution will then be less than one. If, however, Walker's values for friction coefficients were used, the effective coefficient of restitution would be about 1.6. Thus, it appears that for conventionally designed projectiles, the balloting energy will only decrease and a more detailed analysis of balloting motion is unnecessary. An upper bound for the balloting energy growth may easily be obtained in terms of the effective coefficient of restitution. Since the presence of axial torque causes the subsequent impacts to be less and consideration of axial torque would require numerical techniques, the ignoration of this torque will give an upper bound value for balloting-energy growth.

The main conclusion that the balloting-energy will only decrease from its initial value depends heavily on the values utilized for the coefficient of bore friction. These values are known approximately from experiment and it is asserted with some confidence that Walker's [5] values for friction coefficients are in error by perhaps an order of magnitude.

REFERENCES

1. H. P. Gay, "Notes on the Yawing Motion of a Projectile in the Bore," Ballistic Research Laboratory Report No. 2259 (AD 908456L), Aberdeen Proving Ground, Maryland, January 1973.
2. F. V. Reno, "The Motion of the Axis of a Spinning Shell Inside the Bore of a Gun," Ballistic Research Laboratory Report No. 320 (AD 491839), Aberdeen Proving Ground, Maryland, February 1943.
3. L. H. Thomas, "The Motion of the Axis of a Spinning Shell Inside the Bore of a Gun," Ballistic Research Laboratory Report No. 544 (AD PB22102), Aberdeen Proving Ground, Maryland, May 1945.
4. S. H. Chu, and F. K. Soechting, "Transverse Motion of an Accelerating Shell," Technical Report 4314, Picatinny Arsenal, Dover, NJ, June, 1972. AD 894572L.
5. E. H. Walker, "Yawing and Balloting Motion of a Projectile in the Bore of a Gun with Application to Gun Tube Damage," U. S. Army Ballistic Research Laboratory Memorandum Report No. 2411, Aberdeen Proving Ground, Maryland, September 1974. AD 923913L.
6. C. M. Glass, "Fracture of an 8-inch M106 Projectile in an M110E2 Howitzer," U.S. Army Ballistic Research Laboratory Report 1905, Aberdeen Proving Ground, MD, August 1976.
7. R. S. Montgomery, "Friction and Wear at High Sliding Speeds," Wear, Vol. 36, 1976, pp. 275-298.
8. C. M. Herzfeld and R. L. Kosson, "A Theory of Bore Friction," U. S. Army Ballistic Research Laboratory Report No. 851, Aberdeen Proving Ground, Maryland, March 1953. AD 10639.

9. F. P. Bowden, "Recent Experimental Studies of Solid Friction," in Friction and Wear, R. Davies (Editor), Elsevier Publishing Co., Princeton, N.J. 1959. pp. 84-109.
10. H. Goldstein, Classical Mechanics, Addison-Wesley Publishing Co., Inc., Cambridge, MA, March 1956.
11. W. W. Shugarts, Jr., "Frictional Resistance and Wear at High Sliding Speeds," The Frankling Institute Laboratories for Research and Development, IR No. I-2448-2, June 15, 1955.
12. F. M. Sauer, "Fundamental Mechanism of Wear and Friction of Unlubricated Metallic Surfaces at High Sliding Speeds," U.S. Naval Ordnance Test Station Report No. 1729, China Lake, CA, April 1957.
13. F. M. Sauer, "Analysis of Steady-State Metallic Friction and Wear Under Conditions of Molten Metal Film Lubrication," Stanford Research Institute, Technical Report No. 1, Project No. SU-1494, December 5, 1956.
14. J. O. Pilcher and E. M. Wineholt, "Analysis of the Friction Behavior at High Sliding Velocities and Pressures for Gilding Metal, Annealed Iron, Copper, and Projectile Steel," In-Bore Dynamics Symposium sponsored by the TTCP Technical Panel W-2. 1976.
15. H. G. Landau, "Heat Conduction in a Melting Solid," Quarterly Journal of Applied Mathematics 8, No. 1, pp. 81-94, April 1950.

TRANSVERSE DYNAMIC RESPONSE OF GUN BARREL
WITH TIME VARYING SUPPORTS

T.T. FENG

Ebasco Services Inc.
New York, New York

T. HUNG

U.S. Army Armament Command
Rock Island, Illinois

1

TABLE OF CONTENTS

	<u>Page</u>
ABSTRACT	180
I. INTRODUCTION	181
II. PROBLEM FORMULATION	182
III. METHOD OF SOLUTION	185
IV. EXAMPLE	186
V. CONCLUSIONS	188
VI. REFERENCE	198

ABSTRACT

The rising interest in low dispersion, burst fire guns for anti-armor applications has generated a class of gun barrel design which requires a better analytical prediction basis for transverse motion than a conventional simple cantilever model. Inclusion of the effects due to inertia forces of barrel motion, Bourdon load, and travelling projectile load, etc., in the analytical basis appears necessary for useful prediction. Recently, a general model encompassing such effects was formulated [1]. However, no rigorous full solution has yet been obtained.

One of the significant analytical obstacles for this class of barrel design is the multiple time varying supports due to barrel motion. In this paper, the transverse dynamic response of a barrel with a displacement norm for convergence, is established for the governing equations.

A numerical example is given with a 60mm gun barrel having three supports. Transverse and angular deflections at the muzzle end during a single shot cycle are shown. The results indicate possible extended applications for burst fire and a barrel with discontinuous (gap/pad) supports.

1. Introduction

Conventionally, gun barrel analysis is done under the assumption that the barrel is either axially fixed or cantilevered at one end. In some recent designs for low dispersion guns, the barrel is supported transversely. Very small gaps exist between the barrel and the supports, and the barrel moves with respect to the supports during firing. A model of this complex system has not yet been well formulated. However, the beam equation for transverse motion of a cantilevered barrel appears in Appendix B of WVT-TR-75015^[1]. This rather general model includes the effects of barrel weight, inertia force of the barrel motion, Bourdon load, and projectile weight and acceleration force. In this paper, the governing equations of the model are modified and utilized to analyze the transverse dynamic response of a gun barrel with three supports, but without gaps between the supports and the barrel.

A combination of finite difference, modal analysis and Picard's iteration scheme is adopted as the basis for the method of solution. Modal analysis is done in a short time interval considering the location of barrel supports fixed. The iteration scheme is employed to cope with forcing functions which are response dependent. By revising the modes of the barrel and considering the terminal and initial conditions of the problem, dynamic response is obtained in the next short period of time. Continuing in this way, a successive modal analysis in an iterative manner is established.

A numerical example with a 60mm gun barrel is considered. As a specific interest for precision, the transverse and angular deflections at the muzzle end during a single shot firing are shown. The results appear to indicate reasonable physical trends and magnitudes.

The accuracy of the analysis is, in general, dependent on the time intervals and the associated axial movement. Initial estimate of time-space deflection is the prime factor for convergence. A norm for convergence based on deflection is found to be a good estimator of the solution.

2. Problem Formulation

Referring to Figure 1, the equations of the transverse motion of the barrel are [1] :

$$\begin{aligned} (EIy'')'' + \rho A(x)\ddot{y} = & -\rho g A(x) \cos \alpha - p(x,t) a^2 y'' - I \dot{V}^2 y'' + 2V\dot{y}' + \ddot{y} + \dot{V}y' + g \cos \alpha] m_p \delta(\xi-x) \\ & - y' \rho g A(x) (\ddot{X}_0(t)/g - \sin \alpha) + \int_x^{\eta} y'' \rho g A(\bar{x}) (\ddot{X}_0(t)/g - \sin \alpha) d\bar{x} \\ & + P_1 \delta(\eta-x) + P_2 \delta(\eta+\zeta-x) \end{aligned} \quad (1)$$

$$\left. \begin{aligned} y(0,t) &= y'(0,t) = 0 \\ y(\eta,t) &= y(\eta+\zeta,t) = 0 \\ \dot{y}(x,0) &= \dot{y}_0 \\ y(x,0) &= y_0 \end{aligned} \right\} \quad (2)$$

where E = modulus of elasticity

I = moment of inertia of the barrel cross-section

ρ = mass density of the barrel

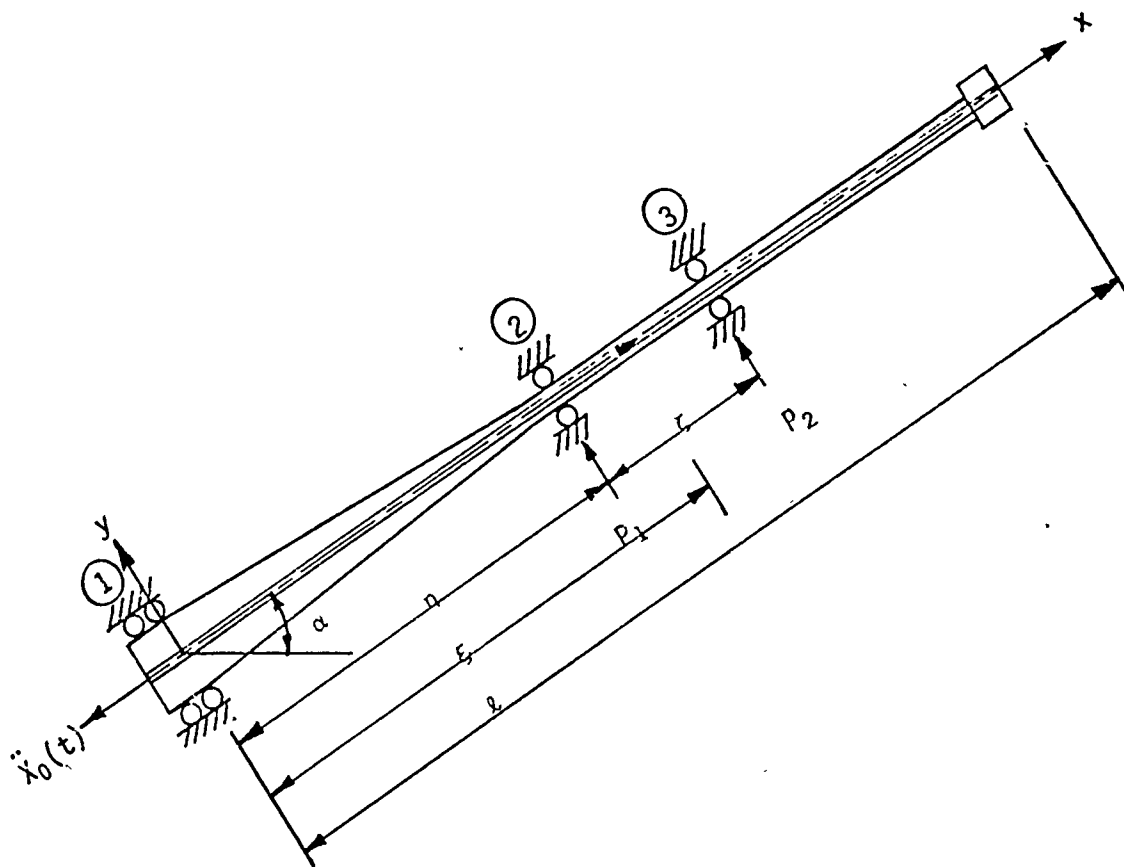


FIGURE 1 Barrel with Three Supports

$A(x)$ = cross-sectional area of the barrel

$p(x,t)$ = bore pressure

a = inner radius

V = velocity of the projectile

g = gravitational acceleration

α = inclined angle of the barrel axis

m_p = projectile mass

δ = Dirac delta function

ξ = projectile travel distance

$X(t)$ = recoil and counter-recoil acceleration

L = total length of the barrel

P_1 = reaction of the second support

η = recoil and counter-recoil distance

P_2 = reaction of the third support

ζ = distance between the last two supports

In the right-hand side of Equation (1), the first term is gravitational force; the second term is Bourdon load; the third term is projectile inertia and gravitational force; the fourth and the fifth terms are recoil and counter-recoil inertia forces; and the last two terms are reactions of the supports.

Bore pressure distribution $p(x,t)$ is obtained by assuming that the charge is uniformly distributed along the barrel and its velocity is zero at the breech and increases linearly to the velocity of the projectile base. Other factor (e.g., friction) are neglected, so from gas dynamics:

$$p(x,t) = p \left[1 - \frac{m_c}{\frac{m_c}{2} + m_p} \cdot \frac{1}{2} \cdot \left(\frac{x}{\ell} \right)^2 \right] \quad (3)$$

where p is the breech pressure and m_c is the weight of the charge.

3. Method of Solution

Since the recoil and counter-recoil distance η is a function of time, Equations (1) and (2) obviously defy a simple analytical solution. If one assumes, however, that η is constant, Equations (1) and (2) can be readily solved by finite difference, modal analysis, or any other suitable methods. It follows that for a short period of time one may attempt to seek an approximate numerical solution by considering η constant. The solution over the whole time interval of concern could be obtained by updating the value of η through successive short time intervals. Furthermore, for a short time interval the barrel modal functions can be treated as fixed. Using several modal functions to expand the solution in the interval would then result in an approximate solution.

A difficulty arises in the right hand side of Equation (1), which involves the unknown transverse loads and must be calculated before the usual modal method can be applied. To overcome this, one may resort to an iterative method. First, one assumes the barrel is under the action of gravitational force, which is a multiple (starting weight factor) of the first term of the right-hand side of Equation (1). The solution of this load gives an amount of deflection, which is used to calculate "transverse load" for the next iteration. This is essentially an adopta-

tion of the generalized Picard's method. Use of modal analysis in such a manner with a finite elements model has two advantages. It avoids calculating the reactions P_1 and P_2 , and it takes account of any attached masses.

Convergence of the iterative process can be determined by considering a displacement norm:

$$||y|| = \sqrt{\int_0^L \int_0^{\Delta T} (y_{k+1} - y_k)^2 dt dx} / \sqrt{\int_0^L \int_0^{\Delta T} y_{k+1}^2 dt dx} \quad (4)$$

where ΔT is the time interval considered and the subscripts of y indicate iteration numbers. If $||y||$ is less than some small number then iteration is terminated. The solution at $t=\Delta T$ is taken as the initial conditions for analysis in the next time interval.

There is another difficulty at the support points. Deflections at support points which are zero in the present time interval are not necessarily zero in the next time interval and vice versa. To overcome this obstacle, one may use revised modal functions to expand the terminal conditions (solutions at $t=\Delta T$ of the current time interval) as the initial conditions for the next time interval. The connection between these two time intervals would then smooth.

4. Example

For a numerical example, a 60mm barrel with given material and geometric data at initial position in Figure 2 is considered. These data simulate an experimental test bed of the Army Medium Caliber Anti-armor Automatic Cannon Program. Breech pressure history, projectile

$E = 30 \times 10^6 \text{ psi}$
 $\rho g = 0.285 \text{ lb/in}^3$
 $m_c = 5.22 \text{ lb}$
 $m_p = 6.00 \text{ lb}$
 $\alpha = 0^\circ$

Unit of measure in Figure 2 is per inch
 p, V, ξ Shown in Figure 3
 n, \dot{X}_0 Shown in Figures 4 and 5

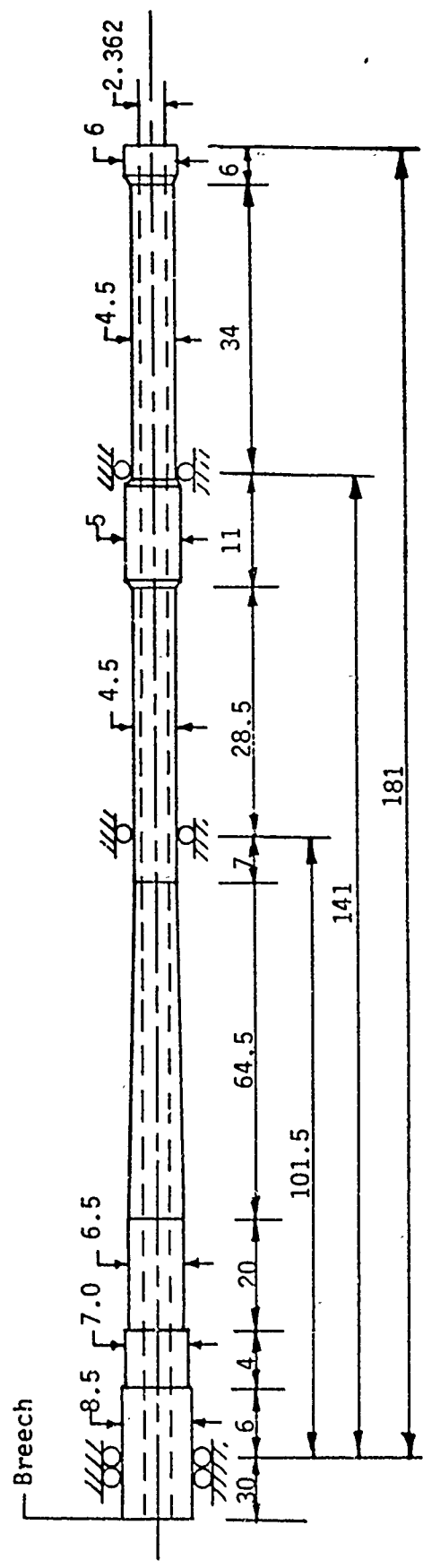


FIGURE 2 Geometric and Material Data of 60mm Barrel at Initial Position

travel velocity and distance, and recoil and counter recoil velocities and distances are shown in Figures 3, 4, and 5. The distance z was kept constant throughout the analysis. The barrel has been divided into 51 finite elements for analysis. The analysis lasted to a complete stroke of one fire. It started with zero velocity of the barrel and deflection due to dead weight of the barrel. Analysis proceeded with time intervals associated with barrel travel distances at 1.2 and 2.4 inches. The projectile passed through the barrel in the first time interval from 0 to 0.0070 seconds.

The first six frequencies at several recoil distances are listed in Table 1. The successive time intervals, time grid points used in the intervals, iteration number of each time interval, and $||y||$ of the initial and final iterations are listed in Table 2. Time-deflection of the muzzle end is shown in Figures 6.1-6.3. The muzzle end oscillates between -0.029 and +0.022 inches at the final stage of counter-recoil. The deflection of the muzzle end at the moment that projectile leaves the barrel is $y = -0.0058$ inches and $y' = -0.00014$ radians. Total computing time for this problem is 5 minutes with a double precision computing area of 300 K bytes on an IBM 360/65 computer.

5. Conclusions

The results in Figures 6.1-6.3 indicate reasonable physical responses at the muzzle end during the firing cycle. The approximate method utilized, therefore, appears to be useful in the analysis of transverse motion of a gun barrel on multiple time varying supports with effects due to gravitational force, Bourdon load, projectile and charge effects, and recoil and counter recoil accelerations.

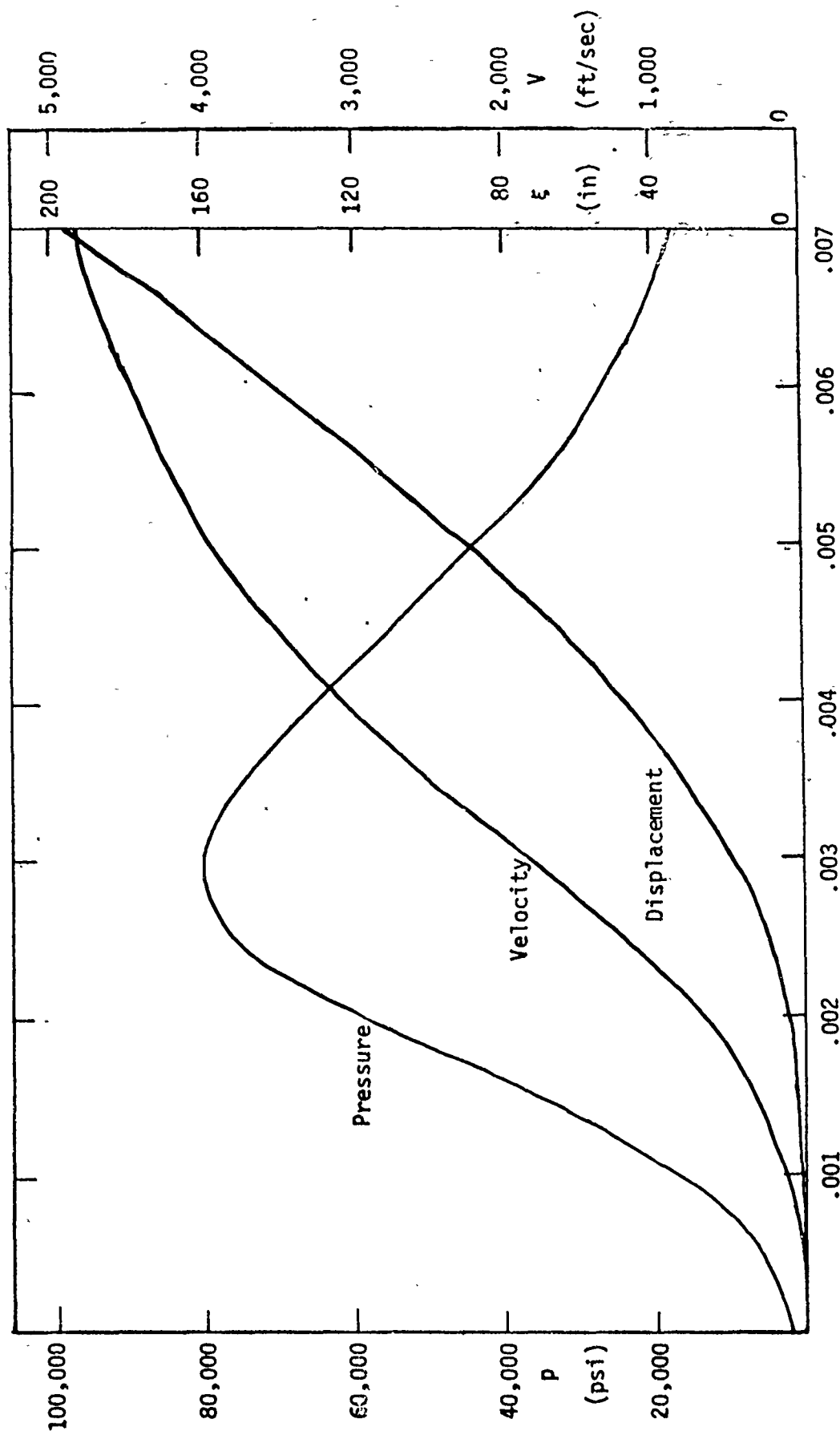


FIGURE 3 Breech Pressure and Projectile Velocity and Displacement

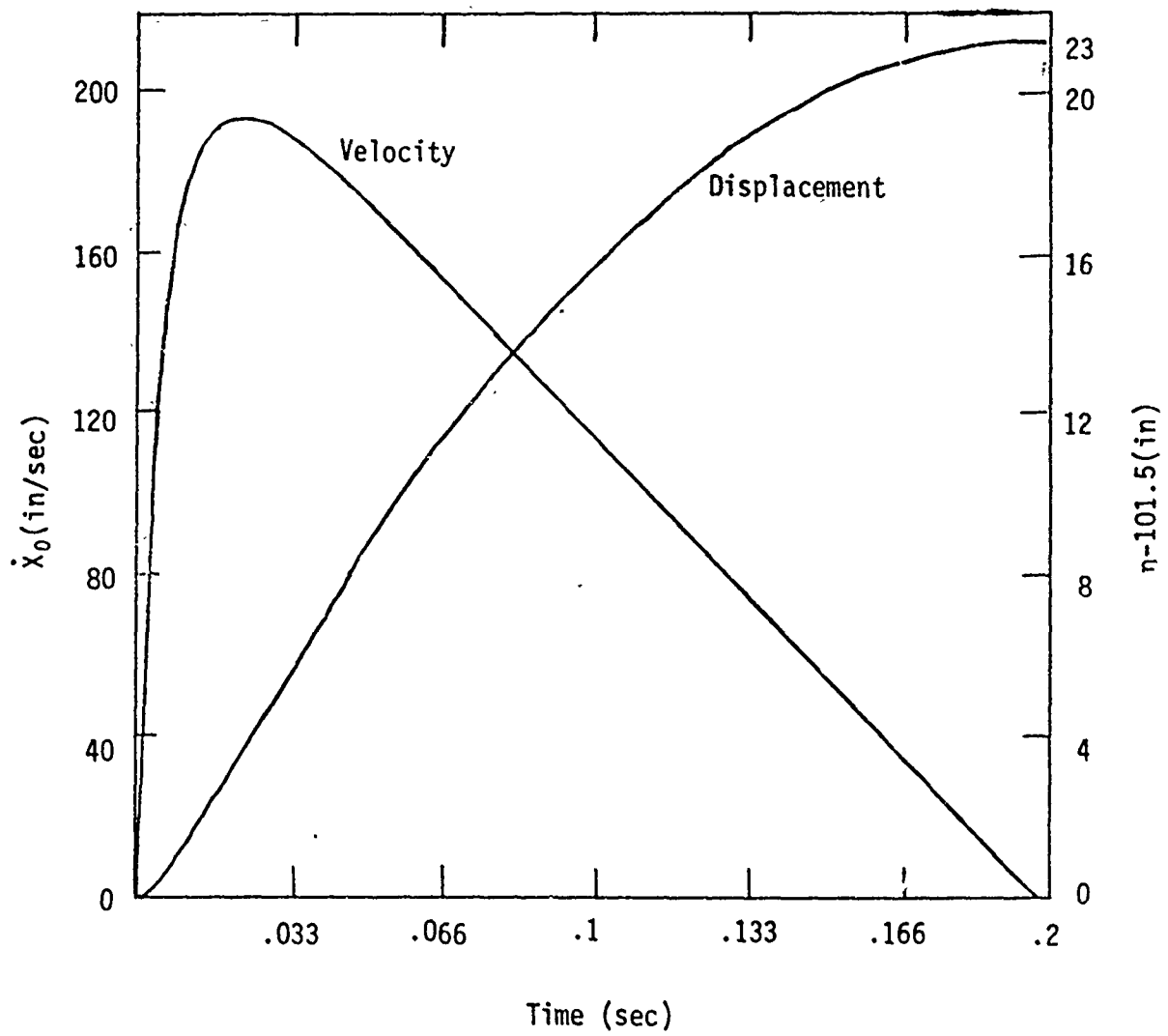


FIGURE 4 Recoil Velocity and Displacement

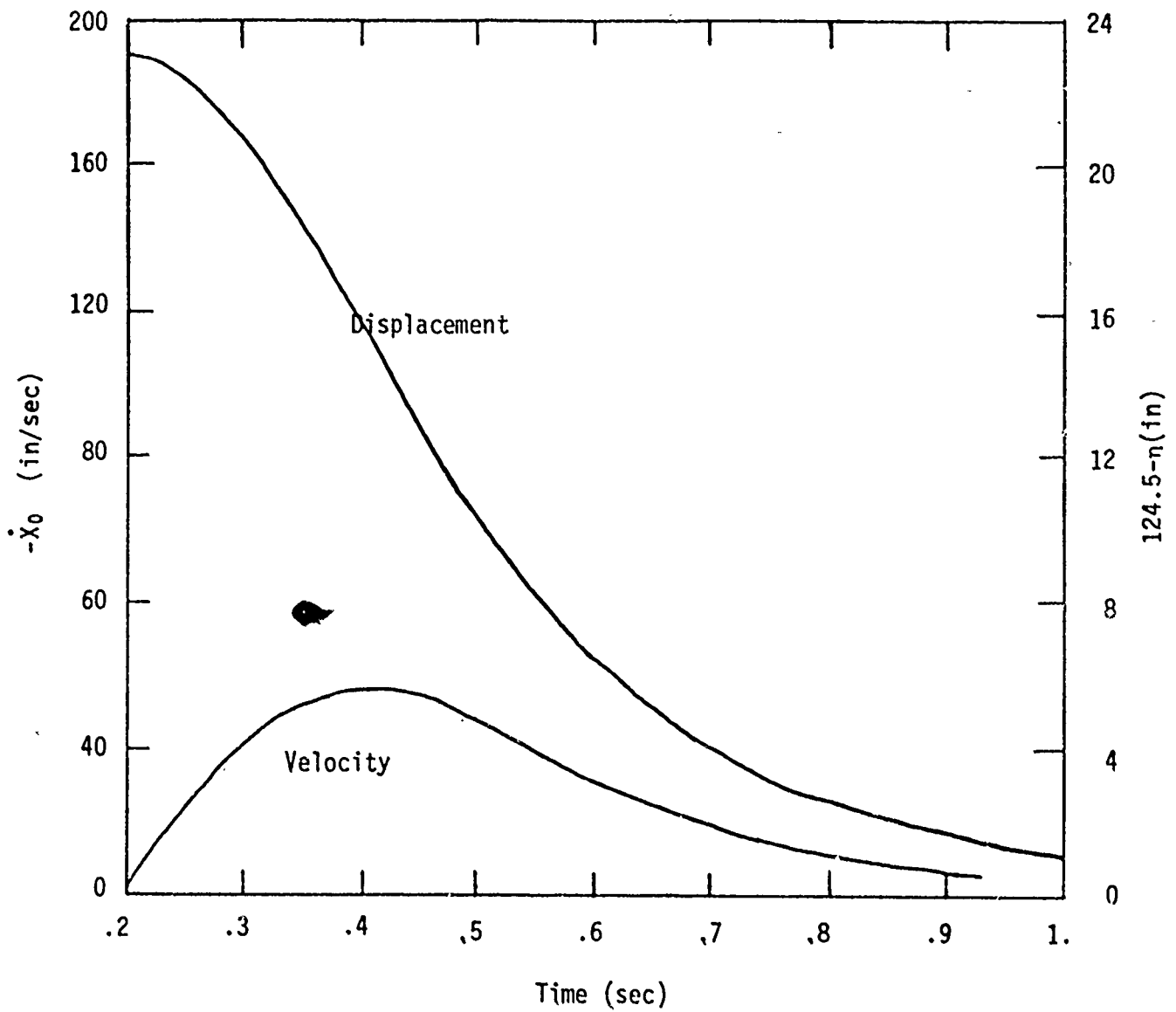


FIGURE 5 Counter Recoil Velocity and Displacement

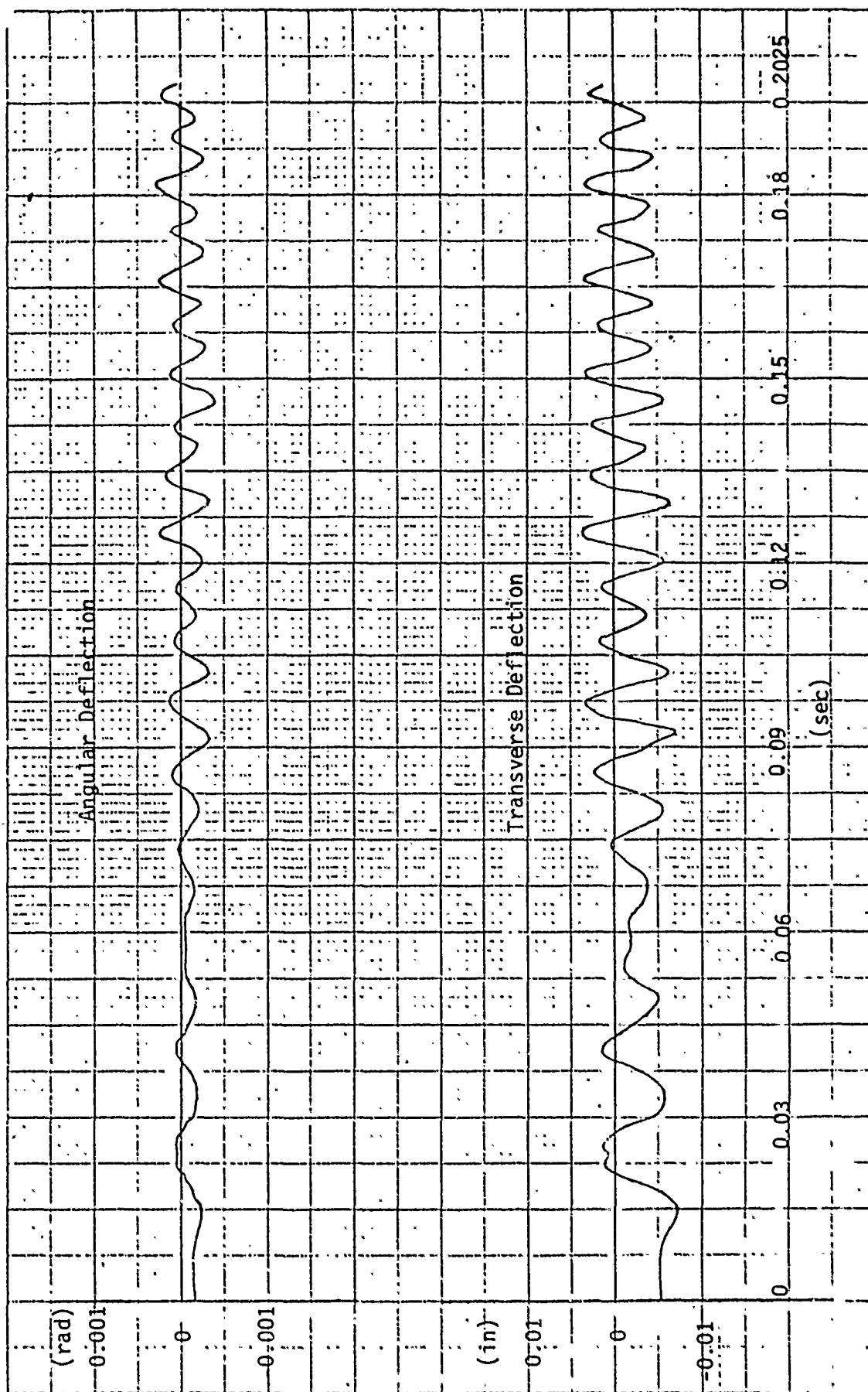


Figure 6.1: Time-Deflection of the Muzzle End.

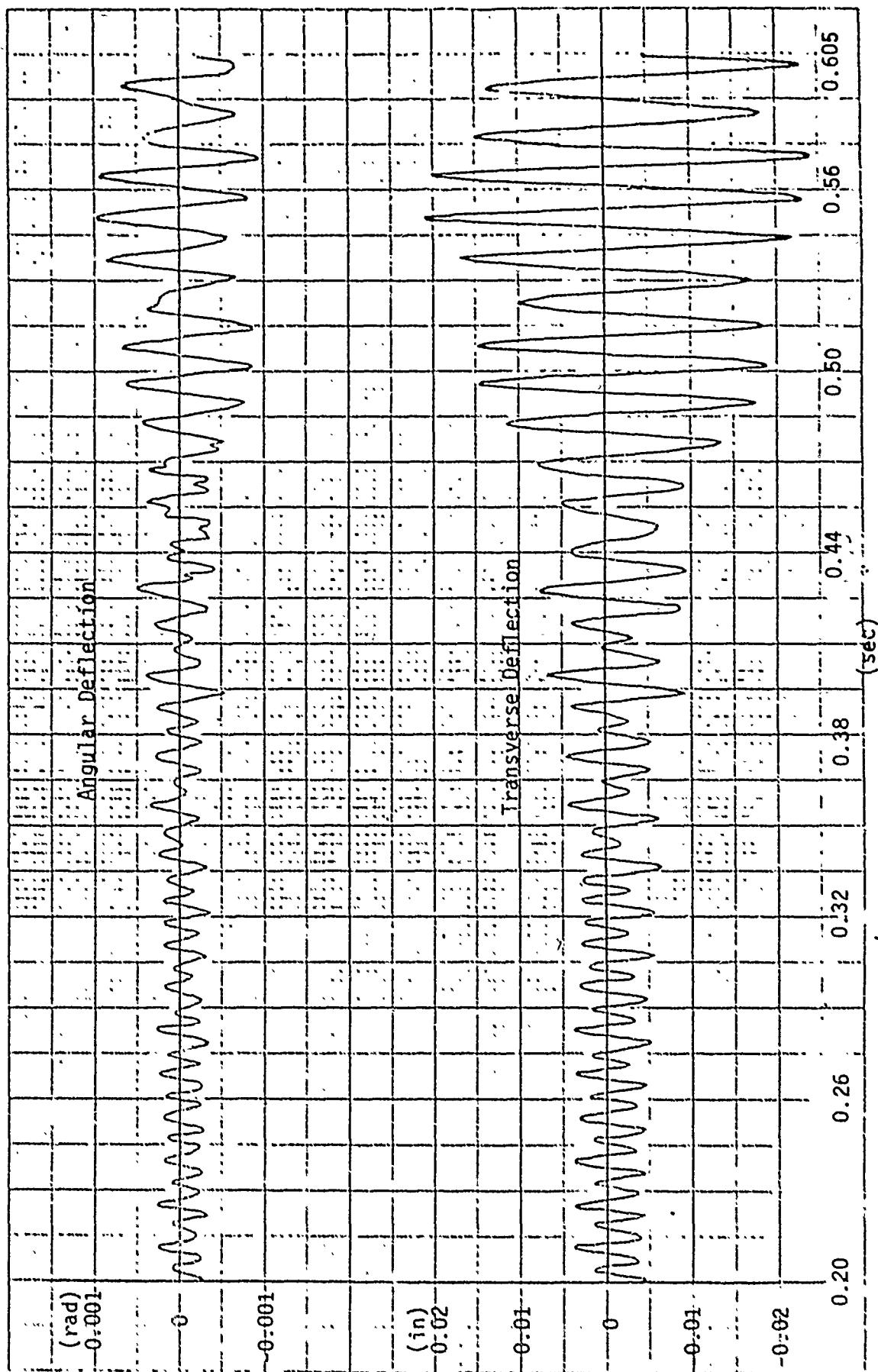


Figure 6.2: Time-Deflection of the Muzzle End.

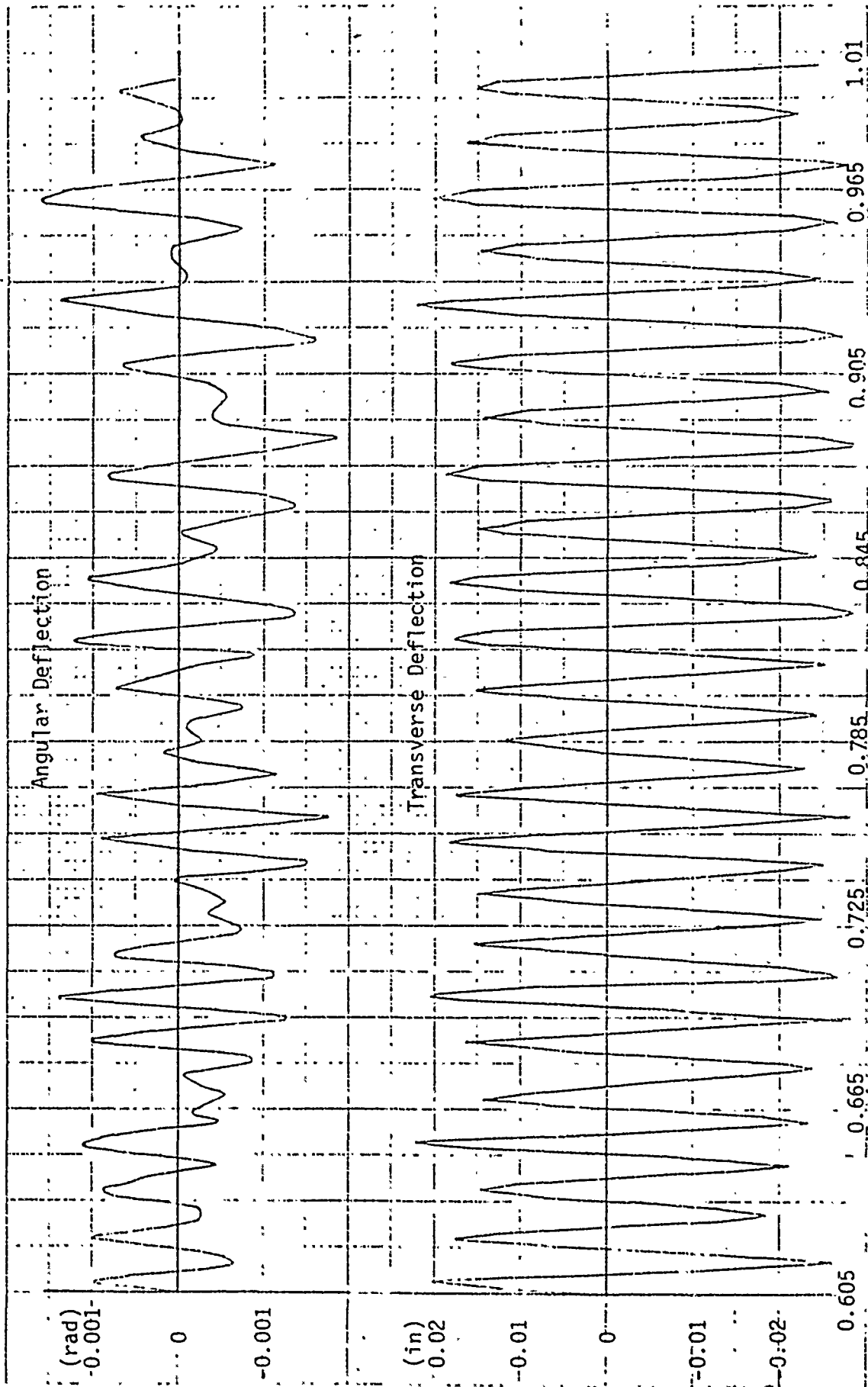


Figure 6.3: Time-Deflection of the Muzzle End.

Table 2 shows the effects of the projectile inertia and the charge pressure in the relevant time interval. The effect of the recoil inertia is small in each time interval, but the recoil distances accumulate the effect. Because of geometric changes, the recoil effect should be shown in successive time intervals.

The method shows its computational effectiveness in the example. It needs very small amount of computing area because space dimension is shortened by modal analysis and time dimension is repeatedly used in the successive time intervals. Moreover, a solution for a burst fire may be obtained by simply applying the method for longer time period without exorbitant computing time.

It appears reasonable to speculate that the method may be extended further to determine the combined effects of the distance η in Figure 1 and the supporting gaps upon the transverse dynamic response of a gun barrel at the muzzle end.

TABLE 1 - Recoil Distances and the Associated Tube Frequencies

<u>n</u> <u>(in)</u>	<u>f1</u> <u>(Hz)</u>	<u>f2</u> <u>(Hz)</u>	<u>f3</u> <u>(Hz)</u>	<u>f4</u> <u>(Hz)</u>	<u>f5</u> <u>(Hz)</u>	<u>f6</u> <u>(Hz)</u>
101.5	51.1	98.4	266	334	467	585
102.7	53.2	96.3	261	341	471	574
103.9	55.5	94.2	256	347	478	564
105.1	57.9	92.3	252	352	486	557
106.3	60.5	90.5	247	357	494	556
107.5	63.2	88.8	242	361	497	562
108.7	66.1	87.3	237	363	495	578
109.9	69.0	86.1	232	366	490	601
111.1	71.8	85.5	228	367	484	628
112.3	73.9	85.9	223	368	477	658
113.5	74.9	88.0	219	368	471	688
114.7	74.7	91.6	215	368	465	705
115.9	74.0	96.4	211	367	459	701
117.1	73.0	102	207	366	455	690
118.3	71.9	108	203	364	450	677
119.5	70.7	115	200	362	447	665
120.7	69.6	123	197	359	444	653
121.9	68.4	132	194	356	443	641
123.1	67.3	141	192	352	442	629

TABLE 2 - Time Interval Information

<u>Time (sec)</u>	<u>No. of Time Grid Points</u>	<u>Starting Weight Factor</u>	<u>No. of Iterations</u>	<u>Initial y </u>	<u>Final y (in 10^{-4})</u>
0.0110	23	1	5	1	8.424
0.0180	15	1	2	1	8.125
0.0240	13	1	2	1	3.212
0.0300	13	1	2	1	0.531
0.0370	15	1	2	1	2.446
0.0430	13	1	2	1	2.978
0.0500	15	1	2	1	2.134
0.0570	15	1	2	1	5.325
0.0645	16	1	2	1	2.210
0.0725	17	1	2	1	5.660
0.0810	18	1	2	1	5.198
0.0900	19	1	2	1	3.899
0.1000	21	1	2	1	5.968
0.1110	23	1	2	1	6.616
0.1235	26	1	2	1	7.027
0.1390	32	1	2	1	7.165
0.1600	43	1	2	1	7.633
0.1990	40	1	3	1	0.022
0.2775	53	1	3	1	0.016
0.3345	58	1	2	1	6.442
0.3805	47	1	2	1	3.027
0.4235	44	1	2	1	0.640
0.4675	45	1	2	1	1.361
0.5165	50	1	2	1	3.316
0.5785	32	1	2	1	3.091
0.6625	43	1	2	1	3.573
0.8165	45	1	2	1	4.238
1.0055	43	1	2	1	1.530

6. Reference

- [1] Dynamic Response of the M113 Gun Tube to Travelling Ballistic Pressure and Data Smoothing as Applied to SM150 Acceleration Data, Technical Report WVT-TR-75015, by T. Simkins, G. Pflegl, and R. Scanton, Benet Weapons Laboratory, Watervliet Arsenal, NJ, April 1975.

AERODYNAMIC INTERFERENCE DURING SABOT DISCARD

E.M. SCHMIDT

Ballistics Research Laboratory
Aberdeen, Maryland

TABLE OF CONTENTS

	<u>Page</u>
I. INTRODUCTION	200
II. EXPERIMENTAL APPARATUS AND TEST PROCEDURE	202
III. EXPERIMENTAL RESULTS	203
IV. ANALYSIS	214
V. SUMMARY AND CONCLUSIONS	214
REFERENCES	216

I. Introduction

Fin-stabilized projectiles are widely employed as anti-armor, kinetic energy rounds. Since sabots are required to launch these projectiles from guns, a unique set of problems is encountered in attempting to design a system with acceptable accuracy. Within the gun, the fins extend aft of the sabot and may interact with the propellant bed or gases and with the gun tube. Since the projectile is manufactured from a dense material, transverse vibration within the less dense and segmented sabot may occur in response to projectile or gun tube asymmetry. At ejection from the launcher, elastic decompression of the sabot, centrifugal, and gas dynamic loadings combine to rupture retaining rings and implement sabot discard. Asymmetries in the discard process may produce transverse loadings upon the projectile and resultant trajectory dispersion. This paper presents the results of an experimental study of the sabot discard from a 60mm fin-stabilized projectile. Particular attention is given to aerodynamic interactions between the discarding sabot components and the sub-projectile.

While aerodynamic interference associated with components of aircraft, e.g., wing-body, airframe-propulsion, and airframe-stores, has been extensively investigated¹, similar interference associated with sabot discard from high speed projectiles has received limited attention²⁻⁴. Gallagher² presents an experimental investigation of projectile deviation from the

desired aim point due to muzzle blast, sabot discard, and projectile asymmetry. Since he neglects any contribution due gun tube/projectile interaction, the value he assigns to deviation due to muzzle blast is orders of magnitude greater than that found in more recent investigations^{5,6}. These show that muzzle blast does not contribute significantly to trajectory deviation and that the actual source lies with gun tube or sabot discard interactions. Gallagher notes that the sabot components open symmetrically, but the center of gravity of the grouped components does not lie along the axis of the projectile. He assumes that there will be a momentum exchange between the sabot and projectile in relation to their masses and the magnitude of the center of gravity separation. However, due to the limitations of his apparatus, Gallagher could not define the magnitude of this deviation which is generated by elastic rebound at muzzle ejection. Gallagher made no attempt to investigate the effects of aerodynamic interactions.

Conn³ investigates the effect of aerodynamic interference between sabots and projectiles fired from a light gas gun. His measurements show that a conical projectile launched with a two-segment sabot has periods of pitch and yaw which are dependent upon the orientation of the sabot plane of separation. He uses oblique shock and Newtonian flow theory to analyze the pressure distribution on a cone at arbitrary attitude relative to a symmetrically discarded, two-segment sabot. The results of his analysis show that aerodynamic interference differentially increases the restoring moments acting on the cone, thereby shortening the periods of oscillation. He notes that by intercepting the sabot components at the point of maximum yaw, the free flight yaw levels are

minimized.

Glauz⁴ uses oblique shock theory to analyze the side forces and moments generated on a fin-stabilized projectile due to a single sabot component flying in close proximity. He assumes that when it intercepts the projectile, the shock wave from the sabot is planar, does not reflect at the projectile, and is not influenced by the projectile viscous or inviscid flow field. In a sample calculation, Glauz predicts a significant alteration of the trajectory of a small caliber flechette by this type discard process; however, his calculated value of discard induced angular velocity is an order of magnitude higher than actually measured⁷. This disagreement is due to both the simplistic nature of the model and the complex, mutually interacting flows established during discard.

The present investigation was conducted to provide detailed information on the aerodynamic interference between sabot components and projectiles for actual kinetic energy round configurations. The results of measurements of sabot and projectile motion from the muzzle, through sabot discard, and into free flight are presented. Observed variations in projectile angular motion is shown to correlate with measured sabot discard asymmetry. A simple model of the interacting flow is used to estimate the projectile behavior. Like previous models, the agreement is not exact; however, the results do support the interpretation as to the cause of anomalous projectile angular motion.

II. Experimental Apparatus and Test Procedure

The test vehicle is a fin-stabilized projectile encapsulated in a four segment sabot. The round is fired from a 60mm gun with a twist of

rifling of one turn in 200 calibers. The launch velocity is 1310 m/s. The projectile and test coordinate system are illustrated in Figure 1.

Data was taken of the projectile launch and flight using a variety of techniques, Figure 2. Near muzzle motion was monitored at a series of six, orthogonal X-ray stations located at five foot intervals. Five smear cameras, set at fifteen foot intervals, provided coverage of the final, aerodynamic discard of sabot components. Downrange motion of the projectile was measured in the BRL Transonic Range.

To permit quantitative reduction of the X-ray data, an *in-situ* calibration procedure was employed. The technique was straightforward; consisting of stringing a calibrated steel wire along the line of fire, taking X-ray photographs of the wire just prior to the shot, removing the wire, and firing the test. In this manner, a double exposure is obtained at each X-ray station, Figure 3. On this X-ray photograph, the wire, with a known spatial location, and the projectile, whose properties we wish to measure, are clearly visible. The reduction of the data on the X-ray is direct for objects located near the calibration wire, e.g., the projectile. The determination of the location and orientation of objects distant from the wire requires correction for parallax.

III. Experimental Results

The measured yawing motion of the projectile gives the clearest indication of the magnitude of aerodynamic interference. A plot of the projectile angles of attack and side slip for five typical firings is presented in Figure 4. Each data point is a separate measurement obtained at an orthogonal X-ray station. These stations are located

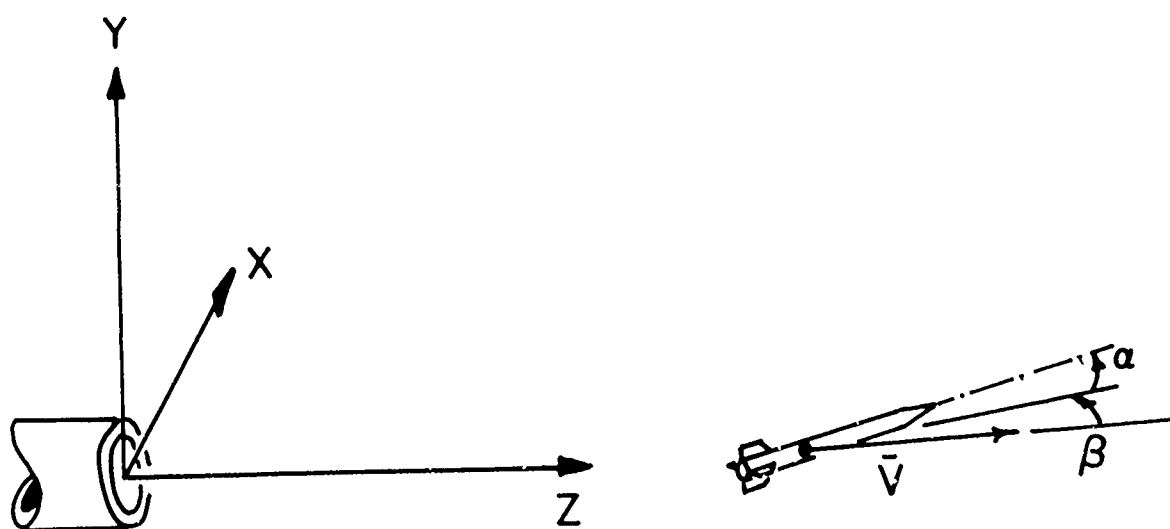
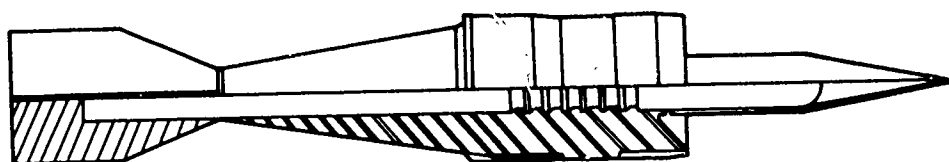


FIGURE I. TEST PROJECTILE &
COORDINATE SYSTEM

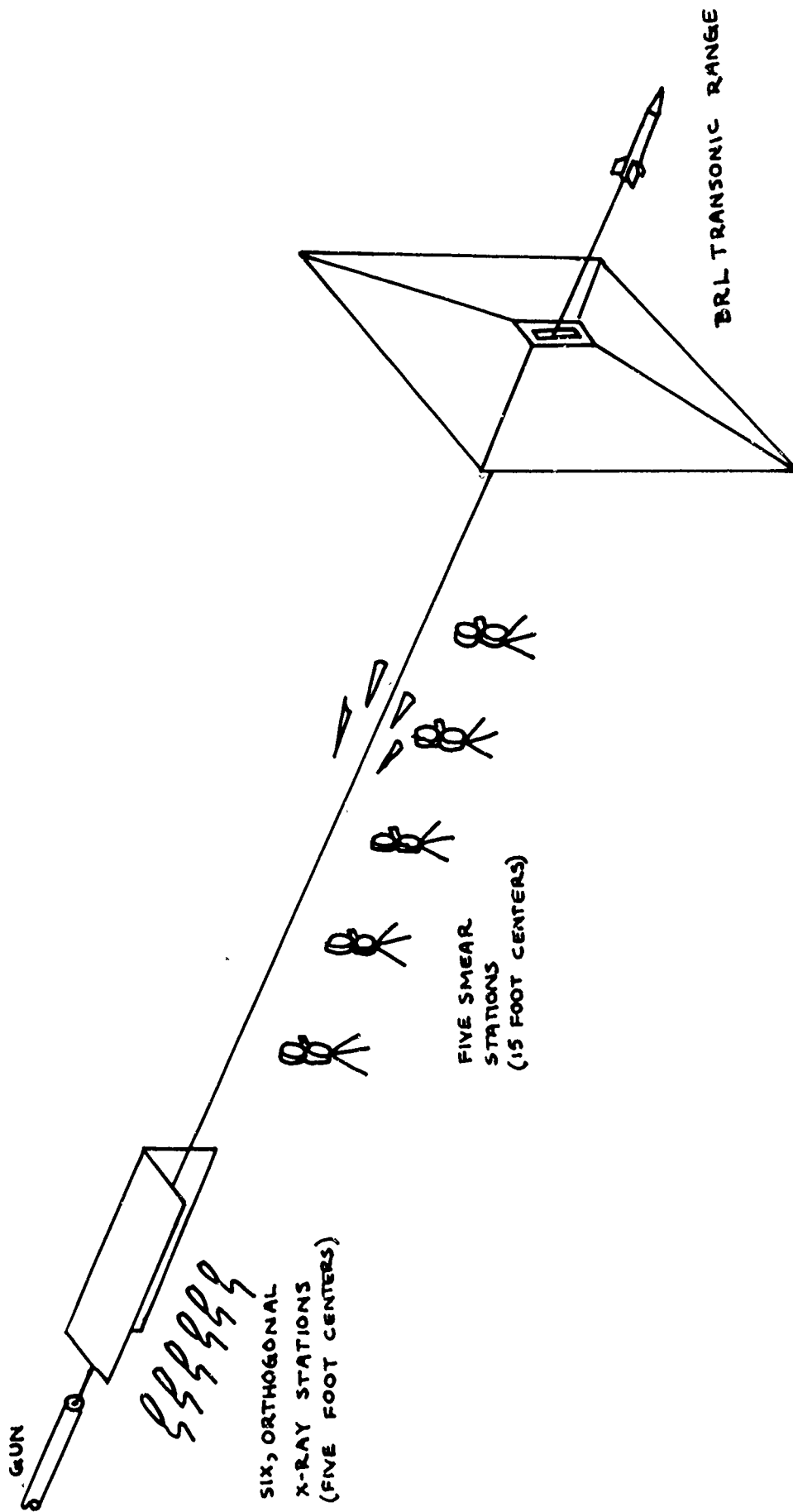


FIGURE 2: SCHEMATIC OF TEST SET-UP



FIGURE 3: SAMPLE X - RAY

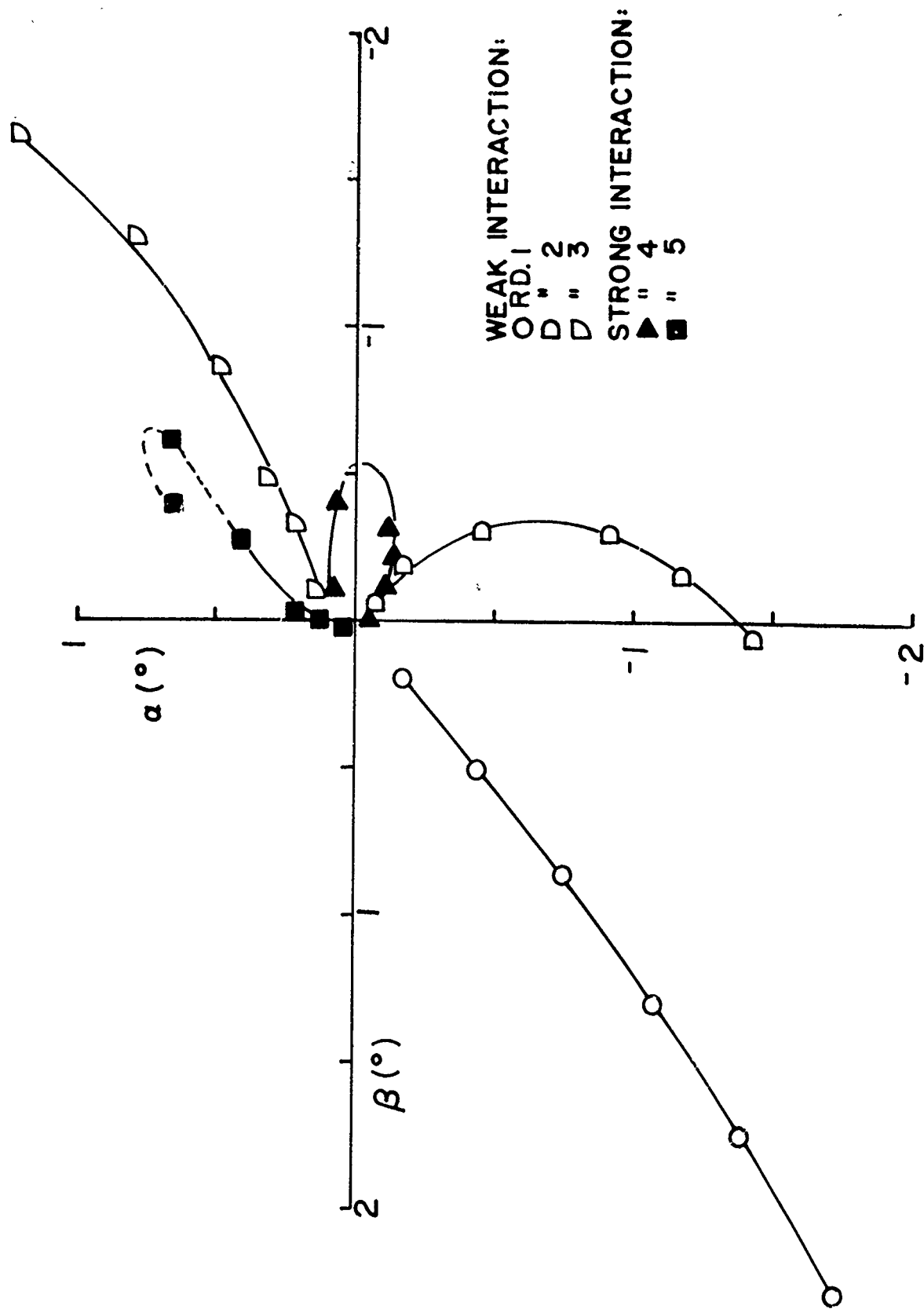


FIGURE 4: PROJECTILE ANGULAR MOTION DURING DISCARD

at approximately five foot intervals with the first station located two feet forward of the gun muzzle. Thus, this figure depicts the variation in projectile attitude as it travels the first 27 feet down-range. The period of yaw (interval between successive minima) for this projectile is 130 feet. If it were assumed that the muzzle represented the initial minimum yaw point and that the round was in free flight, its yaw should increase monotonically to a maximum at 65 feet from the muzzle and then decay to a second minimum at 130 feet. For three of the rounds in Figure 4, this type of yaw motion may be occurring; however, two of the rounds clearly do not exhibit this monotonically increasing behavior.

Rounds 4 and 5 are launched with an angular motion in a given direction which reaches a maximum level at twenty feet from the muzzle. This location is well short of the free flight half period of 65 feet. To confirm the validity of this yawing motion, the X-ray data may be compared with the Transonic Range data, Figure 5. The range measurements cover 680 feet of the projectile trajectory commencing 130 feet from the muzzle. The projectile angular motion, recorded at orthogonal spark shadowgraph station, is fit to the equation of a damped epicycle using a least squares procedure. The comparison between the X-ray measurements and the range data extrapolated back to the muzzle is reasonable. The first plot of Figure 5 is the comparison for a well behaved launch, Round 3. The X-ray data shows similar trends to the Transonic Range data. The second plot is the comparison for Round 5. While the initial motion would not correspond to the extrapolation, the motion measured in

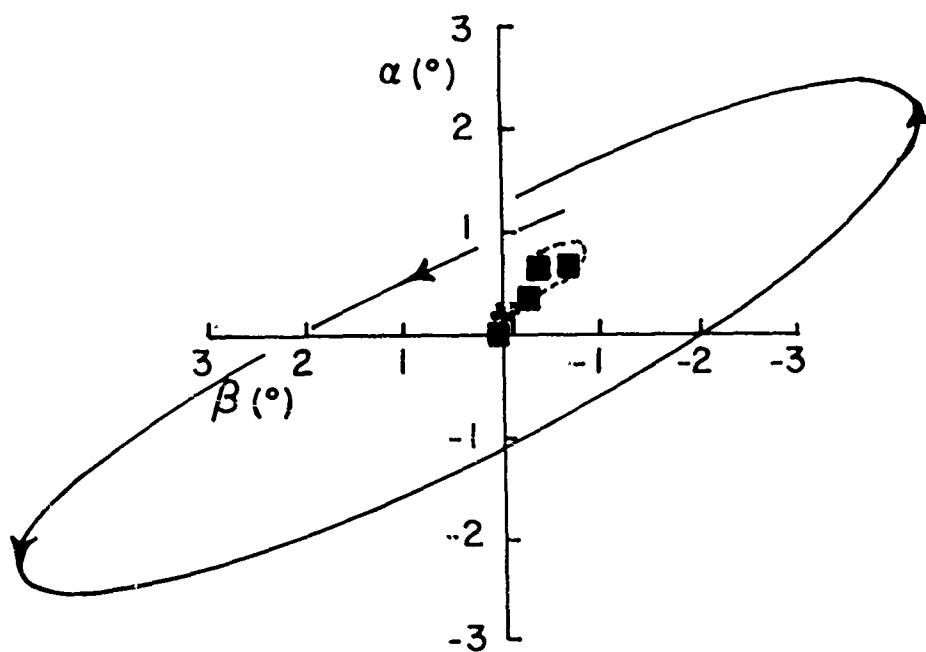
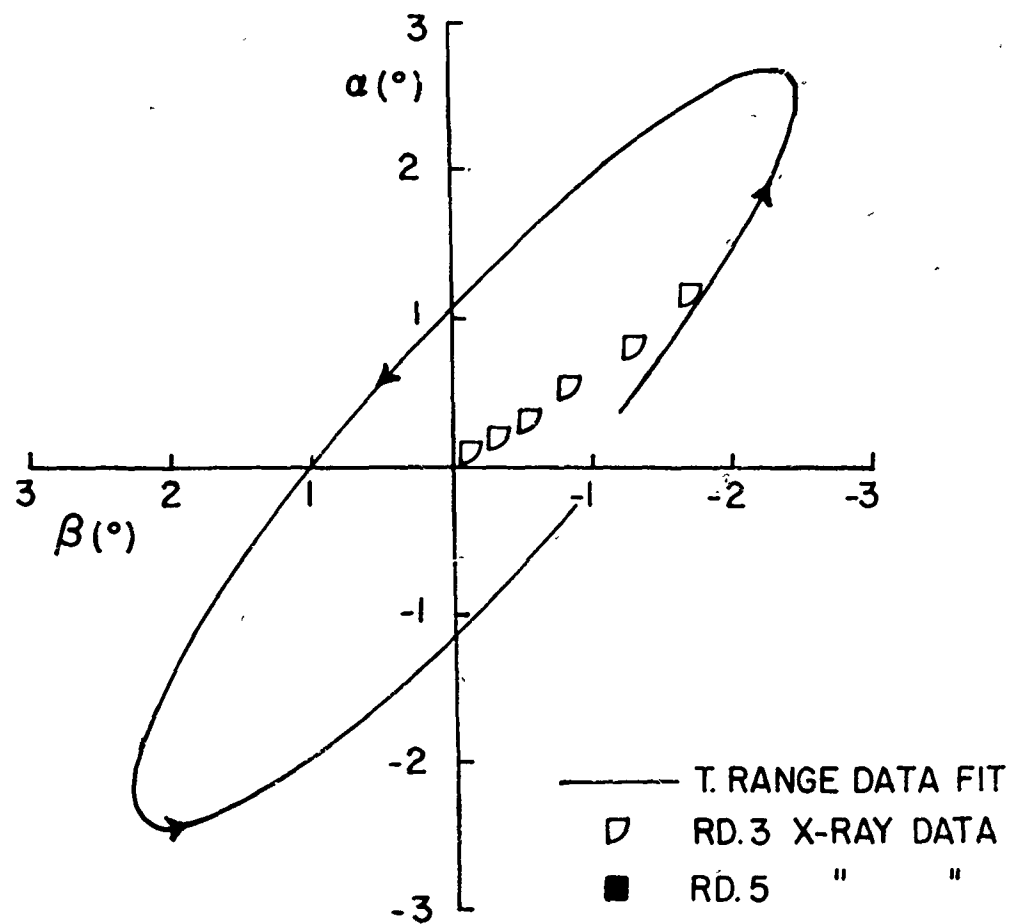
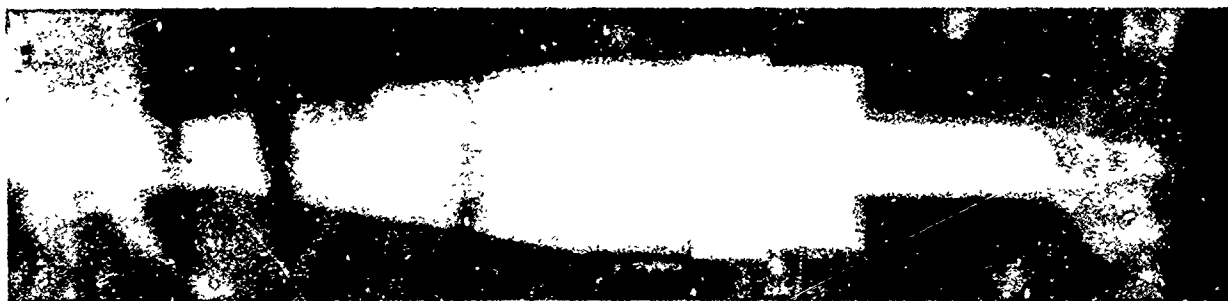


FIGURE 5: COMPARISON OF TRANSONIC RANGE & X-RAY DATA

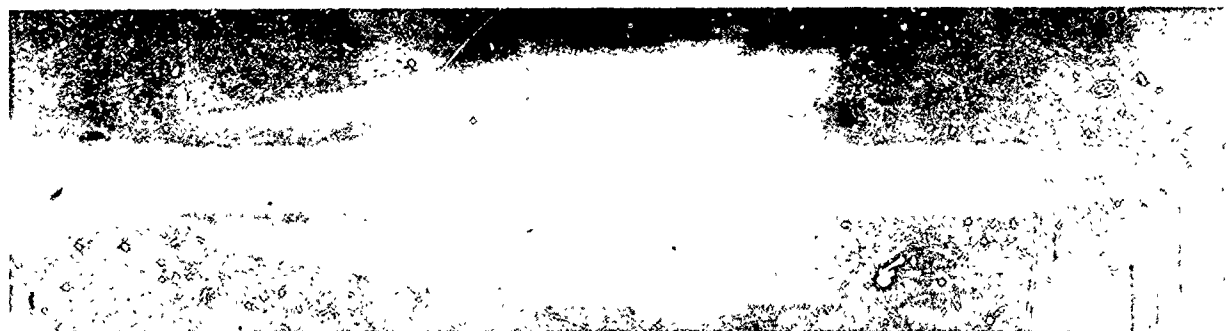
the final X-ray stations does agree with range data. This corroborates what might otherwise be interpreted as anomalous behavior in the X-ray measurements.

When the location of the various sabot components with respect to the projectile is examined, the projectile angular motion may be correlated with discard asymmetry, Figure 6. This is a set of vertical X-ray plates taken for Round 5. The view is that of an observer situated above the flight path and watching the projectile fly downrange beneath him. The X-ray photographs reveal an obvious asymmetry in the geometry of the sabot petals at the final two stations. The petal on the left is closer to the projectile than is the right hand petal. The shock wave from the nearer petal impinges on the fins generating an overpressure and crossflow which would push the fins to the right and the nose to the left (the direction of increasing sideslip). This type aerodynamic interference loading and response is in agreement with the measured projectile motion, Figure 4.

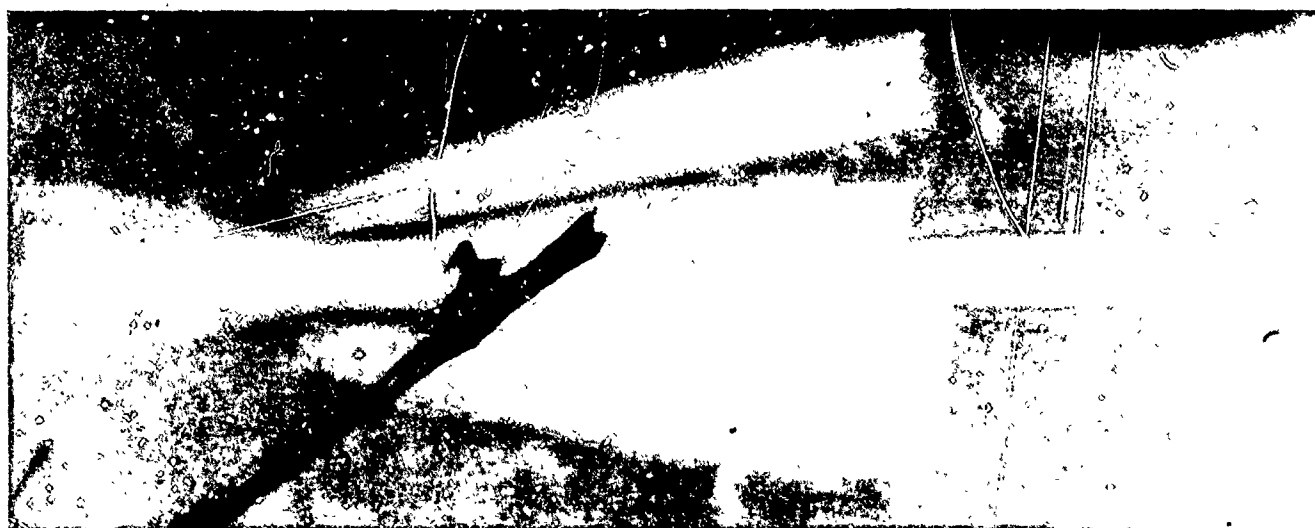
The angular acceleration induced by the aerodynamic interference is substantial, and the resulting angular velocity imparted to the projectile is equivalent in magnitude to the rates observed immediately following separation from the muzzle. For Rounds 4 and 5, aerodynamic interference produced loadings in opposition to the direction of launch angular velocity. This could decrease the level of free flight yaw; however, if the interference loads were in the same sense as the launch angular rate, yaw amplification would occur. Round 3 seems to show a growth in angular velocity during the discard process, Figure 4.



A. $Z = 2.0 \text{ ft}$

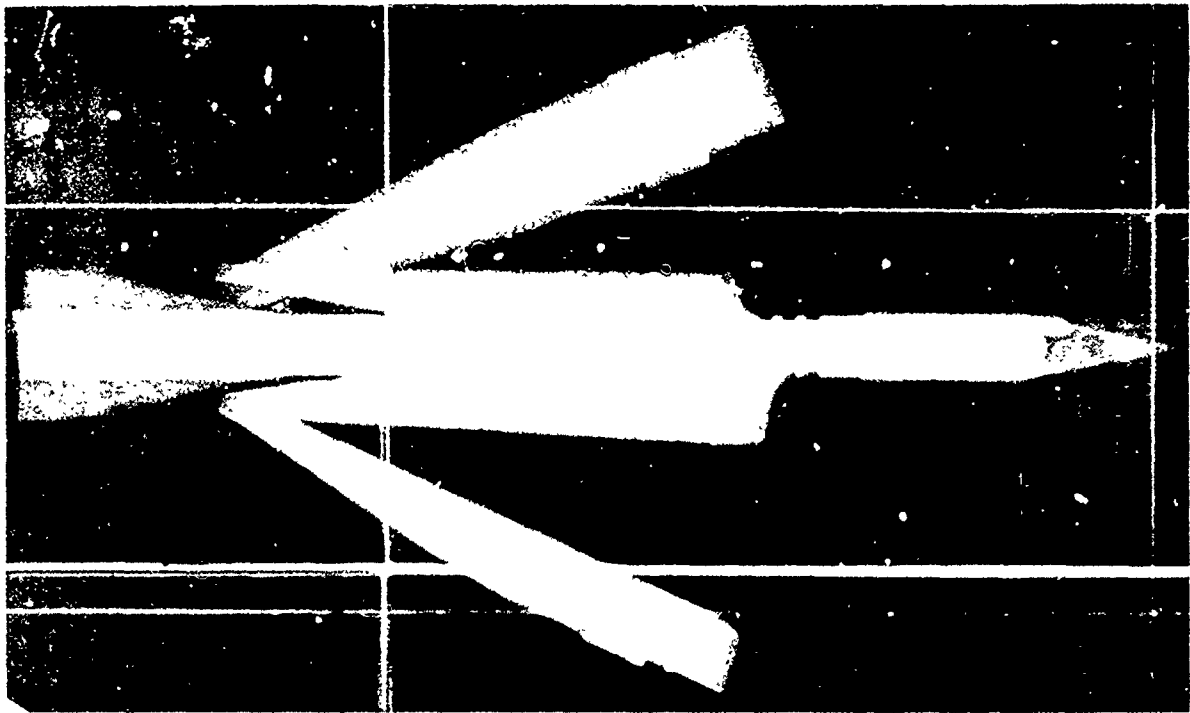


B. $Z = 7.5 \text{ ft}$



C. $Z = 13.0 \text{ ft}$

FIGURE 6: SABOT DISCARD SEQUENCE, RD.5

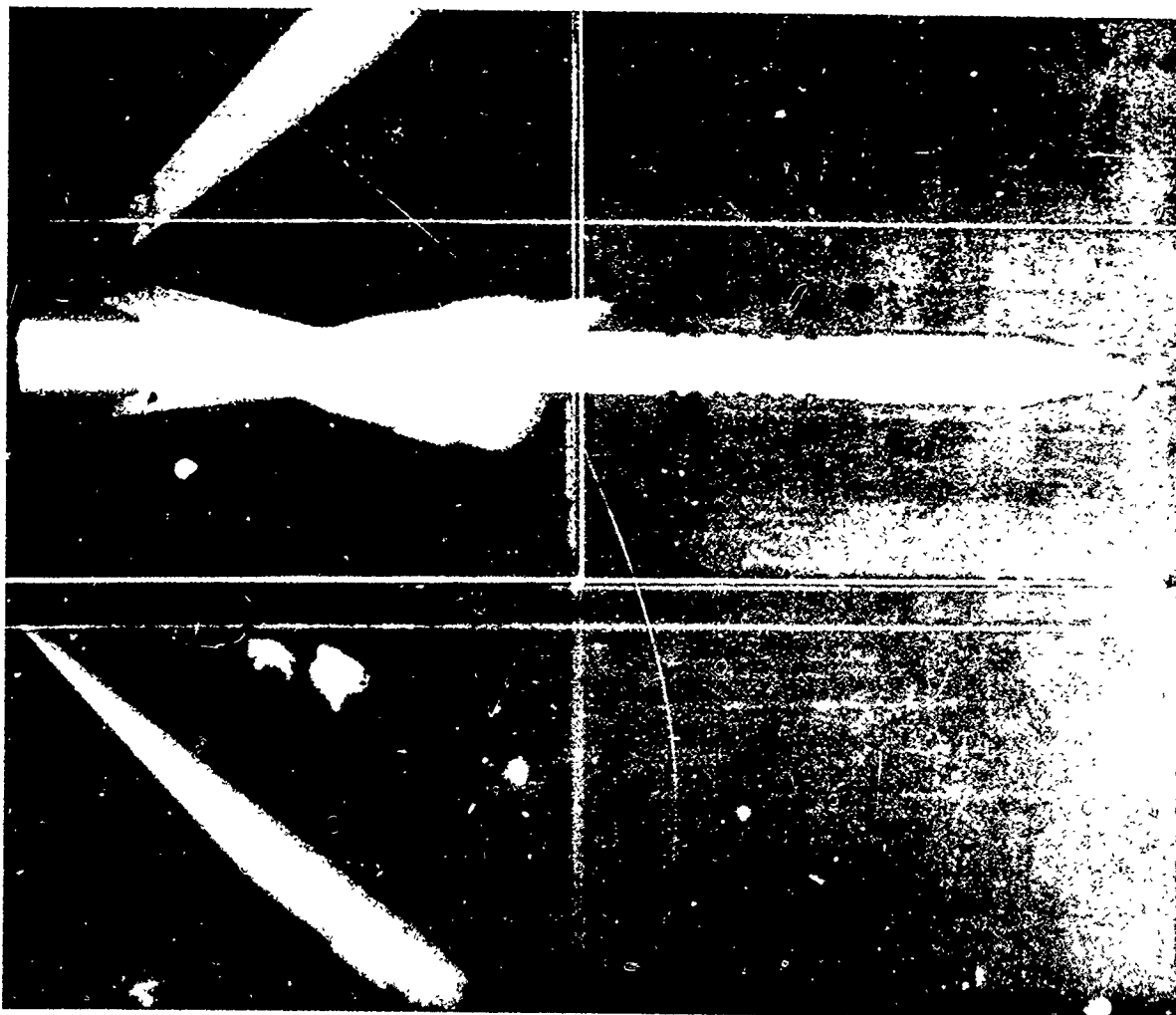


D.Z = 19.5 ft



E.Z = 24.7 ft

FIGURE 6: SABOT DISCARD SEQUENCE, RD. 5



F. Z = 29.9 ft

FIGURE 6: SABOT DISCARD SEQUENCE, RD. 5

Such amplification is undesirable. To control trajectory deviation and dispersion, the designer wishes to reduce aerodynamic jump which is directly proportional to the initial free flight angular velocity. These results indicate an additional area of concern. To decrease the adverse impact of aerodynamic interference, it is necessary to either control discard asymmetry or increase the rate of sabot separation. Since the source of the asymmetry is not immediately obvious, the latter course of action may be more advisable.

IV. Analysis

To determine if the measured angular accelerations could be generated by aerodynamic loading, a simple analysis similar to that of Glauz⁴ is performed. For Round 5, it is observed in Figure 6 that the nearest sabot component is at an angle of approximately 40° with respect to the projectile axis. Assuming the sabot component to be a two-dimensional body and reducing the angle to 38° (to give an attached shock at $M = 3.91$), the flow behind the oblique shock generated by this component may be computed. If the shock impinges on the projectile fin surfaces, the reflected pressure level may be computed. For this type interference, the projectile would experience an angular acceleration of 0.15 deg/ft^2 . The measured angular acceleration for Round 5 is 0.022 deg/ft^2 ; thus, the observed motion is in agreement with that which might be generated by aerodynamic interference.

V. Summary and Conclusions

An experimental program is presented which defines the sabot discard process of a 60mm, fin-stabilized projectile. The data indicate that

strong aerodynamic interference occurs between the discarding sabot components and the projectile. A simple analysis of the magnitude of potential aerodynamic loadings shows that the observed motion of the projectile is well within the upper bound of theory. Since the aerodynamic interaction can adversely affect the trajectory and dispersion of the round, it is advisable to provide for rapid sabot discard thereby decreasing the duration of interference loadings.

REFERENCES

1. Sears, W. R., ed., "Aerodynamic Interference," AGARD, CP-71-71, January 1971.
2. Gallagher, W. J., "Elements which have Contributed to Dispersion in the 90/40mm Projectile," Ballistic Research Laboratory, Aberdeen Proving Ground, MD, R1013, March 1957.
3. Conn, H., "The Influence of Sabot Separation on the Yawing Motion of a Cone," Defense Research Establishment, Valcartier, Canada, June 1970.
4. Glauz, W. D., "Estimation of Forces on a Flechette Resulting from a Shock Wave," Midwest Research Institute, Kansas City, MO, Final Report 19 June 1970 - 18 March 1971, May 1971.
5. Gretler, W., "Intermediate Ballistics Investigations of Wing Stabilized Projectiles," Deutschen Versuchsanstalt für Luft- und Raumfahrt, Aachen, Germany, R67-92, November 1967.
6. Schmidt, E. M., Fansler, K. S., and Shear, D. D., "Trajectory Perturbations of Fin-Stabilized Projectiles due to Muzzle Blast," Journal of Spacecraft and Rockets, May 1977.
7. Schmidt, E. M. and Shear, D. D., "Launch Dynamics of a Single Flechette Round," Ballistic Research Laboratory, Aberdeen Proving Ground, MD, R 1810, August 1975.

A STATE SPACE METHOD FOR OPTIMIZATION
OF WEAPON SYSTEM DYNAMICS

E.J. HAUG AND J.S. ARORA
University of Iowa
Iowa City, Iowa

TABLE OF CONTENTS

	<u>Page</u>
I. INTRODUCTION	219
II. A DYNAMIC OPTIMAL DESIGN PROBLEM	221
III. REVIEW OF THE NONLINEAR PROGRAMMING METHOD	223
IV. A STATE SPACE OPTIMIZATION METHOD	224
V. EXAMPLE I, A NONLINEAR IMPACT ABSORBER	232
VI. EXAMPLE II, A VEHICLE DYNAMIC RESPONSE TEST PROBLEM	236
VII. EXAMPLE III, OPTIMAL DESIGN OF A VEHICLE SUSPENSION	240
VIII. CONCLUSIONS	250
REFERENCES	252

ABSTRACT

A state space method of optimal design of dynamic systems subjected to transient loads is developed and applied. In contrast to the usual nonlinear programming approach of discretizing the time interval and constructing a high dimension nonlinear programming problem, a state space approach is employed which develops the sensitivity analysis and optimization algorithm in continuous state space, resorting to discretization only for efficient numerical integration of differential equations. Comparison of the state space method with the nonlinear programming method is carried out for a nonlinear test problem, in which the state space method requires only one-tenth the computing time reported for the nonlinear programming approach. The method is further illustrated through solution of a five degree of freedom vehicle dynamic response problem, involving multiple input and multiple constraints. Application of the method to weapon dynamics with intermittent motion and to gun tube stiffening optimization for precision are presented in other papers of these proceedings.

I. INTRODUCTION

With the advent of affordable electro-optical devices, digital computers, and precision controls; there is potential on the horizon for extremely precise gun weapons. Such systems are typified by high recoil momentum, intermediate rate of fire, and by long slender tubes. Rational design techniques for recoil control, automatic mechanisms, and interaction of the various mounting and isolation subsystems are needed if one is to achieve the full potential for precision. The very sensitive nature of dynamic response of such systems precludes separate design of the recoil mechanism, mount, and the tube. It is imperative that parametric design techniques be employed, which can account for subsystem interaction and overall system precision, as a function of excitations that are characteristic of each of the subsystems. A practical parametric design technique, therefore, must include sensitivity analysis of the mathematical model of each interacting subsystem.

The existing literature on dynamic effects on precision is reviewed in [1] and other papers of this proceedings, so it will not be repeated here. It suffices to note that analysis capability today is considerably ahead of state-of-art design methodology, the subject to which this paper and [2,3] are addressed. Prior to entering into a technical discussion of the state space dynamic synthesis problem, an important class of weapon design problems involving intermittent motion should be noted. Looseness in supports, the basic intermittent nature of weapon mechanisms, and moving supports render the weapon dynamics problem highly nonlinear [1,4,5]. An extension of the state space method for synthesis of systems with intermittent motion is presented in [6].

The field of mechanical system optimization for dynamic response was advanced significantly in the late 1960's, through application of linear and nonlinear programming methods. A comprehensive summary of this work may be found in the monograph by Sevin and Pilkey [7] and the paper by Karnopp [8]. More recent applications of these programming techniques may be found in [9,10]. Optimal control approaches are suggested in [8] and [11], but no numerical methods are developed or applications presented.

It is important to note that all the nonlinear programming methods presented in [7,9,10] involve placing a finite grid on the time interval and defining the response variables on the time grid as variables of the nonlinear programming problem. The result is a problem of very high dimension. It is universally observed [7,9,10] that the resulting problem requires copious amounts of computer time and limits the size of engineering problems that can be treated.

State space methods of optimization in the controls literature have been developed to a high degree and applied to numerous problems of optimal control, e.g. Bryson [12,13]. These techniques have not, however, been fully exploited for mechanical design optimization. Applications to structures and to some elementary dynamics problems have been treated by the writers [14]. This paper employs these methods and the related gradient methods of Miele [15] for efficient solution of transient dynamic response design problems.

In both the state space approach presented herein and the nonlinear programming approach of [7,9,10], one must employ a discretization of the problem for digital computation. The fundamental difference between the nonlinear

programming and state space methods is the point in the algorithm at which discretization is employed. In the state space method, one develops an optimization algorithm that operates in the design parameter space and only discretizes to carry out numerical integration of the differential equations of motion and certain adjoint differential equations. The trade-off is, thus, high dimensionality in the discretized nonlinear programming problem versus numerical integration of differential equations in the state variable formulation. Following the development of the state space algorithm, example problems are solved and compared with results obtained with the nonlinear programming method.

II. A DYNAMIC OPTIMAL DESIGN PROBLEM

To be more specific, dynamic systems considered here consist of a collection of rigid bodies that are connected by combinations of springs and dampers. The system is described by a vector of design parameters $b = [b_1, \dots, b_m]^T$, where the b_i include spring stiffness, damping coefficient, element mass, or physical dimensions of the system. The design problem has as its objective the choice of this design parameter vector so that the mechanical system satisfies performance constraints, under given excitation, and is optimum in some sense.

In order to impose dynamic performance constraints, a state variable vector (generalized displacement and velocity coordinates) $z(t) = [z_1(t), \dots, z_n(t)]^T$ is required to describe the system dynamics. The differential equations of motion are written in the form

$$\left. \begin{aligned} P(b)\dot{z} &= F(t,z,b) \quad , \quad 0 \leq t \leq \tau \\ z(0) &= z^0 \end{aligned} \right\} \quad (1)$$

where \dot{z} denotes the time derivative of the state variable, $P(b)$ is an $n \times n$ matrix whose elements depend on the design parameters, $F(t,z,b)$ is an $n \times 1$ matrix of forcing functions and support reactions, and z^0 is a vector of given initial conditions. It should be noted that these equations are in general nonlinear.

The specific class of problems treated here concerns minimization of extreme dynamic response, subject to performance constraints that must hold over the entire time interval of concern, $[0, \tau]$. The cost function ϕ_0 that is to be minimized is written as

$$\phi_0 = \max_{t \in [0, \tau]} f_0(t, z(t), b) \quad . \quad (2)$$

Cost functions of this form arise in precision instruments and weapon system design. In case f_0 does not depend on t or $z(t)$, the max-value operation is not required and a much simpler problem results.

Just as the cost function may be taken as the extreme value of a measure of dynamic response, constraints may be written in a similar form. Such extreme value performance constraints may be written in the form

$$\phi_i = \max_{t \in [0, \tau]} f_i(t, z(t), b) - \theta_i \leq 0 \quad , \quad i = 1, \dots, k \quad . \quad (3)$$

Constraints of this form arise as excursion limits on the motion of mechanical components and as stress limits in structural members. In addition to these dynamic performance constraints, explicit bounds must generally be placed on allowable values of the design parameters. That is,

$$b_i^L \leq b_i \leq b_i^U, \quad i = 1, \dots, m, \quad (4)$$

where b_i^L and b_i^U are lower and upper limits on the design parameters.

It may be noted that pointwise constraints $\phi(t, z(t), b) - \theta \leq 0$, for all $0 \leq t \leq \tau$, may be rewritten in the form of Eq. (3). That is,

$\max_{t \in [0, \tau]} \phi(t, z(t), b) - \theta \leq 0$. In addition to the extreme value functionals in Eqs. (2) and (3), functionals of the form

$$\psi = \int_0^\tau h(t, z, b) dt \quad (5)$$

often arise. Such cost and constraint functionals may be used to represent a cumulative measure of performance over the time interval $[0, \tau]$, and are readily incorporated into the state space formulation of the design problem.

III. REVIEW OF THE NONLINEAR PROGRAMMING METHOD

Discretization of the problem of Section II can be carried out by fixing a time grid on the interval $[0, \tau]$, $0 = t_0 \leq t_1 \leq t_s = \tau$. One then defines $z^i = z(t_i)$, $i = 0, \dots, s$ and uses some form of finite difference technique to approximate the dynamic Eqs. (1), e.g.

$$P(b) \left(\frac{1}{h_i} \right) (z^i - z^{i-1}) = F(t_i, z^i, b), \quad i = 1, \dots, s, \quad (5)$$

where z^0 is given by the initial conditions and $h_i = t_i - t_{i-1}$.

One may now define a parameter d by the inequalities

$$f_0(t_i, z^i, b) - d \leq 0, \quad i = 0, 1, \dots, s, \quad (7)$$

and replace the cost function of Eq. (2) by

$$\bar{\phi}_0 = d \quad (8)$$

Finally, one may replace the constraints of Eq. (3) in the discretized formulation by

$$\begin{aligned} f_j(t_i, z^i, b) - \theta_j &\leq 0 \\ j &= 1, \dots, k \\ i &= 0, 1, \dots, s \end{aligned} \quad (9)$$

In addition, one has the design parameter constraints of Eq. (4).

One may now solve the nonlinear programming problem of minimizing the cost function of Eq. (8), subject to the constraints of Eqs. (6), (7), (9), and (4). However, with the dimension of z being n , there are $ns + m + 1$ variables and $(n + k + 1)s + k + 2m + 1$ constraints. Even for a single degree of freedom vibration isolator with $n = 2$, $m = 2$, $k = 2$, and only $s = 50$, there are 103 variables and 257 constraints. For more realistic mechanical systems with transient response, there will be an order of magnitude more variables and constraints. As noted in [7,9,10] problems of such dimension require excessive amounts of computer time. As a result, the examples solved in [7,9,10] involve only one or two degrees of freedom and require in excess of one minute of computer time on third generation computers (IBM 360-65, CDC 6400, and Univac 1108).

IV. A STATE SPACE OPTIMIZATION METHOD

The formulation of the dynamic optimization problem of Section II is troublesome, from an analytical point of view, because of the difficulty in

treating the max-value functions of Eqs. (2) and (3). In this section, the problem is reformulated so that integrals replace the max-value functions. A state space sensitivity analysis method and an optimization algorithm are then presented.

First, following the idea of Eq. (7), one defines an upper bound, b_{m+1} , on f_0 according to the inequality.

$$f_0(t, z(t), b) - b_{m+1} \leq 0, \quad 0 \leq t \leq \tau. \quad (10)$$

The cost function that is to be minimized can, thus be taken as

$$J = b_{m+1}. \quad (11)$$

Next, note that for a continuous function $\eta(t)$, one may replace the inequality $\eta(t) \leq 0$, $0 \leq t \leq \tau$, by the "equivalent" integral constraint

$$\int_0^\tau \langle \eta(t) \rangle^2 dt = 0, \quad (12)$$

where

$$\langle \eta(t) \rangle = \begin{cases} \eta(t), & \eta(t) \geq 0 \\ 0, & \eta(t) < 0 \end{cases}. \quad (13)$$

It is important to note that, even though $d/dt \langle \eta(t) \rangle$ is discontinuous at points where the graph of $\eta(t)$ intersects and abscissa, $d/dt \langle \eta(t) \rangle^2 = 2 \langle \eta(t) \rangle d\eta(t)/dt$ is continuous there if $d\eta/dt$ is continuous.

One may now replace the inequality constraints of Eqs. (3) and (10) by

$$\psi_0 \equiv \int_0^\tau \langle f_0(t, z, b) - b_{m+1} \rangle^2 dt = 0 \quad (14)$$

and

$$\psi_i \equiv \int_0^\tau \langle f_i(t, z, b) - \theta_i \rangle^2 dt = 0, \quad i = 1, \dots, k. \quad (15)$$

Thus, the dynamic optimal design problem is reduced to the "equivalent" problem of minimizing the cost function of Eq. (11), subject to the constraints of Eqs. (4), (14), and (15). This form of the problem may now be treated by known optimization methods [13,14,15].

Before presenting the algorithm, another method of reducing the max-value functions to integral form may be noted. Presuming $f_0(x, z, b)$ is continuous and greater than zero, which can be achieved by adding a fixed constant, then it is known [10,11,12] that

$$\max_{t \in [0, \tau]} f_0(t, z(t), b) = \lim_{p \rightarrow \infty} \left[\frac{1}{\tau} \int_0^\tau [f_0(t, z, b)]^p dt \right]^{1/p}. \quad (16)$$

This fact suggests replacing the constraints of Eq. (3) by

$$\frac{1}{\tau} \int_0^\tau [f_i(t, z, b)]^p dt - \theta_i^p \leq 0, \quad i = 1, \dots, k \quad (17)$$

and the cost function of Eq. (2) by

$$\bar{J} = J^p \approx \int_0^\tau (f_0(t, z, b))^p dt. \quad (18)$$

One could then minimize \bar{J} subject to constraints of Eqs. (1), (4), and (17) and then increase p and re-solve, until a limiting approximation is reached. This method has been justified on theoretical grounds in [11] and

applied in [16] and in references cited in [7]. A comparative study [19] of this approach and the "equivalent" formulation above showed that:

(a) the constraint formulation of Eq. (17) is inaccurate, for practical values of p , (b) use of the equivalent constraints of Eq. (15) and the cost functions of Eqs. (11) and (18) yields equivalent results, and (c) convergence properties and computer time required favor the "equivalent" formulation.

The key to solving any integral form of the design problem is to calculate derivatives of the constraint integrals with respect to the design variables, using the state equation (1) to eliminate the dependence on z . To do this, one may introduce an adjoint variable $\lambda(t)$ through the identity

$$\int_0^T \lambda^T [P\dot{z} - F(t, z, b)] dt = 0 \quad (19)$$

Perturbing b by an amount δb results in a change δz in z . If δb is small, one can expand the left side of Eq. (19), to first order, as

$$\int_0^T \lambda^T \left(P\delta\dot{z} - \frac{\partial F}{\partial z} \delta z + \frac{\partial(P\dot{z})}{\partial b} \delta b - \frac{\partial F}{\partial b} \delta b \right) dt = 0 \quad (20)$$

where

$$\frac{\partial F}{\partial z} = \left[\frac{\partial F_i}{\partial z_j} \right]_{n \times n} \quad \text{and} \quad \frac{\partial F}{\partial b} = \left[\frac{\partial F_i}{\partial b_j} \right]_{n \times m}.$$

Integrating the first term in Eq. (20) by parts, noting that because of the initial condition of Eq. (1) $\delta z(0) = 0$ and requiring that $\lambda(\tau) = 0$, one has the identity

$$- \int_0^T \left(P^T \dot{\lambda} + \frac{\partial F^T}{\partial z} \lambda \right)^T \delta z dt = \int_0^T \left(-\lambda^T \frac{\partial(P\dot{z})}{\partial b} + \lambda^T \frac{\partial F}{\partial b} \right) \delta b dt \quad (21).$$

One may now write first-order approximations for Eqs. (14) and (15), as

$$\begin{aligned} \psi_0 + \delta\psi_0 \equiv \int_0^\tau \left[\left\langle f_0 - b_{m+1} \right\rangle^2 \right. \\ \left. + 2 \left\langle f_0 - b_{m+1} \right\rangle \left(\frac{\partial f_0}{\partial z} \delta z + \frac{\partial f_0}{\partial b} \delta b - \delta b_{m+1} \right) \right] dt = 0 \end{aligned} \quad (22)$$

and

$$\begin{aligned} \psi_i + \delta\psi_i \equiv \int_0^\tau \left[\left\langle f_i - \theta_i \right\rangle^2 \right. \\ \left. + 2 \left\langle f_i - \theta_i \right\rangle \left(\frac{\partial f_i}{\partial z} \delta z + \frac{\partial f_i}{\partial b} \delta b \right) \right] dt = 0, \quad i = 1, \dots, k \end{aligned} \quad (23)$$

The identity of Eq. (21) may now be employed to eliminate explicit dependence of Eq. (22) and (23) on δz . Requiring the adjoint variables

$\lambda^i(t)$, $i = 0, 1, \dots, k$, to satisfy

$$P^T \dot{\lambda}^0 + \frac{\partial F^T}{\partial z} \lambda^0 = 2 \left\langle f_0 - b_{m+1} \right\rangle \frac{\partial f_0^T}{\partial z}, \quad (24)$$

$$P^T \dot{\lambda}^i + \frac{\partial F^T}{\partial z} \lambda^i = 2 \left\langle f_i - \theta_i \right\rangle \frac{\partial f_i^T}{\partial z}, \quad i = 1, \dots, k$$

and

$$\lambda^i(\tau) = 0, \quad i = 0, 1, \dots, k,$$

one may use Eq. (21) to reduce Eqs. (22) and (23) to the form

$$\psi_0 + \ell^0{}^T \delta b - \int_0^T \langle f_0 - b_{m+1} \rangle dt \quad b_{m+1} = 0$$

and

$$\psi_i + \ell^i{}^T \delta b = 0, \quad i = 1, \dots, k$$

(25)

where

$$\ell^0 = \int_0^T \left[2 \langle f_0 - b_{m+1} \rangle \frac{\partial f_0^T}{\partial b} + \frac{\partial (P\dot{z})^T}{\partial b} \lambda^0 - \frac{\partial F^T}{\partial b} \lambda^0 \right] dt$$

and

$$\ell^i = \int_0^T \left[2 \langle f_i - \theta_i \rangle \frac{\partial f_i^T}{\partial b} + \frac{\partial (P\dot{z})^T}{\partial b} \lambda^i - \frac{\partial F^T}{\partial b} \lambda^i \right] dt, \quad i = 1, \dots, k$$

(26)

The terms ψ_0 and ψ_i in Eq. (25) are zero if the constraints are satisfied.

If not, they play the role of errors that must be satisfied by the change δb in b .

Completing the perturbation calculation, one has from Eqs. (4) and (11)

$$b_i^L \leq b_i + \delta b_i \leq b_i^U \quad (27)$$

and

$$\delta J = \delta b_{m+1}. \quad (28)$$

One may now define $\bar{b} = [b^T, b_{m+1}]^T \in \mathbb{R}^{m+1}$ and determine $\delta \bar{b}$ to minimize δJ of Eq. (28), subject to constraints of Eqs. (25) and (27) and a stepsize limitation. To write all equations in terms of the augmented design parameter \bar{b} , one defines $\bar{\ell}^0 = [\ell^0{}^T, - \int_0^T \langle f_0 - b_{m+1} \rangle dt]^T$ and $\bar{\ell}^i = [\ell^i{}^T, 0]^T$

The optimization method employed is the gradient projection technique of [14,20] which is patterned after methods developed by Bryson [12,13]. First, one notes that if $\langle f_i - \theta_i \rangle = 0$ everywhere in $[0, \tau]$, then $\bar{\ell}^i = 0$. Thus, only constraints $\psi_i > 0$ need to be included in the iterative calculation. The reduced vector $\tilde{\psi} = [\psi_i]$, $\psi_i > 0$, is employed. Defining $\Lambda^T = [\bar{\ell}^i]^T$, $\psi_i > 0$, the constraints of Eq. (25) become

$$\tilde{\psi} + \Lambda^T \delta \bar{b} = 0 \quad . \quad (29)$$

The gradient projection algorithm of [14] may now be stated as:

Step 1. Select an estimated design $\bar{b}^{(j)}$ (j denotes the iteration number).
Solve Eq. (1) for the associated state $z^{(j)}(t)$.

Step 2. Evaluate constraints of Eq. (15) and form the index set

$$A = \{i \geq 0 : \psi_i > 0\} \quad .$$

Step 3. For each $i \in A$, integrate the initial value problems of Eq. (24) from τ to 0.

Step 4. For each $i \in A$ compute $\bar{\ell}^i$ from Eq. (26) and form the matrix $\Lambda^T = [\bar{\ell}^i]^T$, $i \in A$.

Step 5. Choose the desired reduction ΔJ in J , (normally $\Delta J = -0.03J$ to $-0.10J$ at the first iteration) and compute

$$\gamma_0 = -\frac{1}{2\Delta J} e^T [I - \Lambda(\Lambda^T \Lambda)^{-1} \Lambda^T] e \quad ,$$

where $e = [0, \dots, 0, 1]^T$. The parameter γ_0 is normally held constant for iterations beyond $j = 0$, but may be adjusted to accelerate convergence.

Step 6. Compute $\mu = - (\Lambda^T \Lambda)^{-1} [2\gamma_0 \tilde{\psi} - \Lambda^T e]$.

Step 7. Compute $\delta \bar{b} = - \frac{1}{2\gamma_0} \delta \bar{b}^{-1} + \delta \bar{b}^{-2}$, where

$$\delta \bar{b}^{-1} \equiv [I - \Lambda (\Lambda^T \Lambda)^{-1} \Lambda^T] e$$

$$\delta \bar{b}^{-2} \equiv \Lambda (\Lambda^T \Lambda)^{-1} \tilde{\psi}$$

and put $\bar{b}^{(j-1)} = \bar{b}^{(j)} + \delta \bar{b}$.

Step 8. If all constraints are satisfied and $||\delta \bar{b}^{-1}||$ is sufficiently small, terminate. Otherwise, return to Step 1 with the new design estimate $\bar{b}^{(j+1)}$.

This computational algorithm has been used to solve a wide range of optimal trajectory, control, and design problems. A comprehensive treatment of the version of the steepest descent algorithm given above may be found [14]. While there is some computational art involved in application of this algorithm, no real difficulty has been encountered in obtaining convergence. Further, efficient numerical integration methods can be used to solve the equations numerically. Based on experience in control theory, such methods are expected to be far more efficient than previously used discrete time approximations of [7,9,10].

The test problems solved herein are presented for the purpose of illustration and algorithm evaluation only. For more realistic and weapon oriented applications, the reader is referred to [8,9,12,14,19]. The computational efficiency of the algorithm illustrated herein and in [8] illustrates that it is capable of treating problems of the complexity encountered in weapon design.

V. EXAMPLE I, A NONLINEAR IMPACT ABSORBER

In order to evaluate the effectiveness of the state space method presented herein, a single degree of freedom impact absorber problem is first solved and results compared with a solution obtained by the nonlinear programming method [10]. The nonlinear single degree of freedom system of Fig. 1 has a fixed mass M and two design parameters b_1 and b_2 that represent spring and damper coefficients, respectively. The exponents n and m are held fixed for each design.

The system impacts a fixed wall at time $t = 0$, so the equations of motion are

$$M\ddot{x} + b_2|\dot{x}|^m \operatorname{sgn}(\dot{x}) + b_1|x|^n \operatorname{sgn}(x) = 0$$

$$x(0) = 0, \quad \dot{x}(0) = v,$$

where $\operatorname{sgn}(\alpha) = \alpha/|\alpha|$ if $\alpha \neq 0$ and 0 if $\alpha = 0$. Defining $z_1 = x$ and $z_2 = \dot{x}$, one may write the equations of motion in the form of Eq. (1) as

$$\begin{bmatrix} 1 & 0 \\ 0 & M \end{bmatrix} \begin{bmatrix} \dot{z}_1 \\ \dot{z}_2 \end{bmatrix} = \begin{bmatrix} z_2 \\ -b_2|z_2|^m \operatorname{sgn}(z_2) - b_1|z_1|^n \operatorname{sgn}(z_1) \end{bmatrix}$$

$$\begin{bmatrix} z_1(0) \\ z_2(0) \end{bmatrix} = \begin{bmatrix} 0 \\ v \end{bmatrix}.$$

It is desired to minimize the maximum acceleration, so an artificial design parameter b_3 is defined by

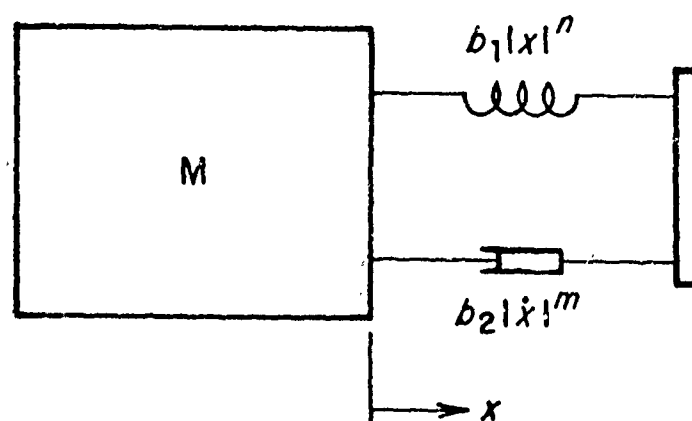


Figure 1. Nonlinear Impact Absorber

$$\frac{1}{M} \left| b_2 |z_2|^m \operatorname{sgn}(z_2) + b_1 |z_1|^n \operatorname{sgn}(z_1) \right| - b_3 \leq 0, \quad 0 \leq t \leq \tau$$

and the cost function is

$$J = b_3.$$

Because it is clear that acceleration will be high at impact, $t = 0$, an additional constraint is imposed as

$$(b_2 v^m / M) - b_3 \leq 0,$$

where the initial conditions have been employed. Finally, a constraint on extreme displacement is imposed, as

$$|z_1(t)| - z_{1\max} \leq 0, \quad 0 \leq t \leq \tau.$$

The problem is in the form treated in Section IV. It may be solved by direct application of the iterative algorithm of Section IV. In order to compare results with [10], numerical data are taken as $M = 1$, $v = 1$, $z_{1\max} = 1$, and $\tau = 12$ sec. A time grid with 0.15 seconds between points was used to solve the above problem for $n = 2$ and $m = 1, 2, 3$, and 4. A 5% reduction in cost function was requested and a constraint error limit of 0.2% was used as stopping criteria.

Numerical results are presented in Table 1. These results agree with those presented in [10] and were obtained in 6.6 sec, or 10% of the CPU time reported in [10]. Further, calculations presented herein were carried out on an IBM 360-65, which is slower than the CDC 6400 used in [10]. Convergence was obtained in six to ten iterations, in all cases. The regularity of the iterative process is illustrated by the plot of b_1 , b_2 , and b_3 versus iteration number in Fig. 2.

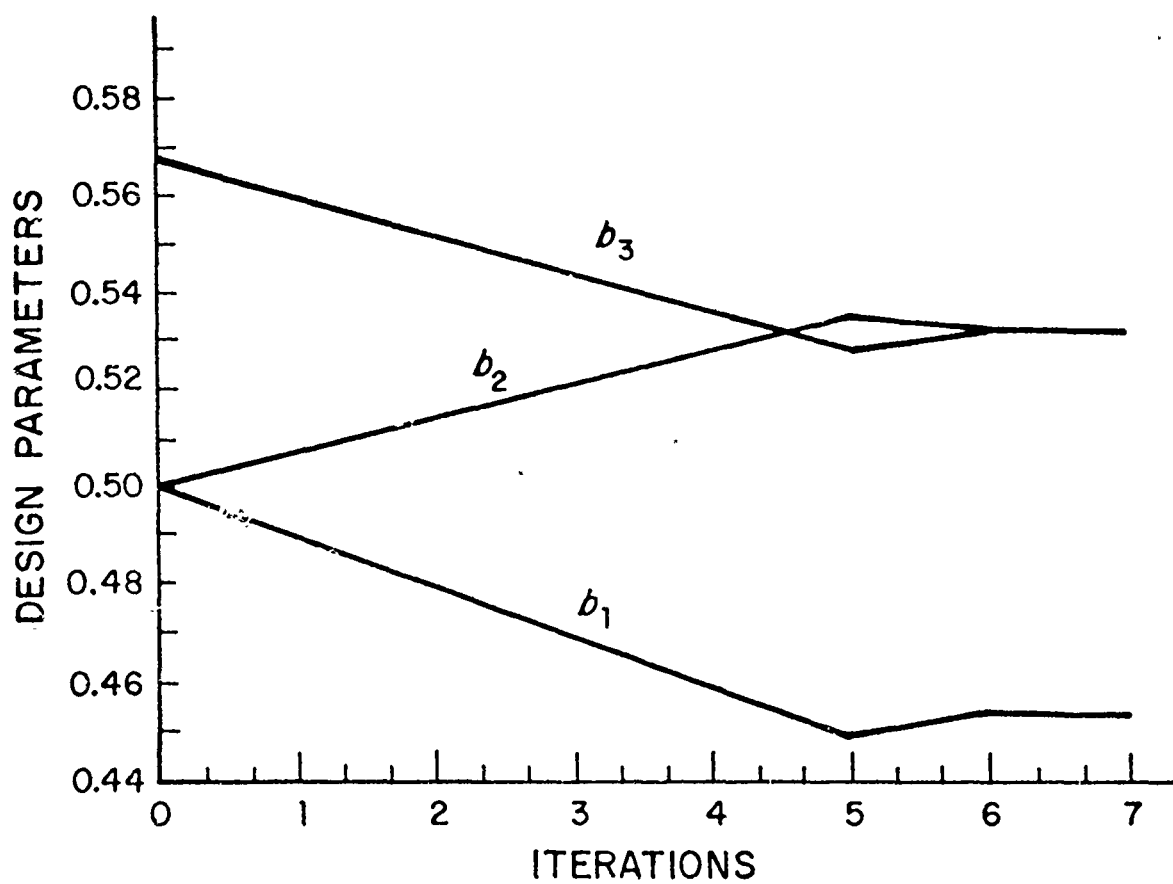


Figure 2. Design Variable Histories

VI. EXAMPLE II, A VEHICLE DYNAMIC RESPONSE TEST PROBLEM

The idealized, two degree of freedom model of a vehicle shown in Fig. 3 is used here to illustrate the method. Design parameters for this simple system include spring constants k_1 and k_2 and damping coefficients c_1 and c_2 , so $b = [k_1, k_2, c_1, c_2]^T$. Vehicle dynamic state variables are the vertical displacement and velocity of the center of gravity, $z_1(t)$ and $\dot{z}_1(t)$, and the pitch angle and roll rate $z_2(t)$ and $\dot{z}_2(t)$. Defining $z_3 = \dot{z}_1$ and $z_4 = \dot{z}_2$, the state variable is $z = [z_1, z_2, z_3, z_4]^T$. The equations of motion may be written in first-order form as

$$\dot{z}(t) = Q(b)z(t) + F(t) \quad , \quad (30)$$

where $F(t) = [0, 0, F_1(t), F_2(t)]^T = \left[0, 0, \frac{G(t)}{m}, \frac{M(t)}{m}\right]^T$

$$Q(b) = \begin{bmatrix} 0 & 0 & 1 & 0 \\ 0 & 0 & 0 & 1 \\ \frac{-k_1 - k_2}{m} & \frac{k_1 L_1 - k_2 L_2}{m} & \frac{-c_1 - c_2}{m} & \frac{c_1 L_1 - c_2 L_2}{m} \\ \frac{k_1 L_1 - k_2 L_2}{I} & \frac{-k_1 L_1 - k_2 L_2^2}{I} & \frac{c_1 L_1 - c_2 L_2}{I} & \frac{-c_1 L_1^2 - c_2 L_2^2}{I} \end{bmatrix} .$$

Here, m is the vehicle mass and I is its moment of inertia about the mass center. The cost function in this example is taken as

$$J = \lambda_1 \max_{t \in [0, T]} |z_4(t)| + \lambda_2 \max_{t \in [0, T]} |\dot{z}_4(t)| \quad ,$$

where λ_1 and λ_2 are nonnegative weighted parameters and $\dot{z}_4(t)$ is substituted from Eq. (30).

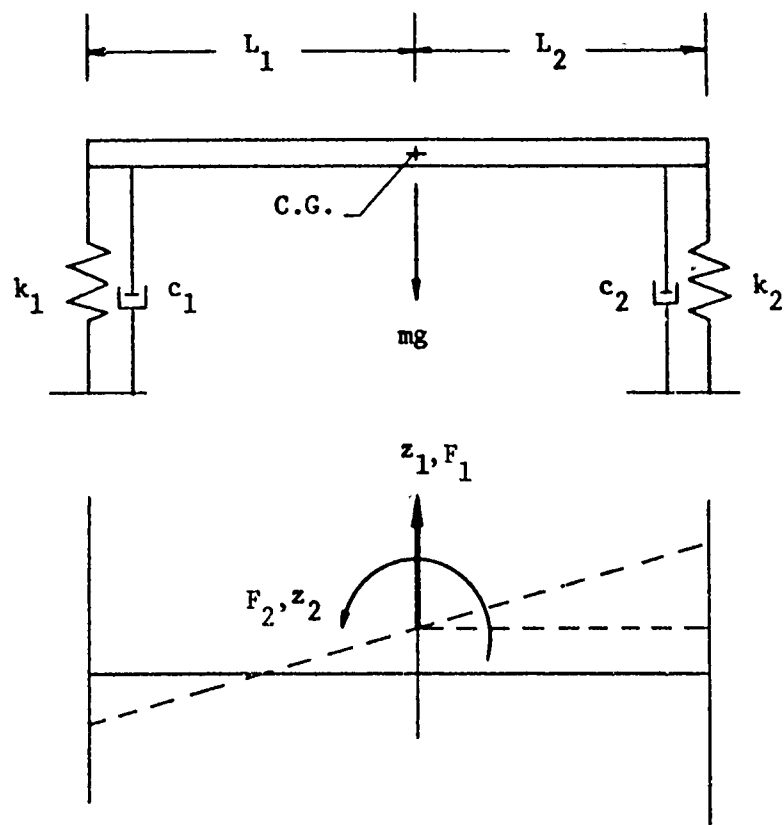


Figure 3. Two Degree of Vehicle Model

Extreme value constraints are placed on excursions z_1 and z_2 , velocities \dot{z}_3 and \dot{z}_4 , and accelerations \ddot{z}_3 and \ddot{z}_4 , in the form

$$\left. \begin{aligned} \phi_1 &\equiv \max_{t \in [0, T]} |z_1(t)| - \theta_1 \leq 0, & i = 1, 2, 3, 4 \\ \phi_5 &\equiv \max_{t \in [0, T]} |\dot{z}_3(t)| - \theta_5 \leq 0 \\ \phi_6 &\equiv \max_{t \in [0, T]} |\ddot{z}_4(t)| - \theta_6 \leq 0 \end{aligned} \right\}$$

where the θ_i 's are bounds on acceptable performance and $\dot{z}_3(t)$ and $\ddot{z}_4(t)$ are evaluated from Eq. (30). Finally, physical design constraints limit the range of admissible stiffness parameters, as in Eq. (4).

For purposes of computing example solutions, a forced motion vehicle optimization problem is solved. A forcing function simulating firing of a high impulse weapon from a light vehicle was chosen as $F_1(t) = 0$ and $F_2(t)$ as shown in Fig. 4. Homogeneous initial conditions are specified. Other numerical data for the model were selected as: $L_1 = 61$ in., $L_2 = 59$ in., $W = 4,500$ lb, and $I = 40,200$ lb-in.-sec². The weighting parameters in the cost function were chosen as $\lambda_1 = \lambda_2 = 1$.

Table 2 shows pertinent data and results for the equivalent formulations and the p-norm approximation of the cost function of Eq. (18). Both formulations converged to the same optimal solution. However, there was significant difference in the computing times. Average computing time was 21.4 seconds for the p-norm formulation and 9.2 seconds for the equivalent formulation. Thus, for a system with a large number of degrees of freedom, the equivalent formulation is formed.

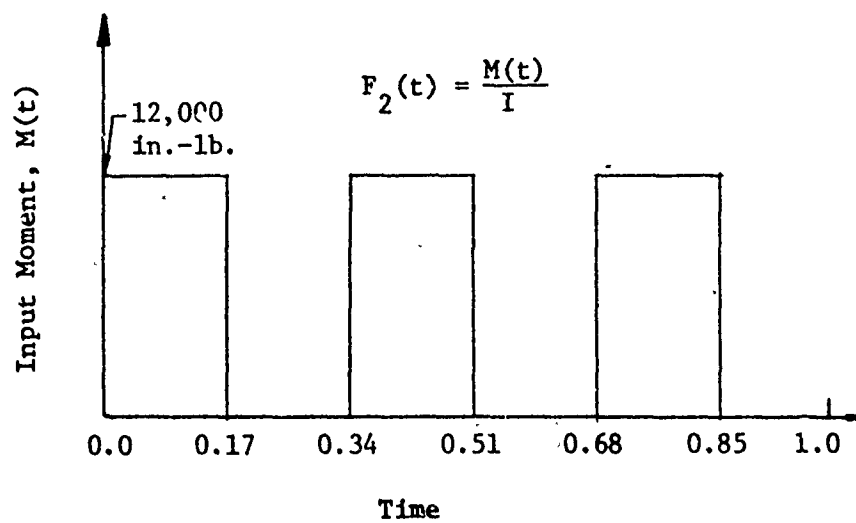


Figure 4. Excitation Moment

VII. EXAMPLE III, OPTIMAL DESIGN OF A VEHICLE SUSPENSION

A larger scale vehicle suspension design problem with five degrees of freedom, 6 design parameters, and a number of extreme value constraints is now solved. Figure 5 shows the model, which was used in [21] to minimize the maximum steady state response, over a given range of excitation frequency. The purpose of this section is to design the vehicle suspension system to minimize the extreme acceleration of the driver's seat, for different combinations of vehicle speeds and road conditions, while satisfying constraints on dynamic response and design parameters. Spring constants and damping coefficients are chosen as the design parameters.

Referring to Fig. 5, m_1 represents the mass of the seat and driver, which is supported by a spring k_1 and damper c_1 that are attached to the main body of the vehicle. The mass of the main body of the vehicle is m_2 and m_4 and m_5 are the masses of wheels and axles. The main body of the vehicle is supported by springs k_2 and k_3 and dampers c_2 and c_3 , which are attached to the axles and wheels. The parameters k_4 and k_5 represent the stiffness coefficients of the tires and c_4 and c_5 represent the damping coefficient of the tires. The moment of inertia of the main body about its mass center is denoted as I and L is the total length of the vehicle. The displacement functions $f_1(t)$ and $f_2(t)$ represent undulations of the road surface as the vehicle is traveling. The state equations that govern the motion of the vehicle are derived by an energy technique [19] and are

$$\dot{z}(t) = Q(b)z(t) + F(t) ,$$

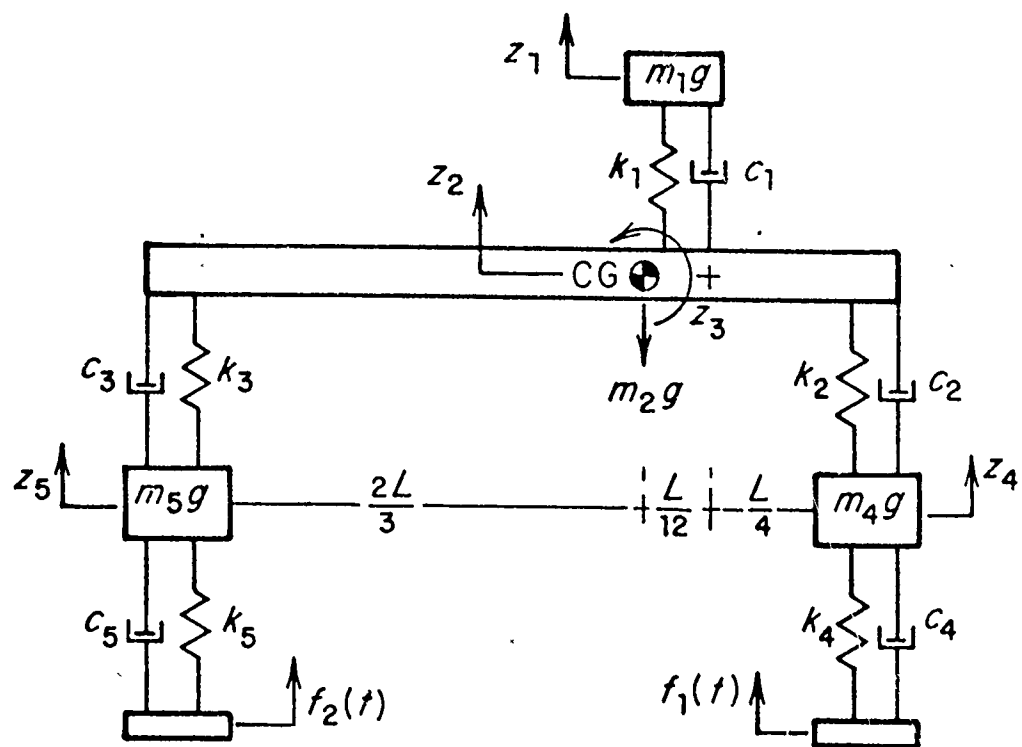


Figure 5. Five Degree of Freedom Vehicle

where $z(t) = [z_1, \dots, z_5, \dot{z}_1, \dots, \dot{z}_5]^T$ and $Q(b) = [Q_{ij}]_{10 \times 10}$. The non-zero elements of $Q(b)$ and $F(t)$ are: $Q_{1,6} = 1$; $Q_{2,7} = 1$; $Q_{3,8} = 1$; $Q_{4,9} = 1$; $Q_{5,10} = 1$; $Q_{6,1} = -k_1/m_1$; $Q_{6,2} = k_1/m_1$; $Q_{6,3} = Lk_1/(12m_1)$; $Q_{6,6} = -c_1/m_1$; $Q_{6,7} = c_1/m_1$; $Q_{6,8} = Lc_1/(12m_1)$; $Q_{7,1} = k_1/m_2$; $Q_{7,2} = -(k_1 + k_2 + k_3)/m_2$; $Q_{7,3} = -L(k_1 + 4k_2 - 8k_3)/(12m_2)$; $Q_{7,4} = k_2/m_2$; $Q_{7,5} = k_3/m_2$; $Q_{7,6} = c_1/m_2$; $Q_{7,7} = -(c_1 + c_2 + c_3)/m_2$; $Q_{7,8} = -L(c_1 + 4c_2 - 8c_3)/(12m_2)$; $Q_{7,9} = c_2/m_2$; $Q_{7,10} = c_3/m_2$; $Q_{8,1} = Lk_1/(12I)$; $Q_{8,2} = -L(k_1 + 4k_2 - 8k_3)/(12I)$; $Q_{8,3} = -L^2(k_1 + 16k_2 + 64k_3)/(144I)$; $Q_{8,4} = Lk_2/(3I)$; $Q_{8,5} = -2Lk_3/(3I)$; $Q_{8,6} = Lc_1/(12I)$; $Q_{8,7} = -(c_1 + 4c_2 - 8c_3)L/(12I)$; $Q_{8,8} = -(c_1 + 16c_2 + 64c_3)L^2/(144I)$; $Q_{8,9} = Lc_2/(3I)$; $Q_{8,10} = -2Lc_3/(3I)$; $Q_{9,2} = k_2/m_4$; $Q_{9,3} = Lk_2/(3m_3)$; $Q_{9,4} = -(k_2 + k_4)/m_4$; $Q_{9,7} = c_2/m_4$; $Q_{9,8} = Lc_2/(3m_4)$; $Q_{9,9} = -(c_2 + c_4)/m_4$; $Q_{10,2} = k_3/m_5$; $Q_{10,3} = -2Lk_3/(3m_5)$; $Q_{10,5} = -(k_3 + k_5)/m_5$; $Q_{10,7} = c_3/m_5$; $Q_{10,8} = -2Lc_3/(3m_5)$; $Q_{10,10} = -(c_3 + c_5)/m_5$; $F_9 = [k_4 \dot{f}_1(t) + c_4 \ddot{f}_1(t)]/m_4$; $F_{10} = [k_5 \dot{f}_2(t) + c_5 \ddot{f}_2(t)]/m_5$.

Since this is a transient dynamic response problem, the input road conditions are quite important. The dynamic response depends strongly on the displacement history of the wheels on the road surface. Referring to Fig. 6, road conditions are defined as a sinusoidal undulation, with constant amplitude x_0 and variable half-wavelengths λ_1 . The tire displacement is defined as

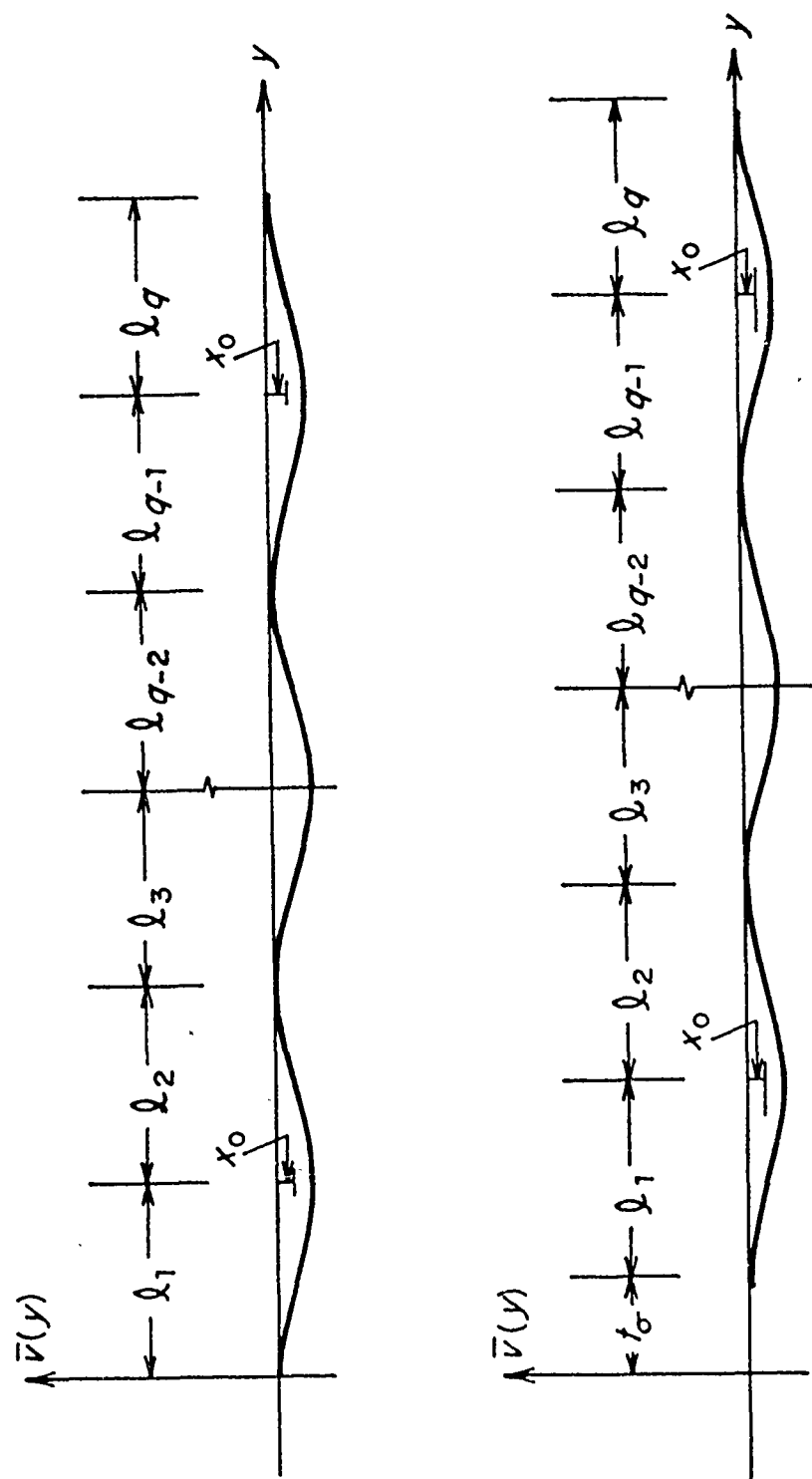


Figure 6. Variable Wavelength Road Conditions

$$\bar{v}(y) = \begin{cases} x_0 \left[1 - \cos \frac{\pi(y - y^{i-1})}{\ell_i} \right] & y^{i-1} \leq y \leq y^i, \quad i \text{ odd} \\ x_0 \left[1 + \cos \frac{\pi(y - y^{i-1})}{\ell_i} \right] & y^{i-1} \leq y \leq y^i, \quad i \text{ even}, \end{cases}$$

where y is a coordinate measured along the road, and $y^i = \sum_{j=1}^i \ell_j$.

If the speed of the vehicle is a constant S , the elapsed time between front and rear tire encounter of the same point on the road surface is $t_0 = L/S$. Since S is the speed of the vehicle, $y = St$, and

$$v(t) = \begin{cases} x_0 \left[1 - \cos \omega_i(t - t^{i-1}) \right] & t^{i-1} \leq t \leq t^i, \quad i \text{ odd} \\ x_0 \left[1 + \cos \omega_i(t - t^{i-1}) \right] & t^{i-1} \leq t \leq t^i, \quad i \text{ even}, \end{cases}$$

where $\omega_i = \pi S / \ell_i$ and $t^i = y^i / S$. The vertical displacement history for the road surface at the front wheel can, therefore, be defined as

$$f_i(t) = \begin{cases} v(t) & 0 \leq t \leq T_1 \\ 0 & \text{otherwise} \end{cases},$$

where T_1 is the time at which the road undulation ceases. The vertical displacement of the road surface at the rear wheel has the same value as the front wheel, but with a time lag t_0 . That is

$$f_2(t) = f_1(t - t_0), \quad t_0 \leq t \leq T_1 + t_0.$$

With these displacement functions and equations of motion, one may now define the optimization problem. The design problem is to minimize the

maximum passenger acceleration, such that certain relative displacements do not exceed established limits. The cost function is thus chosen as

$$\phi_0 = \max_{\substack{t \in [0, \tau] \\ i=1, 2, \dots, \alpha}} |\ddot{z}_1^i(t; b)| ,$$

where α is the number of road conditions treated and $\ddot{z}_1^i(t; b)$ is the acceleration of the passenger seat for the i -th road condition. One may define

$$\psi_0 = b_7 ,$$

with the additional constraints

$$\phi_i = \max_{t \in [0, \tau]} |\ddot{z}_1^i(t; b)| - b_7 \leq 0 , \quad i = 1, 2, \dots, \alpha .$$

The performance constraints are

$$\phi_i = \max_{t \in [0, \tau]} |\ddot{z}_1^i(t; b)| - \theta_1 \leq 0 , \quad i = \alpha + 1, \dots, 2\alpha \quad (31)$$

where θ_1 is a fixed maximum allowable acceleration. The motion of the vehicle must be constrained so that the relative displacements between the main body and the driver's seat, the front wheel, and the rear wheel; as well as the relative displacements between the road surface and the front and rear wheels; are within given limits for each road condition considered. These constraint equations may be written as follows:

$$\phi_{2\alpha+i} = \max_{t \in [0, \tau]} |z_2^i(t; b) + \frac{L}{12} z_3^i(t; b) - z_1^i(t; b)| - \theta_2 \leq 0 , \quad (32)$$

$$i = 1, 2, 3, \dots, \alpha ,$$

$$\phi_{3\alpha+1} = \max_{t \in [0, \tau]} |z_4^i(t; b) - z_2^i(t; b) - \frac{L}{3} z_3^i(t; b)| - \theta_3 \leq 0, \quad i = 1, 2, 3, \dots, \alpha \quad (33)$$

$$\phi_{4\alpha+1} = \max_{t \in [0, \tau]} |z_5^i(t; b) - z_2^i(t; b) + \frac{2L}{3} z_3^i(t; b)| - \theta_4 \leq 0, \quad i = 1, 2, 3, \dots, \alpha, \quad (34)$$

$$\psi_{5\alpha+1} = \max_{t \in [0, \tau]} |z_4^i(t; b) - f_1^i(t)| - \theta_5 \leq 0, \quad i = 1, 2, 3, \dots, \alpha, \quad (35)$$

$$\phi_{6\alpha+1} = \max_{t \in [0, \tau]} |z_5^i(t; b) - f_2^i(t)| - \theta_6 \leq 0, \quad i = 1, 2, 3, \alpha, \quad (36)$$

where θ_2 through θ_6 are the maximum allowable displacements. Equations (31) through (36) are transformed to the form of Eq. (14). Bounds must also be placed on the design parameters as follows:

$$b_j^L \leq b_j \leq b_j^U, \quad j = 1, 2, 3, \dots, 6, \quad (37)$$

where $b = [k_1, k_2, k_3, c_1, c_2, c_3]^T$.

For an example calculation, numerical data are $m_1 g = 290$ lb, $m_2 g = 4,500$ lb, $m_4 g = m_5 g = 96.6$ lb, $I = 41,000$ lb-in.-sec², $L = 120$ in., $k_4 = k_5 = 1,500$ lb/in., and $c_4 = c_5 = 5$ lb-sec/in., lower and upper bounds are for b are $[50, 200, 200, 2, 5, 5]^T$ and $[500, 1000, 1000, 50, 80, 80]^T$, respectively. The units for z_1, z_2 ,

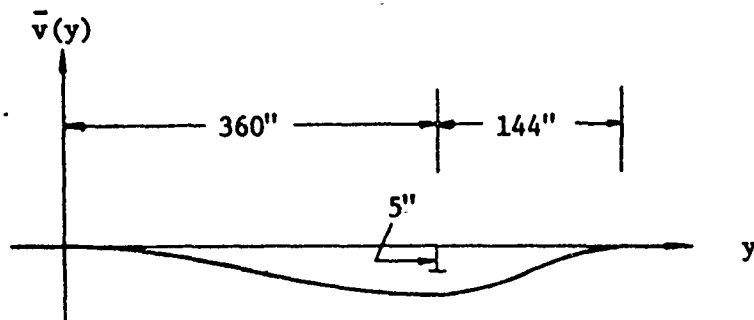
z_4 , and z_5 are inches and for z_3 are radians. Bounds for the constraints in Eqs. (38) through (43) are $\theta = [400, 2, 5, 5, 2, 2]^T$. Homogeneous initial conditions are used in all calculations.

Two different road profiles ($\alpha = 2$) are imposed as shown in Fig. 7. Profile (1) is a combination of two sinusoidal curves with different half-wavelengths $\ell_1 = 360$ in. and $\ell_2 = 144$ in. and an amplitude $x_0 = 5$ in. This profile represents a severe bump condition that may be encountered at moderate speed. Profile (2) is a continuous sinusoidal curve with a constant half-wavelength $\ell_1 = \ell_2 = \ell_3 = \ell_4 = 480$ in. and an amplitude $x_0 = 2$ in. This condition is typical of a high speed highway condition. For the design problem, two vehicle speeds associated with these two road conditions are considered. The second displacement function is determined by Profile (2) with a vehicle speed of 960 in./sec. This results in $t_\sigma = 0.125$ sec and $\omega_i = 2\pi$, $i = 1, 2, 3, 4$. The first displacement function is determined by Profile (1), with a vehicle speed of 450 in./sec. This results in $t_\sigma = 0.2667$ sec, $\omega_1 = 1.25\pi$, and $\omega_2 = 3.125$. The cost function is chosen to be the maximum driver acceleration in the highway condition, of profile (2) only,

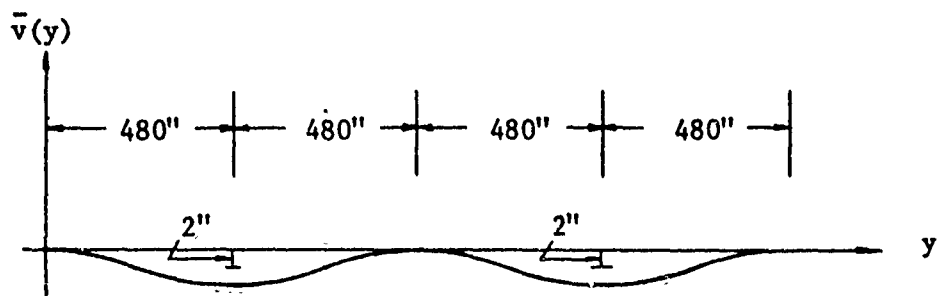
$$J = \max_{t \in [0, \tau]} |\ddot{z}_1^1(t; b)| \quad (38)$$

Constraints of Eqs. (32) through (36) are imposed for both road conditions.

The requested cost function reduction was one percent in the first iteration and the initial design was as shown in Table 3. This resulted in $||\delta b^1|| = 0.8131$ and $||\delta b^2|| = 12.78$. The initial cost function value was 198.6. Maximum value of \ddot{z}_1^1 was 332.6. The constraint on \ddot{z}_1^2



(a) Profile (1)



(b) Profile (2)

Figure 7. Test Road Conditions

was active and constraints of Eqs. (32) and (33) were violated for Profile (1). After 3 iterations, a constraint of Eq. (34) was violated for Profile (1). For all iterations after the seventh, Eqs. (36) were satisfied, and Eqs. (33) and (34) remained active. At the optimum design, after 44 iterations, $||\delta b^1|| = 0.4147 \times 10^{-1}$, $||\delta b^2|| = 0.9584 \times 10^{-2}$, and the optimum cost function was 103.5. The maximum value of \ddot{z}_1^1 was 258.5. The design parameters b_1 , b_2 , and b_3 reached their lower bounds. The average computing time was 35 seconds for each iteration. Numerical results are given in Table 3.

VIII. CONCLUSIONS

The state space method of optimal design of dynamic systems compares favorably both theoretically and computationally, with direct nonlinear programming methods. In the shock isolator example of Section V, the state space method required only one-tenth of the computing time employed in a nonlinear programming formulation [10]. As the dimension of design problems increases, it is expected that the ratio of computing times will still further favor the state space approach. A larger scale, five degree of freedom vehicle dynamic optimization problem with multiple input conditions was also solved with the state space algorithm, with good results. This problem involved twelve max-value constraints, a max-value cost function, and six design variables.

Numerical results for each of these problems indicate that the cost function reduces rapidly in the first few iterations. Although the rate of convergence slows when the cost function is within one to two percent of the optimum, this is not seen to be a practical hindrance of the method. Further, a more sophisticated optimization algorithm may yield fine convergence more rapidly.

The steady performance of the state space method on the example problems solved herein and the authors' experience with such methods in problems involving up to 41 degrees of freedom [2] lead them to conclude that the method can be effectively applied to practical dynamic system optimization problems. Improvements in the algorithm may be made by (a) employing more efficient numerical integration techniques, such as stiff integration methods, (b) constructing a modular program to allow rapid problem set up

and solution, and (c) use of methods such as the augmented Lagrangian for constructing the descent aspect of the algorithm.

Experience obtained with the algorithm on the problems presented herein, on larger scale problems [2,3], and on the important problem of dynamics of systems with intermittent motion lead the writers to conclude that the state space method is practical for the type of design problems encountered in advanced weapon design. It is suggested that the advances in dynamic analysis of precision weapons presented in these proceedings can be employed, with the state space sensitivity analysis and optimization method, to practically carry out parametric design of systems such as the Anti-Armor Automatic Cannon. Advancements needed include algorithm development for larger scale nonlinear systems that incorporate intermittent motion. Further, user oriented codes may be developed for classes of applications that will allow the designer to determine sensitivity of dynamic performance to design variables that are at his control. This will aid him in deciding on needed design changes based on his experience, or in proceeding with automated iterative optimization. The writer recommends the former approach, to take advantage of design experience, prior to launching into a large scale effort in automated optimal design.

REFERENCES

- [1] A. S. Elder, "Survey of Transient Vibrations and Stress Waves in Gun Tubes," This proceedings, January, 1977.
- [2] T. T. Feng, J. S. Arora, and E. J. Haug, Optimal Design of Elastic Structures Under Dynamic Loads, Technical Report No. 10, Materials Division, College of Engineering, University of Iowa, Iowa City, Iowa, May, 1975.
- [3] J. S. Arora, E. J. Haug, and T. T. Feng, "A Finite Element Method of Optimizing Precision of a Vibrating Weapon," This Proceedings, January, 1977.
- [4] T. Hung and T. T. Feng, "Transverse Dynamic Response of a Gun Barrel with Time Varying Supports," This proceedings, January 1977.
- [5] V. Komkov, "Fundamentals of Weapon Dynamic Effects on Precision," This Proceedings, January, 1977.
- [6] R. Huang, E. J. Haug, and J. G. Andrews, "Sensitivity Analysis and Optimization of Mechanisms with Intermittent Motion," This Proceedings, January, 1977.

- [7] E. Sevin and W. D. Pilkey, Optimum Shock and Vibration Isolation,
Monograph No. 6, The Shock and Vibration Center, Naval Research
Laboratory, Washington, D.C., 20390, 1971.
- [8] D. C. Karnopp and A. K. Trikha, Journal of Engineering for Industry 91,
1128-1132 (1969).
- [9] K. D. Wilmert and R. L. Fox, Journal of Engineering for Industry 94,
465-471 (1972).
- [10] K. A. Afimiwala and R. W. Mayne, Journal of Engineering for Industry 96,
124-130 (1974).
- [11] V. A. Troitskii, Journal of Optimization Theory and Application 15,
No. 6, 615-632 (1975).
- [12] A. E. Bryson and W. F. Denham, Journal of Applied Mechanics 29, 247-257,
(1962).
- [13] A.E. Bryson, Jr. and Y. C. Ho, Applied Optimal Control, Blaisdell,
Waltham, Mass., 1969.
- [14] E. J. Haug, Jr., Computer Aided Design of Mechanical Systems, Army
Material Command Engineering Design Handbook, AMCP 706-192 & 193,
1973 & 1977.

- [15] A. Miele, Journal of Optimization Theory and Application 17, Nos. 5/6, 361-430 (1975).
- [16] W. F. Powers, AIAA Journal 10, No. 10, 1291-1296 (1972).
- [17] J. W. Bandler and C. Charalambous, Journal of Optimization Theory and Application 11, No. 5, 556-566 (1973).
- [18] W. Rudin, Real and Complex Analysis, McGraw-Hill, New York, 1966.
- [19] M. H. Hsiao, E. J. Haug, Jr., and J. S. Arora, Mechanical Design Optimization with Transient Dynamic Response, Technical Report No. 23, Division of Materials Engineering, University of Iowa, Iowa City, Iowa, 1976.
- [20] E. J. Haug, Jr., K. C. Pan, and T. D. Streeter, International Journal of Numerical Methods in Engineering 5, 171-184 (1972).
- [21] J. McMunn, "Multi-Parameter Optimum Damping in Linear Dynamical Systems," Ph.D. Thesis, University of Minnesota, Minneapolis, Minnesota, 1967.

TABLE 1
RESULTS FOR NONLINEAR IMPACT ABSORBER

m		1	2	3	4
Initial Design	b_1	0.500	0.500	0.500	0.500
	b_2	0.500	0.500	0.500	0.5
	$ \delta b^1 $	0.53	0.80	0.65	0.47
Final Design	b_1	0.453	0.597	0.682	0.752
	b_2	0.531	0.597	0.682	0.752
	b_3	0.531	0.597	0.682	0.752
	$ \delta b^1 $	0.57×10^{-6}	0.57×10^{-6}	0.83×10^{-6}	0.51×10^{-6}

TABLE 2

DATA AND RESULTS FOR TWO DEGREE OF FREEDOM SYSTEM WITH DAMPING

Lower Bounds on $B = [10, 10, 0.5, 0.5]^T$ Upper Bounds on $b = 1000, 1000, 50, 50]^T$ $\theta_s = [0.007, 0.005, 0.5, 0.5, 0.15, 0.5]^T$ $P = 6$

Variable	Starting Values	Optimal Values P-Norm Formulation	Optimal Values Equivalent Formulation
k_1	2.000×10^2	2.091×10^2	2.092×10^2
k_2	2.000×10^2	2.101×10^2	2.101×10^2
c_1	4.000×10^1	4.934×10^1	4.944×10^1
c_2	4.000×10^1	5.000×10^1	5.000×10^1
Max $ z_1 $	9.224×10^{-3}	6.999×10^{-3}	6.999×10^{-3}
Max $ z_2 $	5.550×10^{-3}	4.999×10^{-3}	4.999×10^{-3}
Max $ z_3 $	3.015×10^{-2}	2.303×10^{-2}	2.306×10^{-2}
Max $ z_4 $	2.511×10^{-2}	2.215×10^{-2}	2.215×10^{-2}
Max $ \dot{z}_3 $	1.888×10^{-1}	1.491×10^{-1}	1.497×10^{-1}
Max $ \dot{z}_4 $	2.985×10^{-1}	2.985×10^{-1}	2.985×10^{-1}

TABLE 3
RESULTS FOR THE 5-DEGREE OF FREEDOM VEHICLE

	Starting Values	Optimal Values
k_1	100.0	50.00
k_2	300.0	200.00
k_3	300.0	200.0
c_1	10.0	46.58
c_2	25.0	78.44
c_3	25.0	26.21
d	198.6	103.50

SENSITIVITY ANALYSIS AND OPTIMAL DESIGN
OF THE 75mm AUTOMATIC CANNON MECHANISM

R.C. HUANG, E.J. HAUG and J.G. ANDREWS
University of Iowa
Iowa City, Iowa

TABLE OF CONTENTS

	<u>Page</u>
I. INTRODUCTION	259
II. DESCRIPTION OF THE MECHANISM AND DEFINITION OF SPECIAL TIMES	260
III. FORMULATION OF THE DESIGN PROBLEM	269
IV. SENSITIVITY ANALYSIS	274
V. NUMERICAL RESULTS AND DISCUSSION	284
VI. APPENDIX A: EQUATIONS OF MOTION	293
VII. APPENDIX B: SENSITIVITY COEFFICIENTS OF THE FUNCTIONAL CONSTRAINTS	296
VIII. REFERENCES	302

I. Introduction

Recent emphasis on precision in the development of automatic weapons systems with high impulse has led to the need for a well designed automatic mechanism with intermittent motion. While design craftsmanship has served well in the past in development of such automatic weapons, their design has not received the level of analytical support it deserves. Typical of this situation is the lack of literature on mechanisms with intermittent motion. Reference [1] presents a survey and explanation of the functioning of mechanisms occurring in clocks, process machinery, and weapons. It is, however, not at all analytically oriented. A survey of the literature on dynamics of mechanisms quickly reveals that, while intermittent motion is acknowledged as an important mechanism problem, virtually no literature is devoted to this subject.

The purpose of this paper is to present an analytical design formulation of a specific automatic weapon mechanism, characterize its motion with piecewise smooth differential equations, and employ methods of optimal control [2] to obtain the sensitivity of its dynamic performance to design variation. A dynamic model is developed and the sensitivity of several measures of dynamic performance to design variation are calculated. A computer program to carry out the dynamic analysis and sensitivity calculation is described and numerical examples of design sensitivity analysis are solved. In addition to a dynamic analysis the program generates sensitivity coefficients that tell the designer what the effect of design changes will be consistent with the performance constraints that he has imposed.

The logical analytical extension of this capability for automatic iterative optimization of weapon dynamics is then presented. An optimization algorithm is derived and numerical results presented, which determine optimum performance of a 75 mm automatic weapon.

II. Description of the Mechanism and Definitions of Special Times

The 75 mm mechanism shown in Fig. 1 consists of three main masses: the barrel assembly B, the sleeve S, and the sear SR. A camming action is used to move the sleeve over the telescoped cartridge so that one can safely ignite the charge during each cycle of system operation. The B-cam path is fixed in the barrel assembly B, while the R-cam path is fixed in the receiver R. The base of this receiver makes an angle α with the horizontal. The sleeve S is connected by a rigid bar PQ to a pin at point P that is constrained to slide without friction along the cam paths.

Two forces, b_{10} and b_{11} , drive the barrel during its forward (counter recoil) and backward (recoil) motions, respectively. In order to slow the barrel assembly during extreme motion, a front buffer D_1 and a rear buffer D_2 are added to the system. Both front and rear buffers are designed to produce constant retarding forces when the barrel is in contact with them.

Special times t_i at which impact or some other irregularity of intermittent motion occur are introduced as an integral element of the dynamic model. Between these times, the motion of the system is quite regular. At these times, however, discontinuities or changes in system configuration can occur. Special times will now be defined for two modes of weapon operation:

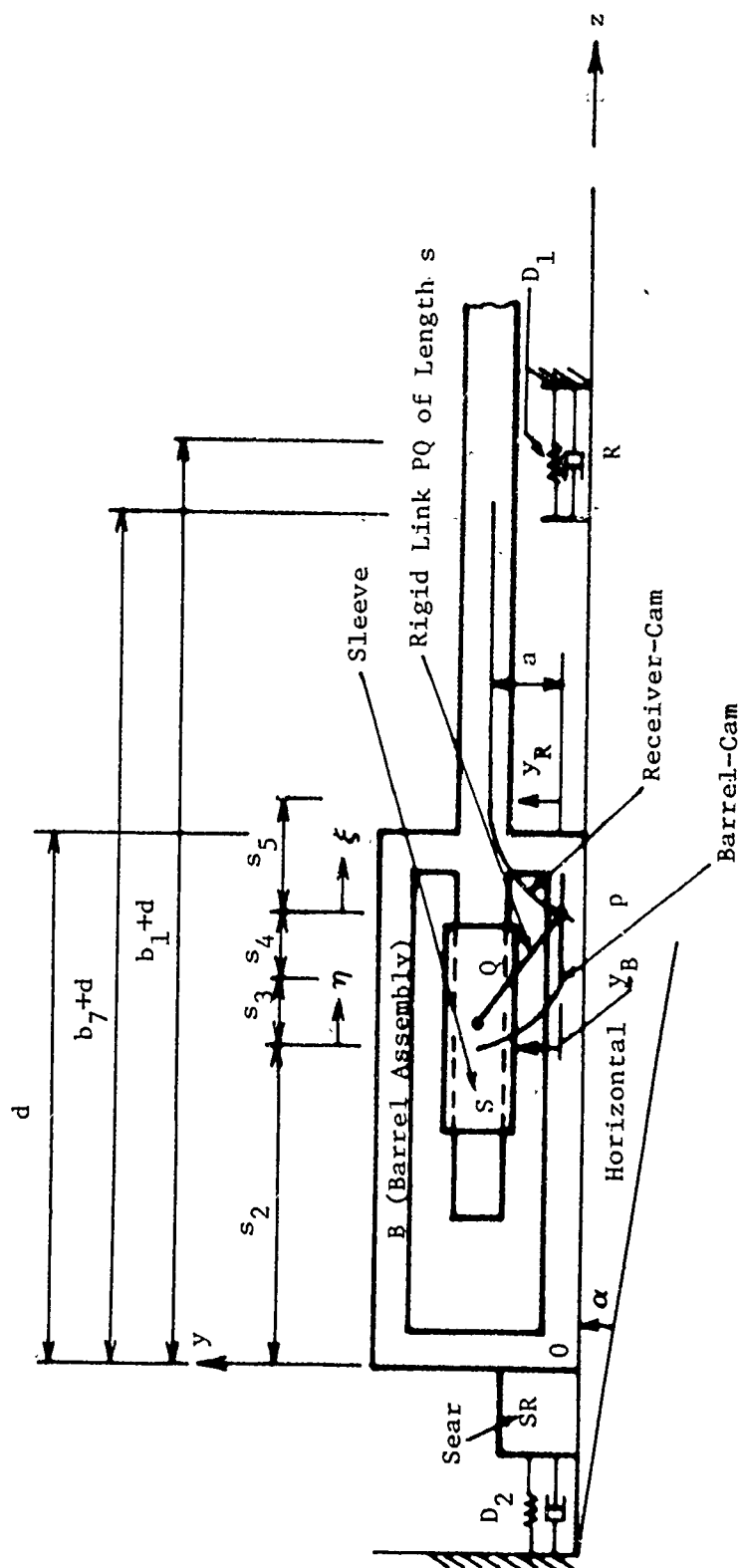


Figure 1. 75 mm Cannon System

A. Firing from run-out.

1. $t_0 = 0$: At this instant, the barrel assembly B leaves the sear position O with velocity b_8 . (Fig. 1)
2. t_1 : At this instant, the pin P starts to move along the R-cam path, and the rigid bar PQ connecting P to S starts to move the sleeve S forward. (Fig. 2)
3. t_2 : At this instant, P reaches the flat portion of the R-cam path and the bar PQ becomes parallel to the z-axis. The sleeve S then moves with the barrel assembly B at the same velocity, and the charge is therefore ready to fire. (Fig. 3)
4. t_3 : At this instant, B contacts the front buffer D_1 . (Fig. 4)
5. t_4 : At this instant, the charge is ignited (impulse = b_9). (Fig. 5)
6. $t_4 + \Delta t$: At this instant, B and S start to move rearward. ($0 < \Delta t \ll 1$)
7. t_5 : At this instant, contact between B and D_1 ceases. (Fig. 6)
8. t_6 : At this instant, S starts to move forward relative to B (i.e., the pin P reaches the curves portion of the R-cam path). (Fig. 3)
9. t_7 : At this instant, P reaches the lower cusp of the R-cam path, and the sleeve S comes to rest relative to R. (Fig. 2)

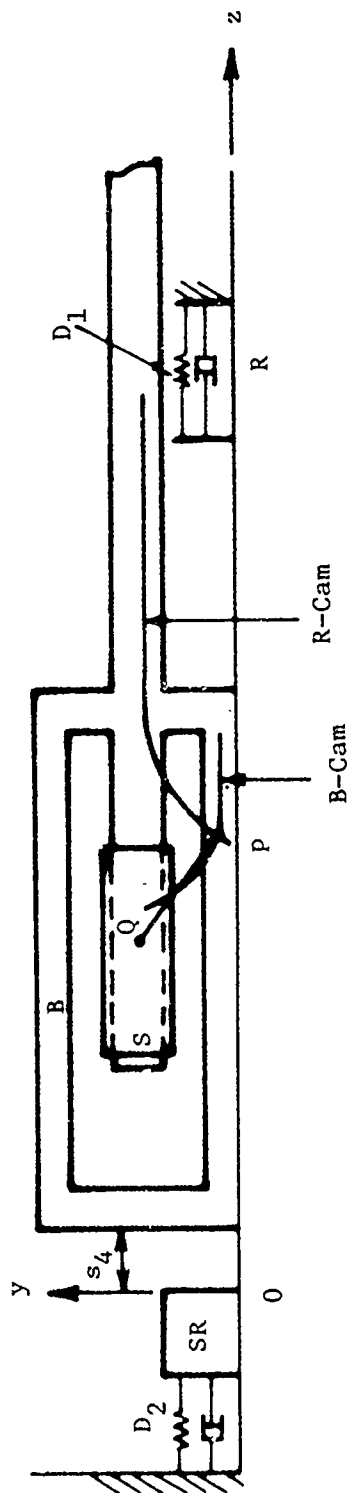


Figure 2. Position where Sleeve Starts to Move Forward or Comes to Rest W.R.T. the Receiver R ($z = s_4$)

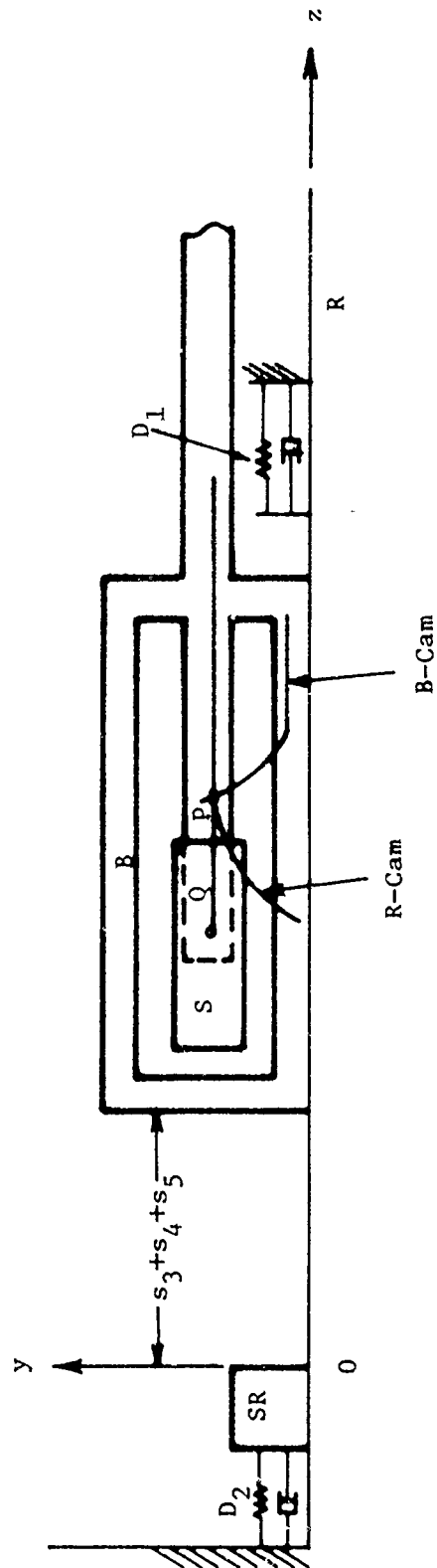


Figure 3. Position where Sleeve Starts to Move with Barrel, with the Same Velocity, or Starts to Move Forward W.R.T. Barrel ($z = s_3 + s_4 + s_5$)

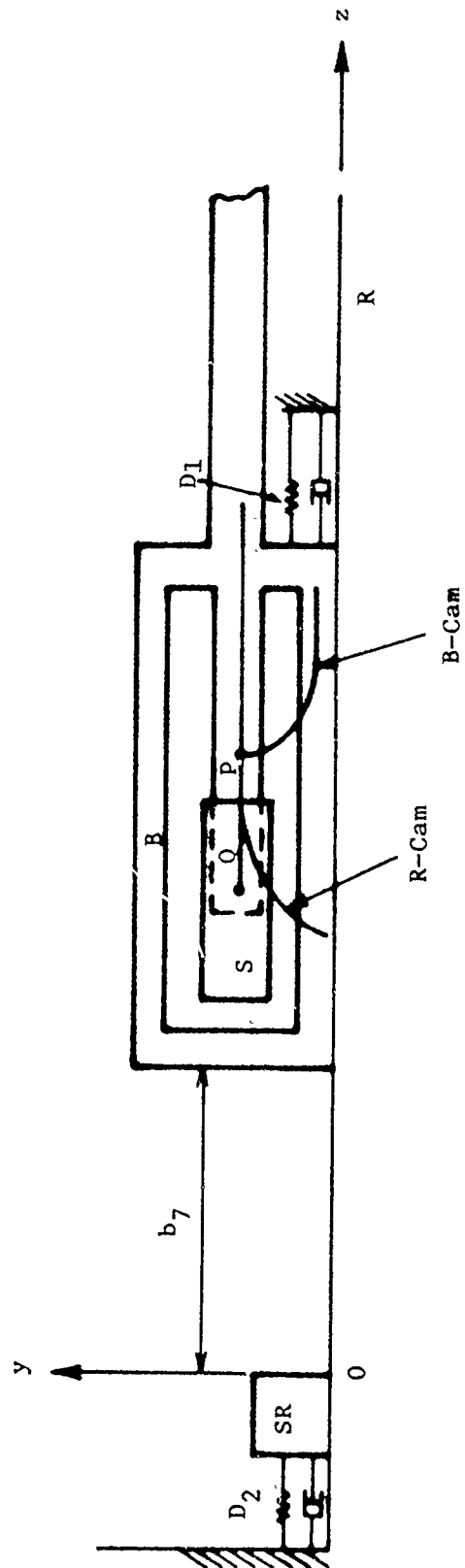


Figure 4. Barrel Assembly at the Position where it Starts to Ceases to Contact the Front Buffer ($z = b_7$)

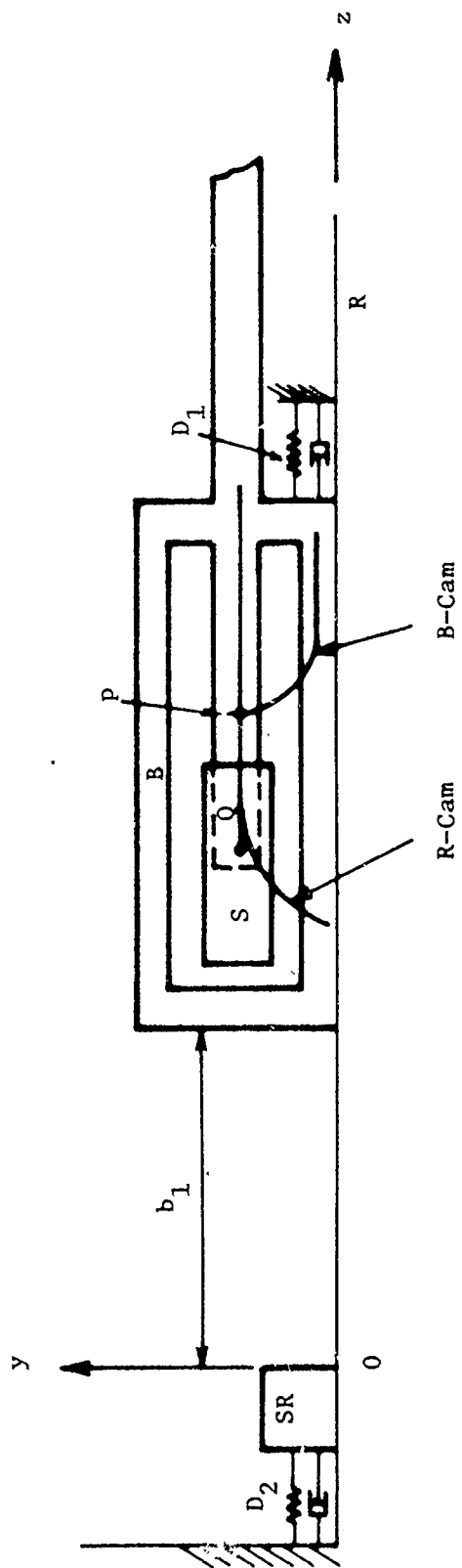


Figure 5. Firing Position ($z = b_1$)

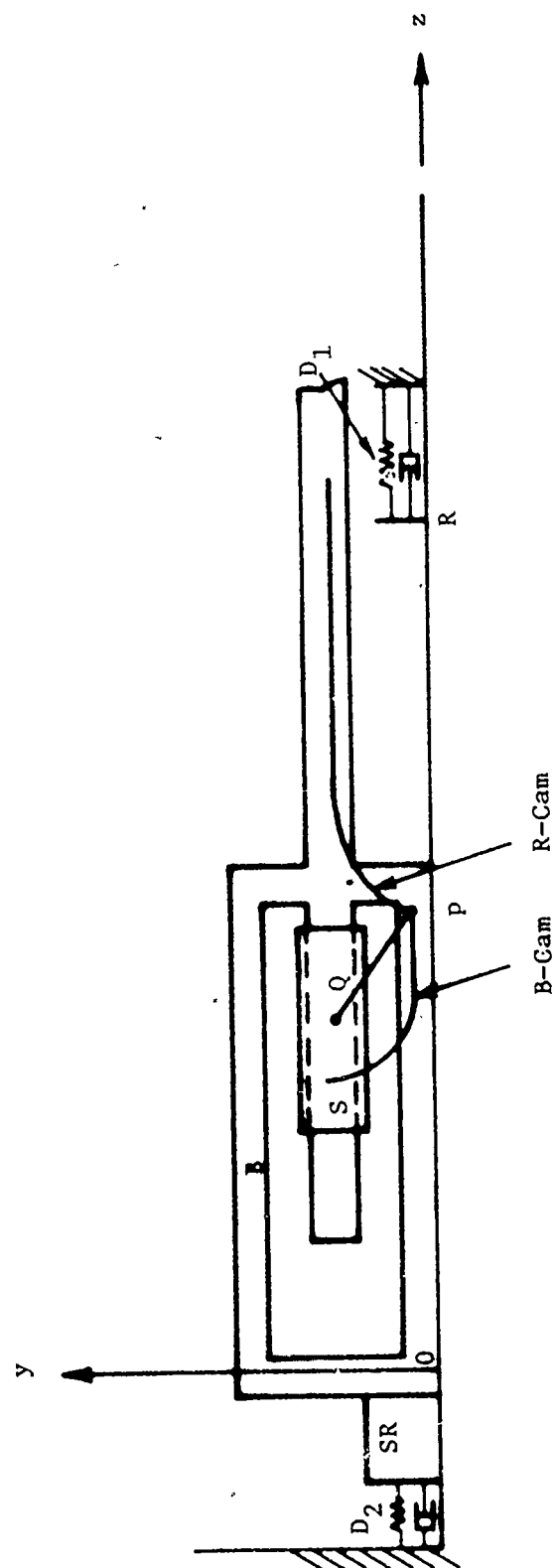


Figure 6. Barrel Assembly at Rearmost Position

10. t_8 : At this instant, B passes the sear position 0 and starts to move rearward with the sear SR, both moving with the same velocity while compressing the rear buffer D_2 . (Fig. 1)
11. t_9 : At this instant, B reaches zero velocity prior to its forward motion due to the driving force b_{10} . (Fig. 6)
12. t_{10} : At this instant, B returns to the sear position 0. This completes one cycle of system operation. (Fig. 1)

B. Firing from in-battery position.

1. $t_0 = 0$: At this instant, B rests at $x = b_1$ and the charge is ignited. (Fig. 5)
2. $t_0 + \Delta t$: At this instant, B starts to move rearward.
3. t_1 : At this instant, contact between B and the front buffer D_1 ceases. (Fig. 4)
4. t_2 : At this instant, S starts to move forward relative to B. (Fig. 3)
5. t_3 : At this instant, S comes to rest on R. (Fig. 2)
6. t_4 : At this instant, B passes the sear position 0 and starts to move rearward with the sear SR, both moving with the same velocity while compressing the rear buffer D_2 . (Fig. 1)

7. t_5 : At this instant, B and SR reach their rearmost position. (Fig. 6)
8. t_6 : At this instant, B passes the sear position 0 and SR comes to rest on R. (Fig. 1)
9. t_7 : At this instant, P starts to move along the R-cam path. (Fig. 2)
10. t_8 : At this instant, P reaches the flat portion of the R-cam path. (Fig. 3)
11. t_9 : At this instant, B first contacts the front buffer D_1 . (Fig. 4)
12. t_{10} : At this instant, B comes to rest on R, and one cycle of system operation is completed. (Fig. 5)

III. Formulation of the Design Problem

In this section, the design problem is formulated first for the specific 75 mm automatic weapon under consideration. This problem is then embedded in a general formulation that will lead to a sensitivity analysis and optimization algorithm.

A. The 75 mm design problem.

Let the design parameters b_j and the state variables z be defined as follows (see Fig. 1):

- b_1 = firing distance measured from the sear position 0
- b_2 = barrel assembly mass
- b_3 = sleeve mass
- b_4 = sear mass

b_5 = constant front buffer contact force

b_6 = constant rear buffer contact force

b_7 = distance between the sear position and the front buffer

b_8 = initial velocity of the barrel

b_9 = imposed impulse

b_{10} = driving force acting on the barrel during its
forward motion

b_{11} = driving force acting on the barrel during its
rearward motion

z_1 = z-coordinate of the barrel

z_2 = velocity of the barrel (\dot{z}_1)

Optimal design problems for the two distinct modes of weapon system operation are formulated as follows:

1. Firing from run-out. Minimize the objective function

$J \equiv t_8 - t_{10}$ (i.e., maximize $t_{10} - t_8$, the time available to feed the charge), subject to the following constraints:

- a. equations of motion:

$$dz/dt = f(z, b, t), \quad 0 < t < t_{10}, \quad t \neq t_i, \quad i = 1, 2, \dots, 9,$$

with initial conditions, $z_1(0) = 0$ and $z_2(0) = b_9$.

The equations of motion are listed in Appendix A.

- b. definitions of the special times t_i (see Fig. 1):

$$z_1(t_1) - S_4 = 0,$$

$$z_1(t_2) - S_3 - S_4 - S_5 = 0,$$

$$z_1(t_3) - b_7 = 0 ,$$

$$z_1(t_4) - b_1 = 0 ,$$

$$z_1(t_5) - b_7 = 0 ,$$

$$z_1(t_6) - s_3 - s_4 - s_5 = 0 ,$$

$$z_1(t_7) - s_4 = 0 ,$$

$$z_1(t_8) = 0 ,$$

$$z_2(t_9) = 0 ,$$

$$z_1(t_{10}) = 0 .$$

c. constraints on the design parameters:

$$\psi_i \equiv b_i - b_i^U \leq 0 \quad \text{and} \quad b_i^L - b_i \leq 0 , \quad i = 1, 2, \dots, 11 ,$$

where b_i^U and b_i^L are the upper and lower bounds on b_i .

d. $\psi_{12} \equiv t_{10} - h_1 \leq 0$. This constraint requires that the cycle time not exceed h_1 .

e. $\psi_{13} \equiv t_2 - t_6 + h_2 \leq 0$. This constraint requires that the time during which the sleeve is in its functional position be not less than h_2 .

f. $\psi_{14} \equiv |z_1(t_9)| - h_3 \leq 0$. This constrains the rearmost position of the barrel assembly.

2. Firing from in-battery. Minimize the objective function

$$J \equiv t_4 - t_6 \text{ (i.e., maximize the feeding time } t_6 - t_4),$$

subject to the following constraints:

a. equation of motion:

$$\frac{dz}{dt} = f(z, bt) , \quad 0 < t < t_{10} , \quad t \neq t_i , \quad i = 1, 2, \dots, 9 ,$$

with initial conditions, $z_1(0) = b_1$ and

$z_2(\Delta t) = b_9 / (b_2 + b_3)$. The equations of motion

are listed in Appendix A.

b. definitions of the special times t_i :

$$z_1(t_1) - b_7 = 0 ,$$

$$z_1(t_2) - S_3 - S_4 - S_5 = 0 ,$$

$$z_1(t_3) - S_4 = 0 ,$$

$$z_1(t_4) = 0 ,$$

$$z_2(t_5) = 0 ,$$

$$z_1(t_6) = 0 ,$$

$$z_1(t_7) - S_4 = 0 ,$$

$$z_1(t_8) - S_3 - S_4 - S_5 = 0 ,$$

$$z_1(t_9) - b_7 = 0 ,$$

$$z_2(t_{10}) = 0 .$$

c. constraints on the design parameters:

$$\psi_i \equiv b_i - b_i^U \leq 0 \quad \text{and} \quad b_i^L - b_i \leq 0 , \quad i = 1, 2, \dots, 11 .$$

$$\underline{d.} \quad \psi_{12} \equiv t_{10} - h_1 \leq 0 \quad .$$

$$\underline{e.} \quad \psi_{13} \equiv z_1(t_{10}) - h_2 \leq 0. \quad \text{This constrains the location of the barrel assembly at } t_{10}.$$

$$\underline{f.} \quad \psi_{14} \equiv |z_1(t_5)| - h_3 \leq 0 \quad .$$

B. General Formulation.

From Section A, one can see that the general mechanical design problem of intermittent motion can be restated as follows [3,4]: Determine the design parameter vector $b \in R^m$, the state variable vector $z(t) \in R^n$, and the special times t_1, t_2, \dots, t_n to minimize the cost functional

$$J = g_0(b, \tilde{t}, \tilde{z}) + \int_0^{t_n} f_0[t, z(t), b] dt \quad , \quad (1)$$

where $\tilde{t} = (t_1, t_2, \dots, t_n)^T$ and $\tilde{z} = (z(t_1), z(t_2), \dots, z(t_n))^T$, subject to the following conditions:

1. State equations

$$\frac{dz_i}{dt} = f_i(t, z, b) \quad , \quad i = 1, 2, \dots, n \quad , \quad 0 < t < t_n \quad , \quad t \neq t_j \quad , \quad (2)$$

2. Initial conditions

$$z(0) - \mu(b) = 0 \quad . \quad (3)$$

3. Equations defining the special times

$$\Omega_i(z(t_{\ell_i}), b) = z_{\ell_i}(t_{\ell_i}) - \omega_i(b) = 0 \quad , \quad i = 1, 2, \dots, n \quad , \quad (4)$$

where $1 \leq \ell_i \leq n$.

4. Functional constraints

$$\psi_{\alpha} \begin{cases} = 0 & , \quad \alpha = 1, \dots, r' \\ \leq 0 & , \quad \alpha = r' + 1, \dots, r \end{cases} \quad (5)$$

where

$$\psi_{\alpha} = g_{\alpha}(b, t, z) + \int_0^{t_{\eta}} L_{\alpha}[t, z(t), b] dt \quad (6)$$

5. Pointwise constraints

$$\phi_{\beta}(t, u) \begin{cases} = 0 & , \quad 0 \leq t \leq t_{\eta} & , \quad \beta = 1, \dots, q' \\ \leq 0 & , \quad 0 \leq t \leq t_{\eta} & , \quad \beta = q' + 1, \dots, q \end{cases} \quad (7)$$

If there is a constraint of the form $H(t, z, b) \leq 0$, $0 \leq t \leq t_{\eta}$, it can be transformed to the functional form of Eq. (5); i.e.,

$$\int_0^{t_{\eta}} \{H[t, z, b] + |H[t, z, b]|\} dt = 0 \quad (8)$$

IV. Sensitivity Analysis

In order to solve the design problem, it is necessary to determine how changes in the design parameters effect the cost functional J , the constraint functionals ψ_{α} , and the constraint functions ϕ_{β} . Here, an initial sensitivity analysis is made, and the result is then applied to both firing from run-out and firing from in-battery.

From Eqs. (1) and (6), it can be seen that J and ψ_α have the same form. Hence, results obtained for the functional J can be immediately applied to ψ_α .

The change in J that is associated with first-order changes in the variables b , t_j , and $z(t)$ is given by

$$\begin{aligned} \delta J = & \frac{\partial g_0}{\partial b} \delta b + \sum_{i=0}^{\eta} \frac{\partial g_0}{\partial z(t_i)} \Delta z(t_i) + \sum_{i=1}^{\eta} \frac{\partial g_0}{\partial t_i} \delta t_i \\ & + \sum_{i=1}^{\eta-1} [f_0(t_i - 0) - f_0(t_i + 0)] \delta t_i + f_0(t_\eta - 0) \delta t_\eta \\ & + \int_0^{t_\eta} \left(\frac{\partial f_0}{\partial z} \delta z + \frac{\partial f_0}{\partial b} \delta b \right) dt, \end{aligned} \quad (9)$$

where $\Delta z(t_j)$ is the total change in z at point t_j , and $\frac{\partial f_0}{\partial z} = \left[\frac{\partial f_0}{\partial z_1}, \dots, \frac{\partial f_0}{\partial z_n} \right]$, etc. If $z(t)$ is continuous, then it follows that at the times t_i ,

$$\Delta z(t_i - 0) = \delta z(t_i - 0) + f(t_i - 0) \delta t_i = \delta z(t_i + 0) + f(t_i + 0) \delta t_i = \Delta z(t_i + 0), \quad (10)$$

where $\delta z(t)$ and δt_i are independent first-order changes in $z(t)$ and t_i .

If $z(t)$ is discontinuous at t_i , with jump $S(b)$, then

$$\Delta z(t_i - 0) + \frac{\partial S}{\partial b} \delta b = \Delta z(t_i + 0). \quad (11)$$

Taking the first variation of the state Eq. (2) gives the following relationship among the independent changes $\delta z(t)$ and δb :

$$\frac{d}{dt} \delta z = \frac{\partial f}{\partial z} \delta z + \frac{\partial f}{\partial b} \delta b, \quad 0 < t < t_\eta, \quad t \neq t_i. \quad (12)$$

The initial conditions of Eq. (3) require that

$$\Delta z(0) - \frac{\partial \mu}{\partial b} \delta b = 0 \quad . \quad (13)$$

Further, Eq. (4) requires that

$$\Delta z_{\lambda_i}(t_i) - \frac{\partial \omega_i}{\partial b} \delta b = 0 \quad . \quad (14)$$

It is desirable to express δJ solely in terms of δb . To reach this goal, the adjoint equation

$$\frac{d\lambda}{dt} = - \frac{\partial f^T}{\partial z} \lambda - \frac{\partial f_o^T}{\partial z} \quad (15)$$

is introduced, where $\lambda(t) \in R^n$ is an adjoint vector variable corresponding to the functional J . Integrating the equation

$$\frac{d}{dt} (\lambda^T \delta z) = \left(\frac{d\lambda^T}{dt} \right) \delta z + \lambda^T \frac{d(\delta z)}{dt} \quad , \quad (16)$$

from t_i to t_{i+1} , with $0 \leq i \leq \eta - 1$, and using Eqs. (12) and (15), one obtains

$$\begin{aligned} & \lambda^T(t_{i+1} - 0) \delta z(t_{i+1} - 0) - \lambda^T(t_i + 0) \delta z(t_i + 0) \\ &= \int_{t_i}^{t_{i+1}} \left(- \frac{\partial f_o}{\partial z} \delta z + \lambda^T \frac{\partial f}{\partial b} \delta b \right) dt \quad . \end{aligned} \quad (17)$$

Summing terms from Eq. (17) over $i = 0, 1, 2, \dots, \eta - 1$ yields

$$\int_0^{t_n} \frac{\partial f_o}{\partial z} \delta z \, dt + \left\{ -\lambda^T(0+) \delta z(0+) + \sum_{i=1}^{n-1} [\lambda^T(t_i - 0) \delta z(t_i - 0) - \lambda^T(t_i + 0) \delta z(t_i + 0)] + \lambda^T(t_n - 0) \delta z(t_n - 0) \right\} = \int_0^{t_n} \left(\lambda^T \frac{\partial f}{\partial b} \delta b \right) dt \quad (18)$$

Here, only the case in which $z(t)$ is continuous in $(0, t_n)$ is treated. The case in which $z(t)$ is discontinuous at some points t_i can be treated in a similar way using Eq. (11). This is done in the example.

Substituting Eq. (10) into Eq. (18) gives

$$\begin{aligned} \int_0^{t_n} \frac{\partial f_o}{\partial z} \delta z \, dt &= \lambda^T(0+) \Delta z(t_o) + \sum_{i=1}^{n-1} \left\{ -[\lambda^T(t_i - 0) - \lambda^T(t_i + 0)] \Delta z(t_i) \right. \\ &\quad \left. + [\lambda^T(t_i - 0) f(t_i - 0) - \lambda^T(t_i + 0) f(t_i + 0)] \delta t_i \right\} - \lambda^T(t_n - 0) \Delta z(t_n - 0) \\ &\quad + \lambda^T(t_n - 0) f(t_n - 0) \delta t_n + \int_0^{t_n} \left(\lambda^T \frac{\partial f}{\partial b} \delta b \right) dt \quad (19) \end{aligned}$$

Substituting Eq. (19) into Eq. (9) leads to the following expression.

$$\begin{aligned} \delta J &= \frac{\partial g_o}{\partial b} \delta b + \left[\frac{\partial g_o}{\partial z(0)} + \lambda^T(0+) \right] \Delta z(0) + \sum_{i=1}^{n-1} \left[\frac{\partial g_o}{\partial z(t_i)} - \lambda^T(t_i - 0) + \lambda^T(t_i + 0) \right] \Delta z(t_i) \\ &\quad + \left[\frac{\partial g_o}{\partial z(t_n)} - \lambda^T(t_n - 0) \right] \Delta z(t_n) + \sum_{i=1}^{n-1} \left[\frac{\partial g_o}{\partial t_i} + f_o(t_i - 0) - f_o(t_i + 0) \right. \\ &\quad \left. + \lambda^T(t_i - 0) f(t_i - 0) - \lambda^T(t_i + 0) f(t_i + 0) \right] \delta t_i + \left[\frac{\partial g_o}{\partial t_n} + f_o(t_n - 0) \right. \\ &\quad \left. + \lambda^T(t_n - 0) f(t_n - 0) \right] \delta t_n + \int_0^{t_n} \left[\left(\frac{\partial f_o}{\partial b} + \lambda^T \frac{\partial f}{\partial b} \right) \delta b \right] dt \quad (20) \end{aligned}$$

Substituting Eqs. (13) and (14) into Eq. (20), one obtains

$$\begin{aligned}
\delta J = & \left\{ \frac{\partial g_o}{\partial b} + \left[\frac{\partial g_o}{\partial z(0)} + \lambda^T(0+) \right] \frac{\partial \mu}{\partial b} + \sum_{i=1}^{n-1} \left[\frac{\partial g_o}{\partial z_{\ell_i}(t_i)} - \lambda_{\ell_i}(t_i - 0) + \lambda_{\ell_i}(t_i + 0) \right] \frac{\partial \omega_i}{\partial b} \right. \\
& + \left. \left[\frac{\partial g_o}{\partial z_{\ell_n}(t_n)} - \lambda_{\ell_n}(t_n - 0) \right] \frac{\partial \omega_n}{\partial b} \right\} \delta b + \sum_{i=1}^{n-1} \sum_{\substack{\ell=1 \\ \ell \neq \ell_i}}^n \left[\frac{\partial g_o}{\partial z_{\ell}(t_i)} - \lambda_{\ell}(t_i - 0) \right. \\
& + \left. \lambda_{\ell}(t_i + 0) \right] \Delta z_{\ell}(t_i) + \sum_{\substack{\ell=1 \\ \ell \neq \ell_n}}^n \left[\frac{\partial g_o}{\partial z_{\ell}(t_n)} - \lambda_{\ell}(t_n - 0) \right] \Delta z_{\ell}(t_n) \\
& + \sum_{i=1}^{n-1} \left[\frac{\partial g_o}{\partial t_i} + f_o(t_i - 0) - f_o(t_i + 0) + \lambda^T(t_i - 0)f(t_i - 0) - \lambda^T(t_i + 0)f(t_i + 0) \right] \delta t_i \\
& + \left[\frac{\partial g_o}{\partial t_n} + f_o(t_n - 0) + \lambda^T(t_n - 0)f(t_n - 0) \right] \delta t_n \\
& + \int_0^{t_n} \left[\left(\frac{\partial f_o}{\partial b} + \lambda^T \frac{\partial f}{\partial b} \right) \delta b \right] dt. \quad (21)
\end{aligned}$$

Thus far, the initial and intermediate conditions for the adjoint variables have not been specified. It is desirable to specify these conditions in such a way that Eq. (21) is independent of $\Delta z(t_i)$ and δt_i ; i.e.,

$$\begin{aligned}
& \sum_{i=1}^{n-1} \sum_{\substack{\ell=1 \\ \ell \neq \ell_i}}^n \left[\frac{\partial g_o}{\partial z_{\ell}(t_i)} - \lambda_{\ell}(t_i - 0) + \lambda_{\ell}(t_i + 0) \right] \Delta z_{\ell}(t_i) \\
& + \sum_{\substack{\ell=1 \\ \ell \neq \ell_n}}^n \left[\frac{\partial g_o}{\partial z_{\ell}(t_n)} - \lambda_{\ell}(t_n - 0) \right] \Delta z_{\ell}(t_n)
\end{aligned}$$

$$\begin{aligned}
& + \sum_{i=1}^{n-1} \left[\frac{\partial g_o}{\partial t_i} + f_o(t_i - 0) - f_o(t_i + 0) + \lambda^T(t_i - 0)f(t_i - 0) - \lambda^T(t_i + 0)f(t_i + 0) \right] \delta t_i \\
& + \left[\frac{\partial g_o}{\partial t_n} + f_o(t_n - 0) + \lambda^T(t_n - 0)f(t_n - 0) \right] \delta t_n = 0 .
\end{aligned} \tag{22}$$

Since all $\Delta z(t_i)$ and δt_i in Eq. (22) are independent, it is necessary that

$$\frac{\partial g_o}{\partial z_\ell(t_n)} - \lambda_\ell(t_n - 0) = 0 , \quad \ell = 1, 2, \dots, n , \quad \ell \neq \ell_n \tag{23}$$

and

$$\frac{\partial g_o}{\partial t_n} + f_o(t_n - 0) + \lambda^T(t_n - 0)f(t_n - 0) = 0 \tag{24}$$

For each $i = n - 1, n - 2, \dots, 2, 1,$

$$\frac{\partial g_o}{\partial z_\ell(t_i)} - \lambda_\ell(t_i - 0) + \lambda_\ell(t_i + 0) = 0 , \quad \ell = 1, 2, \dots, n , \quad \ell \neq \ell_i \tag{25}$$

and

$$\frac{\partial g_o}{\partial t_i} + f_o(t_i - 0) - f_o(t_i + 0) + \lambda^T(t_i - 0)f(t_i - 0) - \lambda^T(t_i + 0)f(t_i + 0) = 0 . \tag{26}$$

Equations (23) through (26) are used to solve for the adjoint variable $\lambda(t)$.

As a result of Eq. (22), Eq. (21) becomes

$$\begin{aligned}
\delta J = & \left\{ \frac{\partial g_o}{\partial b} + \left[\frac{\partial g_o}{\partial z(0)} + \lambda^T(0+) \right] \frac{\partial \mu}{\partial b} \right. \\
& \left. + \sum_{i=1}^{n-1} \left[\frac{\partial g_o}{\partial z_{\ell_i}(t_i)} - \lambda_{\ell_i}(t_i - 0) + \lambda_{\ell_i}(t_i + 0) \right] \frac{\partial \omega_i}{\partial b} \right.
\end{aligned}$$

$$+ \left[\frac{\partial g_o}{\partial z_{\ell_\eta}(t_\eta)} - \lambda_{\ell_\eta}(t_\eta - 0) \right] \frac{\partial \omega_\eta}{\partial b} + \int_0^{t_\eta} \left(\frac{\partial f_o}{\partial b} + \lambda^T \frac{\partial f}{\partial b} \right) dt \left\} \delta b. \quad (27)$$

As noted in the foregoing, Eq. (27) can be applied to both J and ψ_α . For convenience, define

$$\begin{aligned} \ell^{JT} &= \frac{\partial g_o}{\partial b} + \left[\frac{\partial g_o}{\partial z(0)} + \lambda^{JT}(0+) \right] \frac{\partial \mu}{\partial b} \\ &+ \sum_{i=1}^{n-1} \left[\frac{\partial g_o}{\partial z_{\ell_i}(t_i)} - \lambda_{\ell_i}^J(t_i - 0) + \lambda_{\ell_i}^J(t_i + 0) \right] \frac{\partial \omega_i}{\partial b} \\ &+ \left[\frac{\partial g_o}{\partial z_\eta(t_\eta)} - \lambda_{\ell_\eta}^J(t_\eta - 0) \right] \frac{\partial \omega_\eta}{\partial b} + \int_0^{t_\eta} \left(\frac{\partial f_o}{\partial b} + \lambda^{JT} \frac{\partial f}{\partial b} \right) dt; \end{aligned} \quad (28)$$

and

$$\begin{aligned} \psi_\alpha^T &= \frac{\partial g_\alpha}{\partial b} + \left[\frac{\partial g_\alpha}{\partial z(0)} + \lambda^{\psi_\alpha T}(0+) \right] \frac{\partial \mu}{\partial b} \\ &+ \sum_{i=1}^{n-1} \left[\frac{\partial g_\alpha}{\partial z_{\ell_i}(t_i)} - \lambda_{\ell_i}^{\psi_\alpha}(t_i - 0) + \lambda_{\ell_i}^{\psi_\alpha}(t_i + 0) \right] \frac{\partial \omega_i}{\partial b} \\ &+ \left[\frac{\partial g_\alpha}{\partial z_{\ell_\eta}(t_\eta)} - \lambda_{\ell_\eta}^{\psi_\alpha}(t_\eta - 0) \right] \frac{\partial \omega_\eta}{\partial b} + \int_0^{t_\eta} \left(\frac{\partial L_\alpha}{\partial b} + \lambda^{\psi_\alpha T} \frac{\partial f}{\partial b} \right) dt; \end{aligned} \quad (29)$$

Here, ℓ^J and ℓ^{ψ_α} are the sensitivity coefficients of J and ψ_α with respect to the design parameter b .

With this notation,

$$\delta J = \ell^{JT} \delta b \quad (30)$$

and

$$\delta\psi_\alpha = \ell_\alpha^{\psi^T} \delta b. \quad (31)$$

Thus, δJ and $\delta\psi_\alpha$ are now expressed solely in terms of δb , as was desired.

One can now proceed to find the sensitivity coefficients for the cost functional J and the functional constraints ψ_{12} , ψ_{13} , and ψ_{14} defined in Sections III A(1) and (2). Only the sensitivity coefficients for the cost functionals of both modes will be given here. Those for the functional constraints are given in Appendix B.

A. Firing from run-out.

Let λ_1 and λ_2 be the adjoint variables of the state variables z_1 and z_2 with respect to the cost functional $J \equiv t_8 - t_{10}$. Equation (27) becomes

$$\begin{aligned} \delta J = & [-\lambda_1(t_4^-) + \lambda_1(t_4^+)]\delta b_1 + [-\lambda_1(t_3^-) + \lambda_1(t_3^+) - \lambda_1(t_5^-) + \lambda_1(t_5^+)]\delta b_7 \\ & + \lambda_2(0^+)\delta b_8 + \lambda_2(t_4^+)\delta \left(\frac{b_9}{b_2 + b_3} \right) + \int_0^{t_{10}} \lambda^T \frac{\partial f}{\partial b} \delta b \equiv \ell^{JT} \delta b. \end{aligned}$$

Here, $\ell^J = (\ell_1^J, \ell_2^J, \dots, \ell_{11}^J)^T$ is the desired sensitivity coefficient vector of the design parameters, with

$$\begin{aligned} \ell_1^J &= -\lambda_1(t_4^-) + \lambda_1(t_4^+) \int_0^{t_{10}} \lambda^T \frac{\partial f}{\partial b_1} dt, \\ \ell_2^J &= -\lambda_2(t_4^+) \frac{b_9}{(b_2 + b_3)^2} + \int_0^{t_{10}} \lambda^T \frac{\partial f}{\partial b_2} dt, \\ \ell_3^J &= -\lambda_2(t_4^+) \frac{b_9}{(b_2 + b_3)^2} + \int_0^{t_{10}} \lambda^T \frac{\partial f}{\partial b_3} dt, \end{aligned}$$

$$x_7^J = -\lambda_1(t_3^-) + \lambda_1(t_3^+) - \lambda_1(t_5^-) + \lambda_1(t_5^+) + \int_0^{t_{10}} \lambda^T \frac{\partial f}{\partial b_7} dt ,$$

$$x_8^J = \lambda_2(0^+) + \int_0^{t_{10}} \lambda^T \frac{\partial f}{\partial b_8} dt ,$$

$$x_9^J = \frac{\lambda_2(t_4^+)}{b_2 + b_3} + \int_0^{t_{10}} \lambda^T \frac{\partial f}{\partial b_9} dt ,$$

$$x_i^J = \int_0^{t_{10}} \lambda^T \frac{\partial f}{\partial b_i} dt , \quad i = 4, 5, 6, 10, 11 .$$

The end conditions and jump conditions for the adjoint variables are (Eqs. (23)-(26)):

$$\lambda_2(t_{10}^-) = 0 .$$

$$-\lambda_2(t_j^-) + \lambda_2(t_j^+) = 0 , \quad j = 8, 7, 6, 5, 4, 3, 2, 1 ,$$

$$-\lambda_1(t_9^-) + \lambda_1(t_9^+) = 0 ,$$

$$\sum_{i=1}^2 [\lambda_i(t_j^-) f_i(t_j^-) - \lambda_i(t_j^+) f_i(t_j^+)] = 0 , \quad j = 9, 7, 6, 5, 4, 3, 2, 1 ,$$

$$1 + \sum_{i=1}^2 [\lambda_i(t_8^-) f_i(t_8^-) - \lambda_i(t_8^+) f_i(t_8^+)] = 0 ,$$

$$-1 + \sum_{i=1}^2 [\lambda_i(t_{10}^-) f_i(t_{10}^-)] = 0 ,$$

With these conditions, one can solve the adjoint equation backward in the time variable t , where this equation is

$$\frac{d\lambda}{dt} = - \frac{\partial f^T}{\partial z} \lambda, \quad t \in (0, t_{10}) .$$

The procedure used to solve for the adjoint variables can be found in Section 2.5 of [5].

B. Firing from in-battery position.

Proceeding in a similar manner, one obtains

$$\begin{aligned} \delta J = & \lambda_1(0+) \delta b_1 + [-\lambda_1(t_1-) + \lambda_1(t_1+) - \lambda_1(t_9-) + \lambda_1(t_9+)] \delta b_7 \\ & + \lambda_2(0+) \delta \left(\frac{b_9}{b_2 + b_3} \right) + \int_0^{t_{10}} \lambda^T \frac{\partial f}{\partial b} \delta b \, dt, \end{aligned}$$

where again, $\delta J = \lambda^J \delta b$. The end conditions and the jump conditions for the adjoint variables are:

$$-\lambda_1(t_{10}) = 0, \quad$$

$$-\lambda_1(t_5-) + \lambda_1(t_5+) = 0, \quad$$

$$\lambda_2(t_j-) + \lambda_2(t_j+) = 0, \quad j = 9, 8, 7, 6, 4, 3, 2, 1, \quad$$

$$\sum_{i=1}^2 [\lambda_i(t_j-) f_i(t_j-) - \lambda_i(t_j+) f_i(t_j+)] = 0, \quad j = 9, 8, 7, 5, 3, 2, 1, \quad$$

$$\sum_{i=1}^2 [\lambda_i(t_{10}-) f_i(t_{10}-)] = 0, \quad$$

$$1 + \sum_{i=1}^2 [\lambda_i(t_4^-) f_i(t_4^-) - \lambda_i(t_4^+) f_i(t_4^+)] = 0 ,$$

$$-1 + \sum_{i=1}^2 [\lambda_i(t_6^-) f_i(t_6^-) - \lambda_i(t_6^+) f_i(t_6^+)] = 0 .$$

V. Numerical Results and Discussion

With the sensitivity coefficients developed in Section IV and Appendix B, one can apply the algorithm given in Section 3.4 of [5] or Section 8.2 of [4] to obtain the solution to the optimal design problem. The numerical results presented here utilize inches as length units, seconds for time and slugs/12 for mass. The following input data were used.

a. Physical dimensions of the system:

S	S ₁	S ₂	S ₃	S ₄	S ₅
2.5357	6.0	16.0	1.6198	11.668	3.125

b. Approximate cam path shape functions:

$$\begin{aligned} \text{R-cam: } y_R(\eta) = & 1.7038 - 0.7988\eta^2 + 0.3355\eta^3 \\ & - 0.0769\eta^4 + 0.0071\eta^5 \end{aligned}$$

$$\begin{aligned} \text{B-Cam: } y_B(\xi) = & 2.5357 - 5.6869\xi + 0.90071\xi^2 \\ & - 8.8329\xi^3 + 4.3107\xi^4 - 0.8154\xi^5 \end{aligned}$$

c. Values of h_i in the functional constraints:

	h_1	h_2	h_3
Run-Out Case	0.65 sec	0.61 sec	3.0 inches
On-Battery Case	0.65 sec	28.0 inches	3.0 inches

d. Friction coefficient:

$$\mu = 0.17$$

The optimal solution for the run-out case is 0.19 seconds (compared with an experimental result of 0.13 sec) as shown in Fig. 9. The program converges within six iterations, and the history of $||\delta b^1||$ is shown in Fig. 10. The optimal design and the sensitivity coefficients at the optimum point are given in Table I. This table shows that the design parameters b_1 (firing distance), b_2 (mass of barrel), b_3 (mass of sleeve), b_4 (mass of sear), b_7 (distance between sear position and front buffer) and b_8 (initial velocity) have more effect on the feeding time than the other design parameters. The solution of the equations of motion is shown in Figs. 7 and 8.

The optimal solution for the on-battery case is 0.29 seconds (compared to an experimental result of 0.12 sec) as shown in Fig. 13. The optimal design and the sensitivity coefficients are given in Table II. Again, the design parameters b_1 , b_2 , b_3 , b_4 and b_7 have more effect on the objective functional than the other design parameters. The corresponding dynamical solution is shown in Figs. 11 and 12.

The dynamic equations and the adjoint equations are solved by the fourth-order Runge-Kutta method. The solutions of the equations of motion are compatible with experimental results.

The results which follow show that the optimal design in both cases satisfies the basic requirements. The number in parentheses is required value.

A. Run-out case.

1. firing point 20.75 inches in front of sear position
(20.5 inches),

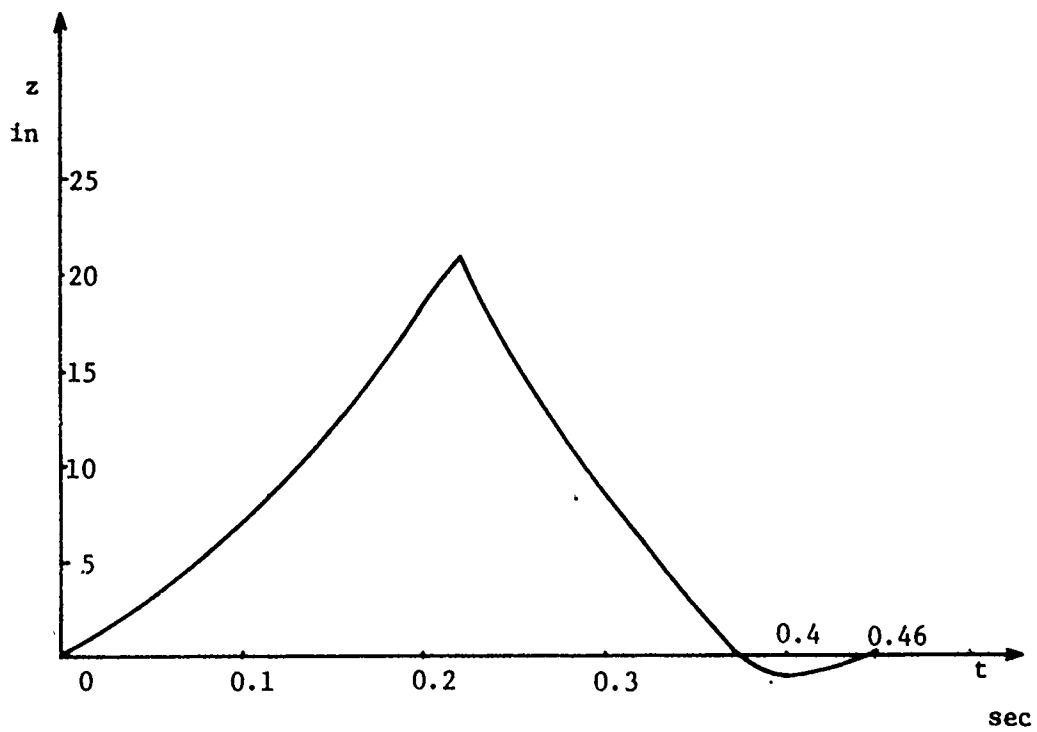


Figure 7. Displacement Curve of the Barrel for the Run-Out Case at the Optimal Point

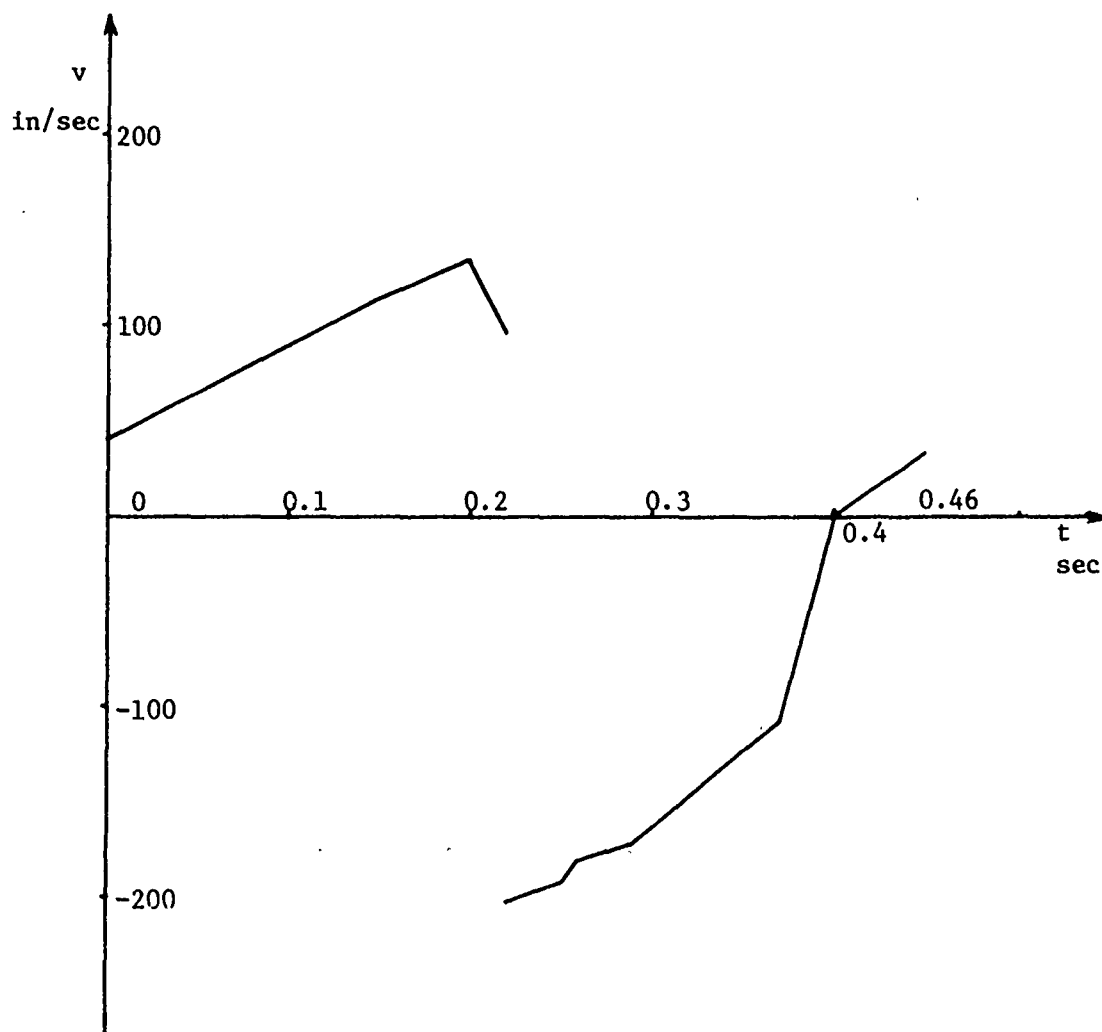


Figure 8. Velocity Curve of the Barrel for the Run-Out Case at the Optimal Point

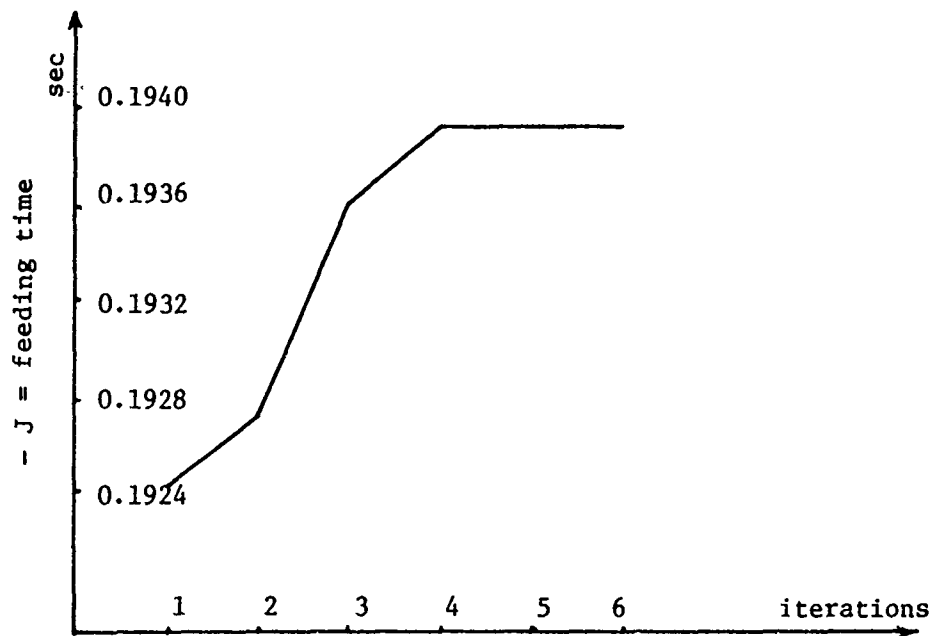


Figure 9. History of the Cost Functional for the Run-Out Case

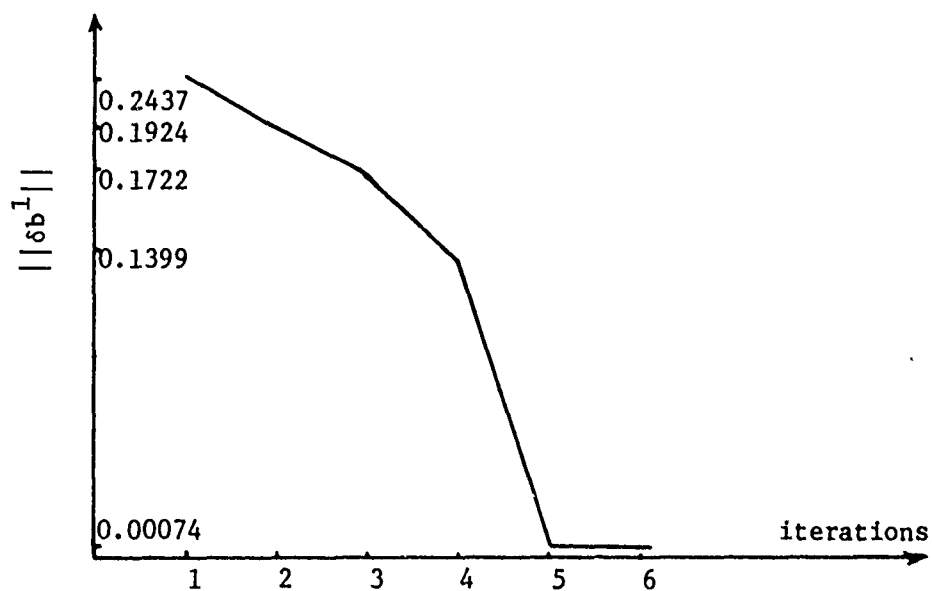


Figure 10. History of $||\delta b^1||$ for the Run-Out Case

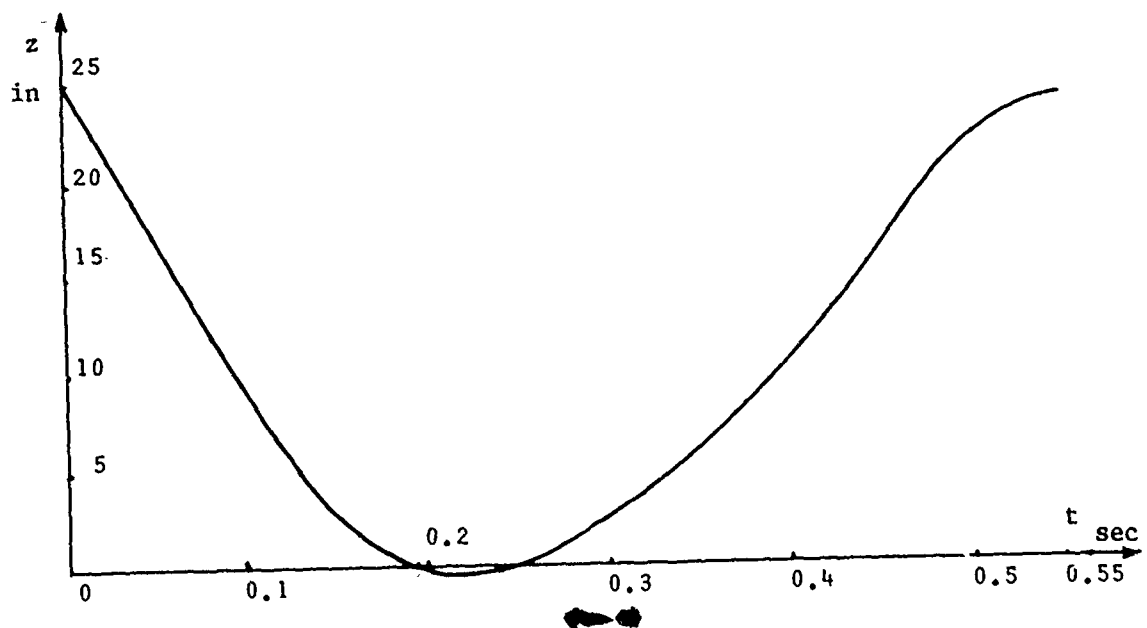


Figure 11. Displacement Curve of the Barrel for the On-Battery Case at the Optimal Point

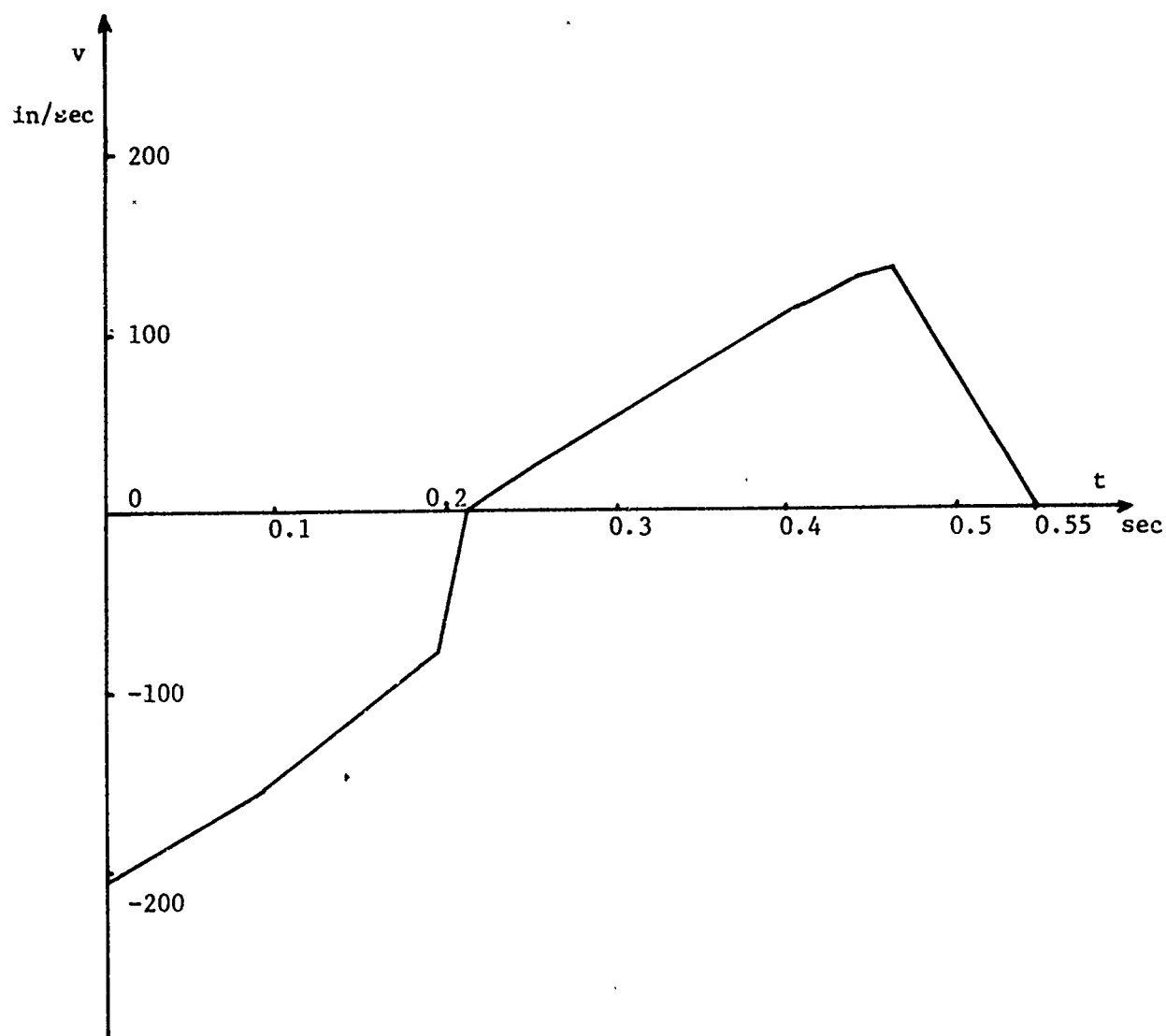


Figure 12. Velocity Curve of the Barrel for the On-Battery Case at the Optimal Point

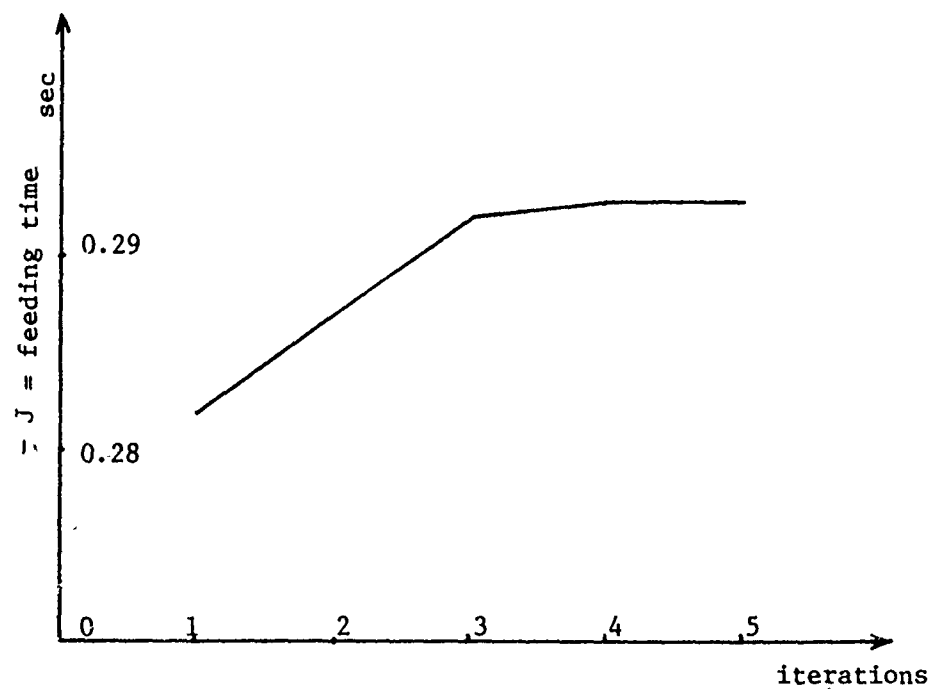


Figure 13. History of the Cost Functional for the On-Battery Case

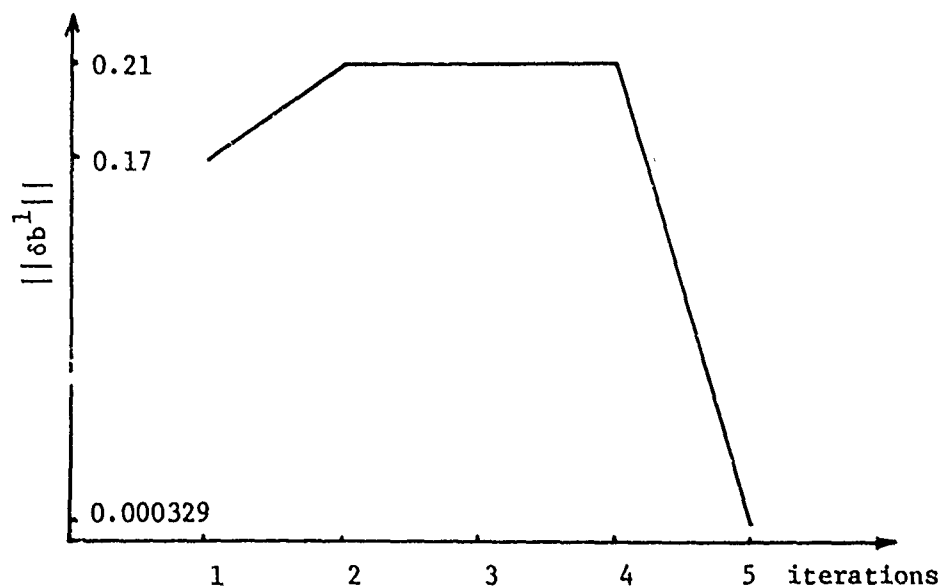


Figure 14. History of $||\delta b^1||$ for the On-Battery Case

2. firing to sleeve unlock time of 38.5 milliseconds
(30 ms minimum),
3. recoil velocity at sear position of 9.17 fps
(4 to 10 fps).

B. On-battery case.

1. firing point 25.19 inches in front of sear position
(25 inches),
2. firing to sleeve unlock time of 62 milliseconds
(30 ms minimum),
3. recoil velocity at sear position of 6.33 fps
(4 to 10 fps).

The optimally designed front and rear buffers produce constant forces of 6900 lb and 12,100 lb, respectively. The optimal fore and aft driving forces b_{10} and b_{11} for the run-out case are 1600 lb and 2000 lb, respectively. For the on-battery case, these forces are 1970 lb and 2175 lb, respectively. These values are satisfactory because their ratio is between 1 and 2 as desired.

The foregoing solutions are obtained for the case when the elevation angle $\alpha = 0^\circ$. For any other angle α in the range -10° to 40° , one can obtain the corresponding driving forces simply by adding or subtracting the component of the gravity force that is parallel to the barrel axis.

VI. Appendix A: Equations of Motion

A. Firing from run-out.

$$\underline{0 < t < t_1}$$

$$b_2 \ddot{z}_1 = b_{10} - b_2 g(\mu + 1) \sin \alpha ,$$

where μ is the friction coefficient.

$$\underline{t_1 < t < t_2}$$

$$b_2 \ddot{z}_1 = b_{10} - b_2 g(\mu + 1) \sin \alpha + \frac{\alpha_\beta}{\alpha_R - \alpha_B} \left\{ M_P (\alpha_R \ddot{y}_P + \ddot{z}_P) - \frac{(\alpha_R \sin \theta + \cos \theta)}{\cos \theta} [b_3 \ddot{z}_S + b_3 g(\mu + 1) \sin \alpha] \right\} .$$

This equation of motion (for the cam reaction interval) is derived in [5].

$$\underline{t_2 < t < t_3}$$

$$(b_2 + b_3) \ddot{z}_1 = b_{10} - (b_2 + b_3) g(\mu + 1) \sin \alpha$$

$$\underline{t_3 < t < t_4}$$

$$(b_2 + b_3) \ddot{z}_1 = b_{10} - (b_2 + b_3) g(\mu + 1) \sin \alpha - b_6$$

$$\underline{t_4 + \Delta t < t < t_5}$$

$$(b_2 + b_3) \ddot{z}_1 = b_{11} - (b_2 + b_3) g(1 - \mu) \sin \alpha$$

$$\underline{t_5 < t < t_6}$$

$$(b_2 + b_3)\ddot{z}_1 = b_{11} - (b_2 + b_3)g(1 - \mu) \sin \alpha$$

$$\underline{t_6 < t < t_7}$$

$$b_2\ddot{z}_1 = b_{11} - b_2g(1 - \mu) \sin \alpha - \frac{\alpha_\beta}{\alpha_\beta - \alpha_R} \left\{ M_p (\alpha_R \ddot{y}_p + \ddot{z}_p) \right. \\ \left. - \frac{(-\alpha_R \sin \theta + \cos \theta)}{\cos \theta} [-b_3\ddot{z}_S - b_3g(1 - \mu)g \sin \alpha] \right\}$$

$$\underline{t_7 < t < t_8}$$

$$b_2\ddot{z}_1 = b_{11} - b_2g(1 - \mu) \sin \alpha$$

$$\underline{t_8 < t < t_9}$$

$$(b_2 + b_4)\ddot{z}_1 = b_{11} - (b_2 + b_4)g(1 - \mu) \sin \alpha + b_6$$

$$\underline{t_9 < t < t_{10}}$$

$$(b_2 + b_4)\ddot{z}_1 = b_{10} - (b_2 + b_4)g(1 + \mu) \sin \alpha$$

B. Firing from in-battery position.

$$\underline{\Delta t < t < t_1}$$

$$(b_2 + b_3)\ddot{z}_1 = b_{11} - (b_2 + b_3)g(1 - \mu) \sin \alpha$$

$$\underline{t_1 < t < t_2}$$

$$(b_2 + b_3)\ddot{z}_1 = b_{11} - (b_2 + b_3)g(1 - \mu) \sin\alpha$$

$$\underline{t_2 < t < t_3}$$

$$b_2\ddot{z}_1 = b_{11} - b_2g(1 - \mu) \sin\theta - \frac{\alpha_\beta}{\alpha_\beta - \alpha_R} \left\{ M_p(\alpha_R\ddot{y}_p + \ddot{z}_p) \right. \\ \left. - \frac{(-\alpha_R \sin\theta + \cos\theta)}{\cos\theta} [-b_3\ddot{z}_s - b_3g(1 - \mu) \sin\alpha] \right\}$$

$$\underline{t_3 < t < t_4}$$

$$b_2\ddot{z}_1 = b_{11} - b_2g(1 - \mu) \sin\alpha$$

$$\underline{t_4 < t < t_5}$$

$$(b_2 + b_4)\ddot{z}_1 = b_{11} - (b_2 + b_4)g(1 - \mu) \sin\alpha + b_6$$

$$\underline{t_5 < t < t_6}$$

$$(b_2 + b_4)\ddot{z}_1 = b_{10} - (b_2 + b_4)g(1 + \mu) \sin\alpha$$

$$\underline{t_6 < t < t_7}$$

$$b_2\ddot{z}_1 = b_{10} - b_2g(1 + \mu) \sin\alpha$$

$$\underline{t_7 < t < t_8}$$

$$b_2 \ddot{z}_1 = b_{10} - b_2 g(1 + \mu) \sin \alpha + \frac{\alpha_\beta}{\alpha_R - \alpha_\beta} \left\{ M_p (\alpha_R \ddot{y}_p + \ddot{z}_p) \right. \\ \left. - \frac{(\alpha_R \sin \theta + \cos \theta)}{\cos \theta} [b_3 \ddot{z}_s + b_3 g(1 + \mu) \sin \alpha] \right\}$$

$$\underline{t_8 < t < t_9}$$

$$(b_2 + b_3) \ddot{z}_1 = b_{10} - (b_2 + b_3) g \sin \alpha$$

$$\underline{t_9 < t < t_{10}}$$

$$(b_2 + b_3) \ddot{z}_1 = b_{10} - (b_2 + b_3) g \sin \alpha - b_5$$

VII. Appendix B: Sensitivity Coefficients of the Functional Constraints

A. Firing from run-out.

$$1. \quad \psi_{12} = t_{10} - h_1 \leq 0$$

$$\delta \psi_{12} = [-\lambda_1(t_4 -) + \lambda_1(t_4 +)] \delta b_1 + [-\lambda_1(t_3 -) + \lambda_1(t_3 +) \\ - \lambda_1(t_5 -) + \lambda_1(t_5 +)] \delta b_7 + \lambda_2(0+) \delta b_8 \\ + \lambda_2(t_4 +) \delta \left(\frac{b_9}{b_2 + b_3} \right) + \int_0^{t_{10}} \lambda^T \frac{\partial f}{\partial b} \delta b \, dt .$$

The end conditions and the jump conditions for λ_1 and λ_2 are

$$- \lambda_2(t_{10}^-) = 0 ,$$

$$- \lambda_1(t_9^-) + \lambda_1(t_9^+) = 0 ,$$

$$- \lambda_2(t_j^-) + \lambda_2(t_j^+) = 0 , \quad j = 8, 7, 6, 5, 4, 3, 2, 1 ,$$

$$1 + \sum_{i=1}^2 [\lambda_i(t_{10}^-) f_i(t_{10}^-)] = 0 ,$$

$$\sum_{i=1}^2 [\lambda_i(t_j^-) f_i(t_j^-) - \lambda_i(t_j^+) f_i(t_j^+)] = 0 ,$$

$$j = 9, 8, \dots, 2, 1 .$$

$$2. \quad \psi_{13} = t_2 - t_6 + h_2 \leq 0$$

$$\delta\psi_{13} = [-\lambda_1(t_4^-) + \lambda_1(t_4^+)]\delta b_1 + [-\lambda_1(t_3^-) + \lambda_1(t_3^+)]$$

$$- \lambda_1(t_5^-) + \lambda_1(t_5^+)]\delta b_7 + \lambda_2(0^+) \delta b_8$$

$$+ \lambda_2(t_4^+) \delta \left(\frac{b_9}{b_2 + b_3} \right) + \int_0^{t_{10}} \lambda^T \frac{\partial f}{\partial b} \delta b \, dt .$$

The end conditions and jump conditions for λ_1 and λ_2 are

$$- \lambda_2(t_{10}^-) = 0 ,$$

$$\sum_{i=1}^2 [\lambda_i(t_{10}^-) f_i(t_{10}^-)] = 0 ,$$

$$-\lambda_1(t_9^-) + \lambda_1(t_9^+) = 0 ,$$

$$-\lambda_2(t_j^-) + \lambda_2(t_j^+) = 0 , \quad j = 8, 7, 6, 5, 4, 3, 2, 1 ,$$

$$\sum_{i=1}^2 [\lambda_i(t_j^-) f_i(t_j^-) - \lambda_i(t_j^+) f_i(t_j^+)] = 0 ,$$

$$j = 9, 8, 7, 5, 4, 3, 1 .$$

$$-1 + \sum_{i=1}^2 [\lambda_i(t_6^-) f_i(t_6^-) - \lambda_i(t_6^+) f_i(t_6^+)] = 0 ,$$

$$1 + \sum_{i=1}^2 [\lambda_i(t_2^-) f_i(t_2^-) - \lambda_i(t_2^+) f_i(t_2^+)] = 0 .$$

$$3. \quad \psi_{14} = |z_1(t_9)| - h_3 \leq 0$$

$$\delta\psi_{14} = [-\lambda_1(t_4^-) + \lambda_1(t_4^+)] \delta b_1 + [-\lambda_1(t_3^-) + \lambda_1(t_3^+)$$

$$- \lambda_1(t_5^-) + \lambda_1(t_5^+)] \delta b_7 + \lambda_2(0^+) \delta b_8$$

$$+ \lambda_2(t_4^+) \delta \left(\frac{b_9}{b_2 + b_3} \right) + \int_0^{t_{10}} \lambda^T \frac{\partial f}{\partial b} \delta b \, dt .$$

The end conditions and jump conditions are

$$-\lambda_2(t_{10}^-) = 0 ,$$

$$\sum_{i=1}^2 [\lambda_i(t_{10}^-) f_i(t_{10}^-)] = 0 ,$$

$$-1 - \lambda_1(t_9^-) + \lambda_1(t_9^+) = 0 ,$$

$$- \lambda_2(t_j^-) + \lambda_2(t_j^+) = 0 , \quad j = 8, 7, 6, 5, 4, 3, 2, 1 ,$$

$$\sum_{i=1}^2 [\lambda_i(t_j^-) f_i(t_j^-) - \lambda_i(t_j^+) f_i(t_j^+)] = 0 ,$$

$$j = 9, 8, 7, 6, 5, 4, 3, 2, 1 .$$

B. Firing from in-battery position.

$$1. \quad \psi_{12} = t_{10} - h_1 \leq 0$$

$$\delta\psi_{12} = \lambda_1(0+) \delta b_1 + [-\lambda_1(t_1^-) + \lambda_1(t_1^+) - \lambda_1(t_9^-)$$

$$+ \lambda_1(t_9^+)] \delta b_7 + \lambda_2(0+) \delta \left(\frac{b_9}{b_2 + b_3} \right)$$

$$+ \int_0^{t_{10}} \lambda^T \frac{\partial f}{\partial b} \delta b \, dt .$$

The end and jump conditions for λ_1 and λ_2 are

$$- \lambda_1(t_{10}^-) = 0 ,$$

$$1 + \sum_{i=1}^2 [\lambda_i(t_{10}^-) f_i(t_{10}^-)] = 0 ,$$

$$- \lambda_1(t_5^-) + \lambda_1(t_5^+) = 0 ,$$

$$- \lambda_2(t_j^-) + \lambda_2(t_j^+) = 0 , \quad j = 9, 8, 7, 6, 4, 3, 2, 1 ,$$

$$\sum_{i=1}^2 [\lambda_i(t_j^-) f_i(t_j^-) - \lambda_i(t_j^+) f_i(t_j^+)] = 0 ,$$

$$j = 9, 8, 7, 6, 5, 4, 3, 2, 1 .$$

$$2. \quad \psi_{13} = z_1(t_{10}) - h_2 \leq 0$$

$$\delta\psi_{13} = \lambda_1(0+) \delta b_1 + [-\lambda_1(t_1^-) + \lambda_1(t_1^+) - \lambda_1(t_9^-)$$

$$+ \lambda_1(t_9^+)] \delta b_7 + \lambda_2(0+) \delta \left(\frac{b_9}{b_2 + b_3} \right)$$

$$+ \int_0^{t_{10}} \lambda^T \frac{\partial f}{\partial b} \delta b \, dt$$

The end and jump conditions for λ_1 and λ_2 are

$$1 - \lambda_1(t_{10}^-) = 0 ,$$

$$\sum_{i=1}^2 [\lambda_i(t_{10}^-) f_i(t_{10}^-)] = 0 ,$$

$$- \lambda_1(t_5^-) + \lambda_1(t_5^+) = 0 ,$$

$$- \lambda_2(t_j^-) + \lambda_2(t_j^+) = 0 , \quad j = 9, 8, 7, 6, 4, 3, 2, 1 ,$$

$$\sum_{i=1}^2 [\lambda_i(t_j^-) f_i(t_j^-) - \lambda_i(t_j^+) f_i(t_j^+)] = 0 ,$$

$$j = 9, 8, 7, 6, 5, 4, 3, 2, 1 .$$

$$3. \quad \psi_{14} = |z_1(t_5)| - h_3 \leq 0$$

$$\delta\psi_{14} = \lambda_1(0+) \delta b_1 + [-\lambda_1(t_1-) + \lambda_1(t_1+) - \lambda_1(t_9-)$$

$$+ \lambda_1(t_9+)] \delta b_7 + \lambda_2(0+) \delta \left(\frac{b_9}{b_2 + b_3} \right)$$

$$+ \int_0^{t_{10}} \lambda^T \frac{\partial f}{\partial b} \delta b \, dt$$

The end and jump conditions for the adjoint variables

λ_1 and λ_2 are

$$- \lambda_1(t_{10}-) = 0 \quad ,$$

$$\sum_{i=1}^2 [\lambda_i(t_{10}-) f_i(t_{10}-)] = 0 \quad ,$$

$$- 1 - \lambda_1(t_5-) + \lambda_1(t_5+) = 0 \quad ,$$

$$- \lambda_2(t_j-) + \lambda_2(t_j+) = 0 \quad , \quad j = 9, 8, 7, 6, 4, 3, 2, 1 \quad ,$$

$$\sum_{i=1}^2 [\lambda_i(t_j-) f_i(t_j-) - \lambda_i(t_j+) f_i(t_j+)] = 0 \quad ,$$

$$j = 9, 8, 7, 6, 5, 4, 3, 2, 1 \quad .$$

VII. References

- [1] J. H. Bickford, Mechanisms for Intermittent Motion, Industrial Press Inc., New York, N.Y., 1972.
- [2] A. E. Bryson, Jr. and Y. C. Ho, Applied Optimal Control, Ginn and Company, Waltham, Mass., 1969.
- [3] W. F. Denham, "Steepest-Ascent Solution of Optimal Programming Problems," Ph.D. Dissertation, Harvard University, 1963.
- [4] E. J. Haug, Jr., Engineering Design Handbook, Computer Aided Design of Mechanical System, AMC Pamphlet No. 706-192, U.S. Army Material Command, Rock Island, Ill., August 1969.
- [5] R. C. Huang, E. J. Haug, Jr. and J. G. Andrews, Optimal Design of Mechanical Systems with Intermittent Motion, Technical Report No. 24, Division of Materials Engineering, University of Iowa, Iowa City, Iowa, 1976.

Table I. Optimal Design, Upper and Lower Bounds, Sensitivity Coefficients, and Weighting Functions of the Design Parameters for the Run-Out Case

	b_1	b_2	b_3	b_4	b_5	b_6
upper bounds	20.75	3.1702	0.2872	0.2044	7000	12300
optimum design	20.75	2.919	0.2368	0.2044	6900	12100
lower bounds	20.25	2.916	0.2356	0.15128	6800	11900
sensitivity coefficients	-0.2675×10^{-1}	0.1355	0.2841	-0.2654×10^{-1}	-0.1586×10^{-4}	0.3991×10^{-5}
weighting functions	0.2596×10	0.1954	0.1790×10^{-1}	0.5111	1.0	1.0

	b_7	b_8	b_9	b_{10}	b_{11}
upper bounds	18.75	60.0	-1900	1700	2100
optimum design	18.26	40.35	-1910	1600	2000
lower bounds	18.25	40.0	-1920	1500	1900
sensitivity coefficients	0.1211×10^{-2}	0.8752×10^{-2}	0.6106×10^{-3}	0.4176×10^{-3}	0.6406×10^{-4}
weighting functions	$0.4511 \times 10^{+2}$	$0.2360 \times 10^{+3}$	1.0	1.0	1.0

Table II. Optimal Design, Upper and Lower Bounds, Sensitivity Coefficients, and Weighting Functions of the Design Parameters for the On-Battery Case

	b_1	b_2	b_3	b_4	b_5	b_6
upper bounds	25.05	3.1702	0.2872	0.2044	7200	14000
optimum design	25.19	3.0919	0.2253	0.2006	6900.0	12100.0
lower bounds	23.0	2.9115	0.2250	0.1528	6600.0	11900.0
sensitivity coefficients	-0.8226×10^{-1}	0.7328×10^{-1}	0.3529	-0.6291×10^{-1}	0.0	0.1294×10^{-4}
weighting functions	$0.6980 \times 10^{+1}$	0.8240×10^{-1}	0.5780×10^{-1}	0.1100	1.0	0.5185×10^7

	b_7	b_8	b_9	b_{10}	b_{11}
upper bounds	18.75	0.0	-1600	2200	2200
optimum design	18.27	0.0	-1910.0	1970.0	2174.7
lower bounds	18.25	0.0	-2200.0	1950.0	1000.0
sensitivity coefficients	0.3405×10^{-2}	0.0	-0.3282×10^{-3}	-0.3274×10^{-4}	-0.4546×10^{-3}
weighting functions	0.5869×10^2	1.0	1.0	1.0	1.0

A FINITE ELEMENT METHOD OF OPTIMIZING
PRECISION OF A VIBRATING WEAPON

J.S. ARORA AND E.J. HAUG

University of Iowa
Iowa City, Iowa

T.T. FENG

Ebasco Service Inc.
New York, New York

TABLE OF CONTENTS

	<u>Page</u>
ABSTRACT	306
I. INTRODUCTION	307
II. STRUCTURAL ANALYSIS	309
III. OPTIMAL DESIGN FORMULATION	312
IV. A COMPUTATIONAL ALGORITHM	315
V. NUMERICAL EXAMPLES	325
VI. DISCUSSIONS AND CONCLUSIONS	333
VII. REFERENCES	334

ABSTRACT

This paper presents a method for optimal design of elastic structures that are subjected to transient dynamic loads. The finite element method, modal analysis, and a generalized steepest descent method are employed in developing a computational algorithm. Structural weight is minimized subject to constraints on displacement, stress, structural frequency, and member size. Optimum results are presented for a cantilever beam model of a gun barrel, subjected to shock input.

I. INTRODUCTION

Design of a weapon for precision is a problem of current interest in modern weapon design. This paper integrates the finite element and generalized steepest descent [1] methods to develop an algorithm for optimal design of structures under dynamic loads. To date, this problem has received very little attention, due to its complexity. Complexity in the problem arises from the fact that stress and displacement constraints for the structure are functions of both the space and the time variables.

Literature in the area of optimal structural design under dynamic loads is quite scarce. Pierson [2] presented a survey of optimal structural design under dynamic constraints in 1972. In this review, dynamic constraints are classified as constraints on structural frequency and on transient dynamic response. A minimum of literature exists on the latter class of problems. Brach [3] considered a class of simply supported beams of constant total mass and minimized the maximum dynamic deflection at the center of the beam. Plaut [4] and Yau [5] also dealt with optimal design of a simply supported beam of given total mass, minimizing an upper bound on its dynamic response. Icerman [6] and Mróz [7] presented optimum designs of structures that were excited by a single harmonic load. Both of these treatments, however, are limited to harmonic excitation and cannot be used to solve the general transient response problem.

Fox and Kapoor [8] used a bounding technique to obtain approximate peak response of planar truss-frames, subjected to shock loads. They employed a feasible direction technique of optimization. Levy [9] presented fully-stressed designs of a rod and beam, subjected to impulsive loads. He

determined maximum stress by setting the derivative of stress with respect to time equal to zero and checking the total energy of the system at these time grid points.

In the present paper, a general method for optimal design of elastic structures under dynamic loads is presented. Constraints are imposed on stress, displacement, natural frequency and design variable magnitudes. The well known modal method of dynamic structural analysis is used to obtain the dynamic response of the structure. A design sensitivity analysis method is developed and the Kuhn-Tucker conditions of nonlinear programming [10] are employed to define an iterative algorithm. The method is then applied for optimal design of a long barrel cannon.

II. STRUCTURAL ANALYSIS

Considering the entire structure as a free body and neglecting damping effects, its dynamic response can be described by the following general matrix equation [11]:

$$\ddot{\tilde{M}}(b)\ddot{\tilde{z}}(t) + \tilde{K}(b)\tilde{z}(t) = \tilde{Q}(t) \quad , \quad (1)$$

with initial conditions

$$\dot{\tilde{z}}(0) = \dot{\tilde{z}}^0 \quad , \quad \tilde{z}(0) = \tilde{z}^0 \quad , \quad (2)$$

where $\tilde{M}(b)$ and $\tilde{K}(b)$ are mass and stiffness matrices of the structure, respectively, $\tilde{Q}(t)$ is the vector forcing function, b is a vector of design parameters, $\tilde{z}(t)$ is a state variable vector of displacements, and t is time. In all subsequent equations, the stiffness and mass matrices are understood to be functions of the design parameter vector b , and the argument b will be omitted. If some of the components of $\tilde{z}(t)$ are known, the solution of the dynamic equations can be obtained by solving a subset of Eq. (1). Furthermore, the reduced initial conditions can be transformed to homogeneous form [12]. After reductions and transformations, the dynamic equations may be written as

$$M_0 \ddot{z}(t) + K_0 z(t) = Q(t) \quad (3)$$

and

$$\dot{z}(0) = 0 \quad , \quad z(0) = 0 \quad , \quad (4)$$

where $z(t)$ is an n -dimensional relative displacement vector corresponding the independent degrees of freedom of the structure and M_0 and K_0 are the

corresponding $n \times n$ mass and stiffness matrices. $Q(t)$ is a subvector of $\bar{Q}(t)$ and is a function of b if the structure undergoes a prescribed boundary motion.

The eigenvalue problem associated with Eq. (3) may be written as

$$M_0 V \Omega - K_0 V = 0 \quad , \quad (5)$$

where V is an $n \times m$ matrix, whose columns are m eigenmodes of the structure and Ω is an $m \times m$ diagonal matrix of the corresponding eigenvalues. The number of eigenmodes necessary to obtain an approximate solution of Eqs. (3) and (4) is frequently less than the dimension of these equations, so $m < n$. To reduce the dimension of the analysis problem, one introduces a transformation

$$z(t) = V \zeta(t) \quad , \quad (6)$$

where $\zeta(t)$ is a generalized coordinate, or reduced state variable, of dimension m . Premultiplying Eqs. (5) and (3) by V^T , one obtains

$$M \Omega - K = 0 \quad (7)$$

and

$$M \ddot{\zeta}(t) + K \zeta(t) = S(t) \quad , \quad (8)$$

with

$$\dot{\zeta}(0) = 0 \quad , \quad \zeta(0) = 0 \quad , \quad (9)$$

where

$$M \equiv V^T M_0 V , \quad (10)$$

$$K \equiv V^T K_0 V , \quad (11)$$

and

$$S(t) \equiv V^T Q(t) \quad (12)$$

are $m \times m$ mass and stiffness matrices and a reduced m -dimensional applied load, respectively. The effect of this substitution is to decouple the equations into m separate equations. Each equation represents a modal response to the factored input, $V^T Q(t)$.

III. OPTIMAL DESIGN PROBLEM FORMULATION

The weight of a truss-frame structure is to be minimized. Thus, the objective function is

$$J(b) = \sum_{i=1}^N \rho_i l_i A_i(b_i) , \quad (13)$$

where ρ_i is the density, l_i is the length, $A_i(b_i)$ is the cross-sectional area of the i -th element and N is the total number of elements.

It is required that displacements and stresses at critical points of the structure be within specified limits, throughout the time interval under consideration. These constraints can be expressed as

$$|z_i(t)| - \bar{z}_i \leq 0 , \quad \text{for all } t , \quad i = 1, 2, \dots, k_1 \quad (14)$$

and

$$|\sigma_j(z, b)| - \bar{\sigma}_j \leq 0 , \quad \text{for all } t , \quad j = 1, 2, \dots, k_2 , \quad (15)$$

where \bar{z}_i and $\bar{\sigma}_j$ are specified bounds on displacement and stress. The constraint inequalities (14) and (15) can be combined and expressed in a vector form as

$$h(z, b, t) \leq 0 , \quad \text{for all } t , \quad (16)$$

where the inequality applies to each component of the vector function. The inequality constraint (16) may be transformed to the equivalent vector functional equality

$$\tilde{\phi}_1(z, b) \equiv \int_0^T [|h(z, b, t)| + h(z, b, t)] dt = 0 \quad (17)$$

Since $h(z, b, t)$ is a continuous function of t , the integrand in Eq. (17) is continuous and is non-negative. If any constraint in expression (16) is violated, the corresponding functional constraint in Eq. (17) is violated and vice versa. Finally, frequency and design parameter constraints are expressed as

$$\omega_j^L \leq \omega_j \leq \omega_j^U, \quad j = 1, 2, \dots, k_3 \quad (18)$$

and

$$b_r^L \leq b_r \leq b_r^U, \quad r = 1, 2, \dots, k_4 \quad (19)$$

where ω_j^L and ω_j^U are lower and upper bounds on the j -th eigenvalue and b_r^L and b_r^U are lower and upper bounds on the r -th design parameter. Expressions (18) and (19) can be further combined and written in vector form as

$$\tilde{\phi}_2(\omega, b) \leq 0 \quad (20)$$

The dynamic optimal design problem may now be defined as follows:

Find a design parameter vector b that minimizes the cost function of Eq. (13), subject to the constraints (3), (4), (5), (17), and (20). Let this problem be denoted by ODP $_n$, where n is the dimension of the state variable. Using Eq. (6), the constraint functional of Eq. (17) can be transformed into

$$\tilde{\phi}_1'(\zeta, b) \equiv \int_0^T [|h'(\zeta, b, t)| + h'(\zeta, b, t)] dt = 0 \quad (21)$$

The problem ODP_n can now be transformed into an approximate problem, with a state variable $\zeta(t)$ of reduced dimension m . One now wishes to find a design parameter vector b that minimizes the cost function (13), subject to the constraints (7), (8), (9), (20) and (21). Let this problem be denoted by ODP_m.

IV. A COMPUTATIONAL METHOD FOR OPTIMAL DESIGN

To take advantage of the structure of the problems ODPn and ODPm, a state space steepest descent method is employed [10]. The method is related to the gradient projection technique of nonlinear programming which seeks a descent direction in the design space. Sensitivity analysis is first employed to approximate the effect of small variations in design on the cost function and constraints. Direct relationships between changes in the cost and constraint functions and a design change δb are established, by eliminating $\delta z(t)$ (or $\delta \zeta(t)$) and $\delta \omega$ from linearized forms of these functions. A reduced optimal design problem for δb is then obtained and solved, using the Kuhn-Tucker conditions of nonlinear programming.

Analyses of five possible methods of optimization for the solution were considered in [12]. A method was selected to obtain a balance between accuracy, effectiveness, and computational efficiency. The basic idea of this method is to use the modal matrix V to transform the transient analysis problem, the eigenvalue problem, and the system sensitivity problem to lower dimensional spaces. The solution of the original problem is then obtained by back substitution. The method is briefly described as follows: As a result of a design change, denote

$$M_1 = M_0 + \delta M_0 \quad (22)$$

and

$$K_1 = K_0 + \delta K_0 \quad (23)$$

Since V is found from Eq. (5), it is not orthogonal with respect to the perturbed matrices M_1 and K_1 . Define the $m \times m$ matrices

$$M' \equiv V^T M_1 V \quad (24)$$

and

$$K' \equiv V^T K_1 V, \quad (25)$$

the reduced eigenvalue problem is

$$M' V' \Omega' - K' V' = 0, \quad (26)$$

where V' is an $m \times m$ matrix of eigenvectors and Ω' is an m -dimensional diagonal matrix of eigenvalues. The solution of this m -dimensional eigenvalue problem gives the modified eigenvalues and eigenvectors

$$\Omega_1 = \Omega', \quad V_1 = VV' \quad (27)$$

of the original problem. That is,

$$M_1 V_1 \Omega_1 - K_1 V_1 = 0. \quad (28)$$

The matrix V' can serve as a transformation to uncouple the state Eq. (8) after a design change.

After several design cycles, V may lose its effectiveness as a transformation matrix, because the design has changed significantly. The criterion for recomputing the transformation matrix V is determined by considering the rate of change of the eigenvalues,

$$e_i \equiv \frac{|\omega'_i - \omega_i|}{\omega_i}, \quad i = 1, 2, \dots, m, \quad (29)$$

where ω'_i and ω_i are diagonal elements of Ω' and Ω , respectively. If any e_i exceeds a prescribed limit, a revised matrix V is found from Eq. (5).

At a given design point, one or more constraints may be violated or ϵ -active [13]. Since design changes are required to be small in the iterative algorithm, only these constraints are treated in the determination of a design change. Denoting the active constraint functionals in Eq. (17) as $\phi_1(z, b)$ and active constraint functions in expression (20) as $\phi_2(\omega, b)$, one may combine them in vector form as

$$\phi(z, \omega, b) \equiv q(\omega, b) + \int_0^T p(z, b, t) dt, \quad (30)$$

where

$$q(\omega, b) \equiv \begin{bmatrix} 0 \\ \phi_2(\omega, b) \end{bmatrix} \quad (31)$$

and

$$\int_0^T p(z, b, t) dt \equiv \begin{bmatrix} \phi_1(z, b) \\ 0 \end{bmatrix}. \quad (32)$$

A typical element of Eq. (30) is denoted by

$$P(z, \omega, b) = G(\omega, b) + \int_0^T F(z, b, t) dt. \quad (33)$$

The first variation of Eq. (33) is

$$\delta P = \frac{\partial G(\omega, b)}{\partial \omega} \delta \omega + \frac{\partial G(\omega, b)}{\partial b} \delta b + \int_0^T \left[\frac{\partial F(z, b, t)}{\partial z} \delta z + \frac{\partial F(z, b, t)}{\partial b} \delta b \right] dt. \quad (34)$$

In order to eliminate $\delta z(t)$ from Eq. (34), one takes the first variation of Eq. (3), to obtain

$$M_0 \ddot{\delta z}(t) + K_0 \delta z(t) = \frac{\partial R(b,t)}{\partial b} \delta b, \quad (35)$$

in which

$$R(b,t) = Q(t) - M_0 \overset{\sim}{\ddot{z}}(t) - K_0 \tilde{z}(t), \quad (36)$$

$$\dot{\delta z}(0) = 0, \quad \delta z(0) = 0, \quad (37)$$

where the notation " $\overset{\sim}{}$ " above an argument indicates that argument is held constant for the calculation. Premultiplying Eq. (35) by the transpose of an adjoint vector $\lambda(t)$, integrating by parts over the time interval, and using Eq. (37), yields the identity

$$\begin{aligned} & \lambda^T(T) M_0 \dot{\delta z}(T) - \dot{\lambda}^T(T) M_0 \delta z(T) \\ & + \int_0^T [\dot{\lambda}^T(t) M_0 + \lambda^T(t) K_0] \delta z \, dt \\ & = \int_0^T \lambda^T(t) \frac{\partial R(b,t)}{\partial b} \delta b \, dt. \end{aligned} \quad (38)$$

The adjoint vector $\lambda(t)$ is now defined to be the solution of the following equations:

$$M_0 \ddot{\lambda}(t) + K_0 \lambda(t) = \left[\frac{\partial F(z,b,t)}{\partial z} \right]^T \quad (39)$$

$$\dot{\lambda}(T) = 0, \quad \lambda(T) = 0. \quad (40)$$

Solutions of Eqs. (39) and (40) can be obtained by modal analysis using the same eigenvectors employed in solving Eqs. (3) and (4). Once $\lambda(t)$ is obtained,

$$\left\{ \int_0^T \lambda^T(t) \frac{\partial R(b,t)}{\partial b} dt \right\} \delta b \text{ replaces } \int_0^T \frac{\partial F(z,b,t)}{\partial z} \delta z dt$$

in Eq. (34), which eliminates δz from the linearized form of Eq. (33).

In order to eliminate $\delta \omega$ from Eq. (34), one takes the first variation of Eq. (5). For the i -th equation, one obtains

$$\begin{aligned} \frac{\partial [M_0 \tilde{v}_i \tilde{\omega}_i]}{\partial b} \delta b + \frac{\partial [\tilde{M}_0 \tilde{v}_i \tilde{\omega}_i]}{\partial b} \delta b + \frac{\partial [\tilde{M}_0 \tilde{v}_i \tilde{\omega}_i]}{\partial b} \delta b \\ - \frac{\partial [K_0 \tilde{v}_i]}{\partial b} \delta b - \frac{\partial [K_0 \tilde{v}_i]}{\partial b} \delta b = 0 \end{aligned} \quad (41)$$

Premultiplying Eq. (41) by \tilde{v}_i^T and using symmetry of M_0 and K_0 , one obtains

$$\delta \omega_i = \frac{\partial \omega_i}{\partial b} \delta b = M^{-1} \left\{ \frac{\partial [\tilde{v}_i^T K_0 \tilde{v}_i]}{\partial b} - \frac{\partial [\tilde{v}_i^T M_0 \tilde{v}_i \tilde{\omega}_i]}{\partial b} \right\} \delta b \quad (42)$$

Collecting all $\delta \omega_i$'s, one may form the vector equation

$$\delta \omega \equiv \frac{\partial \omega}{\partial b} \delta b \quad (43)$$

The first variation of the functional $P(z, \omega, b)$ can now be written in terms of δb alone, as

$$\delta P = \left\{ \frac{\partial G(\omega, b)}{\partial \omega} \frac{\partial \omega}{\partial b} + \frac{\partial G(\omega, b)}{\partial b} \right. \\ \left. + \int_0^T \left[\lambda^T(t) \frac{\partial R(b, t)}{\partial b} + \frac{\partial F(z, b, t)}{\partial b} \right] dt \right\} \delta b . \quad (44)$$

From this result, the first variation of the constraint functional of Eq. (30) is written as

$$\delta \phi = \Lambda^T \delta b , \quad (45)$$

where

$$\Lambda^T \equiv \frac{\partial q(\omega, b)}{\partial \omega} \frac{\partial \omega}{\partial b} + \frac{\partial q(\omega, b)}{\partial b} \\ + \int_0^T \left[\lambda^{\phi T}(t) \frac{\partial R(b, t)}{\partial b} + \frac{\partial p(z, b, t)}{\partial b} \right] dt , \quad (46)$$

Similarly, the variation of the cost function of Eq. (13) may be written as

$$\delta J = \varrho^J{}^T \delta b , \quad (47)$$

where

$$\varrho^J{}^T \equiv \frac{\partial J}{\partial b} . \quad (48)$$

A reduced optimal design problem for δb is now stated as follows:

Find δb to minimize δJ of Eq. (47), subject to the constraints

$$\delta \phi_i = \Lambda_i^T \delta b = - \phi_i , \quad \text{for all } i \in C , \quad (49)$$

$$\delta \phi_j = \Lambda_j^T \delta b \leq - \phi_j , \quad \text{for all } j \in D , \quad (50)$$

and

$$\delta b^T W \delta b \leq \xi^2, \quad (51)$$

where C and D are the index sets of $\phi_1(z,b)$ in Eq. (32) and $\phi_2(\omega,b)$ in Eq. (31), respectively; ξ is a small real number; and W is a positive definite weighting matrix. The constraint of Eq. (51) is used to ensure a small design change, as required for validity of the linear approximations employed in the foregoing sensitivity analysis.

A state space, generalized steepest descent method [10] is used to derive the algorithm. If the matrix Λ^T in Eq. (46) is of full row rank, the gradients of all constraint functions in Eq. (30), with respect to design parameters, are linearly independent. Then, there exist a vector multiplier μ , where $\mu_j \geq 0$ for all $j \in D$, and a scalar multiplier $v \geq 0$, such that

$$\frac{\partial H}{\partial (\delta b)} = \lambda^J{}^T + \mu^T \Lambda^T + 2v \delta b^T W = 0, \quad (52)$$

$$\mu_j (\Lambda_j^T \delta b + \phi_j) = 0, \quad \text{for all } j \in D, \quad (53)$$

and

$$v(\delta b^T W \delta b - \xi^2) = 0, \quad (54)$$

where

$$H \equiv \lambda^J{}^T \delta b + \mu^T (\Lambda^T \delta b + \phi) + v(\delta b^T W \delta b - \xi^2).$$

The solution of Eqs. (49), (52), (53), and (54) is as follows [1,10,13]:

$$\mu = \mu^1 + 2v\mu^2 \quad (55)$$

and

$$\delta b = -\eta \delta b^1 + \delta b^2, \quad (56)$$

where

$$\mu^1 = -B^{-1} \Lambda^T W^{-1} \ell^J, \quad (57)$$

$$\mu^2 = B^{-1} \phi, \quad (58)$$

$$\eta \equiv \frac{1}{2\nu}, \quad (59)$$

$$\delta b^1 = W^{-1} (\ell^J + \Lambda \mu^1), \quad (60)$$

$$\delta b^2 = -W^{-1} \Lambda \mu^2, \quad (61)$$

and

$$B \equiv \Lambda^T W^{-1} \Lambda. \quad (62)$$

Here, δb^1 is the projection of the gradient ℓ^J onto the tangent hyperplane of the constraint surfaces and δb^2 corrects constraint violations. The quantity

$$||\delta b^1|| = \sqrt{\delta b^{1T} W \delta b^1} \quad (63)$$

must approach zero as the algorithm converges [1], so it can serve as a convergence criterion. A computational algorithm, may now be stated as follows:

Step 1. Estimate b , and assemble M_0 and K_0 , as in Eq. (3).

Step 2. Construct ODPn and solve Eq. (5).

Step 3. Use V to transform Eqs. (3) and (4) into Eqs. (8) and (9), respectively.

Step 4. If control comes from Step 2, let all e_i in Eq. (29) be zero and go to Step 5. Otherwise, solve Eq. (26), calculate e_i from Eq. (29), and compute Ω_1 and V_1 in Eq. (27) as new Ω and V . Compute M , K , and $S(t)$ in Eqs. (10), (11), and (12).

Step 5. Calculate $\zeta(t)$ from Eqs. (8) and (9), $z(t)$ from Eq. (6), and stresses at various points of the structure. Check constraints.

Step 6. Form $\phi(z, \omega, b)$ in Eq. (30). Calculate $\frac{\partial R(b, t)}{\partial b}$ in Eq. (35), $\frac{\partial \omega}{\partial b}$ in Eq. (43), and ℓ^{JT} and Λ^T in Eqs. (48) and (46), respectively. Eliminate dependent constraints from $\phi(z, \omega, b)$ and remove the corresponding rows from Λ^T .

Step 7. Choose $\eta = \frac{1}{2\nu} > 0$, compute μ^1 , μ^2 , and μ from Eqs. (57), (58) and (55), respectively.

Step 8. Check the sign of each component of μ , corresponding to the constraint $\phi_2(\omega, b)$ in Eq. (31). If any of these components are negative, remove the corresponding rows from $\phi(z, \omega, b)$ and Λ^T and return to Step 7.

Step 9. Compute δb^1 from Eq. (60) and $||\delta b^1||$ in Eq. (63). If $||\delta b^1||$ is small enough and all constraints are satisfied, terminate the process.

Step 10. Compute δb^2 and δb from Eqs. (61) and (56), respectively. Calculate $b + \delta b$ as a new b . Assemble M_1 and K_1 in Eqs. (22) and (23) as new M_0 and K_0 , respectively.

Step 11. If all e_i obtained in Step 4 are less than a prescribed value, return to Step 3; otherwise, return to Step 2.

The choice of η in Step 7 is made to seek a given reduction in the cost function, normally $\Delta J = -0.01J$ to $-0.10J$. With the desired reduction ΔJ selected, and ignoring constraint error correction, one may calculate δb^1 from Eq. (60) and substitute into Eq. (47) to obtain $\Delta J = -\eta \ell^{JT} \delta b^1$. Thus, one obtains $\eta = -\Delta J / (\ell^{JT} \delta b^1)$. In effect, one is requesting a given percentage reduction in the cost function as the basis for step size selection.

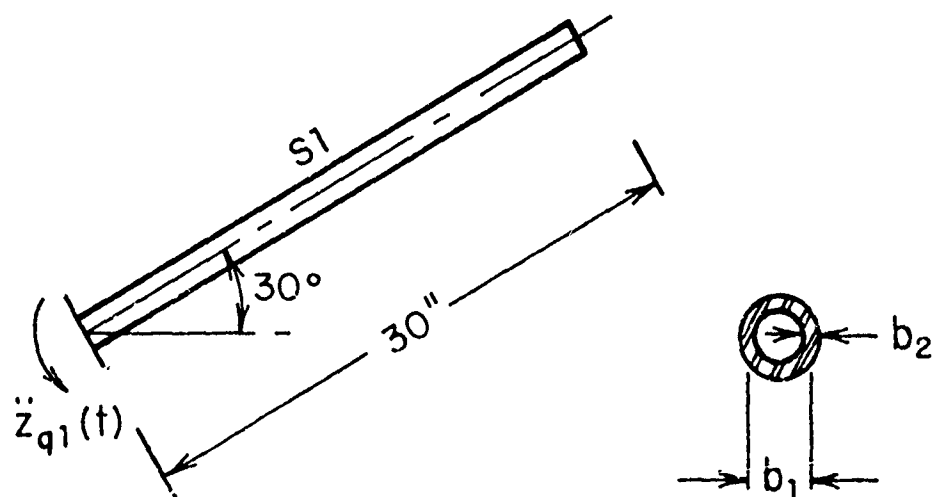
V. NUMERICAL EXAMPLES

A computer program based on the algorithm of Section IV for minimum weight design of beam and truss-frame type of structures was developed in FORTRAN IV(H) on an IBM 360-65 computer. The method of subspace iteration [14] was used in frequency analysis of the problem.

Example 1: A Uniform Tubular Cantilever Beam Subjected
to a Shock Input at the Fixed End

A uniform tubular cantilever beam is tipped up at an angle of 30 degrees to the horizontal. The fixed end is forced to rotate in a prescribed manner, as shown in Fig. 1. The beam is divided into four elements of equal length for analysis. Axial deformation is considered, so the system has 12 degrees of freedom. The design constraints are listed in Table I. The modulus of elasticity and material density are 30×10^6 psi and 0.28 lb/in.^3 , respectively. The initial conditions of motion are zero, and the mean diameter and the wall thickness are considered as design parameters.

The first five of nine eigenvectors, from subspace iteration, were used in the analysis. The starting design weight was 4.354 lb with frequencies of 67.20, 419.8, 1,175, 1,706, and 2,294 cps. This design resulted in $||\delta b^1|| = 6.225$ in the first iteration. The stopping criteria were satisfied in the nineteenth iteration, where $||\delta b^1|| = 3.182 \times 10^{-6}$ and no constraint violation occurred. The final design weight was 2.723 lb with frequencies of 46.36, 290.1, 814.9, 1,600, and 1,706 cps. The fifth frequency of 1,706 cps corresponds to axial deformation. At the optimum, the maximum vertical and angular displacements of the free end were 0.582 in. and 0.0308 rad,



$$\ddot{z}_{q1}(t) = \begin{cases} 1000 \sin(80\pi t) \text{ rad./sec}^2, & 0 \leq t \leq .0125 \text{ sec} \\ 0 \text{ rad./sec}^2, & .0125 \leq t \leq .0150 \text{ sec} \end{cases}$$

Fig. 1. Structure and Load for Example 1

respectively. The maximum stress at the fixed end was 44,700 psi. The total computing time was 22.50 sec for 20 iterations. Numerical results are shown in Table II and Fig. 2 (Solution 1).

This problem was also solved by starting from a different design point with an initial design weight of 3.958 lb and initial frequencies of 45.25, 283.0, 795.1, 1,561, and 1,706 cps. This design resulted in $||\delta b^1|| = 4.082$ in the first iteration. At the fifth iteration, $||\delta b^1|| = 2.413 \times 10^{-6}$. The final design weight was 2.671 lb with frequencies of 45.48, 284.6, 799.5, 1,570, and 1,706 cps. At the optimum, maximum stress at the fixed end was 45,200 psi. The total computing time was 9.65 sec for six iterations. Numerical results are shown in Table II and Fig. 2 (Solution 2).

Example 2: Dynamic Optimization of a Long Barrel Cannon

The problem of design of a precision long barrel cannon is considered next. The cannon is assumed to be a cantilevered tube with eight radial ribs of rectangular cross-section evenly space around the circumference to dissipate heat and stiffen the barrel (see Fig. 3). Heat transfer and stresses due to barrel pressure are not considered in this analysis. When the cannon is fired, the impulsive load on the vehicle causes a pitch motion that occurs at the fixed end of the cannon. It is assumed that the mass of the vehicle is much larger than that of the cannon, so the dynamic response of the vehicle is not altered appreciably as a result of a small change in design of the barrel. The pitch at the base of the gun has both translational and rotational components of motion. The design objective in this problem is to bound the angular amplitude of motion of the muzzle end of the cannon, since this amplitude correlates with the accuracy of the cannon. Numerical

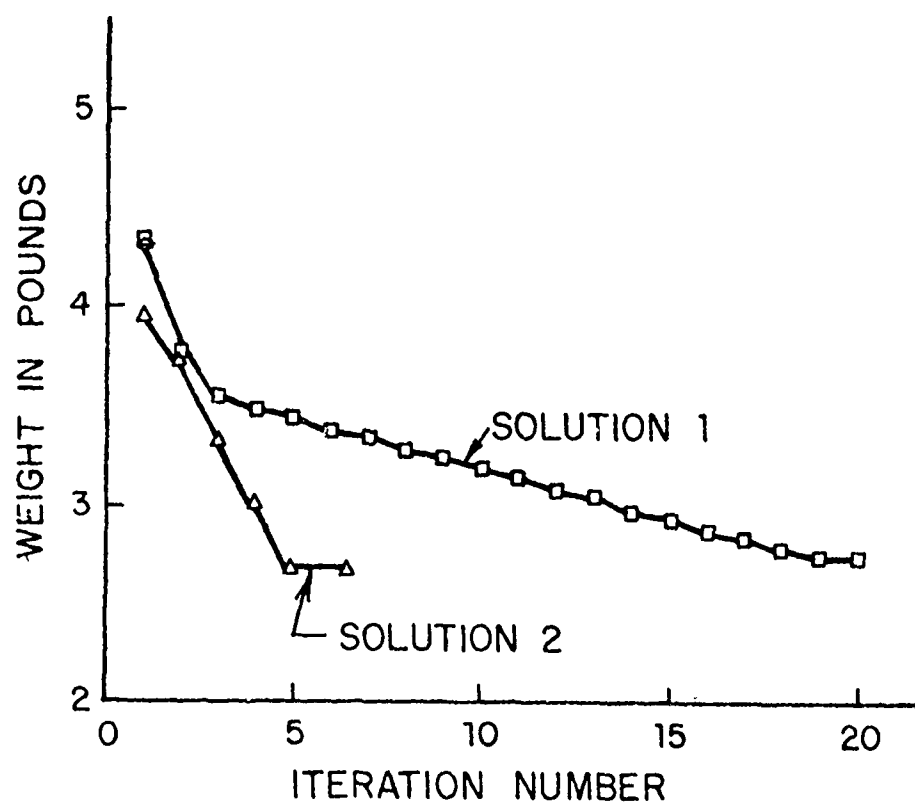


Fig. 2 Weight-Iteration Curves of Examples 1

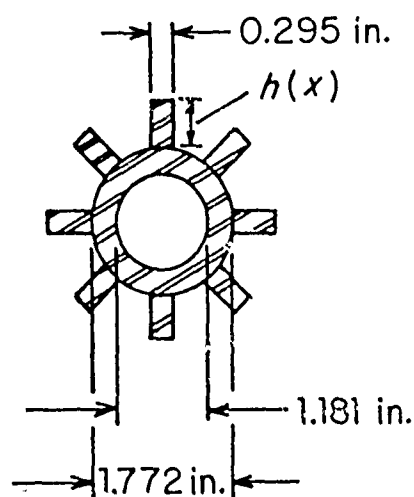
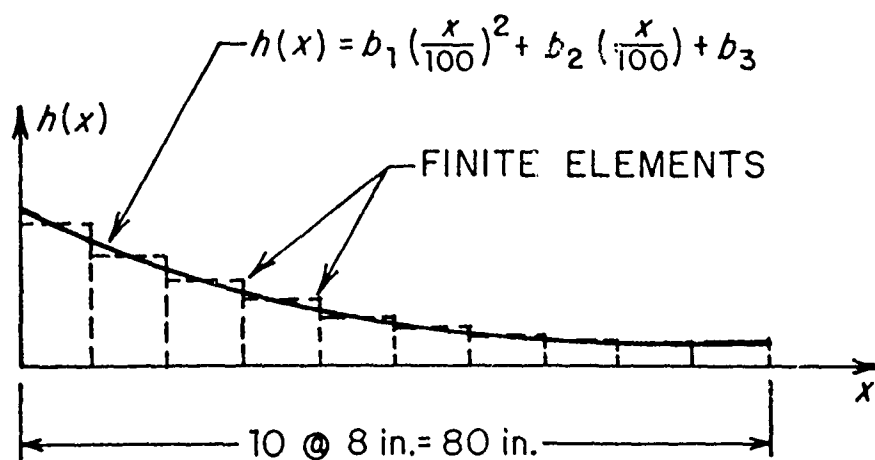
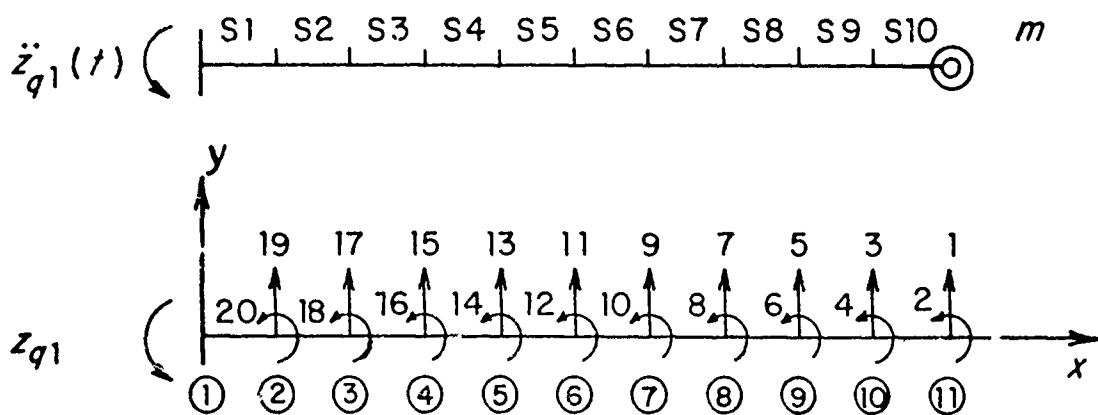
data for this problem are associated with the RARDEN 30 mm, long tube, precision automatic cannon developed by the British, and the initial conditions of motion (z^0, \dot{z}^0) are taken equal to zero.

The width of the ribs is constant, but the depth of the ribs varies as a quadratic polynomial along the barrel as shown in Fig. 3. Design parameters are then taken as the coefficients of this polynomial. Two design configurations have been studied. One design considers an additional concentrated mass of fixed magnitude attached to the muzzle. The other design considers a similar concentrated mass of variable magnitude attached to the muzzle as an additional design parameter.

The finite element method is used in the optimization algorithm, and the constant depth of each finite rib element is taken equal to the actual depth of the real rib at the middle of the finite element. The barrel is approximated by ten finite beam elements of equal length, and axial deformation is ignored. The discretized system has twenty degrees of freedom shown by the arrows in Fig. 3. Design constraints are listed in Table III.

The first six of ten eigenvectors, obtained from subspace iteration, were used in the dynamic analysis. The problem set-up required 0.41 sec on an IBM 360/65 computer.

The first design has a four pound concentrated mass attached to the muzzle. The cost function is the total weight of the tube plus the weight of the ribs. The fixed weight of the concentrated mass has no effect on the optimum design, so it is not included in the cost function. The algorithm was started at a point with a design weight of 46.521 lb. The natural frequencies were 12.02, 64.27, 174.8, 343.6, 571.7, and 860.1 cps. The cost function reduction ratio ΔJ was 0.04. The convergence measure $||\delta b^1||$ was



$$E = 30 \times 10^6 \text{ psi}, \rho = 0.28 \text{ lb/in.}^3$$

$$\dot{z}(0) = z(0) = 0$$

$$\text{DESIGN NO. 1 } m = 4 \text{ lb}$$

$$\text{DESIGN NO. 2 } m = b_4 \text{ lb}$$

$$\ddot{z}_{q1}(t) = -0.001 e^{-3.358(t-0.25)} [165.6584 \sin(6.2657t + 0.004692) + 249.1162 \cos(6.2657t + 0.004692)]$$

$$\text{rad/sec}^2 \quad 0 \leq t \leq 0.625 \text{ sec}$$

Fig. 3. Long Barrel Cannon and Load

19.12 at this point. The measure of convergence reduced to $||\delta b^1|| = 3.677 \times 10^{-4}$ at the eleventh iteration, where the maximum constraint error was 2.8%. This design is selected because further computation showed constraints were more severely violated and weight reduction was small. The dynamic response constraint was active throughout the design process. The final design weight was 42.16 lb (muzzle mass of 4 lb is not included), with natural frequencies of 12.21, 62.39, 168.0, 330.0, 549.5, and 827.2 cps. Total computing time was 30.15 sec for 11 iterations. Numerical results are given in Table IV and Fig. 4.

The second problem treats the concentrated mass as an additional design parameter. The system therefore has a total of 4 design parameters. The design weight is the total weight of the barrel, the ribs, and the concentrated mass. The starting design weight was 38.636 lb, with frequencies of 11.93, 66.10, 178.4, 346.4, 570.4, and 851.0 cps. with $\Delta J = 0.08$ and the first calculation yielded $||\delta b^1|| = 18.28$. The dynamic response constraint was active in some of the initial iterations and was active in every iteration after the eleventh. The convergence criterion was satisfied in the twenty-first iteration, where $||\delta b^1|| = 4.75 \times 10^{-5}$ and all constraints were satisfied. The final design weight was 37.464 lb, with frequencies of 12.11, 66.12, 178.0, 345.3, 568.4, and 847.9 cps. Total computing time was 55.34 sec for 22 iterations. Results are shown in Table IV and Fig. 4.

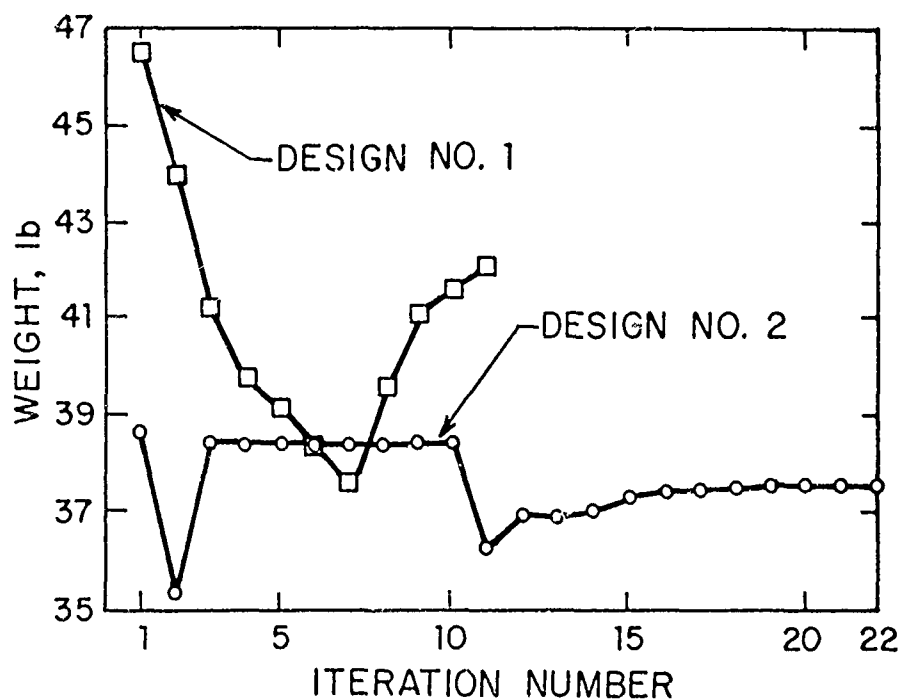
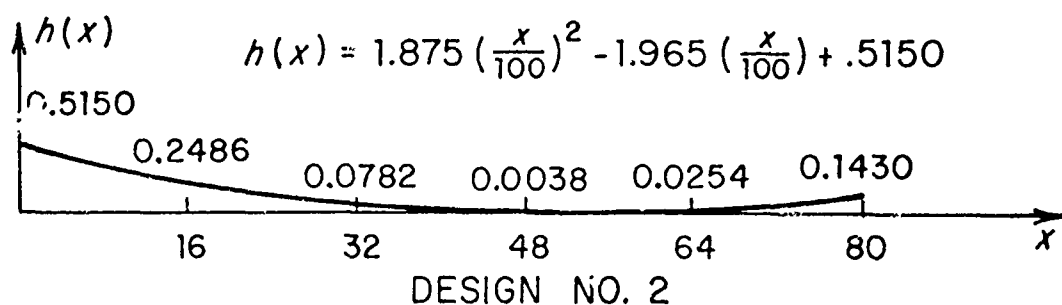
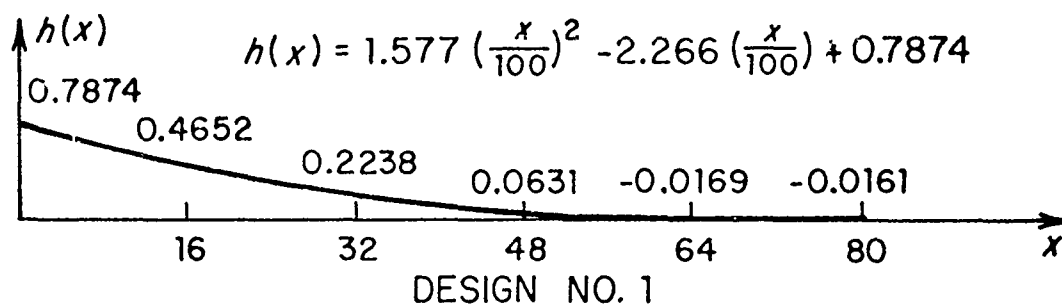


Fig. 4. Rib Profiles and Weight-Iteration Curves of Design No. 1 and No. 2

VI. DISCUSSION AND CONCLUSIONS

The state space steepest descent method, with the modal method of structural analysis and the subspace iteration method for eigenvalue analysis, has demonstrated an ability to optimize design, with constraints on dynamic response (stress and displacement), natural frequencies, and design parameters.

The algorithm developed is applicable for general dynamic loads applied to nodal points of general structures. It does not presently account for static loading, dynamic buckling, and some other important design factors; but it can be extended to include them.

Numerical results for two simple examples are presented to show applicability of the method. These results should be considered as preliminary. The effect of moving masses, thermal loads, time dependent support, and initial bending of the tube are additional factors that remain to be included in the analysis.

Numerical results of some additional examples of elastic structures are presented in [12] and [17]. Recently Cassis and Schmit [18] have also treated the problem of optimal design of elastic structures under dynamic loads. They have used the Davidon-Fletcher-Powell method for exterior penalty function (SUMT) formulation of the problem. Comparisons of the present method with the Cassis and Schmit technique are not yet available.

VII. REFERENCES

- [1] E. J. Haug, Jr., Engineering Design Handbook: Computer Aided Design of Mechanical Systems, AMC Pamphlet No. 706-192, U.S. Army Materiel Command, Washington, D. C., July, 1973.
- [2] B. L. Pierson, Int. J. for Num. Meth. in Eng. 4, 491-499 (1972).
- [3] R. M. Brach, Int. J. Mech. Sci. 10, 429-439 (1968)
- [4] R. H. Plaut, J. of Appl. Math. and Phys. 21, 1004 (1970).
- [5] W. Yau, J. of Appl. Mech., Trans. ASME 41, Ser. E, No. 1, 301-302 (1974).
- [6] L. J. Icerman, Int. J. Solids and Structures 5, No. 5, 473-490 (1969).
- [7] Z. Mróz, ZAMM 50, 303-309 (1970).
- [8] R. L. Fox and M. P. Kapoor, AIAA J. 8, No. 10, 1798-1804 (1970).
- [9] H. J. Levy, Minimum Weight Design under Dynamic Loading, Ph.D. Dissertation, New York University, April, 1972.
- [10] E. J. Haug, Jr., K. C. Pan, and T. D. Streeter, Int. J. for Num. Meth. in Eng., 171-184 (1972).
- [11] J. S. Przemienicki, "Theory of Matrix Structural Analysis," McGraw-Hill Book Co., 1968.

- [12] T-T. Feng, Optimal Design of Elastic Structures Under Dynamic Loads, Ph.D. Dissertation (also Departmental Report No. 18), Mechanics and Hydraulics Program, College of Engineering, University of Iowa, July, 1975.
- [13] B. M. Kwak and E. J. Huag, Jr., J. of Opt. Th. and Appl., to appear 1977.
- [14] K-J. Bathe and E. L. Wilson, J. of Eng. Mech. Div., Proc. ASCE 98, No. EM6, 1471-1485 (1972).
- [15] J. S. Arora, E. J. Haug, Jr., and K. Rim, J. of the Struct. Div., Proc. ASCE 101, No. ST10, 2063-2078 (1975).
- [16] J. S. Arora and E. J. Haug, Jr., Int. J. for Num. Meth. in Eng. 10, No. 4, 747-766 (1976) and Vol. 10, No. 6, 1420-1427.
- [17] T. T. Feng, J. S. Arora, and E. Jr. Haug, Jr., Int. J. for Num. Meth. in Eng., to appear, 1977.
- [18] J. H. Cassis and L. A. Schmit, Jr., J. of the Struct. Div., ASCE 102, No. ST10, 2053-2071 (1976).

TABLE I. DESIGN CONSTRAINTS FOR EXAMPLE 1

The verical and angular deflections of the free end must be less than or equal to 0.6 in. and 0.04 rad., respectively

$$|\sigma_i(t)| \leq 45,000 \text{ psi} , \quad \text{for all } t \text{ and } i$$

$$30 \leq f_1 \leq 60 \leq f_2 \leq 400 \text{ cps}$$

$$0.8 \leq b_1 \leq 2.0 \text{ in.} , \quad 0.1 \leq b_2 \leq 0.15 \text{ in.}$$

TABLE II. INITIAL AND FINAL DESIGNS OF EXAMPLE 1

Design		Solution 1		Solution 2	
		Initial	Final	Initial	Final
S1	b_1	1.500	1.032	1.000	1.012
	b_2	0.110	0.100	0.150	0.100
Wt. lb		4.354	2.723	3.958	2.671
Time/Iteration sec		1.13		1.61	

TABLE III. DESIGN CONSTRAINTS FOR LONG BARREL CANNON

Design No. 1

$$|z_2(t)| \leq 0.0004 \text{ rad.} \quad \forall t$$

$$0 \leq h(x) \leq 0.7874 \text{ in.} \quad \forall x: 0 \leq x \leq 80 \text{ in.}$$

Design No. 2

$$|z_2(t)| \leq 0.0004 \text{ rad.} \quad \forall t$$

$$0 \leq h(x) \leq 0.7874 \text{ in.} \quad \forall x: 0 \leq x \leq 80 \text{ in.}$$

$$0 \leq b_4 \leq 12.01b$$

TABLE IV. INITIAL AND FINAL DESIGNS OF THE LONG BARREL CANNON

Designs	Design No. 1		Design No. 2	
	Initial	Final	Initial	Final
b_1 (in.)	1.500	1.577	2.200	1.875
b_2	-2.000	-2.266	-2.200	-1.963
b_3	0.780	0.7874	0.560	0.515
b_4	-----	-----	0.100	0.000
wt. (lb)	46.521	42.160	38.636	37.464
violation	$v_1 = 0.0336^*$	$v_1 = 0.0278$ $v_2 = 0.0264$	$v_1 = 0.0199$	-----
Time/It. (sec)	2.74		2.52	

* $v_1 = 0.0336$ implies a constraint violation of 3.36%

A REPORT OF THE FINITE ELEMENT METHOD (FEM) ANALYSIS
OF THE MEDIUM CALIBER, ANTI-ARMOR AUTOMATIC CANNON

G.A. PFLEGL

Watervliet Arsenal
Watervliet, New York

TABLE OF CONTENTS

	<u>Page</u>
ABSTRACT	341
DISCUSSION OF MODEL	342
CONCLUSION	359
REFERENCES	360

ABSTRACT

This report discusses the use of the NASTRAN finite element program in the dynamic analysis and modeling effort associated with the Medium Caliber, Anti-Armor, Automatic Cannon (MCAAAC) development program. The finite element method (FEM) has been used in the analysis of both individual components and a simplified version of the entire weapon. Results range from the static analysis of the barrel to determine normal rest configuration, to direct dynamic analysis of the entire weapon over a three-round burst in order to determine muzzle orientation at time of shot ejection.

The discussion includes the reasons for selecting this method of modeling, the significant problems encountered in this approach, and the current status of the effort including results of the analyses. Also included are present plans for further development of the model and its uses.

DISCUSSION OF MODEL

The first thing that must be determined when forming a model is what actually is to be represented. In this particular case the desire was to be able to model the basic configuration of the weapon as it existed at the time of initiation of the effort. This was to include the receiver with its feeder housing; barrel with its breech coupling, bolt and bolt carrier; and the barrel return spring with its housing. But since this was at an early stage of development it was also necessary to have a model which could readily adapt to changes in geometry, stiffness, damping, etc. Along with these design variations in the basic structure, the model would also have to account for changes in requirements.

Changes in modelling requirements were envisioned to include increased complexity (such as the cam actuated bolt carrier), provision for gun - vehicle interaction (requiring the ability to simulate a vehicle) and changes in the operation of the weapon (such as a constant recoil force mode). These are certainly demanding specifications for a model, especially one that is supposed to be able to describe muzzle motion throughout a three round burst of fire. At our particular installation these various requirements appeared to best be met by using a finite element method (FEM) approach implemented with the NASTRAN computer program.

NASTRAN was chosen because it seemed to fit most of the requirements. It appeared that it could be used to develop the basic configuration with little difficulty and then permit changes in any of the components and their characteristics without altering other portions

it also appeared that the model could be developed sequentially to include the envisioned changes in complexity, operation and mounting. Also in favor of NASTRAN was the fact that it was very general with six degrees of freedom for most points. This would permit the analysis to include the vertical and transverse motion of the muzzle of the barrel and thus provide input for a program used to determine weapon accuracy.

Since the NASTRAN program is so very general in nature and uses the direct integration of the equation of motion that it has set up, it can handle changes in the prescribed time variant loads, as well as linear and non-linear loads based on the deflection and motion of the structure. Such loadings permit relatively good modelling of contact conditions. NASTRAN also allows for various types of damping and permits eigenvalue (fundamental modes) analysis of the structure and its individual components with various support conditions.

NASTRAN has another feature which was seen to be of considerable importance early in the modelling effort. This is the fact that NASTRAN is essentially the same at the approximately two hundred and seventy locations which support the program. Because the program is so very general, more data is generated, transferred, manipulated, and stored than in a program written for a specific problem. This means that any reasonable model would quickly outgrow the capabilities of Watervliet Arsenal's computer, which is the smallest of those having NASTRAN, and a larger machine would be needed. However, since the code is the same all over, all of the development and ground work

for the model could be done at Watervliet and the outside computer would only be needed for extended timeframe (full- or multi-cycle) solutions.

The acronym "NASTRAN" has been used many times in the last few paragraphs with little explanation other than that it is a finite element method computer program. This title is derived from the origin and basis of the program - Nasa STRuctural ANalysis. In the mid 1960's, NASA saw the need for a general purpose, all inclusive program based on a unified finite element approach. This program was to use the best elements and computer methods to solve problems in the research and development of aerospace and related structures. The program was to be of modular construction such that at regular intervals parts of it could be updated without requiring a re-write of the entire program. The first public version released in 1970 is the result of five years of work headed by people at Goddard Space Flight Center.

In a most general and simplistic explanation of the program, the user specifies an array of points (called grid points) in the structure to be analyzed. The nature of the connection between adjacent grid points is specified on element cards. The program then uses numerical methods to determine the stiffness between the grid points of each individual element and the mass associated with each such point. These values are set up in matrix form. The matrices for all the elements are then combined to form the set of simultaneous equations of motion of the defined points in the structure. This system of

equations is then modified to account for damping, added stiffness, constrained degrees of freedom and degrees of freedom which are defined as linear combinations of other remaining degrees of freedom - that is the boundary conditions.

Given this reduced set of simultaneous equations, the program can then find the displacements of the grid points for specified static loads. From the displacements and the individual element matrices it can find the element stresses. Or from the set of equations it can determine the normal modes of vibration including complex modes if damping is present. Or, if a time variant load is given, it will do double integration in the time domain to determine acceleration, velocity, and displacement for each degree of freedom. Further interest in the operation of the program should be directed to the NASTRAN theory manual or a text on the method.

Having introduced the intent of the model and the method of affecting it, it is now possible to go on to discuss particular features of the model. There are actually five different areas of consideration in the model; they are 1) loading and constraints, 2) the barrel, 3) the receiver, 4) the bolt, bolt carrier and cam, 5) the deflection compensating truss and 6) the shock absorbers and dampers. In each of these sections the requirements on the model can be determined from looking at the proposed weapon design, while the ability of the model to meet these demands can be assessed from the features of NASTRAN that were employed in the model. To aid in this assessment some description of the NASTRAN features will be given without, however, going into the

the theoretical development or the computer implementation. The NASTRAN Programmer's Manual are available to provide this information in the depth that it requires. To include a detailed explanation in this presentation would only serve to bore some readers and confuse others while not adding materially to how the model was made and performed.

The first area of consideration is that of the loading and the constraints (i.e., boundary conditions) to be applied. Since this is a recoil actuated weapon, it is essentially the breech pressure acting on the net bore area which causes barrel motion. The time variant values of breech pressure during projectile inbore travel come from the computer program used in the weapon design. A gas dynamics program provides data on the breech pressure during blow down. This project is not designed to assess radial and longitudinal motion within the tube wall (although that has been shown to be possible) so, therefore, the pressure distribution within the tube is not used. Torsional motion of the barrel is not considered, either, since the relation between projectile acceleration and the loading of rifling is still unknown.

This loading is accomplished in NASTRAN by the use of a TLOAD card. This card references a TABLED card and a DAREA card such that at any time in the solution the tabular value as determined from the former is applied to a degree of freedom specified on the latter multiplied by the coefficient there stated. This procedure allows the breech pressure versus time data to be defined as a table to any degree

of precision required; that is, the increment of time used in the table can be made as small as necessary to define the behavior. During the solution, the NASTRAN program will do linear interpolation between the specified data points as necessary. By use of the coefficient on the DAREA card, the definition of the net bore area can be kept separate from the definition of the breech pressure allowing easy alteration of either one. For the simulation of a multiple round burst of fire, the table entries are just repeated with the addition of the appropriate time interval. Since the ballistic pressure is the only outside force driving the weapon, these free items are all that are needed to define the loading.

It is envisaged that the weapon may be mounted on several different vehicles and most likely in a constant recoil force mode on one of them. The structure which transmits the forces of the gun to the vehicle (and the vehicle forces to the gun) have not been designed and therefore have not been included in the model. To provide some form of constraint to the model, all the grid points on the bottom of the receiver were held fixed in all six degrees of freedom. These single point constraints, as they are known in NASTRAN, lock the receiver to the frame of reference. It is then possible to have the program print out the reaction forces at each such point as a function of time. This information will be useful in designing the vehicle mounts.

The most important component of the weapon is the barrel, since all other items are there to support the barrel as it guides and launches the projectile. It is the barrel which undergoes the largest

deflections. Also, the intent of this modelling effort is to provide values of muzzle motion to be used in an exterior ballistics program in an attempt to assess weapon accuracy. It is because of these requirements that considerable effort was expended to determine the extent to which NASTRAN would be able to approximate the behavior of the barrel in a dynamic response situation. To assist in this evaluation and in the preparation of the model itself, an auxiliary program was created (using FORTRAN IV) which would generate all the necessary cards for a finite element representation of the gun tube based on NASTRAN's BAR element.

The BAR element is a metric element which encompasses extension, torsion and bending properties. (The ROD and TUBE elements were not chosen as they fail to include bending.) The BAR element is the most mathematically complete element of the NASTRAN program, a fact that has been demonstrated repeatedly. This completeness is based on three assumptions (1) the element is initially straight, (2) it is unloaded except at its two ends, and (3) its properties (cross section area, area moments of inertia, etc.) are uniform along its length. Because a gun barrel is designed to be essentially straight and because there is no attempt at an interior ballistic analysis which might demand a distributed pressure load, the first two criteria are met. The third assumption is accounted for in the FORTRAN program by integrating the properties of the element over its assigned length and then normalizing with respect to the length rather than simply averaging the properties of the element at its two ends. Using the output of this program as

input, NASTRAN was used to generate results which were compared to experimental values for an M68 Tank Cannon.

The comparison was of both a static and a quasi-dynamic nature. The static portion was accomplished by adding to the tube elements the lumped masses (complete with offset centers-of-gravity) for the breech ring and the bore evacuator assembly and executing NASTRAN's Grid Point Weight Generator. The NASTRAN results were a total barrel weight of 2521 pounds and a center of gravity of 54.80 inches forward of the rear face of the gun tube. This compares very well with average measured values of 2492 pounds weight and 54.83 inches for the c.g.. These are errors of only 1.2% and .05% respectively, when compared to measured values. The quasi-dynamic analysis involved the comparison of calculated normal modes of the barrel with those measured during actual gun firings. The first frequency of vibration had a measured value of about 26.3 cycles per second and the calculated value was 26.7 cps. This is an error of only 1.5%. Later in the recoil cycle the barrel has an altered support condition such that its frequency becomes about 8.4 cycles per second. When these support conditions are applied in NASTRAN, the result is a frequency of 8.6 cps. The closeness of these results were sufficient to encourage the modelling effort and to provide confidence in the output of the FORTRAN program.

As a further check on the expected performance and as a test to determine the number of BAR elements required, two models of an early gun tube design were made - one using sixteen elements and one using sixty-four elements. The two models were constrained in cantilever

fashion from the breech end and had a static load applied at the muzzle. The muzzle deflections varied by less than four percent. The eigenvalues were extracted for the two models with the one having four times the total number of modes as the other. For those modes which were present in each model the correspondence was remarkable - within two percent (and usually less) at almost every frequency. Since it was known at the start that this model was to be a rather loose approximation, the sixteen element representation was chosen. Later it became necessary to locate two additional grid points on the barrel so that two of the elements were each divided into two parts with the element properties recalculated. This eighteen element representation is the way the barrel model has remained.

The receiver is the second most massive portion of the weapon. It is basically a rectangular structure fabricated from steel plate. Fine features of the model such as weld fillets, bearing blocks and surfaces, attachment lugs, etc. were not considered for the model. Such refinements could be added at a later time if the behavior of the model indicates that such items could show up in the results. With the exclusion of such details it becomes relatively simple to represent the receiver as a collection of quadrilateral and triangular plate bending elements - NASTRAN's QUADZ and TRIAZ elements respectively. These metric elements are designed to handle inplane tension, compression and shear and out of plane bending of a homogeneous, isotropic material (Fig.1.).

Attached to the side of the receiver is a structure which contains the feeder mechanism which itself contains a three round clip of ammunition. The external configuration was somewhat defined at the start of the model construction but with the interior details not only vague but of questionable value to the model, just as the interior details of the receiver. So to account for the additional mass of the feeder and ammunition, a non-structural mass density was specified in the definition of the top and bottom plates of the feeder housing (Fig. 2.). This parameter specifies an area mass density to be included with the normal calculation which is based solely on the thickness of the element. The value of the coefficient was set to reflect the total mass of two rounds plus a percentage of the basic feeder housing.

Bolted to the front of the receiver and coaxial with the barrel is a cylindrical steel sleeve surrounding the barrel return spring which is also coaxial with the barrel (Fig. 3). At the front (muzzle end) of the sleeve is a rather massive steel collar which acts as a bearing surface during recoil motion of the tube. Thus the sleeve not only covers the barrel return spring but also acts as a barrel support. The sleeve itself is modeled as a series of Bar elements because the BAR element can be defined to have the same properties (area, moments, etc) as the sleeve which is acting primarily in a bending mode. The mass of the collar is accounted for by a concentrated, lumped mass (CONMZ) at the end of the series of BAR's representing the sleeve.

The support condition between the weapon barrel and the steel collar is modeled by a NASTRAN constraint feature - the MPC or multi-point constraint. This feature provides that the motion of a degree of freedom is directly related to one or more other degrees of freedom according to the coefficients defined by the user. Using this capability, a point that at rest is slightly forward of the collar position and at full recoil is slightly rearward of the collar, is defined to have the same vertical and horizontal displacement as the grid point representing the location of the collar. A point at the rear of the barrel is similarly associated with points on the sides of the receiver where support rails are located in the real weapon. It is obvious that such a definition of support conditions does not account for the accumulative effect of tolerances commonly referred to as play. To include such non-linear behavior would have added undue complexity to the model and would have required a measurement of the play which was not possible.

The barrel return spring is actually a large coil spring which is around the barrel with one end compressed against the receiver and the other forced against a collar locked to the gun barrel. In the normal rest position there is a considerable preload in the spring. The spring itself is modeled by a series of NASTRAN elastic spring (ELAS) elements with concentrated masses at the nodes between the elements. The elastic elements represent simple scalar springs which act only on one degree of freedom to resist the rigid body motion of the gun barrel in recoil. These elements were chosen because they are not metric elements and therefore have no material representation which in NASTRAN is

based on small displacement theory. A series of elements is used so that the lumped masses at the series of modes will provide some sort of distributed mass for the barrel return spring. This effort was deemed necessary in light of the fact that the real spring weighs one-hundred and twenty-five pounds.

The preload in the spring is modeled by simply specifying its reaction forces on the receiver and the barrel. This is accomplished by requesting a time dependent load (TLOAD). This load is defined by a Table which specifies a value constant in time and a DAREA which directs the load to be applied to the receiver and barrel with the correct magnitude and directions.

Another portion of the weapon which received considerable attention is a part of the internal workings of the receiver comprised of the bolt, bolt carrier and cam. The breech closure of the barrel is accomplished by an externally threaded cylindrical plug (the bolt) which is inserted into the opening in a cylindrical coupling affixed to the rear of the gun tube. This coupling behaves as part of the tube and is included in its representation. This bolt is supported and controlled in rotation by a bolt carrier which recoils in the same line of action as the barrel. In the actual operation of the weapon, when the barrel recoils, a lever on the carrier engages a cam on the side of the receiver forcing the bolt to rotate and unlock and then accelerating both the carrier and the bolt rearward away from the barrel. The acceleration forces the carrier rearward against a compression spring until it is latched and held awaiting release. Upon release,

it is driven forward, advancing a round of ammunition into the chamber and locking the bolt. Since this is a recoil operated weapon, energy is transferred from the barrel to these moving parts through the action of the lever and cam and it was wondered if NASTRAN could model this energy transfer.

A model of this action was constructed by using a NASTRAN multi-point constraint (MPC; described previously) between a point with lumped mass representing the carrier and bolt, a point on the breech end of the barrel and a third point separate from the physical representation of the model. Since the design of the cam had determined a table of values relating barrel recoil distance and carrier - barrel separation, this tabular data was entered directly into NASTRAN via a TABLE card. A non-linear load was then defined which applied a load to the separate point (which was supported by a scalar spring) to enforce the desired deflection. The MPC thus caused the displacement of the carrier to be the total of the barrel and the separate point displacements. Since the scalar spring of the separate point was several orders of magnitude greater in stiffness than either the barrel return spring or the bolt carrier spring, the interaction and energy transfer between these two parts was effected by this use of the MPC. In spite of this success, it was decided that this phase was too complex to be incorporated into the early multi-round model and so only the lumped mass of the bolt and carrier was retained along with the carrier spring.

A very prominent portion of the weapon, the deflection compensating truss, was actually very simple to model as a collection (Fig. 4.) of BAR elements. Once assembled, its stiffness at possible points of forward tube support were calculated with a single NASTRAN run. The affect of these support conditions on the normal modes of the barrel were then evaluated in an attempt to determine the best locations and the final modal behavior of the weapon.

The final portion of the weapon to be described seemed very trivial at the start and end of the effort but in the middle caused considerable anguish and delay. NASTRAN provides for the direct specification of viscous type damping (DAMPi card, $i = 1-4$) between degrees of freedom. It is very easy to thus represent the main recoil buffer (Fig. 5.) which is attached to the rear of the barrel and the front of the receiver and works in both recoil and counter recoil modes. However, a very important part of the operation is the counter-recoil buffer which only acts over the last five inches of counter recoil motion. This prevents the barrel from slamming into the receiver at high speed and yet allows rapid cycling of the barrel. A detailed scheme was devised to define the model equivalent of this real life situation.

The intent was to use a non-linear load which is a linear function of the product of two displacements (NOLIN2). One of these would be the displacement of a separate point supported by a scalar spring which would be deflected to unit value when acted upon by a tabularly defined non-linear load (NOLIN1). The table would only have non-zero value

for barrel displacements of less than the required five inches. The other displacement would be of a separate point, too, but one where the displacement would be proportional to the positive velocity of the barrel. This would be accomplished by loading the separate point with a third type of non-linear load (NOLIN3). This type defines a load as an exponential function of the displacement of a degree of freedom but only when it is a positive displacement. The displacement used to define this load must then be equal to the velocity of a point on the breech of the barrel. And NASTRAN has a very simple means of defining this equivalence called the transfer function.

The transfer function (TF) allows the user to define a linear relationship between the displacement and/or higher order time derivatives of it for a grid point and the displacement of an extra point (EPOINT) added for just this purpose. This procedure was tried on Watervliet's IBM computer with disastrous results as large oscillations of barrel motion built up. Several variations of the same arrangement were tried with the same results. The NASTRAN office at Langely, AFB could give no explanation. A test deck with twelve different combinations of derivatives defined by twelve different transfer functions was tested. Some results were reasonably good while others (those that related derivatives of unequal power) were not. A single case was tried on the NAVY's CDC computer at NSRDC and appeared to work. So the trouble was attributed to NASTRAN's use of a mixture of single- and double-precision subroutines on the

IBM computers. Since the size of the model (particularly the number of integration time steps) required that the final form be run on the larger CDC computer of the NAVY, the last obstacle appeared to be out of the way.

But when the problem was first run to check it out on the CDC machine, the same problem showed up after about one hundred time steps. The rate of growth of the problem was smaller but it was still there. The solution became very simple, however, when it was learned that the version of NASTRAN at NSRDC had been modified to allow non-linear loads to be based on velocity directly by simply adding ten to the associated degree of freedom when listing it on a NOLINI card. This enabled the counter recoil buffer to work as originally intended.

The model was run on NSRDC's computer for about sixteen hundred integration time steps which simulated a three round burst of fire. Data for various portions of the finite element model are shown in Table 1. Plots of some of the output are shown in Figs. 6 - 11. Since the structure has not been fully assembled, let alone fired, it is impossible to provide real data for comparison. It does appear from the data of muzzle motion that the weapon may be reasonably accurate but that the interval between firings may have to be adjusted to reduce dispersion. Current plans call for static and modal testing of the assembled weapon when available for comparison to NASTRAN.

The model itself is being updated with the inclusion of damping on the horizontal and vertical motion of the structure. The values to be used for damping are currently being determined from the comparative testing and modeling of an M68 Tank Cannon. The version of NASTRAN at Watervliet Arsenal has been modified to provide the critical non-linear velocity dependent loads and to run this problem as a series of successive segments of the overall integration time span. Further improvements in the model are anticipated to be inclusion of the bolt, bolt-carrier, and cam operation and an approximation of the mass transfer of the feeder mechanism. The model will be altered to include a constant recoil force mode and also mounting on a vehicle.

CONCLUSION

It has been shown that the finite element method as implemented by the NASTRAN computer program is capable of modeling weapon components with considerable accuracy. This has been demonstrated both by other user's success with the same elements and in certain portions of the development of the weapon model. It has also been shown that the user does not have to be directly involved with the analytical calculations of the model once the assumptions involved with the features of the program are understood and met. This approach to dynamic modeling can lead to a report lacking in mathematical expression but still containing results. In such an approach to modeling the actual physical dimensions become of secondary importance compared to the distinct features of the weapon and the means chosen to represent them. This particular model has shown that it can be used to represent a three round burst of fire. The final determination of accuracy awaits completion of the weapon and its initial testing.

REFERENCES

- Butler, T. G., et al; NASTRAN: A Summary of the Functions and Capabilities of the NASA Structural Analysis Computer Systems; NASA-SP-260; 1971.
- McCormick, C. S.; MSC/NASTRAN Basic Training Manual; The MacNeal-Schwendler Corp; 1975.
- MacNeal, R. H. ed; The NASTRAN Theoretical Manual; NASA SP-221 (01); 1972.
- McCormick, C. S., ed; The NASTRAN User's Manual; NASA SP-222 (01); 1972.

TABLE 1 - WEAPON PARAMETERS

Barrel Dimensions

Length	229.0 inches
Maximum Outside Diameter	8.7 inches
Minimum Outside Diameter	3.9 inches
Bore Diameter	2.4 inches
Weight	2050. pounds
Coupling Weight	220.0 pounds
Return Spring Weight	125.0 pounds

Bolt Carrier and Bolt Weight 65.0 pounds

Receiver Dimensions

Length	62.0 inches
Width	10.0 inches
Height, Maximum	18.5 inches
Weight	1550.0 pounds

Maximum Height of Truss

Above Receiver	24.0 inches
Above Base Plate	42.5 inches

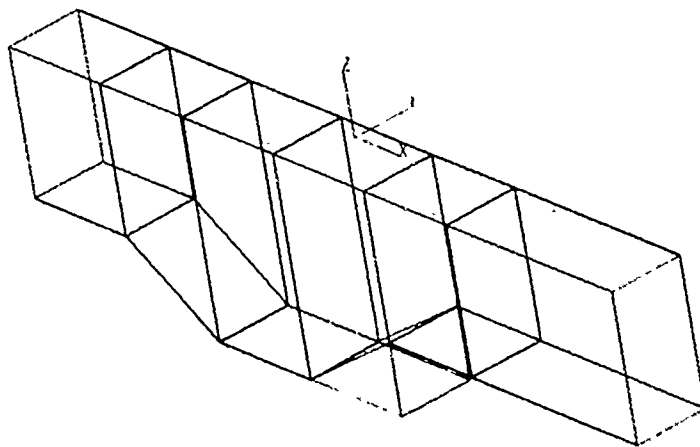


Figure 1. THE RECEIVER

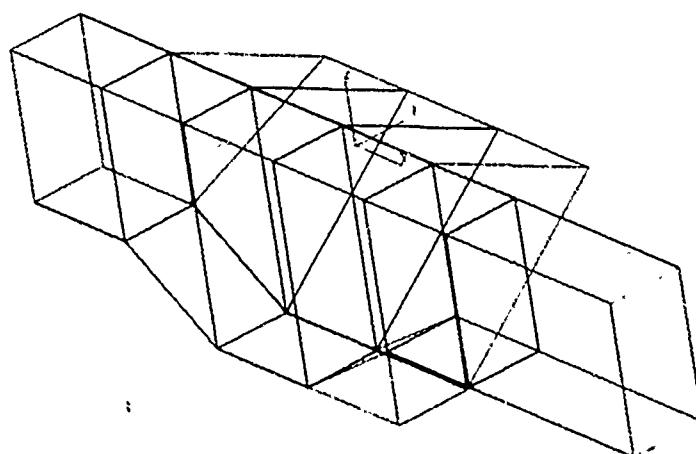


Figure 2. THE RECEIVER
WITH FEEDER HOUSING

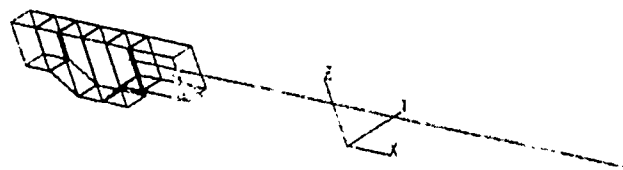


Figure 3. THE RECEIVER
WITH BARREL

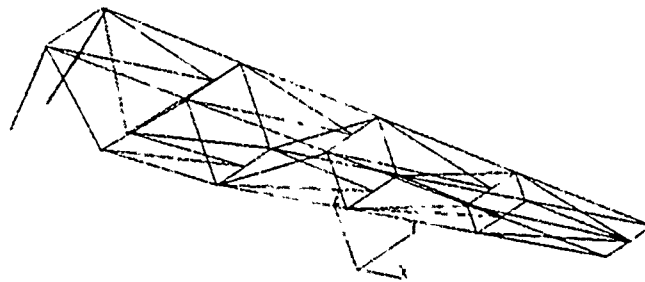


Figure 4. THE TRUSS

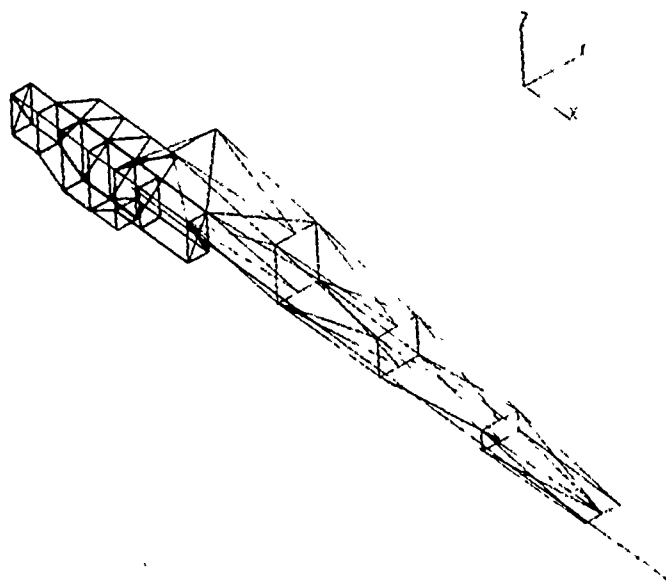
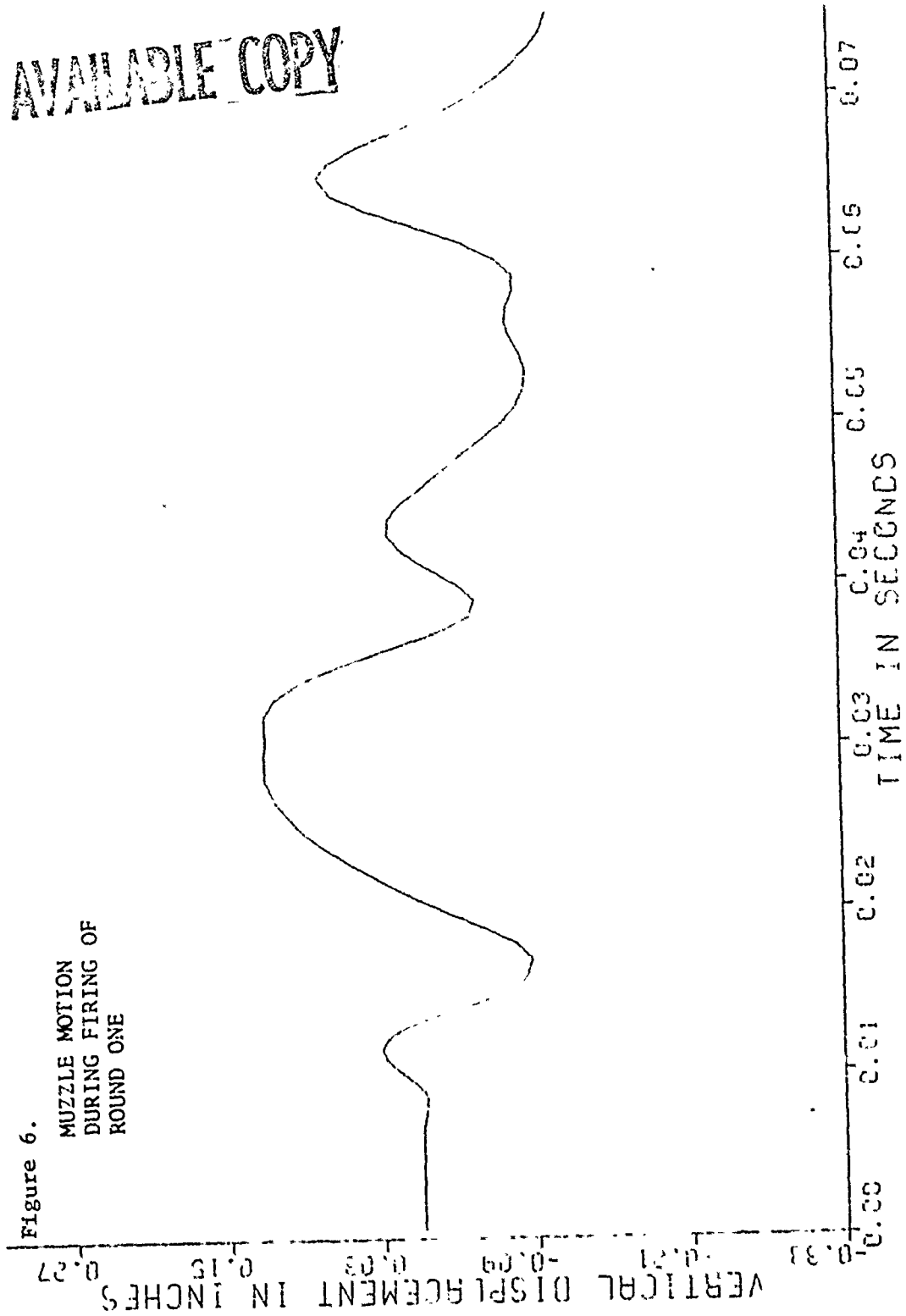


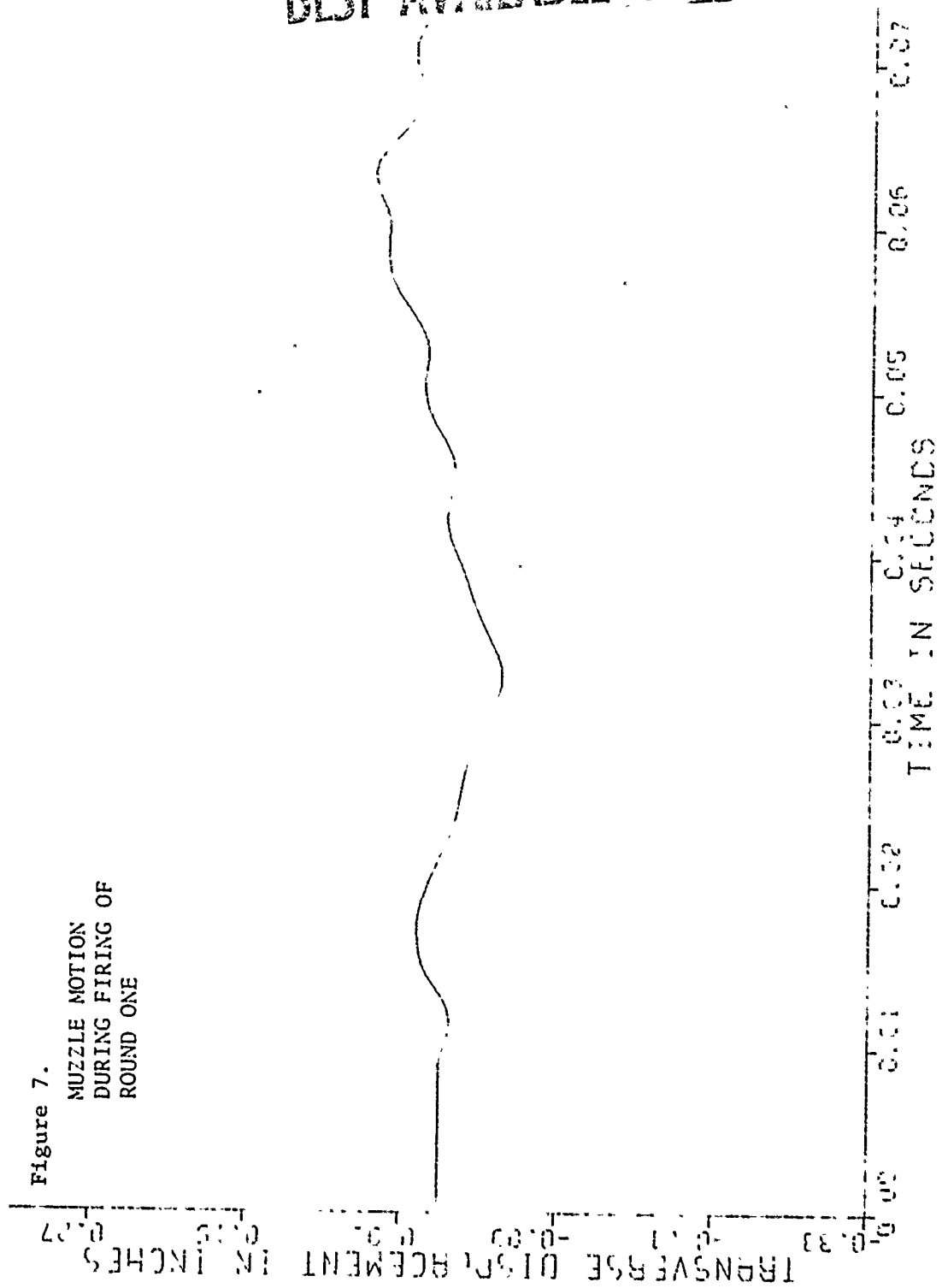
Figure 5. THE COMPLETE
MODEL

BEST AVAILABLE COPY



BEST AVAILABLE COPY

Figure 7.
MUZZLE MOTION
DURING FIRING OF
ROUND ONE



BEST AVAILABLE COPY

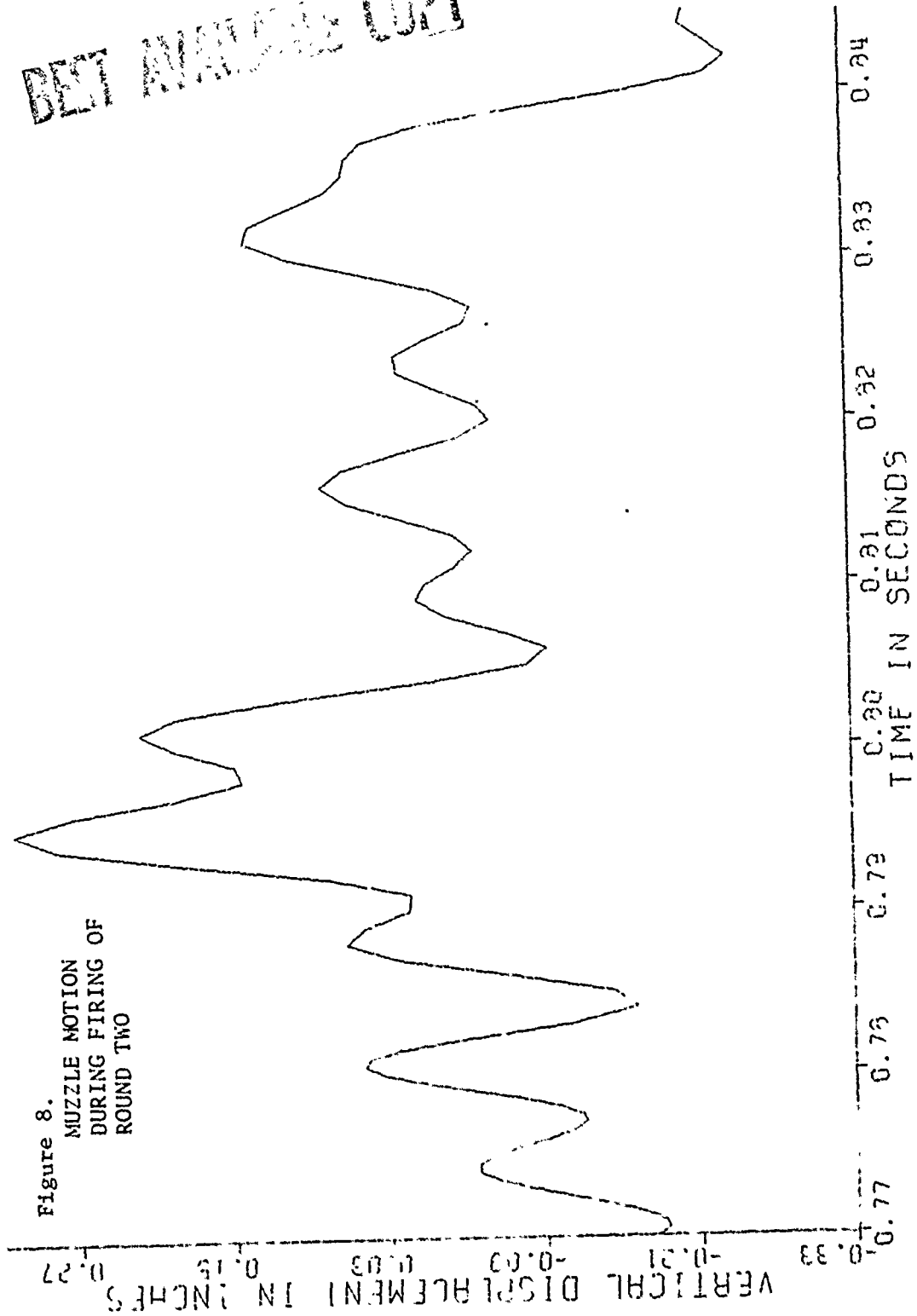
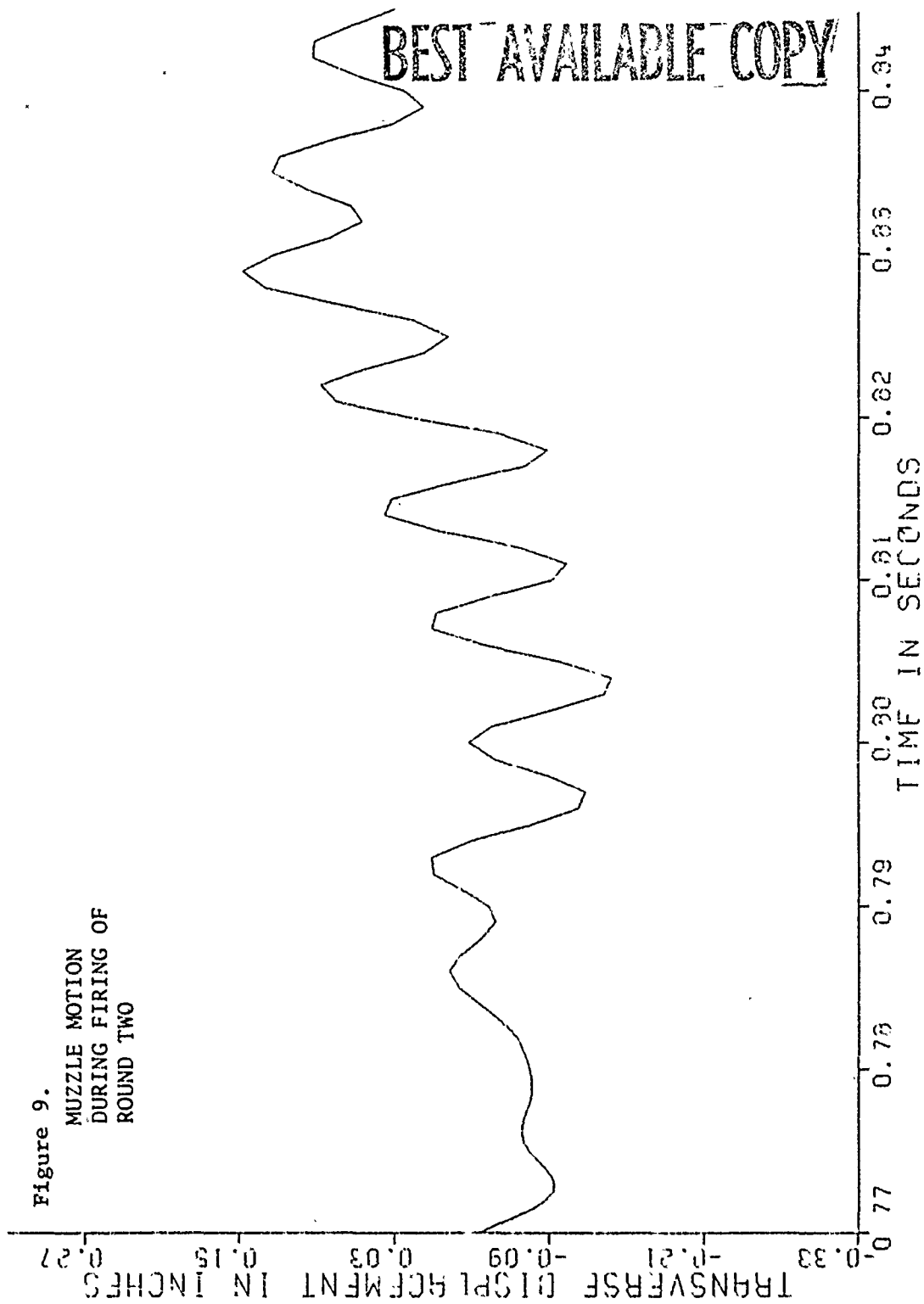
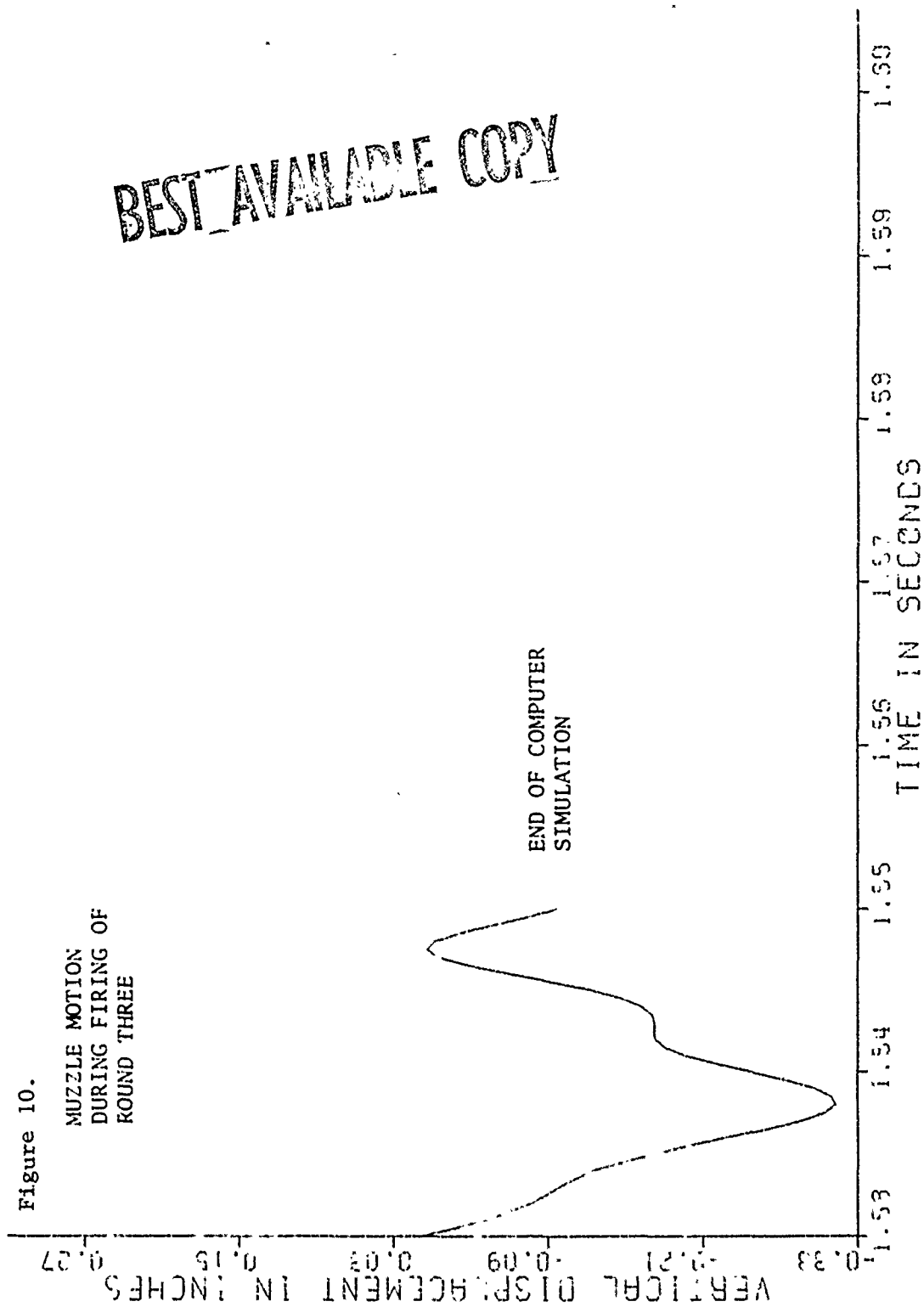


Figure 9.
MUZZLE MOTION
DURING FIRING OF
ROUND TWO

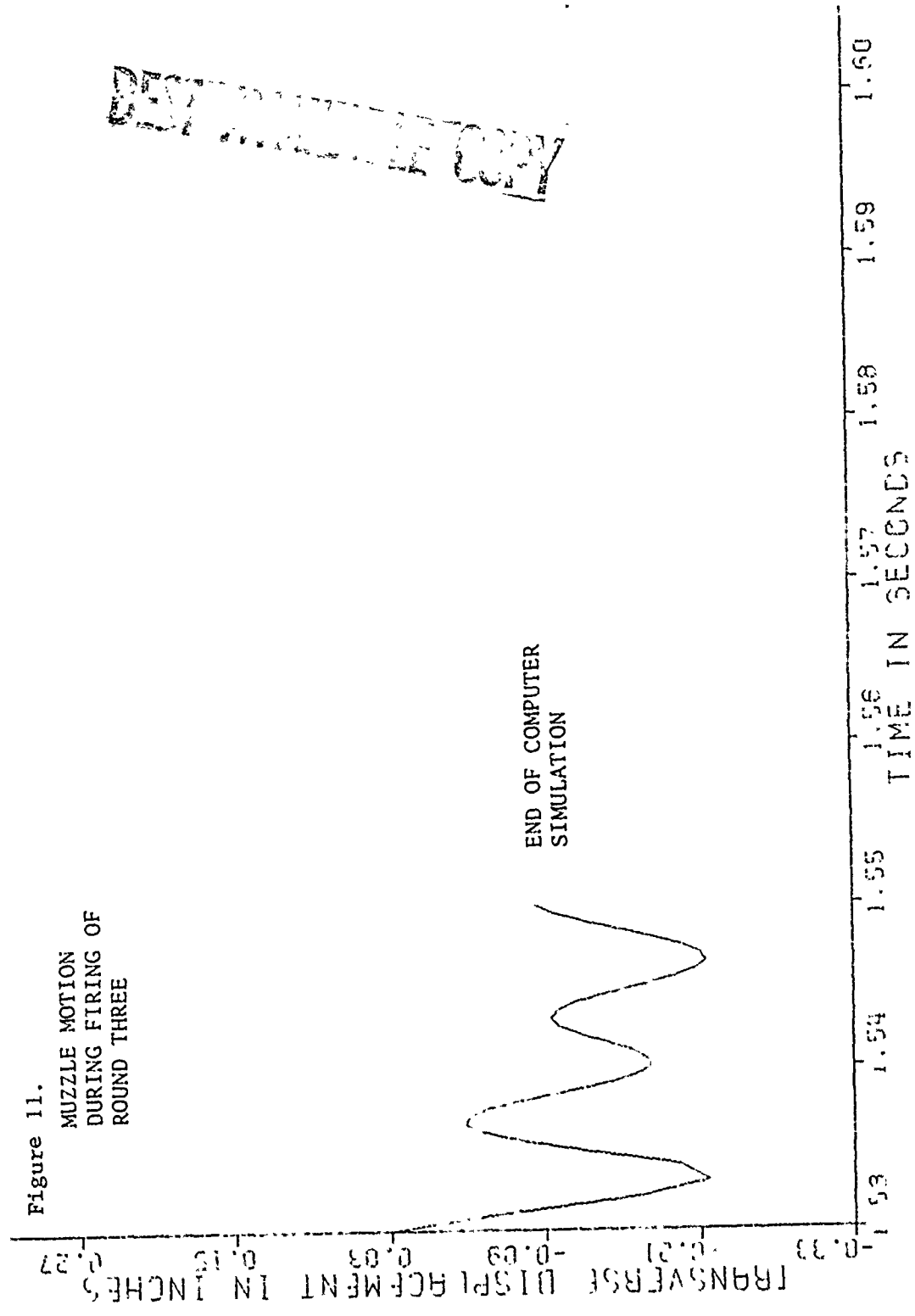


BEST AVAILABLE COPY



BEST AVAILABLE COPY

Figure 11.
MUZZLE MOTION
DURING FIRING OF
ROUND THREE



RADIAL AND TRANSVERSE RESPONSE OF GUN TUBES

BY FINITE ELEMENT METHODS

T.E. SIMKINS

Watervliet Arsenal

Watervliet, New York

TABLE OF CONTENTS

	<u>Page</u>
ABSTRACT	374
CHAPTER ONE	376
Section I - Finite Element Response of a 175mm (M113) Gun Tube to Ballistic Pressurization	376
Section II - Transverse Response of the M113 Tube to 'Bourdon' loads	396
References (Chapter One)	400
CHAPTER TWO	421
State of the Art in Moving Mass Problems	422
Continuum Description of the Moving Mass Problem	426
The Finite Element Displacement Method	428
Structure Equations of Motion	435
Boundary Conditions	440
Problem Statement and Solution	441
Results - Moving Force	446
Results - Moving Mass	450
References (Chapter Two)	459
APPENDIX - The Beam Equation for Transverse Motions of the M113 Tubes	461

ABSTRACT

RADIAL AND TRANSVERSE RESPONSE OF GUN TUBES BY THE FINITE ELEMENT METHOD

Previous work published by the author is reviewed treating several problems associated with in-bore ballistics and a limited comparison with experimental work accomplished more recently is also given.

The most ambitious work involves computation (via NASTRAN) of the radial response of a tube bore to travelling ballistic pressure. Tube geometry and ballistic pressures corresponding to the 175mm M113 gun tube were followed very closely. The computation employed an integration time step small enough to predict vibration activity as high as 20 khz - the upper limit of typical tape recording equipment. While such a time step leads to an inordinate amount of computer time, all results were achieved in a single computer run leading to a finely detailed set of response graphs at many stations along the tube. Comparisons with later test firing records show remarkably good agreement considering the limitations of the 250 degree of freedom model. Results indicate that the Lamé' design formula used for tube design errs on the unsafe side, stresses being greater than those predicted by this formula. The high state of vibrational activity actually evidenced in test records is predicted in the NASTRAN results.

Another study estimates the response of this slightly curved 175mm tube when exposed to the ballistic pressure function - the term 'Bourdon load' being coined in the process. Muzzle response in the

vertical plane is predicted as a function of time up through shot ejection. Further work develops the finite element technique for handling the moving mass aspects of the problem, treating the projectile as a moving point mass. A sample application of this work compares results with the only experiments of record - those of Ayre, Jacobsen and Hsu. Very good agreement with these results was obtained using only a few finite elements. Finally, a systematic derivation governing transverse tube motions is derived and incorporates the most comprehensive load set to date.

CHAPTER ONE

Section I of this chapter presents the radial displacement response of a 175mm (M113) bore surface to firing as computed by the method of finite elements. Experimental test firings of record are also offered for comparison. Section II employs a second finite element model to explore the transverse response (vertical plane) of an initially curved tube following a sudden internal pressurization. Both Sections I & II of this chapter employ the NASTRAN finite element code and no recognition is given to the presence of projectile mass. In Chapter Two, however, it is shown how the method of finite elements may be used to account for inertial effects induced by the projectile as a moving mass. NASTRAN - it turns out - is unsuitable for this purpose, however, and a special finite element code was necessary.

SECTION I - FINITE ELEMENT RESPONSE OF A 175MM (M113) GUN TUBE TO BALLISTIC PRESSURIZATION

Statement of the Problem:

The problem is defined as follows:

An isolated 175mm gun tube, open at each end and unsupported or unconstrained in any way, is loaded along its interior bore surface by radially applied interior ballistic pressure. In addition, the rearward thrust of the ballistic pressure is applied axisymmetrically over the breech end of the tube. (No account of the breech plug is included.) The ballistic pressure input to the problem is computed from FORTRAN program, IBAL, authored and refined at Watervliet Arsenal. The loading

(and geometry) is fully axisymmetric and can be conceived as a time-variant pressure following the motion of a fictitious projectile. Other than defining the region of pressurization in time, the 'projectile' has no additional purpose or properties. No structural damping or temperature effects are included in the problem and the primary objective is to predict the radial displacements of the bore surface in response to the ballistic pressure load.

NASTRAN Problem Definition:

From the problem as defined above, the NASTRAN formulation is composed. As in any finite element technique, the body of interest is divided into a number of elements each of which deforms according to a general law when either forces or displacements are prescribed along portions of its boundaries. This deformation law is not completely arbitrary in that the deformation must retain continuity across the boundaries between elements and furthermore the explicit formulation of the law should satisfy some principle of mechanics - such as virtual work, minimum energy, etc.

In the NASTRAN model for the 175mm tube, 62 trapezoidal ring elements are utilized - creating a problem of 250 degrees of freedom. These ring elements (see Figure 1) are axisymmetric and can only be used in cases where the

applied loads and deformations are also axisymmetric. Consequently any transverse deformations of a gun tube during firing must be treated using elements of a different type. The latter of course, fall beyond the scope of work to be reported in this section. In Section II however, some of the rudimentary aspects of transverse tube behavior are treated.

The discretization of tube geometry is rather straight forward and is shown in figure 2. Bore stations or Grid Points, are listed in Table I. Discretizing the load - which is travelling along the bore at projectile velocity - is not as simple and presents some unusual and interesting considerations.

The ballistic load function falls within the general category of travelling loads. Each element of the finite element model therefore, receives in turn a time-variant loading. While this in itself is not an unusual condition to be modeled by Nastran, the matter of transforming a continuous pressure distribution to discrete loads acting at the element attachments, i.e., the Grid Points, creates a bit of a problem. In statics for example, the engineer may discretize a pressure distribution by some intuitive averaging procedure, perhaps with the aim of preserving force or moment equipollence at some particular station. In finite element theory however, there is only one

TABLE I
BORE STATIONS
(GRID POINTS)

<u>Grid Point No.</u>	<u>Distance from Muzzle</u>	<u>Distance from Breech</u>	<u>Grid Point No.</u>	<u>Distance from Muzzle</u>	<u>Distance from Breech</u>
1	413	0	64	203	210
4	406	7	66	196	217
7	399	14	68	189	224
10	392	21	70	182	231
12	385	28	72	175	238
14	378	35	74	168	245
16	371	42	76	161	252
18	364	49	78	154	259
20	357	56	80	147	266
22	350	63	82	140	273
24	343	70	84	133	280
26	336	77	86	126	287
28	329	84	88	119	294
30	322	91	90	112	301
32	315	98	92	105	308
34	308	105	94	98	315
36	301	112	96	91	322
38	294	119	98	84	329
40	287	126	100	77	336
42	280	133	102	70	343
44	273	140	104	63	350
46	266	147	106	56	357
48	259	154	108	49	364
50	252	161	110	42	371
52	245	168	112	35	378
54	238	175	114	28	385
56	231	182	116	21	392
58	224	189	118	14	399
60	217	196	120	7	406
62	210	203	122	3.5	409.5
			124	0.	413

procedure that is consistent with the finite element formulation per se and even this procedure is only correct when the loads are statically applied. For dynamic loading conditions there is no truly consistent procedure for discretizing continuous load distributions. In view of this fact and the approximate nature of the assumed linear displacement function by which an element is forced to deform, it is questionable as to how far one can trust the conventional procedure of producing statically consistent discrete loads to replace the pressure distribution. (The displacement function is directly used in this procedure).

In view of these arguments it seemed expedient and justifiable to describe the travelling load intuitively, rather than to work through the statically consistent procedure. Only after the final computer run was performed, was time taken to compare the two methods of load description.* As it turned out the loads calculated by either procedure differ by an average amount of only 8.3% and the total load applied to an element at any given time is the same by either calculation. Discontinuities in loading rate, present in the intuitively derived load functions, may tend however, to favor the excitation of natural frequency vibrations in the results.

* See Comparison, Appendix A.

Load Definition:

Along with each of the grid points to receive a load, we assign a domain of load definition. If the ballistic pressure (at some point in time) is applied over all or part of the bore surface contained within this domain, then the corresponding grid point receives a load. The value of the load is made proportional to the fraction of the domain exposed to the pressure. In the NASTRAN model the domains of each loaded grid point extend between the mid-planes of the trapezoidal elements as shown in figure 3. Thus as the 'projectile' (i.e., the ballistic pressure) arrives at a location midway between say, Grid Points 42 and 44, a load begins to build at Grid Point 44. The load at all times will be proportional to the amount of penetration into the domain $\dots x/\ell$ where ℓ is the length of the grid point domain of load definition.

In practice the grid point loads are tabulated vs. time and because of their number and irregular character, a great deal of load data is required for an accurate modeling of the load condition.

NASTRAN SOLUTION FORMAT

The transient response in the radial direction is sought at stations along the bore axis of the tube. In

NASTRAN one has a choice of two transient response formats... Rigid Format Number 12 entitled "Modal Transient Response" and Rigid Format Number 9 - "Direct Transient Response". The former is more approximate than the latter unless all of the vibration modes are employed in the solution in which case the two formats involve virtually the same amount of computation. If a modal transient response calculation is to be made, the user must be sure that enough modes are employed to yield the accuracy demanded. Because of the spatial distribution of the instantaneous load applied to the 175mm tube, a modal transient response calculation is not practical since an accurate description of the deformation of the bore surface would require a large number of eigenvectors - even though their corresponding frequencies may remain virtually unexcited.¹ The only other choice is therefore to actually integrate the two-hundred and fifty coupled equations of motion - NASTRAN's Rigid Format Number 9.

The main decision to be made in using the direct integration algorithm concerns the choice of the time step to be used in the numerical integration procedure. Even though the algorithm employed by NASTRAN is Unconditionally stable (i.e., no unbounded quadratures will result) gross errors will result unless the time step of integration is

¹ BURTON, R., Vibration and Impact (1958), Addison-Wesley, p. 261.

chosen sufficiently small. Since one is generally seeking the integrations over a specific time length, i.e., the ballistic period, smaller time steps imply a corresponding increase in the number of iterations required. This in turn is limited by available funds and computation time. The time step for this problem was chosen on the basis of the largest loading rate present in the problem. Since this loading rate is nearly proportional to the projectile velocity, the rate will achieve its greatest value near the muzzle where the load varies from zero to full value in roughly 250 microseconds. To describe this load in fine tabular detail, minimizing sharp 'corners' or discontinuities, the time step was chosen as 10 microseconds. Such a time step would also clearly define any response as high as 15 khz. It can also be shown that a time step of this value is sufficient to predict a response over 36 periods of the lowest natural frequency with an error not exceeding 10% in amplitude or phase in all frequencies up to ten times the fundamental. For details of this appraisal the reader is invited to examine section 11.3 of the NASTRAN Theoretical Manual.

MATERIAL PROPERTIES AND INITIAL CONDITIONS

Only the simplest material properties were assumed for the model:

$$E = \text{Young's Modulus} = 30 \times 10^6 \text{ psi}$$

$$\nu = \text{Poisson's Ratio} = 0.3$$

The initial conditions of velocity and displacement are null.

PROGRAM OUTPUT

Of the 124 grid point locations defined within the NASTRAN model of the 175mm tube, radial displacement and load output was requested from 32 of the 61 grid points along the bore surface. The output was requested on magnetic tape as well as 35mm film - ready for slide mounting. 8-1/2" x 10" plots were made from this film and the corresponding X-Y data printed from the magnetic tape. The printed output for the problem solution is quite voluminous and therefore only seven load and response curves will be presented in this report - four for discussion purposes and three for comparison with instrumental test firings at Aberdeen and Yuma Proving Grounds. The loads and responses at these points are generic to the extent that those at other bore stations can be understood in similar terms.

DISCUSSION - Grid Point 10

Figure 4 shows the pressure (lower curve) and displacement as functions of time at Grid Point 10 located in the breech, to the rear of the projectile at all times. Superposed is the displacement as conventionally computed for

design purposes via the static Lamé solution.² This solution corresponds to a uniformly pressurized, infinitely long uniform tube of cross section equal to that at the grid point under discussion, i.e. GP 10.

One first notes that due to its location aft the projectile, GP 10 receives pressure continuously and smoothly from time zero. Consequently the rate of load application at this station is only dependent upon the rate at which the burning propellant produces pressure and not on the velocity of the projectile (except possibly in a very secondary way). Thus the rate of load application at GP 10 is not nearly as severe as that at grid points located further along the bore.

The next item of note is the increasingly apparent excitation of a natural frequency of approximately 2600 hz as time continues through the ballistic period. We will see later that this frequency agrees quite well with the observed frequency of 2380 hz in the BRL records. In that no structural damping has been included in the model, one is not surprised that the predicted frequency is somewhat higher than that produced during these actual test firings. Superposed on the 2600 hz frequency is a 'beat' whose frequency is estimated at about 130 hz. This beat frequency appears at different values as one observes from stations further along the bore. At GP 56 we estimate this frequency at about 400 hz and at GP 64 - 600 hz.

²ROARK, R. J., Formulas for Stress and Strain, 2nd Edition, McGraw Hill Book Company, Inc.

The production of beats suggests that several natural frequencies exist close in value to the observed 2600 hz vibration. To determine if indeed this is the case, a NASTRAN eigenvalue analysis was applied to the finite element model. The results are shown in figure 5 in the form of a frequency density distribution. Together with a plot of projectile velocity versus bore travel (figure 6) one not only gains insight to the production of beats but also the reason for the observed vibrational behavior at about 2600 hz.

As figure 6 shows, the projectile velocity exceeds 2600 ft/sec. over the latter half of bore travel. Velocities of this magnitude are clearly sufficient to create Grid Point loading rates large enough to excite natural frequencies in the neighborhood of 2600 hz, i.e., the observed vibration. That there indeed exist a multitude of frequencies near this value is born out by the frequency density plot which shows no less than 17 natural frequencies between the values of 2400 and 2800 hz. All of these are excitable by the projectile velocity which exists throughout the latter half of bore travel and easily combine to form the observed beat phenomena. The existence of beats has physical significance in that a beat amplitude surpasses that of either of the amplitudes of the component vibrations.

A third point of interest is the comparison between the response predicted by the Lamé solution and that from the NASTRAN model. The Lamé response is conservative in that it exceeds the time-averaged dynamic response. The explanation is that the Lamé problem assumes the pressure to be uniform throughout the entire length (infinite) of the tube. In reality - and in the NASTRAN model - the pressure only exists of course, in the region to the rear of the projectile. The non-pressurized region in front of the projectile tends to assume its unloaded configuration exerting a contractile effect on the region to the rear of the projectile. Only when there exists a considerable input of kinetic energy to a vibration mode of period close to the rise time of load application, will the Lamé peak displacement be exceeded. It is evident that this condition is not fulfilled at GP 10. We shall witness different behavior further down-bore.

Grid Point 24

Figure 7 shows the pressure (lower curve) and displacement at GP 24, not far in front of the projectile prior to firing. The distinctive feature as compared with GP 10 is the time delay prior to load application at this station. During this delay period a negative, i.e., inward, radial displacement occurs at this grid point. This is caused by the existence of adjacent pressurized and nonpressurized

regions. The Lamé counterpart cannot of course predict such a displacement since all regions of the tube are assumed uniformly pressurized.

At approximately 6.5 milliseconds following ignition, the 'projectile' passes GP 24 exposing this portion of the surface (i.e., the load domain of GP 24) to the pressure of the propellant gas. Thus the initial time rate of load application at this station is determined almost wholly by the value of the projectile velocity at this time rather than the propellant burn characteristic as at GP 10.

In all other respects the response at Grid Point 24 is similar to that previously described at Grid Point 10.

Grid Point 72

Figure 8 shows the pressure (lower curve) and displacement - Nastran and Lamé - at Grid Point 72, located roughly half way down the tube bore. As at GP 24 we observe a negative displacement until the projectile passes the station approximately 15 milliseconds following ignition. At this time the projectile possesses a rather large velocity creating a rapid time rate of pressurization at this location. The rate is great enough to appreciably excite the observed natural frequency (approx. 2600 hz), causing a peak response 35% greater than that predicted by the Lamé solution.

Grid Point 120

Grid Point 120 is only 9 inches from the muzzle end of the tube. The maximum pressure (figure 9) is seen to be roughly half that at GP 72. Consequently, the negative radial displacement prior to the arrival of the projectile is correspondingly less. The high velocity of the projectile, however, causes great excitation of the 2600 hz natural frequency oscillation. This results in a NASTRAN radial displacement which exceeds the static Lamé computation by nearly 50%.

Again we observe a strong 'beat' at this grid point. To what degree such beats are actually realized in practice is clearly a matter which should be determined.

COMPARISON WITH PREVIOUS TEST FIRINGS OF RECORD

The NASTRAN model of the 175mm tube was formulated and computer-executed prior to the examination of any particular experimental results. With the NASTRAN-predicted response in hand, a request for experimental results of test firings was made to Mr. Herman Gay of the Ballistic Research Laboratories, Aberdeen, Md. Mr. Gay recommended BRL Technical Note No. 1722 authored by Mr. John M. Hurban in September 1969. Mrs. Joyce Mayo of the Watervliet Arsenal Technical Library was quick (as always) to provide a copy of this report.

The BRL note reports on the response of strain gages mounted on the exterior surface of a 175mm gun tube. This tube differed slightly from that used for the NASTRAN model. The presence of a breech and tube support created further dissimilarities. Nevertheless, surprisingly close agreement was achieved wherever quantitative and qualitative comparisons could be made.

Figure 10 shows the strain gage response to the firing of a zone 3 charge,^{*} at several stations along the tube exterior. Complete quantitative comparison with the BRL results is not possible here since the ordinate is "pressure" rather than strain or displacement as in the NASTRAN results. This so called "pressure" is computed from the measured strains ϵ_θ , ϵ_z according to the relation:

$$P = \frac{E(W^2-1)}{2(1-\nu^2)} [\epsilon_\theta + \nu \epsilon_z]$$

where W is the wall ratio at the particular station where ϵ_θ , ϵ_z are measured and E , ν are Young's modulus and Poisson's ratio. If, however, it is assumed that $\epsilon_z \ll \epsilon_\theta$ then the ordinate used in the BRL report is approximately proportional to ϵ_θ , and the NASTRAN-predicted radial displacement response at stations along the bore surface differs only by a scalar multiplier from this exterior circumferential strain. Thus the two may be qualitatively compared.

^{*}The load functions used in the NASTRAN model also correspond to a Zone 3 charge.

In comparing the NASTRAN results (Grid Points 34, 48, 68 - figures 11, 12, 13) with similarly located stations 4,5,6 of the 175mm tube used by BRL, one first notes the negative ordinate values prior to the arrival of the projectile at each of these locations. Good qualitative agreement can easily be observed. Next we see that NASTRAN successfully replicates the abrupt loading condition experienced at each station as the projectile passes. Finally, figure 7 yields an estimated natural frequency of 2380 hz visible mostly during the latter portion of the ballistic cycle. This compares closely with the 2600 hz prediction of the NASTRAN model. (Including structural damping into the model should provide even closer agreement).

The amplitude of the oscillation as predicted by NASTRAN is considerably greater than that in evidence in figure 10 - the BRL results. In connection with this it is interesting to compare the BRL results at the same stations when a Zone 2 charge was fired. Figure 14 shows these results and it is immediately obvious that the amplitude of the natural frequency oscillations is greater than that observed from figure 10. This is surprising in that a zone 2 charge is weaker than a zone 3 charge. The explanation was provided when it was learned that BRL employs a filtering technique in the process of analogue to digital conversion.

Conversations with Mr. John Hurban - author of the BRL work - indicated that the extent of such filtering is not known at this time. He allowed, however, that the degree of filtering employed could very well vary from case to case.

Table II shows the maximum bore expansions from the BRL report. As noted, the results correspond to a Zone 1 type charge and stations 5 on tube numbers 4136 and 4137 are at the same location as station 4 on tube number 1185; i.e., all stations are 259 in. from the muzzle end of the tube (corresponding to NASTRAN Grid Point number 48). A computation of the Lane displacement at this point agrees within 12% with Nastran results (figures 11 and 12) so that one does not expect a great deal of dynamic effect on bore displacements at this location. Consequently one might also expect good agreement between the NASTRAN predicted displacements and those measured and reported in Table II - in spite of the use of filtering. However, the difference between NASTRAN's assumed Zone 3 charge and the Zone 1 charge used in these test firings must of course be accounted for. The peak pressure ratio for these two charges is 0.218^3 . If the Nastran peak response of .007 in. is multiplied by this ratio, the result gives a .0015 in. expected bore expansion for a zone 1 charge - a figure which agrees quite well with those listed in the right hand column of Table II.

³ANDERSON, H.B., Aberdeen Proving Ground, Development and Proof Services Report No. 1375, Eleventh revision, Jan. 1968.

TABLE II

MAXIMUM BORE EXPANSIONS - BRL DATA

<u>TUBE NUMBER</u>	<u>STRAIN GAGE STATION*</u>	<u>LAND DIAMETER (IN.)</u>	<u>GROOVE DIAMETER (IN.)</u>	<u>RADIAL BORE EXPANSION (IN.)</u>
4136	5	6.891	7.036	0.0012
4137	5	6.891	7.035	0.0013
1185	4	6.892	7.032	0.0014

*ALL STATIONS CORRESPOND TO GRID POINT NO. 48 WHERE A PEAK DISPLACEMENT OF .007 IN. IS PREDICTED VIA NASTRAN (ZONE 3 CHARGE).

USING THE PEAK PRESSURE RATIO FOR ZONES 1 & 3:

$(.007)(.218) = .0015$ " WHICH AGREES FAIRLY WELL WITH THE ABOVE DATA TAKEN FROM 1968 BRL TESTS.

It is a matter of considerable importance that the true degree of natural frequency excitation be assessed - for it is this excitation which is responsible for the major difference between the peak response as predicted by the NASTRAN model and that estimated by the Lamé solution. A review of figure 8, for example, shows that the 35% increase in peak response as compared to that predicted from the Lamé formula is entirely due to excitation at this 2600 hz frequency. Filtering the strain gage response at or below this 2600 hz frequency level could very well lead to erroneous and possibly unsafe conclusions. Mr. Hurban found that the original unfiltered analogue tape recordings no longer exist. More recently, however, new tests at Yuma Proving Grounds have been conducted and a comparison verifies our suspicions.

Owing to the unknown degree of filtering employed in the BRL test records, it was highly desirable that new tests be conducted without filtration. This opportunity arose in the Spring of 1974 when M113 firings were scheduled (for other purposes) at Yuma Proving Grounds. Watervliet Arsenal succeeded in their request to have strain gages mounted along the outer surface of the tube at four axial stations. Figures 15 and 16 show the experimental results at stations #3 and #4 which correspond to grid points #72 and #120 (Figure 8 & 9). It was gratifying to observe natural

frequency excitations far in excess of these of the filtered BRL records. The general similarity of these experimental records with those produced by the NASTRAN model is apparent. Two prominent comparisons are the production of large amplitude 'beats' and the possibility that the phase of a natural oscillation may be such as to produce an extraordinary strain above the Lane value immediately upon passage of the projectile at a particular station. Such phase agreement is unfulfilled in figure 15 but is clearly evident in figure 16. In that no damping was employed in the NASTRAN model, the generally larger amplitudes of vibration in figures 8 and 9 are to be expected. The dominant frequency excited in the NASTRAN model which is in excellent agreement with the BRL test records, does not at all agree with that appearing in the YPG results - the latter being done to 1600 hz and the former near 2600 hz as previously noted. The discrepancy can be explained by the fact that the tube fired at YPG has a considerably thinner wall than that employed in the NASTRAN model.

SECTION II - TRANSVERSE RESPONSE OF THE M113 TUBE TO

'BOURDON' LOADS

In addition to the radial response of the M113, some progress has been made in estimating the transverse response to a pressure load along the bore surface.

As a first approach we have imagined the 175mm tube to be in a state of readiness, inclined to the vertical as shown in figure 17. Only the bore axis is depicted here - the curvature (exaggerated) being due to the action of gravity (vernacularly referred to as 'droop'). Because of this initial deformation at least three non-elementary forces act upon the tube when fired - the so-called 'Bourdon' force (due to unequal upper and lower bore surface areas), the recoil acceleration moment, and the forces due to the curved path traversed by the projectile while in-bore. A fourth non-elementary force arises due to the action of the gravity on the moving, in-bore, projectile. In addition to these (and possibly others) one also has the elementary forces of transverse beam inertia as well as the constant gravitational force acting directly on the tube. The resulting equation of motion* - based on the beam flexure formula is:

$$(EIy'')'' + K(x,t)y'' - [\rho g A \sin \alpha][(x-L)y']' + \\ + M_p[\ddot{y} + 2V_p y' + V_p^2 y'' + g \cos \alpha] \delta(x-V_p t) + \rho A y - \rho g A \cos \alpha$$

*For complete derivation see Appendix.

In order to obtain some idea as to the motion to be expected from say, the 'Bourdon' loading, we have treated a simplified case in which only the 'Bourdon' load acts in conjunction with gravity upon the tube. If we let $\alpha = 0$, the equation of motion reduces to:

$$(EIy'')'' + K(x,t)y'' + \rho A \ddot{y} = -\rho Ag$$

with initial conditions $y(x,0) = Y(x)$ and $\dot{y}(x,0) = 0$ and boundary conditions corresponding to a cantilevered beam. $Y(x)$ is the 'static' deformation due to gravitational forces acting upon the structure prior to $t = 0$. To keep the problem as simple as possible in this first attempt we consider a Bourdon loading which arises from the application of a uniform ballistic pressure applied stepwise in time at $t = 0$ along the entire bore surface of the tube. Choice for the amplitude of the step was more or less arbitrarily based on the time-averaged value of the ballistic pressure cycle for the M113; $P_{av} = 13,420$ psi. As shown in the Appendix this leads to a Bourdon term in the previous equation of motion:

$$K(x,t)y''(x,t) = P_{av}\pi a^2 y''(x,t)$$

Except for this term, the equation of motion can be viewed as a typical beam problem which, if one so chooses, can be solved via NASTRAN. Provided that the above distributed Bourdon load can be discretized into concentrated loadings at the nodal (grid) points of a finite element beam model

of the M113, the Bourdon forced motion problem can be made amenable to NASTRAN solution also. The discretization of any distributed loading over the surface of an element can be accomplished as follows:

The concentrated 'forces' at the nodes of a finite element may be obtained from knowledge of any distributed loading $f(\xi)$ through the following relation:

$$\underline{F} = L \int_0^1 \underline{a}^T f(\xi) d\xi$$

where ξ is the non-dimensional length variable x/L and L is the beam element length. $\underline{a}(x)$ is defined through the relation:

$$y(x) = \underline{a}(x) \underline{U}$$

where \underline{U} is the vector of nodal displacements for the element. In a finite beam element $\underline{a}(x)$ is determined 'exactly' by solving for $y(x)$, the transverse displacement of the element, given the imposed displacements \underline{U} (generalized) at the ends (nodes) of the element.

Utilization of these formulae will result in a force vector \underline{F} having the form $\underline{F} = \underline{\alpha} \cdot \underline{U}$; i.e., a form accommodated by one of the NASTRAN load formats (NOLIN2). Thus the problem of Bourdon-forced excitation of a non-uniform beam may be converted to finite-element form suitable for solution via the NASTRAN finite element program.

An eighteen-element beam model of the M113 tube was employed for solving the previously described problem. The details of this model and the preparation of the load input to the program will be covered in a later report which will also deal with more realistic ballistic functions-a task which presents only moderate difficulty.

Figures 18 and 19 show the NASTRAN results for this case of infinite projectile velocity and constant pressure loading. In figure 18 we show the shape of the M113 at shot ejection (estimated to occur at about 25 milliseconds after ignition) whereas figure 19 shows the predicted muzzle movement in time.

REFERENCES - CHAPTER ONE

1. BURTON, R., Vibration and Impact (1958), Addison-Wesley, p. 261.
2. ROARK, R. J., Formulas for Stress and Strain, 2nd Edition, McGraw Hill Book Company, Inc.
3. ANDERSON, H. B., Aberdeen Proving Ground, Development and Proof Services Report No. 1375, Eleventh revision, Jan. 1968.
4. HILDEBRAND, Advanced Calculus for Engineers, p. 353.
5. SIMKINS, T., PFLEGL, G., SCANLON, R., Dynamic Response of the M113 Gun Tube to Travelling Ballistic Pressure and Data Smoothing as Applied to XM150 Acceleration Data - WVT-TR-75015, April 1975.

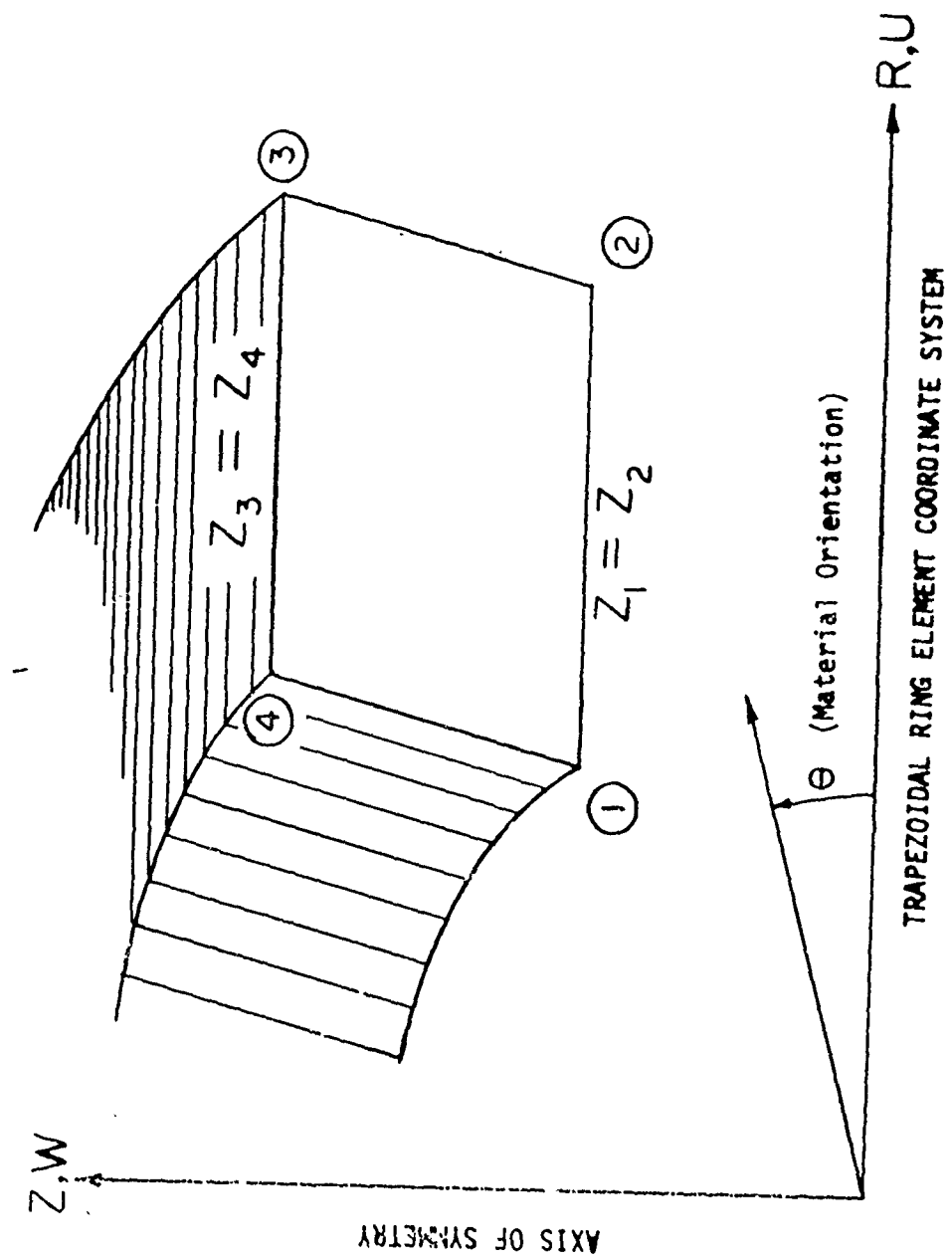


Figure 1. Ring Elements Used in NASTRAN Analysis.

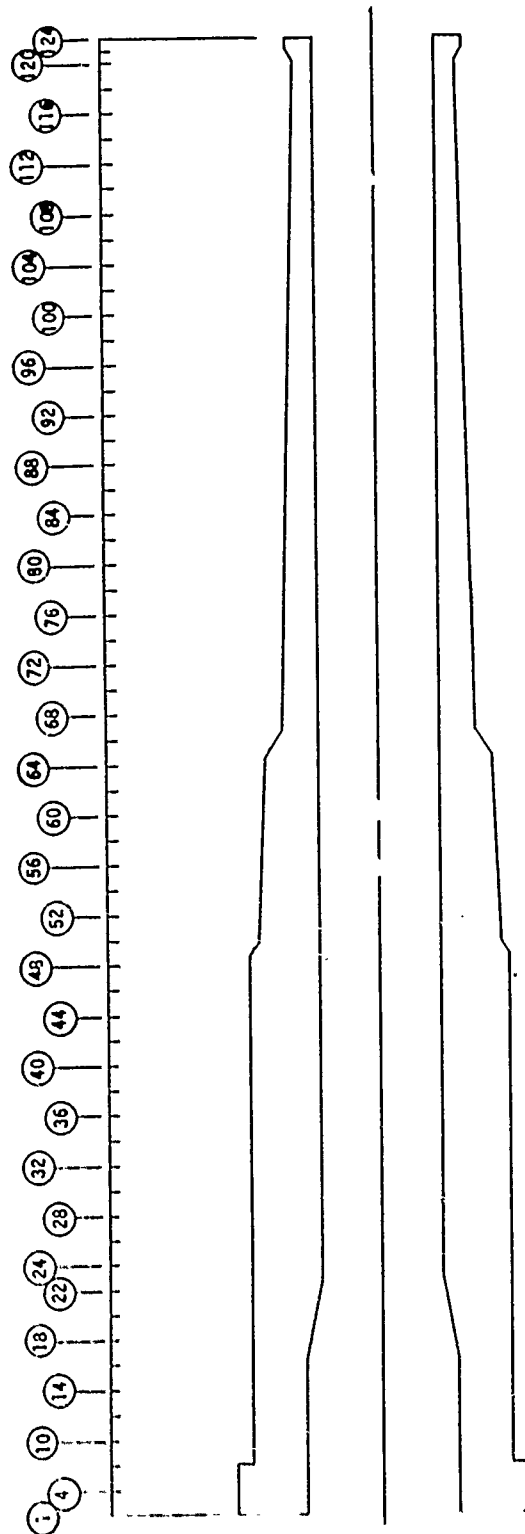


Figure 2. Finite Element Representation of M113 Gun Tube.

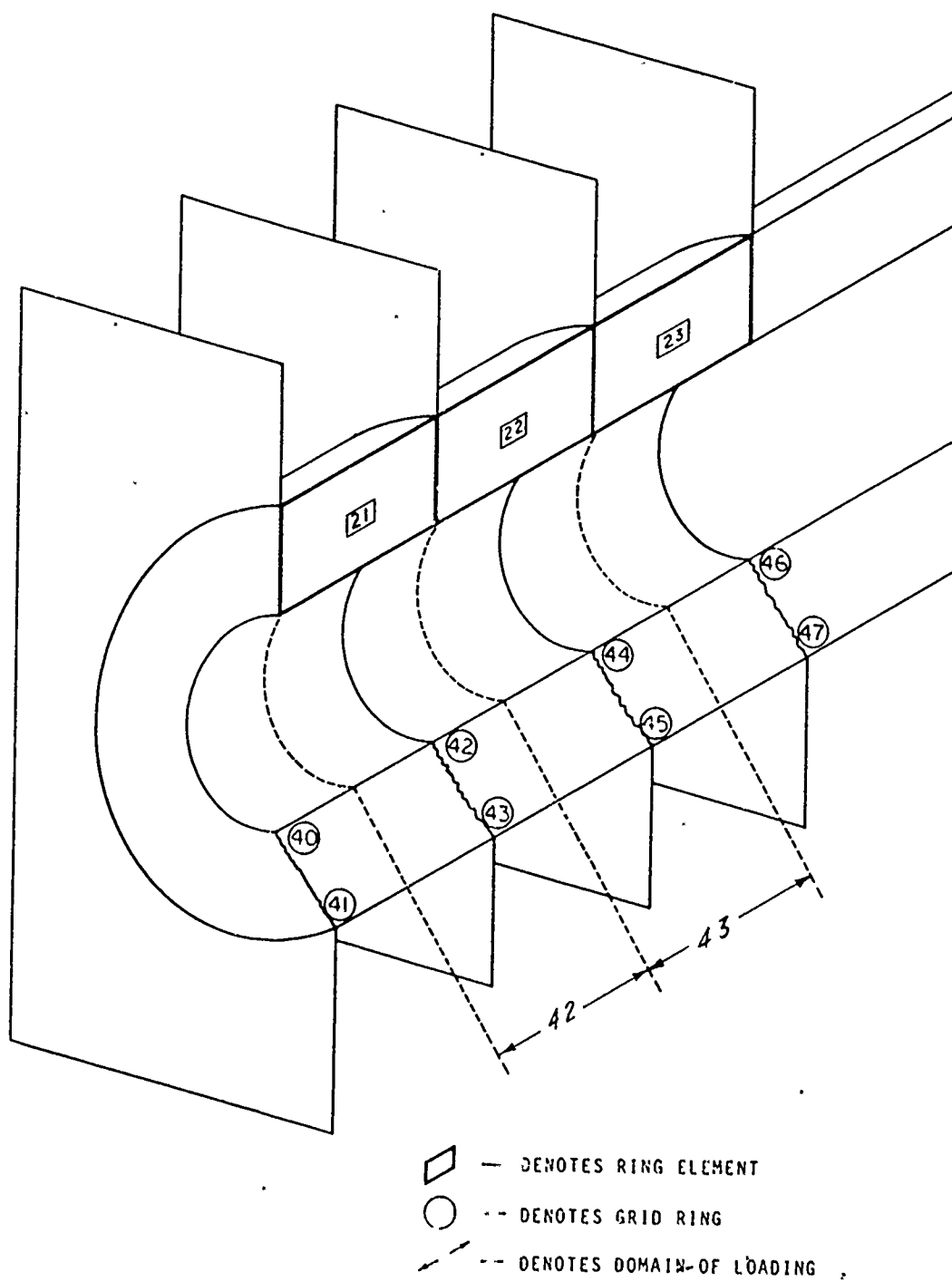


Figure 3. Domains of Load Definition.

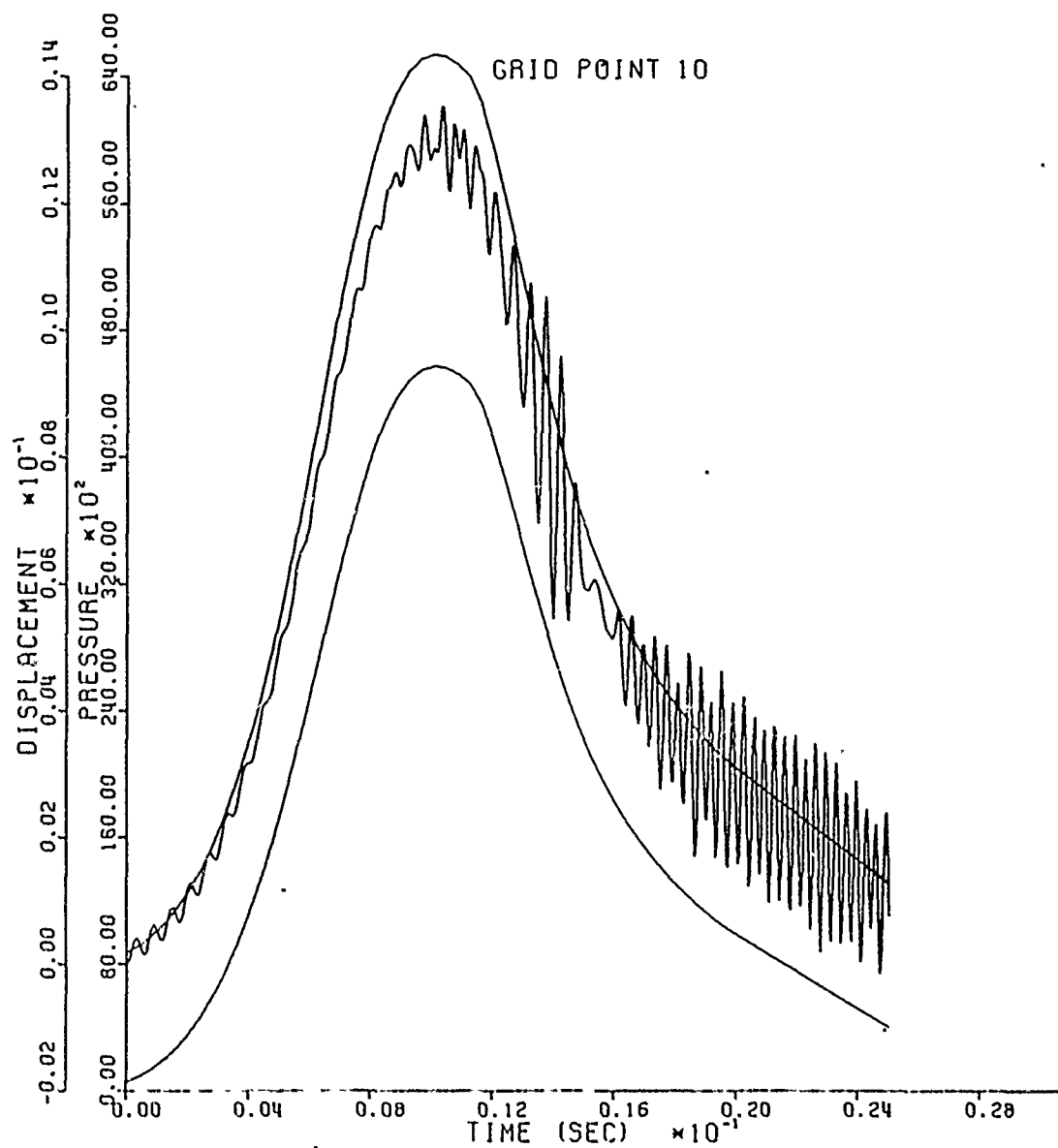


Figure 4. Grid Point 10 - Pressure, Lamé Displacement, and NASTRAN Displacement vs. Time.

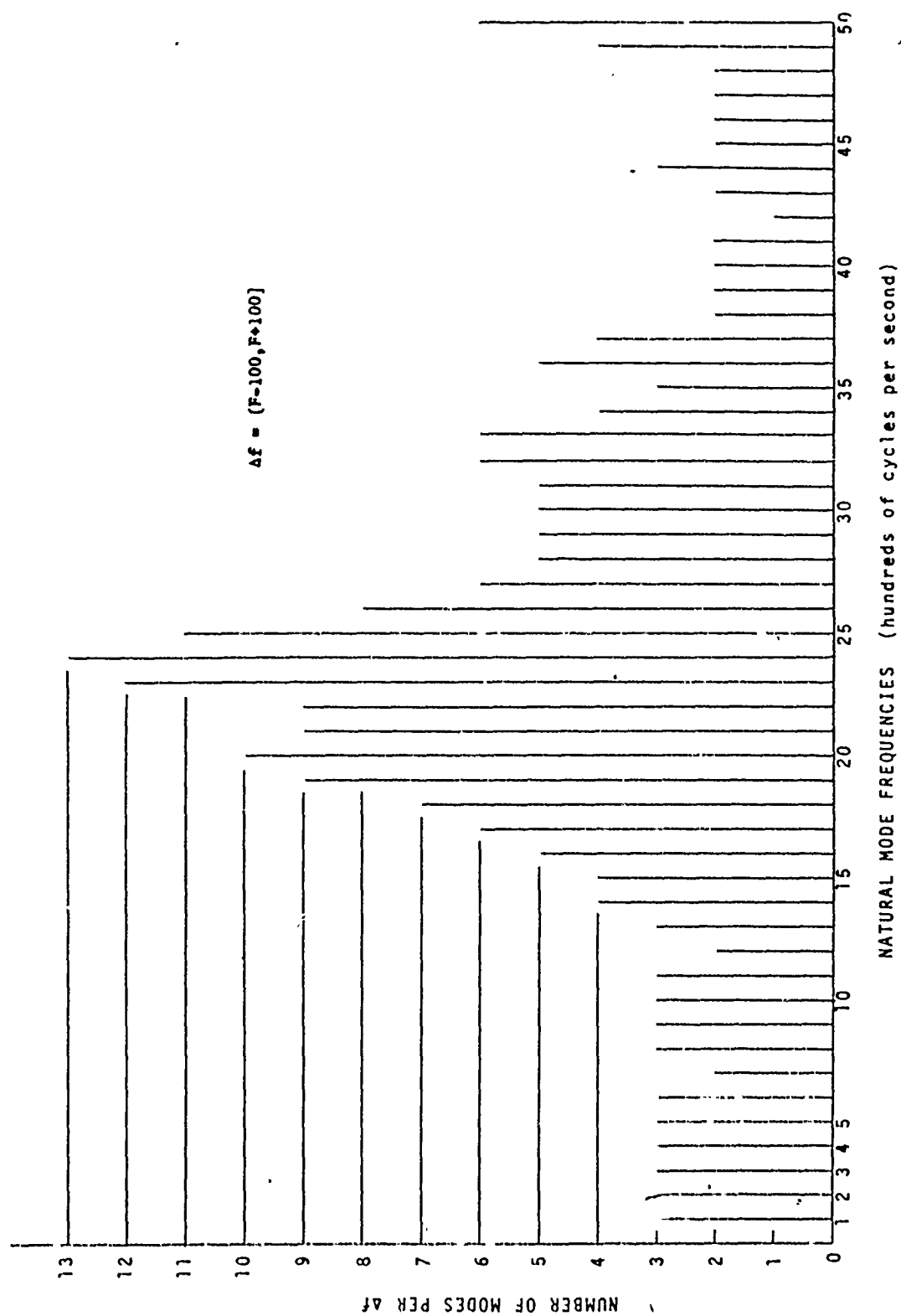


Figure 5. Density Distribution of Tube Natural Frequencies.

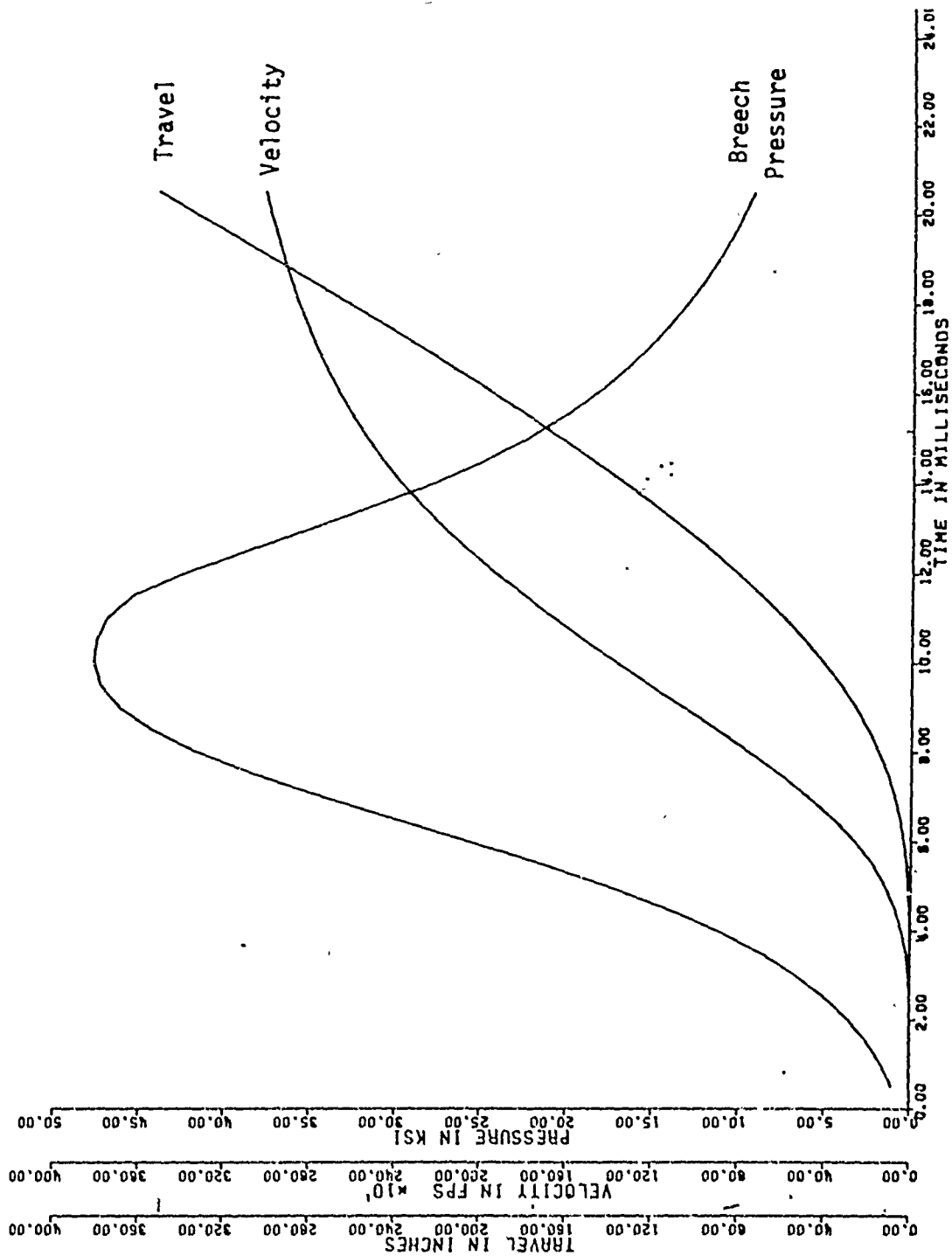


Figure 6. Projectile Velocity and Bore Travel vs. Time

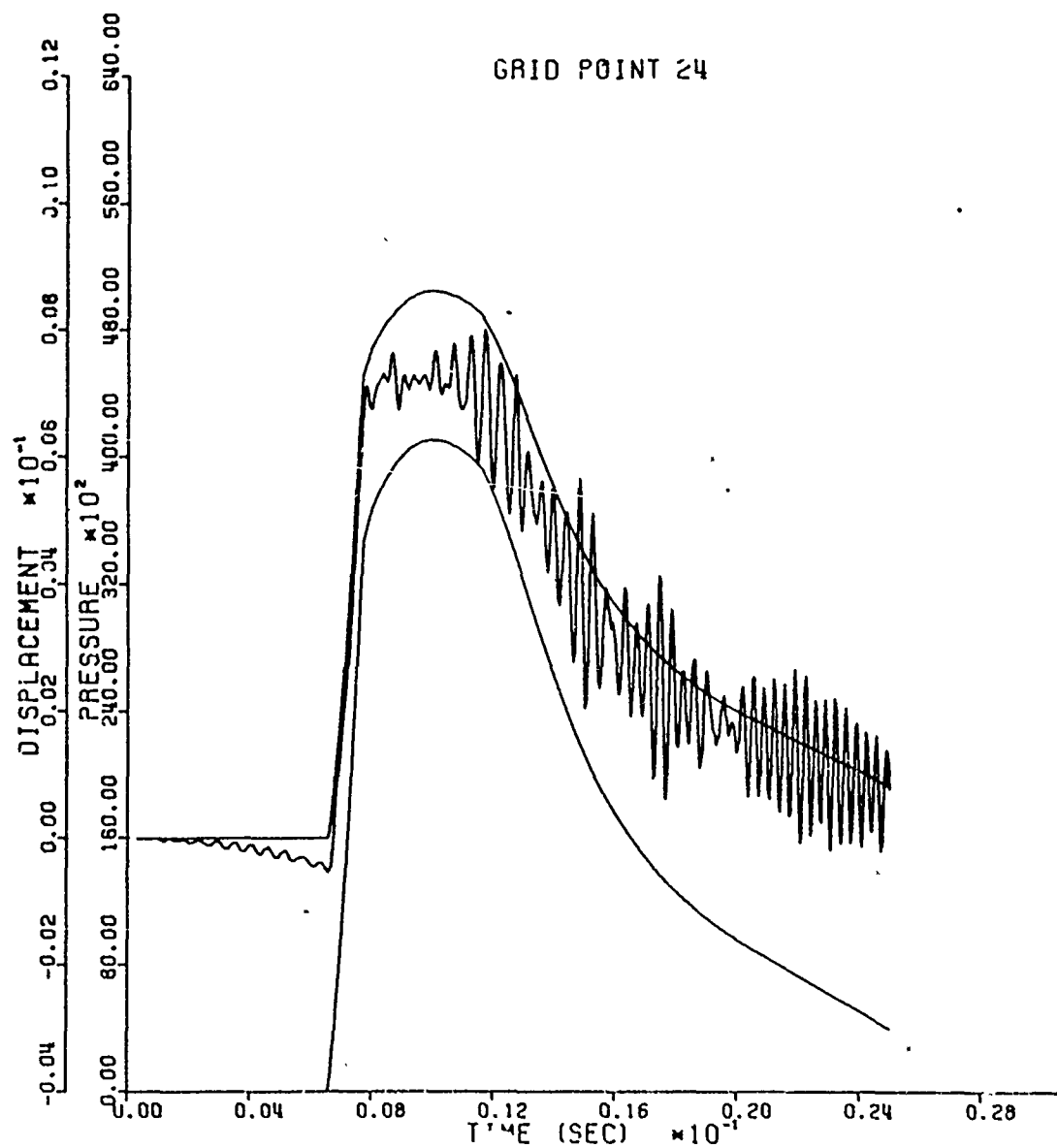


Figure 7. Grid Point 24 - Pressure, Lamé Displacement, and NASTRAN Displacement vs. Time.

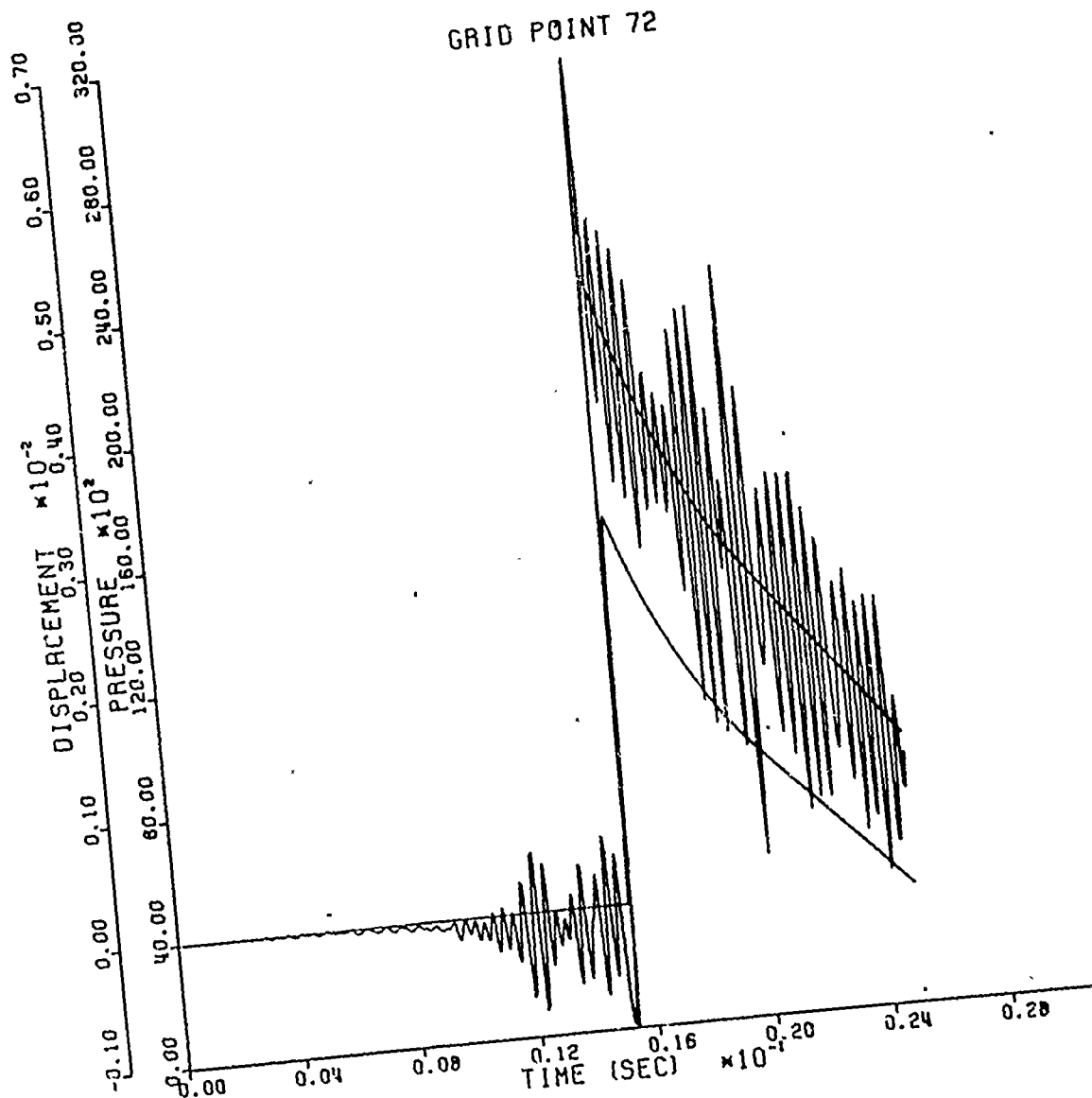


Figure 8. Grid Point 72 - Pressure, Lamé Displacement, and NASTRAN Displacement vs. Time.

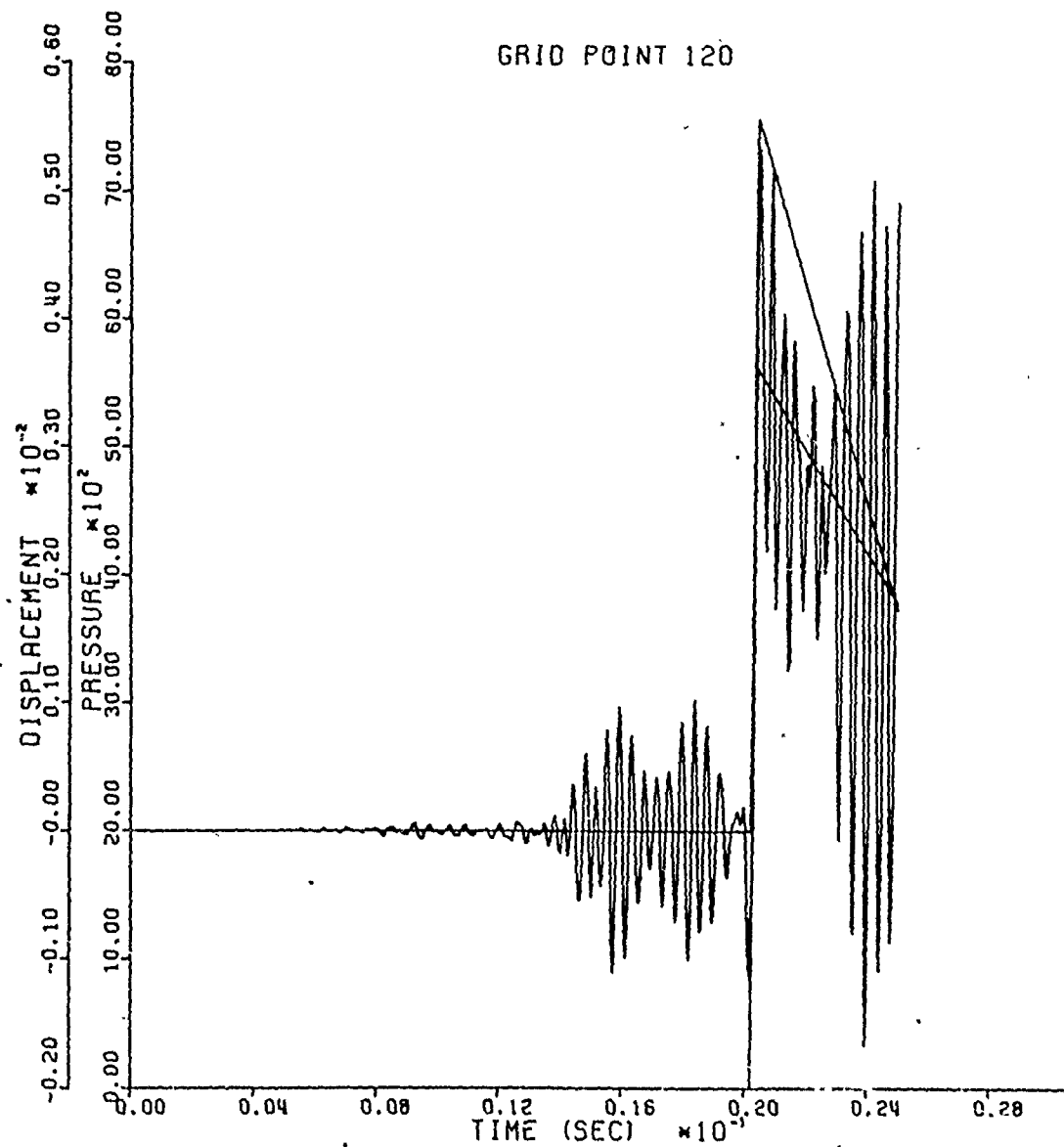
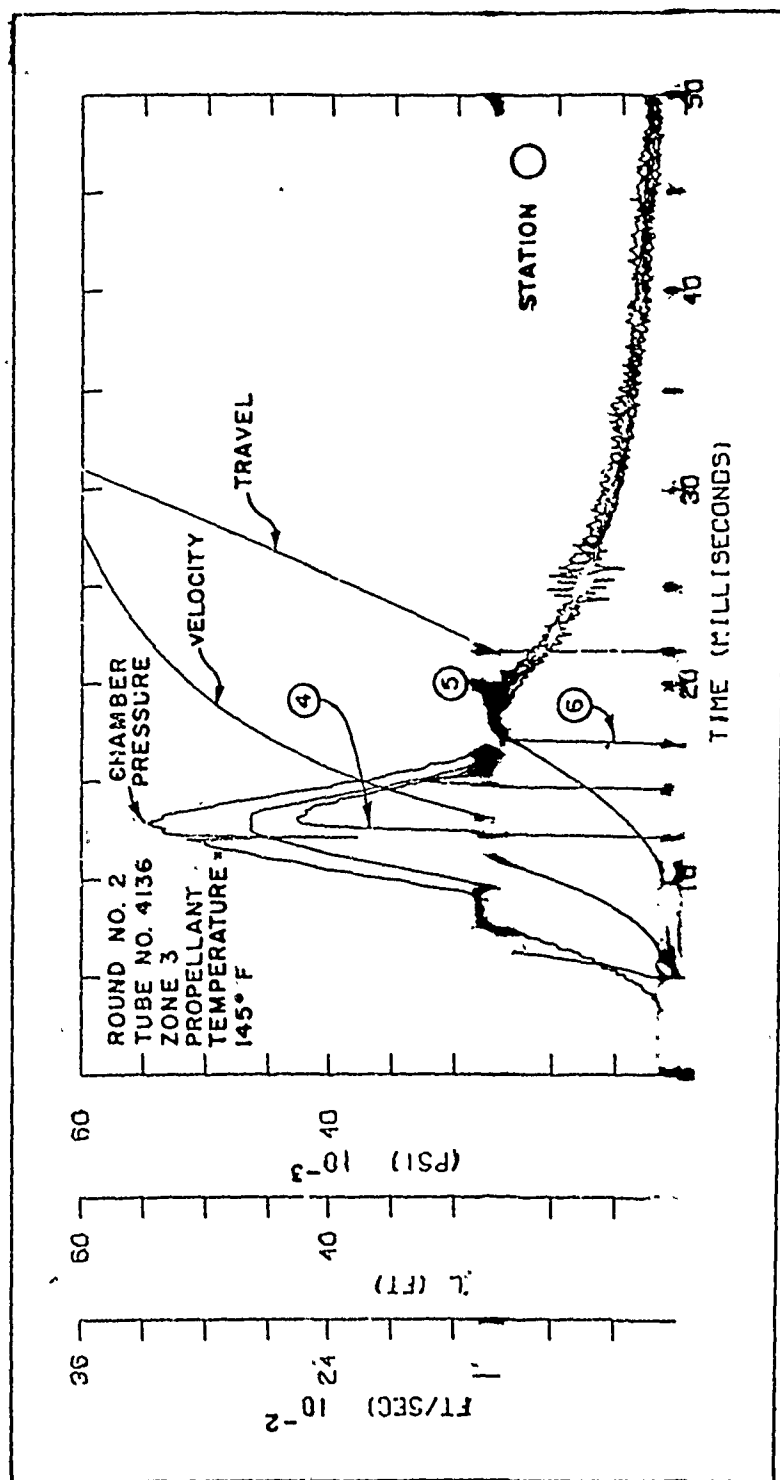


Figure 9. Grid Point 120 - Pressure, Lamé Displacement, and NASTRAN Displacement vs. Time.



Velocity, Travel and Pressure versus Time for a
Zone 3 Charge.

Figure 10. BRL Test Record - Zone 3 Charge. Stations 4-6 correspond to NASTRAN Points 34, 48 and 6B.

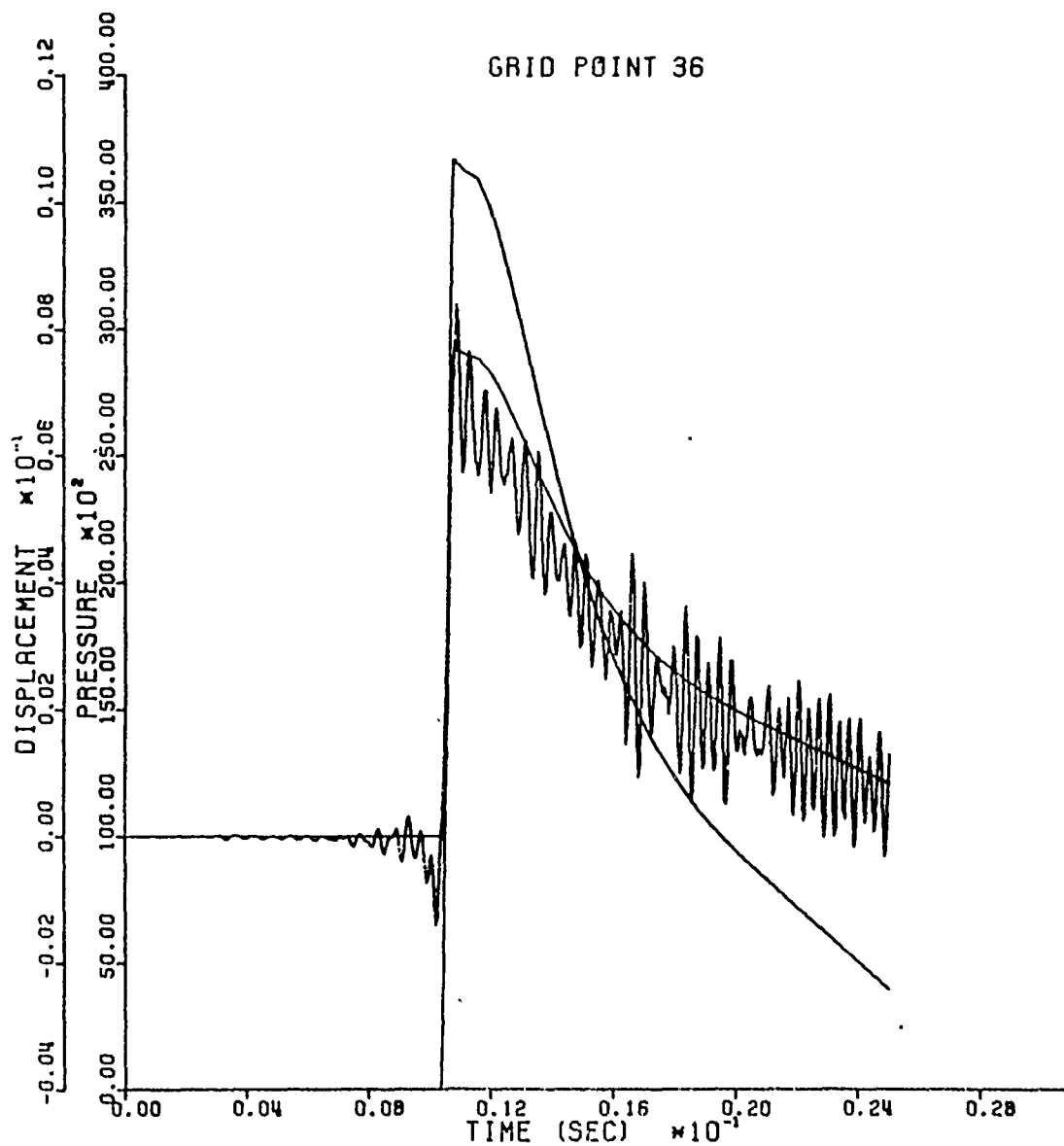


Figure 11. Grid Point 36 - Pressure, Lamé Displacement, and NASTRAN Displacement vs. Time.

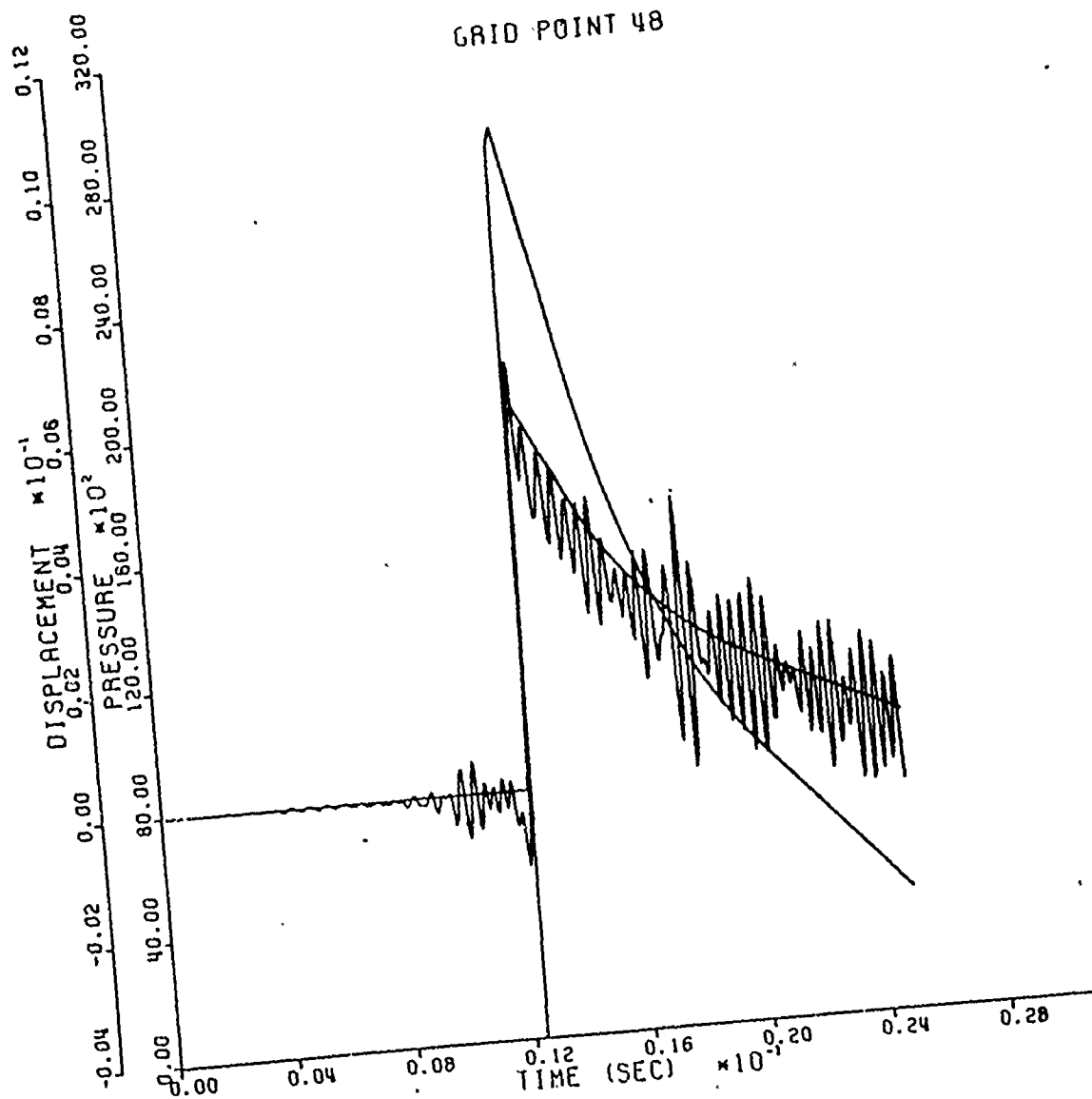


Figure 12. Grid Point 48 - Pressure, Lamé Displacement, and NASTRAN Displacement vs. Time.

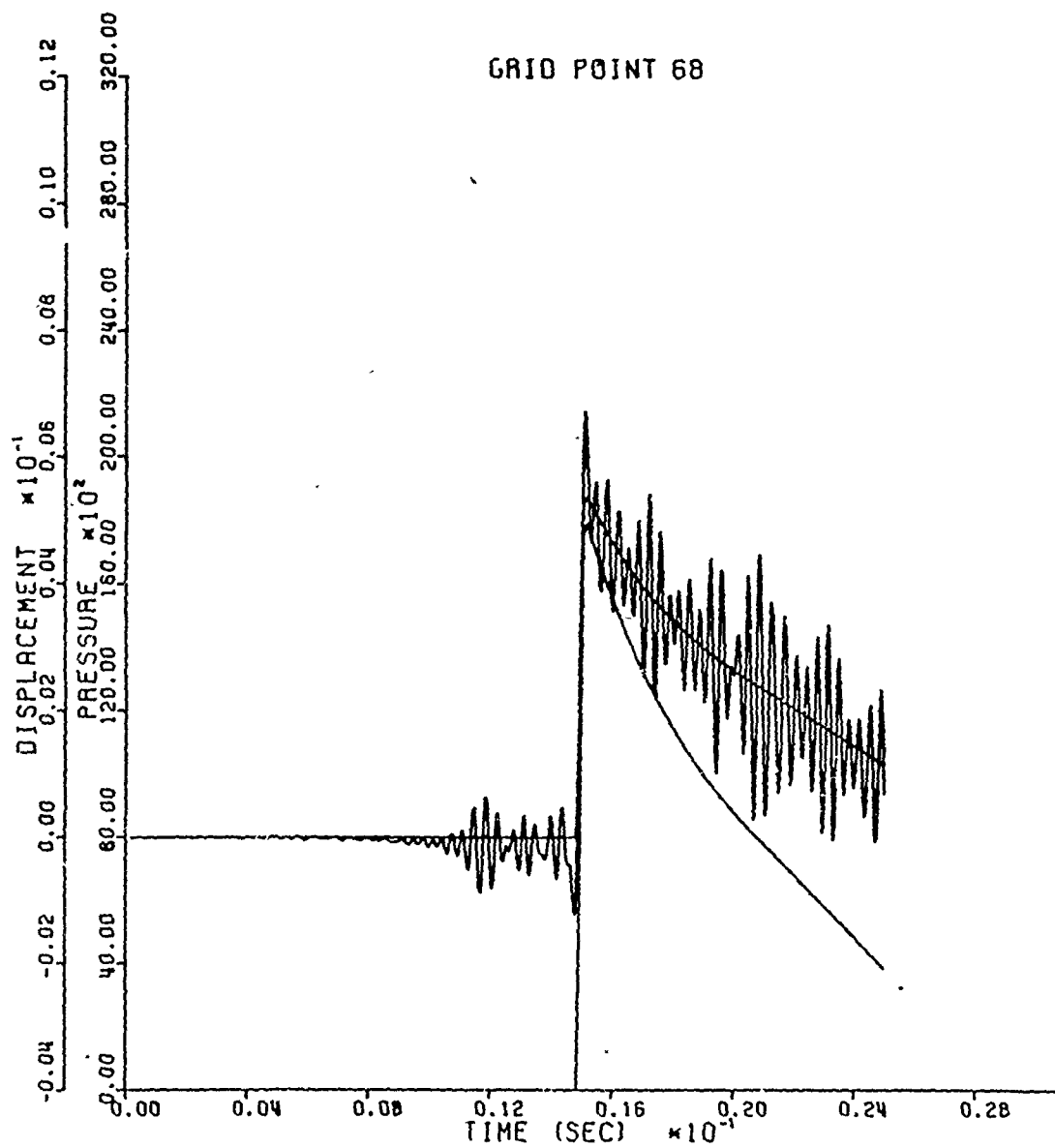
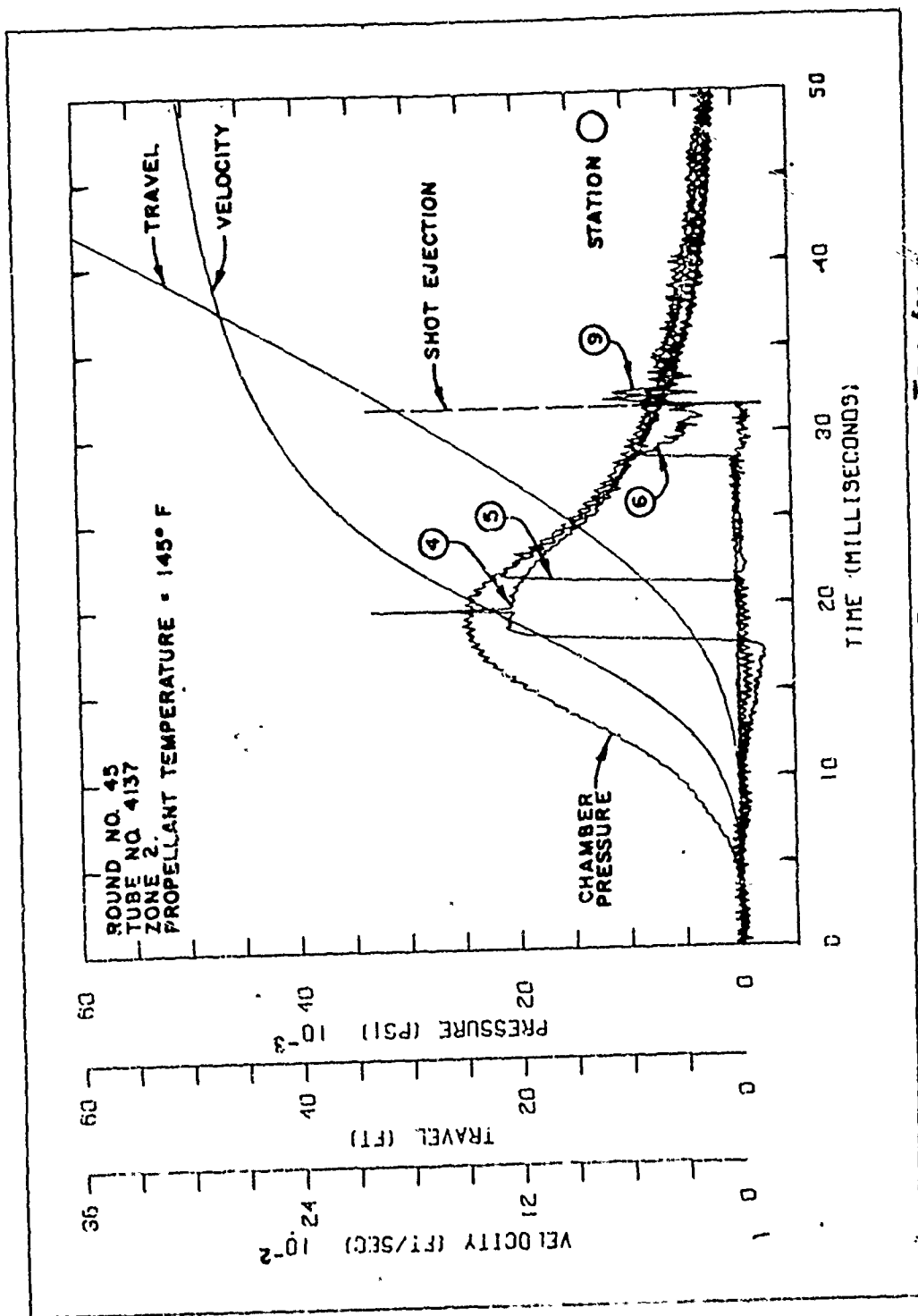


Figure 13. Grid Point 68 - Pressure, Lamé Displacement, and NASTRAN Displacement vs. Time.



Velocity, Travel and Pressure versus Time for Zone 2 Charge.

Figure 14. BRL Test Record - Zone 2 Charge. Stations 4-6 correspond to NASTRAN Grid Points 34, 48, & 68.

175 MM GUN TEST

YUMA RD. 11 ST. 3

175 INCHES FROM MUZZLE

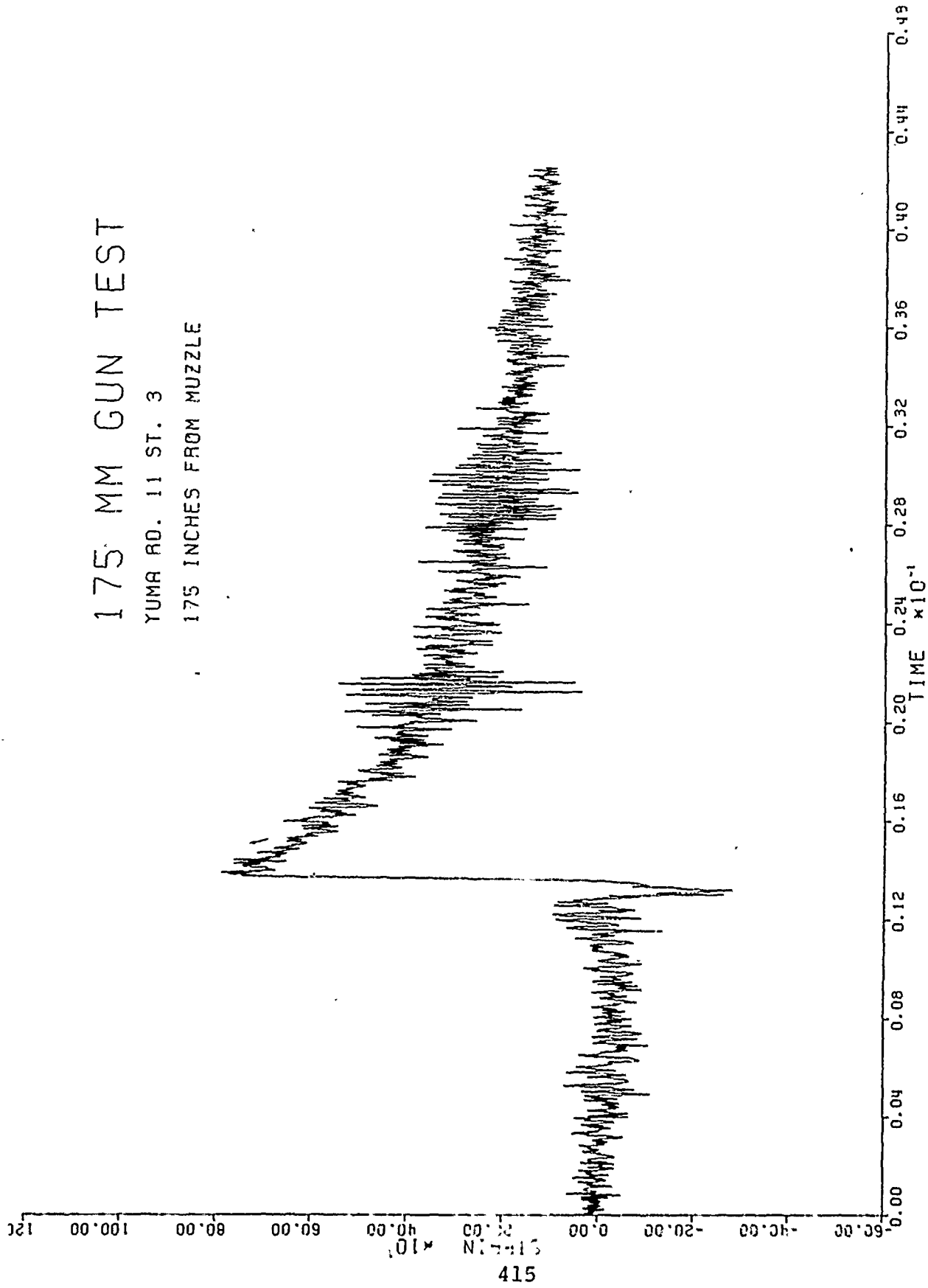


Figure 15. Yuma Test Record -- Zone 3 Charge. Station 3 Corresponds to NASTRAN Grid Point 72.

175 MM GUN TEST

YUMA RD. 11 ST. 4

009 INCHES FROM MUZZLE

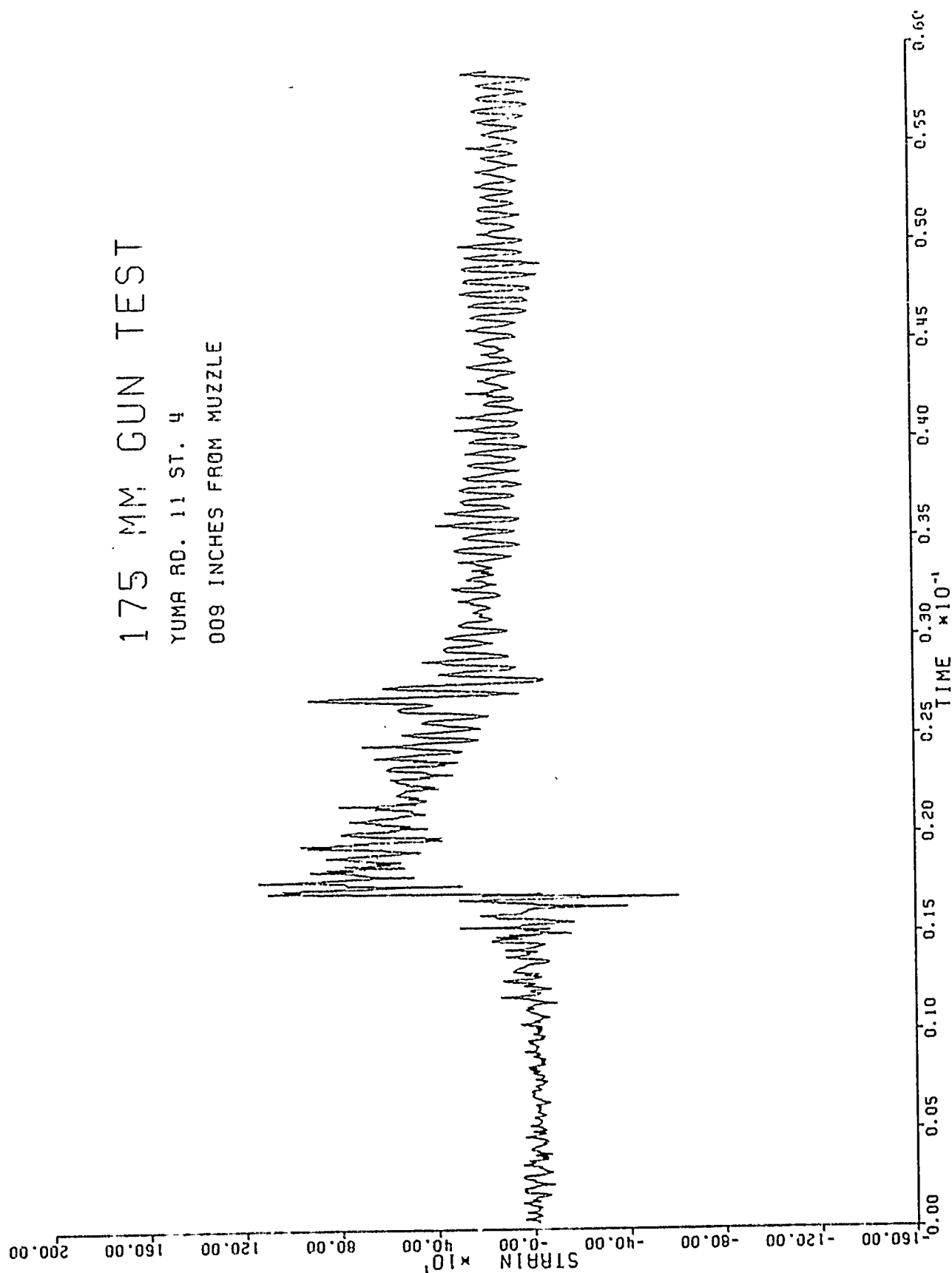


Figure 16. Yuma Test Record - Zone 3 Charge. Station 4 Corresponds to NASTRAN Grid Point 120.

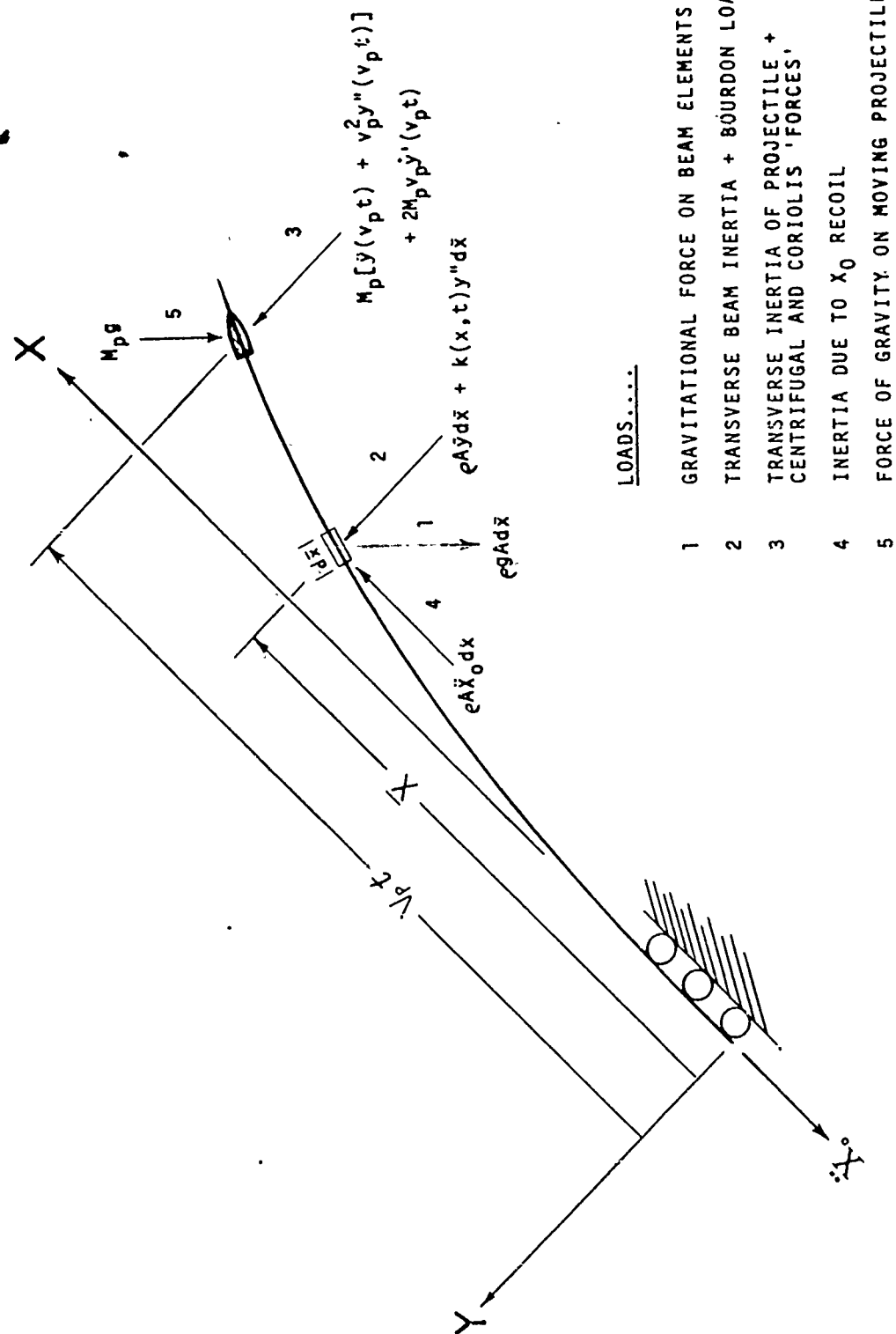


Figure 17. Deformed Tube Axis and Loads.

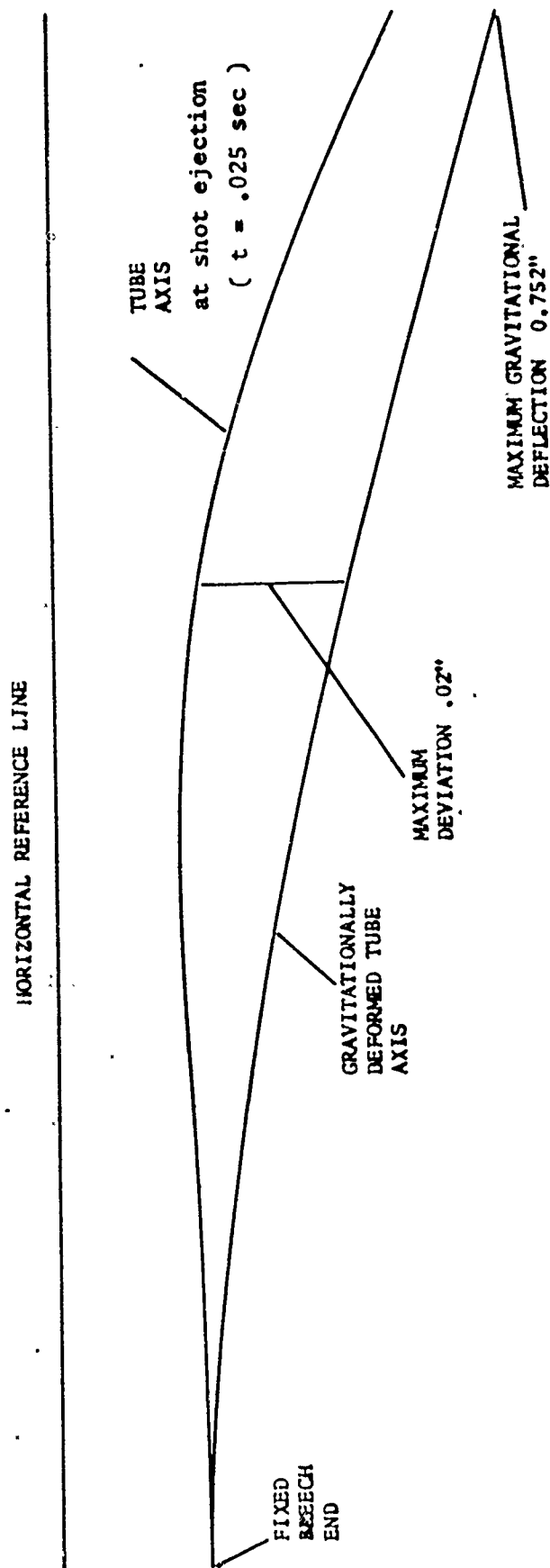


Fig. 18. Statically and Dynamically Deformed Axis'

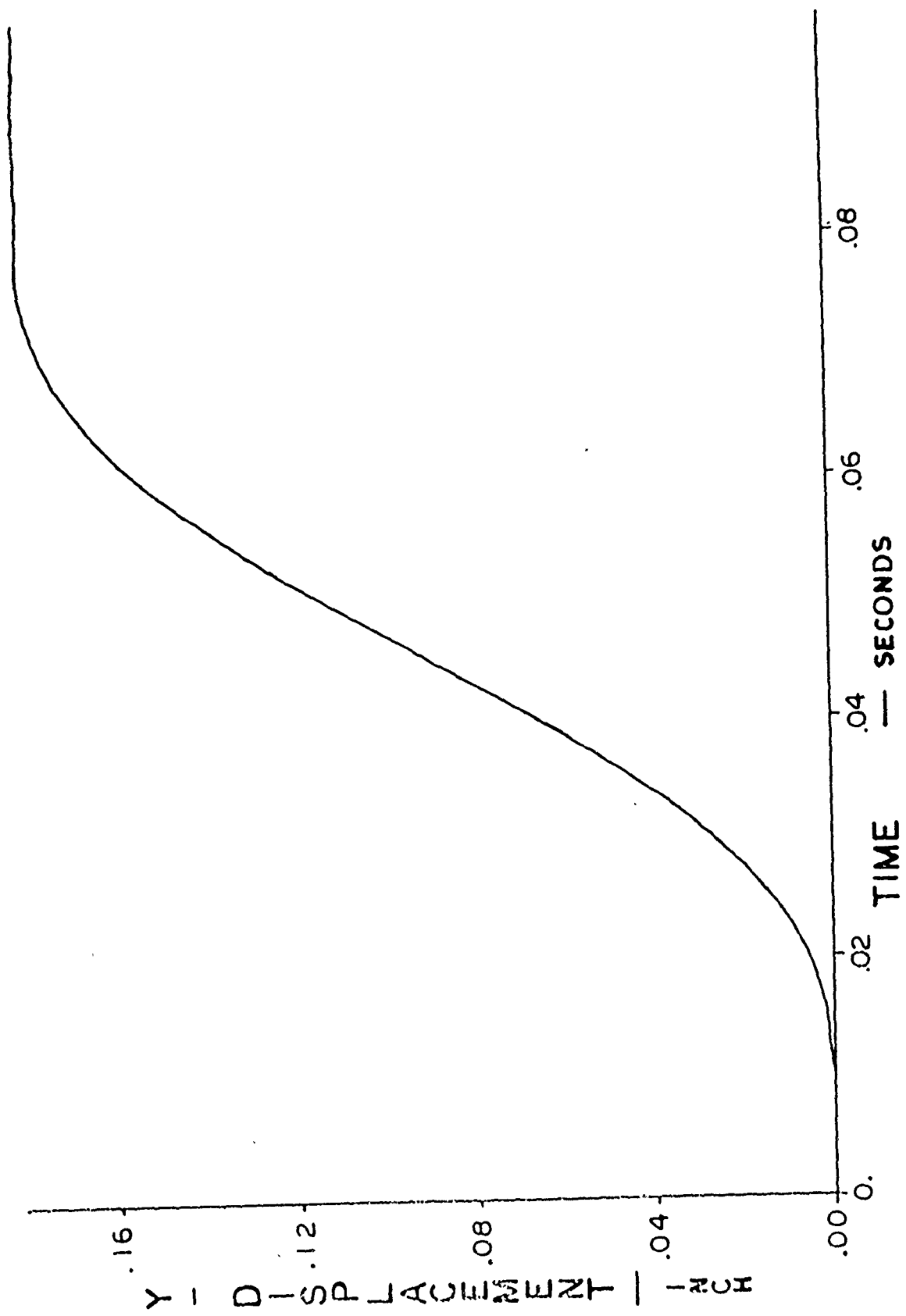


Fig 19a Displacement of Muzzle

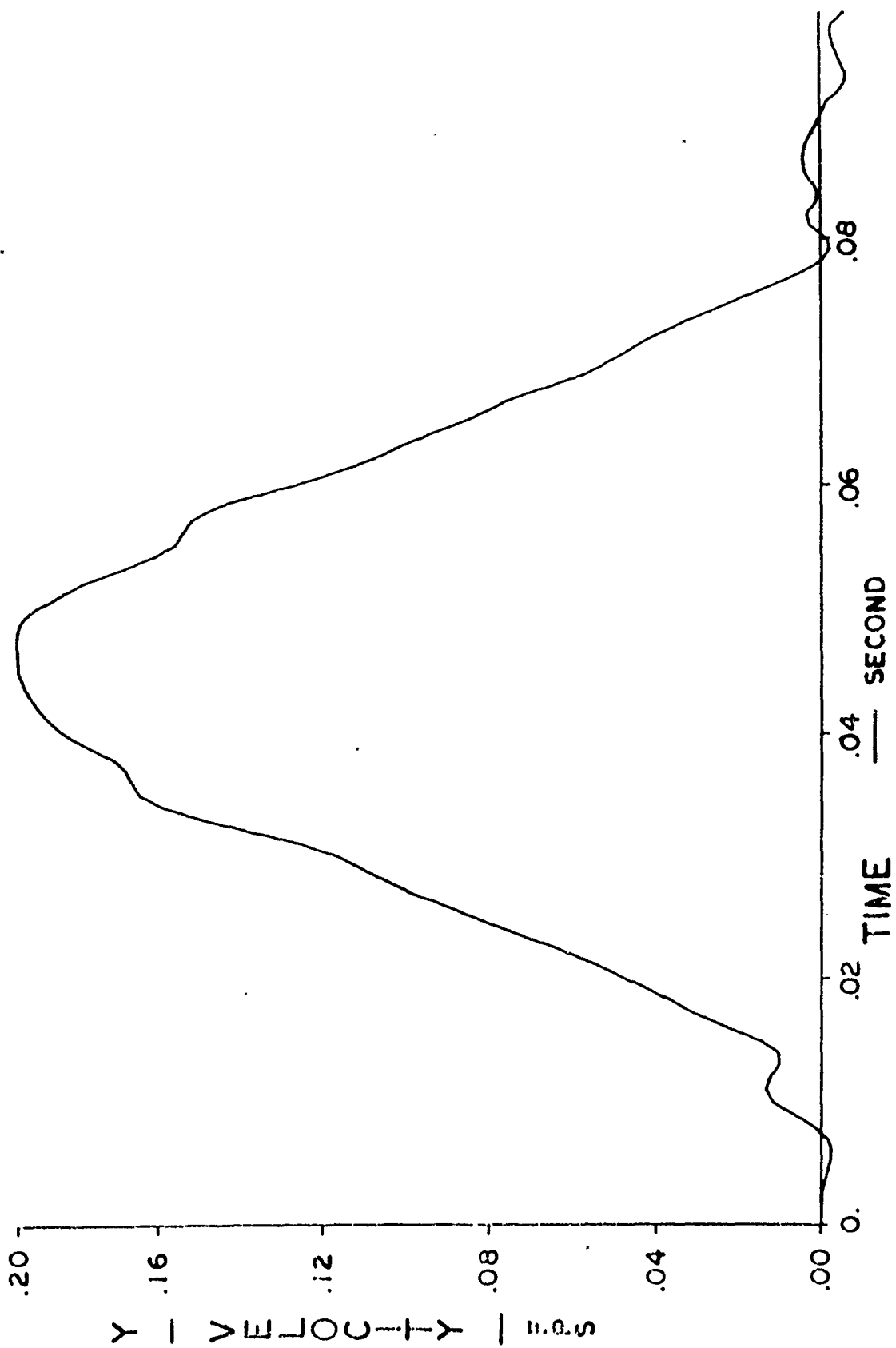


Fig 19b Transverse Muzzle Velocity

CHAPTER TWO

The Importance of the Moving Mass Problem

In more conventional applications the difference in the response of a structure to a moving mass and to the weight of this mass is not very great. However, if the moving mass is an appreciable fraction of the total structural mass of the problem - or if the velocity of the mass is very large, an unconventional structural problem is defined in which the difference may be quite pronounced. There are at least two illustra-

tions which come to mind: (1) - a railroad train crossing a long trestle¹ (in which the moving mass compares to the mass of the trestle) and (2) - a projectile traversing a long tube (in which uncommonly high velocities are evident). We are professionally interested in the latter as a knowledge of the response of a tube to a moving mass leads immediately to a good estimate of the resultant interface pressure between the projectile and the bore surface - an important first step toward the ultimate understanding of the causes of bore and muzzle wear problems and proper design of projectile casings and rotating bands. The importance of the structural response of the tube in altering the round trajectory is also apparent. Thus treatment of the moving mass problem has a wide base of military justification.

State of the Art in Moving Mass Problems

Although the method of computation reported herein is immediately applicable to a finite element beam model of a gun tube, it is first necessary to assess the accuracy of the method by applying it to a problem which has received prior treatment and reported in the literature. The most common base for comparison has been the experimental work of Ayre, Jacobsen, and Hsu² - presumably because of the lack of

(1) Stokes, Sir George G., "Discussion of a Differential Equation Relating to the Breaking of Railway Bridges," Trans Cambridge Phil Soc, 8, p. 707, 1849

(2) Ayre, R.S., Jacobsen, L.S., and Hsu, C.S., "Transverse Vibration of One and of Two Span Beams Under the Action of a Moving Mass Load," Proc. of First National Congress on Applied Mechanics, June 1951

any simple analytical solution with which to compare results. (The analytical solution of Schallenkamp is not convenient for general application - this will be mentioned further on in the report)

This report is therefore concerned with predicting the response of a uniform, simply supported beam while subjected to a concentrated mass moving along its length at constant velocity under the influence of gravity. The method employed, however, is immediately applicable to time variant mass velocities as well as other boundary conditions and variable beam cross section.

Before commencing with the details of the moving mass problem it may be worthwhile to point out the theoretical differences between problems in which masses are in motion and those which involve only moving forces.

To begin with, moving loads* are but special cases of time and space variant forcing functions $f(x,t)$ for one dimensional structures such as beams. The customary beam equation of forced motion can be written ³:

$$MW + Lw = f(x,t) \quad \dots (1)$$

where M and L are operators:

$$M = \rho A; \quad L = (EI \partial^2 / \partial x^2)$$

(3) Tong, K., Theory of Mechanical Vibrations, J. Wiley & Sons, 1960
p. 300

* The term 'load' is intended to be general and to represent applied loads such as moving forces and/or masses

Solving the homogeneous form of equation (1) ($f(x,t) = 0$), i.e., the free vibration problem—leads to the eigenfunctions $r_n(x)$ and the eigenvalues ω_n with which any forced motion problem ($f(x,t) \neq 0$) can be solved.

Transforming to modal coordinates $p_i(t)$ defined in the expansion:

$$w(x,t) = \sum_1^{\infty} p_i(t) r_i(x) \quad \dots(2)$$

leads to an infinite number of differential equations which are uncoupled:

$$\text{i.e.} \quad m_{ii}(\ddot{p}_i + \omega_i^2 p_i) = \int_0^l f(x,t) r_i(x) dx \quad \dots(3)$$

$$\text{where} \quad m_{ii} = \int_0^l r_i^2 M(r_i) dx$$

Now if $f(x,t)$ is a moving concentrated force, i.e.,

$$f(x,t) = -P_0 \delta(x-vt)$$

then (3) becomes:

$$m_{ii}(\ddot{p}_i + \omega_i^2 p_i) = -P_0 r_i(vt) \quad \dots(4)$$

The solution to (4) can be written immediately in terms of the eigenfunctions and eigenvalues of the free vibration problem.

For a moving mass, however,

$$f(x,t) = -m_p \ddot{w} \delta(x-vt)$$

When substituted in (3), the right hand side becomes:

$$-m_p \int \frac{\partial^2 w}{\partial t^2} r_i(x) \delta(x-vt) dx = \left. \frac{\partial^2 w}{\partial t^2} r_i(x) \right|_{x=vt} (-m_p)$$

$$\text{but } \left. \frac{\partial^2 w}{\partial t^2} \right|_{x=vt} = \ddot{w}(vt) + 2\dot{w}'(vt) + v^2 w''(vt) ; \quad ' = \partial/\partial x$$

$$\text{using (2): } \left. \frac{\partial^2 w}{\partial t^2} \right|_{x=vt} = \sum_j \{ r_j(vt) p_j + 2v r_j'(vt) p_j + v^2 r_j''(vt) p_j \}$$

then (3) becomes:

$$m_{ii} (\ddot{p}_i + \omega^2 p_i) = -m_p \sum_j \{ r_j(vt) p_j + 2v r_j'(vt) p_j + v^2 r_j''(vt) p_j \} \quad \dots (5)$$

In contrast to (4), equations (5) are not uncoupled. In fact all of the variables p_i , $i = 1, \infty$, appear in each of the infinite number of differential equations. To make matters worse, each variable has a time-variant coefficient. To date the only exact mathematical treatment appears to be that due to Schallenkamp⁴ involving a triple infinite series equation for unknown Fourier coefficients.

Thus the whole concept of natural frequencies and modes of vibration loses its value in quantitative determination of the response of a system with time variant properties - of which the moving mass is but a special case. For every location of the mass along the beam we have a new infinity of eigenvalue solutions. With an infinite num-

(4) Schallenkamp, A., "Schwingungen von Trägern bei bewegten Lasten," Ingenieur-Archiv, v.8, 1937, pp. 182-198

ber of locations for the mass to occupy, we thus have a double infinity of eigenfunctions and eigenvalues.

Equation (1) can, however, be solved numerically - regardless of the space and time dependent material properties and the forcing term. In what follows we eliminate the space variable through the finite element process. The time variable is handled by a numerical integration procedure of common variety (predictor-corrector). In essence therefore, we approximate our continuum description (1), by a finite number of ordinary differential equations with time dependent coefficients.

Continuum Description of the Moving Mass Problem

In the Appendix a derivation is given for the equation of forced transverse motion of a beam model of the M13 gun tube:

$$(EIy'')'' = -k(x,t)y'' + (\rho A \ddot{X}_0(t) + \rho A g \sin \alpha)y''(x-l) + (\rho A \ddot{X}_0(t) + \rho A g \sin \alpha)y' - m_p(\ddot{y} + 2v\dot{y}' + g \cos \alpha + v^2 y'')\delta(x-vt) - \rho g A \cos \alpha - \rho A \ddot{y} \quad \dots(6)$$

This equation assumes that A, the beam cross section is uniform and that v - the velocity of the moving mass m_p is constant. In that we will be applying the equation to beam elements of uniform and equal cross section the former assumption is consistent. This restriction is not necessary to the generality of the method. The assumption of

constant velocity is motivated by our desire to compare results with the work of Ayre, Jacobsen and Hsu. In (6) the term $k(x,t)y''$ is the so called 'Bourdon' force. Terms in \ddot{X}_0 represent transverse forces induced by axial recoil acceleration when beam curvature and slope are non-zero. Terms in ρAg are due to the beam weight. None of these forces are of interest in this report which deals exclusively with forces induced by the moving mass:

$$\text{i.e.} \quad f(x,t) = -m_p(\ddot{y} + 2v\dot{y}' + g + v^2 y'')\delta(x-vt) \quad \dots(7)$$

where α , the tube elevation angle, has been made equal to zero. Thus the special version of equation (6) we will be concerned with in this report:

$$EIy'''' + \rho A \ddot{y} = -m_p(\ddot{y} + 2v\dot{y}' + g + v^2 y'')\delta(x-vt) \quad \dots(8)$$

where E, I, ρ , and A assume constant values. The left hand side of (8) is recognized as originating from the simplest of beam theory, i.e., where the entire transverse deflection of the beam is assumed to be due to bending moment only. The right side of (8) therefore represents the totality of applied loads, the first term corresponding to the inertia of m_p ; the second is a 'Coriolis' type load; the third is due to the gravitational force on m_p (its weight) and the fourth is the 'centrifugal' force due to m_p following the beam curvature. The Dirac - delta function δ - specifies that each of these forces acts in a concentrated fashion at the location $x = vt$ along the beam.

As written equation (8) is a continuum description of the problem.

Using the method of finite elements the space variable, x , will be discretized - resulting in a set of ordinary differential equations with time as the independent variable.

THE FINITE ELEMENT DISPLACEMENT METHOD

The basic procedure in finite element procedures is to consider the structure of interest as being composed of elements connected together at adjacent attachment points - called nodes or grid points. For the case at hand, the elements will be considered as short beams connected end to end to form the longer beam structure of interest. One then seeks to relate (at least approximately) the displacement at any point interior to an element solely in terms of certain generalized displacements assumed at its attachments.

Figure 1a shows the beam structure of interest (corresponding to equation (8)) broken down into three shorter beam segments or elements. The generalized displacements at the points of attachment consist of one translation and one rotation. (We could define more). It is obvious that when adjacent elements are connected the element displacements at each point of attachment must agree, i.e., must be continuous.

$$\text{e.g.} \quad u_3^1 = u_2^2, \text{ etc.}$$

This continuity requirement between element displacements therefore reduces the number of generalized grid point displacements. For the three beam elements shown in fig 1(a), the number of independent displacements is thus reduced from twelve to eight upon connection of the elements as shown in figure 1(b).

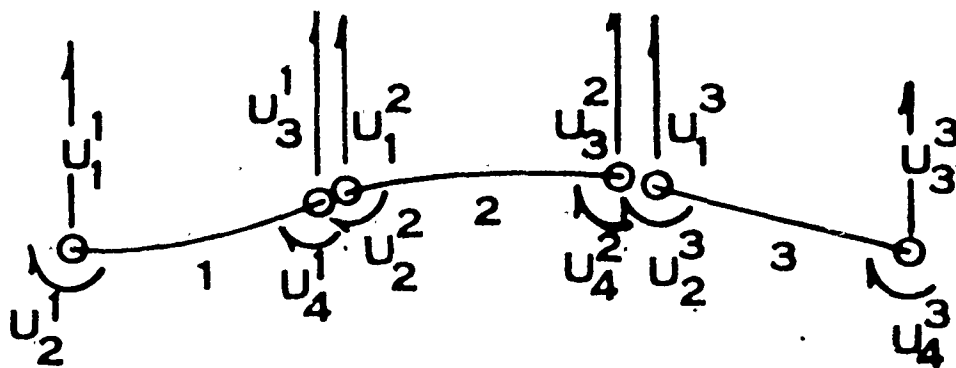


Figure 1(a). Finite Element Breakdown of Beam Structure.

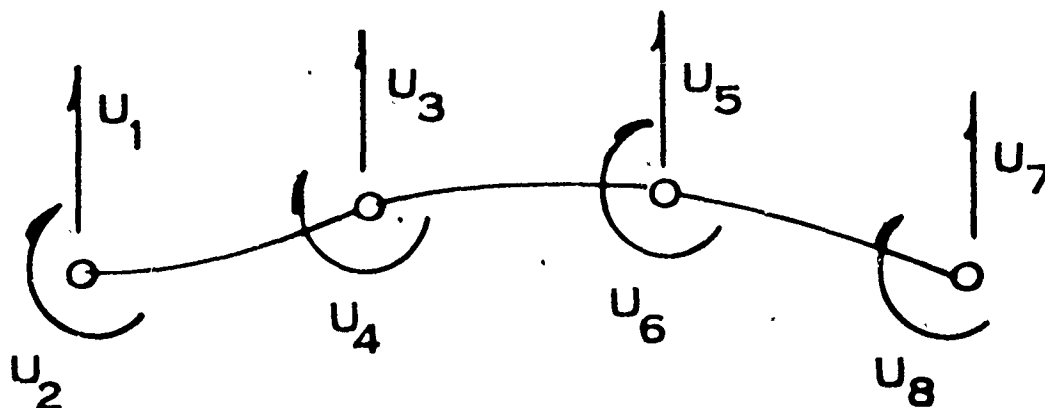


Figure 1(b). Interconnection of Beam Elements to Form Beam Structure.

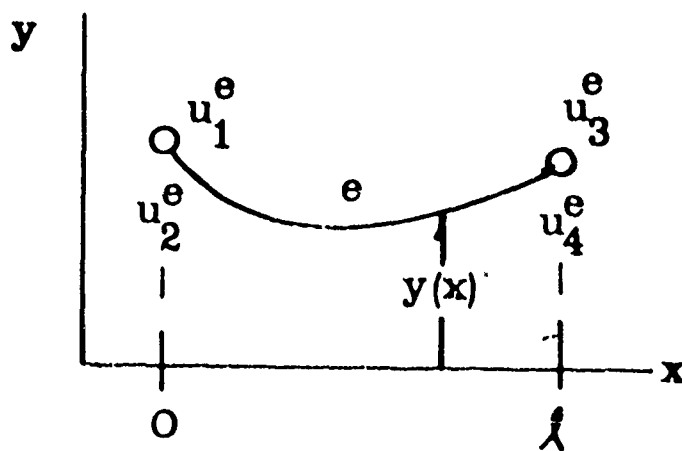


Figure 1(c). A General Beam Element in Deformed Configuration.

Letting $y(x,t)$ represent the transverse displacement of the beam continuum between the end points of a given element (fig 1(c)) the procedure is then to approximate $y(x,t)$ as a linear function of the generalized element displacements u_i^e . (The assumption of linearity will lead to linear differential equations in the u_i^e) Since there are four u_i^e per element - all of which are as yet arbitrary - we can try a polynomial expression with four arbitrary constants, i.e. a cubic:

$$y(x) = a_0 + a_1 x + a_2 x^2 + a_3 x^3 = a_i x^i$$

where, in the latter notation we intend that a sum be performed over repeated index i , with i ranging from 0 to 3.

The a_i can easily be determined from the four conditions:

$$y(0,t) = u_1^e ; \quad y'(0,t) = u_2^e ;$$

$$y(l,t) = u_3^e ; \quad y'(l,t) = u_4^e ;$$

The result can be expressed as the vector product:

$$y(x,t) = \underline{a}(x) \underline{u}^e ; \quad 0 \leq x \leq l \quad \dots (9)$$

explicitly,

$$y(x,t) = \left\{ \begin{array}{c} 1 - 3\xi^2 + 2\xi^3 \\ l(\xi - 2\xi^2 + \xi^3) \\ 3\xi^2 - 2\xi^3 \\ (\xi^3 - \xi^2)l \end{array} \right\} \begin{vmatrix} u_1^e \\ - \\ u_2^e \\ - \\ u_3^e \\ - \\ u_4^e \end{vmatrix}$$

where $\xi = x/l$

Equation (9) constitutes a formal discretization of the continuum in that all interior displacement information has been referred to the end point, or element, displacements. The goal then is to determine these displacements $u_i^e(t)$.

When subjected to sets of applied forces and constraints (boundary conditions), the beam element responds according to the laws of mechanics from which we are free to choose any one of several in which to formulate the equations of motion of the element. It is very convenient to employ the principle of virtual work for dynamic loading⁵ - which states that in a virtual displacement $\delta y(x)$, of the beam element from its instantaneous state of equilibrium, the increment in strain energy, i.e., the virtual strain energy, is equal to the sum of the virtual work done by all the forces including the inertia loads.

$$\text{i.e.} \quad \delta U = \delta W - \int_0^L \rho \delta y \ddot{y} A dx \quad \dots(10)$$

where δU represents the virtual elastic strain energy resulting from the virtual work δW of the applied forces and the virtual work of the inertia forces. (ρ is the material density and A the beam cross-sectional area.) In general the elastic strain energy due to a virtual displacement can be written:

$$\delta U = \int_V \sigma \delta \epsilon dx dy dz \quad \dots(11)$$

where σ is the induced stress due to virtual strain $\delta \epsilon$.

(5) Przemieniecki, J.S., Theory of Matrix Structural Analysis, McGraw Hill, 1968, p. 267

The virtual work due to applied forces $f(x,t)$ per unit length:

$$\delta W = \int_0^l f(x,t) \delta y dx$$

Thus (10) becomes:

$$\int_V \sigma \delta \epsilon dx dy dz = \int_0^l f(x,t) \delta y dx - \int_0^l \rho \ddot{y} \delta y A dx \quad \dots (12)$$

Hooke's Law specifies:

$$\sigma = \beta \epsilon$$

In beam theory, $\beta = E$, Young's modulus, and $\epsilon = hy''$, h being the distance from the beam neutral axis to the fiber in which σ is being defined. Substituting in (12), the left term becomes:

$$\int_0^l \int_A E h^2 y'' \delta y'' dx dy dz = EI \int_0^l y'' \delta y'' dx$$

so that (12) becomes:

$$EI \int_0^l y'' \delta y'' dx = \int_0^l f(x,t) \delta y dx - \int_0^l \rho \ddot{y} \delta y A dx \quad \dots (13)$$

Making use of the approximation (9), i.e., $y = \underline{a}(x) \underline{u}^e$;

$$\delta y = \underline{a}(x) \delta \underline{u}^e \quad \text{and} \quad \delta y'' = \underline{a}''(x) \delta \underline{u}^e$$

Substituting these expressions in (13):

$$EI \int_0^l \delta \underline{u}^e \underline{a}'' \underline{a}'' \underline{u}^e dx = \int_0^l \delta \underline{u}^e \underline{a} f(x,t) dx - \rho A \int_0^l \delta \underline{u}^e \underline{a} \underline{a} \underline{u}^e dx$$

Since the virtual displacements \underline{u}^e are arbitrary:

$$\left\{ \rho A \int_0^l \underline{\bar{a}} \underline{\bar{a}} dx \right\} \underline{\ddot{u}}^e + \left\{ EI \int_0^l \underline{\bar{a}}'' \underline{\bar{a}}'' dx \right\} \underline{u}^e = \int_0^l \underline{\bar{a}} f(x,t) dx \quad \dots (14)$$

(a bar over a quantity denotes its transpose)

The $n \times n$ matrix coefficient expressions ($n = 4$ for the problem at hand) of $\underline{\ddot{u}}$ and \underline{u} deserve to be called \underline{m}^e and \underline{k}^e respectively and the right hand term is the force vector \underline{f}^e whose elements replace the distributed and applied forces present in the continuum problem. These forces are considered as being applied to the ends of the element e . The matrices \underline{m}^e and \underline{k}^e have been evaluated many times in the literature⁶ and will simply be repeated here for beam elements of four degrees of freedom.

$$\underline{k}^e = EI/l^3 \cdot \begin{bmatrix} 12 & & & \\ 6l & 4l^2 & \text{symm} & \\ -12 & -6l & 12 & \\ 6l & 2l^2 & -6l & 4l^2 \end{bmatrix}$$

$$\underline{m}^e = \rho A l / 420 \cdot \begin{bmatrix} 156 & & & \\ 22l & 4l^2 & \text{symm} & \\ 54 & 13l & 156 & \\ -13l & -3l^2 & -22l & 4l^2 \end{bmatrix}$$

(6) Przemieniecki, J.S., Theory of Matrix Structural Analysis, McGraw Hill, 1968, p. 81, 297

To form the force vector \underline{f}^e , the expression $f(x,t)$ from equation (7) is substituted into the right side of equation (14).

$$\text{thus } \underline{f}^e = - \int_0^l \underline{\bar{a}} \underline{m}_p (\ddot{y} + 2v\dot{y}' + g + v^2 y'') \delta(x-vt) dx$$

substituting the relation $y(x) = \underline{au}^e$:

$$\begin{aligned} \underline{f}^e &= - \underline{m}_p \int_0^l \underline{\bar{a}}(x) \{ \underline{a} \ddot{u}^e + 2v \underline{a}' \dot{u}^e + g + v^2 \underline{a}'' u^e \} \delta(x-vt) dx \\ &= - \underline{m}_p \{ c_1(t) \underline{u}^e + c_2(t) \dot{u}^e + c_3(t) u^e \} - \underline{m}_p g \underline{\bar{a}}(vt) \\ &\quad \dots 0 \leq vt \leq l \\ &= 0 \quad \text{otherwise} \end{aligned}$$

$$\begin{aligned} \text{where } c_1(t) &= \underline{\bar{a}}(vt) \underline{a}(vt) \\ c_2(t) &= 2v \underline{\bar{a}}(vt) \underline{a}'(vt) \\ c_3(t) &= v^2 \underline{\bar{a}}(vt) \underline{a}''(vt) \end{aligned}$$

Equation (14) can then be written:

$$\begin{aligned} (\underline{m}^e + \underline{m}_p c_1(t)) \ddot{u}^e + \underline{m}_p c_2(t) \dot{u}^e + (\underline{k}^e + \underline{m}_p c_3(t)) u^e &= - \underline{m}_p g \underline{\bar{a}}(vt) \\ \dots 0 \leq vt \leq l \end{aligned}$$

or simply,

$$\underline{u}^e(t) \ddot{u}^e + \underline{\gamma}(t) \dot{u}^e + \underline{\kappa}(t) u^e = \underline{\phi}^e(t) \quad \dots (15)$$

Outside the interval $0 < vt \leq l$, the time variant coefficients $c_i(t)$ and $a(vt)$ must be replaced by zeros. This can be accomplished by nullifying the m_p factor outside this interval.

Equation (15) represents a set of n ordinary differential equations with time dependent coefficients. They are the differential equations of motion for any beam element of density ρ and section modulus EI as well as cross-sectional area A . All of these element properties may differ from element to element.

STRUCTURE EQUATIONS OF MOTION

The equations of motion for the combined structure, i.e.,

$$\underline{M}(t)\ddot{\underline{U}} + \underline{C}(t)\dot{\underline{U}} + \underline{K}(t)\underline{U} = \underline{F}(t) \quad \dots(16)$$

are formed as follows.

Each term of equation (15) constitutes a force - ψ_i^e , at the element attachment points, $i = 1$ thru n . When all elements are joined the resultant force at the connections (grid points) is the sum of the individual forces at the attachments. For example, the inertia forces at the right end of the first element (cf. fig 1) are to be added to those at the left end of the second element to yield the total inertia force at the connection grid point.

i.e., the inertia forces acting on the first element - element #1 in figure 1 - in the u_1, u_2, u_3 , and u_4 directions are the vector components:

$$\psi_i^1 = \mu_{ij}^1 \ddot{u}_j$$

Summation over repeated subscripts is intended and i & j range from 1 to n . Similarly for element #2:

$$\psi_i^2 = \mu_{ij}^2 \ddot{u}_j^2$$

Upon joining these two elements, ψ_3^1 combines with the force ψ_1^2 and ψ_4^1 with ψ_2^2 so that the resulting forces on the two-beam substructure are, for the case $n = 4$:

$$\begin{bmatrix} \psi_1^1 \\ \psi_2^1 \\ \psi_3^1 + \psi_1^2 \\ \psi_4^1 + \psi_2^2 \\ \psi_3^2 \\ \psi_4^2 \end{bmatrix} = \begin{bmatrix} \mu_{11}^1 & \mu_{12}^1 & \mu_{13}^1 & \mu_{14}^1 & 0 & 0 & 0 & 0 \\ \mu_{21}^1 & \mu_{22}^1 & \mu_{23}^1 & \mu_{24}^1 & 0 & 0 & 0 & 0 \\ \mu_{31}^1 & \mu_{32}^1 & \mu_{33}^1 & \mu_{34}^1 & \mu_{11}^2 & \mu_{12}^2 & \mu_{13}^2 & \mu_{14}^2 \\ \mu_{41}^1 & \mu_{42}^1 & \mu_{43}^1 & \mu_{44}^1 & \mu_{21}^2 & \mu_{22}^2 & \mu_{23}^2 & \mu_{24}^2 \\ 0 & 0 & 0 & 0 & \mu_{31}^2 & \mu_{32}^2 & \mu_{33}^2 & \mu_{34}^2 \\ 0 & 0 & 0 & 0 & \mu_{41}^2 & \mu_{42}^2 & \mu_{43}^2 & \mu_{44}^2 \end{bmatrix} \begin{bmatrix} \ddot{u}_1^1 \\ \ddot{u}_2^1 \\ \ddot{u}_3^1 \\ \ddot{u}_4^1 \\ \ddot{u}_1^2 \\ \ddot{u}_2^2 \\ \ddot{u}_3^2 \\ \ddot{u}_4^2 \end{bmatrix}$$

Enforcing the equality of the displacements, velocities, and accelerations of the attachments, i.e.

$$\ddot{u}_3^1 = \ddot{u}_1^2 \equiv \ddot{U}_3 \quad \text{and} \quad \ddot{u}_4^1 = \ddot{u}_2^2 \equiv \ddot{U}_4$$

where the upper case letter denotes that \ddot{U}_3 , \ddot{U}_4 are grid point accelerations in conformance with figure 1(b).

Hence in terms of grid point notation:

$$\begin{bmatrix} \psi_1 \\ \psi_2 \\ \psi_3 \\ \psi_4 \\ \psi_5 \\ \psi_6 \end{bmatrix} = \begin{bmatrix} \mu_{11}^1 & \mu_{12}^1 & \mu_{13}^1 & \mu_{14}^1 & 0 & 0 \\ \mu_{21}^1 & \mu_{22}^1 & \mu_{23}^1 & \mu_{24}^1 & 0 & 0 \\ \mu_{31}^1 & \mu_{32}^1 & (\mu_{33}^1 + \mu_{11}^2) & (\mu_{34}^1 + \mu_{12}^2) & \mu_{13}^2 & \mu_{14}^2 \\ \mu_{41}^1 & \mu_{42}^1 & (\mu_{43}^1 + \mu_{21}^2) & (\mu_{44}^1 + \mu_{22}^2) & \mu_{23}^2 & \mu_{24}^2 \\ 0 & 0 & \mu_{31}^2 & \mu_{32}^2 & \mu_{33}^2 & \mu_{34}^2 \\ 0 & 0 & \mu_{41}^2 & \mu_{42}^2 & \mu_{43}^2 & \mu_{44}^2 \end{bmatrix} \begin{bmatrix} \ddot{U}_1 \\ \ddot{U}_2 \\ \ddot{U}_3 \\ \ddot{U}_4 \\ \ddot{U}_5 \\ \ddot{U}_6 \end{bmatrix}$$

$\equiv \underline{M}(t)\ddot{\underline{U}}(t)$... the inertia forces acting on the grid points of a 2-element substructure. The other forces in the equations of motion for this structure are formed by similar superposition. Thus the structure equations of motion are formed by overlapping and summing the element matrices wherever a grid point connection is made. For an N - element beam there will be N-1 such overlaps (shown schematically in figure 2). Each overlap will contain n/2 entries from the lower right corner of the nxn matrix corresponding to the element to the left of the grid point - and n/2 entries from the upper left corner of the matrix corresponding to the element to the right of this grid point. These overlapping elements are to be summed.

$$\begin{aligned}
& \begin{bmatrix} \mu^1 \\ \mu^2 \\ \mu^3 \\ \vdots \\ \mu^{2M-2} \end{bmatrix} + \begin{bmatrix} \ddots & & & & \\ & \mu^1 & & & \\ & & \mu^2 & & \\ & & & \ddots & \\ & & & & \mu^{2M-2} \end{bmatrix} \begin{bmatrix} \ddot{u}_1 \\ \ddot{u}_2 \\ \ddot{u}_3 \\ \vdots \\ \ddot{u}_{2M-2} \end{bmatrix} \\
& + \begin{bmatrix} \gamma^1 \\ \gamma^2 \\ \gamma^3 \\ \vdots \\ \gamma^{2M-2} \end{bmatrix} \begin{bmatrix} \ddot{u}_1 \\ \ddot{u}_2 \\ \ddot{u}_3 \\ \vdots \\ \ddot{u}_{2M-2} \end{bmatrix} \\
& = \begin{bmatrix} \kappa^1 \\ \kappa^2 \\ \kappa^3 \\ \vdots \\ \kappa^{2M-2} \end{bmatrix} + \begin{bmatrix} \ddots & & & & \\ & \kappa^1 & & & \\ & & \kappa^2 & & \\ & & & \ddots & \\ & & & & \kappa^{2M-2} \end{bmatrix} \begin{bmatrix} F_1 \\ F_2 \\ F_3 \\ \vdots \\ F_{2M-2} \end{bmatrix}
\end{aligned}$$

Figure 2. Matrix Equations of Motion for the Moving Mass Problem.

It is to be noticed from equation (15) that in general, the coefficient matrices $\underline{\mu}^e$, $\underline{\gamma}^e$, and $\underline{\kappa}^e$ consist of a constant part (null in the case of $\underline{\gamma}^e$) and a time variant part which derives from the moving mass m_p . These time variant elements are null except when t is such that m_p is located within the length of a particular beam element. Only then are the time-variant components of the corresponding element matrix finite. Thus in figure 2, one conceives of a conventional matrix of constant coefficient multipliers of the acceleration, velocity, and displacement terms plus a time variant set of components which propagate in a band along the diagonal of each structure coefficient matrix as the moving mass traverses the beam in time. Thus at any instant only n of the structure equations of motion possess time variant coefficients - n being the number of element displacements (degrees of freedom) considered for each beam element - four for the case at hand. Thus the prospect of solving the full set of equations numerically - without incurring extraordinarily long computer run times - would appear to be good. For example it is not uncommon to solve via computer, a fifty degree of freedom transient problem in conventional structure dynamics via the finite element technique - where all of the coefficients are constant in time. It should therefore involve only a moderate increase in computation time to allow four of these equations to take on time-variant coefficients as in our problem of the moving concentrated mass. Roughly speaking one might expect that each time-variant matrix element will create additional computation no greater than that caused by adding another degree of freedom to a conventional constant coefficient problem. Thus a 50 degree of freedom problem - e.g.,

twenty-four connected beam elements subjected to a moving concentrated mass - could be solved with a computation time not in excess of a ninety-eight degree of freedom problem in which all the matrix coefficients are constant. ($\underline{u}^e(t)$, $\underline{y}^e(t)$, and $\underline{\kappa}^e(t)$ each comprise sixteen time dependent components).

Boundary Conditions

A great convenience of the finite element procedure - as compared say, to the Ritz or Galerkin procedures - is that all ambiguity is removed in choosing the boundary conditions to enforce. (This is due to the particular stage of deduction at which the finite element idealization is invoked in a variational procedure*). In practice all one has to do is mimic physical reality. For example, a beam with hinge (simple) supports at each end requires that the corresponding displacements vanish; e.g., in a three-element beam model, $U_1 = U_7 = 0$. Similarly a clamped cantilevered beam would insist that $U_1 = U_2 = 0$. Instead of specification of particular zero values, however, it is more efficient to merely delete the corresponding rows and columns from the coefficient matrices \underline{M} , \underline{C} , and \underline{K} of equation (16). Thus for the case of a three-element hinged-hinged beam, we simply delete the first and the seventh rows and columns from these matrices. Similarly we delete the corresponding elements from any force vector \underline{F} , appearing on the right hand side of this equation.

*Conversations with Dr. Gary Anderson, Applied Mathematics and Mechanics Div, Benet Weapons Laboratory, Watervliet Arsenal, Watervliet, N.Y.

PROBLEM STATEMENT AND SOLUTION

For the purpose of comparing results achieved by finite elements with those appearing in the literature, the problem to be solved is one of three beam elements connected end to end to form a simply supported beam having uniform cross section and material properties. A moving mass, m_p , is assumed to traverse the beam from left to right at a constant velocity v - see figure 3.

Deleting the first and seventh rows and columns from the coefficient matrices \underline{M} , \underline{C} and \underline{K} along with the first and seventh components of the vector \underline{F} of equation (16) results in a six degree of freedom problem - that is, six coupled equations of forced motion. These equations will be solved numerically with m_p and its velocity v , serving as parameters.

In reality we have no clairvoyance to guide the choice of values for m_p and v except, of course, to repeat those used in the literature so that a comparison may be made. It appears, however, that the values chosen by Ayre, et al, were not completely arbitrary in that certain values of v will cause resonant (secular) behavior in the moving force problem. From equation (3) we can verify that resonance will indeed occur for any value $v = v^*$, such that $m_{ii}(v^*) = 0$. Although applicable only to moving force problems, it is intuitively plausible that extraordinary behavior in the moving mass problem might occur for values of velocity not far removed from these values v^* . Having no 'closed form' analytical solution with which to anticipate points of singular - or otherwise interesting - behavior, one

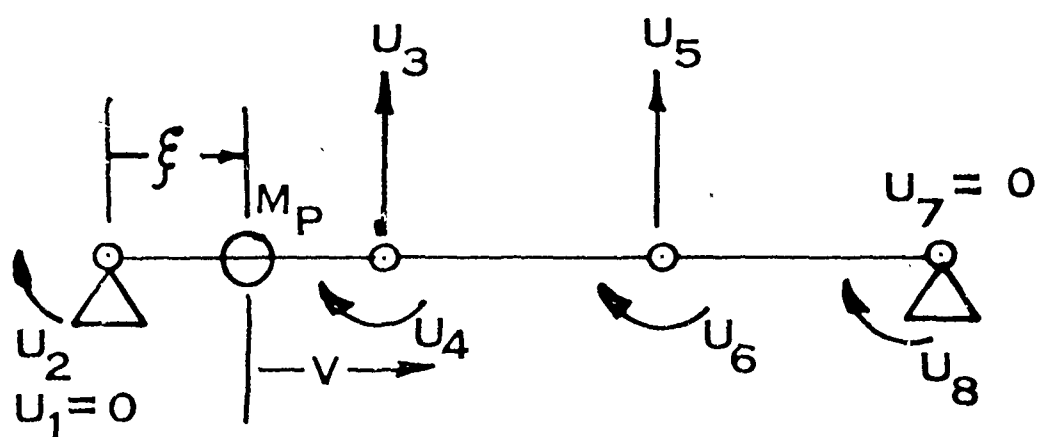


Figure 3. Finite Element Model for Moving Mass Problem.

can do no better than to at least allow the velocity of the mass to range through the lowest v^* which will cause m_{ii} to vanish. This apparently was the reasoning behind the choice of velocities investigated by Ayre, et al, who performed experiments in which v was chosen as $v^*/4$, $v^*/2$, and v^* for the moving force and $v^*/4$ and $v^*/2$ for the moving mass - v^* being the first value of v to cause m_{ii} to vanish, i.e., the first resonant or 'critical' velocity of the moving force solution. (Maintaining contact between the beam and mass for velocities higher than $v^*/2$ was apparently impossible.)

For the simply supported beam being considered:

$$m_{ii}(v) = \alpha_i^2 v^2 - \omega_i^2 \quad \dots (17)$$

where $\alpha_i = i\pi/L$, L being the overall length of the combined beam structure and $\omega_i = \alpha_i^2 \sqrt{EI/\rho A}$ ⁸

Table 1 lists the material constants and dimensions employed for the three identical beam elements used in this work. From these values one calculates from (17) for $i=1$:

$$v^* = 899.13 \text{ in/sec}$$

We intend to examine numerical solutions for the moving force and the moving mass throughout the range $0 < v \leq v^*$.

Two primary references will be used as basis of comparison:

- (i) The exact solution for the moving force solution⁸ which for

(8) Nowacki, W. Dynamics of Elastic Systems, Chapman & Hall Ltd, London, 1963, p. 136

TABLE 1. MATERIAL PROPERTIES AND NOMENCLATURE

	Material	aluminum
ρ	Density	$3.14 \times 10^{-4} \text{ lbsec}^2/\text{in}^4$
L	Overall Beam Length	32
l	Length of each element	120.0 in
ρAL	Beam Mass	
m_p	Moving Mass	0.0, $\rho AL/4$, $\rho AL/2$
E	Young's Modulus	$1.0 \times 10^7 \text{ psi}$
A	Beam Cross Sect. Area	31
I	Beam Area Moment of Inertia (fixed by choice of ω_1 below)	
h	Beam Thickness	2.0 in.
$\omega_1/2\pi$	Beam Fundamental Frequency	1.25 hz
v	Mass Velocity	100., $v^*/4$, $v^*/2$, v^*
v^*	Fundamental Resonant Velocity	899.13 in/sec

the case of a moving concentrated downward force $-m_p \delta(x-vt)$ is :

$$y(x,t) = -2m_p g / \rho A L \sum_{n=1}^{\infty} \sin \alpha_n x (\alpha_n v \sin \omega_n t - \omega_n \sin \alpha_n v t) / \omega_n (\alpha_n^2 v^2 - \omega_n^2) \dots (18)$$

The finite element solutions for the moving mass problem (Equation (16) after imposing support constraints) with $m_p = 0$ will be compared with computations of (18) above.

(ii) The experimental work of Ayre, Jacobsen and Hsu². The mass velocities employed in this work were quasi-static $v \doteq 0$, and $v \doteq v^*/4$, $v^*/2$, and v^* . The moving mass values chosen were $m_p = 0$, and $m_p = \rho A L/4$ and $\rho A L/2$ where $\rho A L$ is the total beam mass.

Equation (16) is solved using Hamming's modified predictor-corrector method which uses fourth order Runge-Kutta method suggested by Ralston¹⁰ for adjustment of the initial increment and for computation of starting values. The method is taken directly from the IBM Scientific Subroutine Package for the IBM System #360, re: Programmer's Manual # H20-0205 available this laboratory. The method was found to be about four times faster than using the Runge-Kutta method throughout the entire problem. In general, run times in the order of 20 - 30 minutes on the IBM model 44 computer.

(2) Ayre, R.S., Jacobsen, L.S., and Hsu, C.S., "Transverse Vibration of One and of Two Span Beams Under the Action of a Moving Mass Load," Proc. of First National Congress on Applied Mechanics, June 1951

(10) Ralston and Wilf, Mathematical Methods for Digital Computers, Wiley and Sons, New York, London, 1960, pp. 95-109

Results - Moving Force

Figures 4 through 7 show the transverse displacement of the beam at the grid point locations $x = L/3, 2L/3$ as computed either by the finite element method or by evaluation of the exact solution (18) - any discrepancy between the results being too small to be discerned even in plots of this scale. This is substantially less error than appears in other treatments yielding approximate results.^{4,9}

Using the relationship (9), i.e., $y(x,t) = \underline{a}(x)\underline{u}^e(t)$ with $x = vt$, gives the displacement directly beneath the moving load to be compared with the results of Ayre, et al, who recorded displacement information exclusively at this location. Figures 8 - a,b,c show these comparisons and it is obvious that the agreement with experiment is much better in figures b and c than in a. Actually, Ayre and his co-workers experienced considerable experimental difficulty when the force was translated at $v^*/4$. Quoting from their publication² in which the authors remark on their disagreement with Schallenkamp's theoretical solution for the moving force (evidently a three term approximation of expression (18)):
..."The agreement is generally good [except at $v^*/4$] where it has been found that comparatively small errors in velocity may result in marked differences in the shape of the trajectory." ... In 8a the theoretical curve used by Ayre as a basis of comparison has been included.

(2) Ayre, R.S., Jacobsen, L.S., and Hsu, C.S., "Transverse Vibration of One and of Two Span Beams Under the Action of a Moving Mass Load," Proc. of First National Congress on Applied Mechanics, June 1951

(4) Schallenkamp, A., "Schwingungen von Trägern bei bewegten Lasten," Ingenieur-Archiv, v.8, 1937, pp. 182-198

(9) Hutton, D.V., and Counts, J., "Deflections of a Beam Carrying a Moving Mass," Trans. ASME, Sept, 1974, p. 803

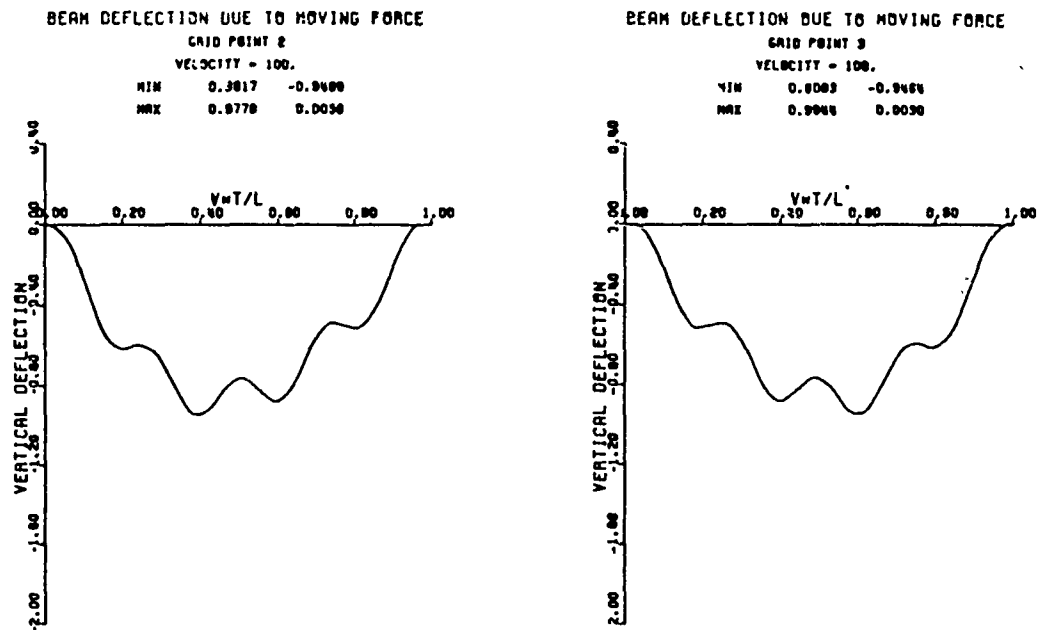


Figure 4

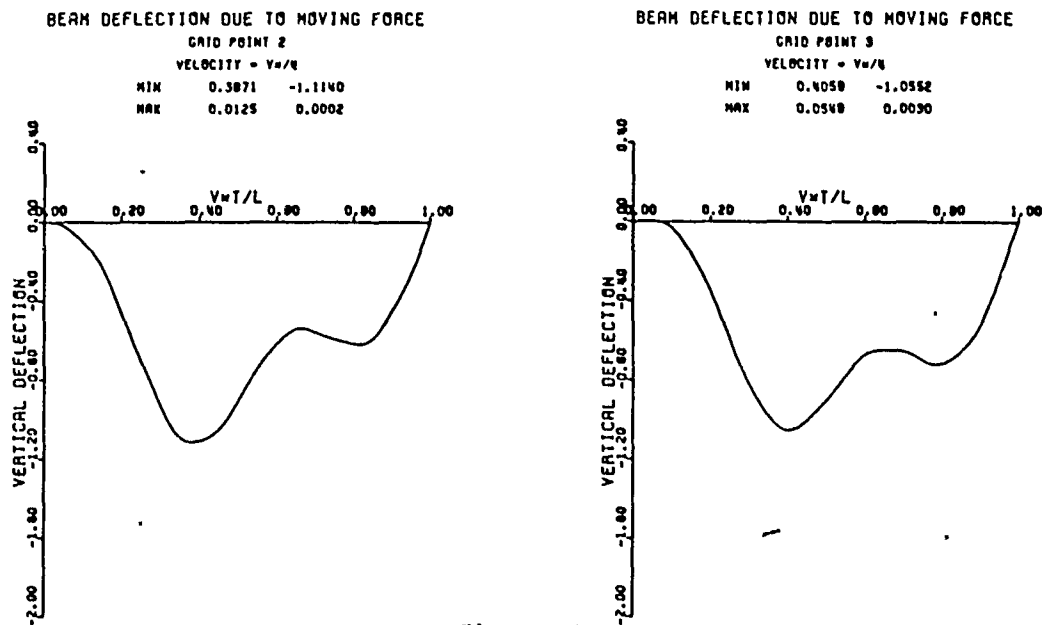


Figure 5

Transverse Motion at Grid Points in Response to Moving Force

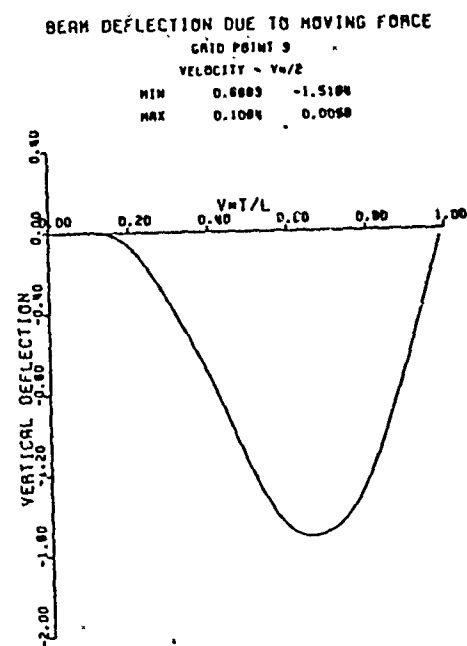
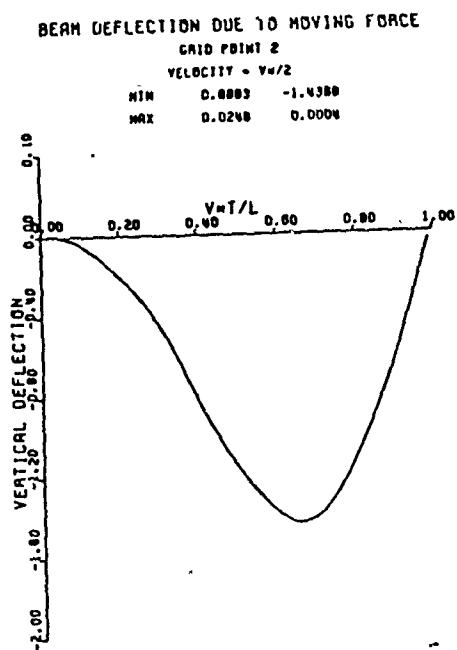


Figure 6

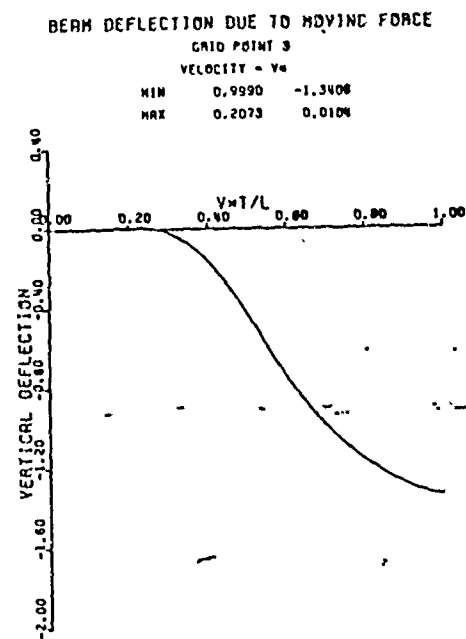
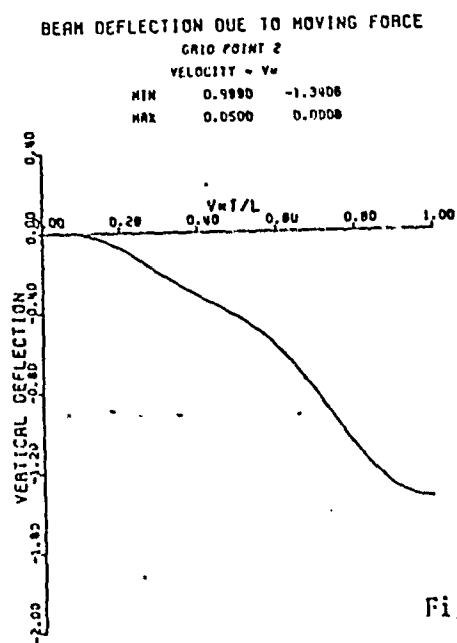


Figure 7

Transverse Motion at Grid Points in Response to Moving Force

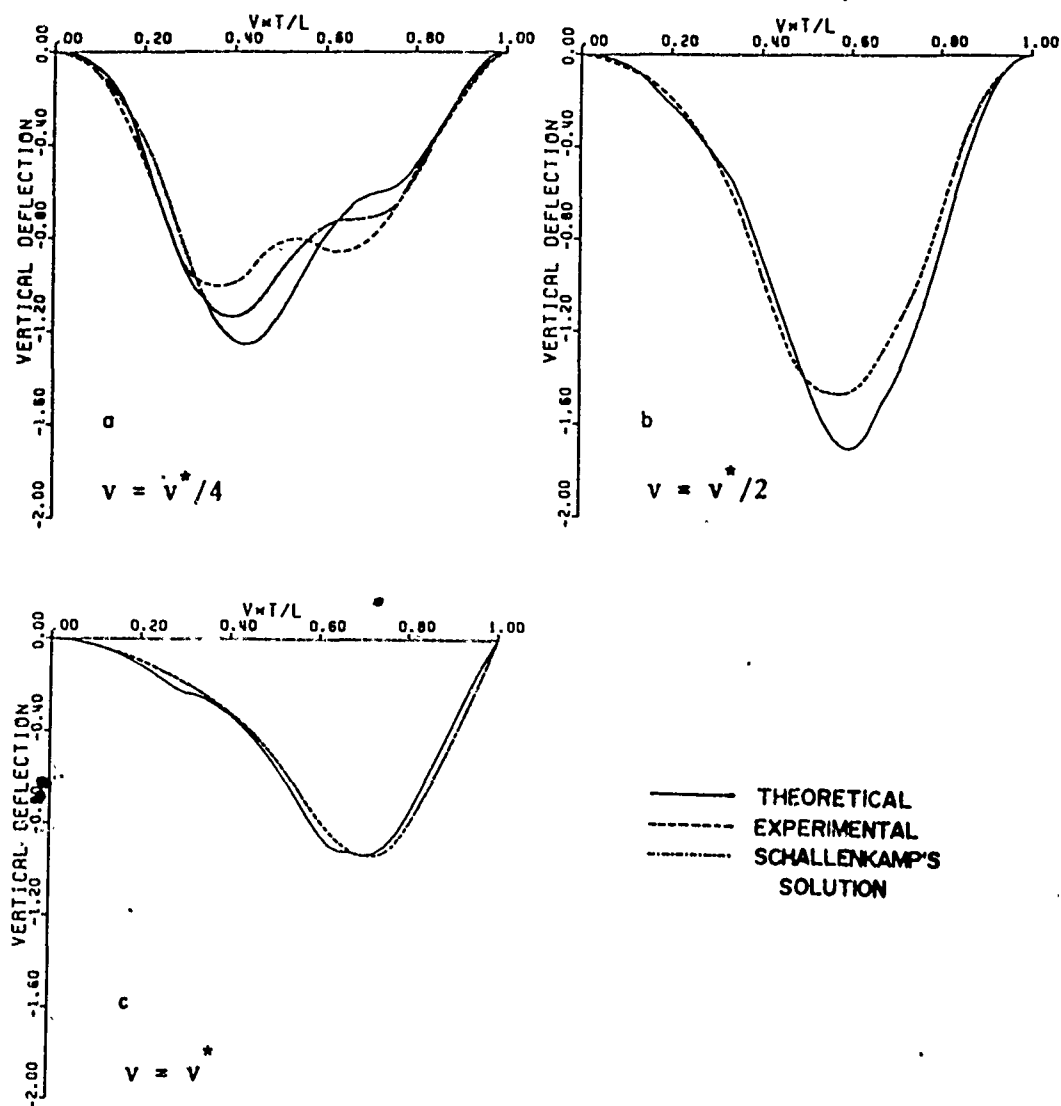


Figure 8. Transverse Motion at $x = vt$ in Response to Moving Force.

The exceptional agreement* (using only three finite beam elements) of the finite element results for the moving force gives confidence in extending the technique to the moving mass problem - for which no simple solution as (18) exists.

Results - Moving Mass

Figures 9 through 14 show the transverse displacement of the beam at the grid point locations $x = L/3, 2L/3$ as computed by the finite element procedure for various cases of velocity and mass values. Again use will be made of relationship (9) to convert this information to displacement beneath the moving mass so that a direct comparison with the experimental results of Ayre, Jacobsen, and Hsu can be made. Figure 15 - a,b,c shows this comparison to be quite good - excellent agreement occurring at the grid point locations. A closer look shows, however, that the slopes of the curves generated by the finite element analysis are discontinuous at the grid point locations. The reason for this is that the displacement approximation (9) is built from cubic polynomials which are not continuous in the second derivative at the grid point connections. Indeed, only continuity in y and y' were demanded in constructing these polynomials.

The discontinuities of $y''(x)$ at grid points might not be serious if it was not for a 'force' in the continuum equation of motion (8)... $m_p v^2 y''(x)$. Thus at higher velocities jump discontinuities in y'' will cause increasingly powerful disturbances which are nonphysical in character. This is apt to be especially influential in armament

*Note: All displacements are normalized with respect to the displacement which occurs at midspan due to a static load at this point.

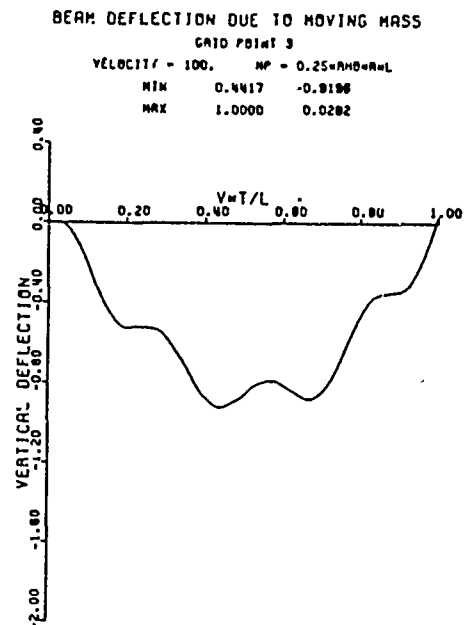
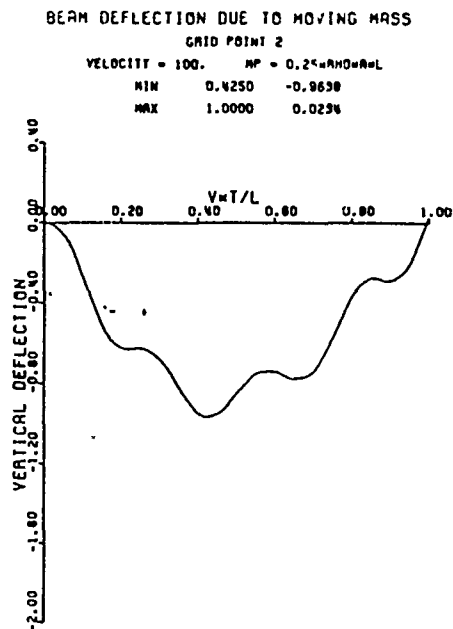


Figure 9

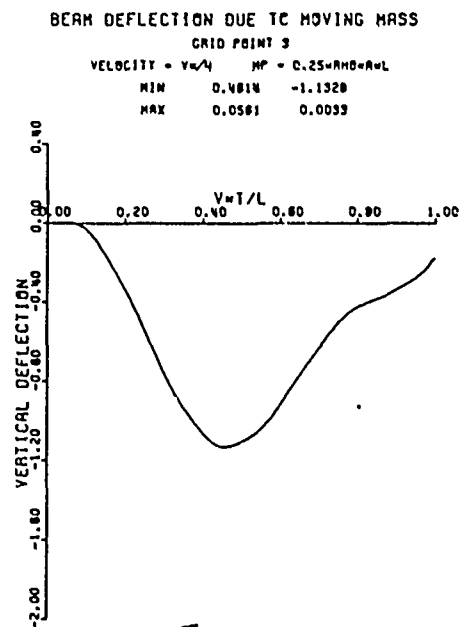
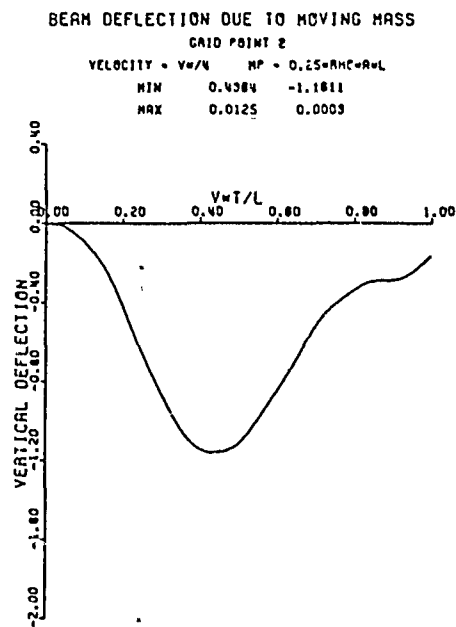


Figure 10

Transverse Motion at Grid Points in Response to Moving Mass

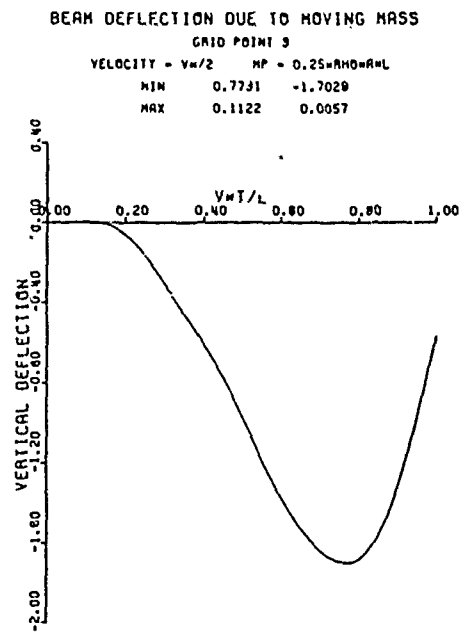
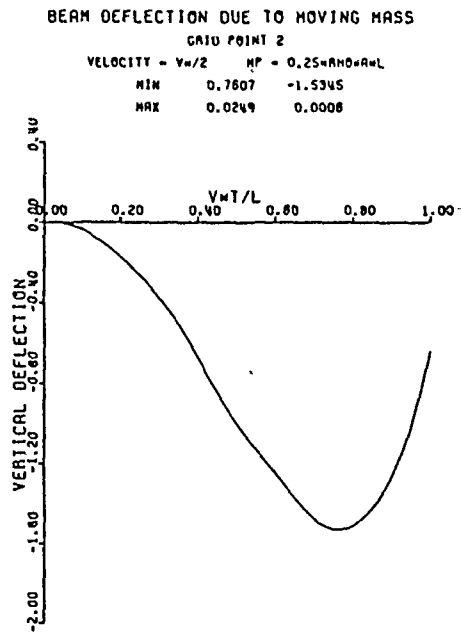


Figure 11

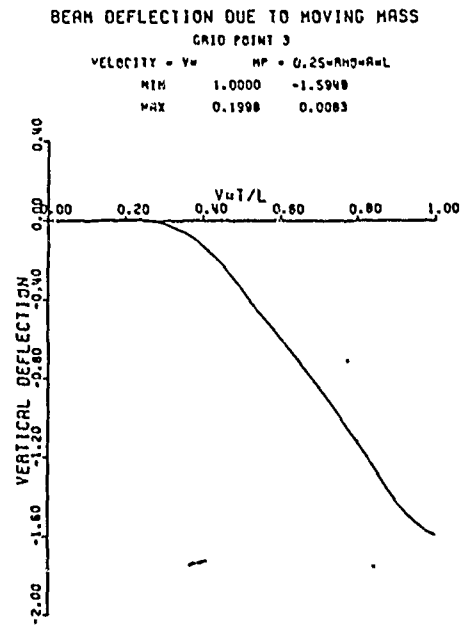
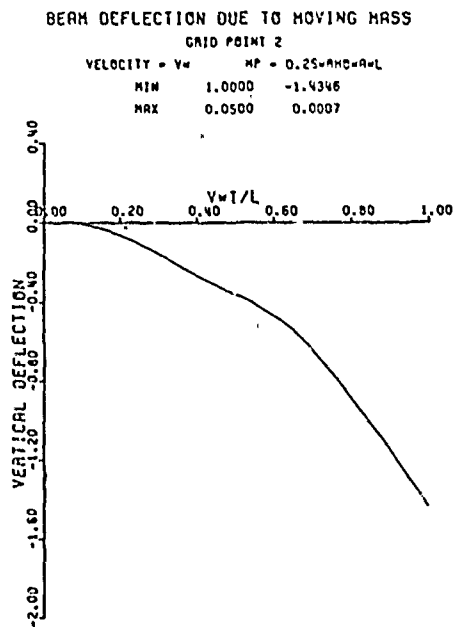


Figure 12

Transverse Motion at Grid Points in Response to Moving Mass

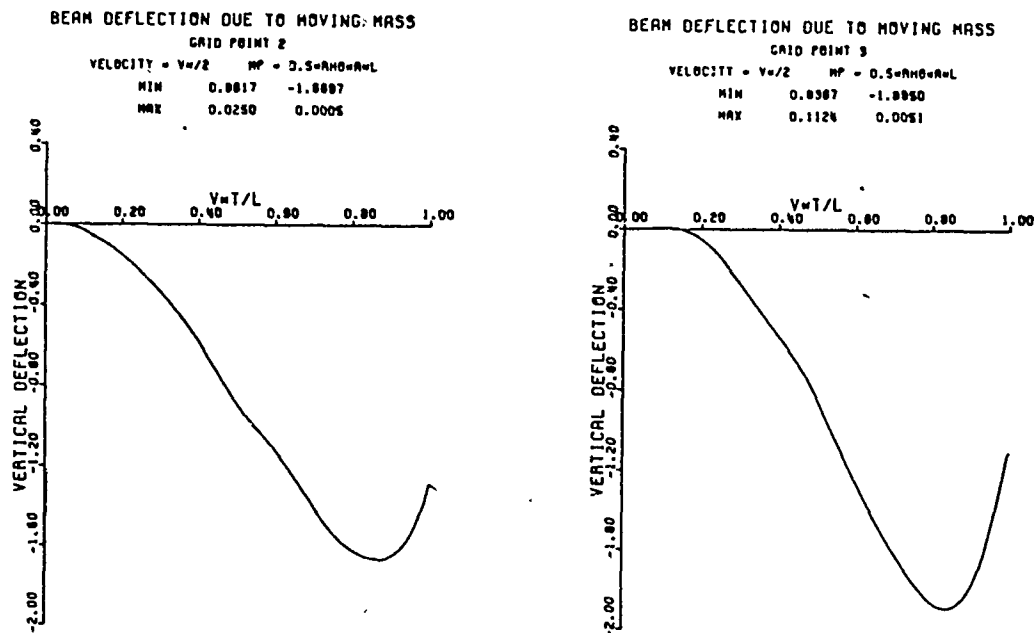


Figure 13

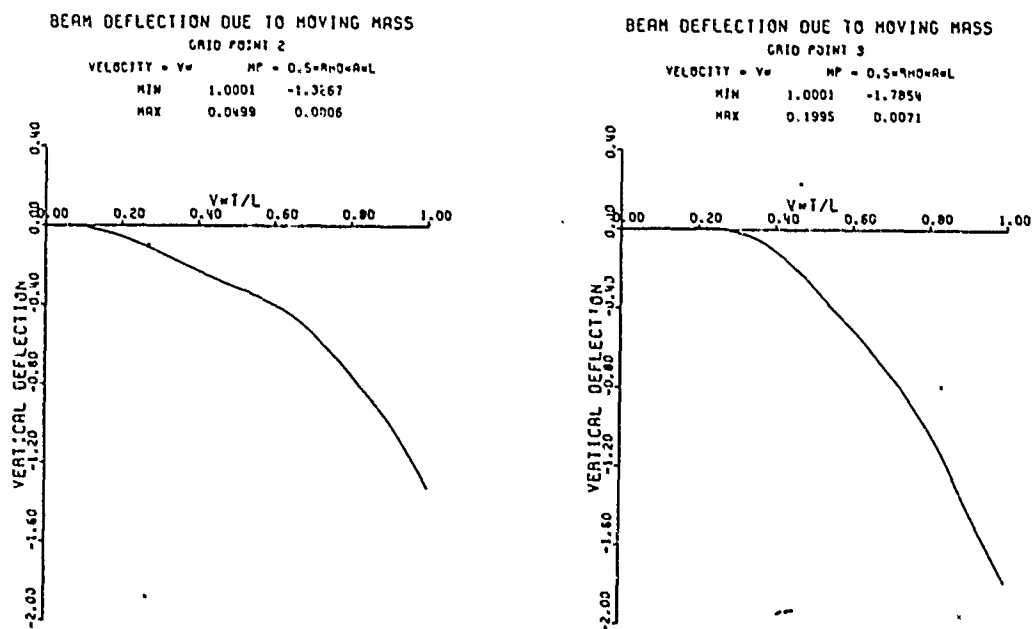


Figure 14

Transverse Motion at Grid Points in Response to Moving Mass

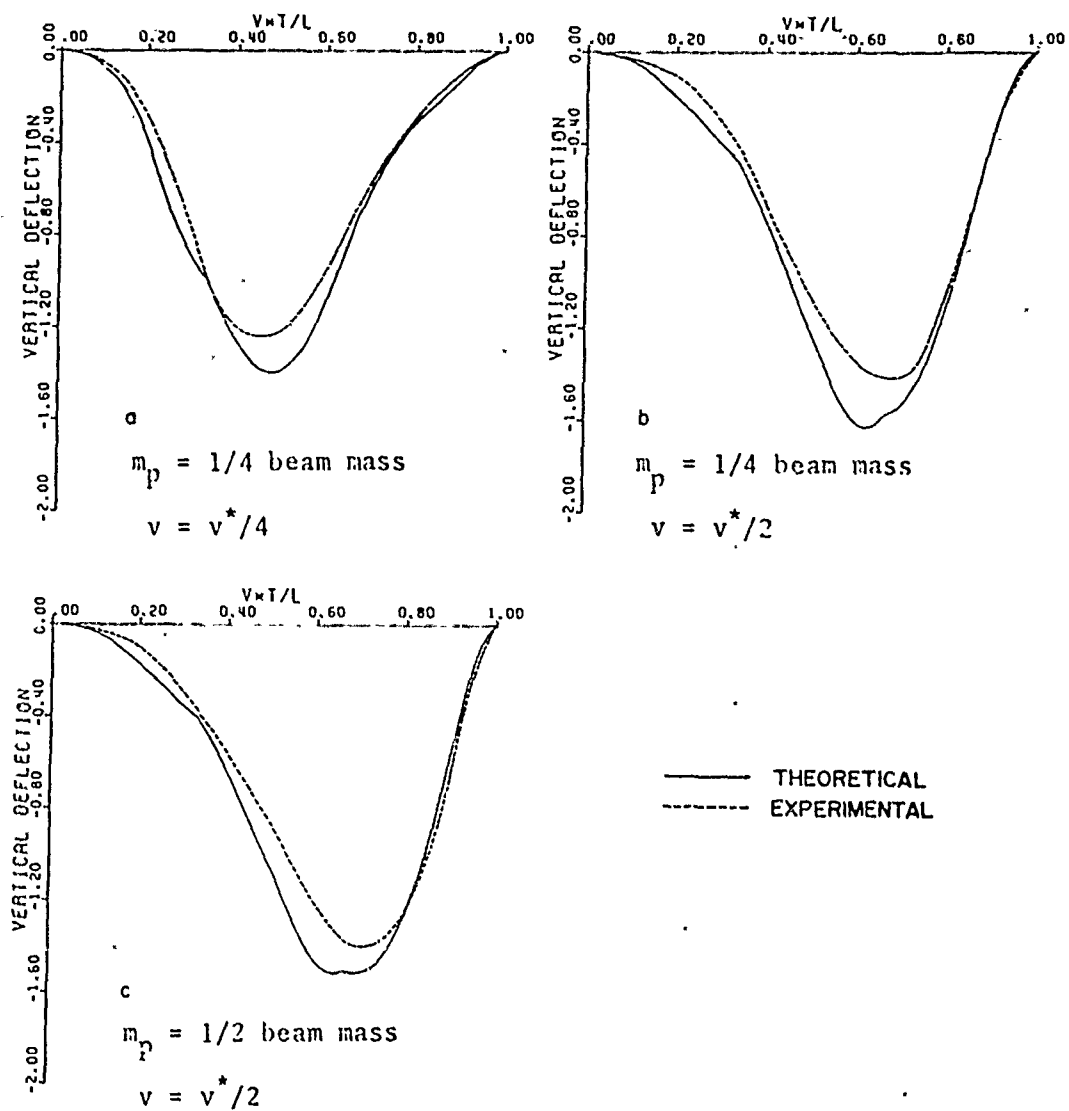


Figure 15. Transverse Motion of Moving Mass.

applications involving velocities considerably larger than v^* .

One approach toward rectification of this problem requires the formation of higher-ordered polynomials which are continuous in the second derivative across the grid points of the structure. Higher polynomials have additional coefficients and, as in the previous derivation, these coefficients are equal in number to the element degrees of freedom, i.e., the generalized displacements u_i^e .

The establishment of polynomial displacement functions proceeds in the same manner as before, with the added conditions:

$$y''(0) = u_3^e \quad ; \quad y''(L) = u_6^e$$

The result is that $y(x)$ will be approximated interior to an element by:

$$y(x) = \underline{\hat{a}}(x)\underline{u}^e ;$$

where $\underline{\hat{a}}$ and \underline{u}^e are now vectors with six components instead of four.

The new $(\hat{})$ element matrices are calculated according to equation (14). The multiplication and integration was accomplished analytically by a computer program called MANIP which was written in the FORMAC language - giving analytical expressions as output. Similarly, new expressions for c_1 , c_2 , and c_3 for use in equation (15) were formed using this program. $\underline{\hat{k}}^e$ and $\underline{\hat{m}}^e$ compose the constant elements of the matrices $\underline{\hat{u}}^e$ and $\underline{\hat{u}}^e$ and are found to be:

$$\underline{\hat{k}} = \frac{EI}{7\ell^3} \cdot \begin{bmatrix} 120 & 60\ell & 3\ell^2 & -120 & 60\ell & -3\ell^2 \\ & (192/5)\ell^2 & (11/5)\ell^3 & -60\ell & (108/5)\ell^2 & -4/5\ell^3 \\ & & (3/5)\ell^4 & -3\ell^2 & (4/5)\ell^3 & \ell^4/10 \\ & & & 120 & -60\ell & 3\ell^2 \\ & \text{symm} & & & (192/5)\ell^2 & -\frac{11\ell^3}{5} \\ & & & & & 3\ell^4/5 \end{bmatrix}$$

$$\underline{\hat{m}}^e = \frac{o\Lambda\ell}{231} \cdot \begin{bmatrix} 181/2 & (311/20)\ell & (281/240)\ell^2 & 25 & -151\ell/20 & \frac{181\ell^2}{240} \\ & 52\ell^2/15 & 23\ell^3/80 & 151\ell/20 & -133\ell^2/60 & \frac{13\ell^3}{60} \\ & & \ell^4/40 & \frac{181\ell^2}{240} & -13\ell^3/60 & \frac{\ell^4}{48} \\ & & & 181/2 & -311\ell/20 & \frac{281\ell^2}{240} \\ & & & & (52/15)\ell^2 & -\frac{23\ell^3}{80} \\ & & & & & \frac{\ell^4}{40} \end{bmatrix}$$

Figure 16 shows the improved results obtained through the use of the quintic polynomial. Comparison should be made with the results obtained via the cubic polynomial as shown in figure 15(a). The price paid, however, is increased computation time due to the additional degrees of freedom induced through the use of the quintic. One also faces increasing amount of ill-conditioning in the matrix equations of motion due to the widely differing magnitudes induced in the coefficient matrices and their corresponding output variables. Future work will concentrate on these problems and the use of less time-consuming integration algorithms.

BEAM DEFLECTION UNDER A MOVING LOAD

$$\text{VELOCITY} = V \times / 4 \quad \text{MP} = 0.25 \times \text{RHO} \times A \times L$$

MIN	0.4739	-1.3598
MAX	1.0001	0.0000

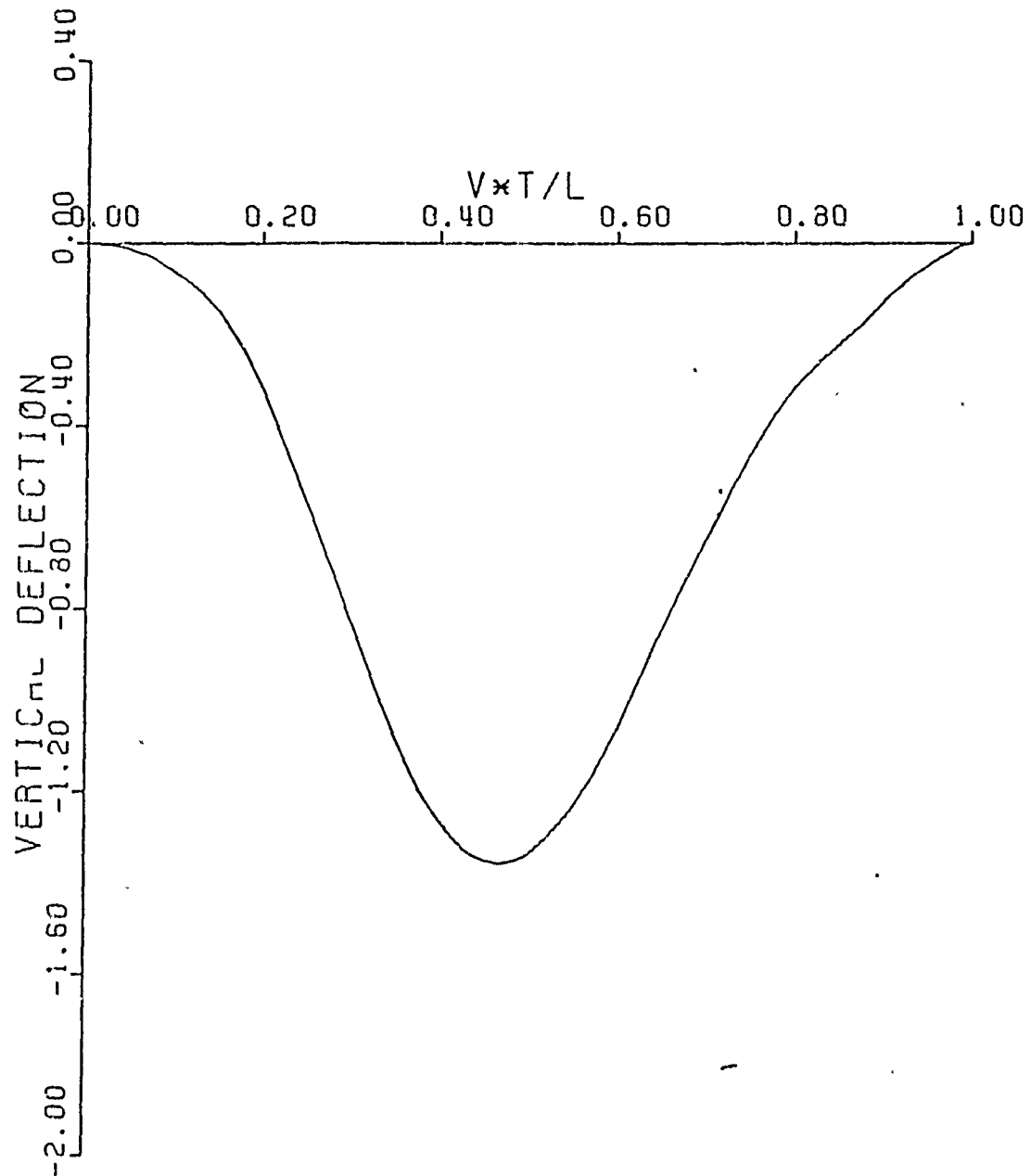


Figure 16. Improved Results Using Quintic Shape Function.

REFERENCES - CHAPTER TWO

1. Stokes, Sir George G., "Discussion of a Differential Equation Relating to the Breaking of Railway Bridges", Trans. Cambridge Phil. Soc., 8, p. 707, 1849.
2. Ayre, R. S., Jacobsen, L. S., & Hsu, C. S., "Transverse Vibration of One and of Two Span Beams Under the Action of a Moving Mass Load", Proc. of First National Congress on Applied Mechanics, June 1951.
3. Tong, K., Theory of Mechanical Vibrations, J. Wiley & Sons, 1960, p. 300.
4. Schallenkamp, A., "Schwingungen von Trägern bei bewegten Lasten", Ingenieur - Archiv, V. 8, 1937, pp. 182-198.
5. Przmieniecki, J. S., Theory of Matrix Structural Analysis, McGraw-Hill, 1968, p. 267.
6. Przmieniecki, J. S., Theory of Matrix Structural Analysis, McGraw-Hill, 1968, p. 81, 297.
7. Simkins, T. E., Pflegl, G., and Scanlon, R. S., "Dynamic Response of the M113 Gun Tube to Travelling Ballistic Pressure and Data Smoothing as Applied to XM150 Acceleration Data", Watervliet Arsenal Technical Report WVT-TR-75015, April 1975.
8. Nowacki, W., Dynamics of Elastic Systems, Chapman & Hall Ltd, London, 1963, p. 136.
9. Hutton, D. V., and Counts, J., "Deflections of a Beam Carrying a Moving Mass", Trans ASME, Sept 1974, p. 803.

10. Ralston and Wilf, Mathematical Methods for Digital Computers.
Wiley and Sons, New York, London, 1960, pp. 95-109.
11. Simkins, T., "Structural Response to Moving Projectile Mass by the
Finite Element Method", WVT-TR-75044, July 1975.

APPENDIX

THE BEAM EQUATION FOR TRANSVERSE MOTIONS OF THE M113 TUBE

The beam equation for the deflection of the neutral axis assumes that a restoring moment proportional to the second spatial derivative of the deflection $y(x,t)$, will be induced in response to any applied moment $M(x,t)$:

$$\text{i.e., } M(x,t) = EIy''(x,t) \quad (\text{B-1})$$

where E and I are Young's modulus and the cross sectional area moment of inertia respectively.

The applied moments $M(x,t)$ are due to distributed and concentrated loads acting on the tube. Some of these loads act at locations which change in time. Figure 15 depicts the general loading condition at any time and shows (exaggerated) the initial beam curvature due to the action of gravity. Because of this curvature, both transverse and axial load components will possess moment arms with respect to any generic point x along the beam neutral axis.

Thus the total moment induced by a particular load distribution per unit length is:

$$M_w(x,t) = \int_x^L \{w_t(\bar{x},t)[\bar{x}-x] + w_a(\bar{x},t)[y(\bar{x})-y(x)]\}d\bar{x} \quad (\text{B-2})$$

where L is the overall tube length and w_t , w_a are the

transverse and axial components of the load intensity distribution $w(x,t)$.

Similarly, concentrated loads $P(x,t)$ located at various points $\xi(t)$ and having transverse and axial components P_t , P_a respectively, will induce a total moment

$$M_p(x,t) = \{[\xi-x]P_t - [y(\xi)-y(x)]P_a\}H(\xi-x) \quad (B-3)$$

where $H(z)$ is the Heaviside function:

$$\begin{aligned} H(z) &= 0 & z < 0 \\ &= 1 & z > 0. \end{aligned}$$

As indicated in figure 15, four distributed type loads exist as well as two concentrated loads. (Since the beam inertia and bourdon loadings both act in a purely transverse direction, they have been grouped together in the figure.)

These loads will be considered individually, in the order depicted in the figure.

(i) Gravitational force acting upon the tube at angle α . The tube weight per unit length is constant in time although in general it will be space-variant thru the cross-sectional area function $A(x)$.

$$w_t = w_t(x) = -\rho g A(x) \cos(\alpha)$$

$$w_a = w_a(x) = -\rho g A(x) \sin(\alpha)$$

(ii) (a) Inertial Loads due to Transverse Beam Motion.

The inertia force acting upon an element of beam mass $dm = \rho A(x)dx$ is simply:

$$-\ddot{y}(x,t)dm = -\ddot{y}(x,t)\rho A(x)dx$$

thus

$$w_t = w_t(x,t) = -\rho A(x)\ddot{y}(x,t).$$

(b) Bourdon Loads.

Due to the curvature of the gun axis, the bore surface area is not axially symmetric, i.e., there is an unequal distribution of bore surface area above and below the neutral axis of the tube. Therefore, when the tube is pressurized a moment will be created. In the initially deformed configuration as shown in figure 15, such a moment will tend to straighten the tube initially. At later times in the ballistic cycle however, the sign of the moment will vary with the different modes of vibration. (In general one might reasonably expect, however, that the fundamental mode will dominate the deflection pattern and the net result would be a moment tending to straighten the tube).

To derive the expression for the bourdon load, it is simpler to first consider a beam with a rectangular, rather than circular, hole (bore) of height h and having unit width into the plane of the figure. A section of such a beam is shown in figure (a).

Since equation (B-1) contains the assumption that the deflection at any point along the beam neutral axis is circular, there exists therefore a radius of curvature $R(x)$ which describes the elastic deflection curve of the neutral axis.

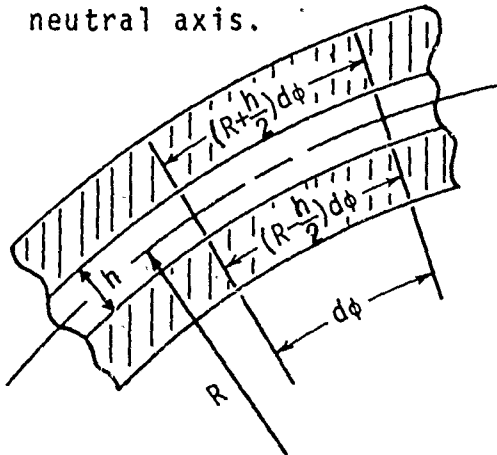


Figure (a)

Referring to figure (a), the difference in bore surface area above and below the neutral axis is observed to be:

$$d\sigma = (R + \frac{h}{2})d\phi - (R - \frac{h}{2})d\phi = hd\phi$$

Since $d\phi = \frac{d\phi}{dx} dx$ and since $\phi = y'$, we have that $d\sigma = hy''dx$.

Consequently, the 'Bourdon' load intensity for a rectangular bore of unit width:

$w_t(x,t) = p(x,t)hy''$; where $p(x,t)$ is the internal ballistic pressure applied to the bore area.

For a circular hole we proceed in the same manner:

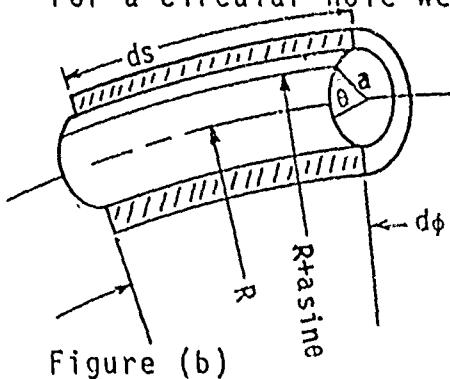


Figure (b)

$$\begin{aligned} ds &= (R + a \sin(\theta))d\phi \\ &= (R + a \sin(\theta))dx/R \end{aligned}$$

The projected elemental bore surface area:

$$ads(\sin\theta d\theta) = (R + a \sin\theta)(a \sin\theta)dx/R$$

Thus the net bore surface area corresponding to a differential beam element:

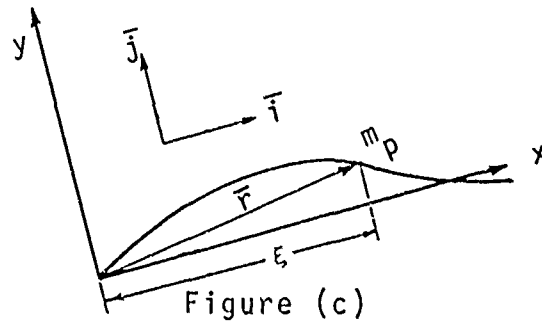
$$\int_0^{2\pi} \left\{ \frac{a^2 \sin^2 \theta}{R} + a \sin \theta \right\} d\theta dx = a^2 \pi y'' dx$$

i.e., the upper bore surface (above the neutral plane) has a greater area per unit length than the lower bore surface by the amount $a^2 \pi y''$ and the Bourdon load intensity is therefore:

$$w_t(x, t) = -p(x, t) a^2 \pi y'' \equiv -k(x, t) y''.$$

(iii) Projectile Inertial Forces.

The curved bore path followed by the projectile causes reactionary inertial loads to be applied to the tube. Figure (c) represents the projectile as a point mass m_p travelling with velocity $V(t)$ along the curved bore axis so that at time t , its position along the bore is $x = \xi(t)$.



The position vector $\bar{r}(t)$ as measured from the origin of an inertial reference frame:

$$\bar{r} = \xi \bar{i} + y(\xi, t) \bar{j}; \quad \xi = \int_0^t V dt$$

$$\dot{\vec{r}} = \dot{\xi}\vec{i} + \left[\frac{\partial y}{\partial \xi} \dot{\xi} + \dot{y} \right] \vec{j}; \quad (\dot{}) = \partial/\partial t$$

$$\ddot{\vec{r}} = \ddot{\xi}\vec{i} + \left\{ \frac{\partial}{\partial \xi} \left[\frac{\partial y}{\partial \xi} \dot{\xi} + \dot{y} \right] \dot{\xi} + \frac{\partial}{\partial t} \left[\frac{\partial y}{\partial \xi} \dot{\xi} + \dot{y} \right] \right\} \vec{j}$$

noting that $\partial/\partial \xi = \partial/\partial x$, we have:

$$= \dot{V}\vec{i} + \{V^2 y'' + 2V\dot{y}' + \ddot{y} + \dot{V}y'\} \vec{j}$$

where (') denotes derivatives with respect to the independent space variable, x .

The transverse forces acting on the projectile are the transverse component of its weight and the reaction of the bore surface. This reaction must be equal and opposite to P_t , the transverse component of force acting on the tube.

$$\text{thus, } -P_t - m_p g \cos \alpha = [V^2 y'' + 2V\dot{y}' + \ddot{y} + \dot{V}y'] \Big|_{x=\xi}$$

$$\text{or, } P_t = -m_p [V^2 y''(\xi, t) + 2V\dot{y}'(\xi, t) + \ddot{y}(\xi, t) + \dot{V}y'(\xi, t) + g \cos \alpha]$$

(iv) Recoil Inertia Loads

For this purpose we consider the axial motion of the tube to be uniform, i.e., at any point x the tube accelerates rearward with the same prescribed acceleration $X_0(t)$.

Thus $w_a(x,t) = -\rho A \ddot{X}_0(t)$ is the axial load intensity function representing the inertia load due to recoil.

Let $\bar{w}(x,t)$ and $\bar{P}(x,t)$ denote the totals of the distributed and concentrated loads respectively. With this notation the equation of motion becomes:

$$\begin{aligned} EI y''(x,t) = & \int_x^L \{ \bar{w}_t(\bar{x},t)[\bar{x}-x] - \bar{w}_a(\bar{x},t)[y(\bar{x},t)-y(x,t)] \} d\bar{x} + \\ & + \{ [\xi(t)-x] \bar{P}_t - [y(\xi,t)-y(x,t)] \bar{P}_a \} H(\xi-x) \end{aligned} \quad (B-4)$$

\bar{x} is merely a dummy variable for integration, and $\xi(t)$ is the point of application of the particular concentrated load.

Ultimately, we desire a differential equation devoid of integral forms. We proceed, therefore, to differentiate with respect to the space variable, x , noting⁴ that

$$d/dx \int_x^L h(x,\bar{x}) d\bar{x} = \int_x^L \partial h / \partial x d\bar{x} - h(x)$$

thus,

$$\begin{aligned} (EI y'')' = & - \int_x^L \{ \bar{w}_t(\bar{x},t) - y' \bar{w}_a(\bar{x},t) \} d\bar{x} - (\bar{P}_t - y' \bar{P}_a) H(\xi-x) + \\ & \{ \bar{P}_t(\xi-x) - [y(\xi,t)-y(x,t)] \bar{P}_a \} \delta(\xi-x), \end{aligned}$$

where $\delta(z)$ is the Dirac-delta function.

⁴HILDEBRAND, Advanced Calculus for Engineers, p. 353.

Now if $f(z)$ is a continuous function:

$$f(z)\delta(z) = f(0)\delta(z),$$

so that

$$\begin{aligned} (EIy''')' &= -\int_{-\infty}^L \{\bar{w}_t(\bar{x}, t) + y' \bar{w}_a(\bar{x}, t)\} d\bar{x} - \\ &= (\bar{P}_t + y' \bar{P}_a) H(\xi - x) + [y(\xi, t) - y(x, t)] \bar{P}_a \delta(\xi - x). \end{aligned}$$

Differentiating once more:

$$\begin{aligned} (EIy''')'' &= \bar{w}_t(x, t) - y' \bar{w}_a(x, t) + \int_x^L y'' \bar{w}_a(\bar{x}, t) d\bar{x} + \bar{P}_t \delta(\xi - x) - \\ &= \bar{P}_a \{2y' \delta(\xi - x) + [y(\xi, t) - y(x, t)] \frac{d\delta(\xi - x)}{d(\xi - x)} + \\ &= y'' H(\xi - x)\}^*, \end{aligned} \quad (B-5)$$

where

$$\begin{aligned} \bar{w}_t(x, t) &= -\rho g A(x) \cos \alpha - \rho A(x) \ddot{y} - k(x, t) y'' \\ \bar{w}_a(x, t) &= -\rho A(x) \ddot{X}_0(t) - \rho g A(x) \sin \alpha \\ \bar{P}_a &= 0; \\ \bar{P}_t &= -m_p (V^2 y'' + 2V \dot{y}' + \ddot{y} + \dot{V} y') \Big|_{x=\xi} + m_p g \cos \alpha. \end{aligned}$$

If A is uniform, then

$$\int_x^L y'' \bar{w}_a(\bar{x}, t) d\bar{x} = \rho A y'' [g \sin \alpha + \ddot{X}_0(t)] (x - L),$$

and if, further, $V = \text{const.}$, so that $\xi = Vt$, the final equation of motion is:

* where $\delta'(z)$ is a function having the property $\int_{-\infty}^{\infty} \delta'(z) \phi(z) dz = -\phi'(0)$.

$$\begin{aligned}
 (EIy'')'' &= -k(x,t)y'' + [\rho A \ddot{X}_0(t) + \rho A g \sin \alpha] y''(x-L) + \\
 &+ [\rho A \ddot{X}_0(t) + \rho A g \sin \alpha] y' - m_p(\ddot{y} + 2V\dot{y}' + g \cos \alpha + \\
 &+ V^2 y'') \delta(x-Vt) - \rho g A \cos \alpha - \rho A \ddot{y}
 \end{aligned}
 \tag{B-6}$$

INVESTIGATION OF CAUSES OF DISPERSION IN LOW-DISPERSION
AUTOMATIC CANNON SYSTEM (LODACS) CONCEPT

R.S. NEWELL
Battelle Memorial Institute
Columbus, Ohio

TABLE OF CONTENTS

	<u>Page</u>
INTRODUCTION	471
METHODOLOGY	473
DISCUSSION OF DISPERSION-CAUSING FACTORS	475
Yaw of the Projectile at Launch	475
Initial Yaw Rate of the Projectile	478
Effects of Variation in Muzzle Velocity	480
Fire-Control Influence	480
Effect of Variation in Projectile Mass	480
Effect of Lateral Throw-Off of Projectile	483
Launch-Angle Error	486
Eccentricity of Projectile	493
SUMMARY AND COMMENTARY ON DISPERSION SOURCES	493
REFERENCES	496

INTRODUCTION

Causes of dispersion in guns is not a new topic in the armament development community. Scores of reports treat the problem in general or in a detailed examination of one or more of the factors which contribute to dispersion. Much of the early work, although at least partially applicable to any dispersion question, dealt with artillery, mortar, or tank rounds. Dispersion in automatic cannon is discussed less frequently in the literature. Besides there being comparatively fewer automatic cannon systems over the years, the application of dispersion has been different in automatic cannon as contrasted with larger caliber weapons. In automatic cannon, the design of both ammunition and gun has generally proceeded along pure engineering lines. In production, after integration on the vehicle, the mount is tuned to provide a system dispersion which falls in the 3 to 4-mrad range. For the targets, engagement ranges, rates of fire and available fire-control accuracy, this level of dispersion was generally acceptable and, hence, no great attention has been devoted to causes of dispersion in automatic cannon.

Comparatively recently, however, a new role for and approach to automatic cannon has developed. The potential for building a tank-killing automatic cannon in the 60 to 90-mm caliber ranges is being considered in separate but related technology programs at the U. S. Army Armament Command (60 mm) and Defense Advanced Research Projects Agency (75 mm). The British have fielded a 30-mm automatic cannon, the Rarden, for use against light armor. The U. S. Army Armament Command is conducting a technology program to explore the necessary attributes of a precise, smaller caliber automatic cannon system in the Low Dispersion Automatic Cannon System (LODACS) program. All of these efforts share the goal of a system dispersion of less than 1 mrad; the Rarden system has demonstrated such precision.

In terms of dispersion, the fundamental question is asked, "What are the important contributors to system dispersion?" As mentioned before, much of the dispersion effort has been directed toward single-shot concepts. For an automatic cannon, one rule of thumb suggests that, after completion of development, the Mann barrel dispersion of the ammunition is 0.25 mrad; the dispersion from a single-barrel automatic cannon on a hard stand is about 1 mrad, and the dispersion of a burst from a vehicle-mounted automatic cannon is 3 to 4 mrad. This suggests that there are phenomena associated with burst fire and with vehicle mounting which contribute to dispersion. Interestingly, the Rarden gun achieves (occasionally) less dispersion from the vehicle mount than from the hard stand. This gun, incorporating a sliding breech, a heavy barrel with flash hider, and damping pads to reduce lateral motion of the barrel is currently being studied and tested in the LODACS program.

This present BCL task effort was initiated to take a brief look at factors which contribute to dispersion in an automatic cannon system. The intent here is to identify trends and relative orders of magnitude of individual dispersion-inducing phenomena, rather than to perform an exhaustive and definitive study of the subject. The results would then be available for consideration in initiating or adding emphasis to investigations of specific phenomena, and to assist in planning subsequent system tests, and in interpreting results.

This effort has considered the following causes of dispersion in an automatic cannon:

- Projectile yaw
- Projectile yaw rate
- Muzzle-velocity variation
- Fire-control effects
- Projectile mass variation
- Throw-off
- Launch-angle error
- Eccentricity of projectile

For convenience, characteristics of the Rarden round have been assumed. The effects of variations in dispersion-causing factors have been calculated. An attempt has been made to identify the parameter bounds to be anticipated in a LODACS system. Owing to the quick-look nature of this investigation, this has not been done in great depth, nor has the cross-coupling of two or more of the phenomena causing dispersion been attempted. Thus, the results are only to be considered indicative of trends.

METHODOLOGY

The problem is analyzed with an adaptation of point-mass trajectory analysis of exterior ballistics. The basic equations are:

$$\frac{d^2x}{dt^2} = -\frac{\pi \rho d}{8m} C_D v^2 \cos \theta ,$$

$$\frac{d^2y}{dt^2} = -\frac{\pi \rho d^2}{8m} C_D v^2 \sin \theta - g ,$$

where

x = down-range coordinate

y = vertical coordinate

ρ = density of air

d = diameter of projectile

m = mass of projectile

C_D = drag coefficient

v = velocity of projectile $\left[\left(\frac{dx}{dt} \right)^2 + \left(\frac{dy}{dt} \right)^2 \right]^{1/2}$

θ = angle of trajectory with horizontal

g = acceleration due to gravity .

Initially,

$$\frac{dx}{dt} (0) = v_0 \cos \theta_0 ,$$

$$\frac{dy}{dt} (0) = v_0 \sin \theta_0 .$$

The trajectory is calculated with variations of v_o , θ_o , m in order to determine the change in impact point at the given range of interest (ranges considered were 1000 and 2000 m).

Yaw and yaw-rate effects were analyzed with techniques adapted from Reference 1*. The effect of an initial yaw or yaw rate is properly analyzed by considering the motion of the projectile in a six-degree-of-freedom representation; however, an approximation to the change in the angle of departure is:

$$\theta_J = \frac{C_{L_\alpha}}{C_{M_\alpha} m v_o d} (I_Y \dot{\delta}_o - i I_X p_o \delta_o) ,$$

which is positive up (real term) and left (imaginary term), where $\dot{\delta}_o$ and δ_o are complex values and where:

C_{L_α} = lift coefficient

C_{I_α} = moment coefficient

I_Y = transverse moment of inertia

I_X = axial moment of inertia

$\dot{\delta}_o$ = yaw rate of projectile

p_o = spin rate of projectile .

This, of course, represents a dispersion source whose result can have a component in the horizontal direction perpendicular to the line of sight. By the nature of its definition, this formulation of aerodynamic jump represents an upper bound on the actual effect of yaw when the impact point is less than the maximum range of the ammunition.

* References are given at the end of the report.

Throw-off, in which the launch mechanism imparts a lateral velocity to the center of gravity of the projectile, is handled by adding a component to the appropriate initial velocity component. It is assumed that the velocity component in the deflection (horizontal) direction is small and can be neglected for drag computations.

Projectile characteristics used in this study were taken from Reference 2. For reference, some of the values and curves have been reproduced in the Appendix.

DISCUSSION OF DISPERSION-CAUSING FACTORS

Yaw of the Projectile at Launch

Table 1 gives the difference in impact point at 1000 and 2000 m for given yaw of the projectile at launch. As can be seen from Table 1, small initial yaw angles give relatively small deflections downrange, amounting to up to 0.013 mrad for an initial yaw of 0.4 mrad, or 0.023°. These deflections scale with initial yaw, as long as the values of initial yaw remain reasonably small. A yaw of 1 mrad to the right, for example, causes a downward deflection of 31.4 mm at a range of 1000 m.

Yaw of the projectile at launch can be caused by a number of factors. If, for example, the gun is moving lateral to the direction of fire at a velocity which is not negligible relative to the muzzle velocity, yaw will occur. This occurs in low-performance, side-firing aircraft cannon, but not in the configuration of the LODACS weapon. Even if the LODACS gun turns out to be a Gatling gun, an 8-in.-diameter, six-barrel cluster firing 2000 rounds per minute, the associated yaw is repeatable for every round and is about 3 mrad for 3500 ft/sec muzzle velocity. Unlikely as this choice is because of other considerations, the lateral velocity of the projectile at the muzzle will greatly exceed anticipated levels of a single-barrel concept, and still will not cause large random deflection. However, throw-off associated with this lateral velocity can cause significant deflections. This will be discussed subsequently.

TABLE 1. EFFECT OF PROJECTILE YAW ON IMPACT POINT

Yaw, mrad		Errors in Impact Point, mm			
		1000 m		2000 m	
		δy	δz	δy	δz
Up	Left				
-0.2	0.	0.	6.28	0.	15.26
-0.14	-0.14	- 3.79	4.44	- 7.58	10.79
0.	-0.2	- 5.36	0.	-10.72	0
0.14	-0.14	- 3.79	- 4.44	- 7.58	-10.79
0.2	0.		- 6.28	0.	-15.26
0.14	0.14	3.79	- 4.44	7.58	-10.79
0.	0.2	5.36	0.	10.72	0.
-0.14	0.14	3.79	4.44	7.58	10.79
-0.4	0.	0.	12.56	0.	30.52
-0.28	-0.28	- 7.58	8.88	-15.17	21.58
0.	-0.4	-10.72	0.	-21.45	0.
0.28	-0.28	- 7.58	- 8.88	-15.17	-21.58
0.4	0.	0.	-12.56	0.	-30.52
0.28	0.28	7.58	- 8.88	15.15	-21.58
0.	0.4	10.72	0.	21.43	0.
-0.28	0.28	7.58	8.88	15.15	21.58

Another cause of yaw is loose fit between projectile and bore, as illustrated in Figure 1 (Reference 3). The degree of yaw is a function of the length, L , of the main body from the bourrelet to the beginning of the boat-tail, and of the difference, d , between the projectile diameter and the bore. The yaw θ is then:

$$d/L = \tan \theta \approx \theta$$

It has been observed in the Rarden gun that d is negligible. If L is taken as 45.6 mm and d is assumed to be 0.0456 mm, initial yaw is 0.1 mrad. In larger shell⁽⁸⁾, yaw of 4.5 mrad has been observed prior to 5-msec travel in-bore. Yaw this large can cause a significant contribution to dispersion in the aerodynamic jump representation used.

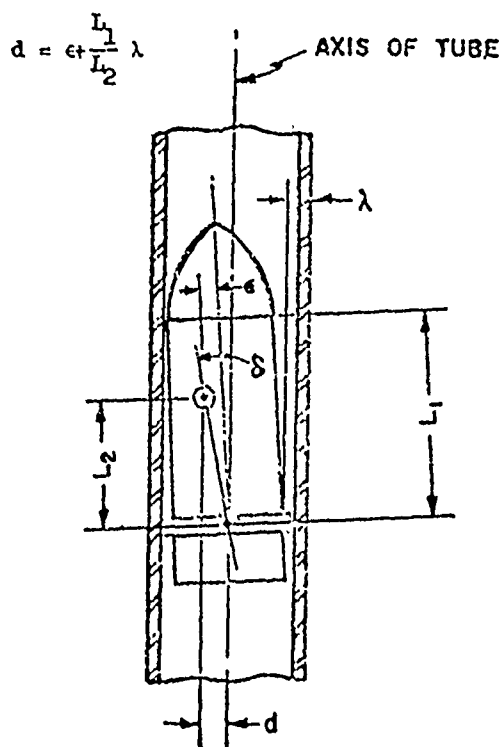


FIGURE 1. COMBINED EFFECTS OF CLEARANCE AND ECCENTRICITY

In a similar way, the projectile can be improperly seated in the forcing cone, one side of the rotating band being fully engaged, the other side not in full contact, and the projectile accordingly cocked. Since the rotating band

is 0.9 mm deep, this corresponds to a yaw of, at most, 20 mrad; if the engraving is 0.3 mm off-center, there is a resulting deflection at 1000 m of 17.8 mm.

The maximum values of this parameter should be established by test to verify that no pathological conditions exist, but large contributors to dispersion from aerodynamic factors associated with initial yaw will probably not be encountered. Another yaw-related phenomenon will be discussed later.

Initial Yaw Rate of the Projectile

The effect of initial yaw rate on dispersion is displayed in Table 2. As can be seen, the effect is considerably less than that of yaw. Yaw rate is caused by balloting of the projectile upon exit from the muzzle, from tip-off of the projectile by a laterally accelerating muzzle, and by muzzle acceleration.

A balloting projectile representation⁽⁴⁾ applied to the Rarden suggests that the yaw rate is 1.5 mrad/sec which does not produce significant dispersion. On the other hand, tip-off produces a yaw rate due to acceleration on the projectile after the center of gravity has cleared the muzzle, as illustrated in Figure 2. If r is the distance from the center of gravity to the start of the boat-tail, the associated yaw rate is a function of r/v_0 . Since no significant lateral acceleration is observed in the Rarden during shot ejection and v_0 is small, the yaw rate will be small, as will the dispersion associated with it. In future designs, if a projectile is considered with a long distance between bore contacts, these considerations will have to be reopened.

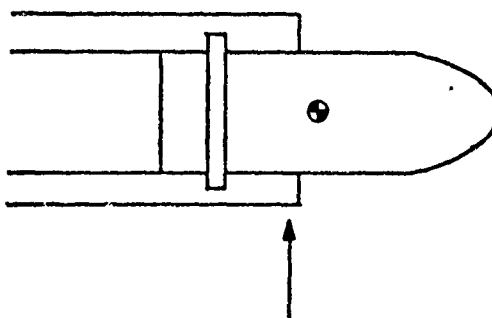


FIGURE 2. TIP-OFF OF PROJECTILE BY LATERAL MOTION OF MUZZLE

TABLE 2. EFFECT OF PROJECTILE YAW RATE ON IMPACT POINT

Yaw Rate, mrad/sec		Errors in Impact Point, mm			
Up	Left	1000 m		2000 m	
		δy , mm	δz , mm	δy , mm	δz , mm
-0.4	0.	-0.01	--	-0.02	0.
-0.28	-0.28	-0.01	-0.01	-0.02	-0.02
0.	-0.4	0.	-0.01	0.	-0.03
0.28	-0.28	0.01	-0.01	0.02	-0.02
0.4	0.	0.01	--	0.02	0.
0.28	0.28	0.01	0.01	0.02	0.02
0.	0.4	--	0.01	0.	0.02
-0.28	0.28	-0.01	0.01	-0.02	0.01
-0.8	0.	-0.02	0.	-0.05	0.
-0.56	-0.56	-0.02	-0.02	-0.03	-0.05
0.	-0.8	0.	-0.03	0.	-0.06
0.56	-0.56	0.02	-0.02	0.03	-0.05
0.8	0.	0.02	0.	0.05	0.
0.56	0.56	0.02	0.02	0.03	0.05
0.	0.8	0.	0.03	0.	0.06
-0.56	0.56	-0.02	0.02	-0.03	0.05

Effects of Variation in Muzzle Velocity

Results of variation in muzzle velocity are displayed in Figure 3 for 1000 and 2000-m range. Note that two different scales are used in the graph, and that results do not scale with range. This is basically because of the greater gravity drop for the longer time of flight at 2000 m. Note also that, while this is not a significant error source at close ranges, it becomes significant at long ranges. Moreover, recent tests of the Rarden system indicate a round-to-round spread in muzzle velocity of 25.9 ft/sec. If this represents a standard deviation of 7 m/sec, a typical dispersion could be 1/3 mrad at 2000 m, which is significant. Moreover, if the round-to-round variation proves to be the trend, these observations could indicate a need for an effort to reduce muzzle-velocity variation.

Fire-Control Influence

One of the time-honored adages in system design is that fire control can neither improve nor worsen the dispersion of an automatic cannon. In the case of LODACS, however, a firing rate of 90 shots per minute and a burst size of seven rounds requires 2 seconds of firing time. If, during the firing of the burst, because of system reaction to firing, aim wander, or any other factor, the fire control inappropriately influences the aim point, the results could be interpreted as dispersion. Therefore, a test program which is concerned with small dispersion and its causes must at all times monitor the influence of fire control during firing.

Effect of Variation in Projectile Mass

The effect of variation in projectile mass is displayed in Figure 4. A typical value for the variation in projectile mass, according to Reference 1, is 0.25 percent. For the Rarden round, this is 0.9 g. Note that considerably larger deviations result in negligible influences or error in impact point.

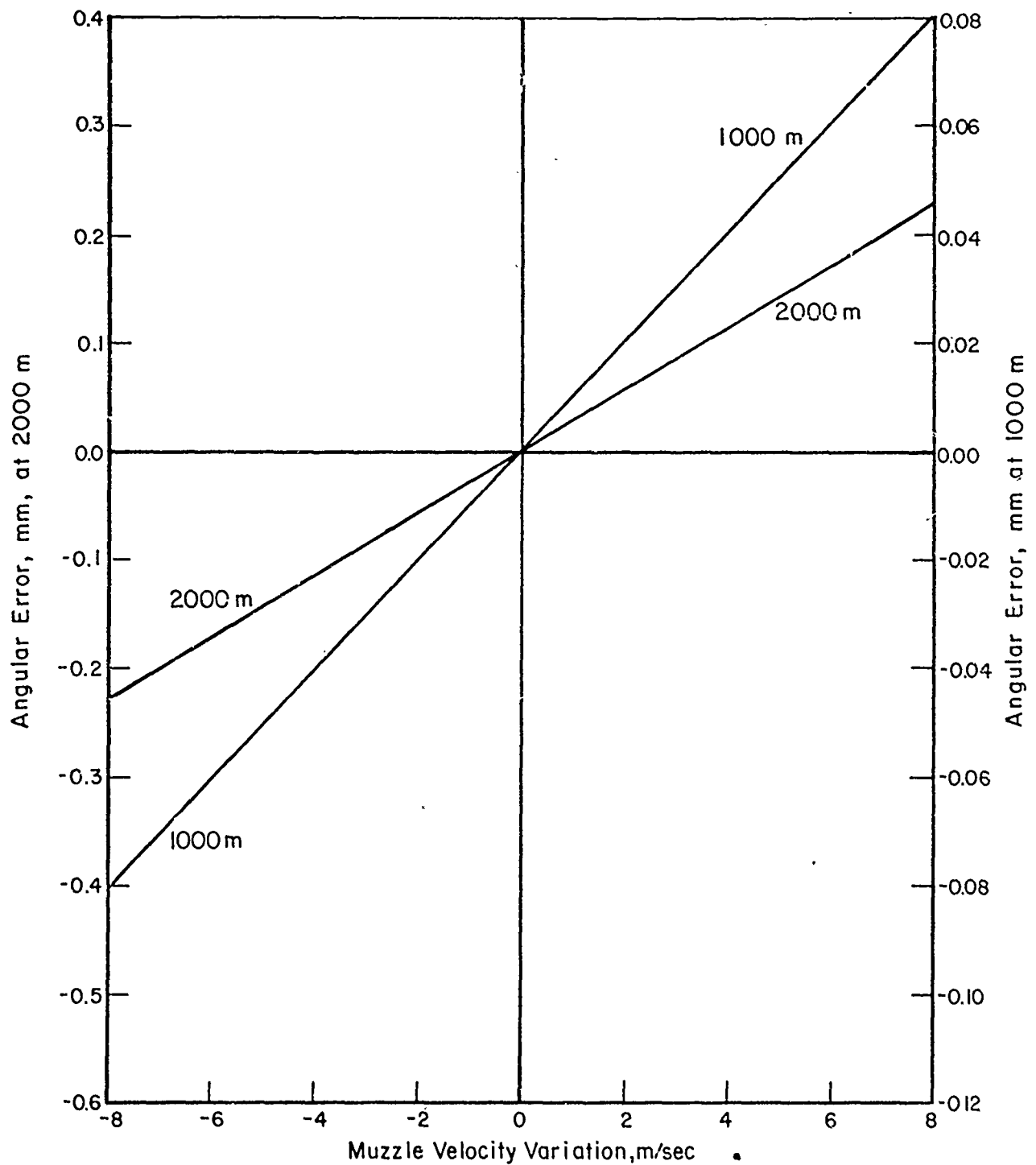


FIGURE 3. EFFECT OF VARIATION IN MUZZLE VELOCITY ON IMPACT POINT

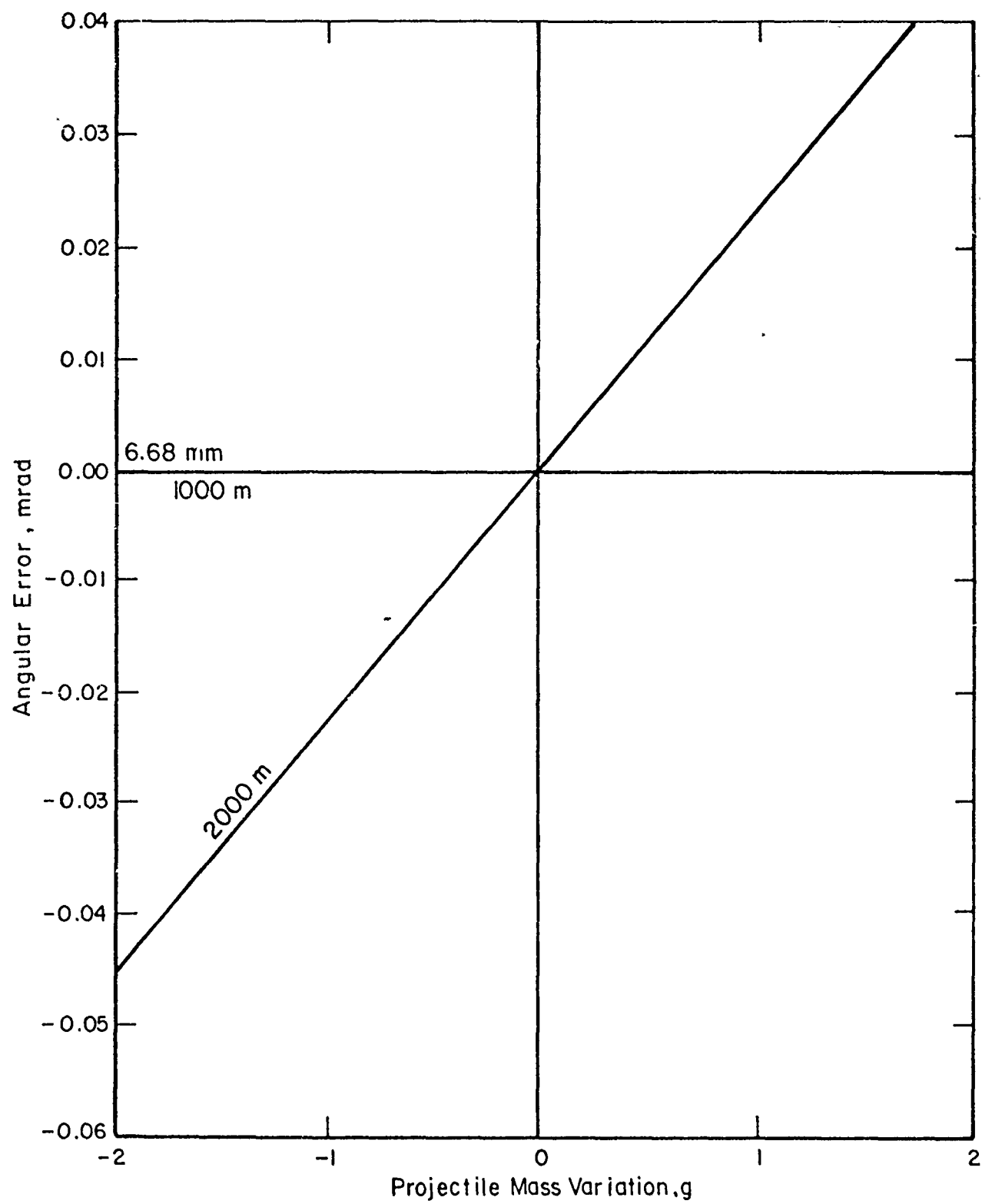


FIGURE 4. EFFECT OF PROJECTILE MASS VARIATION ON IMPACT POINT

Effect of Lateral Throw-Off of Projectile

The effect of lateral throw-off of the projectile is shown in Table 3. As seen in this table, a lateral velocity of 300 mm/sec on launch can cause a deflection of up to 325 mm, or 0.325 mrad, at 1000 m. A muzzle disturbance of this size can be a significant error source. If, however, lateral motion is small at the time of projection, throw-off is a small, even negligible contributor to dispersion.

The lateral motion of the projectile can be caused by a number of factors, including:

- Rigid body rotation of
 - Vehicle relative to the ground
 - Gun relative to the vehicle
 - Barrel relative to the gun
- Barrel whip
- Eccentricity of a spinning projectile (effect of the center of mass not lying at center of in-bore rotation with resultant lateral velocity upon exit from muzzle).

The Rarden has been instrumented during burst firing from a vehicle. Based on the first series of such tests, gross motion of the muzzle is small at times of shot ejection for rounds in a burst subsequent to the first. Lateral motion for the first round is virtually zero. This effect is not observed in other weapons, however. Depending upon how much the centerline of the bore is off from the mount trunnions, and on how much rigidity there is in the elevating struts, a mount reaction can exist which causes a rigid body motion of the barrel before shot ejection. This has been observed in the 90-mm tank gun⁽⁶⁾. The point is that, even though not observed in the Rarden, rigid body rotation of the barrel is a possible contributor to dispersion.

A similar observation can be made concerning throw-off due to barrel whip in the Rarden. If the dynamic response of the barrel due to firing loads is generally described as a sum of functions of the form $y(x,t) = A_m e^{-b_m t} \sin \omega_m t \cos \zeta_m x$ except for phase angles, with y the deflection and the subscript m denoting each mode. The parameters of interest then become dy/dt

TABLE 3. EFFECT OF THROW-OFF ON PROJECTILE IMPACT POINT

Throw-Off, mm/sec		Error in Impact Point, mm			
		1000 m		2000 m	
δy	δz	δy	δz	δy	δz
100.	0.	92.59	0.	185.13	0.
70.71	70.71	65.47	76.7	130.91	186.37
0.	100.	0.	108.47	0.	263.57
- 70.71	70.71	- 65.47	76.7	-130.91	186.37
-100.	0.	-92.59	0.	-185.13	--
- 70.71	- 70.71	- 65.47	- 76.7	-130.91	-186.37
0.	-100.	0.	-108.47	0.	-263.57
70.71	- 70.71	65.47	- 76.7	130.91	-186.37
200.	0.	185.18	0.	370.27	0.
141.4	141.4	130.94	153.40	261.82	372.74
0.	200.	0.	216.94	0.	527.14
-141.4	141.4	-130.94	153.40	-261.82	372.74
-200.	0.	-178.27	0.	-370.27	0.
-141.4	-141.4	-130.94	-153.40	-261.82	-372.74
0.	-200.	0.	-216.94	0.	-527.14
141.4	-141.4	130.94	-153.40	261.82	-372.74
300.	--	277.77	0.	559.4	0.
212.13	212.13	196.41	230.10	392.73	559.12
0.	300.	0.	325.42	0.	790.71
-212.13	212.13	-179.51	230.00	-392.73	559.12
-300.	0.	-260.86	0.	-538.01	0.
-212.13	-212.13	-179.51	-230.	-392.73	-559.11
0.	-300.	0.	-325.42	0.	-790.71
212.13	-212.13	196.41	-230.10	392.73	-559.12

for throw-off. For tip-off, the parameter d^2y/dt^2 is of interest. In a subsequent section, the slope of the barrel dy/dx will be discussed. Although the modes are not known for the Rarden gun, this type of analysis might yield some insight into the throw-off. The presence of the damping pads could conceivably cause a greater throw-off contribution at the muzzle than is common. The mode shape that might be observed could be as in Figure 5.

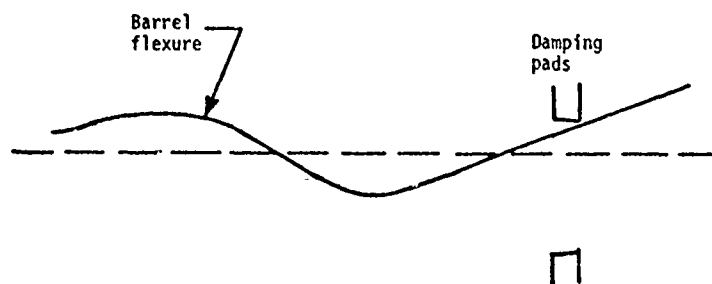


FIGURE 5. POSSIBLE BARREL-MODE SHAPE DUE TO PRESENCE OF DAMPING PADS

Eccentricity of the projectile is a source of throw-off error. This is caused by the center of mass of the projectile not lying on the axis of rotation during in-bore acceleration. Upon exit from the muzzle, center of rotation moves to the center of mass. In the transition, there is a lateral velocity imparted which is a function in magnitude of the angular rate of rotation and the distance from the center of mass to the in-bore center of rotation. The direction is a function of the orientation of the center of mass on exit from the muzzle. If the mass eccentricity is 0.026 mm from the centerline, if the twist is one turn in 30 calibers, and if the muzzle velocity is 1090 m/sec, the throw-off will be 200 mm/sec. Further comment on this source of dispersion will be made in the section, "Eccentricity of Projectiles".

Another cause of throw-off is related to in-bore yaw of the projectile. In this case, the yawed projectile effectively has its center of mass off the centerline of the tube. In a manner like the throw-off resulting from the eccentric projectile, a lateral velocity can occur upon exit from the muzzle. In a large shell (Reference 3), this can be comparable to the magnitude of the eccentricity throw-off. At 2 mrad in in-bore yaw, the

moment arm throw-off of the Rarden round is 0.6 m/sec. This is based on a yaw condition in which the front edge of the boat-tail and the rear edge of the ogive are in contact with the bore. However, it is possible for a projectile yaw to exist without the center of mass being off the centerline of the bore. If this occurs, this contribution to throw-off and, hence, to dispersion, is zero. There is, thus, considerable latitude for the yaw parameter to influence dispersion. In one reference (Reference 5) it is shown that the yaw throw-off in a 37-mm proof slug is an order of magnitude greater than aerodynamic jump. In another reference (Reference 3) the two phenomena contribute about equally for a 175-mm artillery round.

To summarize, throw-off is not an error source which can be ignored. Its causes are varied and include dynamic system response to firing loads, barrel whip and yaw, and eccentricity of the projectile. Attention should be given to each of these sources of throw-off error for a low dispersion system.

Launch-Angle Error

Variation in orientation of the barrel from round to round, of course, is traditionally considered to be the prime source of dispersion. The Rarden data available for this effort did not include sufficient muzzle-position data for burst fire to shed light on the changing angle of departure. Parametric variation of this parameter is indicated in Table 4. This table indicates little more than the approximation used in many weapon systems analyses: a small angular error at the gun causes a comparable angular error at the target. The degree to which the various causes contribute to angular error are being investigated in ARMCOM and BRL efforts. The following is a discussion of error phenomena and possible orders of magnitude.

Dynamic Response

Dynamic response of the vehicle is a common source of dispersion. In this case, the response of the vehicle's suspension due to firing a previous round or rounds has not damped out at the time of fire of a subsequent round. In the Rarden, the rate of fire is such that the vehicle response may be damped out. This should, in any case, be verified. However, for fire-on-the-move,

TABLE 4. EFFECT OF LAUNCH-ANGLE ERROR ON
PROJECTILE IMPACT

Launch Angle Error, $\delta\theta$ mrad	Error in Impact Points,	
	mm	
	1000 m, δy	2000 m, δy
-0.14	-140	-279.92
-0.12	-120	-239.93
-0.10	-100	-199.95
-0.08	- 80	-159.96
-0.06	- 60	-119.97
-0.04	- 40	- 79.98
-0.02	- 20	- 39.99
0.02	20	39.99
0.04	40	79.98
0.06	60	119.97
0.08	80	159.96

the low rate of fire can allow a dispersionlike effect to be observed due to a changing orientation of the vehicle and errors in the stabilization during the firing of a burst.

Mount Motion

A report by Gay and Elder⁽⁶⁾ includes a simple model of mount dynamics for a 90-mm tank cannon. Although not general, it includes some aspects of the problem which could bear on dispersion in a LODACS configuration. In this representation,

I_w = moment of inertia of weapon about trunnions,

θ = angular rotation,

ϵ = vertical distance from center of gravity of recoiling mass to centerline of bore,

A = area of bore,

$P(t)$ = powder pressure,

and force of elevating strut is neglected as small compared to powder pressure. Thus:

$$I_w \ddot{\theta} = \epsilon A P(t),$$

or

$$\dot{\theta}(t) = \frac{\epsilon A}{I_w} \int_0^t P(t) dt,$$

and

$$\theta(t) = \frac{\epsilon A}{I_w} \int_0^t \int_0^t P(t) dt dt.$$

As an approximation,

$$A \int_0^T P(t) dt = \left(w_p + \frac{w_c}{2} \right) \frac{v_p}{g},$$

where τ is time projectile is ejected, w_p and w_c are weights of projectile and charge, respectively, and v_p is muzzle velocity of projectile. Using this approximation,

$$\begin{aligned} A \int_0^{\tau} \int_0^t p(t) dt dt &= \left(w_p + \frac{w_c}{2} \right) \frac{1}{g} \int_0^{\tau} v dt \\ &= \left(w_p + \frac{w_c}{2} \right) \frac{1}{g} \int_0^L \frac{dx}{dt} dt, \\ &= \left(w_p + \frac{w_c}{2} \right) \frac{L}{g}, \end{aligned}$$

where L is length of projectile travel in bore. Then,

$$\begin{aligned} \dot{\theta}(\tau) &= \frac{\epsilon}{I_w} \left(w_p + \frac{w_c}{2} \right) \frac{v_p}{g}, \\ \theta(\tau) &= \frac{\epsilon}{I_w} \left(w_p + \frac{w_c}{2} \right) \frac{L}{g}. \end{aligned}$$

Thus, under this model, there could be a reaction before shot ejection which contributes to dispersion. By adding a damping term and changing moments and geometry, one could look at the effect of mount dynamics at the time of the next round. It is the author's understanding that such an investigation is underway for the Rarden mount; if not, it should be undertaken. Using numbers motivated by the Rarden gun ($\epsilon = 2.54$ cm, $I_w = 71.3$ kg/m², $w_p = 360$ g, $w_c = 160$ g, $v_p = 3580$ ft/sec, $L = 244$ cm, $\tau = 0.0048$ sec), one finds that the angular rate is 0.4 rad/sec and the angular displacement is 0.4 mrad. Note that the angular rate thus determined corresponds to a linear velocity at the muzzle, a source of dispersion discussed in a previous section.

Motion of the Barrel

Barrel flexure as a cause of both lateral motion and angular change of the muzzle at shot ejection is being investigated by ARMCOM. This area is

an important dispersion source and its investigation should be encouraged. The following discussion is intended as a commentary on the problem. Definitive analysis is deferred to either a follow-on effort or the on-going ARMCOM investigations. The significant aspect of the on-going efforts is the presence and effect of damping pads on the Rarden Gun. These pads can greatly alter mode shapes of the response, and are not considered in any of the references used in this effort.

The reaction of the tube to an angular loading at the breech has been analyzed by Gay and Elder⁽⁶⁾ for a 90-mm tank gun. In this representation,

$$\frac{\partial^2}{\partial x^2} EI(x) \frac{\partial^2 y}{\partial x^2} + \mu \frac{\partial^2 y}{\partial t^2} = \mu(x-\lambda) \ddot{\theta} ,$$

where

y = deflection of barrel

x = distance along barrel

E = Young's modulus

$I(x)$ = area moment of inertia

$\mu(x)$ = mass of beam per unit length

θ = rotation of breech

λ = distance to start of flexible portion of barrel

The complete solution of the forced vibration is given by:

$$y = \sum Y_n(x) q_n(t) .$$

where

Y_n = the normal functions

q_n = the generalized coordinates.

Although the response is influenced by the presence of a muzzle device, the first several mode shapes are as illustrated in Figure 6. These mode shapes correspond to slopes of the barrel at the muzzle of the sort presented in Table 5 for the 90-mm tank gun⁽⁶⁾.

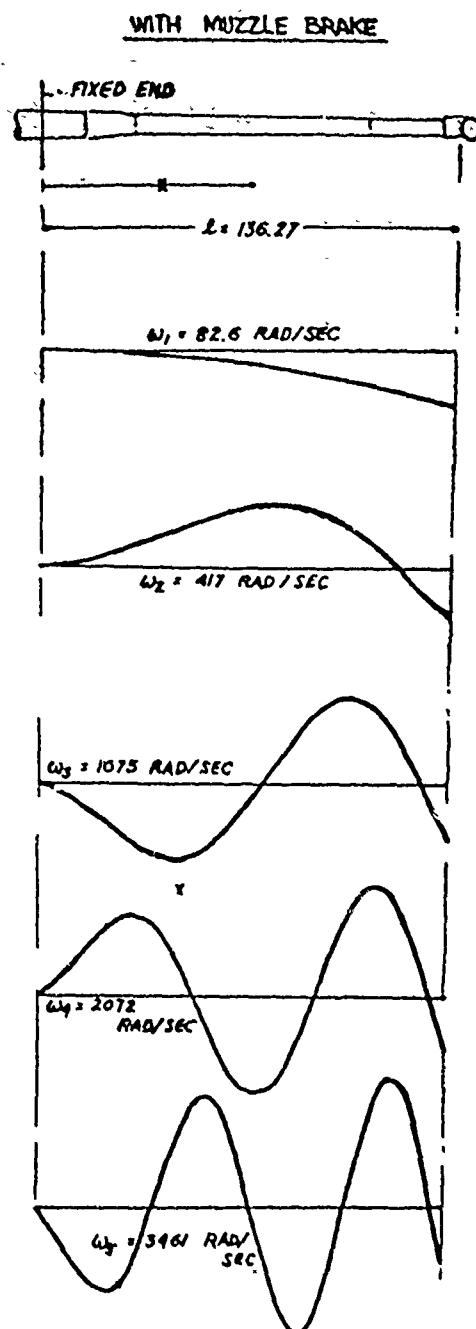


FIGURE 6. FUNCTIONS AND FREQUENCIES OF LATERAL VIBRATION

TABLE 5. FIRST FIVE MODES IN LARGE-CALIBER
BARREL RESPONSE

Mode	Frequency, rad/sec	Slope
1	105.6	0.0118
2	489	0.0373
3	1208	0.0605
4	2282	0.0846
5	3757	0.1095

For the Rarden, however, the presence of the damping pads can cause a mode shape as discussed in the previous section and illustrated in Figure 5. It is conceivable that either the slope of a lower mode could be higher or, more likely, a higher lateral velocity could be present.

The effect of droop of the barrel (or any curvature of the barrel such as dynamic response remaining from previous rounds) can be a contributor to an impact point other than intended. If the droop condition changes from round to round during a burst, a dispersion effect can develop. Darpas⁽⁵⁾ has analyzed the effect of droop by representing the barrel as a cantilever beam and calculating the radius of curvature at the muzzle. The lateral force on the projectile due to this curvature is then calculated. This force is:

$$F = \frac{m p_o L^2 v^2}{2EI}$$

where p_o is the weight of the tube per unit length. A Rarden projectile can be expected to exert a significant force on the barrel. In other cannon, this phenomenon has been observed to influence the position of the muzzle prior to shot ejection. In the Rarden, no such motion is observed, but a pronounced motion is observed immediately after exit of the projectile.

In an analogous way, a projectile whose center of mass does not coincide with its center line exerts a centrifugal force on the barrel as it is traversed by the rotating-barrel.

A report by Elder⁽³⁾ discusses some of the dispersion sources, which are discussed in this and other sections, for a 175-mm gun. Bearing in mind

that this is strictly one shot, and that the particular forces involved (such as those associated with projectile eccentricity) may be out of proportion to lower caliber guns, the breakdown of dispersion sources is still interesting. For Zone 3, for example, a total error of 1.62 mrad is observed consisting of 0.36-mrad angular change, 0.72-mrad transverse muzzle motion, 0.54-mrad throw-off due to eccentricity, and 0.43-mrad aerodynamic jump. Firing in a burst mode would certainly not make the contribution of angular change and transverse muzzle motion smaller, but would probably not greatly affect the other sources.

Eccentricity of Projectile

The effect of eccentric projectiles and the effect of eccentricity on dispersion was not addressed in this effort. This phenomenon certainly occurs, and probably contributes a measurable factor to dispersion particularly at long ranges. However, as mentioned in the introduction, Mann barrel ammunition dispersion is quite small. Since this includes projectile eccentricity effects, both in the sense of aerodynamic factors and the throw-off discussed earlier, it is argued that eccentricity of the projectile does not offer a significant contribution to dispersion.

SUMMARY AND COMMENTARY ON DISPERSION SOURCES

Without having considered the Rarden system in great detail, suggestions of an error budget for that concept would be conjectural at best. Based on the investigations of parameters motivated by Rarden, the following observations are made as to principal causes of dispersion.

Several causes of dispersion are seen as not being particularly large. These include aerodynamic jump due to in-bore yaw and yaw rate. Also seen as not being large are variations in projectile mass. In a precision system, change of effective aim point during a long burst should be at worst a small effect. At short range (less than 500 m), variation in muzzle velocity should have a small effect.

More significant dispersion sources include the effect of throw-off of the projectile upon exit from the muzzle. This can be either a yaw effect

(possibly only a small contributor) or the effect of barrel motion. At long ranges, variation in muzzle velocity will have an effect on dispersion. The effect of launch-angle variation is related to throw-off and is probably the most significant factor in dispersion.

It is observed that the dispersion-causing effects all have identifiable directions for the observed dispersion at the target, given the conditions at the gun. Variation in muzzle velocity, for example, is an effect which is observed in a vertical orientation. On the other hand, throw-off can conceivably occur in any direction. However, the mounting configuration of the Rarden, and of most guns, is such that most of the barrel motion occurs in the vertical plane. Muzzle velocity variation, projectile-mass variation, most of throw-off and most of launch angle deviation all occur in the vertical direction.

Over large numbers of rounds fired, effects of yaw and yaw rate will probably exhibit groupings of impact points, for firings at the same range, and with the contribution of other factors accounted for. These groupings will be a result of a discrete number of initial yaw and yaw-rate conditions, caused by the position of the rifling in the barrel. It may be possible to identify a nonrandom factor in yaw-related errors, such as a correlation between orientation of the barrel on shot ejection and a particular grouping at impact. An observation of this sort could be evidence of a projectile-induced barrel response. An attempt should be made to perform a statistical analysis of data to determine whether any such correlations exist. Some of these activities are being pursued in the present LODACS program but are cited here as recognition of the need for the effort.

There are several areas that deserve attention for determining dispersion-causing factors for the LODACS concept:

- The work currently underway to investigate barrel response to the firing of a burst should be encouraged and pursued. This effort should be coordinated with testing to validate the analytical representation and in this manner gain insight into barrel-related causes of dispersion.
- Although not expected to be a significant source of dispersion, tests to determine yaw and yaw rate should be conducted.

- Statistical analysis should be performed on available data on firings to date to determine whether any known correlation exists among dispersion-causing parameters and observed impact points.

The effort reported here was intended as only an initial look at the problem. There are a few ways in which the analysis can be extended to provide meaningful insight into the dispersion of a LODACS concept. First, the adequacy of the aerodynamic jump formulation needs to be verified with a six-degree-of-freedom representation of this problem; this has an impact on the conclusion that projectile in-bore yaw is not a large dispersion source. Second, additional test data from efforts concurrent to this investigation can be used to extend the basis of the analysis in the LODACS concept. Third, the ammunition should be inspected to insure variations in projectile mass and symmetry are known before firing. But most importantly, this effort did not consider the cross-coupling effects of two or more phenomena simultaneously. What, for example, is the effect of concurrent throw-off and yaw, or of the projectile imbalance and a variation in muzzle velocity? The investigation of these cross-coupled phenomena can be of significant benefit in subsequent analysis of test results and in the attempt to understand what events occurred on a given burst during system testing.

REFERENCES

- (1) *Design for Control of Projectile Flight Characteristics*, Engineering Design Handbook, AMCP 706-242, Headquarters, U. S. Army Materiel Command, Washington, D. C. (September 1966).
- (2) Neitzel, G. P., Jr., *Aerodynamic Characteristics of 30MM HS831-L Ammunition Used in the British 30MM Rarden Gun*, Memorandum Report No. 2466, U. S. Army Ballistic Research Laboratories, Aberdeen Proving Ground, Maryland (March 1975).
- (3) Elder, A. S., *The Lateral Motion of a 17MM Gun Tube Produced by an Eccentric Projectile*, Memorandum Report No. 1418, U. S. Army Ballistic Research Laboratories, Aberdeen Proving Ground, Maryland (July 1962), AD 286 860.
- (4) Gay, H. P., *On the Motion of a Projectile as It Leaves the Muzzle*, Technical Note No. 1425, U. S. Army Ballistic Research Laboratories, Aberdeen Proving Ground, Maryland (August 1961), AD 801 974.
- (5) Darpas, J. G., *Transverse Forces on Projectiles Which Rotate in the Barrel*, Memorandum Report No. 1208, U. S. Army Ballistic Research Laboratories, Aberdeen Proving Ground, Maryland (March 1959).
- (6) Gay, H. P., and Elder, A. S., *The Lateral Motion of a Tank and Its Effect on the Accuracy of Fire*, Report No. 1070, U. S. Army Ballistic Research Laboratories, Aberdeen Proving Ground, Maryland (March 1959), AD 217 657.
- (7) Lieske, R. F., and McCoy, R. L., *Equations of Motion of a Rigid Projectile*, Report No. 1244, U. S. Army Ballistic Research Laboratories, Aberdeen Proving Ground, Maryland (March 1964), AD 441 598.
- (8) Kirkendall, R. D., *The Yawing Motion of Projectiles in the Bore*, Technical Note No. 1739, Interior Ballistics Laboratory, U. S. Army Ballistics Research Laboratories, Aberdeen Proving Ground, Maryland (September 1970), AD 878 327.

APPLICATION OF ACCELEROMETERS FOR THE
MEASUREMENT OF GUN TUBE MOTION

J.O. PILCHER, C.L. HENRY AND R.B. MURRAY
Ballistics Research Laboratory
Aberdeen, Maryland

TABLE OF CONTENTS

	<u>Page</u>
I. INTRODUCTION	498
II. LOCAL TUBE MOTION	498
III. ACCELEROMETER SENSITIVITY	503
IV. ACCELEROMETER OUTPUT	503
V. ANALYSIS	503
VI. THE MEASUREMENTS	507
VII. OPTICAL MEASUREMENTS	507
VIII. SUMMARY	511
REFERENCES	513

I. INTRODUCTION

Recent efforts to model gun tube motion, projectile motion and momentum transfer from gun tube to projectile at muzzle exit have made the measurement of gun tube motion more important from the standpoint of validation of models and determining initial conditions for aeroballistic flight.

Although previous measurements have been successfully made by using various optical techniques, these techniques do not lend themselves to rapid implementation in the field and are generally limited to horizontal firings. The following is a discussion of current investigation into the use of accelerometers to measure the motion of a gun muzzle during the interior ballistic cycle.

II. LOCAL TUBE MOTION

The accelerations at a station along a gun can be described in terms of a moving Cartesian coordinate system with its origin on the centerline of the tube and in the transverse plane of the station. Figure 1 shows the coordinate system with an accelerometer positioned on the circumference of the tube. The sensitivity of the accelerometer is described by the vector, \vec{S} ; the accelerometer position is described by the vector, \vec{P} , emanating from the origin of the tube coordinate system to the accelerometer coordinate system.

The unit vectors of the accelerometer coordinate system are assumed to

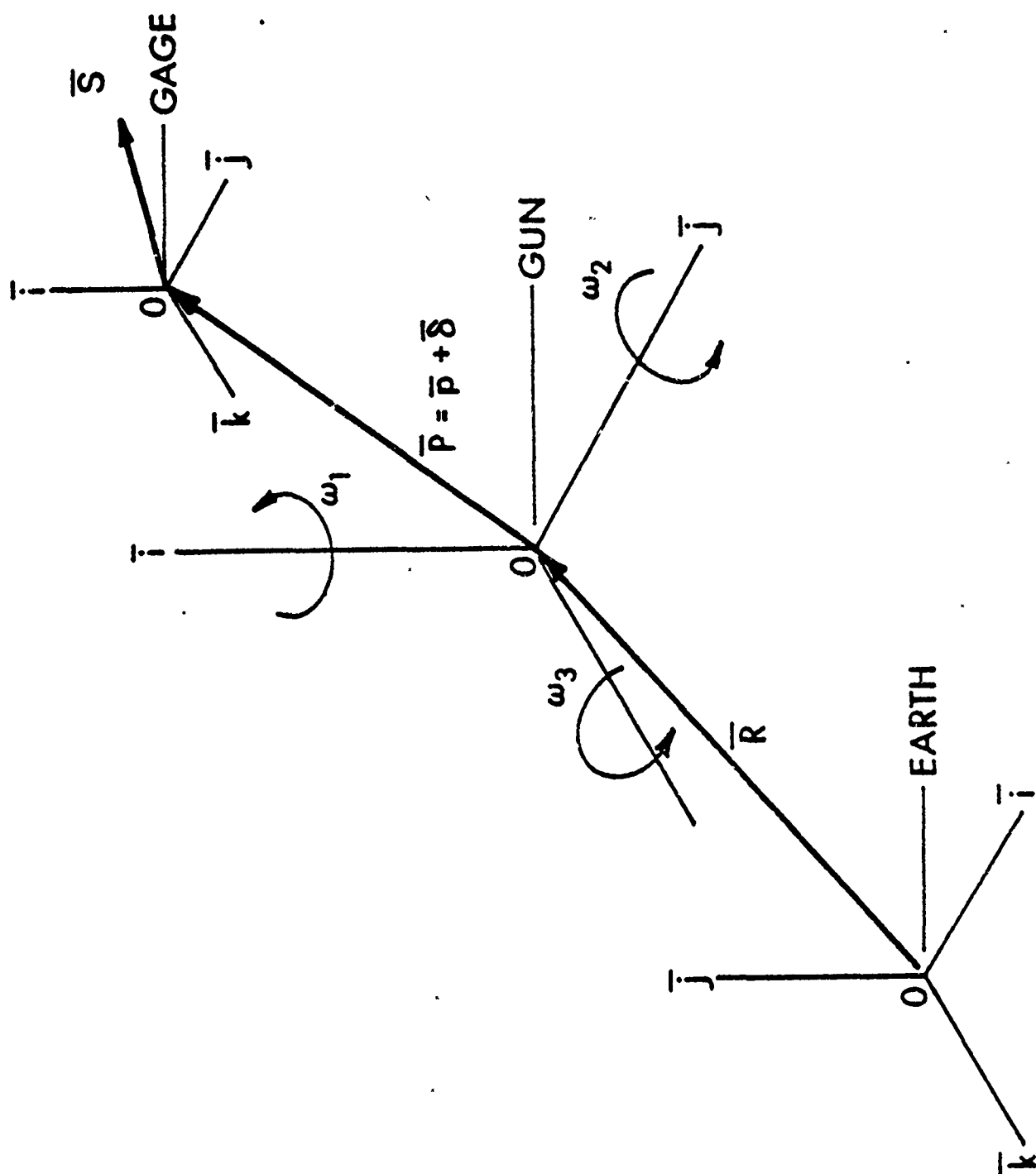


Figure 1. Gun and Accelerometer Coordinate System

remain co-parallel with the tube coordinate system. The position of the tube coordinate system is defined by vector, \bar{R} , which emanates from the origin of an arbitrary fixed reference coordinate system that is initially co-parallel with the tube coordinate system. The tube coordinate system is assumed to translate and rotate with respect to the reference coordinate system with time.

The motion of the accelerometer can be described by taking the second time derivative of the position vector

$$\bar{L} = \bar{R} + \bar{P} = \bar{R} + \bar{p} + \bar{\delta} \quad (1)$$

where \bar{R} = the tube position vector, a function of time, t

\bar{p} = the nominal accelerometer position vector, a constant

$\bar{\delta}$ = the local deformation vector due to local stresses at the accelerometer position, a function of time

It can be shown¹ that the second derivative with respect to time is

$$\bar{A} = \ddot{\bar{R}} + \frac{\partial^2 \bar{\delta}}{\partial t^2} + 2 \bar{\omega} \times \frac{\partial \bar{\delta}}{\partial t} + \bar{\omega} \times (\bar{p} + \bar{\delta}) + \bar{\omega} \times (\bar{\omega} \times \bar{\delta}) + \bar{\omega} \times (\bar{\omega} \times \bar{p}) \quad (2)$$

where $\bar{\omega} = \omega_1 \bar{i} + \omega_2 \bar{j} + \omega_3 \bar{k}$

In order to minimize the number of terms in the expansion of equation (2) the position vector \bar{p} is chosen so that it coincides with one of the unit vectors \bar{i} , \bar{j} , \bar{k} . For the purpose of this discussion, we set

$$\bar{p} = p_1 \bar{i}, p_2 = p_3 = 0 \quad (3)$$

Next we must examine the sources for the local displacement vector $\bar{\delta}$. The local displacement vector $\bar{\delta}$ is composed of:

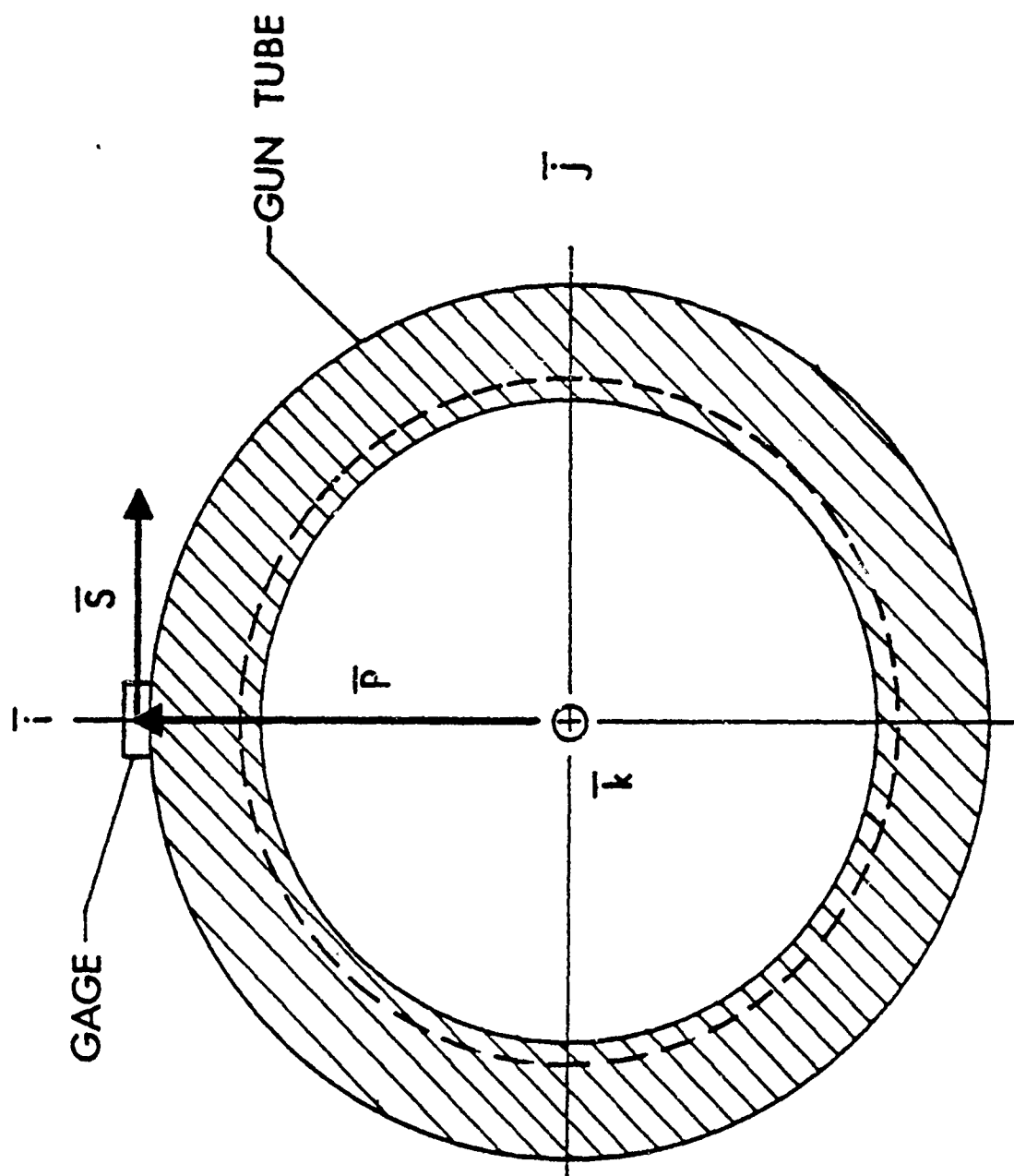


Figure 2. Accelerometer Position and Alignment.

o Radial displacement due to the Poisson effect in response to the longitudinal and torsional strains in the tube generated from the tube recoil body forces.

o Radial displacement generated by the passage of the projectile and propellant gas loadings

o Orthogonal displacement components due to the longitudinal, dilational and torsional strain waves propagated in the tube.

These components have properties that make data separation and analysis quite amenable:

o Radial displacements due to the Poisson effect can be eliminated from the data by proper orientation of the primary sensitivity axis of the accelerometer.

o Radial displacement generated by the passage of the projectile can be eliminated by proper filtering techniques; these components are pulses in the 14KHz frequency regime for the test series under investigation.

o The displacement generated by stress waves are pulses in the frequency regime above 20KHz and are also amenable to filtering techniques.

By filtering out components above a nominal 10Khz which is well above the 26th mode of vibration of the gun tube $\bar{\delta}$ can be assumed to be

$$\bar{\delta} = \bar{\delta}_1 \bar{i} \quad (4)$$

In addition, $\ddot{\delta}_1$ is due to tube body forces and is approximately three orders of magnitude smaller than the acceleration of the gun tube and can be neglected.

Thus equation (2) expands to the following expression,

$$\begin{aligned}\bar{A} = & (\ddot{R}_1 + \omega_3^2 p_1 + \omega_2^2 p_1) \bar{i} + (\ddot{R}_2 + \dot{\omega}_3 p_1 - \omega_2 \omega_1 p_1) \bar{j} \\ & + (\ddot{R}_3 - \dot{\omega}_2 p_1 - \omega_1 \omega_3 p_1) \bar{k}\end{aligned}\quad (5)$$

III. ACCELEROMETER SENSITIVITY

The vector \bar{S} is defined as

$$\bar{S} = s_1 \bar{i} + s_2 \bar{j} + s_3 \bar{k} \quad (6)$$

Ideally, the accelerometer sensitivity can be defined

$$\bar{S} = s_2 \bar{j} \quad (7)$$

where $s_1 = s_3 = 0$.

However, the cross axis sensitivity of a piezoelectric accelerometer follows a cosine law² where

$$s_1^2 + s_3^2 = \frac{s_2^2}{400} \quad (8)$$

for a nominal cross axis sensitivity of five percent.

In the case of the gun tube vibration problem to be discussed later, the acceleration components are of the same order of magnitude thus we can use equation (7) by assuming a + five percent error in the measurement. This error could be minimized if accelerometers were calibrated to determine the secondary and tertiary axes of sensitivity.

IV. ACCELEROMETER OUTPUT

Using equation (7) and equation (5) the accelerometer output is as follows:

$$C = \bar{S} \cdot \bar{A} = s_2 (\ddot{R}_2 + \dot{\omega}_3 p_1 - \omega_2 \omega_1 p_1) \quad (9)$$

Figure 2 shows schematically the physical arrangement of the accelerometer and tube.

V. ANALYSIS

In order to separate the translational and rotational terms in equation (9), accelerometers are used in pairs as shown in Figure 3.

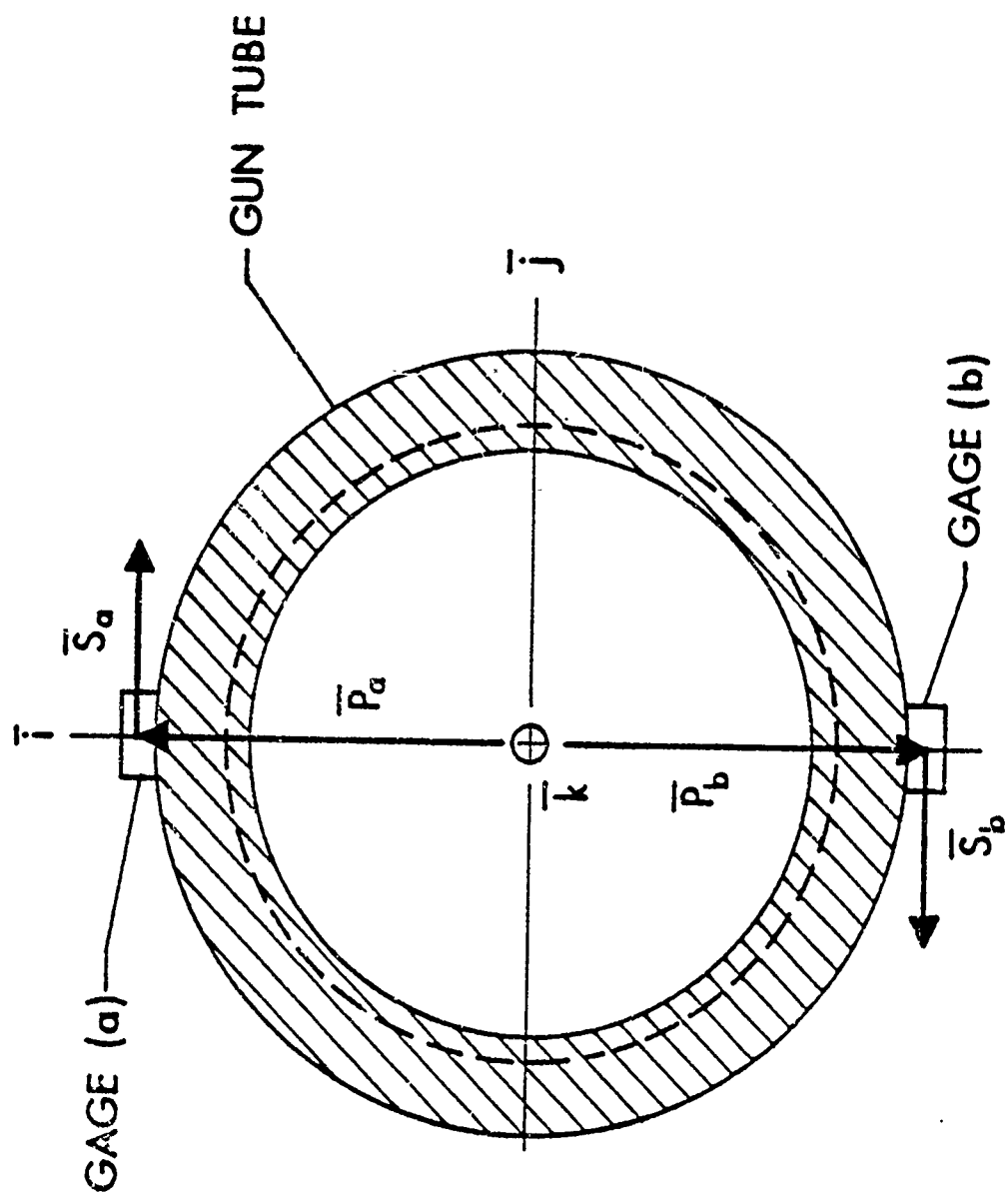


Figure 3. Diagram of Acceleration Measurement Geometry

The output of the two accelerometers are shown below

$$\begin{aligned} C_a &= S_a (\ddot{R}_2 + \dot{\omega}_3 p_1 - \omega_2 \omega_1 p_1) \pm 5\% \\ C_b &= S_b (-\ddot{R}_2 + \dot{\omega}_3 p_1 - \omega_2 \omega_1 p_1) \pm 5\% \end{aligned} \quad (10)$$

By differencing the two outputs and collecting terms, we get

$$\ddot{R}_2 = \frac{1}{2} \left(\frac{C_a}{S_a} - \frac{C_b}{S_b} \right) \pm 5\% \quad (11)$$

By summing the two outputs and collecting terms, we obtain

$$\dot{\omega}_3 - \omega_2 \omega_1 = \frac{1}{2p} \left(\frac{C_a}{S_a} + \frac{C_b}{S_b} \right) \pm 5\% \quad (12)$$

For the case shown in Figure 3

$\dot{\omega}_3$ = torsional acceleration about the tube centerline

p = outside radius of the tube

\ddot{R}_2 = horizontal translational acceleration of the tube.

By adding a second pair of accelerometers mounted in the same fashion as the first pair and at the same station along the tube with their position vector coincident with the J axis, a second set of equations are similarly derived.

$$\ddot{R}_1 = \frac{1}{2} \left(\frac{C_c}{S_c} - \frac{C_d}{S_d} \right) \pm 5\% \quad (13)$$

$$\dot{\omega}_3 + \omega_2 \omega_1 = \frac{1}{2p} \left(\frac{C_c}{S_c} + \frac{C_d}{S_d} \right) \pm 5\% \quad (14)$$

By summing the outputs of the four accelerometers the following relationship is obtained

$$\dot{\omega}_3 = \frac{1}{4p} \left(\frac{C_a}{S_a} + \frac{C_b}{S_b} + \frac{C_c}{S_c} + \frac{C_d}{S_d} \right) \pm 5\% \quad (15)$$

The four accelerometer array is shown in Figure 4.

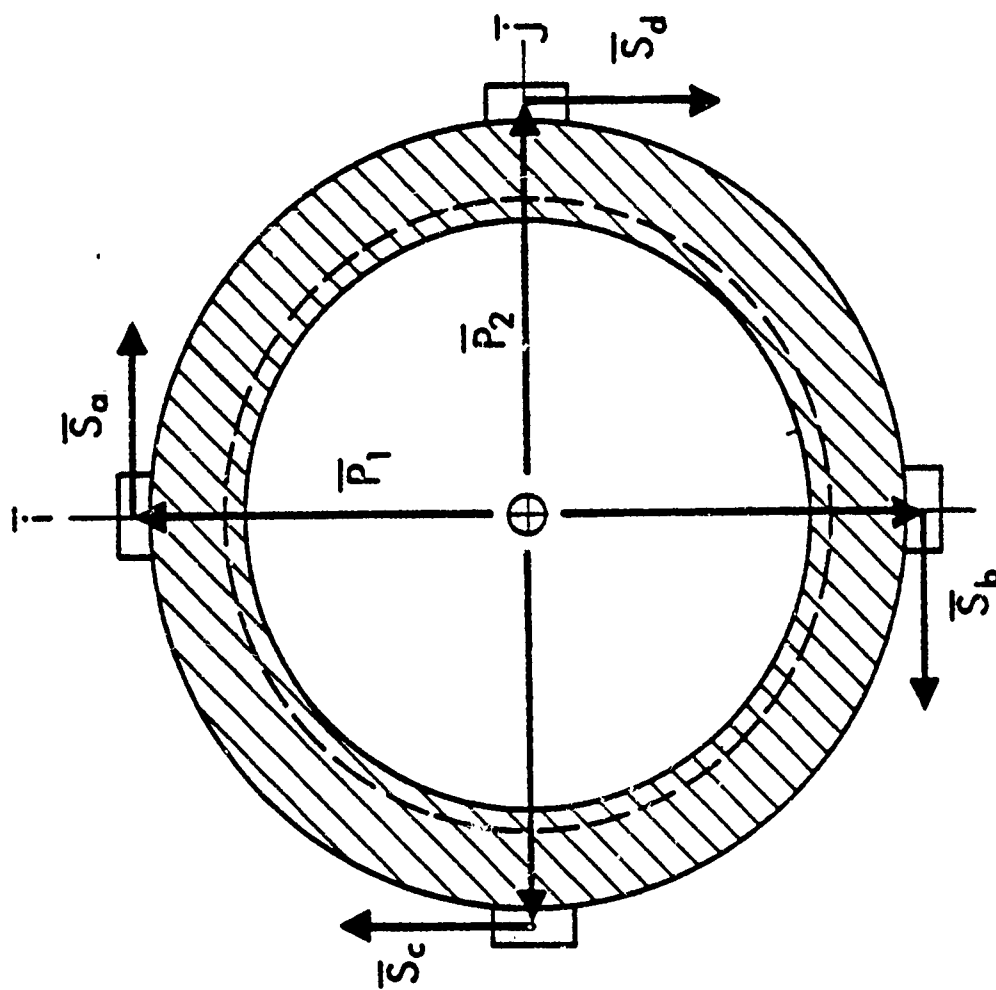


Figure 4. Four Accelerometer Array

VI. THE MEASUREMENTS

Preliminary measurements of the lateral motion of the M68 tank gun were made using a pair of triaxial accelerometers. The data for y-axis (horizontal) were recorded and analyzed. The configuration used was that shown in Figure 3. Using the previous discussed analyses as a basis for data reduction, the accelerometer outputs were filtered through a 20KHz pass filter and a 10KHz low pass filter. These filtered data showed that components of acceleration in this frequency regime were negligible and that the prime data lay below 10KHz.

A considerable amount of high frequency data was evident starting above 25KHz. The high frequency components must be considered when establishing accelerometer requirements.

Once the data were in the form shown in equation 11 they were integrated twice with respect to time to obtain displacement versus time. Figure 5 shows the horizontal acceleration data; Figure 6 shows the horizontal velocity data; Figure 7 shows the horizontal displacement data.

These preliminary tests results were compared with calculated results from a computerized gun vibration model.

Although the general character of the displacement-time data is similar to the model predictions, amplitudes were not in agreement. Before a definitive statement as to the validity of the data and the accuracy of the model can be made, a series of comparative tests must be made. In progress at the BRL is a series of tests to compare the accelerometer measurements with direct optical measurement of displacement versus time.

VII. OPTICAL MEASUREMENTS

Concurrent with accelerometer measurements using the four element array shown in Figure 4, three electro-optical systems for measuring displacement are being used to measure the muzzle motion of a 37mm test cannon. The electro-

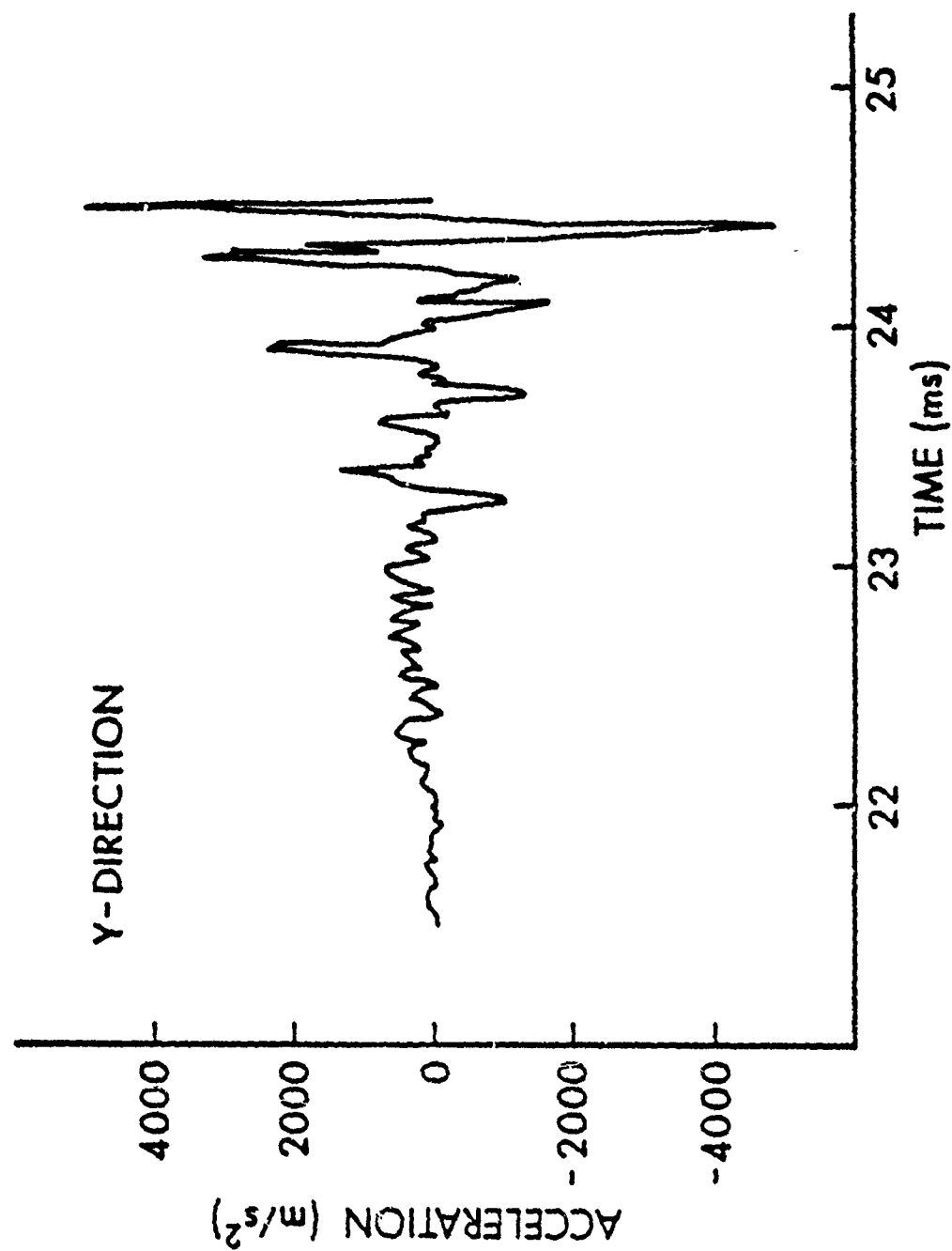


Figure 5. Horizontal Acceleration Data from Equation (11).

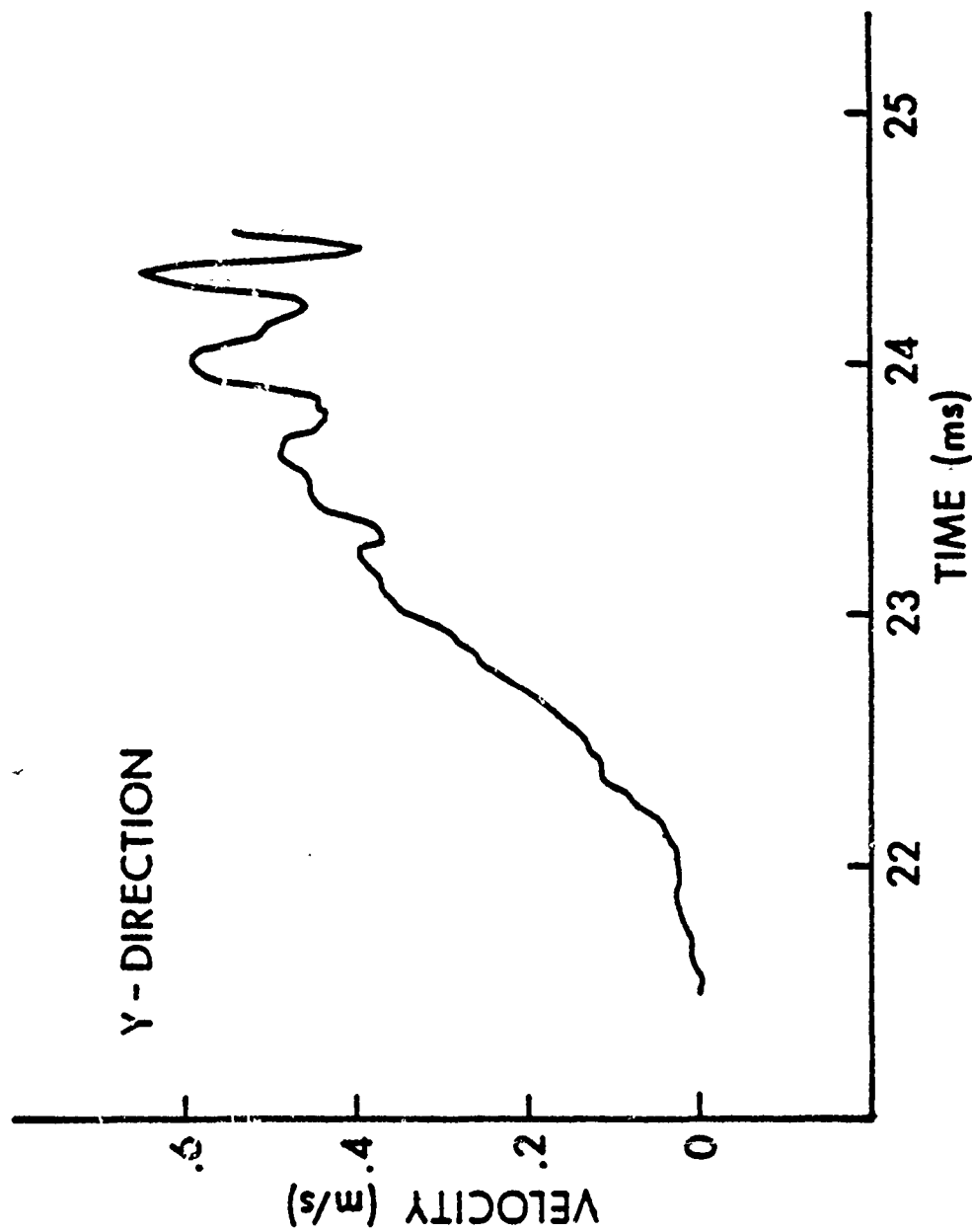


Figure 6. Horizontal Velocity Data from the First Integration of Equation (11).

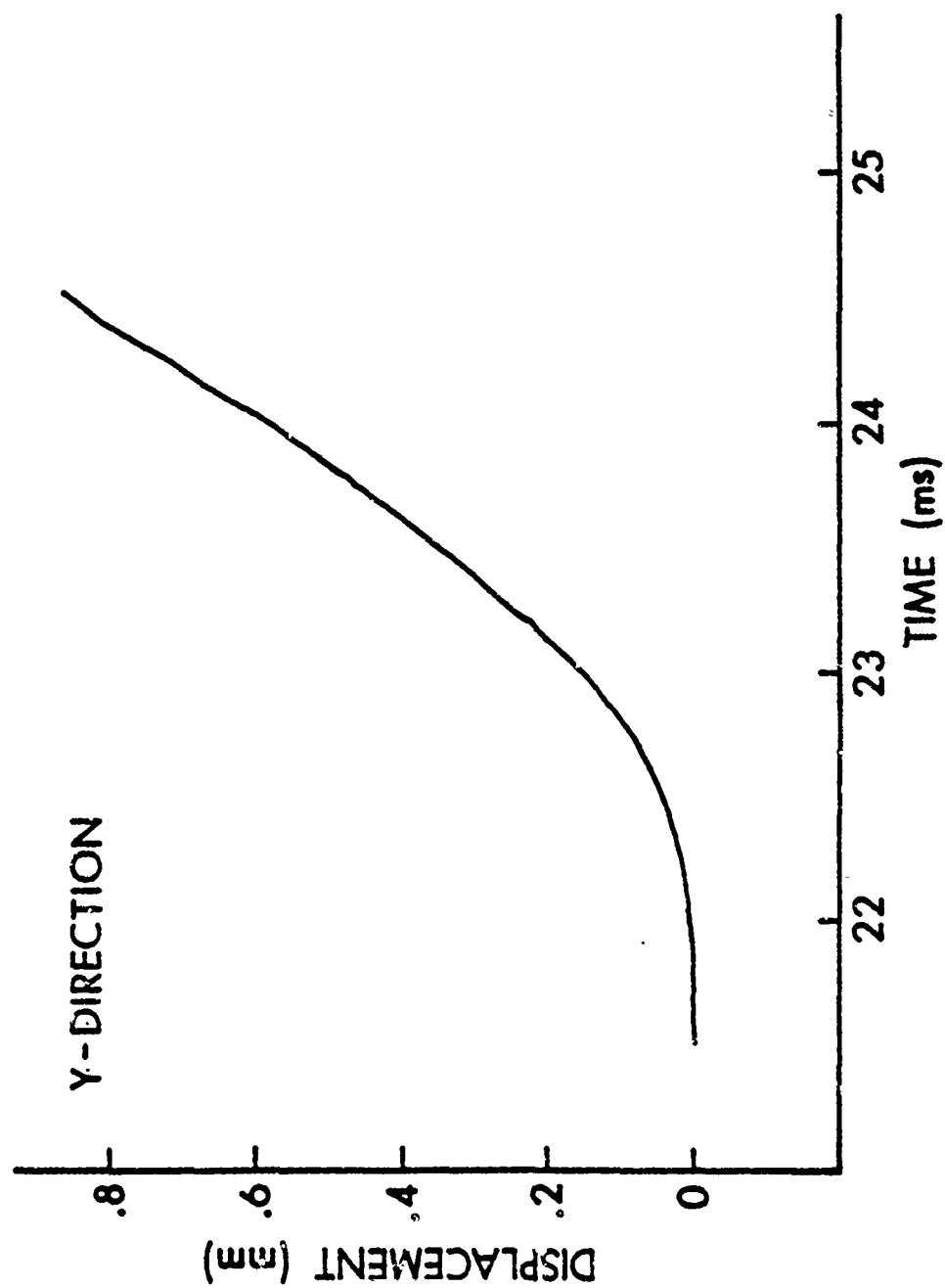


Figure 7. Horizontal Displacement Data from the
Second Integration of Equation (11).

optical system is a servo controlled photo multiplier system that provides an output voltage linearly proportional to the displacement of target normal to the line of sight of the instrument. By using three systems, the two orthogonal lateral displacements and angular displacement about the gun axis can be measured. At this writing tests and data reduction have not been completed. The new data will be presented at the workshop.

VIII. SUMMARY

Analysis of six degree of freedom response of accelerometers shows that particular arrays of four accelerometers can yield the two translational cross-axis components and the coaxial rotational component of muzzle motion. Preliminary tests and current test series for the technique have made the following accomplishments

- o Improved mounting techniques for gun application
- o Improved filtering technique for data reduction
- o Established accelerometer requirements such as response and capacity
- o Data reduction package has been developed

The accuracy and precision of the technique with "off the shelf" commercial components is currently being determined; the advances in the "state-of-the-art" in accelerometry, particularly calibration, required to increase the accuracy are being determined. In addition to gun tube motion, application of these techniques are being examined for projectile measurements.

Results may be summarized as follows:

Bonded accelormeters have been used successfully by using a highly flexible epoxy bonding agent. The main problem, particularly in small caliber tests, is that the bonding agent must be insensitive to shock loading.

Filtering systems most applicable to these types of measurements must have constant time delays over the band pass of the filter and must be inserted between the sensor and data conditioning electronics to minimize distortion in the multiplex and recording systems one might use.

One of the major difficulties in using accelerometers is the zero shift experienced during measurement. To alleviate zero shift problems, high range shock accelerometers are required with some sacrifice of sensitivity. Sensitivity can be regained by using the state of the art solid state charge amplifiers which exhibit much improved stability and noise rejection at high gains.

Recent tests show that to establish potential accuracy for accelerometer measuring systems, comparative tests using long lever arm optical systems, such as the Oddsam System to be discussed by B.T. Haug later this morning and accelerometers having known crossaxis response must be conducted. Efforts to obtain the desired accelerometers with the required calibration information are now in progress.

In order to extend the usefulness of existing equipment, mathematical techniques for eliminating zero shifts in the data are being made to characterize the zero shifts and determine the limits of such characterization.

REFERENCES

1. R. N. Arnold and L. Maunder, "Gyrodynamics", Academic Press, New York, 1961, pp 52-56.
2. C. M. Harris and Charles E. Crede, "Shock and Vibration Handbook", Vol. I, McGraw-Hill, New York, 1961, Chapter 16, pp 19-20.

DEFLECTING PENETRATOR SIMULATION

W.H. HATHAWAY, B.K. STEARNS AND R.H. WHYTE
General Electric Company
Burlington, Vermont

TABLE OF CONTENTS

	<u>Page</u>
SUMMARY	515
INTRODUCTION AND BACKGROUND	516
THEORETICAL FORMULATION	517
A. MATHEMATICAL MODELING	517
B. YAW AND DISPERSION COMPUTATION	521
EXPERIMENTAL CORRELATION	524
CONCLUSIONS	525

SUMMARY

A dynamic simulation has been developed for describing the angular distortion of a slender penetrator contained within an armor piercing projectile as it traverses the length of a gun barrel. The dynamic model considers flexing of the penetrator under the influence of acceleration and centrifugal forces. Linear accelerations of 70000 g's and spin rates of 120000 revolutions per minute are encountered by the projectile. The high spin rate is required for gyroscopic stability. The penetrator is constrained by linear springs which represent the support of the penetrator by the carrier and the complete projectile by the barrel. This simulation has been coupled to exterior ballistics programs in order that the effect of this deflection on round to round launch yaw and dispersion can be predicted. Dispersion data has been gathered for several different penetrator configurations and the results have compared favorably with dynamic simulation predictions.

INTRODUCTION AND BACKGROUND

An Armor Piercing Projectile has been developed for use with the GAU-8/A Gun System and A10 Close Air Support Aircraft. The Armor Piercing Projectile (AP) is part of an ammunition family also consisting of Target Practice and High Explosive Projectiles.

During phases of full scale development of the AP, considerable dispersion (Mann Barrel) was encountered. The AP contains a depleted uranium core to enhance penetration. Normal "jump" type computations, even assuming excessive clearance (bore to barrel) and bourrelet engraving did not account for the observed large first maximum yaws and subsequent large dispersions.

The program schedule and the performance requirements (penetration) provided considerable constraints on the problem solving phase and, in effect, ruled out an extended cut and try approach.

The following factors were considered possible causes of poor performance:

- 1) Spin rate - penetrator flexing resonance
- 2) Structural failure of the carrier (massive engraving)
- 3) Penetrator deflection (bending)

Eglin Air Force Base photographed by X-ray an early design which showed considerable distortion. General Electric constructed steel bourrelet carriers which exhibited no engraving, but still excessive dispersion.

At this point, General Electric concentrated on penetrator deflection as the probable cause and set out to develop an analytical model which could be used as a design tool.

THEORETICAL FORMULATION

A. Mathematical Modeling

The basic assumptions made in developing the mathematical model follow:

1. The projectile is loaded at its base with a uniformly distributed pressure acting in the direction of the barrel centerline.
2. Lateral support is provided by linear springs.
3. The projectile is initially misaligned with the barrel axis.

The initial misalignment of the penetrator with the barrel axis is illustrated in Figure 1. The parameters used to position the penetrator relative to the barrel and projectile are:

X_p = projectile base thickness to penetrator

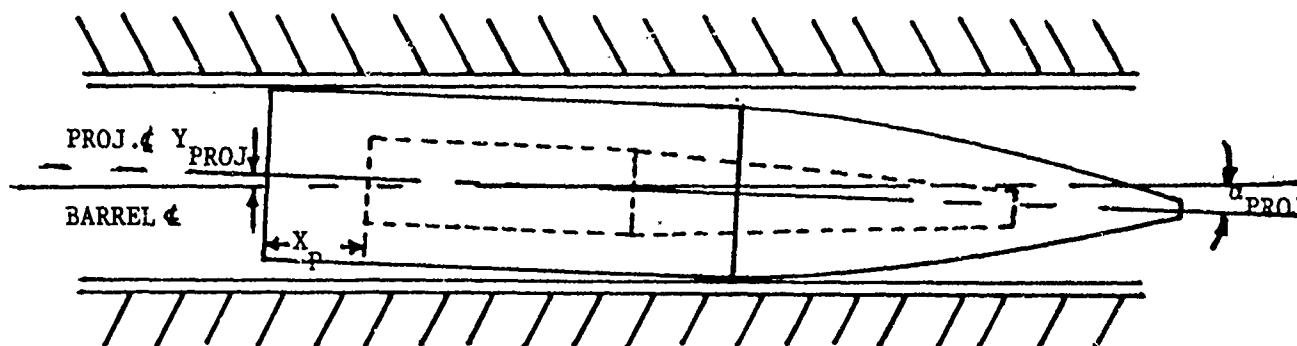
Y_T = total base offset of penetrator

α_T = total misalignment angle of penetrator

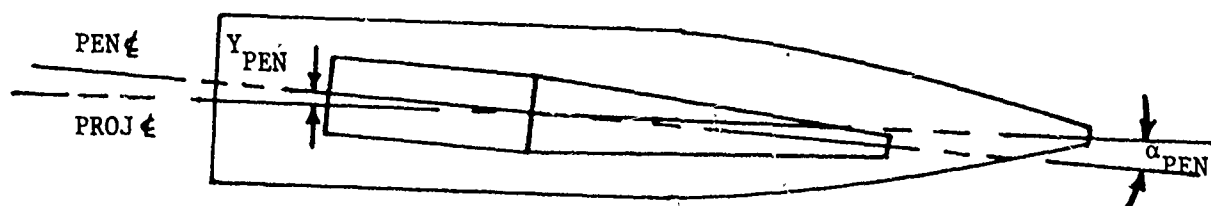
The base offset and misalignment angle, Y_T and α_T , are made up of two components as illustrated in Figure 1. The components are due to barrel versus projectile diameter (tolerances) and manufacturing tolerances involved in assembling the penetrator and carrier.

Structural modeling of the penetrator is done using a lumped mass finite element technique. Using this technique a stiffness matrix, K , is formed which describes the deflection of any element in terms of the forces and moments acting on that element. Deflections in translation and rotation are considered with shear effects being included. Figure 2 illustrates the mathematical modeling and forcing functions. The system of differential equations (one for each degree of freedom) describing the transient response of the penetrator follows.

$$[M] [\ddot{X}] + [K] [X] = [F] \quad (1)$$

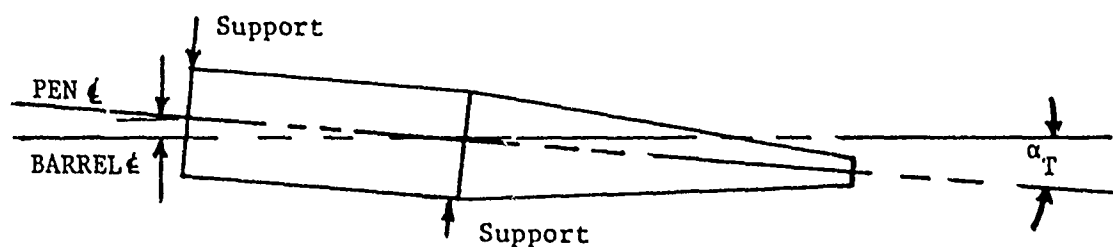


Y_{PROJ} - Base Offset of Projectile
 α_{PROJ} - Misalignment Angle of Projectile



Y_{PEN} - Relative Base Offset of Penetrator
 α_{PEN} - Relative Misalignment Angle of Penetrator

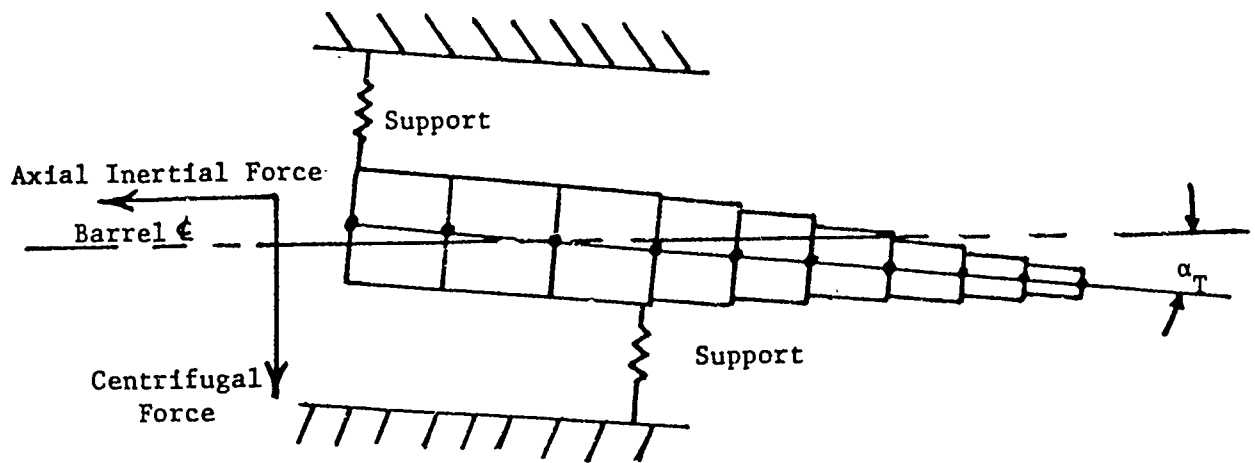
PENETRATOR RELATIVE TO PROJECTILE AXIS



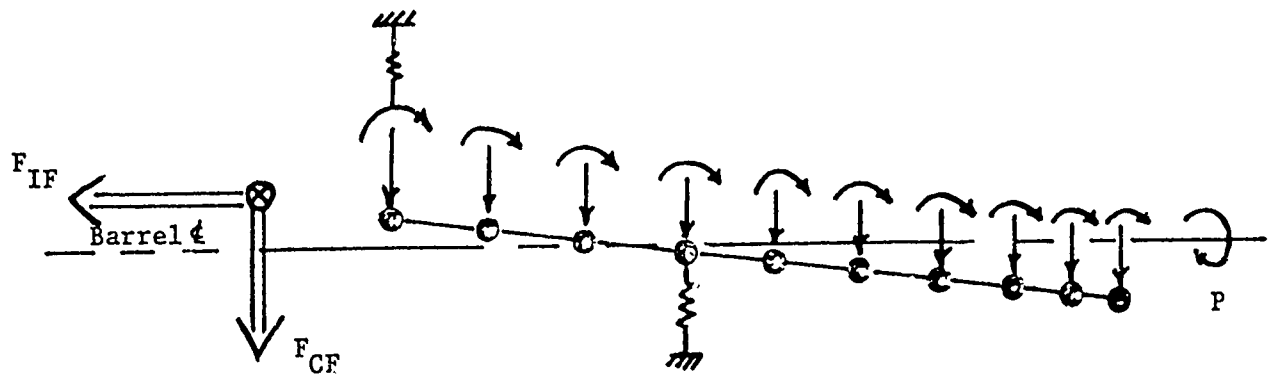
α_T - Total Misalignment Angle of Penetrator = $\alpha_{PROJ} + \alpha_{PEN}$
 Y_T - Total Base Offset of Penetrator = $(Y_{PROJ} - X_p \sin(\alpha_{PROJ})) + Y_{PEN}$

PENETRATOR RELATIVE TO BARREL AXIS

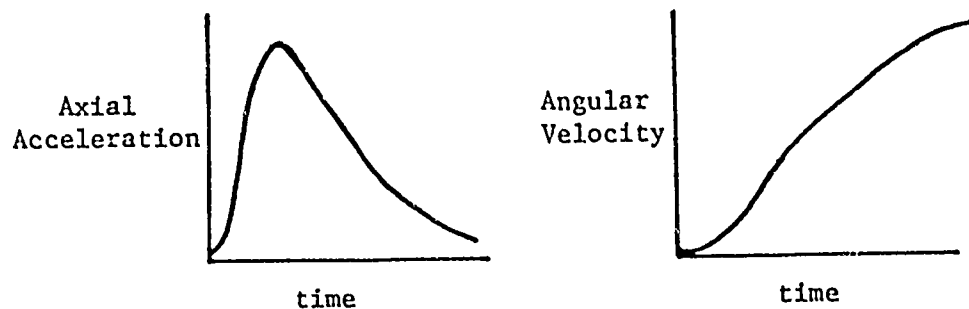
Figure 1 Penetrator Skewness



Penetrator Geometry Modeling - Solid Cylinders
Lateral Support Modeling - Linear Springs



Dynamic Modeling - Lumped Mass
Linear Springs



FORCING FUNCTIONS

Figure 2 Math Modeling
 519

where:

$[M]$ = mass matrix

$[X]$ = displacements in translation and rotation
for each node

$\left[\ddot{X}\right] = \frac{d^2}{dt^2} X$

$[K]$ = structural stiffness matrix

$[F]$ = external forces and moments acting at
each node.

The external forces and moments are computed as follows. The axial acceleration of the projectile results in bending moments on each element of the penetrator due to its misalignment. The angular velocity results in centrifugal forces on each element due to offset of the elements from the barrel centerline. The acceleration and spin profiles used are based on an interior ballistics simulation.

Theoretical verification of the dynamic simulation was accomplished in two phases: (1) verification of the numerical integration technique, and (2) static verification of the structural model. Three numerical integration techniques were employed for comparison of efficiency and accuracy: (1) constant velocity or lumped impulse procedure, (2) Hombolt's approximation, and (3) fourth order Runge-Kutta. The results indicated comparable accuracies due to the nature of the differential equations and external forces. It was therefore concluded that the lumped impulse procedure would be used due to its higher efficiency over the other two methods. Structural verification of the technique used to model the penetrator was accomplished by computing the deflection of a statically loaded uniform rod for which a closed form solution is available. The same problem was solved using the Penetrator Bending Analysis (modified to solve a static situation). The resulting end deflection of the rod from the two solution techniques differed by approximately 5%. This checked the structural modeling of the penetrator thru the stiffness matrix.

The penetrator constraints are simulated by linear springs. The placement of these springs is defined by the carrier. The results of the dynamic simulation are obviously very critical to the location of those constraints, i.e., the support given to the penetrator by the carrier. The problem of determining the location and magnitude of these springs to accurately describe the carrier is very complex. It was decided that the most expedient method of determining these supports would be a static test. Stated briefly, the test set-up consisted of a 30 mm API projectile without the wind screen engraved into a barrel section. The penetrator tip was statically loaded. Deflections along the penetrator were measured for various levels of loading. In correlating the static test data with the theoretical model, tip deflection was the primary indicator used. Repeatability of the test was approximately $\pm 5\%$ on tip deflection. Correlation of the theoretical model with the test results was achieved by using linear springs of 5×10^6 lb/in with the last location of spring support coming at the edge of the carrier support. This provided an estimate of the spring constant which should be used for modeling of the constraints.

B. Yaw and Dispersion Computation

The result of primary interest from this analysis is the penetrator mode shape as the projectile exits from the barrel. This mode shape results in an initial angular motion of the projectile and consequently higher dispersion. From the known physical properties of the carrier and penetrator, stability properties of the projectile at barrel exit, and the mode shape, the first maximum yaw and dispersion are computed as follows:

Let: $C_{m\alpha}$ = Pitch moment coefficient derivative
 $C_{N\alpha}$ = normal force coefficient derivative
 C_D = drag force coefficient

C_{PN} = normal force center of pressure coordinate, in.
 X_{cg} = axial center of gravity position coordinate, in.
 D = projectile diameter, in.
 I_x, I_y = axial, transverse moment of inertia, lb-in²
 W = total projectile weight, lb.
 Y_{cg} = radial center of gravity position coordinate, in.
 T = rifling twist, cal/rev
 B = misalignment angle at projectile exit of centroidal axis relative to barrel centerline, radians
 $TDISP$ = dispersion, mils at 1000 inches
 $TABAR$ = projectile first maximum yaw

$$TDISP = \sqrt{D_1^2 + D_2^2} (1000.) \quad (2)$$

where:

$$C_{m\alpha} = C_{N\alpha} (C_{PN} - X_{cg})/D$$

$$D_1 = \left[\left(\frac{C_{N\alpha} - C_D}{C_{m\alpha}} \right) \left(\frac{2\pi}{T} \right) \left(\frac{I_y - I_x}{WD^2} \right) \right] (B)^2$$

$$D_2 = \left[(Y_{cg}) \left(\frac{2\pi}{TD} \right) \right]^2$$

$$TABAR = \left[2 \frac{I_y}{I_x} - 1 \right] (B)/\sigma \quad (3)$$

where

$$\sigma = \left(1 - \frac{1}{GYRO} \right)^{1/2}$$

$$GYRO = \frac{(568784)(I_x)^2}{I_y D^5 C_{ma} T^2}$$

The dispersion and first maximum yaw as computed above are assumed to represent three standard deviations of what should be expected in actual firings. This assumption is based on correlation to testing done on 30 mm API configurations. The values for these parameters are adjusted, based on this assumption, to represent one standard deviation.

The misalignment angle, B, is computed based on known physical properties of the carrier and bent penetrator configuration. This will be illustrated as follows. Consider that the moments of inertia and weights of each element of the modeled penetrator have been computed.

Let: I_{xi}, I_{yi}, I_{xyi} = axial inertia, transverse inertia, and product of inertia of i^{th} element

R_i = radius of i^{th} element

W_i = mass of i^{th} element

X_{cgi}, Y_{cgi} = center of gravity coordinates of i^{th} element

I_{xT}, I_{yT}, I_{xyT} = total axial, transverse, and product of inertia relative to the barrel centerline

X_{cgT}, Y_{cgT} = total center of gravity coordinates

$$I_{xT} = \sum_{i=1}^N \left[I_{xi} + W_i (Y_{cgi} - Y_{cgT})^2 \right] \quad (4)$$

$$I_{yT} = \sum_{i=1}^N \left[I_{yi} + W_i (X_{cgi} - X_{cgT})^2 \right] \quad (5)$$

$$I_{xyT} = \sum_{i=1}^N \left[W_i (W_{cgi} - X_{cgT})(Y_{cgi} - Y_{cgT}) \right] \quad (6)$$

$$B = \sin^{-1} \left[\frac{2I_{xyT}}{I_{yT} - I_{xT}} \right] / 2. \quad (7)$$

Typical dimensions and performance parameters are given in Table I for the GAU-8/A weapon.

EXPERIMENTAL CORRELATION

For positive verification of the method, the distorted shape of a penetrator at muzzle exit, as predicted by the simulation, should be compared with X-ray photographs of actual firings. Even though this has not been done on the final candidate configuration, the analytical approach has been successfully used to design penetrators with desired stability and stringent dispersion characteristics. X-ray photographs do exist at muzzle exit for one configuration. The bending is readily apparent in the photographs and is within the range predicted (.25 predicted, .20 measured) for that configuration. This is illustrated in Figure 3.

GAU-8/A Parameters

Bore Diameter	1.1845 ± .002 inches
Projectile Diameter	1.1795 ± .0015 inches
Muzzle Velocity	3200 to 3500 ft/sec
Muzzle Spin Rate	11360 to 12425 rad/sec
Peak Linear Acceleration	70,000 g's
Peak Angular Acceleration	8,000,000 rad/sec ²
Projectile Weight	.80 to .95 pounds
Penetrator Weight	.57 to .67 pounds

TABLE I
524

During the design evolution, various penetrator shapes were investigated both for penetration and dispersion. A summary of predicted versus actual measured dispersion is shown in Figure 4. As these designs are still competition sensitive between the ammunition subcontractors, they are only described by letters. Each letter represents a different design of penetrator or penetrator carrier interface. An exact prediction would have followed the dotted line. As the penetrator deflections become larger, more variations between predicted and actual are apparent. This is caused by the less rigid designs being more susceptible to variations in initial conditions.

The configurations D and E were predicted to deflect less than .002 inches while A is predicted to deflect about .010 inches.

Table II shows the computed effect of the following characteristics on dispersion.

1. Penetrator Diameter
2. Penetrator Length
3. Location of Support
4. Penetrator Material (Depleted Uranium or Kennertium)

Penetrator weight is held constant during 5 of the 6 examples shown. Small changes in dimensions are shown to make large changes in dispersion.

CONCLUSIONS

The model developed in this paper has been shown to be a reliable engineering tool for the design of Armor Piercing Projectiles. Tradeoffs can be performed analytically to select those configurations which will be structurally rigid enough to withstand gun launches without resulting in excessive dispersion.

DISPERSION OF CANDIDATE DESIGNS

TARGET AT 3600 INCHES

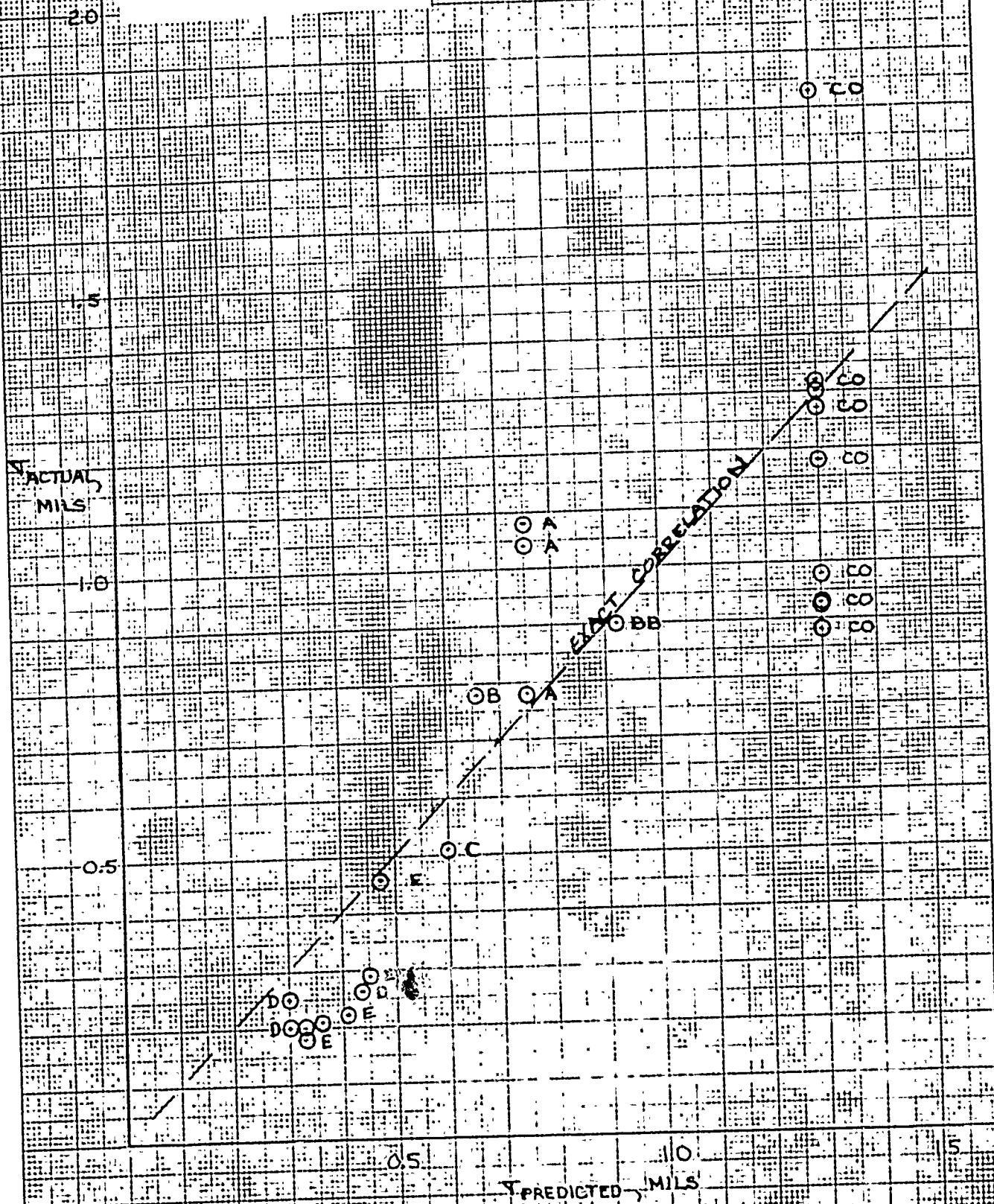


FIGURE 4

DISPERSION DUE TO PENETRATOR BENDING

CYLINDRICAL PENETRATOR CONFIGURATIONS

DIAMETER INCHES	LENGTH INCHES	LAST SUPPORT INCHES	MATERIAL	WEIGHT LBS.	TIP DEFLECTION (INCHES)		FIRST MAX. - YAW (DEGREES)		DISPERSION (MILS)	
					INITIAL	FINAL	INITIAL	FINAL	INITIAL	FINAL
.55	4.209	1.7	DU	.670	.0110	Did not make it	2.37	Did not make it	1.16	Did not make it
.60	3.537	1.7	DU	.670	.0093	.1565	1.71	18.43	.61	6.34
.65	3.014	1.7	DU	.670	.0080	.0124	1.26	1.65	.42	.54
.60	3.537	1.7	KEN	.670	.0093	.0216	1.71	3.18	.61	1.10
.60	3.337	1.7	DU	.632	.0088	.0295	1.54	3.71	.52	1.19
.60	3.537	1.9	DU	.670	.0093	.0317	1.72	4.19	.61	1.43

INITIAL PENETRATOR ORIENTATION RELATIVE TO BARREL CENTERLINE: - .0007" BASE OFFSET

.162° MISALIGNMENT ANGLE

TABLE II

THE EXPERIMENTAL VERIFICATION OF BUFFER
DISCHARGE COEFFICIENTS

A. AKERS
Iowa State University
Ames, Iowa

TABLE OF CONTENTS

	<u>Page</u>
SUMMARY	529
I. INTRODUCTION	530
II. THEORY	531
III. EXPERIMENTAL APPARATUS AND PROCEDURE	533
IV. PRESENTATION OF RESULTS AND DISCUSSION	536
V. FUTURE INVESTIGATIONS	541
VI. CONCLUDING REMARKS	542
VII. ACKNOWLEDGMENTS	543
VIII. REFERENCES	544

SUMMARY

A summary of how the buffer load is resisted in a conventional artillery system is given. The main geometric and dynamic properties of British guns manufactured during the twentieth century are then listed, and it is shown how these properties were achieved in a recoil test rig and in a static test rig, both pieces of apparatus being designed to measure orifice discharge coefficient. The mean experimental results are then presented and an indication of the corrections applied is given. The range of Reynolds number used was 40 to 40,000, and the ratio of length/gap of orifice was varied between 0.12 and 20.0. Comparisons between the e results and those produced by other authors using steady conditions were given, and the total spread of the value of discharge coefficient was around 0.08.

Finally, some indication is given as to how a test rig, presently being designed, will furnish further information on appropriate values of discharge coefficient at the extreme driving pressures generated in modern recoil systems.

I. INTRODUCTION

The orifice in a conventional artillery system used to absorb the energy of the recoil is normally annular in nature: one wall is moving while the other is stationary, and the area presented to the oil flow, together with the orifice geometry, changes during the recoil stroke. For a simplified diagrammatic representation of the buffer operation, see Figure 1. In addition to the above nonstandard conditions for a fluid orifice, the flow is quasi-static in nature; the pressure generated can be extremely high (up to 55 MPa), and cavitation is occurring. It is not therefore surprising that design information on orifice coefficient falls short of what is required for purposes of buffer design.

In [1] experimental results were obtained for annular orifices with one wall moving (dynamic) and for side wall orifices with stationary walls (static). Values of the ratio orifice length/orifice gap (l/h) varied between 0.12 and 20.0, and Reynolds numbers lay between 40 and 40,000. These controlled tests were performed on pieces of apparatus designed to approximate to the conditions within recoil buffers on British guns constructed in the twentieth century. See Table 1.

Values of discharge coefficient obtained were compared with those of previous authors [2,3] for steady flows and stationary walls. Good agreement was obtained, and mean curves have been drawn through the experimental points and presented here in order to provide design curves of discharge coefficient.

An attempt had been made in [1] to correlate experimental results from the point of view of cavitation, but no success was achieved. Some pertinent details are given, however, on a rig expressly being designed

to measure discharge coefficients when the flow velocities (u) are 110 m/s, the driving pressures (p) are 14 MPa, and cavitation numbers (K) are as high as 12.0. These values of p and K are considerably in excess of those used to date [4], although lower than those which may be expected in future armament systems [5].

II. THEORY

The type of orifice considered, together with geometrical and other quantities, is shown in Figure 1. When the recoil buffer force B is exerted on the outer cylinder, a pressure p_1 is generated in the upstream area, together with a velocity U of the cylinder. This gives rise to a theoretical value of velocity given by

$$U = \sqrt{\frac{2(p_1 - p_2)}{\rho \left[\left(\frac{A}{a}\right)^2 - 1 \right]}} \quad (1)$$

where ρ is the density of the fluid [6]. The value A/a is greater than 10 in practice, and the following corrections are also applied:

- velocity of approach phenomenon,
- extension of the rod,
- compression of the oil, and
- expansion of the cylinder.

These corrections lead to the following result for discharge coefficient

$$C_d = \left[\frac{U - \phi \left\{ \frac{d(p_1 - p_2)}{dt} \right\}}{a} \right] \sqrt{\frac{\rho}{2(p_1 - p_2)}} \quad (2)$$

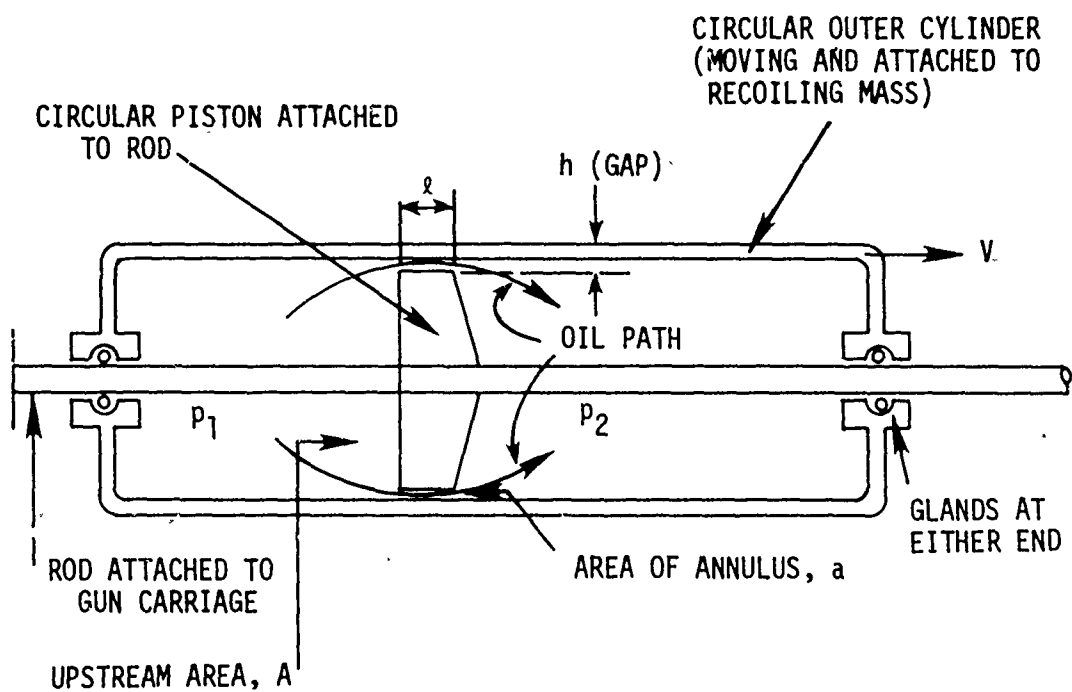


Figure 1. Diagrammatic representation of a recoil buffer and orifice.

The term in Eq. (2) which includes pressure variation with time is due to the effects of elasticity, and the derivation is given more fully in [1].

The effects of metal strain on orifice area and of volumetric flow due to the influence of viscosity in the annulus were ignored.

The discharge coefficient was plotted as a function of orifice Reynolds number. The reference length was taken to be the hydraulic mean diameter

$$D_M = \frac{(4) \text{ (area of orifice)}}{\text{(perimeter of orifice)}} \quad (3)$$

and with the dynamic rig, the value was approximately equal to twice the annular gap (which was identical to the representative length used in [3]). For the static rig, the value of D_M approximated to 1.95 h.

III. EXPERIMENTAL APPARATUS AND PROCEDURE

A. Dynamic Rig

The details of velocities, values of ℓ/h , and lengths of recoil of British guns used in the twentieth century are given in Table 1. This table shows how successful the attempts to achieve these values in the experiments were; the rig layout used is given in [1]. An outer cylinder was driven over the piston by means of an attached piston which was propelled by pneumatic pressure. The magnitude of the pneumatic pressure is dictated by the required cylinder velocity and varied between 0.40 and 1.1 MPa.

Pressure and velocity measurements were obtained from transducer outputs, which were triggered, synchronized, and recorded on the storage

screen of a standard, four-channel memory oscilloscope. Upon each "firing" the synchronized trace obtained from the pressure and velocity transducers was photographed. The stroke of the piston was obtained by numerical integration of the velocity trace in order to check the transducer calibration. Readings of pressure, velocity, slope of the pressure curve, and compressed length were obtained at 40 ms intervals. (The two latter quantities were required in order to calculate the compressibility correction.) The corrected velocity values were then used to give values for C_d and Re .

B. Steady State Rig

The steady flow orifice rig consisted of a square-sectioned chamber having transparent sides, the flow passing through a narrow rectangular slot. The gap width was varied to achieve values of l/h or 20.0, 10.0, 0.56, and 0.405. The entrance and exit pipes were 28 mm in diameter, and downstream of the entrance the flow expanded, passing through perforated plates for flow straightening. Water from the mains was used with this rig, and the exit was at atmospheric pressure. Figure 2 gives the general arrangement for measurement of discharge coefficient. For low flow rates the pressure difference was recorded on a mercury-on-water manometer, and for higher flow rates the difference of readings on two bourdon gages was used. A stop watch was used to determine the time taken for a given quantity of water to pass through the rig under steady flow conditions, and, thus, the mean velocity through the working section was derived. The kinematic viscosity of the water was deduced from its accepted variation with temperature (measured by means of a

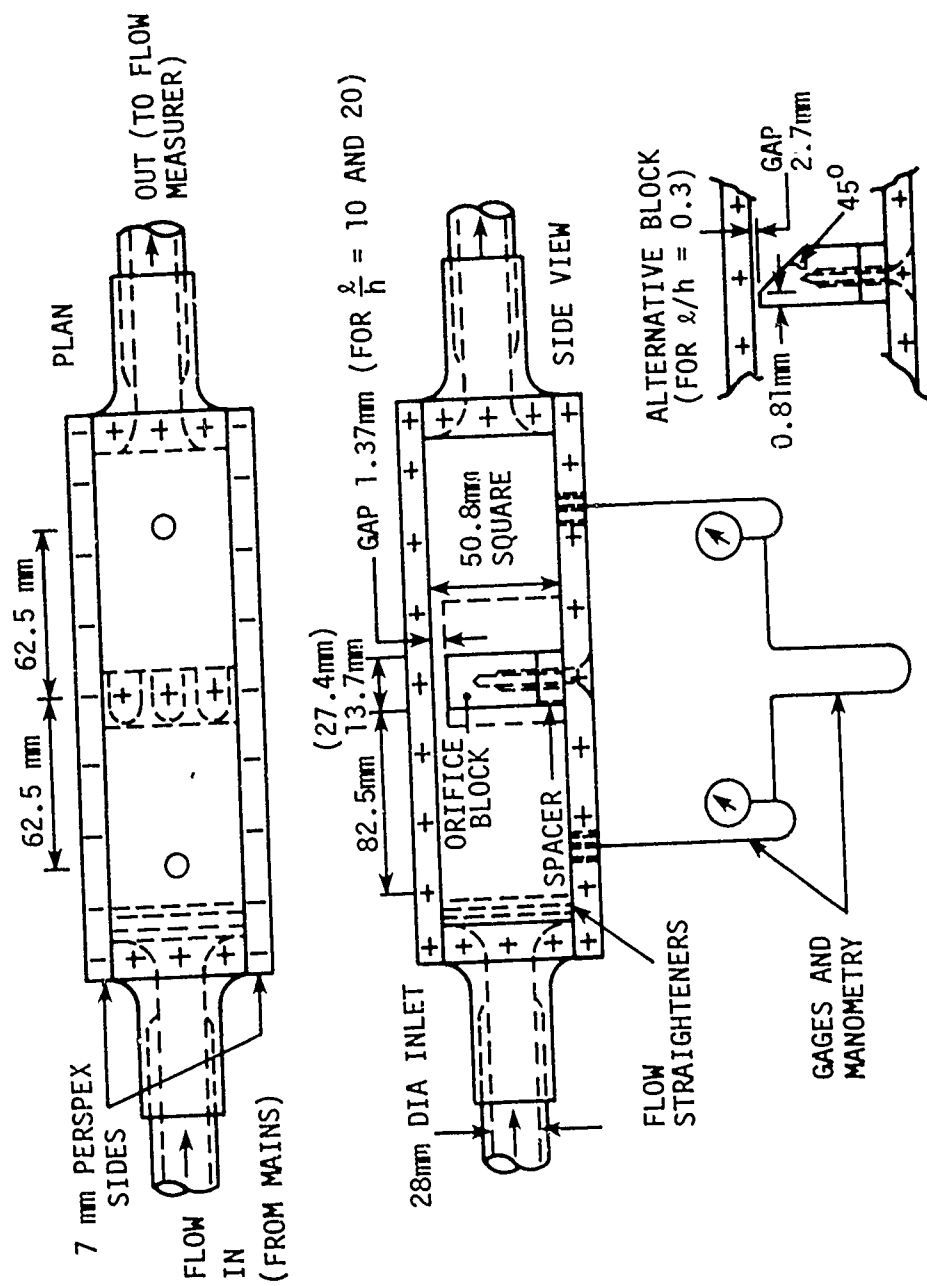


Figure 2. Measurement of discharge coefficient (steady state rig).

mercury in-glass thermometer), and, thus, Reynolds number and C_d were readily calculable.

IV. PRESENTATION OF RESULTS AND DISCUSSION

Orifice flow coefficient values with ℓ/h equal to 20, 10, and 0.3 (average) are shown in Figures 3, 4, and 5 for orifice Reynolds numbers ranging from 40 to 40,000. In addition to the experimental curves obtained from the dynamic and steady flow rigs, concerted results from Lichtarowicz et al. for $\ell/h = 0.5$ and 10.0 are shown [2], together with the results on an annular orifice by Bell and Bergelin [3]. The Reynolds numbers used in [2] were based on conditions within a circular orifice concentric with a circular pipe, whereas in the case of Bell and Bergelin and the experimental results obtained here from both the dynamic and steady state rigs, the hydraulic mean diameter was used.

For well over half of the results, it was expected that transition flow would exist, in a regime where both viscous and inertia phenomena are important; but for Reynolds numbers of greater than 4000, the predominant effects were expected to be kinetic energy losses associated with flow contraction, limited expansion, and turbulent friction. No measurements were taken during these tests for entirely viscous flow, the limit for Reynolds number being 40 for these conditions [3].

It was not possible to plot results for a symmetric circular orifice for $\ell/h = 20.0$ since there were no data available [2]. However, the values obtained here were within 0.08 of those for an annular orifice [2]. The values taken at $\ell/h = 10.0$ show an unexpected scatter of roughly 0.08 in C_d , but there is reasonable agreement between the

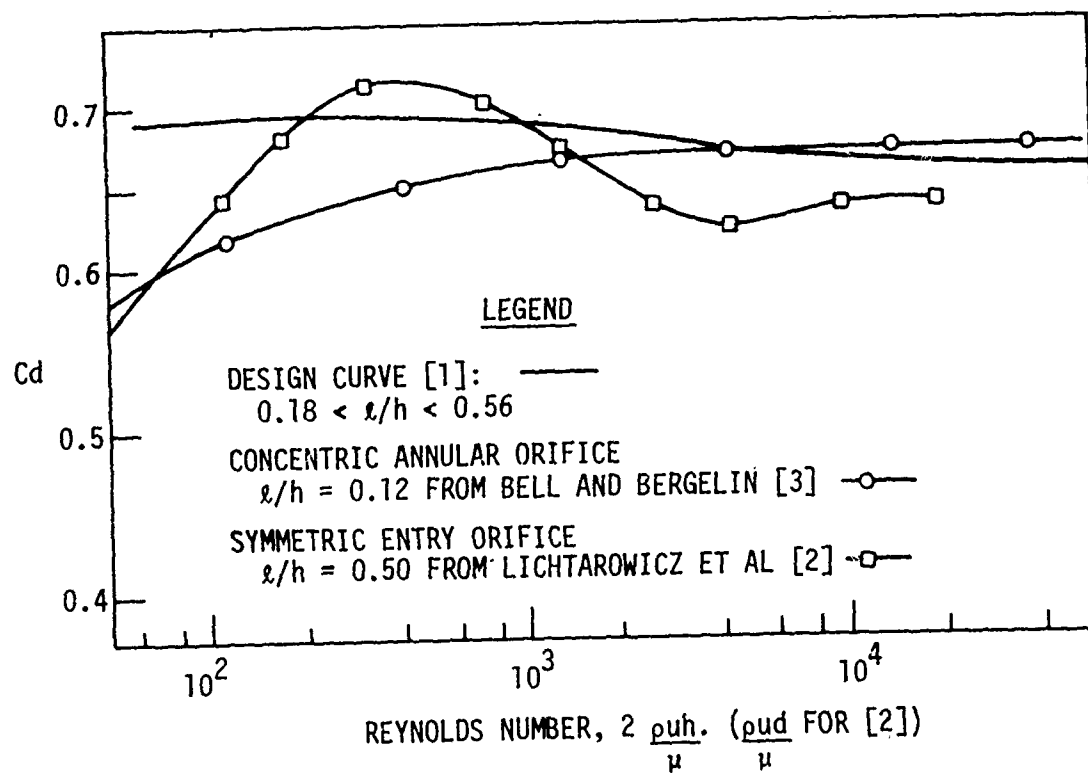


Figure 3. Design values discharge coefficient ($.18 < l/h < .56$).

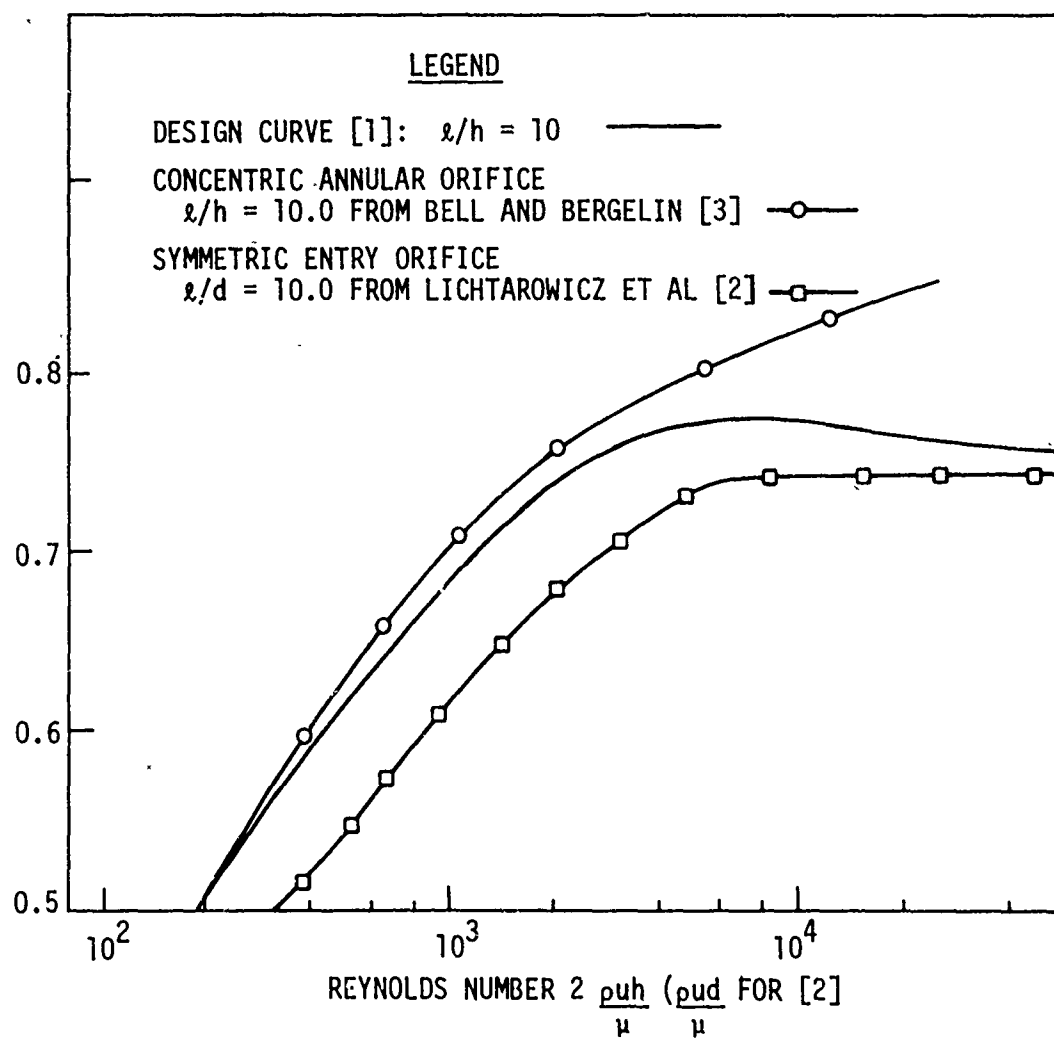


Figure 4. Design values of discharge coefficient ($\ell/h = 10.0$).

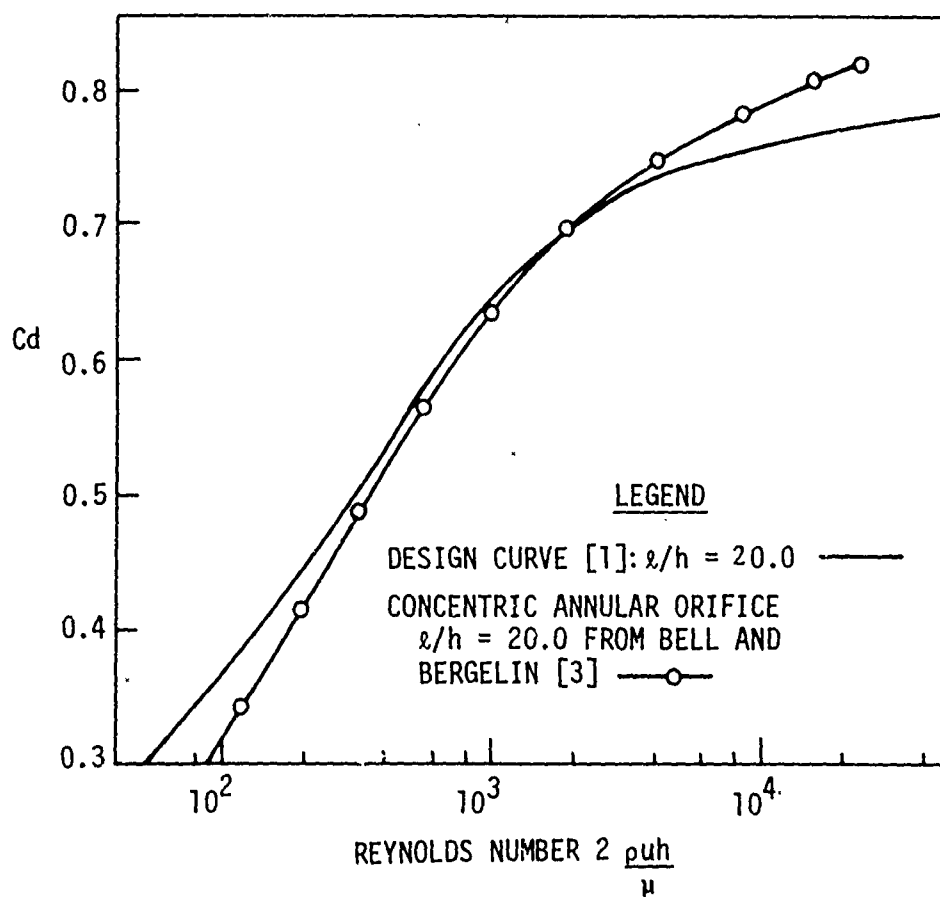


Figure 5. Design values of discharge coefficient ($l/h = 20.0$).

experimental results obtained on both dynamic rigs and with [2] and [3]. The results tend to be nearer those obtained in [3] than to those from [2] for Reynolds numbers of up to 10,000, a possible explanation being the greater similarity of orifice configuration.

Values of $\ell/h = 0.56$ and 0.405 were used for the steady state rig. For the dynamic rig, the value chosen was 0.3 and lay roughly between the values used in [3] and [4]. The results do not show nearly as much scatter as those for $\ell/h = 10.0$, and those obtained on the steady state rig agree tolerably with those obtained from the dynamic rig. The remarkable fact is the better agreement, over a wide Reynolds number range, of the experimental results with those produced in [2] than with those of [3]. The constancy in the values of C_d should also be noted.

The discharge coefficient for an orifice with a moving wall is found to vary less as the value ℓ/h diminishes, and it is tempting to suppose that when $\ell/h = 0$, the least variation is expected. This is, unfortunately, of little help in the design of armament recoil systems since the average value of ℓ/h for artillery pieces appears to be approximately 15.0 . The curves constructed, drawn through the experimental results should provide design values which are better than those used to date.

With regard to pressure traces measured downstream of the piston in the dynamic rig, the situation was not satisfactory. Confusing results were obtained, due possibly to the jet produced by the annular gap and to reflections of pressure and rarefaction waves from the cylinder extreme end. The small pressure pulses shown in the traces did not respond to mathematical treatment, and it was concluded that these could

be ignored compared with upstream values, as they were always less than about 0.07 MPa. On the above grounds, it was decided that no useful purpose could be served at this stage by presentation of these results. It is considered that such effects can be measured using instrumentation now available, but it should be realized that any set of results must be regarded as applicable to the geometry of that particular recoil buffer only.

V. FUTURE INVESTIGATIONS

From recent calculations [5] it has been shown that under overload conditions of certain types of armament, it is possible to achieve the required buffering force only by using cylinder pressures in the order of 55 MPa. Thus, oil velocities in the jet are in the order of 250 m/s. The geometry of the orifice can also be unusual, inasmuch as radially inward flow into the center of a hollow tube is sometimes used, and there will be extensive cavitation and jet impingement. Under these conditions it is not known what values of discharge coefficient should be assumed. Such information is essential for calculation of the dynamics of the recoiling parts, and, thus, the design of a test rig to measure this quantity at extreme pressures is now underway at Iowa State University. It is to be a steady state rig, and values of pressure of only one quarter of those encountered instantaneously in the system described above are contemplated (i.e., pressures up to 14 MPa), but further information will be available from a suitable dynamic test to be used in conjunction with the rig. It is expected that the range of knowledge will be increased significantly by this research.

VI. CONCLUDING REMARKS

1. Flow measurements taken on rigs where fluid passes through a narrow gap adjacent to one wall, where Reynolds numbers have been between 40 and 40,000, and the orifice length to wall gap ratios between 0.3 and 20.0 have been considered. In one rig the gas was annular and the outside wall moving, and in the other the gap consisted of a long rectangle where all walls were stationary. The quasi-steady values for orifice discharge coefficient with a moving wall were not markedly different from those obtained with a stationary wall, although they do tend to be slightly higher. The values are also close to results obtained by previous workers using stationary concentric central or peripheral orifices. Design curves for discharge coefficient have been drawn through the experimental points using the correct orifice configuration, and these should provide better data than those presently available.
2. In the case of the moving wall configuration, corrections were made for compressibility of the fluid and elasticity of the cylinder/piston arrangement. The viscous effect of the moving wall and the effect of loads upon orifice deformation were ignored.
3. The variation of C_d with Reynolds number diminishes as the value of l/h decreases. Although it would be preferable to have a constant C_d for the design of recoil systems, it is not possible to have values of l/h less than approximately 10 and, thus, the above fact is of little practical value in this case.
4. A newly designed experimental rig should provide further information on discharge coefficient at values of pressure and jet velocity

outside those values at which tests have, up to the present, been used. These pressures and velocities will go some way to meeting values experienced in presently designed systems.

5. Although it seems possible that the results of shock waves can be measured, their influence would be difficult to assess, and it seems likely that the phenomena actually observed would only apply to the actual configuration tested.

VII. ACKNOWLEDGMENTS

The work described above was performed partially under the auspices of the Engineering Research Institute of Iowa State University. Their support is gratefully acknowledged.

VIII. REFERENCES

1. A. Akers, Discharge Coefficients for an Annular Orifice with a Moving Wall, in "Proc. Third Int. Fluid Power Symp.," pp. B3-37-B3-51. British Hydrodynamic Research Association, Bedford, England, 1973.
2. A. Lichtarowicz, R. K. Duggins and E. Markland. Discharge coefficients for incompressible flow through long orifices, J. Mech. Eng. Sci., 7(2), 210-219 (1965).
3. K. J. Bell and D. P. Bergelin. Flow Through Annular Orifices, Trans. ASME, 79(3), 593-601 (April 1957).
4. R. H. Spikes and G. A. Pennington. Discharge Coefficient of Small Submerged Orifices, Proc. Inst. Mech. Eng., 173, 661-674 (1959).
5. A. Akers. Unpublished report to Naval Surface Weapons Center, Dahlgren, September 1976.
6. R. A. Dodge and M. J. Thompson. "Fluid Mechanics," First edition. McGraw Hill, New York, 1937.

MAIN DETAILS OF BRITISH RECOIL SYSTEMS

TYPE OF GUN	MUZZLE VELOCITY m/s	DATE OF MANUFACTURE	ORIFICE SHAPE ENTRY	x/h	A/a	RECOIL LENGTH (m)	MAX RECOIL VELOCITY m/s
3.7 IN HOW	296	1920	30° RAMP	4.4	8.85	1.07	10.1
5.5 IN FIELD GUN	90	1941	30° RAMP	8.3	5.2	1.37	10.6
25 POUNDER FIELD GUN	530	1938	45° RAMP	2.5	4.83	0.92	10.4
12 POUNDER COASTAL	680	1910	90° CORNER 0.05 IN RAD	1.65	19.5	0.21	0.68
105 mm SP (ABBOT)	720	1965	90° CORNER 0.1 IN RAD	40.0	9.9	0.31	14.2
4.5 IN ACK ACK	730	1940	45° RAMP 0.15 IN RAD	1.25	10.0	0.42	0.71
77 mm TANK GUN	840	1944	45° RAMP 0.15 IN LONG	24.6	12.4	0.22	10.1
17 POUNDER S.P. GUN	880	1944	90° CORNER 0.05 IN RAD	17.7	14.9	0.36	9.1
6 POUNDER ANTI TANK	890	1941	90° CORNER 0.05 IN RAD	39.6	15.3	0.76	8.6
32 POUNDER ANTI TANK	1070	1945	90° CORNER	21.7	4.3	0.36	8.4
RECOIL RIG	--	--	90° CORNER	0.3 10.0 20.1	13.3	0.58	3.0
STEADY FLOW APPARATUS	--	--	90° CORNER	0.3 0.405 0.56 10.0 20.0	36.4 18.2	--	--

Table 1.

PRECISION POINTING AND STABILIZATION OF A
LOW DISPERSION AUTOMATIC CANNON SYSTEM

R.E. KASTEN
Rock Island Arsenal
Rock Island, Illinois

N. LOH
University of Iowa
Iowa City, Iowa

TABLE OF CONTENTS

	<u>Page</u>
I. INTRODUCTION	547
II. SYSTEM SPECIFICATION	548
III. DERIVATION OF THE CONTROL LAW	559
IV. SPECIFICATION OF CONTROL ELECTRONICS	572
V. SUMMARY AND CONCLUSIONS	574
REFERENCES	576

I. INTRODUCTION

A. BACKGROUND

An increasing number of Army gun type weapon systems, including helicopter gun turrets, artillery, air defense guns and combat vehicles, require high performance gun pointing, tracking and stabilization systems to effectively perform their mission. Consequently, it has become increasingly important for the Army to develop a capability to specify, design and evaluate control and stabilization systems for turreted weapons.

To help meet this need, a procedure for the design of control and stabilization systems has been jointly developed by personnel of the Rodman Laboratory and the Department of Information Engineering at the University of Iowa. This procedure utilizes results of modern control theory, augmented by extensive digital computer simulations to derive and specify a practical controller for both regulating and tracking systems. The optimal design procedure and the numerical techniques required to obtain a solution were derived and utilized initially in an investigation of methods^{1,2,3} to improve the pointing accuracy of helicopter gun turrets, however, it is applicable to any turreted weapon system. It is presently being applied to design of a turret drive system for the Low Dispersion Automatic Cannon System (LODACS) test bed vehicle. The LODACS test bed vehicle consists of a Sheridan vehicle in which the main weapon has been replaced by a RARDEN 30mm automatic cannon.

The LODACS vehicle will have a stabilized sighting system and a sophisticated fire control system including a digital fire control computer, a miss-distance sensor (MDS) and a Closed-Loop Fire Control system. The purpose of the task reported in this paper is to provide the LODACS test bed vehicle with a precision gun pointing system which will respond to position commands received from the sight and fire control systems and maintain the desired aim-point for both stationary and fire-on-the-move conditions.

B. TURRET CONTROLLER DEVELOPMENT

The development of the turret control system can be divided into three stages or tasks:

1. Specification of components for the turret power drive subsystem (i.e., motors, actuators, gearboxes, power supplies, etc.). These components must meet the torque, speed and power requirements established by the performance requirement and the operating environment of the particular weapon system.

2. Derivation of a control law to achieve the desired performance with the components specified in Task 1.

3. Specification and integration of the electronics and sensors needed to implement the control law with the power drive subsystem.

The details of each of these three stages as applied to the development of the LODACS turret and the progress to date, are discussed below.

II. SYSTEM SPECIFICATION

The first step in the design of a turret control system is to determine the performance requirement of the system and the disturbance

environment in which the system must operate.

This information is then used to specify the turret power drive components which will respond to controller commands and maintain the aim line in spite of applied disturbances.

Once the power drive subsystem is determined, the ultimate performance capability of the system is also largely determined. No control law can be derived which will correct for major errors made in this stage of the design. In theory it is possible to choose the poles and zeroes of a controllable linear system at will and thus achieve any desired level of performance. In practice, however, non-linearities, and power and torque limitations always restrict the range over which system characteristics can be modified by feedback control.

In spite of the importance of this stage of the design, it is often difficult or impossible to determine the exact performance requirements or the disturbance environment. Often the parameters of the gun, turret and mount are not completely determined when long lead items for the control system are specified. No general method for determining these requirements is available, but the way in which the LODACS system was specified is discussed and might at least serve as a guide for combat vehicle turrets

PERFORMANCE REQUIREMENTS

Specific performance requirements for the LODACS were derived from the accuracy of the gun and the fire control system and from knowledge of the requirements on other combat vehicles. The LODACS turret control system will slave the gun to a separately stabilized sight. Aimpoint

offsets of the gun line from the gunner's line of sight are computed by the fire control computer and must be maintained by the turret control system.

The principle sources of delivery error for the LODACS weapon system are the gun/ammo dispersion, the fire control system computational error and the gun pointing error. The gun/ammo dispersion and the expected fire control error are random errors of known magnitude. The accuracy requirement for the weapon pointing and stabilization system was chosen so that the total system error would not be seriously degraded.

DISTURBANCE ENVIRONMENT

A complete specification of a turret control system must also include the turret tracking requirement and the disturbance environment. Information on the evasive motion of typical targets or on the evasive maneuvers of an attacking vehicle are not yet available to the designer. Proving ground test of moving fire capability often involve firing at targets with a fixed crossing velocity on firing at fixed targets from a zig-zag course. Because of the long engagement ranges, a maximum tracking rate of 100 mr/sec (corresponding to a crossing velocity of 60 mph at 250 meters) was considered adequate. A higher rate for slewing ($\sim 90^\circ/\text{sec}$) is required but precision tracking is not required at these rates. For design purposes the target was modeled as moving with step-like changes in velocity with fixed velocity between these changes.

The disturbances encountered by a turret control system are a function of the vehicle speed and the terrain roughness as well as the gun and turret mass properties and the properties of the turret drive elements themselves. The torque relationship between these quantities can be expressed as an equation of the form:

$$\text{II-1} \quad T = m \times r \times a_L + N^2 (J_m + J_a) \times a_H + [N^2 (J_m + J_a) + J_L] \times a_C$$

where m is the mass of the load (the turret or the gun, r is the distance between the load center of gravity and its center of rotation, a_L is the component of turret linear acceleration perpendicular to both r and the center of rotation, N is the gear ratio of the turret drive system, J_m is the inertia of the motor rotor, J_a is the equivalent inertia of the gears, a_H is the component of hull angular acceleration about the load center of rotation, J_L is the moment of inertia of the load and a_C is the angular acceleration commanded by the gunner and fire control system. For loads driven by a hydraulic piston, the second term is replaced by a term dependent on the length of the torque arm, the mass of the piston and the effective mass of the torque arm, however, this term is negligible compared to the other components.

The specification of the turret power drive components for the LODACS drive system was based on the statistical properties of the torque obtained from Eq. II-1. The torque capability was specified as the value that would meet the torque requirement 95% of the time (assuming gaussian probability distributions), that is, the torque capability required was twice the rms value of the torque obtained

from the torque relation, evaluated for a typical hull input.

The gun and turret inertias and unbalances were estimated based on known gun and turret properties. The gear ratios and motor rotor and gear inertias vary widely depending on the type of turret drive system selected.

The statistical properties of the system required to evaluate II-1 (except a_c) were obtained from HITPRO⁵ computer simulation of the vehicle moving over the Aberdeen Proving Ground Bump Course at 15mph. It should be noted that a high degree of correlation between a_L and a_H was predicted by the simulation so that the torque was the simple sum of the components rather than the root sum square as for uncorrelated components.

A further requirement on the turret drive components is that they deliver the specified torque at the 2σ value of the gun angular rate relative to the hull. The rms angular velocity of the hull was also estimated from the HITPRO simulation (.25 radians/sec in elevation and .1 radian/sec in azimuth). This velocity requirement is added because the torque output capability of some types of drive system decreases rapidly as the velocity increases. The power requirement was obtained from the torque requirement and the r.m.s. relative velocity of the weapon and the hull obtained from the simulation.

The parameters and statistical averages for the LODACS vehicle are tabulated in Table II-1.

BANDWIDTH REQUIREMENTS

The suspension system of a combat vehicle acts as a low pass filter that attenuates the high frequency inputs from the terrain. Further damping of the high frequency disturbance components is accomplished by the inertia, J, of the gun and turret themselves which add an attenuation factor, A(f) of the form

$$\text{II-2 } A(f) = \frac{1}{J(2\pi f)^2}$$

to the magnitude of the motion resulting from a disturbance at a frequency f. The turret control system must damp out the low frequency components. The bandwidth requirement for the turret control system was determined by estimating the frequency above which the disturbance torque weighted by A (f) becomes negligible. The frequency spectrum was calculated from computer simulation of the linear acceleration (the principle disturbance) and the bandwidth requirements were estimated to be from 0-5hz for the traverse drive and 0-10hz for the elevation drive.

In order to assure that these bandwidths would be achievable in the system, the resonances of the drive system components, i.e., gearbox and hydraulic resonances, were required to be outside this region.

POWER DRIVE SUBSYSTEM

Based on the above requirements on the turret power drive subsystem, a hydraulic system was chosen for the LODACS turret. This hydraulic system employs a bent axis hydraulic motor and gearbox in traverse and a hydraulic piston in elevation.

A hydraulic power supply consisting of an electrically driven hydraulic pump and an accumulator provides the hydraulic system with a 2000 psi operating pressure. This system actually exceed torque and power requirements but larger hydraulic actuators are required to increase the hydraulic stiffness to meet system bandwidth requirements. The linearized block diagrams of these systems are shown in Figures II-1 and II-2. The differential equations representing this system can be written as

$$\text{II-3} \quad \dot{x} = Ax + Bu + Fw$$

$$x(0) = x_0$$

where x is a vector representing the states of the system, w is the external disturbance applied to the system, and u is a control function whose derivation is discussed in the following section. A , B and F are matrices whose elements are a function of the parameters of the turret. A , B , and F for the elevation and azimuth LODACS system are given in Tables II-1 and II-2.

TABLE II-1a

STATISTICAL PROPERTIES OF HULL MOTION USED TO ESTIMATE LODACS TORQUE
AND POWER REQUIREMENTS

ELEVATION

$$a_L = 12 \text{ft/sec}^2 (\text{rms})$$

$$a_A = 2 \text{ rad/sec}^2 (\text{rms})$$

$$a_C = 1/2 \text{ rad/sec}^{2*}$$

$$w_n = .125 \text{ rad/sec (rms)}$$

AZIMUTH

$$a_L = 10 \text{ft/sec}^2 (\text{rms})$$

$$a_A = 1/2 \text{ rad/sec}^2 (\text{rms})$$

$$a_C = 1/2 \text{ rad/sec}^{2*}$$

$$w_H = .1 \text{ rad/sec}^{**}$$

UNLESS OTHERWISE NOTED ALL QUANTITIES WERE ESTIMATED FROM A HITPRO
SIMULATION OF A SHERIDAN VEHICLE AT 15 MPH ON THE APG BUMP COURSE.

*Estimated fire control computer command requirement

**Based on required tracking rate, not hull motion

TABLE II-1b

LODACS TURRET PHYSICAL PROPERTIES

ELEVATION

$$M_{xr} = 250 \text{ #-ft/g}$$

$$N^2(J_M + J_A) \approx 0.$$

$$J_L = 160 \text{ slug-ft}^2$$

AZIMUTH

$$M_{xr} = 4000 \text{ #-ft/g}$$

$$N^2(J_M + J_T) = 400 \text{ slug-ft}^2$$

$$J_L = 4000 \text{ slug-ft}^2$$

TABLE II-2

ELEVATION SYSTEM

REGULATOR

$$A = \begin{bmatrix} 0 & 1 & 0 & 0 & 0 & 0 \\ 0 & -2.62 & .0117 & 0 & 0 & 0 \\ 0 & -2.09 \times 10^5 & 0 & 2.3 \times 10^6 & 0 & 0 \\ 0 & 0 & 0 & 0 & 4.0 & 0 \\ 0 & 0 & 0 & 0 & 0 & 1 \\ 0 & 0 & 0 & -4.11 \times 10^6 & -9.8 \times 10^4 & -500 \end{bmatrix}$$

$$B^T = \begin{bmatrix} 0 & 0 & 0 & 0 & 0 & 4.9 \times 10^4 \end{bmatrix}$$

$$H^T F^T = \begin{bmatrix} 0.0 & -2.625 & -2.0971 \times 10^5 & 0 & 0 & 0 \end{bmatrix}$$

TRACKER

$$p=r$$

$$A_r = \begin{bmatrix} 0 & 0 \\ 0 & 1 \end{bmatrix}$$

DISTURBANCE ACCOMMODATION

$$w=z$$

$$A_z = \begin{bmatrix} 0 & -39.4 \\ 1 & 0 \end{bmatrix}$$

TABLE II-3

AZIMUTH SYSTEM

REGULATOR

$$A = \begin{bmatrix} 0 & 1 & 0 & 0 & 0 & 0 & 0 & 0 \\ 0 & .182 & 0 & 0 & 0 & 0 & 0 & 921 \\ 0 & 0 & -1.17 & 2.59 \times 10^6 & 0 & 0 & -806. & 0 \\ 0 & 0 & 0 & 0 & 4 & 0 & 0 & 0 \\ 0 & 0 & 0 & 0 & 0 & 1 & 0 & 0 \\ 0 & 0 & 0 & -3.05 \times 10^6 & -9.79 \times 10^4 & -500 & 0 & 0 \\ 0 & 0 & 6.2 & 0 & 0 & 0 & 0 & -5760 \\ 0 & -1.0 & 0 & 0 & 0 & 0 & .0016 & 0 \end{bmatrix}$$

$$B^T = \begin{bmatrix} 0 & 0 & 0 & 0 & 0 & 48985 & 0 \end{bmatrix}$$

$$H^T F^T = \begin{bmatrix} 0 & -.182 & 0 & 0 & 0 & 0 & 0 & -1 \end{bmatrix}$$

TRACKER

$$p=r$$

$$A_r = \begin{bmatrix} 0 & 0 \\ 1 & 0 \end{bmatrix}$$

DISTURBANCE

$$w=z$$

$$A_z = \begin{bmatrix} 0 & -39.4 \\ 1 & 0 \end{bmatrix}$$

III. DERIVATION OF THE CONTROL LAW

A. THEORETICAL CONSIDERATIONS

The general optimal control problem is to determine a control function, u , such that an asymptotically increasing cost function, J , is minimized for any initial condition on the state vector, X . The cost function, J , is the time integral of some positive definite function of time, the states of the system and the control function. For most cost functions, the solution for the optimal control is a very difficult, if not intractable problem. There is one particular type of cost function, the quadratic cost function, for which the form of the solution is well known and numerical techniques for the solution are widely available. The application of these techniques to the derivation of a controller for a helicopter gun turret has been reported elsewhere.^{1,2,3}

The results obtained in these studies showed that a practical quadratic optimal controller could be derived which performed better than the existing classical controller, required relatively little engineering effort to design, and could be easily implemented. This design technique was chosen for application to the LODACS turret controller. A brief review and discussion of the theory is included here.

LINEAR OPTIMAL REGULATOR WITH A QUADRATIC COST FUNCTION

A linear system may be described by a set of linear differential equations of the form

$$\begin{aligned} \text{III-1} \quad \dot{x} &= Ax + Bu & y &= Hx \\ x(0) &= x_0 \end{aligned}$$

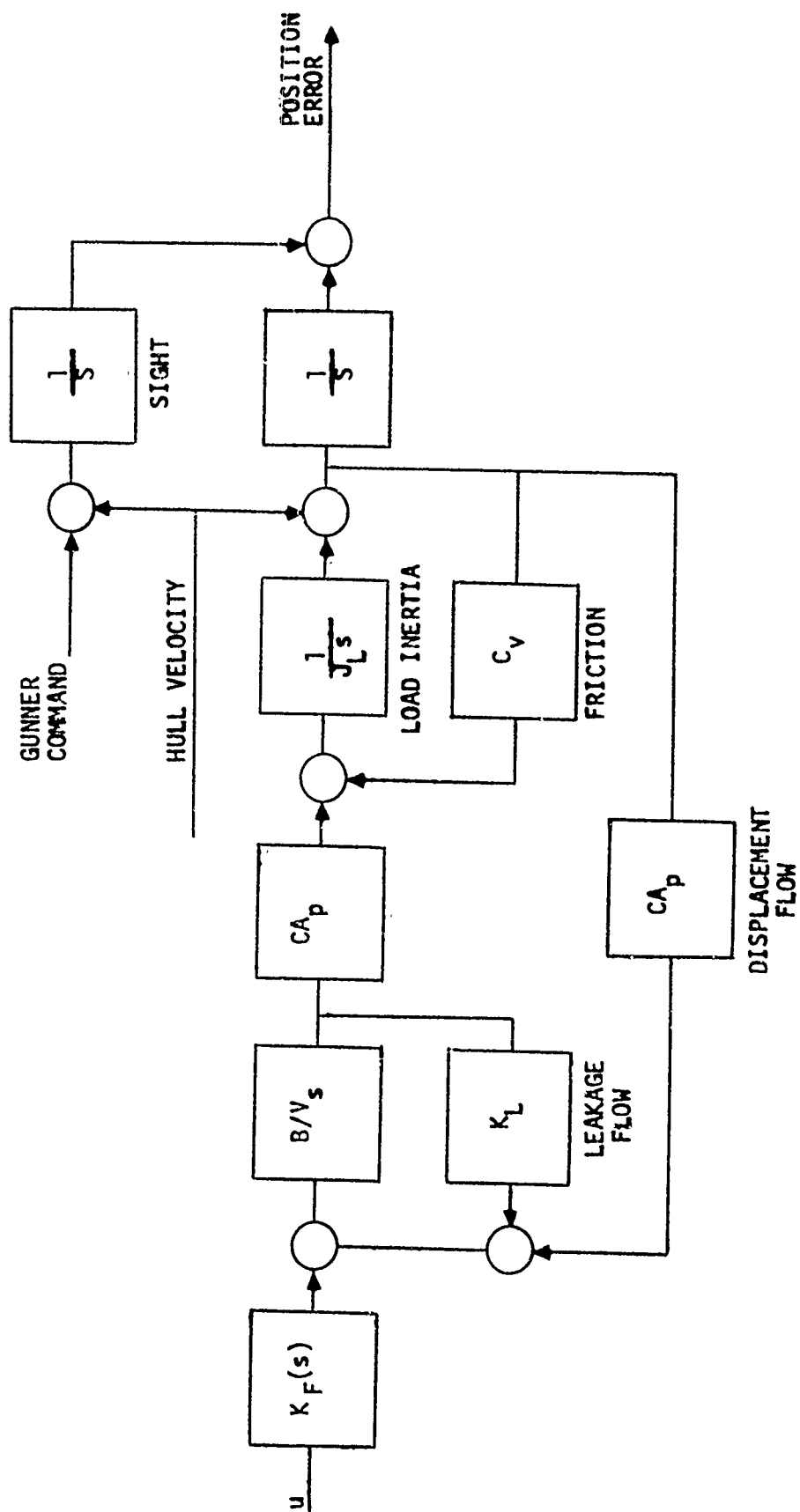


FIG II-1 HYDRAULIC TURRET DRIVE SYSTEM
(ELEVATION)

where x is a vector of the states of the system, u is the control function and A and B are matrices whose elements are determined by the parameters of the system. y is the vector of observed states of the system.

The quadratic cost function, which will be minimized by the choice of u , is of the form

$$\text{III-2} \quad J = \int_0^{t_f} (x^t H^T Q H x + u^T R u) dt + x^t(t_f)^T R_2 x(t_f)$$

where Q and R_2 are positive semidefinite weighting matrices and R is a positive definite weighting matrix. t_f is the final time of interest for the problem.

The control function, u , which will drive the initial state, x_0 , to the zero state with a minimum value for J is known to be of this form:

$$\text{III-3} \quad u_{\text{opt}} = -R^{-1} B^T K x$$

where the K matrix is the solution of matrix Ricatti equation

$$\begin{aligned} \text{III-4} \quad -\dot{K} &= A^T K + K A + H^T Q H - K B R^{-1} B^T K \\ K(t_f) &= R_2 \end{aligned}$$

The solution of this non-linear matrix differential equation can be obtained by numerical methods. The resulting optimal control function can be implemented by weighting the measured states of the system by time varying gains. Often these time varying gains quickly reach a steady state value.

In many cases, including the turret controller, the steady state solution is desired. The feedback gains then become fixed, which permits

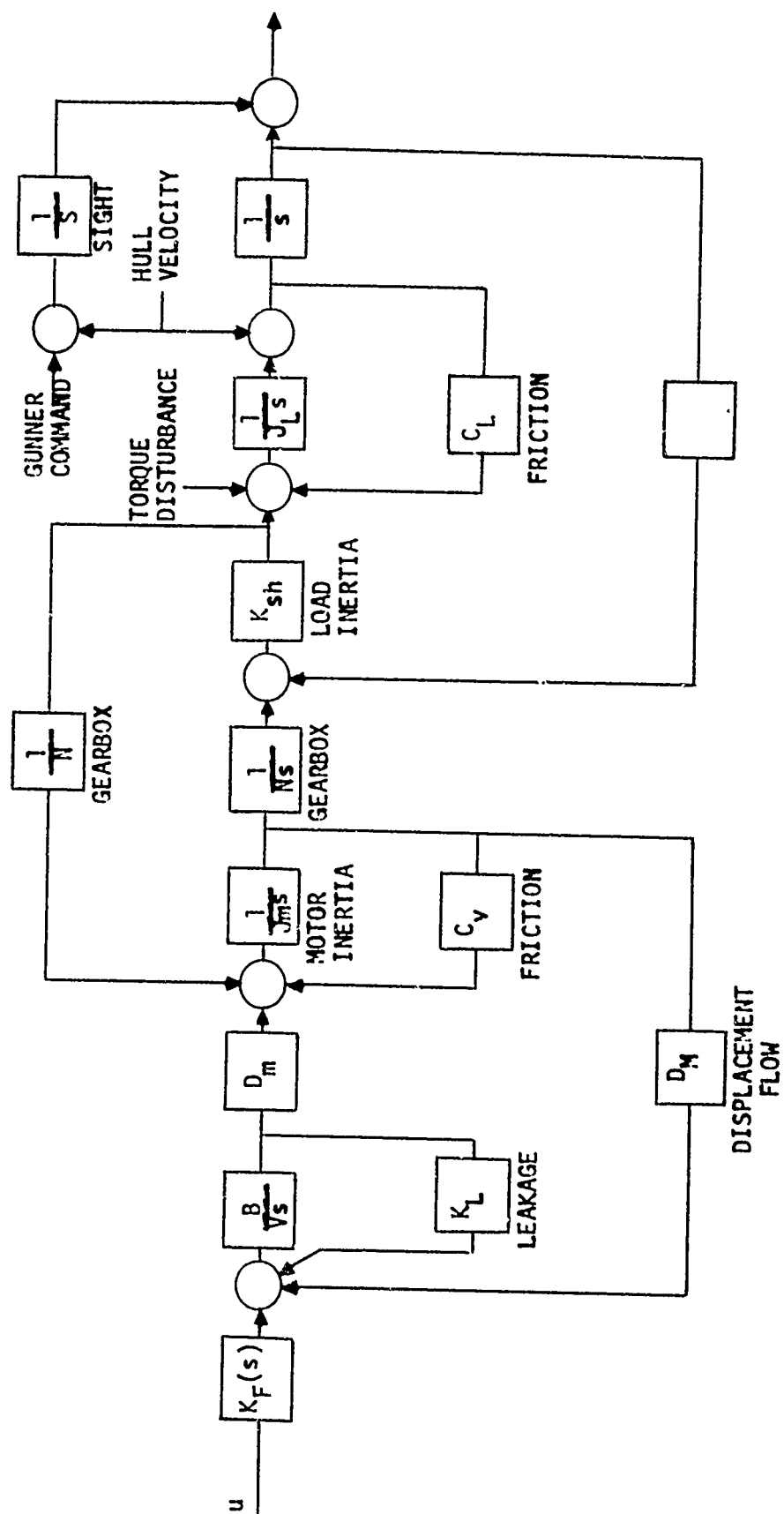


FIG II-2 HYDRAULIC TURRET DRIVE SYSTEM
(AZIMUTH)

them to be easily implemented by analog circuits.

The steady state value of the K matrix can be found by solution of the algebraic equation

$$\text{III-5} \quad 0 = A^T K + KA + H^T QH - KBR^{-1} B^T K$$

This latter technique is computationally more efficient, which becomes important when the design is iterated many times. Note that all states are assumed to be measured and available for forming the feedback control function.

THE TRACKING PROBLEM

The optimal regulator generates a control function which drives the state vector to zero from some initial condition or maintains some set vector in the presence of external disturbances. In many cases, including the turret controller, it is actually desired that one or more states of the system track some input command such as the gunner's tracking command. The tracking problem can easily be put in the form of the regulator problem provided that the tracking commands can be approximated by the output of a stable linear system decaying from some arbitrary initial condition. A wide range of tracking signal including steps, ramps, sinusoids and decaying exponentials can be represented in this way.

The tracking command, p , can be represented as the output of the linear system

$$\begin{aligned} \text{III-6} \quad p &= D_r r \\ \dot{r} &= A_r r \\ r(0) &= r_0 \end{aligned}$$

Now the original regulator states represented by Eq. III-1 can be augmented by the states represented by Eq. III-6 to form a new regulator system with states \bar{x} matrices A, B and D replaced by \bar{A} , \bar{B} and \bar{D} where

$$\text{III-7a} \quad \bar{A} = \begin{bmatrix} A & 0 \\ 0 & A_r \end{bmatrix},$$

$$\text{III-7b} \quad \bar{B} = \begin{bmatrix} B \\ 0 \end{bmatrix}$$

$$\text{III-7c} \quad \bar{D} = [D \quad D_r]$$

and $\bar{x} = \begin{bmatrix} x \\ x_r \end{bmatrix}$

By proper choice of the cost function the control system can be forced to follow the tracking command. For example, if it is desired that x_1 follows p_1 , the cost function can contain a term of the form $(x_1 - p_1)^2$. If this term is heavily weighted in the cost function, then x_1 is forced to follow p_1 and the desired performance is obtained. The form of the solution for the control function for the optimal tracker is exactly the same as for the regulator.

For the LODACS turret system, the tracking command is modeled as a series of step and ramp function of unknown height and slope. The tracking function can be represented by a second order linear system of the form:

$$\text{III-8} \quad \begin{bmatrix} \dot{r}_1 \\ \dot{r}_2 \end{bmatrix} = \begin{bmatrix} 0 & 0 \\ 0 & 1 \end{bmatrix} \begin{bmatrix} r_1 \\ r_2 \end{bmatrix} \quad \text{with } p = r.$$

DISTURBANCE ACCOMMODATION

Any external disturbances which are applied to the optimal regulators and trackers described above, cause the state of the system to deviate from the desired state. The resulting error is sensed and the state feedback control function is applied to the plant to balance the disturbance. Thus some error must result before a corrective action is taken. In the presence of large external disturbances, it is difficult to implement the control function required for precision tracking. This problem is also encountered in classical design controllers and is handled by the use of feedforward signals.

The original LODACS optimal tracker designs were found (by computer simulation) to be overly sensitive to hull motion inputs. It did not appear that the feedback gains could be increased to provide satisfactory performance. This was not completely unexpected since other optimal tracker designs had demonstrated this sensitivity and all existing high performance turret stabilization systems have hull motion feed forward loops.

The optimal design procedure can accommodate the design of feedforward loops for disturbance accommodation in much the same way as the tracking signals are accommodated, that is, the tracker states are augmented by the states of a stable linear system which generates an approximation of the disturbance input as it decays from some initial condition. The disturbance is modeled as a vector, w , which is the output of a system described by:

$$w = H_z$$

$$z = A_z z$$

$$z(0) = z_0$$

the augmented regulator including both the tracking states and the disturbance states has the same form as the original regulator problem except the matrices A , B and D are replaced by \bar{A} , \bar{B} and \bar{D} respectively, where,

$$\text{III-9a} \quad \bar{A} = \begin{bmatrix} A & FH & 0 \\ 0 & A_z & 0 \\ 0 & 0 & A_r \end{bmatrix}$$

$$\text{III-9b} \quad \bar{B} = \begin{bmatrix} B \\ 0 \\ 0 \end{bmatrix}$$

$$\text{III-9c} \quad \bar{D} = [D, D_r, H].$$

The form of the cost function and the solution for the optimal control function is the same as for the optimal regulator, however, for the tracker and the tracker with disturbance accommodation, considerable computational simplification and a pleasing result can be realized if the K matrix is divided into components

$$K = \begin{bmatrix} K_{xx} & K_{xz} & K_{xr} \\ K_{zx} & K_{zz} & K_{zr} \\ K_{rx} & K_{rz} & K_{rr} \end{bmatrix}$$

then the optimal control function can be written as³

$$u_{opt} = \begin{matrix} -R^{-1} B^T K_{xx} X \\ -R^{-1} B^T K_{xr} r \\ -R^{-1} B^T K_{xz} Hz \end{matrix}$$

The resulting control system is represented by the block diagram of Figure 10, III-1.

The optimal tracker block diagram is very similar to the block diagram of a classical turret stabilization system. The chief differences are the number of variables sensed and the absence of compensation networks in the feedback paths.

The LODACS test bed vehicle suspension system resonates at a frequency of about 1hz, therefore, the hull disturbance was modeled as a sinusoid at that frequency. This disturbance can be generated by a linear differential equation of the form:

III-10

$$W=Z$$

$$\begin{bmatrix} \dot{z}_1 \\ \dot{z}_2 \end{bmatrix} = \begin{bmatrix} 0 & 2 \\ 1 & 0 \end{bmatrix} \begin{bmatrix} z_1 \\ z_2 \end{bmatrix}$$

This has not yet been finalized as the design disturbance.

INACCESSIBLE STATES

The optimal control functions generated by the method discussed above assumes that every state of the plant, the tracker and the disturbance is weighted and summed to form the control function u . In practice it is costly and often very difficult to provide sensors for the measurement of all of the states of the system. A practical alternative is to generate estimates of the inaccessible states of the system

from information about the known states and the control function. The estimated states are then weighted and included in the control function as if they had been measured directly. A systematic method for estimating the unknown states is to employ a Luenberger observer. A Kalman filter accomplishes the same function in noisy systems. Other estimation techniques could also be employed.

B. DESIGN PROCEDURE

MODEL DEVELOPMENT

Before the optimal feedback gains can be set, a linearized model of the turret drive system must be derived. The states selected to describe the system are not unique and some care in their selection can greatly simplify the implementation of the control law. In the model of the LODACS turret drive system derived in Section II, a considerable effort was made to ensure that the states of the model correspond to the outputs of the sensor that would be available in the actual system. One unusual result of this procedure is that one of the states of the model, x_1 , is the position error or the difference between the actual gun line and the gun line directed by the gunner's sight and the fire control computer. This corresponds to the signal available from the resolver chain which links these devices. The selection of system states which correspond to measured quantities permits system sensitivity to noise and gain variation to be estimated readily.

SELECTION OF COST FUNCTION

The art of designing a turret control system by this optimal design procedure is to select a cost function which generates a control

function that meets the system performance requirement without requiring the system states to exceed their physical limitations. The relationship between the cost function, the performance requirement and the system non-linearities is not known a priori, and must be determined by an iterative procedure. The iterative procedure consists of selecting a cost function, generating the control function corresponding to that cost function, evaluating the performance of the turret drive system with this control function by computer simulation, and modifying the control law (adjusting the elements of the weighting matrices Q and R) to improve the performance as required. If the system does not perform well enough, additional weight can be given to the error terms in the cost function. If the value of some state exceeds that achievable by the physical system, that state can be weighted in the cost function. A new control function is generated based on the modified control law and the performance of the new drive system is evaluated by computer simulation. This procedure is repeated until either a satisfactory result is obtained or the designer is satisfied that the capability of the turret drives has been achieved.

The selection of the initial cost function on the starting point for the iterative procedure is little more than an educated guess. The control function, u , must be weighted, and it is apparent that a term related to the squared error of the system should be included. The inclusion of other terms to limit the values to be attained by other states of the system depends on the judgement and experience of the designer. The relative weighting to be assigned to these terms

and the sensitivity of the system performance to changes in the weighting must be determined by trial and error.

Before the LODACS turret control design is finalized it will be incorporated in a full scale simulation where realistic external disturbances and tracking signals are applied and subsystem interactions can be evaluated. The HITPRO simulation is presently being modified for this purpose. Some final iterations on the design will probably be required before the control electronics are specified.

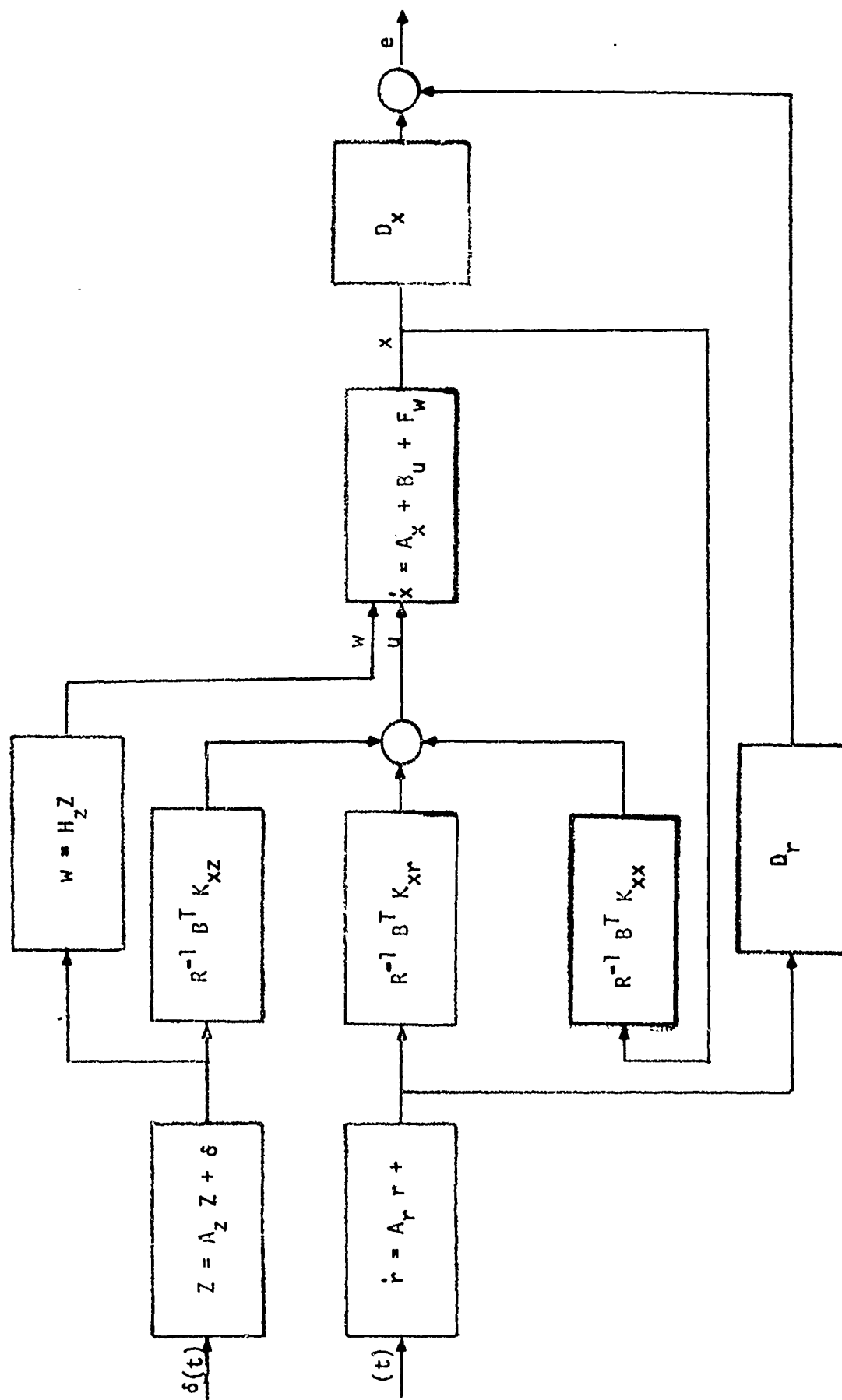


FIG III-1 BLOCK DIAGRAM OF OPTIMAL TURRET CONTROL SYSTEM

IV. SPECIFICATION OF CONTROL ELECTRONICS

The implementation of a control law based on the design procedure in Section III could conceivably be realized with either analog or digital electronics. At the present time, an analog system is easier and less risky to implement than the digital system. As the speed of microprocessors increases and the cost of A-D and D-A converters is reduced, digital processors will become more attractive. Ultimately a single digital processor for both fire control and turret control will very likely be possible.

The analog electronic controller would consist of fixed gain amplifiers, integrators, sensors and signal conditioning electronics as represented by the block diagram of Fig. IV-1. The regulator feedback signal, the tracker feedforward signal and the disturbance accommodation feedforward signal can all be implemented by fixed gain amplifiers. The implementation of the Luenberger observer requires only amplifiers and integrators, the number of integrators being equal to the number of states to be estimated. Signal conditioning in the form of demodulation, filtering, impedance matching, etc., is highly variable from system to system because it is dependent on the types of sensors used. Some adjustments of amplifier gains will undoubtedly be required as the system is integrated and final parameter values become known.

The optimal controller derived by the procedure described in Section III requires no compensation networks in the feedback or feedforward signals, and the electronics required for systems of the same order is the same except for the gains of the amplifiers.

Turret drive system, whether driven electrically or hydraulically are often modelled as systems of about the same order (6-10 states per axis). Therefore, it appears to be feasible to design a single turret controller that could be adapted to a variety of prototype turret drive systems by either a modular design where the number of amplifiers and integrators can be varied, or overdesigning the system to include extra amplifiers and integrators. The chief barrier to such an approach is that signal conditioning requirements vary widely between systems.

The feasibility of implementing the turret control for the LODACS turret with sufficient flexibility that it can be used for other applications is being investigated.

V. SUMMARY AND CONCLUSIONS

A. PROGRESS AND WORK REMAINING

Our program is to implement an optimal controller for a precision turret controller. Specifications for system performance were derived and estimates of the disturbance environment were made. Based on this analysis, a hydraulic turret drive system is being procured. The hydraulic turret drive system was modeled and control laws have been derived. The HITPRO simulation is being modified for use in evaluation these control laws. Luenberger observers for both the traverse and elevating system are being derived.

After the design is completed, the electronics for the controller can be specified and procured and system integration will begin.

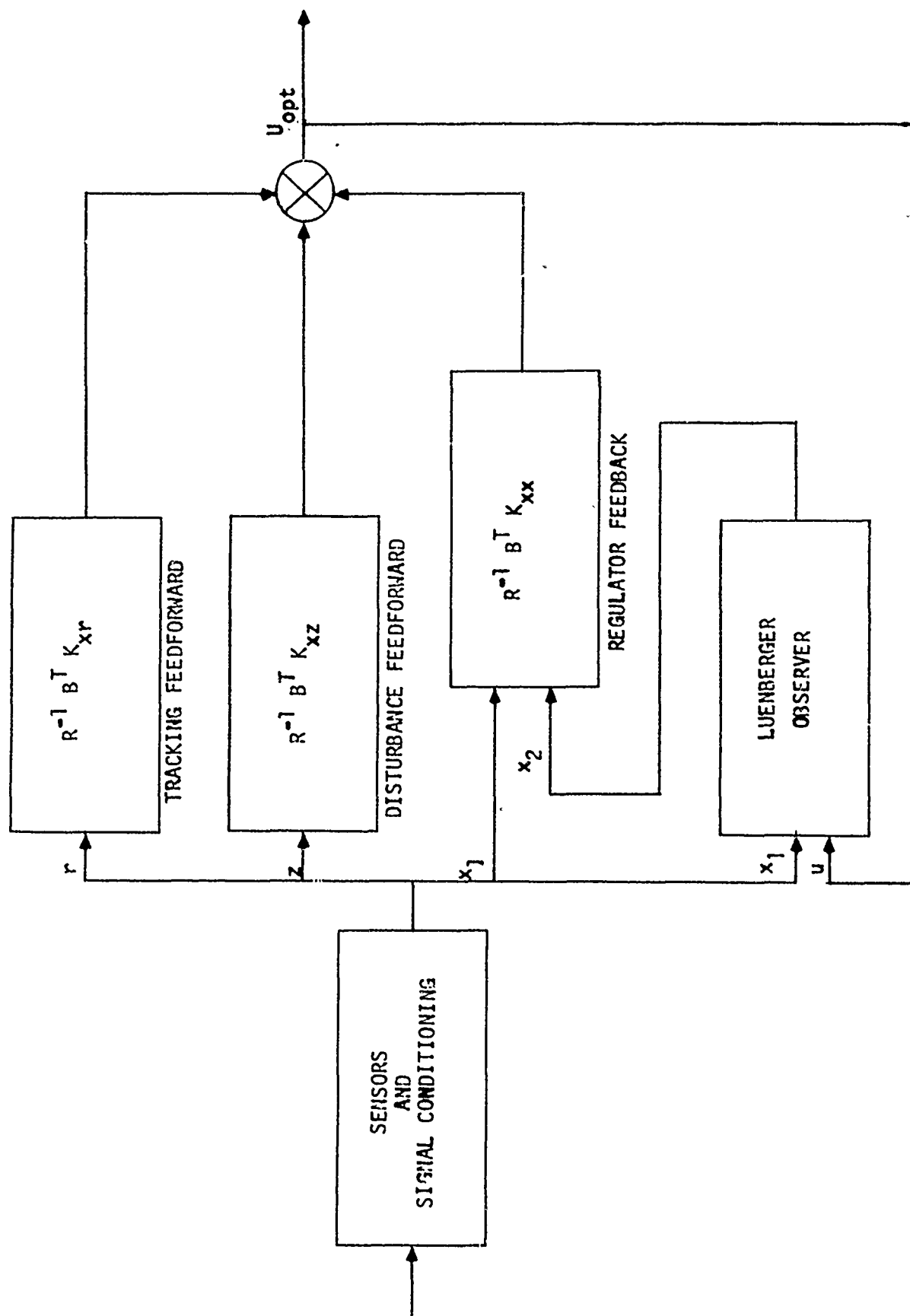


FIG. IV-1 BLOCK DIAGRAM OF ELECTRONIC CONTROLLER.

REFERENCES

1. Loh, N.K., "Optimal Control of a Helicopter Turret Control System," Rock Island Arsenal Report #R-TR-75-019, January 1975
2. Loh, N.K., Kasten, R.E., Walljasper, R.B., and Murdock, J.K., "Optimal Tracking of a Helicopter Turret Control System with Inaccessible State Variables," Proceedings of Seventh Annual Pittsburgh Conference on Modeling and Simulation, Volume 7, 1976.
3. Loh, ET AL, "Study of Disturbance Accommodation Techniques with Application to Control Systems," Report under Preparation for the Rock Island Arsenal, January 1977.
4. Kwakernaak, H., and Swan, R., Linear Optimal Control Systems, New York: Wiley Interscience, 1972.
5. Cushman, P.G., "HITPRO, Volume II, User's Manual;" Rock Island Arsenal Report #SWERR-TR-72-17, April, 1972.

ON THE GUN POINTING ACCURACY OF
AN ANTI-ARMOR AUTOMATIC CANNON

A.P. BORESI, H.L. LANGHAAR AND R.E. MILLER

University of Illinois
Urbana, Illinois

S.C. CHU
Rock Island Arsenal
Rock Island, Illinois

TABLE OF CONTENTS

	<u>Page</u>
I. INTRODUCTION	578
II. A STATEMENT OF THE PROBLEM AND A METHOD OF APPROACH	581
III. ANALYSIS OF THE PROBLEM	582
A. ESTIMATES OF VARIOUS BALLISTIC EFFECTS	585
B. ENERGY FORMULATION OF THE LAGRANGIAN	591
C. RELATIVE IMPORTANCE OF VARIOUS MODES OF MOTION	596
IV. METHOD OF SOLUTION	598
REFERENCES	601

I. INTRODUCTION

The purpose of this paper is to outline a method of approach for a deterministic study of the pointing accuracy of modern anti-armor automatic cannons. Emphasis is given to the evaluation of various factors and their influence upon the gun barrel response to a single projectile firing, as well as to repeated firings.

The accuracy of an anti-armor automatic cannon depends strongly upon the position, the velocity, and the slope of the cannon barrel at the muzzle, as the projectile is ejected. Since upon firing the passage of the projectile through the barrel induces transverse, torsional and recoil motions of the cannon, a precise knowledge of the time dependency of subsequent transverse, torsional and recoil motions of the gun tube is required to predict gun pointing accuracy.

In modern artillery, the cannon consists in part of a slender thick-wall tube with a constant inner diameter and a variable outer diameter. The breech end of the tube is heavily constrained against lateral motion, the supporting yoke serving to constrain lateral bending and lateral displacement of the tube in the yoke. However, the tube may recoil axially rather freely through the yoke. Often, one or more additional lateral supports are placed between the breech yoke and the cannon muzzle, and viscous dashpots may be employed to dampen the lateral motion of the tube. These additional lateral supports restrict lateral displacement of the tube, but allow relatively free bending rotation of the tube at the supports. Another factor that affects the tube motion is the presence of a concentrated (tuning) mass usually located near the muzzle end of the cannon, the purpose of this mass being to serve as a fine tuning (adjustment) device to correct gun pointing errors.

The optimum location of the tuning mass for purposes of reducing the lateral displacement and velocity of the cannon muzzle is of particular importance.

Because of the weight and the slenderness of the tube, the cannon barrel droops in a vertical plane when at rest in a firing position. However, when a projectile is fired down the barrel, pressures produced by the expanding gas in the barrel and forces exerted by the projectile on the barrel as it passes through the barrel induce a lateral motion of the tube. Furthermore, as the projectile travels down the tube, rifling in the inner barrel produces an axial spin of the projectile. In turn, the tube is subjected to a torsional moment which produces torsional motion of the tube.

Observation of the actual response of a cannon muzzle after firing shows that the muzzle moves around in some sort of Lissajous figure. This result has led some investigators to conclude that there is a coupling between the torsional motion and the lateral motion of the barrel. However, the present authors have studied the problem of coupling by the theory of linear elasticity and have found no coupling between torsional and bending modes. In particular, according to linear elasticity theory, a cantilever tube that is vibrating freely in a bending plane will not deviate from that plane if it is given a prescribed torsional oscillation at the root. However, there may be secondary (nonlinear) effects that cause some coupling between torsional and bending vibrations. Then the lateral centrifugal force of the projectile, the Bourdon pressure effect, or other effects may couple bending vibrations and torsional vibrations.

In the absence of nonlinear effects, the fact that the muzzle moves around in some sort of Lissajous pattern may be explained by noting that the

lateral motion, in general, consists of a combination of a vertical motion (in the direction of gravity) and a horizontal motion. Since the vertical and horizontal motions are superimposed, the muzzle moves about in a Lissajous figure.

It is easy to see why one might think that the torsional and bending modes are coupled. For example, consider a cantilever beam of circular cross section that droops in a neutral plane. If the droop of the cantilever beam is due to permanent crookedness, a torsional rotation of the beam will cause the beam to be displaced out of the vertical plane. However, if the droop is due to weight alone, it may be shown that the torsional rotation does not displace the beam from the vertical plane. Accordingly, for small torsional and lateral motions of a gun barrel, the torsional motion of an initially straight gun tube may be studied separately from the bending motion. In other words, the weight of the barrel does not affect the torsional motion.

As noted in part above, the accuracy of an artillery piece under repeated firing depends strongly upon the location of lateral supports, upon the location and the size of the tuning mass, upon the restraint of the breech support during recoil and return to firing position, upon aerodynamic and structural damping, upon the Bourdon pressure effect, upon gas pressures behind the projectile, etc. Consequently, a study of the gun pointing accuracy of an anti-armor cannon must include a study of the transient motion of a variable thickness cannon tube subjected to transient forcing functions and constrained laterally by supports, whose axial positions depend on time.

As noted in [1], by 1950, the problem of the motion of beams had been a subject of discussion for over a century. By 1976, we note that the litera-

ture on the dynamics of beams has increased several fold. However, an extensive study of the technical literature has not revealed any treatment of lateral supports with time dependent axial positions [2,3,4]. We refer to this type of problem as that of lateral-torsional transient motions of variable thickness tubes subjected to lateral constraints with time-dependent axial positions, or briefly as transient motion of tubes subjected to axially-sliding lateral constraints. In the following articles, we further define the problem and propose a method of attack, which is believed will yield a solution that includes the significant effects of various factors.

II. A STATEMENT OF THE PROBLEM AND A METHOD OF APPROACH

The problem of gun pointing accuracy is essentially one of transient motion of thick-wall slender tapered tubes, with axially sliding lateral supports and attached tuning mass, subjected to axial and lateral driving forces. To achieve a solution to this extremely difficult problem of mechanics, one might use a modal analysis approach [5]. Then one requires the natural modes of vibration of the system, preferably in an analytical form. However, in the present complex problem, the determination of analytical expressions for mode forms is not very feasible. Another difficulty lies in the fact that the treatment of forced motion problems in a series of natural modes is useful only if the series converges rapidly. In the present problem, the finite-element treatment of the initial value problem appears more promising than expansions in natural modes. In particular, the finite-element method readily admits representation of air damping, structural damping, and special damping devices by a row of dashpots along the length of the barrel. In addition, natural frequencies may be readily obtained for the

complex barrel-support system and plots of natural modes may be generated as a simple extension of the program.

III. ANALYSIS OF THE PROBLEM

A high performance cannon which is currently being developed at Rodman Laboratory is classified as having an intermediate firing rate, a high recoil energy, and perhaps most importantly, a very long tapered slender thick-wall barrel, approximately 60 mm in bore diameter and 220 inches in length. During each firing of a round, the passage of the projectile through the barrel induces torsional and lateral motions of the barrel, as well as an axial motion (recoil and recovery) of the barrel. A successful design of this anti-armor automatic cannon (AAAC) system depends heavily upon the gun pointing accuracy. Hence, the prediction of transient transverse, torsional and recoil motions of the gun tube is very important to the gun pointing error analysis. An analysis of a constant thickness gun tube under a single shot firing condition, in which the NASTRAN computer program was utilized, has been reported [6, 7]. However, there seemingly have been no studies that incorporate all significant effects, such as tapered barrel, accurate representation of supports, etc. Accordingly, a deterministic model which determines the motion of a gun barrel should take into account ballistic phenomena such as weight of the projectile, centrifugal force of the projectile in a curved barrel, the Bourdon effect, inertial effects accompanying recoil, and reaction of rifling. In addition, axial friction of the projectile must be included, and radial expansions and contractions of the gun barrel (breathing motion) should be considered. Torsional response is

decoupled from bending response except for second-order effects. The overall motion may be divided into two phases: (1) The motion of the barrel while the projectile is in it, letting the initial motion of the barrel be arbitrary. (2) The subsequent motion of the barrel after the projectile leaves.

Since the projectile attains supersonic speed before it leaves the muzzle, there is a shock wave ahead of it. This shock wave is the classical one-dimensional shock wave due to a high-speed motion of a piston. However, the shock wave appears to have negligible effect on the deformation of the barrel. Its main effect is to retard the projectile. There are pressure waves in the gas behind the projectile as well. Consequently, the assumption that the pressure in the gas is uniform at any instant may be questionable.

If there is enough damping in the system to stop the motion of the barrel before the next shot is fired, periodicity of the motion is irrelevant. Then, the problem is reducible to a pure initial-value problem. More generally, however, the motion of the barrel, after firing, may exhibit an exponentially damped pattern of oscillation with fairly regularly spaced beats. Such beats are common in multidegree freedom systems. This motion is repeated approximately, between each firing interval.

There are several practical questions that occur. First, what is the slope of the muzzle when the projectile leaves the barrel? Second, what is the lateral velocity of the muzzle as the projectile leaves the barrel? The slope and lateral velocity at the muzzle affect the aim. There is very little recoil movement of the barrel while the projectile is in the barrel. Consequently, except for inertial effects on the barrel, recoil has little to do with the first phase of the barrel motion. To get the muzzle slope and lateral

velocity, we may consider the solution of the initial value problem over only a small range of time t . As Collatz [8] points out, this condition is extremely useful. It is when we must project over a long range of t that initial value problems become sensitive. A third practical problem is one of free vibration of a damped system. Some estimate of damping caused by recoil is desirable, but damping due to dashpot devices probably is more important. Air damping, structural damping and damping due to special devices might be approximated by a row of dashpots along the barrel. Structural damping may be relatively unimportant for short periods of time and a small number of cycles.

Initially, the barrel accelerates backward. Hence, inertial forces on it act forward and create tension in the barrel. The friction of the projectile is not superposable on this inertial effect, since it acts tangentially (it is a follower force), whereas the inertial force acts along the line of recoil.

There are two ways to approach the problem. One method is to treat the barrel as a continuous tapered beam. The differential equation of the system may be set up relatively easily. However, difficulty occurs with the centrifugal force of the projectile, since it is a traveling point force. It can be represented as a Dirac delta function, but it does not fit well with continuous functions. The other approach is to use a finite element or piecewise polynomial approximation. The discrete nature of the centrifugal force is well suited for this method. In any case, we must discretize the problem to adapt it to the computer. Hence, it appears reasonable to do so at the outset. The supports are readily represented by discrete spring elements.

A. Estimates of Various Ballistic Effects

1. Bourdon Effect. The Bourdon tube used in pressure gauges works because the cross section is oval. The internal pressure tends to make the cross section circular, and there is an elastic coupling that simultaneously tends to straighten the tube.

The tendency of pressure in a gun barrel to straighten the barrel is called the Bourdon effect. However, it is quite different from the Bourdon tube effect. This is seen most clearly if we consider a barrel with bore of rectangular cross section. Figure 1a shows an element of the barrel in the bent position. Since the part below the neutral axis is shortened and the part above the neutral axis is lengthened by bending, there is a difference of area equal to $2by_{xx}dx$. Hence, if internal pressure is p , there is an effective load equal to $2bpy_{xx}dx = pAy_{xx}dx$, where $A = 2ba$ is the area of the bore. If the ends of the barrel were sealed, the net load due to internal pressure p would be zero, but this is not the case here, since the projectile does not act like a sealed end. If the bore is circular an element above the neutral axis has length $(1 + ay_{xx}\sin\theta)dx$, Figure 1b. The corresponding element below the neutral axis has length $(1 - ay_{xx}\sin\theta)dx$. The difference in length is $2ay_{xx}\sin\theta dx$ and the difference in areas is $2a^2y_{xx}\sin\theta d\theta dx$. The projection of this area is $2a^2y_{xx}\sin^2\theta d\theta dx$. Hence, the effective load is

$$2a^2y_{xx}pdx \int_0^{\pi} \sin^2\theta d\theta = \pi a^2py_{xx}dx \quad (1)$$

Since $A = \pi a^2$ is the area of the bore, the load per unit length of the barrel is pAy_{xx} . This is the same result that was obtained for the rectangular section.

To obtain the differential equation for the barrel, we will employ the Lagrange formulation. Consequently, we need an expression for the variation of work, δW . Hence, we write for pressure p

$$\delta W_p = \int_0^{\xi} pAy_{xx} \delta y dx \quad (2)$$

where $\xi(t)$ is the coordinate of the projectile. If we use a piecewise cubic approximation,

$$y = a_0 + a_1x + a_2x^2 + a_3x^3 \quad (3)$$

In turn, we express a_0, a_1, a_2, a_3 in terms of nodal displacements and nodal slopes of an element. These displacements and slopes are the generalized coordinates q_i . Thus,

$$\begin{aligned} \delta y &= \delta a_0 + x\delta a_1 + x^2\delta a_2 + x^3\delta a_3 \\ y_{xx} &= 2a_2 + 6a_3x \end{aligned} \quad (4)$$

and

$$\delta W_p = pA \int_0^{\xi} (2a_2 + 6a_3x) (\delta a_0 + x\delta a_1 + x^2\delta a_2 + x^3\delta a_3) dx \quad (5)$$

Hence, since a_0, a_1, a_2, a_3 are linear functions of the generalized coordinates q_i , we obtain (with the summation convention)

$$\delta W_p = p_{ij} q_i \delta q_j$$

where (p_{ij}) is a matrix in which the elements p_{ij} are functions of time t . Since p and ξ are known functions of t , Eq. (5) represents the contribution to δW from the pressure behind the projectile.

After the projectile leaves the barrel, there are pressure waves in the barrel, but they probably have little effect on the barrel motion. Initially, it seems reasonable to assume that the pressure effect is negligible after the projectile leaves the barrel.

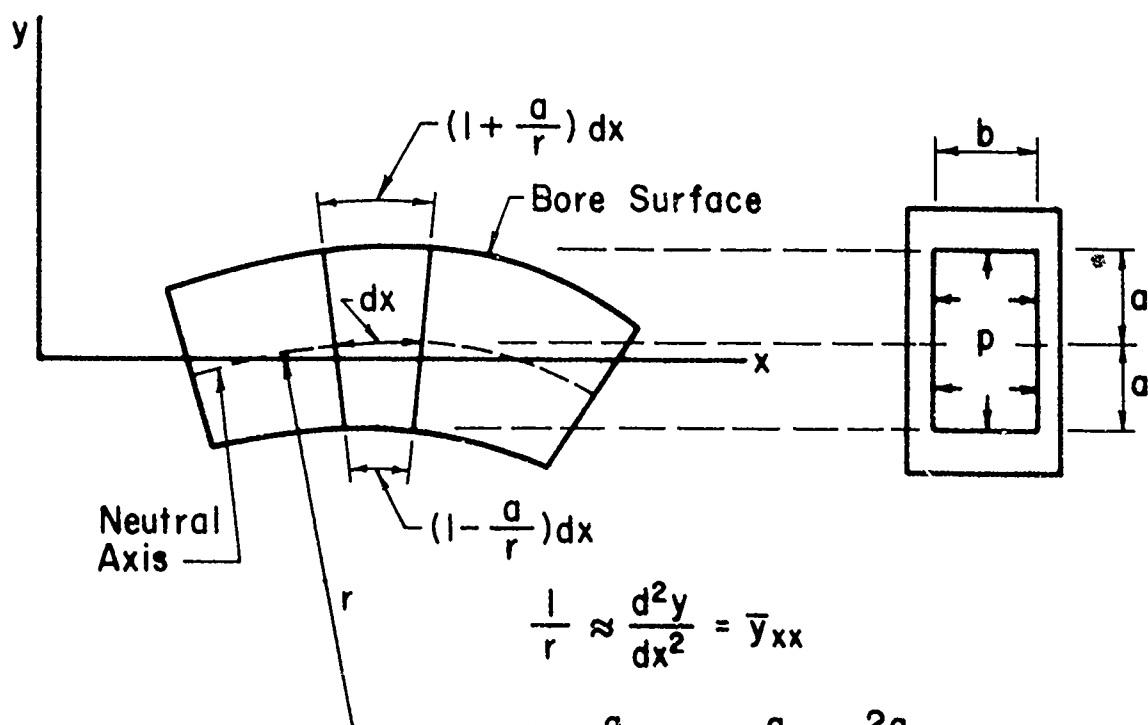
2. Axial Inertia. Axial inertia due to recoil may be calculated as though the barrel were rigid. The tension due to this effect is then a known function $P(x,t)$. If we suppose that the barrel is inextensional, the shortening of the chord due to bending, up to the section at $x = \xi$ is

$$\frac{1}{2} \int_0^{\xi} y_x^2 dx.$$

Effectively, then, an element of length dx is shortened by the amount $\frac{1}{2} y_x^2 dx$, and the potential energy of that element due to shortening is $\frac{1}{2} P y_x^2 dx$. Hence, the strain energy due to bending is augmented by the amount

$$\frac{1}{2} \int_0^{\ell} P y_x^2 dx \quad (6)$$

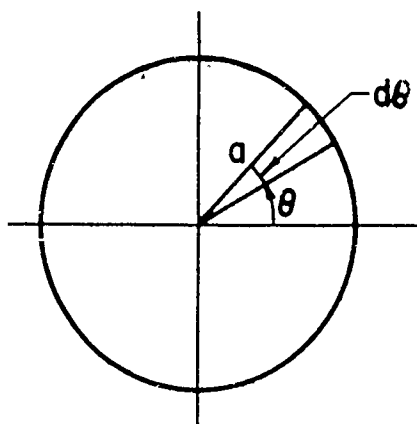
where ℓ is the length of the barrel. This integral is a function of t , since y and P are functions of x and t . Section properties of the barrel do not enter here, except in so far as they affect $P(x, t)$.



$$\frac{1}{r} \approx \frac{d^2 y}{dx^2} = \bar{y}_{xx}$$

$$(1 + \frac{a}{r}) - (1 - \frac{a}{r}) = \frac{2a}{r} \approx 2a y_{xx}$$

(a)



(b)

Figure 1. Bourdon Effect.

From the finite-element viewpoint, the contribution to the potential energy due to axial tension is

$$\frac{1}{2} \int_{\text{All elements}} P(a_1 + 2a_2x + 3a_3x^2)^2 dx \quad (7)$$

This quantity is a quadratic form in the a 's and hence in the q 's, but the coefficients are functions of time t , because P depends on t .

3. Weight of the Projectile. The weight of the projectile is

$$F = - mg \quad (8)$$

where m denotes the mass of the projectile and g denotes the gravity constant. Hence, the contribution to δW of F is

$$\delta W_F = F\delta y = - mg\delta y \cos \alpha \quad (9)$$

where α is the angle of the gun barrel with the horizontal.

In finite-element form

$$\delta W_F = - mg (\delta a_0 + x\delta a_1 + x^2\delta a_2 + x^3\delta a_3)\cos \alpha \quad (10)$$

Only the a 's in the barrel segment containing the projectile are involved.

We note that $x = x(t)$. In terms of the generalized coordinates q_i ,

Eq. (10) becomes

$$\delta W_F = p'_{ij} q_i \quad q_j \quad (11)$$

where most of the coefficients p'_{ij} are zero. Consequently, the Bourdon effect and the weight of the projectile combine to give a contribution to the total δW of the form

$$\delta W = P_{ij} q_i \delta q_j \quad (12)$$

where

$$P_{ij} = P_{ij}(t).$$

4. Weight of Barrel. The potential energy of the barrel due to weight is

$$V = \rho g \cos \alpha \int_0^l \Lambda_1 y dx \quad (13)$$

where Λ_1 is the cross sectional area of the barrel material and ρ is the mass density of the barrel. In finite element form

$$V = \rho g \cos \alpha \int_{\text{All elements}} \Lambda_1 (a_0 + a_1 x + a_2 x^2 + a_3 x^3) dx \quad (14)$$

Hence, this part of the potential energy is a linear form in the generalized coordinates q_i .

5. Axial Friction Due to Projectile. The axial friction force f , produced by the projectile on the barrel, acts tangentially. (Fig. 2) In computing the contribution to δW of f , δW_f , we set $\delta t = 0$. Force f acts at the instantaneous location of the projectile, at a distance s along the curve. Thus, the displacement is determined. The component of f along the displacement determines δW_f .

The expression for δW_f is cumbersome. The tangential frictional force tends to straighten the barrel. However, it probably has only a small effect upon the motion of the barrel. The tangential frictional force may

be included by considering its components along the gun barrel and perpendicular to the gun barrel. These components may then be treated in the same manner as the other lateral and axial forces.

B. Energy Formulation of the Lagrangian Function

1. Strain Energy of Bending of Barrel. The strain energy U of beam bending is

$$U = \frac{1}{2} \int_0^L EI y_{xx}^2 dx \quad (15)$$

where E denotes the elasticity modulus and I denotes the moment of inertia of the cross section area. In terms of finite elements, Eq. (15) becomes

$$U = \frac{1}{2} \int_{\text{All elements}} EI (2a_2 + 6a_3 x)^2 dx \quad (16)$$

Hence, U is a quadratic form in the q_i , that is,

$$U = \frac{1}{2} a_{ij} q_i q_j \quad (17)$$

The coefficients a_{ij} are constants. However, if we include the potential energy of the axial inertia with the strain energy, the coefficients are functions of t . The strain energy of supporting springs must be included. This may be easily done. Also, shear deformation effects may be accounted for [7]. However, for simplicity they are not included in this discussion. Nevertheless the effects of shear deformation may be important and they will be examined in the study.

2. Kinetic Energy. The kinetic energy T of the barrel due to the lateral displacement is

$$T = \frac{1}{2}\rho \int_0^{\ell} A_1 y_t^2 dx \quad (18)$$

In finite element form, Eq. (18) is

$$T = \frac{1}{2}\rho \int_{\text{All elements}} A_1 (\dot{a}_0 + \dot{a}_1 x + \dot{a}_2 x^2 + \dot{a}_3 x^3)^2 dx \quad (19)$$

where dots denote time derivatives. Hence, in terms of generalized coordinates q_i , the kinetic energy of the barrel is a quadratic function of \dot{q}_i , namely

$$T = \frac{1}{2} b_{ij} \dot{q}_i \dot{q}_j \quad (20)$$

If rotary inertia is included, the additional term

$$\frac{1}{2}\rho \int_0^{\ell} I_y^2 \dot{x}_t^2 dx \quad (21)$$

must be included in T . However, the general form (Eq. 20) of T is not changed.

The kinetic energy of the projectile is $T_p = \frac{1}{2} m (\dot{y}_t^2 + v^2)$ where $v(t)$ is the axial velocity of the projectile. The term $\frac{1}{2} m v^2$ is irrelevant in the variational treatment, since it does not involve variations of the q 's. Hence, effectively, $T_p = \frac{1}{2} m \dot{y}_t^2$ or

$$T_p = \frac{1}{2} m (\dot{a}_0 + \dot{a}_1 x + \dot{a}_2 x^2 + \dot{a}_3 x^3)^2$$

where the a 's are the coefficients in the deflection function for the tube

interval in which the projectile lies at time t . For the projectile, x is a known function of t . Hence, if the projectile is considered to be a particle, T_p is a quadratic form in the four \dot{q} 's that pertain to the finite element in which the projectile lies at time t . Hence, the coefficients in this form are functions of t , and furthermore, the relevant \ddot{q} 's change as the projectile (particle) moves from one finite element to another. It is apparent, however, that Eq. (20) remains valid for the combined kinetic energy of the projectile and the tube, provided that the coefficients b_{ij} are suitable functions of time t . We note that it is possible to transfer the exciting effect of the projectile into the expression for δW by introducing the virtual work of the centrifugal force and the Coriolis force of the projectile, but it is simpler to include the effect of the projectile in the kinetic energy term.

3. General Formulation. With the above results, we may write the Lagrangian L of the system

$$L = T - V = \frac{1}{2} b_{ij} \dot{q}_i \dot{q}_j - \frac{1}{2} a_{ij} q_i q_j - a_i q_i \quad (22)$$

where the last term is the weight term. The Lagrange equations of motion are

$$\frac{d}{dt} \left(\frac{\partial L}{\partial \dot{q}_i} \right) - \frac{\partial L}{\partial q_i} = R_i \quad (23)$$

where by

$$\delta W = R_i \delta q_i \quad (24)$$

we obtain

$$R_i = p_{ij} \dot{q}_j \quad (25)$$

The effects of viscous damping can also be included in Eq. (23). Then, the equations of motion of the system take the form

$$b_{ij} \ddot{q}_j + c_{ij} \dot{q}_j + a_{ij} q_j = R_i + a_i \quad (26)$$

Since $R_i = p_{ij} \dot{q}_j$, it can be absorbed in the term $a_{ij} q_j$. Hence, the differential equations of motion take on the form

$$b_{ij} \ddot{q}_j + c_{ij} \dot{q}_j + a_{ij} q_j = a_i \quad (27)$$

The initial conditions for integration of Eqs. (27) are

$$q_i = q_i^{(0)} \quad \text{and} \quad \dot{q}_i = \dot{q}_i^{(0)} \quad \text{for} \quad t = 0 \quad (28)$$

Equations (27) and (28) form a well-defined initial value problem.

4. Dashpot Damping. Let a single dashpot lie at $x = x_m$ (Fig. 3). The resisting force of the dashpot is $c \partial y_m / \partial t$ where c is the dashpot constant. Let the dashpot lie at a nodal point. Then, $y_m = q_k$. Hence, all c_{ij} are zero except $c_{kk} = c$. Then all the differential equations (Eq. 27) are the

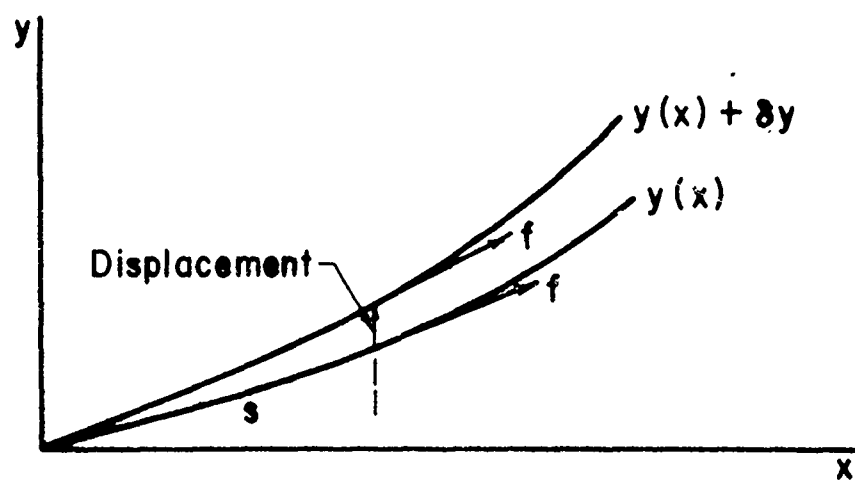


Figure 2. Axial Friction.

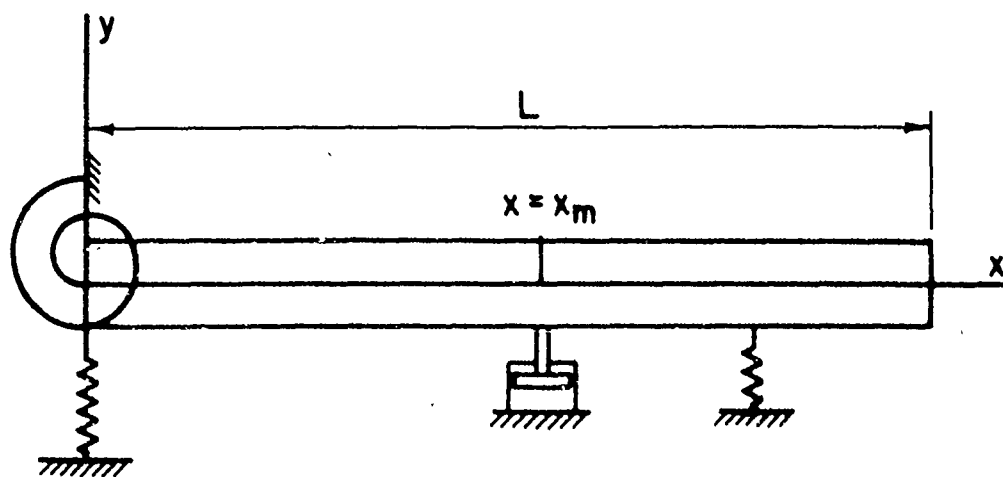


Figure 3. Damping.

same except the one for which $i = k$. That differential equation has the extra c term in it. If several dashpots act at node points, their introduction presents no problem.

C. Relative Importance of Various Modes of Motion

According to linear elasticity theory, there is no coupling between torsional modes and bending modes of a tube since torsional modes entail only shearing strains. In the Bernoulli theory of bending, shear deformation is ignored. However, even if shear deformation is taken into account in bending, it is symmetrical about a diameter and causes no torsion.

As an example of the relative magnitude of frequencies in torsion and bending consider a uniform steel cantilever tube of length $L = 153.225$ in. long, with internal diameter 2.36 in. and external diameter 6.6 in. (These dimensions approximate the dimensions of the Rodman Laboratory cannon forward of the breech.) For steel, the mass density is $\rho = 7.27979 \times 10^{-4}$ lb.sec²/in.⁴, the modulus of elasticity is $E = 30 \times 10^6$ lb/in.², and Poisson's ratio is $\nu = 0.30$. The lowest bending (circular) frequency is $\omega_1^B = 53.27$ rad/sec. This yields a natural frequency of $f_1^B = 53.27/(2\pi) = 8.48$ cycles/sec. The lowest torsional (circular) frequency is $\omega_1^T = 1290$ rad/sec. For higher modes in bending, we get

$$\omega_1^B = 53.27, \omega_2^B = 333.85, \omega_3^B = 934.8$$

$$\omega_4^B = 1831.8, \omega_5^B = 3028$$

Hence, ω_1^T for torsion lies between ω_3^B and ω_4^B for bending.

Breathing (radial expansion and contraction) modes have much higher frequencies. In fact, for the first breathing mode $\omega_1^R = 104790$ rad/sec. (based upon plane strain theory). Thus, the first breathing mode frequency is about equal to the 27th bending mode frequency ω_{27}^B . To compute the higher bending mode frequencies, we may use the close approximation

$$\omega_n^B \approx (n - \frac{1}{2})^2 \frac{\pi^2 r}{L^2} (E/\rho)^{1/2}; n > 4$$

where r is the radius of gyration of the cross section. Hence, the bending frequencies for a tube are approximately

$$\omega_n^B \approx (n - \frac{1}{2})^2 \frac{\pi^2}{2L^2} \sqrt{\frac{E(r_1^2 + r_0^2)}{\rho}}; n > 4$$

where L is the length of the tube and r_0 and r_1 are the inner and outer radii of the tube.

For the torsional frequency, it may be shown that

$$\omega_n^T = (2n - 1) \frac{\pi}{2L} (G/\rho)^{1/2}; n = 1, 2, \dots$$

where L is the length of the tube and $G = E/[2(1 + \nu)]$ is the shear modulus of steel. Formulas for the breathing modes are much more complicated since they contain Bessel functions of the first and second kind.

Since the lowest torsional frequency (1290 sec^{-1}) is much higher than the lowest bending frequency (53 sec^{-1}), one should expect that nonlinear effects would cause negligible coupling between torsional and bending modes, particularly if ω_1^T for torsion does not resonate with some ω_n^B for bending.

Because of the rifling in the cannon bore, the projectile exerts a moving torsional couple on the barrel. It is not particularly difficult to determine the resulting twisting motion of the barrel. Hence, in the analysis, one may let the initial torsional motion of the barrel (when the projectile leaves the breech) be arbitrary.

As noted previously, by the theory of linear elasticity, no coupling exists between torsional and bending modes. Consequently, according to linear theory, a cantilever tube that is vibrating freely in a bending plane (say the vertical plane) will not deviate from that plane if it is given a prescribed torsional oscillation at the root. However, there may be a secondary (nonlinear) effect that causes some coupling between torsional and bending vibrations. If so, then lateral forces (e.g., the lateral centrifugal force of the projectile, the Bourdon effect, etc.) would generate lateral vibrations. In particular, if quadratic (nonlinear) terms in the strain-displacement relations are retained, one may be able to exhibit nonlinear coupling between torsional and bending modes (See the example on p. 271 of reference 8). Another possibility is that an infinitesimal horizontal (or vertical) bending vibration is unstable, in the sense that the firing causes it to increase. The Bourdon effect and the centrifugal force of the projectile tend to aggravate the deflection.

IV. METHOD OF SOLUTION

During the time $0 \leq t \leq t_1$ that the projectile is in the barrel, the a_{ij} of Eqs. (27) are functions of time. Ordinarily, t_1 is of the order of 5

milliseconds, whereas, the interval of time T between firings is of the order of a 1 second or so. The fundamental period of vibration of the barrel is in the neighborhood of 25 milliseconds. Thus, to determine the motion of the barrel as the projectile exits from the muzzle, we must solve the initial value problem (Eqs. 27 and 28) for a range of t covering the few milliseconds that the projectile is in the barrel. Collatz (9) suggests the Runge-Kutta method or the finite difference method for treating initial value problems of ordinary differential equations. Piecewise polynomials may also be used to treat initial-value problems (10). These methods and other methods should be considered in the study.

After projectile exit, the coefficients of Eqs. (27) are constants. Then, the problem reduces to one of damped vibration of the barrel. A particular solution of Eqs. (27) is readily obtained. To obtain the solution of the homogeneous part of Eqs. (27), we let (8)

$$q_j = z_j e^{rt} \quad (29)$$

Then, Eqs. (27) may be written (for n coordinates)

$$\sum_{j=1}^n (r^2 b_{ij} + r c_{ij} + a_{ij}) z_j = 0 \quad (30)$$

The necessary and sufficient conditions that Eq. (30) be satisfied is that

$$\det(r^2 b_{ij} + r c_{ij} + a_{ij}) = 0 \quad (31)$$

Equation (31) has n roots of the type $r = -c + i\omega$ in which $c > 0$ and $\omega > 0$.

Let the n roots be $r_1 = -c_1 + i\omega_1$, $r_2 = -c_2 + i\omega_2$, $r_3 = -c_3 + i\omega_3$, ---, $r_n = -c_n + i\omega_n$. For each of these r 's there corresponds a set of z 's, given by Eq. (30). The z 's are determinate except for an arbitrary constant factor.

Let the z 's be given by

$$z_j = \rho_j e^{i\theta_j} \quad (32)$$

Then the n values

$$z_j^{(1)} = \rho_j^{(1)} e^{i\theta_j^{(1)}}, \quad z_j^{(2)} = \rho_j^{(2)} e^{i\theta_j^{(2)}}, \quad \dots, \quad z_j^{(n)} = \rho_j^{(n)} e^{i\theta_j^{(n)}} \quad (33)$$

The homogeneous solution of Eq. (27) is a linear combination of the z 's.

Thus, the general solution is

$$\begin{aligned} q_j = & A_1 \rho_j^{(1)} e^{-c_1 t} \sin(\omega_1 t + \theta_j^{(1)} - \gamma_1) \\ & + A_2 \rho_j^{(2)} e^{-c_2 t} \sin(\omega_2 t + \theta_j^{(2)} - \gamma_2) \\ & + \dots \\ & + A_n \rho_j^{(n)} e^{-c_n t} \sin(\omega_n t + \theta_j^{(n)} - \gamma_n) \\ & + (\text{particular solution})_j \end{aligned} \quad (34)$$

where the $A_1, A_2, \dots, A_n, \gamma_1, \gamma_2, \dots, \gamma_n$ are the $2n$ arbitrary constants.

These $2n$ arbitrary constants are determined from the initial conditions for the damped vibration, namely

$$q_j = q_j^{(t_1)}, \quad \dot{q}_j = \dot{q}_j^{(t_1)} \quad \text{for } t = t_1 \quad (35)$$

The values of $q_j^{(t_1)}$ and $\dot{q}_j^{(t_1)}$ are thus obtained from the solution of the initial value problem which describes the motion of the barrel from the time of firing to the time that the projectile exits from the muzzle.

In general, the study should yield the transient response of variable thickness gun barrels, including the effects discussed.

REFERENCES

1. E. Saibel and E. D'Appolonia, Forced Vibration of Continuous Beams, ASCE, Proceedings Vol. 77, Nov. 1951.
2. R. D. Mindlin and L. E. Goodman, Beam Vibration with Time-Dependent Boundary Condition, J. of Applied Mechanics, Vol. 17, pp. 377-380, 1950.
3. H. I. Epstein, Vibrations with Time-Dependent Internal Conditions, J. of Sound and Vibrations, Vol. 39, part 3, pp. 297-303, 1975.
4. The Shock and Vibration Bulletin, Vols. 1-46, The Shock and Vibration Information Center, U.S. Naval Research Laboratory, Washington, D. C.
5. L. Meirovitch, Analytical Methods of Vibrations, The MacMillan Company, N. Y., 1967.
6. Simkins, T., Pflegl, G., and Scanlon, R., Dynamic Response of the M113 Gun Tube to Traveling Ballistic Pressure and Data Smoothing as Applied to XM150 Acceleration Data, Watervliet Arsenal Report WVT-TR-75015, April 1975.

7. Simkins, T. E., Structural Response to Moving Projectile Mass By The Finite Element Method, Watervliet Arsenal Report WVT-TR-75044, July 1975.
8. H. L. Langhaar, Energy Methods in Applied Mechanics, John Wiley and Sons, N. Y., 1962.
9. L. Collatz, The Numerical Treatment of Differential Equations, 3rd Ed., Springer Press, Berlin, 1960.
10. H. L. Langhaar and S. C. Chu, Piecewise Polynomials and The Partition Method for Ordinary Differential Equations, Developments in Theoretical and Applied Mechanics, Vol. 8, Pergamon Press, Oxford and New York, 1970, pp. 553-564.

ELECTROMAGNETIC PULSE INSTRUMENTATION AND
MEASUREMENT TECHNIQUE FOR THE DETERMINATION
OF PROJECTILE VELOCITY, SPIN, PRECESSION AND NUTATION

R.K. LODER, E.M. WINEHOLT, J.O. PILCHER,
J.R. GRAMLING AND J.Q. SCHMIDT
Ballistics Research Laboratory
Aberdeen, Maryland

TABLE OF CONTENTS

	<u>Page</u>
I. INTRODUCTION	605
II. BASIC CONCEPT	609
III. MATHEMATICAL FORMULATION	612
IV. COMPUTATION OF THE INDUCED ELECTROMOTIVE FORCE	618
V. DATA EVALUATION PROCEDURE	628
VI. DESIGN CRITERIA	631
VII. CONCLUSION	639
REFERENCES	641

During a recent investigation concerning the interior ballistic causes of the erratic flight behavior of a subcaliber kinetic energy projectile, the requirement arose for an accurate determination of the final launch conditions of the projectile sabot assembly as well as the exterior ballistic performance of the subprojectile. The available instrumentation and measurement techniques proved to be inadequate. Therefore, a new system had to be developed. A series of electromagnetic pulse detector stations, each consisting of any array of coils of wire which are arranged circumferentially in a ring configuration, are employed along the flight path of the projectile. A cylindrical permanent miniature magnet is inserted in the nose of the projectile. As the projectile traverses through the stations, the moving magnetic field of the magnet induces electric currents in the coils of wire which are recorded on tape in analog form. Using 12 coils of wire per station, we are able to determine from the experimental data the 12 unknown variables representing the location of the center of the magnetic dipole, its linear and angular velocities and the direction of its polar axis for each point of time. Reduction of the six degrees-of-freedom motion of the projectile from these quantities is trivial.

1. INTRODUCTION

A. Discussion of Prior State-of-the-Art

A variety of instrumentation/measurement techniques have been developed which can be and are used to obtain individual, mostly distance-averaged, parameters of the early flight trajectory of a projectile. The most encompassing one up to now is based on sequential orthogonal photographic recording employing high-speed photoflash techniques in the visible as well as in the x-ray spectral range and background screens with reference lines. This type of recording requires advanced knowledge of the linear velocity of the projectile to ensure proper timing of the photoflash. Reduction of the photographic data yields, in addition to corrections in the assumed velocity, the yaw, pitch and roll of the projectile averaged over the whole recording distance and, when the projectile is properly marked, the spin also. This measurement system does not lend itself to quick and automatic data processing and evaluation and is contrary to the long term trend which has been away from the use of cameras and photographic film for the recording of the instrumental data. Therefore, attempts are currently being made to replace the optic-photographic recording by optic-electronic witness screen instrumentation/measurement techniques [1]. Most of them are still conceptual and their proper function has yet to be demonstrated. Basically, their principle is simple: a raster of parallel light beams is established horizontally and vertically in a plane which is orthogonal to the flight direction. Two sides, non-opposing, contain the light sources and the other two an array of photodiode sensors. When an object passes through the plane, a shadow will be thrown onto each of the two detector arrays, the extreme positions of which are then recorded as function of time. A sequence of such instrumentation stations permits the obtainment of the same flight information as the optic-

photographic method. In addition, this system can also be used for the determination of the flight performances of individual rounds fired in rapid succession.

Apart from this kind of photographic recording, a combination of instrumentation and measurement techniques is necessary to collect the set of flight data required for the analysis of the flight performance of ballistic objects.

Linear velocities are generally determined either directly by Doppler radar or indirectly by distance versus time measurements. Non-optic examples of the later method are the induction and high-frequency oscillator coil instrumentations. In the induction coil system a projectile magnetized to saturation is shot through two one-loop induction coils which are separated by a well measured distance. The pulses of the induced voltages trigger and stop a time counter. From the distance and the recorded time the average velocity within the measured distance is computed. In the high-frequency oscillator coil instrumentation [2] the projectile is fired through a metallic coil which forms an inductance in a stable high-frequency oscillator. When the projectile flies through the coil, the permeability and the dielectric constant in the cross-sectional area and, therefore, the inductance of the coil change. This causes an increase in the frequency of the oscillator which is recorded as a function of time. The recorded signals are then processed to obtain the contour of the projectile and the time of passage. From that velocity is determined.

The spin of projectiles is mainly measured with a parallel wire spin sensor, besides optic means. In this technique the projectile is magnetized along one side. A long wire antenna parallel to the trajectory of the pro-

jectile monitors the change in the magnetic field due to spin during the bypass of the projectile. The induced current is sinusoidal and its frequency corresponds directly to the spin. However, whenever the magnitude of precession or nutation becomes large, this spin measurement technique fails.

To determine precession and nutation, the projectile is fired through a sequence of yaw cards. The orientation of the projectile axis at the yaw card locations is then estimated from the shape of the penetration holes. From the orientations the precession and nutation averaged over the measured distance are obtained. This method is not only inaccurate but also influences the trajectory of the projectile due to the successive impacts of the projectile on the yaw cards.

Another method for obtaining velocity, spin, precession, and nutation, which is mainly used for investigation in projectile in-bore dynamics, relies on instrumenting the projectile with accelerometers and transmitting the signals via radio telemetry. But this method is extremely expensive and practically cost prohibitive for other than purely research oriented investigations.

Apart from the optic-electronic witness screen technique and the last mentioned method, none of the previous ones allows an adequate determination of the rate of the change of the ballistic parameters in the intermediate ballistic and early free flight regimes. In addition, we do not have an adequate instrumentation/measurement technique for the investigation of the flight performance of salvo rounds.

B. Historical Aspects.

About a year ago the Ballistic Research Laboratories were asked to look into the causes of the erratic flight behavior of the 105mm M392A2 subcaliber kinetic energy round. It was a classical in-bore dynamics problem, in essence. To reveal the interior ballistic causes for the adverse free flight performance of the subprojectile one has to determine the parameters of the initial condition of the projectile-gun system, record the entire in-bore motion of the projectile assembly and the gun tube motion, and evaluate the final performance of the subprojectile in such detail that the initial state of the projectile-gun system can be uniquely related by a temporal sequence of in-bore and launch dynamics data to the exterior ballistic trajectory. Due to the complexity of the projectile itself and the in-bore motion of its assembly components we were forced to put together an experimental and theoretical program which utilizes the available technology to the fullest extent and requires the adaption of new concepts in instrumentation, measurement and theoretical evaluation techniques. The electromagnetic pulse instrumentation and measurement technique was one of them. It arose from the requirement of an accurate determination of the final launch conditions of the subprojectile-sabot assembly as well as the exterior ballistic performance of the subprojectile. For the evaluation of the final launch conditions we needed the spin of the sabot petals, the sabot pot and the subprojectile at muzzle exit. By recording the impact of the sabot petals on a witness board, we can quite easily obtain their spin at muzzle exit from their displacement and time of flight. But, for a concurrent spin measurement of sabot pot and subprojectile, the available instrumentation and measurement techniques proved to be inadequate. We had a similar problem with the determination of the free flight performance of the subprojectile. Although we will record the projectile impact on a

target witness board to evaluate the dispersion about one and a half kilometer from the site of the gun, we needed the precession and nutation of the subprojectile in addition to its spin. Since the standard exterior ballistic method, sequential orthogonal photographic recording, does not lend itself to quick and automatic data processing, we looked for a measurement technique which would provide the spins of the sabot pot and the subprojectile as well as the flight trajectory of the subprojectile.

The exploitation of the magnetic dipole radiation which is produced by a moving magnet seemed to be the most promising way to go. Since the standard parallel wire spin sensor technique to measure spin fails for projectiles with excessive yaw, we fell back to the fundamentals of electromagnetics.

II. BASIC CONCEPT

Let us look at the external magnetic field of a long cylindrical magnet and probe its magnetic induction, B , along an arbitrary straight line (Fig. 1).

As we move from left to right, we see that the magnitude of the magnetic induction increases slowly until it reaches a maximum at point 2. From here on it decreases rapidly to zero. After reaching the minimum, the magnetic induction rises steeply through the points 5, 6, 7, passes through a maximum and decreases asymptotically to zero. Since the magnetic field at a point is only a function of the distance and the orientation of the magnet, we can probe the magnetic field at a point by moving the magnet along an arbitrary path. The results is the same as for a resting magnet and a moving point. In principle, knowing the magnetic field distribution of the magnet as function of time, we can determine the motion of the magnet. Therefore, we have to look for a suitable means of obtaining the magnetic

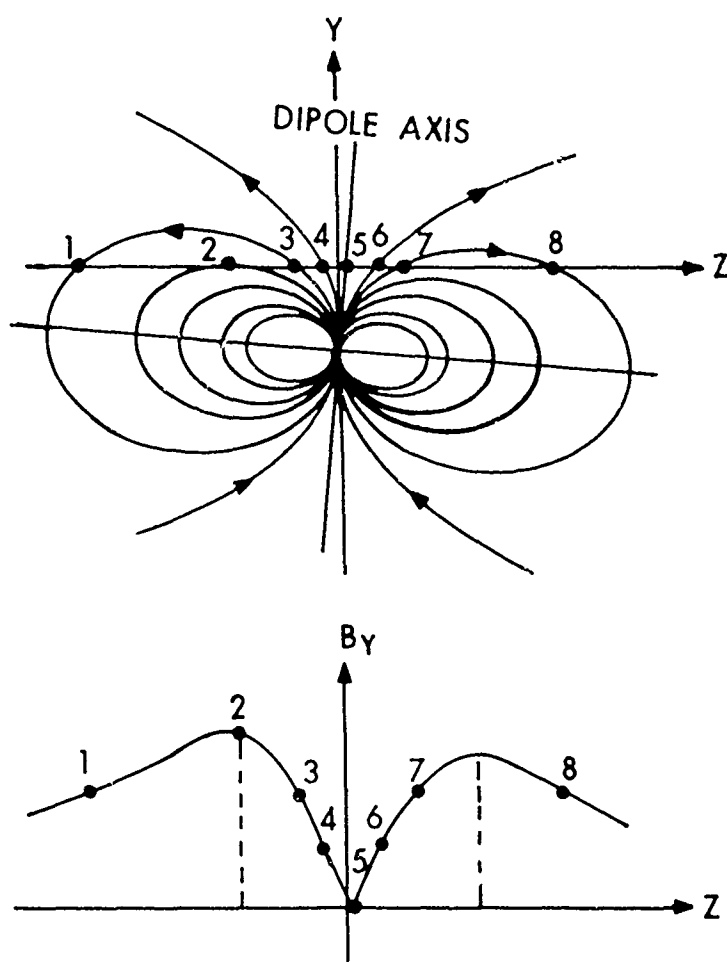


Figure 1. Magnitude of the Magnetic Induction Along a Straight Line Intersection.

induction or a derivative of it. One quantity that we can conveniently measure is the electromotive force which is produced in circuits placed in time-varying magnetic fields. Using Faraday's law of induction we can relate the electromotive force to the time rate of change of the magnetic flux which links the circuit.

Based on this idea we can design an instrumentation to record the six degrees-of-freedom motion of a projectile. A series of electromagnetic pulse

detector stations, each consisting of an array of coils of wire (circuits) which are arranged circumferentially in a ring configuration, is employed along the flight paths of the projectile (Fig. 2). As the projectile traverses the stations, the moving field of a miniature magnet which is inserted in the projectile induces in the circuit an electric current which is recorded by a magnetic tape recorder in analog form.

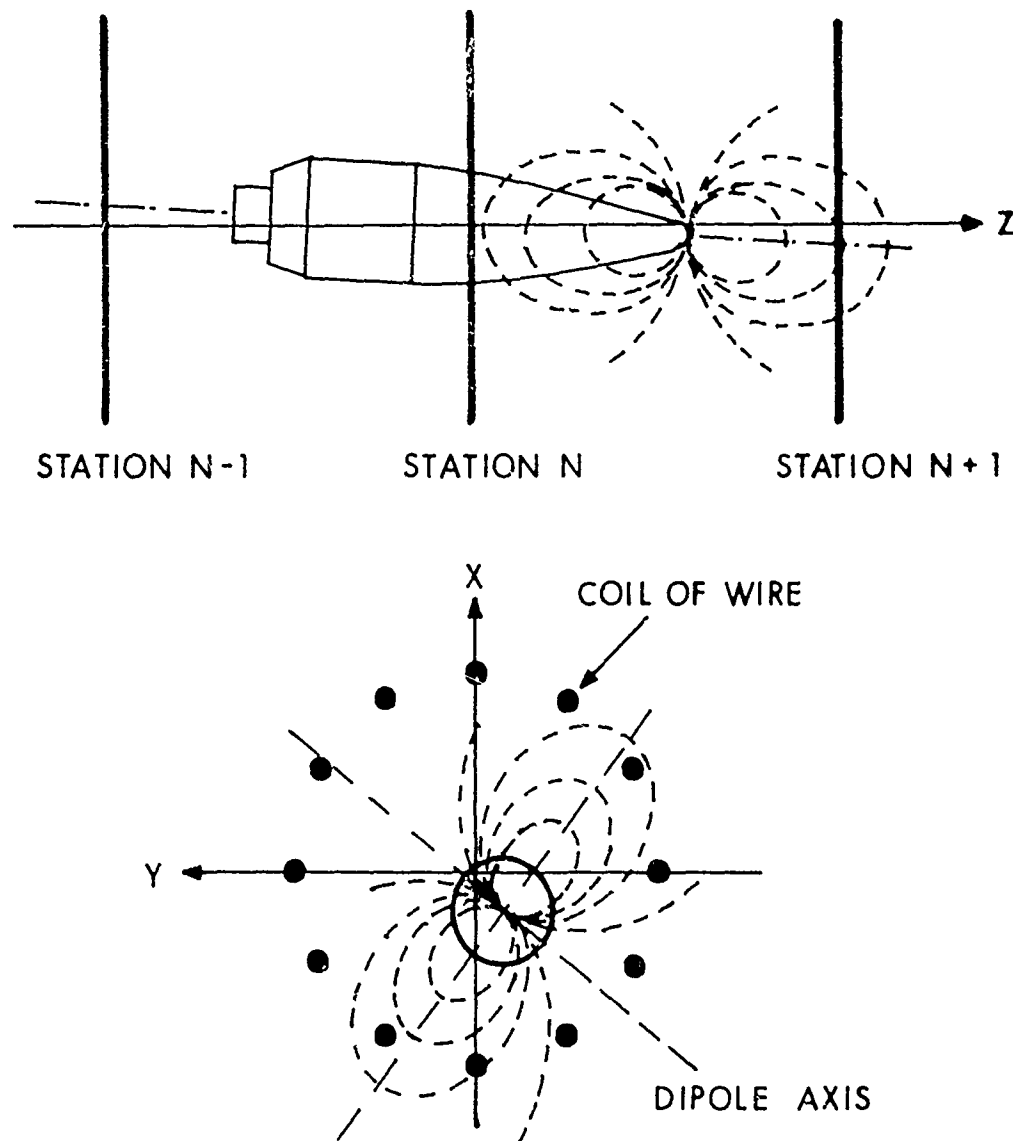


Figure 2. Projectile Traversing Through the N-th Electromagnetic Pulse Station.

The design parameters of the instrumentation have to be obtained from sensitivity analyses using realistic bounds for projectile motion. For that purpose, we must derive explicit equations relating the electromotive force to the motion of the magnet and the projectile, respectively.

III. MATHEMATICAL FORMULATION

Faraday's law of induction [3] relates the electromotive force V produced in a circuit to the time rate of change of the magnetic flux F which links the circuit

$$(3.1) \quad V = \oint_C (\vec{E} \cdot d\vec{\ell}) = - \frac{d}{dt} F = - \frac{d}{dt} \int_S (\vec{B} \cdot d\vec{f}),$$

where C is a closed curve spanned by an arbitrary surface S , both stationary in the observer's frame of reference. $d\vec{\ell}$ and $d\vec{f}$ are the corresponding line and areal elements. \vec{E} and \vec{B} are the electric density and the magnetic induction, respectively. For a "simple" medium like air the magnetic-induction vector $\vec{B}(\vec{x}, t)$ is given by

$$(3.2) \quad \vec{B} = \mu_0 \vec{H},$$

where $\vec{H}(\vec{x}, t)$ is the magnetic field intensity vector, μ_0 is the permeability of the medium and \vec{x} is the position vector from the center of the magnetic dipole to the observation point. The magnetic intensity, in turn, can generally be expressed in terms of potentials [3]

$$(3.3) \quad \vec{H} = \frac{1}{\mu_0} (\vec{\nabla} \times \vec{A}_e) - \vec{\nabla} \phi_m - \frac{\partial}{\partial t} \vec{A}_m,$$

where \vec{A}_e , $\vec{\phi}_m$, and \vec{A}_m are respectively the electric vector, magnetic scalar and magnetic vector potentials. Since a permanent magnet does not have any electric or magnetic vector potentials, the magnetic field intensity vector reduces to the gradient of the magnetic scalar potential

$$(3.4) \quad \vec{H} = -\vec{\nabla} \phi_m.$$

The scalar potential outside the magnet can be written as an expansion in magnetic multipoles

$$(3.5) \quad \phi_m = \sum_n \phi_m^{(n)},$$

where $\phi_m^{(n)}$ is the potential of a magnetic multipole of the n -th order. Because there is no magnetic monopole, the lowest nonvanishing term in the expansion is of first order, corresponding to a magnetic dipole. For a homogeneous and isotropic cylindrical bar magnet magnetized coaxially, its far field is practically identical to that of a dipole because only its near field is influenced by magnetic multipoles of order n , n greater than one. Since in the experimental arrangement the length of the miniature magnet is much smaller than the distance between the center of the magnet and the observation point, the far field condition prevails and we can approximate the field of the magnet by that of a magnetic dipole. The scalar potential of a magnetic dipole of moment \vec{m} is given by [5]

$$(3.6) \quad \phi_m = \phi_m^{(1)} = \frac{\vec{m} \cdot \vec{x}}{4\pi\mu_0 x^3},$$

where x is the magnitude of \vec{x} . The geometric arrangement is shown below (Fig. 3).

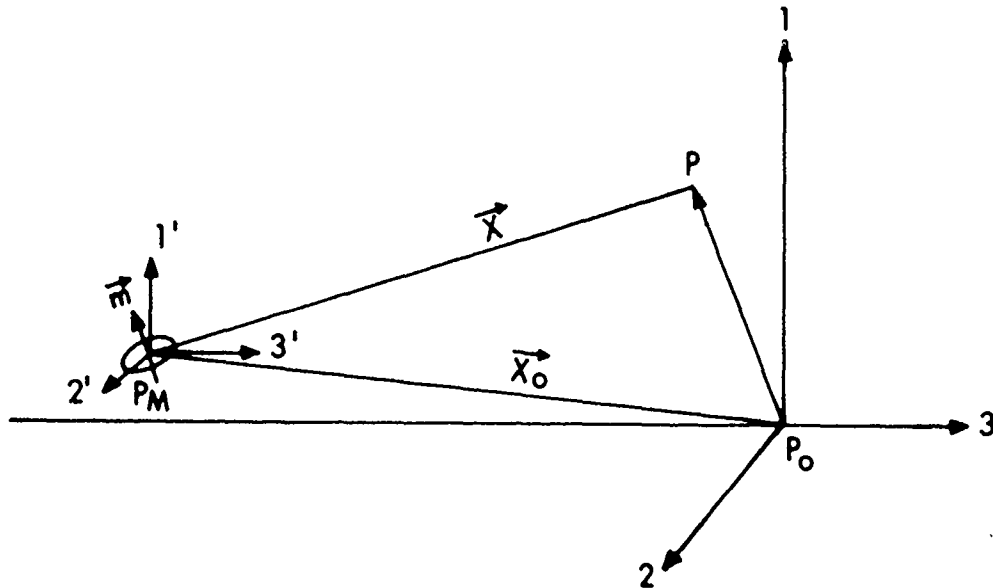


Figure 3. Dipole Geometry Relative to the Observation Point P.

The dashed coordinate frame is parallel to our frame of reference, the origin of which lies in the center of the Nth electromagnetic pulse station. The dipole moment can be presented by

$$(3.7) \quad \vec{m} = m\vec{s}, \quad \vec{s} = (s_1, s_2, s_3),$$

where m is the magnitude of the magnetic dipole moment and \vec{s} is its unit vector of orientation. Combining Eqs. (3.4), (3.5), (3.6) and (3.7) we obtain for the magnetic field intensity vector

$$(3.8) \quad \vec{H} = -\frac{m}{4\pi\mu_o} \vec{\nabla} \frac{(\vec{s} \cdot \vec{x})}{x^3} \\ = -\frac{m}{4\pi\mu_o} \frac{1}{x^3} \left[s_1 - 3x_1 \frac{(\vec{s} \cdot \vec{x})}{x^2}, s_2 - 3x_2 \frac{(\vec{s} \cdot \vec{x})}{x^2}, s_3 - 3x_3 \frac{(\vec{s} \cdot \vec{x})}{x^2} \right].$$

Note that

$$(3.9) \quad \vec{x} = \vec{P}_M \vec{P} = \vec{P}_O \vec{P} - \vec{P}_O \vec{P}_M$$

from Fig. 3.

Let us now express the vector $\vec{P}_O \vec{P}$ as a function of the instrumentation geometry as sketched in Fig. 2. The point $P=P_i$ can be any point on the surface S_i which is formed by the closed loop C_i of the i -th coil of wire in the electromagnetic pulse station. Optimal symmetry in the sensor arrangement and hence in the temporal-induced electromotive force is assured for three distinct orthogonal orientations of the loop surfaces with the unit vector normal to the surface pointing into the radial, tangential and axial (flight) directions, respectively (Fig. 4).

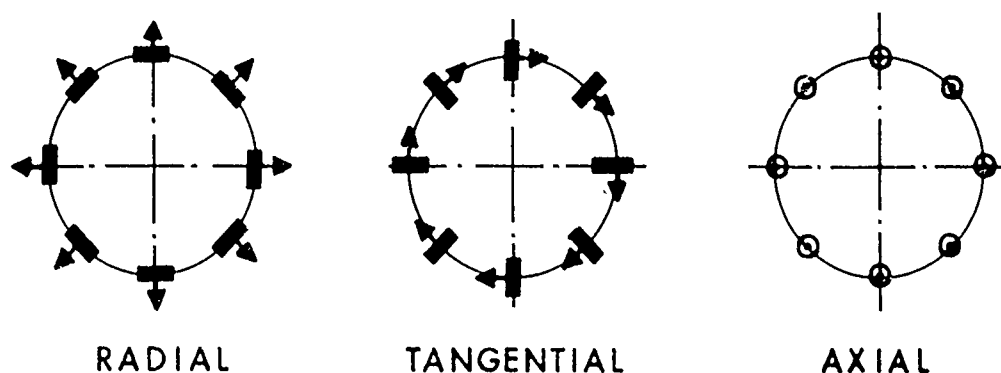


Figure 4. The Three Optimal Orientations of the Loop Surface of the Coil of Wire.

By reference to Figs. 5, 6, 7, and 8 we can derive the vector $\vec{P}_O \vec{P}$ for the loop orientations.

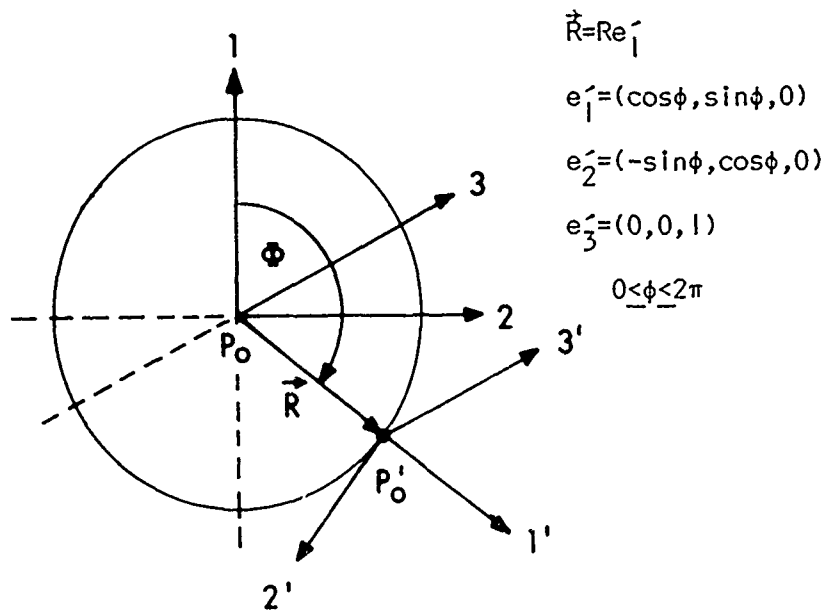


Figure 5. Coordinate Frame for i -th Coil of Wire.

For the first orientation (Fig. 6)

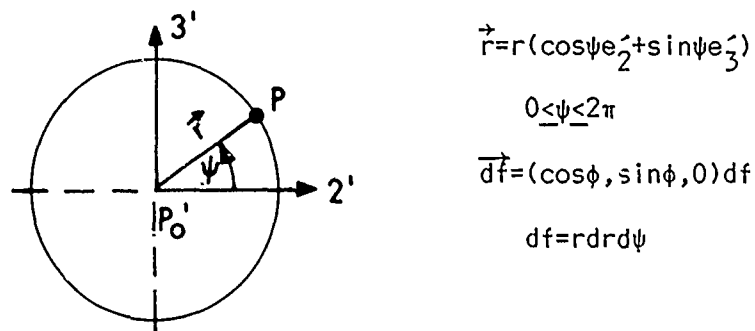
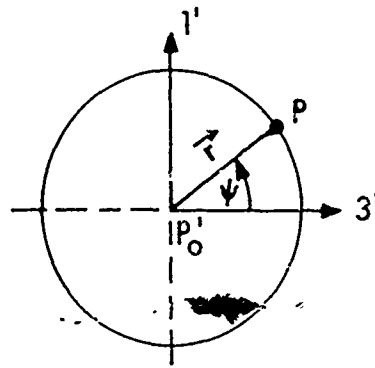


Figure 6. Geometry of the First Loop Orientation Having the Unit Vector Normal to the Loop Surface Pointing Into the Radial Direction.

we obtain

$$(3.10) \quad \vec{P}_0 \vec{P} = \vec{R} + \vec{r} = R \mathbf{e}_1' + r \cos \psi \mathbf{e}_2' + r \sin \psi \mathbf{e}_3' = (R \cos \phi - r \sin \phi \cos \psi, R \sin \phi + r \cos \phi \cos \psi, r \sin \psi).$$

For the second orientation (Fig. 7)



$$\vec{r} = r(\sin\psi \hat{e}_1' + \cos\psi \hat{e}_3')$$

$$0 \leq \psi < 2\pi$$

$$d\vec{f} = (-\sin\phi, \cos\phi, 0) df$$

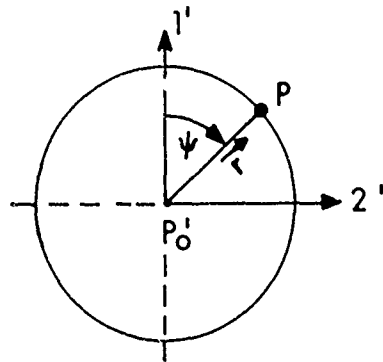
$$df = r d\psi$$

Figure 7. Geometry of the Second Loop Orientation Having the Unit Vector Normal to the Loop Surface Pointing Into the Tangential Direction.

we have

$$(3.11) \quad \vec{P}_0' \vec{P} = \vec{R} + \vec{r} = (R + r \sin\psi) \hat{e}_1' + r \cos\psi \hat{e}_3' = (R \cos\phi + r \cos\phi \sin\psi, R \sin\phi + r \sin\phi \sin\psi, r \cos\psi).$$

For the third orientation (Fig. 8)



$$\vec{r} = r(\cos\psi \hat{e}_1' + \sin\psi \hat{e}_2')$$

$$0 \leq \psi < 2\pi$$

$$d\vec{f} = (0, 0, 1) df$$

$$df = r d\psi$$

Figure 8. Geometry of the Third Loop Orientation Having the Unit Vector Normal to the Loop Surface Pointing Into the Axial Direction.

we derive

$$(3.12) \quad \overrightarrow{PoP} = \overrightarrow{R} + \overrightarrow{r} = (R + r \cos \psi) \mathbf{e}_1' + r \sin \psi \mathbf{e}_2' \\ = (R \cos \phi + r \cos \phi \cos \psi - r \sin \phi \sin \psi, R \sin \phi + r \sin \phi \cos \psi + r \cos \phi \sin \psi, 0).$$

IV. COMPUTATION OF THE INDUCED ELECTROMOTIVE FORCE

Denoting the vector $\overrightarrow{PoP_M}$ by \overrightarrow{XO} and using Eqs. (3.10), (3.11) and (3.12), respectively, we can express the vector $\overrightarrow{X} = \overrightarrow{P_M P}$ for the three sensor orientations as

$$(4.1.1) \quad \overrightarrow{X} = -(u + r \sin \phi \cos \psi, v - r \cos \phi \cos \psi, w - r \sin \psi),$$

$$(4.1.2) \quad \overrightarrow{X} = -(u - r \cos \phi \sin \psi, v - r \cos \phi \sin \psi, w - r \cos \psi), \text{ and}$$

$$(4.1.3) \quad \overrightarrow{X} = -(u - r \cos \phi \cos \psi + r \sin \phi \sin \psi, v - r \sin \phi \cos \psi - r \cos \phi \sin \psi, w),$$

whereby $(u, v, w) = (x_0 - R \cos \phi, y_0 - R \sin \phi, z_0)$.

Substitution of these position vectors, the magnetic field intensity vector, Eq. (3.8), and the areal elements as given in Figs. 5, 6, and 7 into the formula for the electromotive force V , Eq. (3.1), yields

$$(4.2.1) \quad V = \frac{m}{4\pi} \frac{d}{dt} \int_0^{2\pi} d\psi \int_0^r dr r ([\cos \phi \Lambda^3 - 3u D \Lambda^5 - 3 \sin \phi D r \cos \psi \Lambda^5] s_1 \\ + [\sin \phi \Lambda^3 - 3v D \Lambda^5 + 3 \cos \phi D r \cos \psi \Lambda^5] s_2 \\ + [-3w D \Lambda^5 + 3 D r \sin \psi \Lambda^5] s_3),$$

where $\Lambda = \Lambda(r, \psi) = [A - 2(B \cos \psi + C \sin \psi)r + r^2]^{-1/2}$,

$A = u^2 + v^2 + w^2$, $B = -u \sin \phi + v \cos \phi$, $C = w$, $D = u \cos \phi + v \sin \phi$;

$$(4.2.2) \quad V = \frac{m}{4\pi} \frac{d}{dt} \int_0^2 d\psi \int_0^r dr r ([-\sin \psi \Lambda^3 - 3u D \Lambda^5 + 3 \cos \phi D r \sin \psi \Lambda^5] s_1 \\ + [\cos \phi \Lambda^3 - 3u D \Lambda^5 + 3 \sin \phi D r \sin \psi \Lambda^5] s_2 \\ + [-3w D \Lambda^5 + 3 D r \cos \psi \Lambda^5] s_3),$$

where $\Lambda = \Lambda(r, \psi) = [A - 2(B \cos \psi + C \sin \psi)r + r^2]^{-1/2}$,

$$A = u^2 + v^2 + w^2, \quad B = w; \quad C = u \cos \phi + v \sin \phi, \quad D = -u \sin \phi + v \cos \phi;$$

$$(4.2.3) \quad V = \frac{m}{4\pi} \frac{d}{dt} \int_0^{2\pi} \int_0^r dr \, r \left(\begin{aligned} &[-3u D \Lambda^5 + 3D \cos \phi r \cos \psi \Lambda^5 - 3D \sin \phi r \sin \psi \Lambda^5] s_1 \\ &+ [-3v D \Lambda^5 + 3D \sin \phi r \cos \psi \Lambda^5 + 3D \cos \phi r \sin \psi \Lambda^5] s_2 \\ &+ [\Lambda^3 - 3w D \Lambda^5] s_3 \end{aligned} \right),$$

where $\Lambda = \Lambda(r, \psi) = [A - 2(B \cos \psi + C \sin \psi)r + r^2]^{-1/2}$,

$$A = u^2 + v^2 + w^2, \quad B = u \cos \phi + v \sin \phi, \quad C = -u \sin \phi + v \cos \phi, \quad D = w.$$

To express the electromotive force V as an explicit functions of its independent variables, explicit analytical solutions for the four areal integrals

$$(4.3.1) \quad I_1 = \int_0^{2\pi} d\psi \int_0^r dr \, r [A - 2r(B \cos \psi + C \sin \psi) + r^2]^{-3/2},$$

$$(4.3.2) \quad I_2 = \int_0^{2\pi} d\psi \int_0^r dr \, r [A - 2r(B \cos \psi + C \sin \psi) + r^2]^{-5/2},$$

$$(4.3.3) \quad I_3 = \int_0^{2\pi} d\psi \int_0^r dr \, r (r \cos \psi) [A - 2r(B \cos \psi + C \sin \psi) + r^2]^{-5/2}, \text{ and}$$

$$(4.3.4) \quad I_4 = \int_0^{2\pi} d\psi \int_0^r dr \, r (r \sin \psi) [A - 2r(B \cos \psi + C \sin \psi) + r^2]^{-5/2}$$

must be derived. Using Leibnitz's theorem for differentiation of an integral, the quadratures (4.3.2), (4.3.3) and (4.3.4) can be written as derivatives of the first integral

$$(4.4.1) \quad I_2 = -\frac{2}{3} \frac{\partial}{\partial A} I_1,$$

$$(4.4.2) \quad I_3 = \frac{i}{3} \frac{\partial}{\partial B} I_1, \text{ and}$$

$$(4.4.3) \quad I_4 = \frac{1}{3} \frac{\partial}{\partial C} I_1,$$

thereby, reducing the number of integrals to be computed to one. Since, due to the presumed geometric arrangement of the detector system A is always larger than $|r^2 - 2r(B\cos\psi + C\sin\psi)|$, the denominator in Eq. (4.3.1) can be expanded into a binomial series

$$(4.5) \quad [A - 2r(B\cos\psi + C\sin\psi) + r^2]^{-3/2} = A^{-3/2} \sum_{\mu=0}^{\infty} \binom{-3/2}{\mu} A^{-\mu} \sum_{\nu=0}^{\mu} \binom{\mu}{\nu} (-)^{\nu} 2^{\nu} r^{2\mu-\nu} (B\cos\psi + C\sin\psi)^{\nu}.$$

Inserting this series expansion into Eq. (4.3.1)

$$(4.6) \quad I_1 = A^{-3/2} \sum_{\mu=0}^{\infty} \binom{-3/2}{\mu} A^{-\mu} \sum_{\nu=0}^{\mu} \binom{\mu}{\nu} (-)^{\nu} 2^{\nu} \left[\int_0^r dr r^{2\mu-\nu+1} \right] \left[\int_0^{2\pi} d\psi (B\cos\psi + C\sin\psi)^{\nu} \right]$$

and carrying out the quadratures [5]

$$(4.7) \quad \left[\int_0^r dr r^{2\mu-\nu+1} \right] = \frac{r^{2\mu-\nu+2}}{2\mu-\nu+2}$$

$$(4.8) \quad \left[\int_0^{2\pi} d\psi (B\cos\psi + C\sin\psi)^{\nu} \right] = 2\pi \delta(\nu-2n) \frac{\Gamma(n+1/2)}{\Gamma(1/2)\Gamma(n+1)} (B^2 + C^2)^n, \quad n=0,1,2,\dots,$$

we obtain the series

$$(4.9) \quad I_1 = \pi A^{-1/2} \sum_{\mu=0}^{\infty} \binom{-3/2}{\mu} \epsilon^{\mu} \sum_{\nu=0}^{\lfloor \mu/2 \rfloor} \binom{\mu}{2\nu} \frac{2^{2\nu} \Gamma(\nu+1/2)}{(\mu-\nu+1)\Gamma(1/2)\Gamma(\nu+1)} \epsilon^{\lfloor \mu/2 \rfloor - \nu} \eta^{\nu},$$

with $\epsilon = r^2/A$ and $\eta = (B^2 + C^2)/A$.

We can rearrange this series as a series of ascending powers of ϵ . Since

$$(4.10) \quad \binom{-3/2}{\mu} \binom{\mu}{2\nu} \frac{\Gamma(\nu+1/2) 2^{2\nu}}{\Gamma(1/2)\Gamma(\nu+1)(\mu-\nu+1)} = (-)^{\mu} \frac{\Gamma(2\mu+2)}{2^{2\mu} \Gamma(\mu+1) \Gamma^2(\nu+1) \Gamma(\mu-2\nu+1)(\mu-\nu+1)},$$

we have

$$\begin{aligned}
(4.11) \quad \mu=0 & \quad \left[\frac{\Gamma(2)}{2^0 \Gamma(1) \Gamma^2(1) \Gamma(1).1} \right] \epsilon^0 \\
\mu=1 & \quad \left[-\frac{\Gamma(4)}{2^2 \Gamma(2) \Gamma^2(1) \Gamma(2).2} \right] \epsilon^1 \\
\mu=2 & \quad \left[\frac{\Gamma(6)\eta}{2^4 \Gamma(3) \Gamma^2(2) \Gamma(1).2} \right] \epsilon^1 + \left[\frac{\Gamma(6)}{2^4 \Gamma(3) \Gamma^2(1) \Gamma(3).3} \right] \epsilon^2 \\
\mu=3 & \quad \left[-\frac{\Gamma(8)\eta}{2^6 \Gamma(4) \Gamma^2(2) \Gamma(2).3} \right] \epsilon^2 + \left[-\frac{\Gamma(8)}{2^6 \Gamma(4) \Gamma^2(1) \Gamma(4).4} \right] \epsilon^3 \\
\mu=4 & \quad \left[\frac{\Gamma(10)\eta^2}{2^8 \Gamma(5) \Gamma^2(3) \Gamma(1).3} \right] \epsilon^2 + \left[\frac{\Gamma(10)\eta}{2^8 \Gamma(5) \Gamma^2(2) \Gamma(3).4} \right] \epsilon^3 \\
& \quad + \left[\frac{\Gamma(10)}{2^8 \Gamma(5) \Gamma^2(1) \Gamma(5).5} \right] \epsilon^4 \\
\mu=5 & \quad \left[-\frac{\Gamma(12)\eta^2}{2^{10} \Gamma(6) \Gamma^2(3) \Gamma(2).4} \right] \epsilon^3 + \left[-\frac{\Gamma(12)\eta}{2^{10} \Gamma(6) \Gamma^2(2) \Gamma(4).5} \right] \epsilon^4 \\
& \quad + \left[-\frac{\Gamma(12)}{2^{10} \Gamma(6) \Gamma^2(1) \Gamma(6).6} \right] \epsilon^5
\end{aligned}$$

Collecting the coefficients of the same power of ϵ , we derive the new power series

$$(4.12) \quad I_1 = \pi A^{-1/2} \epsilon \sum_{\mu=0}^{\infty} (-)^{\mu} \frac{\Gamma(2\mu+2) \epsilon^{\mu}}{2^{2\mu} \Gamma(\mu+1) \Gamma(\mu+2)} \sum_{\nu=0}^{\mu} (-)^{\nu} \frac{\Gamma(2\mu+2\nu+2) \Gamma^2(\mu+1)}{2^{2\nu} \Gamma(2\mu+2) \Gamma(\mu+\nu+1) \Gamma^2(\nu+1) \Gamma(\mu-\nu+1)} \eta^{\nu}.$$

Let us now define a function

$$(4.13) \quad G_{\ell,k}(\alpha, \beta, \gamma) = \gamma^{-(\ell+k+1/2)} \left(\frac{\alpha}{\gamma}\right) C_{\ell,k} \sum_{m=0}^{\infty} K_m^{\ell,k} \left(\frac{\beta}{\gamma}\right) \cdot \left(\frac{\alpha}{\gamma}\right)^m$$

$$\text{where } C_{\ell,k} = 2^{-2(\ell+k)} \frac{\Gamma(2\ell+2k+2)}{\Gamma(\ell+k+1) \Gamma(k+2)}$$

$$K_m^{\ell k}(\frac{\beta}{\gamma}) = (-)^m 2^{-2m} \frac{\Gamma(2m+2\ell+2k+2)\Gamma(\ell+k+1)\Gamma(k+2)}{\Gamma(2\ell+2k+2)\Gamma(m+\ell+k+1)\Gamma(m+k+2)} \frac{\mathfrak{W}(-)^n 2^{-2n}}{\delta}$$

$$\frac{1}{(n+1)} \binom{m+k}{n+k} \frac{\Gamma(m+k+\ell+1)\Gamma(2n+2m+2\ell+2k+2)}{\Gamma(n+m+k+\ell+1)\Gamma(2m+2\ell+2k+2)} \left(\frac{\beta}{\gamma}\right)^n$$

and derive functional relations for its derivatives $\frac{\partial}{\partial \alpha} G$, $\frac{\partial}{\partial \beta} G$, and $\frac{\partial}{\partial \gamma} G$.

For the first one, we have

$$(4.14) \quad \frac{\partial}{\partial \alpha} G_{\ell, k}(\alpha, \beta, \gamma) = \gamma^{-(\ell+k+3/2)} C_{\ell k} \sum_{\alpha}^{\infty} (m+1) K_m^{\ell k}(\frac{\beta}{\gamma}) \cdot \left(\frac{\alpha}{\gamma}\right)^m.$$

The second one, $\frac{\partial}{\partial \beta} G$, is given by

$$(4.15) \quad \frac{\partial}{\partial \beta} G_{\ell, k}(\alpha, \beta, \gamma) = \gamma^{-(\ell+k+3/2)} \left(\frac{\alpha}{\gamma}\right) C_{\ell k} \sum_{\alpha}^{\infty} \left(\frac{\alpha}{\gamma}\right)^m \left[(-)^m \frac{\Gamma(2m+2\ell+2k+2)\Gamma(\ell+k+1)}{2^{2m}\Gamma(2\ell+2k+2)\Gamma(m+\ell+k+1)} \right. \\ \left. \frac{\Gamma(k+2)}{\Gamma(m+k+2)} \frac{\mathfrak{W}(-)^n 2^{-2n}}{\delta} \frac{n}{\Gamma(n+1)} \binom{m+k}{n+k} \frac{\Gamma(m+k+\ell+1)\Gamma(2n+2m+2\ell+2k+2)}{\Gamma(n+m+k+\ell+1)\Gamma(2m+2\ell+2k+2)} \left(\frac{\beta}{\gamma}\right)^{n-1} \right].$$

Because $\Gamma^{-1}(n) = n\Gamma^{-1}(n+1) = 0$ for $n \leq 0$, the first nonvanishing term begins with $m=1$ and $n=1$. If we let $\mu=m-1$ and $\nu=n-1$, we obtain

$$(4.16) \quad \frac{\partial}{\partial \beta} G_{\ell, k}(\alpha, \beta, \gamma) = \gamma^{-(\ell+k+3/2)} \left(\frac{\alpha}{\gamma}\right)^2 C_{\ell k} \sum_{\alpha}^{\infty} \left(\frac{\alpha}{\gamma}\right)^{\mu} \left[(-)^{\mu+1} \frac{\Gamma(2\mu+2\ell+2k+4)\Gamma(\ell+k+1)}{2^{2\mu+2}\Gamma(2\ell+2k+2)\Gamma(\mu+\ell+k+2)} \right. \\ \left. \frac{\Gamma(k+2)}{\Gamma(\mu+k+3)} \frac{\mathfrak{W}(-)^{\nu+1}}{\delta} \frac{1}{2^{2\nu+2}\Gamma(\nu+1)} \binom{\mu+k+1}{\nu+k+1} \frac{\Gamma(\mu+k+\ell+2)\Gamma(2\nu+2\mu+2\ell+2k+6)}{\Gamma(\nu+\mu+k+\ell+3)\Gamma(2\mu+2\ell+2k+4)} \left(\frac{\beta}{\gamma}\right)^{\nu} \right].$$

Let $\kappa=k+1$ and $\lambda=\ell+1$, we have

$$\begin{aligned}
(4.17) \quad \frac{\partial}{\partial \beta} G_{\ell, k}(\alpha, \beta, \gamma) &= \gamma^{-(\lambda+k+1/2)+1} \left(\frac{\alpha}{\gamma} \right)^2 \left(\left[\frac{\Gamma(2\lambda+2k-2)}{2^{2(\lambda+k)-4} \Gamma(\lambda+k-1) \Gamma(k+1)} \right] \right. \\
&\quad \left. \left[(-) \frac{\Gamma(2\lambda+2k+2) \Gamma(\lambda+k-1) \Gamma(k+1)}{2^2 \Gamma(2\lambda+2k-2) \Gamma(\lambda+k+1) \Gamma(k+2)} \right] \left[(-) \frac{1}{2^2} \right] \right) \sum_{\mu=0}^{\infty} K_{\mu}^{\lambda k} \left(\frac{\beta}{\gamma} \right) \left(\frac{\alpha}{\gamma} \right)^{\mu} \\
&= \alpha G_{\lambda, k}(\alpha, \beta, \gamma) = \alpha G_{\ell+1, k+1}(\alpha, \beta, \gamma);
\end{aligned}$$

hence the derivative $\frac{\partial}{\partial \beta} G$ obeys the recurrence relation

$$(4.18) \quad \frac{\partial}{\partial \beta} G_{\ell, k}(\alpha, \beta, \gamma) = \alpha G_{\ell+1, k+1}(\alpha, \beta, \gamma).$$

The third derivative, $\frac{\partial}{\partial \gamma} G$, is given by

$$\begin{aligned}
(4.19) \quad \frac{\partial}{\partial \gamma} G_{\ell, k}(\alpha, \beta, \gamma) &= -\gamma^{-(\ell+1+3/2)} \left(\frac{\alpha}{\gamma} \right) C_{\ell k} \sum_{\mu=0}^{\infty} \left(\frac{\alpha}{\gamma} \right)^{\mu} \left((-)^m \frac{\Gamma(2m+2\ell+2k+2)}{2^{2m} \Gamma(2\ell+2k+2)} \right. \\
&\quad \left. \frac{\Gamma(\ell+k+1) \Gamma(k+2)}{\Gamma(m+\ell+k+1) \Gamma(m+k+2)} \sum_{n=0}^{\infty} (-)^n \frac{1}{2^{2n} \Gamma(n+1)} \binom{m+k}{n+k} \frac{\Gamma(m+k+\ell+1)}{\Gamma(n+m+k+\ell+1)} \right. \\
&\quad \left. \frac{\Gamma(2n+2m+2\ell+2k+2) (\ell+k+m+n+3/2)}{\Gamma(2m+2\ell+2k+2)} \left(\frac{\beta}{\gamma} \right)^n \right)
\end{aligned}$$

Since

$$\begin{aligned}
(4.20) \quad \frac{\Gamma(m+k+\ell+1) \Gamma(2n+2m+2\ell+2k+2) (\ell+k+m+n+3/2)}{\Gamma(n+m+\ell+k+1) \Gamma(2m+2\ell+2k+2)} &= \left[\frac{1}{2^2} \frac{\Gamma(m+k+\ell+1)}{\Gamma(m+k+\ell+2)} \right. \\
&\quad \left. \frac{\Gamma(2m+2\ell+2k+4)}{\Gamma(2m+2\ell+2k+2)} \right] \left[\frac{\Gamma(2n+2m+2\ell+2k+4)}{\Gamma(2m+2\ell+2k+4)} \frac{\Gamma(m+\ell+k+2)}{\Gamma(n+m+\ell+k+2)} \right],
\end{aligned}$$

we get

$$\begin{aligned}
 (4.21) \quad \frac{\partial}{\partial \gamma} G_{\ell, k}(\alpha, \beta, \gamma) &= -\gamma^{-(\ell+k+3/2)} \left(\frac{\alpha}{\gamma} \right) \left[C_{\ell k} \frac{\Gamma(\ell+k+1) \Gamma(2\ell+2k+4)}{2^2 \Gamma(\ell+k+2) \Gamma(2\ell+2k+2)} \right] \sum_{n=0}^{\infty} \left(\frac{\alpha}{\gamma} \right)^n \\
 &\quad \left[(-)^n \frac{\Gamma(2m+2\ell+2k+4) \Gamma(\ell+k+2) \Gamma(k+2)}{2^{2m} \Gamma(2\ell+2k+4) \Gamma(m+k+\ell+2) \Gamma(m+k+2)} \sum_{n=0}^m (-)^n \frac{1}{2^{2n} \Gamma(n+1)} \left(\frac{\beta}{\gamma} \right)^n \right. \\
 &\quad \left. \frac{\Gamma(2n+2m+2\ell+2k+4) \Gamma(m+\ell+k+2)}{\Gamma(2m+2\ell+2k+4) \Gamma(n+m+\ell+k+2)} \left(\frac{\beta}{\gamma} \right)^n \right] \\
 &= -G_{\ell+1, k}(\alpha, \beta, \gamma).
 \end{aligned}$$

Therefore we can express the derivative $\partial G / \partial \gamma$ by the recurrence relation

$$(4.22) \quad \frac{\partial}{\partial \gamma} G_{\ell, k}(\alpha, \beta, \gamma) = -G_{\ell+1, k}(\alpha, \beta, \gamma).$$

From Eqs. (4.12) and (4.13) it is evident that the first areal integral in terms of the G-function is given by

$$(4.23) \quad I_1 = \pi G_{00}(r^2, B^2 + C^2, A)$$

Inserting this solution into Eqs. (4.4.1), (4.4.2) and (4.4.3) and carrying out the differentiations, we obtain finally

$$(4.24.1) \quad I_2 = \frac{2}{3} \pi G_{10}(r^2, B^2 + C^2, A),$$

$$(4.24.2) \quad I_3 = \frac{2}{3} \pi B r^2 G_{11}(r^2, B^2 + C^2, A), \text{ and}$$

$$(4.24.3) \quad I_4 = \frac{2}{3} \pi C r^2 G_{11}(r^2, B^2 + C^2, A).$$

Substitution of these series solution into Eqs. (4.2.1) to (4.2.3) gives

$$(4.25.1) \quad v = \frac{m}{2} \frac{d}{dt} \left(\begin{aligned} &[1/2 \cos G_{00} - uD(G_{10} - \alpha G_{11}) - \alpha \cos \phi D^2 G_{11}] s_1 + \\ &[1/2 \sin \phi G_{00} - vD(G_{10} - \alpha G_{11}) - \alpha \sin \phi D^2 G_{11}] s_2 + \\ &[-wD(G_{10} - \alpha G_{11})] s_3 \end{aligned} \right),$$

$$(4.25.2) \quad v = \frac{m}{2} \frac{d}{dt} \left(\begin{aligned} &[-1/2 \sin \phi G_{00} - uD(G_{10} - \alpha G_{11}) + \alpha \sin \phi D^2 G_{11}] s_1 + \\ &[1/2 \cos \phi G_{00} - vD(G_{10} - \alpha G_{11}) - \alpha \cos \phi D^2 G_{11}] s_2 + \\ &[-wD(G_{10} - \alpha G_{11})] s_3 \end{aligned} \right),$$

$$(4.25.3) \quad v = \frac{m}{2} \frac{d}{dt} \left(\begin{aligned} &[-uD(G_{10} - \alpha G_{11})] s_1 + \\ &[-vD(G_{10} - \alpha G_{11})] s_2 + \\ &[1/2 G_{00} - wD(G_{10} - \alpha G_{11}) - \alpha D^2 G_{11}] s_3 \end{aligned} \right),$$

where $G_{\ell k} = G_{\ell k}(\alpha, \beta, \gamma)$, $\alpha = r^2$, $\beta = B^2 + C^2$, and $\gamma = A = u^2 + v^2 + w^2$. Only the variables (u, v, w) and (s_1, s_2, s_3) are functions of time; therefore we can represent the differentiation operator by

$$(4.26) \quad \frac{d}{dt} = \frac{\partial u}{\partial t} \cdot \frac{\partial}{\partial u} + \frac{\partial v}{\partial t} \cdot \frac{\partial}{\partial v} + \frac{\partial w}{\partial t} \cdot \frac{\partial}{\partial w} + \frac{\partial s_1}{\partial t} \cdot \frac{\partial}{\partial s_1} + \frac{\partial s_2}{\partial t} \cdot \frac{\partial}{\partial s_2} + \frac{\partial s_3}{\partial t} \cdot \frac{\partial}{\partial s_3}.$$

Using Eqs. (4.26), (4.18) and (4.22) we can carry out the differentiation.

After a few elementary manipulations we finally obtain for the electromotive force

$$(4.27) \quad v = \frac{m}{2} \left(\sigma_1 \dot{s}_1 + \sigma_2 \dot{s}_2 + \sigma_3 \dot{s}_3 + [s_1 \tau_{11} + s_2 \tau_{21} + s_3 \tau_{31}] \dot{u} + [s_1 \tau_{12} + s_2 \tau_{22} + s_3 \tau_{32}] \dot{v} + [s_1 \tau_{13} + s_2 \tau_{23} + s_3 \tau_{33}] \dot{w} \right),$$

where the functions σ_i and τ_{ij} ($i, j=1, 2, 3$) are given by

$$(4.28) \quad \sigma_i = \sum_{j=1}^3 M_{ij}^0 A_j, \quad i=1, 2, 3,$$

$$\tau_{ij} = \sum_{k=1}^5 M_{jk}^2 B_k, \quad i=1, 2, 3 \text{ and } j=1, 2, 3, \text{ with}$$

$$A = \begin{bmatrix} \frac{1}{2} G_{00} \\ D(G_{10} - \alpha G_{11}) \\ \alpha D^2 G_{11} \end{bmatrix}, \quad B = \begin{bmatrix} (G_{10} - \alpha G_{11}) \\ 3\alpha D G_{11} \\ 2D(G_{20} - \alpha G_{21}) \\ 2\alpha D(G_{21} - \alpha G_{22}) \\ 2\alpha^2 D^3 G_{22} \end{bmatrix}$$

The matrices M are different for each of the three distinct cases of sensor orientation. For the first orientation with the unit vector normal to the loop surface pointing in the radial direction, we have

$$(4.29.1) \quad M^0 = \begin{bmatrix} \cos\phi & -u & -\cos\phi \\ \sin\phi & -v & -\sin\phi \\ 0 & -w & 0 \end{bmatrix}$$

$$M^1 = \begin{bmatrix} -(3u\cos\phi + v\sin\phi) & -\cos^2\phi & u^2 & u(u\cos 2\phi + v\sin 2\phi) & \cos^2\phi \\ -(u\sin\phi + v\cos\phi) & -\sin\phi\cos\phi & uv & \frac{1}{2}(u^2 + v^2)\sin 2\phi & \sin\phi\cos\phi \\ -w\cos\phi & 0 & uw & wB\sin\phi & 0 \end{bmatrix}$$

$$M^2 = \begin{bmatrix} -(u \sin \phi + v \cos \phi) & -\sin \phi \cos \phi & vu & \frac{1}{2}(u^2 + v^2) \sin 2\phi & \sin \phi \cos \phi \\ -(u \cos \phi + 3v \sin \phi) & -\sin^2 \phi & v^2 & v(u \sin 2\phi - v \cos 2\phi) & \sin^2 \phi \\ -w \sin \phi & 0 & vw & -wB \cos \phi & 0 \end{bmatrix}$$

$$M^3 = \begin{bmatrix} -w \cos \phi & 0 & wu & wB \sin \phi & 0 \\ -w \sin \phi & 0 & wv & -wB \cos \phi & 0 \\ -D & 0 & w^2 & -w^2 & 0 \end{bmatrix}$$

with $\alpha = r^2$, $\beta = B^2 + C^2$, $\gamma = A$, $A = u^2 + v^2 + w^2$, $B = -u \sin \phi + v \cos \phi$, $C = w$, and $D = u \cos \phi + v \sin \phi$.

For the second orientation with the unit vector normal to the loop surface pointing in the tangential direction, we have

$$(4.29.2) \quad M^0 = \begin{bmatrix} -\sin \phi & -u & \sin \phi \\ \cos \phi & -v & -\cos \phi \\ 0 & -w & 0 \end{bmatrix}$$

$$M^1 = \begin{bmatrix} (3u \sin \phi - v \cos \phi) & -\sin^2 \phi & u^2 & -u(u \cos 2\phi + v \sin 2\phi) & \sin^2 \phi \\ (-u \cos \phi + v \sin \phi) & \sin \phi \cos \phi & uv & -\frac{1}{2}(u^2 + v^2) \sin 2\phi & -\sin \phi \cos \phi \\ w \sin \phi & 0 & uw & -wC \cos \phi & 0 \end{bmatrix}$$

$$M^2 = \begin{bmatrix} (-u \cos \phi + v \sin \phi) & \sin \phi \cos \phi & vu & -\frac{1}{2}(u^2 + v^2) \sin 2\phi & -\sin \phi \cos \phi \\ (u \sin \phi - 3v \cos \phi) & -\cos^2 \phi & v^2 & -v(u \sin 2\phi - v \cos 2\phi) & \cos^2 \phi \\ w \cos \phi & 0 & vw & -wC \sin \phi & 0 \end{bmatrix}$$

$$M^3 = \begin{bmatrix} w \sin \phi & 0 & wu & -wC \cos \phi & 0 \\ -w \cos \phi & 0 & wv & -wC \sin \phi & 0 \\ -D & 0 & w^2 & -w^2 & 0 \end{bmatrix}$$

with $\alpha = r^2$, $\beta = B^2 + C^2$, $\gamma = A$; $A = u^2 + v^2 + w^2$, $B = w$,

$C = u \cos \phi + v \sin \phi$, and $D = -u \sin \phi + v \cos \phi$.

For the third orientation with the unit vector normal to the loop surface pointing in the axial direction, we have

$$(4.29.3) \quad M^0 = \begin{bmatrix} 0 & -u & 0 \\ 0 & -v & 0 \\ 1 & -w & -1 \end{bmatrix}$$

$$M^1 = \begin{bmatrix} -w & 0 & u^2 & -u^2 & 0 \\ 0 & 0 & uv & -uv & 0 \\ -u & 0 & uw & 0 & 0 \end{bmatrix}$$

$$M^2 = \begin{bmatrix} 0 & 0 & vu & -uv & 0 \\ -w & 0 & v^2 & -v^2 & 0 \\ -v & 0 & vw & 0 & 0 \end{bmatrix}$$

$$M^3 = \begin{bmatrix} -u & 0 & wu & 0 & 0 \\ -v & 0 & wv & 0 & 0 \\ -3w & 0 & w^2 & w^2 & 1 \end{bmatrix}$$

with $\alpha=r^2$, $\beta=B^2+C^2$, $\gamma=A$; $A=u^2+v^2+w^2$, $B=u\cos\phi+v\sin\phi$,

$C=-u\sin\phi+v\cos\phi$, and $D=w$.

V. DATA EVALUATION PROCEDURE

It is evident from the anteceding explicit formulae for the induced electromagnetic force, that we have twelve unknown variables, namely the relative position vector between the centers of the magnetic dipole and the coil of wire, $(u,v,w)=(x_0-R\cos\phi, y_0-R\sin\phi, z_0)$, the linear velocity of the magnetic dipole center, $(\dot{u}, \dot{v}, \dot{w})=(\dot{x}_0, \dot{y}_0, \dot{z}_0)$, the orientation of the dipole axis (s_1, s_2, s_3) , and its angular velocity $(\dot{s}_1, \dot{s}_2, \dot{s}_3)$. To uniquely define the dipole motion at any instant of time, we need a set of twelve equations. We

can satisfy this requirement by employing twelve sensors (coils of wire) in a station. To optimize the symmetry in the experimental set up, we arrange the twelve sensors circumferentially and equally spaced in a ring configuration:

$$(5.1) \quad \phi_n = \frac{2\pi}{12} \cdot n, \quad n=1,2,\dots,12.$$

To counterbalance small deviations in the recorded signal strengths of the twelve sensor-amplifier-recorder systems due to minute differences in the instrumentation, we introduce the gauge constants

$$(5.2) \quad C_n; \quad n=1,2,\dots,12,$$

which must be generated by calibrational methods. Let

$$(5.3) \quad V_n, \quad n=1,2,\dots,12,$$

be the recorded voltages, then for any instant of time we have a set of twelve equations

$$(5.4) \quad \sum_{i=1}^3 \sigma_i \dot{s}_i = g^n, \quad g^n = \delta^n - \sum_{j=1}^3 \left[\sum_{k=1}^3 \tau_{kj}^n s_k \right] \dot{x}_j, \quad \delta^n = C_n V_n / m, \quad n=1,2,3,\dots,12, \text{ and}$$

$$(\dot{x}_1, \dot{x}_2, \dot{x}_3) = (\dot{u}, \dot{v}, \dot{w}),$$

with twelve unknown variables. Since the velocities \dot{s}_i and \dot{x}_i , $i=1,2,3$, occur only linearly in the above equations, this set of equations can readily be reduced to a set of six equations with six unknowns. Selecting the v , $v+4$ $v+8$ th equations, $v \in [1,2,\dots,12]$, for the elimination of the \dot{s}_i , $i=1,2,3$,

$$(5.5) \quad \dot{s}_i = - \sum_{j=1}^3 \left(\sum_{k=1}^3 \left[\sum_{\mu \in [v, v+4, v+8]} a_i^{\mu} \tau_{kj}^{\mu} \right] s_k \right) \dot{x}_j + d_j, \quad i=1,2,3, \text{ with}$$

$$a_i^{\mu} = A_i^{\mu} / D, \quad d_i = \left[\sum_{\mu \in [v, v+4, v+8]} A_i^{\mu} \delta^{\mu} \right] / D, \quad D = \sum_{\mu \in [v, v+4, v+8]} \sigma_i^{\mu} A_i^{\mu},$$

$$A_i^{\mu} = \sigma_{i+1}^{\mu+4} \sigma_{i+2}^{\mu+8} \sigma_{i+2}^{-\mu+4} \sigma_{i+1}^{\mu+8}, \quad (i \bmod 3) \in [1,2,3] \text{ and } (\mu \bmod 12) \in [1,2,\dots,12],$$

we obtain a set of nine equations with nine unknowns:

$$(5.6) \quad \sum_{j=1}^3 b_{j\lambda}^K = f^K; \quad b_j^K = \sum_{k=1}^3 [\tau_{kj}^K - \sum_{i=1}^3 \sigma_i^K b_{ijk}] s_k,$$

$$b_{ijk} = \sum_{\mu \in [v, v+4, v+8]} a_i^\mu \tau_{kj}^\mu \quad \text{for all } i, j, k \in [1, 2, 3];$$

$$f^K = \delta^K - \sum_{i=1}^3 \sigma_i^K d_i;$$

$$\kappa \neq v, v+4, v+8 \text{ and } \kappa \in [1, 2, 3, \dots, 12]$$

selecting the $v+2$, $v+6$ and $v+10$ th equations, $v \in [1, 2, \dots, 12]$, to get rid of the \dot{x}_i , $i=1, 2, 3$,

$$(5.7) \quad \dot{x}_j = [\sum_{\kappa \in [v+2, v+6, v+10]} E_j^K f^K] / H;$$

$$H = \sum_K E_1^K b_1^K, \quad E_j^K = b_{j+1}^{K+4} b_{j+2}^{K+8} - b_{j+2}^{K+4} b_{j+1}^{K+8}$$

$$(j \bmod 3) \in [1, 2, 3], (\kappa \bmod 12) \in [1, 2, \dots, 12],$$

we obtain a set of six equations with six unknowns:

$$(5.8) \quad \sum_{j=1}^3 b_j^\lambda e_j = H f^\lambda, \lambda \neq v, v+2, v+4, v+6, v+8, v+10 \text{ and } (\lambda \bmod 12) \in [1, 2, \dots, 12];$$

$$e_j = \sum_{\kappa \in [v+2, v+6, v+10]} E_j^K f^K, \quad j=1, 2, 3.$$

Solutions to these equations can be derived numerically by minimizing the function

$$(5.9) \quad F = \sum_{v=1}^{12} | \sum_{i=1}^3 e_i b_i^v - H f^v |, \quad v=1, 3, 5, 7, 9, 11.$$

This method ensures us a best fit of the variables (x_1, x_2, x_3) and (s_1, s_2, s_3) to the recorded data. Once these variables are obtained, we can use Eqs. (5.7) and (5.5) to determine $(\dot{x}_1, \dot{x}_2, \dot{x}_3)$ and $(\dot{s}_1, \dot{s}_2, \dot{s}_3)$. With this outlined data evaluation method we can determine uniquely the flight trajectory of the center and the motion of the axis of the magnetic dipole. Since the position and orientation of the miniature cylindrical bar magnet represented by a magnetic dipole is fixed within the projectile, the six degrees of freedom motion of the projectile can directly be derived from it using a proper coordination transformation.

VI. DESIGN CRITERIA

The result, Eq. (4.28), cannot only be used for the establishment of a data evaluation package but also for the derivation of proper design criteria. The electromotive force depends on design parameters apart from the twelve unknown variables. Two design parameters, namely the number of sensors per station and their positions in the ring configuration, have already been determined previously:

(6.1) Number of sensors per station: 12,

Angular position of sensor: $\phi_n = \frac{\pi}{6} \cdot n, n=1,2,\dots,12$

Still we have to establish the bounds for the radius of the ring configuration, the radius of the coil of wire, the required amplification of the generated signals, the dipole moment of the miniature magnet, the best orientation of the coils of wire, the number of electromagnetic pulse stations and their separation distance.

To determine the above design parameters of the instrumentation, we carried out a sensitivity analysis for a case where the dipole center moves with a velocity v_z in a straight line along the center axis of the instru-

mentation and the dipole axis rotates with a angular velocity ω about that axis. Varying the shortest distance of approach between the dipole center and the observation point, the radius of the coil of wire at the observation point, and the linear velocity, spin and magnetic moment of the magnetic dipole, we established the design parameters for a prototype instrumentation. Figs. 9, 10, and 11, for instance, show the induced electromotive force in 24 coils of wire arranged circumferentially and equally spaced in a ring configuration for the data set $R = .3\text{m}$, $r = 6.35 \cdot 10^{-3}\text{m}$, $v_z = 1460\text{m/sec}$, $\omega = 5026.5\text{ Hertz } (=800\text{ rps})$, and $m = 2.5 \cdot 10^{-7}\text{ weber m}$, typical for the M392A2 subcaliber round. The magnetic dipole moment assumed in the computation corresponds to a commercially available cylindrical ALNICO or ceramic magnet with a length of 19mm (3/4") and a diameter of 3.2mm (1/8"). For the first orientation, the unit vector normal to the loop surface of the coil of wire pointing in the radial direction, a peak in the voltage envelope of about 1.375mV occurs at about $\pm .11\text{m}$ from the plane of symmetry at $t=0$. During passage at $t=0$ the maximum amplitude is about two thirds of the peak voltage. The signal to noise ratio of our magnetic tape recording and reproducing instrumentation puts a lower limit on the detectable signal amplitude. Any signal below .5 percent of the peak amplitude is buried in the noise. To compare the useful space interval in which the signals can be evaluated for the determination of the flight trajectory we arbitrarily set forth a 10 percent threshold of the maximum amplitude for any instant of time. Approaching from left we start with the evaluation as soon as the maximum of the 24 amplitudes crosses this threshold value and continue through until it reaches the cut-off limit on the descending branch of the right side. Using this criterion we obtain thus a useful space interval of about 80cm. The second orientation, the unit vector normal to the loop surface of the coils

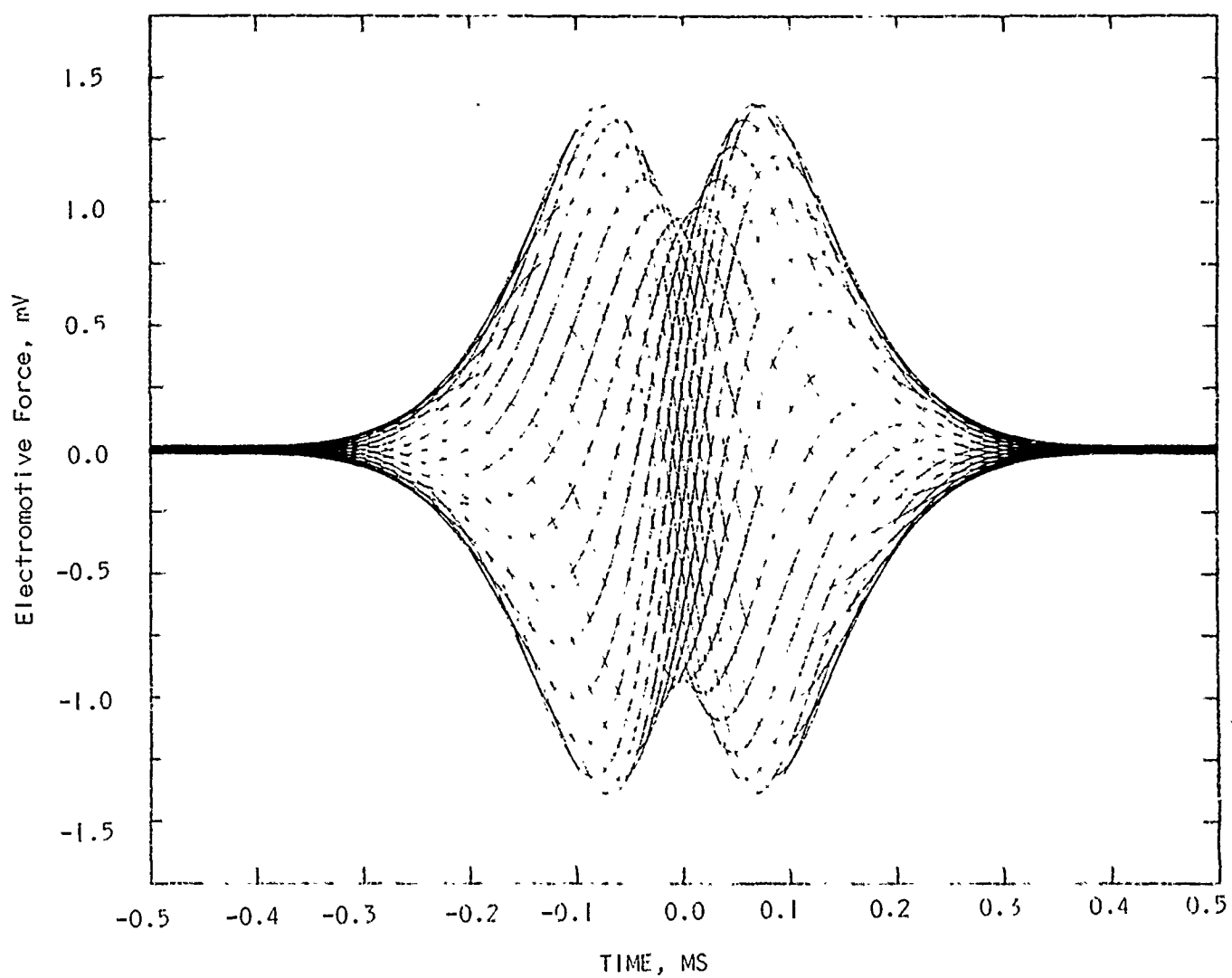


Figure 9. Electromotive Force Versus Time for Element of Loop Area Pointing in the Radial Direction.

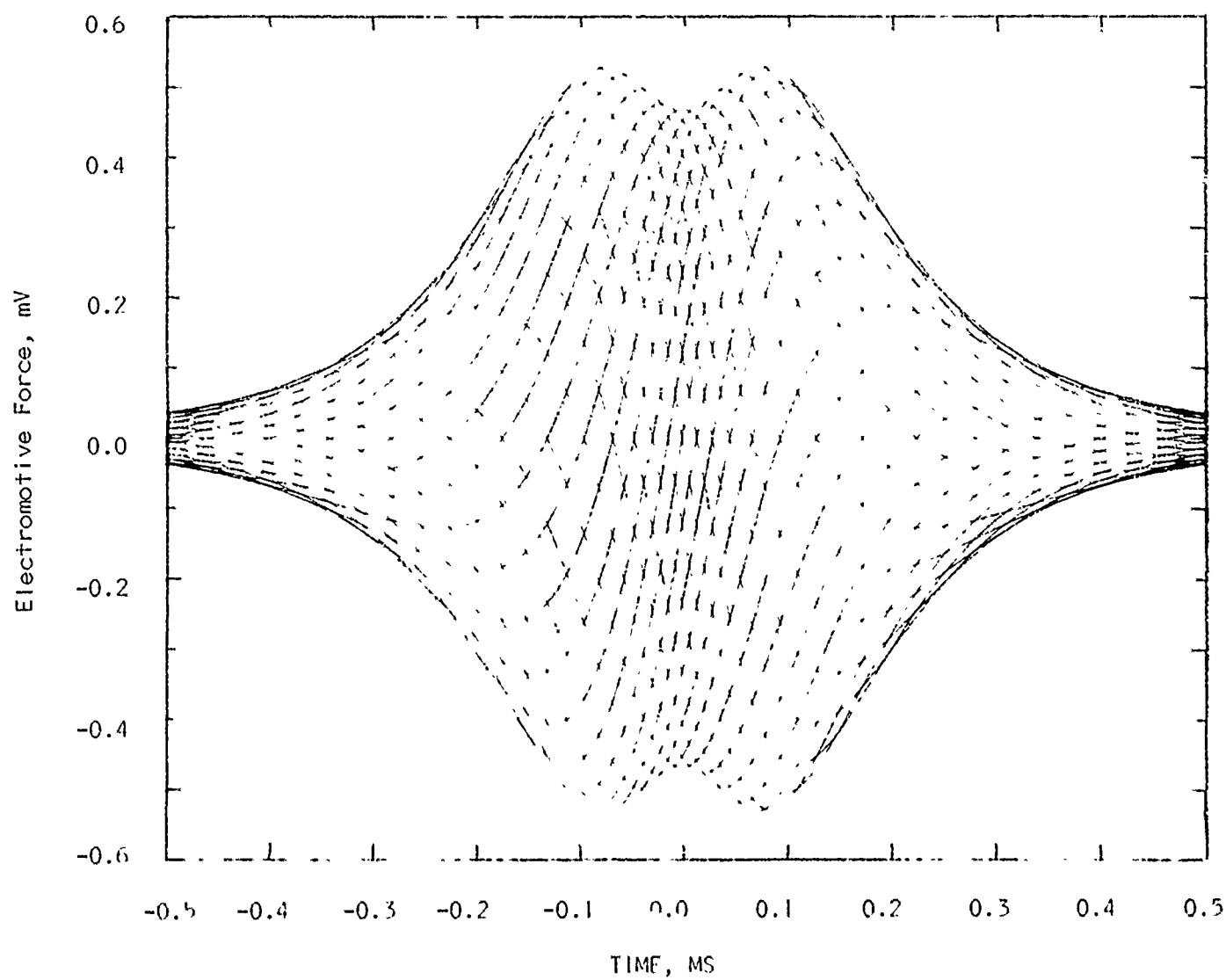


Figure 10. Electromotive Force Versus Time for Element of Loop Area
Pointing in the Tangential Direction.

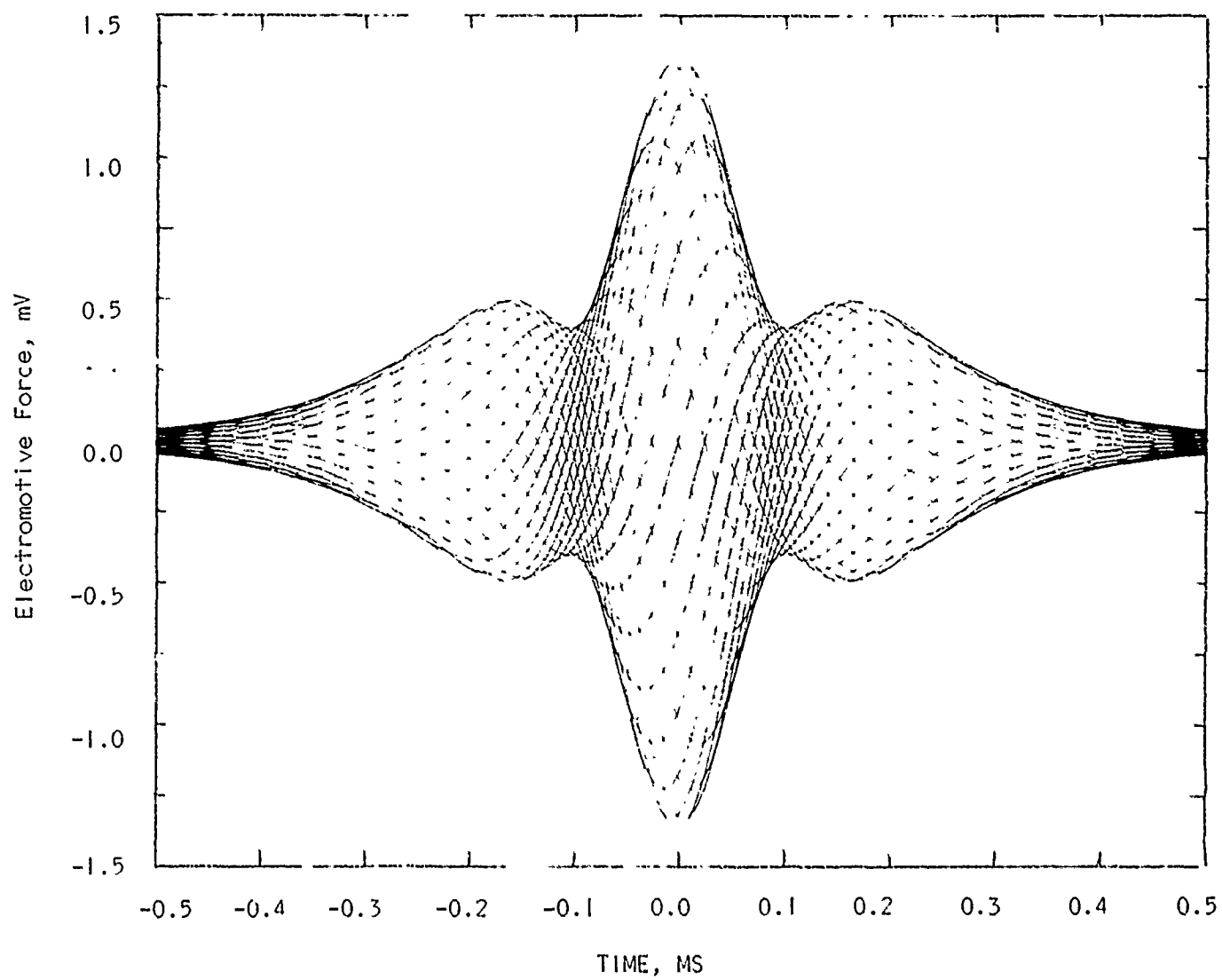


Figure II. Electromotive Force Versus Time for Element of Loop Area Pointing in the Axial Direction.

of wire pointing in the tangential direction, exhibits a behavior similar to the first one. It has a peak voltage of .53mV at 1.11m and a maximum amplitude of .48mV at passage $t=0$. Its useable space domain is about 1.25m. For the third orientation, the unit vector normal to the loop surface of the coil of wire pointing in the axial direction, we observe three maxima of .5, 1.375, and .5mV at -.234, .0, and .234m, respectively, with a useable space domain of about 105cm.

Since we want to discriminate the signal from the magnet as much as possible from the electromagnetic background noise and to disturb the magnetic field of the dipole as little as possible, we must keep the number of loops in the coil of wire and its radius as small as possible and select an orientation which maximizes both the signal strength and the useable time of recording. Based on the sensitivity analysis we picked out the third orientation with the loop surface of the coil of wire pointing in the axial direction for our sensors. By proper expansion of Eq. 4.27 we find, that for the previously discussed third orientation the voltage induced in one loop at $t=0$ is proportional to the moment and the velocity of the dipole, to the square of the loop radius, and to the negative third power of the ring radius.

$$(6.2) \quad V \propto m v_z r^2 / R^3$$

Since the maximum voltage is only in the mV range, we must amplify the signals either by increasing the number of loops in the coils of wire or by the use of amplifiers or by applying both methods simultaneously to the signal range of the magnetic tape recorder.

$$(6.3) \quad V_{\text{max/recorder}} \approx A.N.V_{\text{max/loop}}$$

$V_{\text{max/recorder}}$ is the maximal voltage which can be recorded on the magnetic tape, A is the gain of the amplifier, N is the number of loops in the coil of wire, and $V_{\text{max/loop}}$ is the maximal voltage induced in one loop by the bypassing magnetic dipole.

Based on the sensitivity analysis we established the design parameters for the instrumentation. The analysis showed that we can use a simple parallel coil arrangement for probing the moving magnetic dipole field and time-multiplexed recording of the signals. The block diagram of this parallel spin coil switching method is shown in Fig. 12. In this configuration a sequential series of coils of wire, one coil per station, is tied in parallel and feeds a common amplifier. Since the signal which is induced at the coil of wire by the by-passing magnetic dipole field is of sufficient amplitude as compared to the signals coming from the adjacent stations and the cables are shielded to avoid excessive pick up of extraneous signals, a single amplifier can be used. Due to the temporal sequence in the measurement of the projectile motion we can use data channels for the recording of the electromagnetic pulses which previously were employed to record data while the projectile traveled in-bore. As the projectile exits the muzzle, we can use a sensor at the muzzle to initiate a switching sequence which will remove the previous signal from the input of the data amplifier and switch in the signals from the electromagnetic radiation pick-up coils.

The number of electromagnetic pulse stations and their separation distance basically depends on the precession, nutation and dispersion of the round fired and the required set of data.

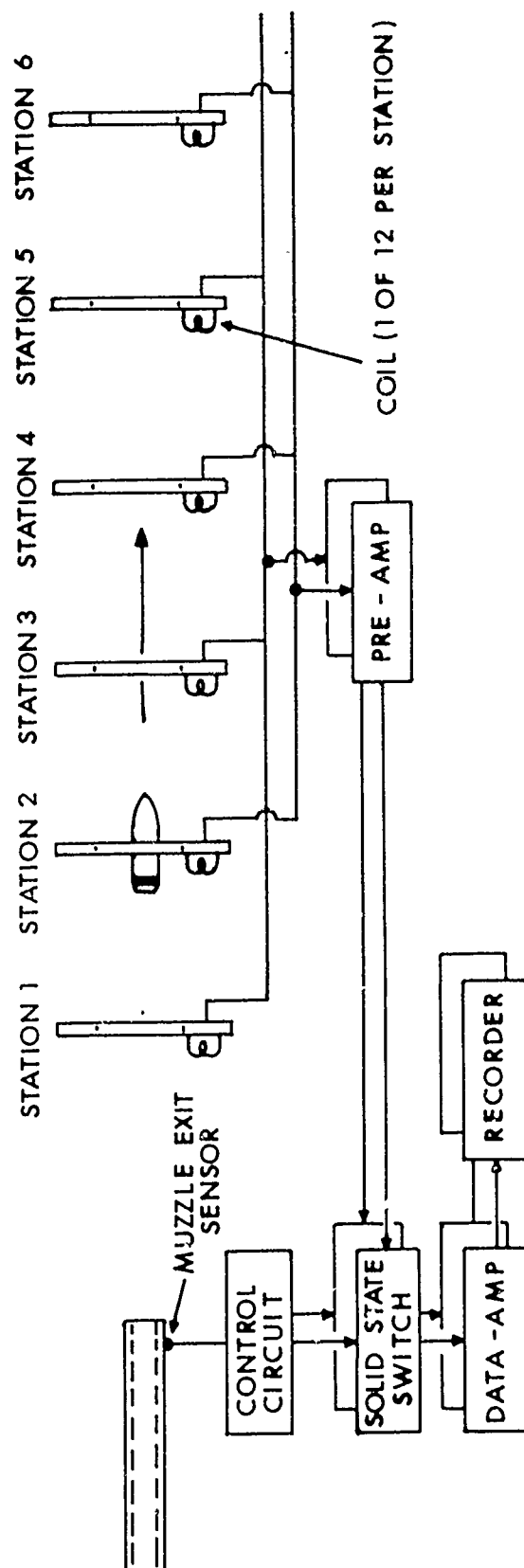


Figure 12. Block Diagram of the Parallel Spin Coil Switching Method.

VII. CONCLUSION

We used the relations (6.3) and (6.2) together with the computed values of $V_{\max/\text{loop}}$ to establish the design parameter of an experimental prototype having two stations each with only four sensors. We inserted a miniature magnet in the nose of a 37mm projectile, fired it, and recorded the signals. The unfiltered and superimposed signals from these four coils of wire at one station are shown in Fig. 13. The recorded data were within the computed

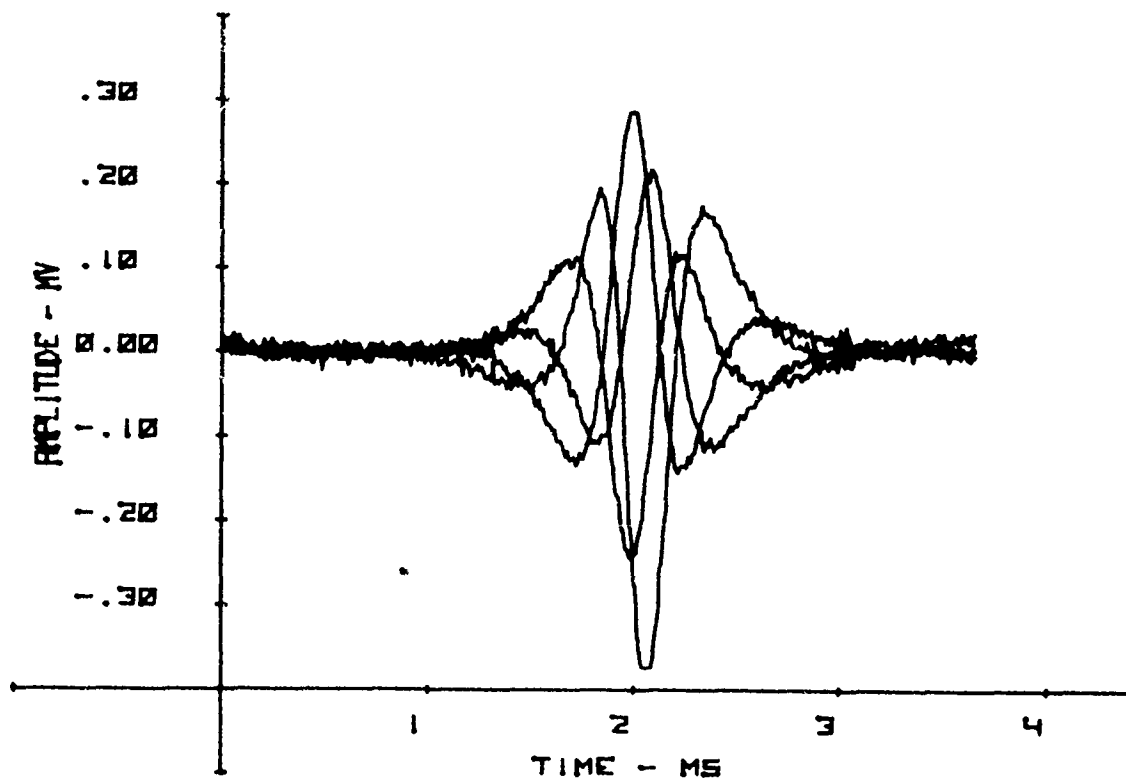


Figure 13. Unfiltered Data from a Station with Four Electromagnetic Pulse Detectors.

envelope of the electromotive force and proved that the theoretically conceived measurement technique is correct and can be applied to the obtainment of continuous flight data in the intermediate ballistic and early free flight regimes of projectiles.

At the moment we are in the midst of building an electromagnetic pulse instrumentation system consisting of eight stations, each having 12 coils of wire which are arranged circumferentially and equally spaced in a ring configuration. The equations for the computer evaluation package for determining the projectile motion from the 12 variables of the magnet motion have been derived and are currently being programmed. As soon as the instrumentation is built, we will carry out an experimental firing program in which we will concurrently record the motion of a medium caliber projectile with this electronic recording technique and with the conventional photo flash method in our transonic indoor range. From the recorded data we will then reduce the position and velocity vector of the center of gravity of the projectile, the spin, the precession and the nutation of the projectile axis as a function of time and compare the two sets of data.

With the preliminary experimental validation of our theoretical concept we have demonstrated that our proposed electromagnetic pulse instrumentation and measurement technique is a very suitable means to electronically monitor the motion of projectiles in the early free flight regime and to process the recorded data quickly and automatically. We believe that this type of instrumentation and measurement technique could become a standard tool for monitoring the instantaneous position, orientation, linear velocity, and angular velocity vector of a ballistic object or a succession of ballistic objects moving in a nonmetallic medium as function of time.

REFERENCES

1. Schuhmann, W., "Physikalische Grundlagen einer mobilen, immateriellen Treffbildscheibe", Colloquium on Ballistic Measurement Techniques, June 6-7, 1973, Institute Franco-Allemand De Recherches De Saint-Louis, France.
2. Schultze, G., "Telemetrische V_0 -Messungen", Colloquium on Ballistic Measurement Techniques, June 6-7, 1973, Institute Franco-Allemand De Recherches De Saint-Louis, France.
3. American Institute of Physics Handbook, Third Edition, 1972, McGraw-Hill Inc., N.Y.
4. Ollendorff, F., "Berechnung Magnetischer Felder", 1952 Springer Verlag, Wien.
5. Ryshik, I.M. and Gradstein, I.S., "Summen-, Produkt-und Integral Tafeln", Second Revised Edition, 1963, Deutscher Verlag der Wissenschaften, Berlin.

EFFECTS OF ECCENTRIC FIRING

B.K. STEARNS
General Electric Company
Burlington, Vermont

TABLE OF CONTENTS

	<u>Page</u>
I. INTRODUCTION	643
II. SINGLE SHOT TEST FIXTURE	644
III. MODEL AND ANALYSIS	646
IV. FIRE TEST INSTRUMENTATION	647
V. COMPARISON OF TEST RESULTS WITH ANALYSIS	648
VI. DISCUSSION	656
REFERENCES	658

INTRODUCTION

A project is currently underway at General Electric to develop an analytical method for more accurately predicting gun dynamic response. In the initial stage of this project, only the effects of eccentric firing, or mis-alignment, are being considered. This phenomenon of unbalance is encountered in many automatic weapon designs when the firing force is not in axial alignment with the center of gravity of the recoiling parts. In such cases, during firing, dynamic pitching and yawing moments are introduced, causing deformation and movement of various weapon components. Dynamic behavior of this kind can seriously affect firing precision.

As a part of the project, a special single shot device was built to provide a basic understanding of the behavior of unbalanced systems. The mis-alignment between firing force and the center of gravity of the recoiling parts can be varied. An attempt was made in the design to minimize dynamic effects other than eccentric loading. The apparatus has a minimum of moving parts, and a very stiff barrel is used to avoid the effects of droop. The support system, however, was designed to exhibit nonlinear behavior typical of actual installations, for support loading is an important consequence of eccentric firing.

A transient dynamic numerical analysis was used to calculate the response of the test device. The analysis considered the non-linearities in loading as well as those in the support structure. The weapon was modelled as a series of concentrated masses and springs.

Fire tests were conducted with the test fixture in different configurations, having varying amounts of eccentricity. Some comparisons have been made between the measurements and the dynamic simulation predictions.

Work on this project is continuing, and this paper presents a report of the progress to date.

SINGLE SHOT TEST FIXTURE

A sketch of the test fixture is shown in figure 1. It consists of a 30mm Mann ballistics barrel (with breech-block) which is held in position by forward and aft supports. These supports are approximately 66 inches apart, but this spacing is variable. An additional block is rigidly attached at the mid-section of the barrel to provide an impact surface for the recoil adapters. The basic design is such that the firing force is nearly in axial alignment with the vertical center of gravity of the recoiling mass. When the gun is fired, the barrel, breech-block and mid-barrel attachment move rearward, sliding in the forward and aft support blocks. Rearward motion is attenuated by the recoil adapters which are contacted after 0.70 inches of free travel. Torsional moments from projectile spin-up are reacted by a sliding joint at the forward support.

Each support block is held in place vertically by two pin-ended rods which are connected to independent cantilevered plates. The support stiffness can be varied by installing plates of different thickness. A similar arrangement of tie-bars provides side support.

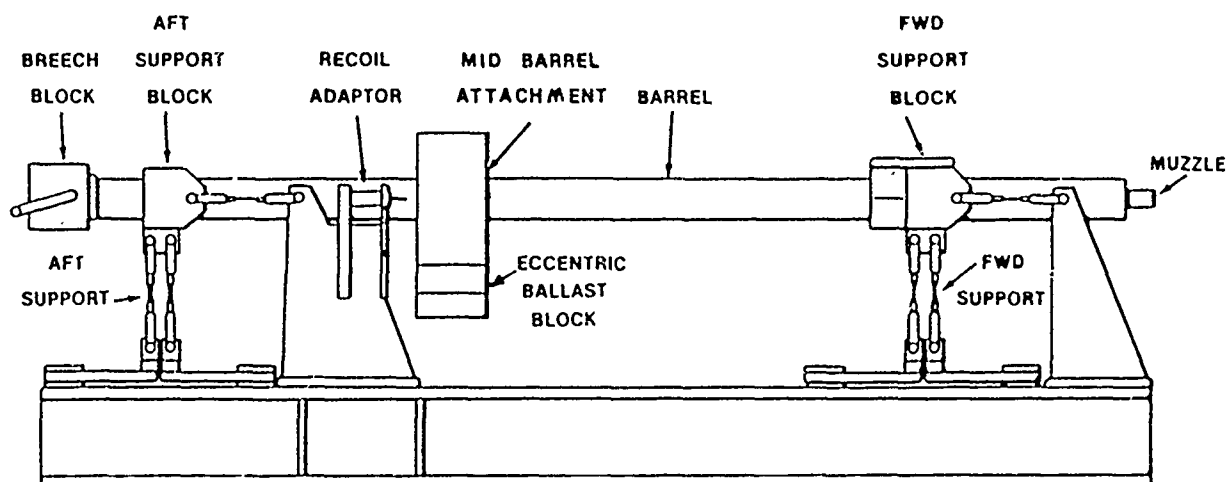


Fig. 1 - Single-barrel Dynamic Test Fixture

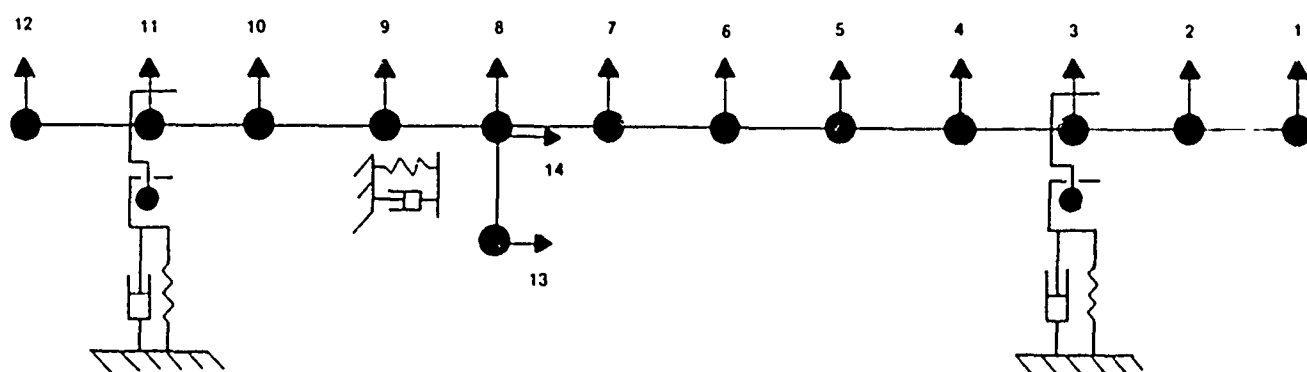


Fig. 2 - Single-barrel Gun Model

The complete design is relatively stiff. Although the Mann barrel is about 90 inches in length, it has a near constant outer diameter of 3.30 inches. Its weight, without the breech block, is 184 lbs. The vertical supports each have a minimum stiffness of about 50000 lbs/in. The total recoiling weight is 334 lbs.

To obtain an unbalanced system, additional weight (ballast), in the form of thick steel plates, is bolted to the mid-section support block. This becomes part of the recoiling mass and lowers the overall center of gravity. With a maximum ballast of 87.5 lbs., the eccentricity between the barrel centerline and the center of gravity becomes 1.42 inches.

MODEL AND ANALYSIS

The test device was modelled with a series of concentrated masses, beam elements, and springs, as shown in figure 2. The stiffness of the beam elements, joining the barrel masses, were calculated using finite element theory.¹ These values compared favorably with actual static test results. The stiffness characteristics of the vertical supports, and the ballast support beam were determined from static tests. These springs were non-linear, showing different behavior in tension than in compression. They also contained gaps from machining tolerances at mating surfaces and pin connections. The total gap, or tolerance buildup, in each support linkage was nearly .025 inches.

The transient dynamic response of the lumped mass model was performed using the linear acceleration time step integration method.² A specific computer program was developed to generate stiffnesses and to carry out the calculations. Two dimensional analysis was used as the eccentricity occurs only in the vertical plane.

The chamber pressure variation with time was used as the forcing function. The firing pulse was approximated with a series of straight line segments.

The non-linear springs were included in the analysis along with friction forces between the support blocks and the recoiling barrel. Because the system was relatively stiff, no viscous damping was included in the initial calculations.

FIRE TEST INSTRUMENTATION

During fire testing, instrumentation was provided for measuring chamber pressure, support forces, axial displacement, barrel vertical displacement, and muzzle pitching angle variation with time. A measurement was also made to determine projectile exit time.

Strain gage bending bridges were applied to the cantilevered plates to measure support forces, and to the recoil adapter support to measure recoil forces. Strain gages recording hoop stress at the muzzle were used to record projectile exit time. Axial movement was determined with linear motion transducers.

Two optical trackers were used to measure muzzle vertical motion as well as pitching angle. One tracker was focused on the tip of the muzzle and the other some 8 inches aft of that point. Both vertical motions were recorded on magnetic tape. Later, the tape was played back through an analog computer which combined the signals to produce angular displacement. Although the recorded pitching angle is between two separated points and not precisely at the muzzle, the results are useful for comparison purposes.

COMPARISON OF TEST RESULTS WITH ANALYSIS

Test shots were fired with the fixture in different ballast configurations, while measurements were recorded on oscillograph and magnetic tape. The traces of support loads were compared with calculated values as one means of checking the capabilities of the analysis.

The measured forward mount load variation with time is plotted in figure 3 for the concentric configuration (in which no ballast was added), and also for the configuration where maximum ballast was applied. Aft support loads are plotted in figure 4. The effects of unbalance can be clearly seen in both figures. By comparison, very little load develops for the concentric case. Although, after the first 8 milliseconds, when the recoil adapters contact the recoiling mass, a noticeable disturbance in the support loads can be observed.

Curves of calculated loads for the maximum ballast condition are also plotted in figures 3 and 4. The comparison with test results is encouraging for a first attempt. The analysis seems to predict fairly closely the near

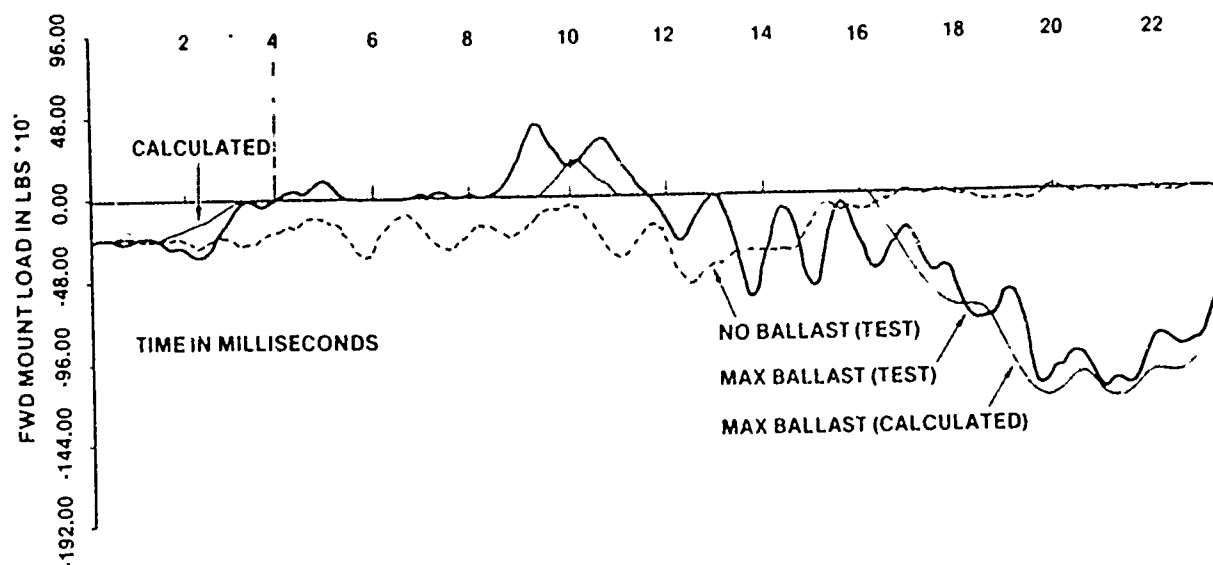


Fig. 3 - Forward Support Load

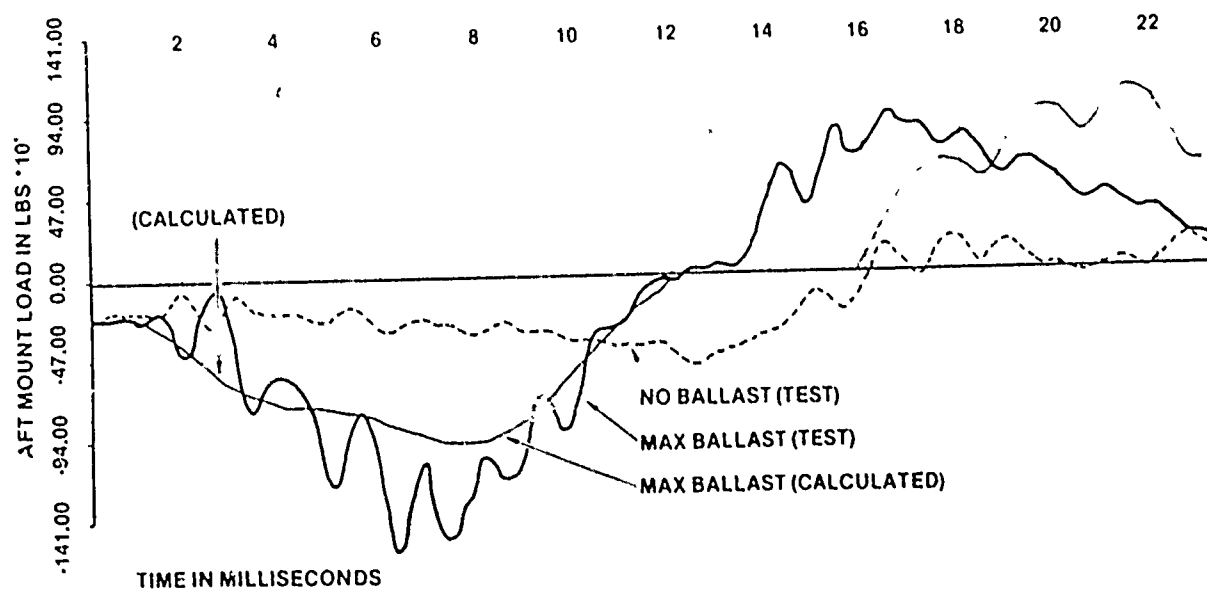


Fig. 4 - Aft Support Load

zero load which occurs when the barrel traverses the gap, or dead-band, in each support spring. The noticeable difference in curve shape between test and analysis of the aft mount load, in the range from 14 to 24 milliseconds, is believed to be produced by rotation of the support block. Over the time span, it can be observed that the area under the two curves is about the same.

The disturbing feature in the comparison is the appearance of the secondary frequency of about 800 hz which appears in the test data superimposed on the primary wave form. The two lowest natural frequencies in the vertical direction, involving large support spring movement, were calculated as 43 cps and 58 cps. These seem to bracket the main frequency shown in the test data. The next three frequencies, which involve barrel bending modes, were calculated to be 185, 561, and 960 cps. Since none of these correspond to the observed high frequency, another approach was taken.

The support systems were remodelled using four individual masses rather than one, to determine if the measured effect might be due to response within the supports themselves. A plot of the computed results is shown in figure 5 along with the measured loading. A comparison of these curves shows a closer agreement and the presence of a high frequency response. Refined modelling and the inclusion of damping could undoubtedly improve the correlation, but one questions the need for closely reproducing such a high frequency in the support structure itself.

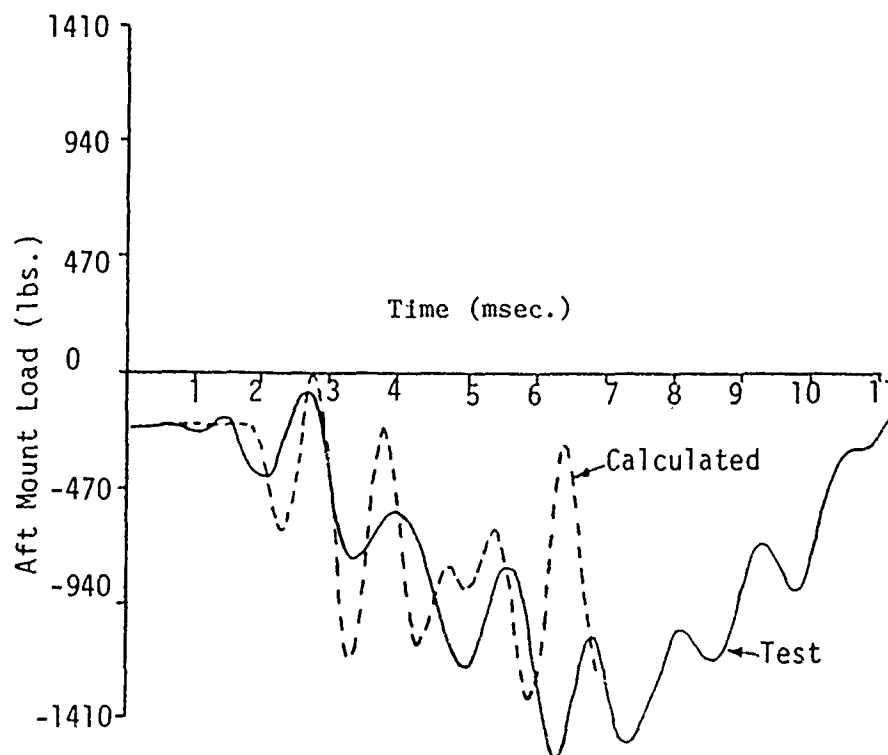


Figure 5. Aft Support Load with Maximum Ballast

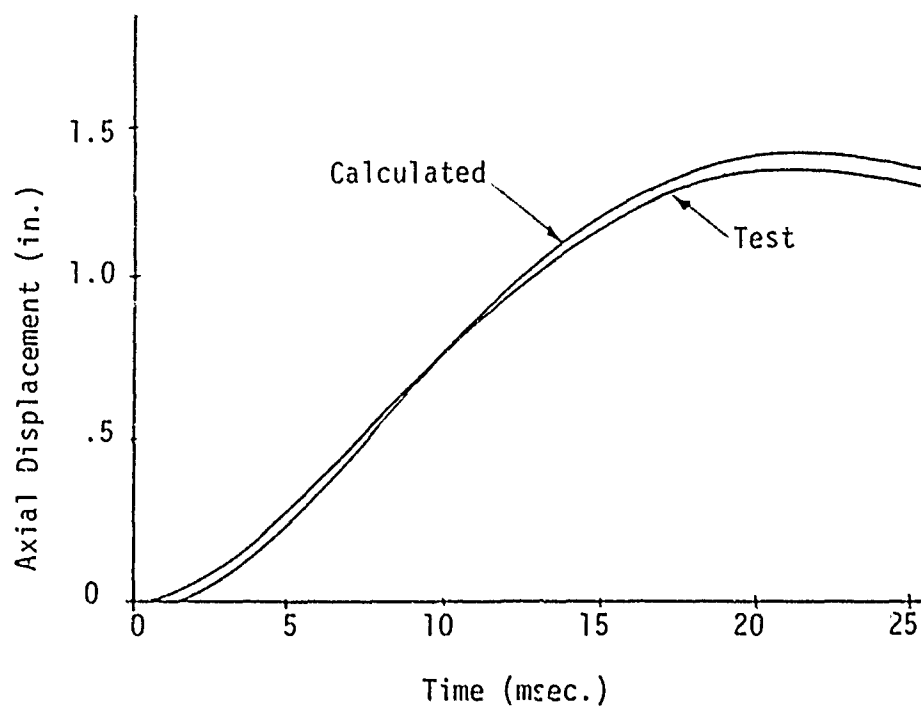


Fig. 6 - Recoil Motion

Calculations of recoil motion were also compared with test data. The results are plotted in figure 6. Agreement could be improved with a more detailed consideration in the analysis of friction between the projectile and the barrel, and that between the powder gas and barrel.³ These effects have been included in the analysis, but only as a linear function of chamber pressure.

It is interesting to consider the motion of the test apparatus prior to projectile exit. The calculated deformed shape of the barrel is plotted at four different time intervals in figure 7. Although the primary motion of the stiff structure is rigid body pitching, there also is evidence of transverse bending. This effect would, of course, be significantly greater with a more flexible barrel.

Plots of the calculated vertical displacements of the two end nodes are given in figure 8. Optical tracker test measurements are also shown. The analytical predictions seem to be drastically in error at the time of projectile exit. Although the displacement measurements were taken some weeks after the load data was obtained, and with a re-assembled test fixture, a consistency would be expected. It can be noted that the peak upward load at the forward mount (see figure 3) occurred around 10 milliseconds, at the same time the peak vertical displacements occurred. This tends to give credibility to the test data and makes the analysis questionable for the stiff system. Although very small movements are involved, the analysis predicts opposite displacement and pitching angle from test results at exit time. There appears to be a lag in response which is not included in the analysis.

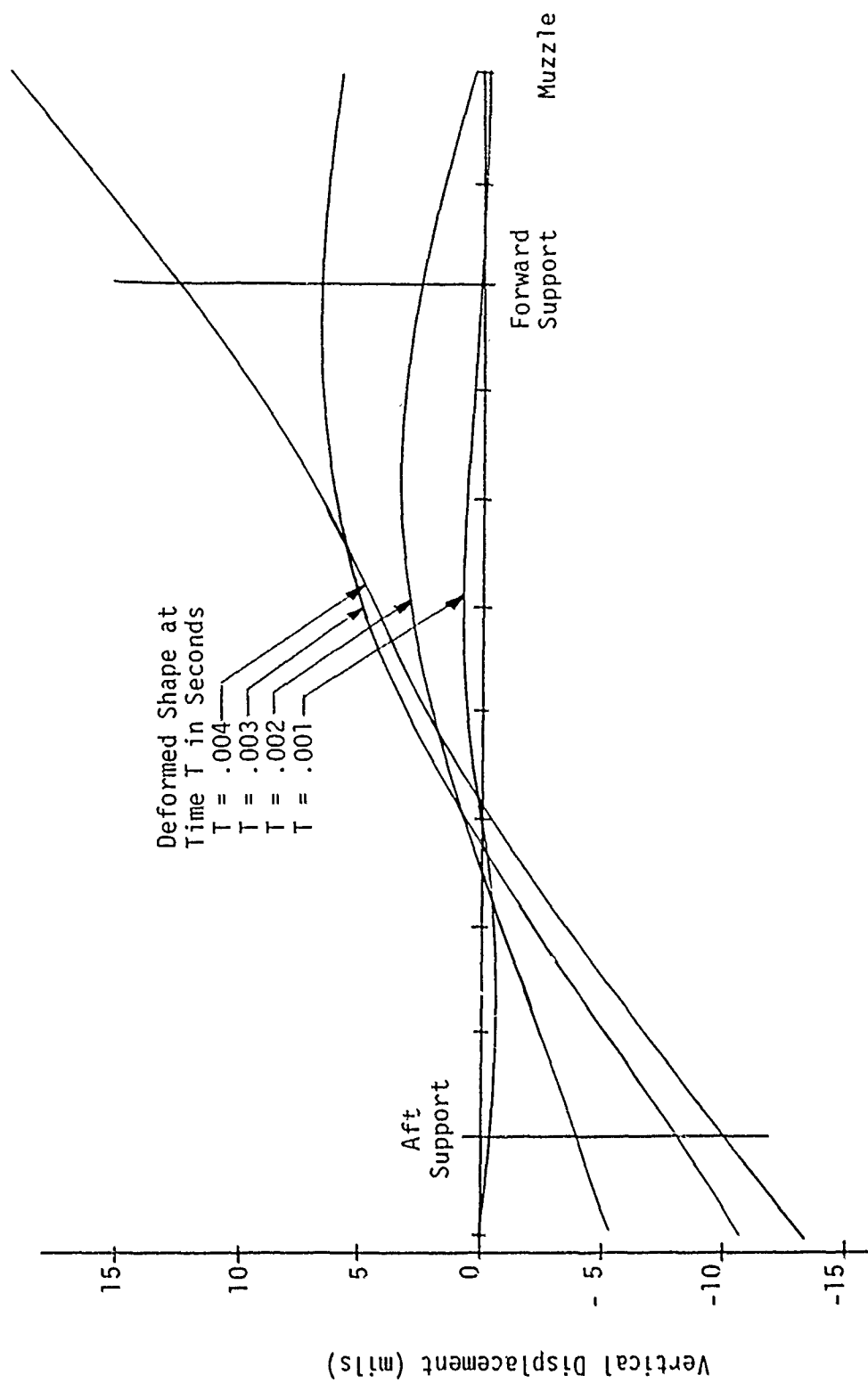


Fig. 7 - Calculated Barrel Deformed Shape

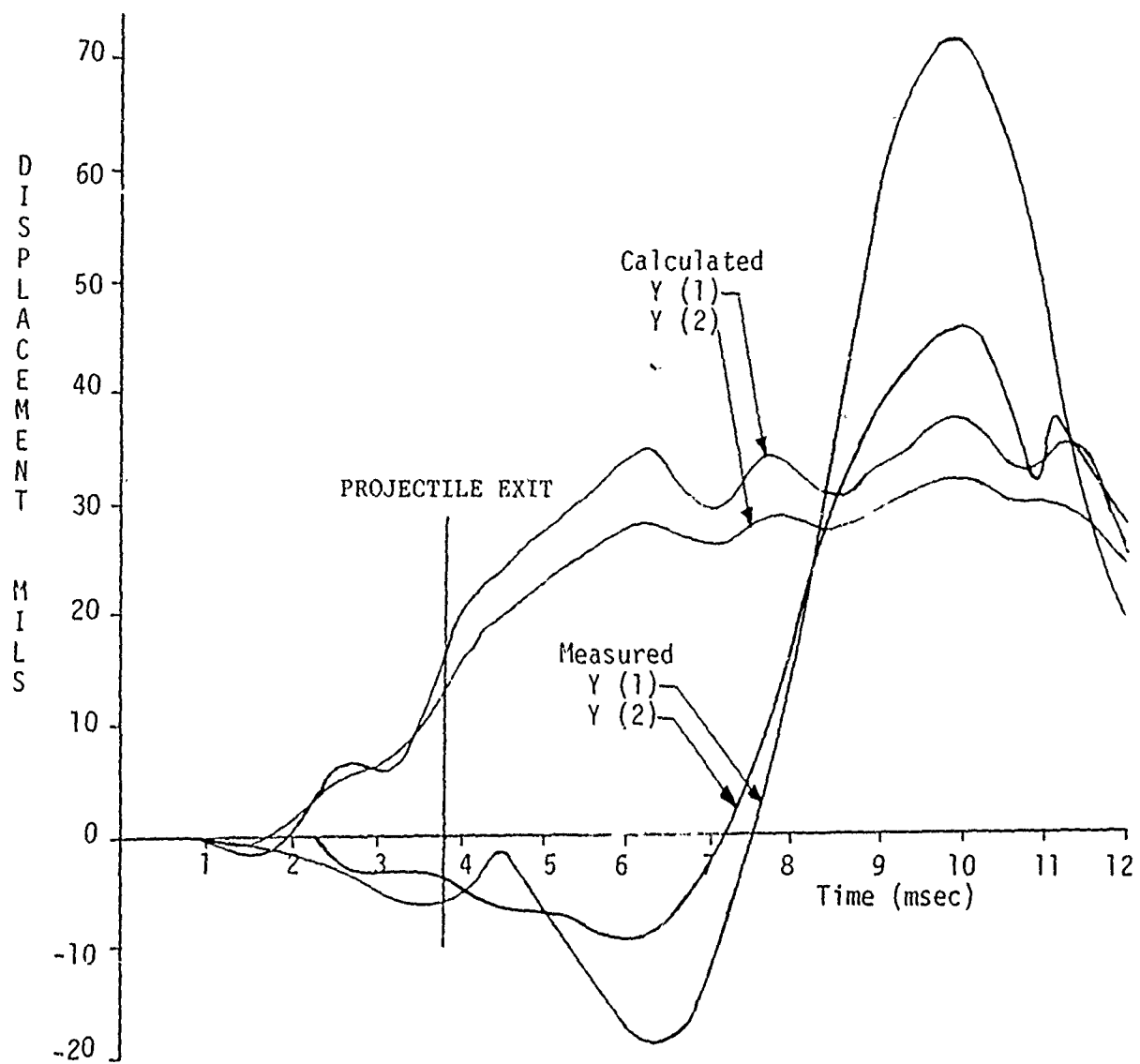


Fig. 8 - Vertical Displacement of Nodes at Muzzle

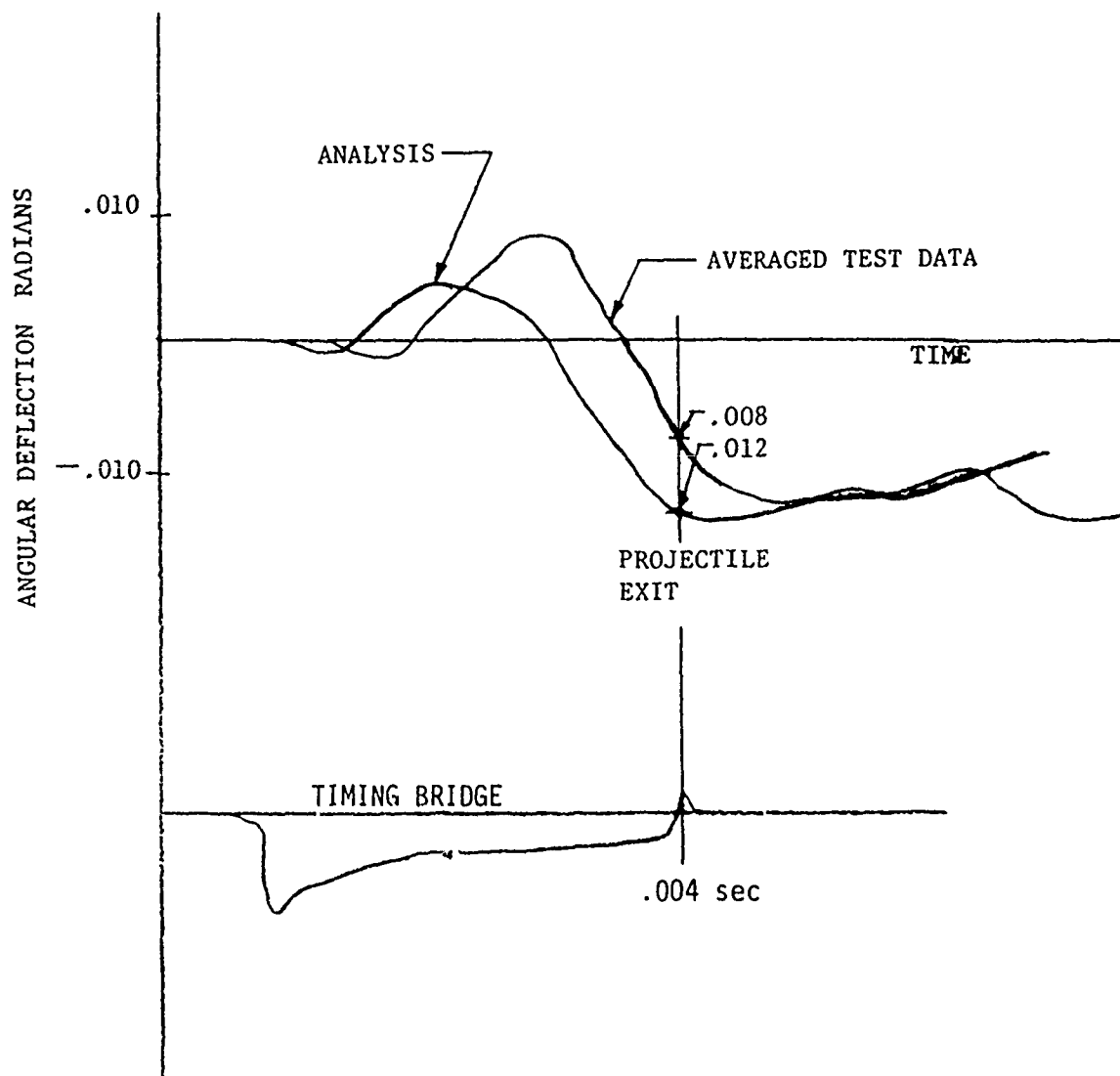


Fig. 9 - Angular Deflection at End of Barrel

Similar single shot tests have been conducted with a lightweight barrel having much greater flexibility than that of the Mann barrel. Fire testing resulted in much greater motion at the muzzle. Optical trackers were focused some 5 inches apart near the muzzle to measure the pitching angle. A plot of the results is shown in figure 9 along with analytical predictions. The measured pitching angle at time of projectile exit was .008 radians. The test was repeated several times and targets were taken. All shots hit the target (1000 inches) between 7 and 9 inches below boresight.

The calculated displacements agree somewhat better for the flexible system. However, it is still not known from testing such an arrangement, whether the analysis is in error, or whether barrel droop, or some other effects are responsible for the disagreement between test and prediction.

DISCUSSION

An attempt has been made to isolate the effects of eccentric firing with a simple single shot test device in a fundamental investigation. In this study, both analytical and test results have shown the apparatus to display a highly complex behavior when fired. An extrapolation from the fundamental test results substantiates what is presently surmised about eccentric firing of production precision gun weapons, including single barrel, multi-barrel, and rotating barrel cluster weapons.

Eccentric firing has an effect on gun dynamic response, which directly or indirectly, can influence weapon accuracy. Firing with an unbalanced

recoiling mass will result in muzzle tipping at the time of projectile exit, even if the gun has infinitely stiff transverse supports. Not only does the tipping affect initial yaw, but a transverse velocity is also imparted to the projectile. The transverse loads, developed from the unbalanced system, deflect the supporting structure to produce a further pitching of the barrel. In turret applications, the transverse loads developed from eccentric firing can be expected to influence servo load torques.

It can be argued that no real inaccuracy is developed from eccentric firing if each shot, although several mils from boresight, passes through the same hole, or is a mil or so from point of impact. However, the problem arises in automatic weapons when slight variations in action occur with repeated shots. The starting position may be different, the round impulse may vary, or the recoil adapter may behave abnormally. The result of slight mis-timing may be observed from figure 9. A delay of 0.1 millisecond could, in this case, produce a 2 or 3 mil difference in initial heading of the projectile.

From the results obtained thus far, it appears that the lumped mass method of analysis might be used satisfactorily for the prediction of support load variation with time. And also, it should be suitable for determining servo load torques in turret applications. However, its suitability for predicting muzzle tipping is still in doubt, and a continuation of the project is planned to resolve this question.

REFERENCES

1. J. S. Przemieniecki, Theory of Matrix Structural Analysis, McGraw-Hill, 1968.
2. J. M. Biggs, Introduction to Structural Dynamics, McGraw-Hill, 1964.
3. H. P. Gay, An Interim Report on the Dynamics of Automatic Weapons. (U). Ballistic Research Labs Aberdeen Proving Ground Md., Sept. 1974.

OPTICAL DEVICE FOR DETERMINING
SMALL ANGULAR MOTION

B.T. HAUG
Ballistics Research Laboratory
Aberdeen, Maryland

TABLE OF CONTENTS

	<u>Page</u>
I. INTRODUCTION	660
II. EQUIPMENT	661
A. THE OPTICAL SYSTEM	662
B. THE LASER	663
C. THE SPATIAL FILTER	663
D. THE BEAM SPLITTER	663
E. THE PARABOLOIDAL MIRROR	664
F. THE PHOTODIODE	665
III. DATA ACQUISITION AND REDUCTION	665
IV. RESULTS AND CURRENT EFFORT	672

I. INTRODUCTION

A. BACKGROUND

In the early sixties, at the Ballistic Research Laboratory (B.R.L.), Messrs. Stanley S. Lentz and Richard B. Kirkendall developed an instrumentation system to measure the off-axial in-bore motion of medium to large caliber projectiles. An optical lever system was used with a carbon arc lamp as a light source and a displacement time camera to record the motion. They faced four major problems in this effort: (1) Due to the white light source the system had to be used at night to prevent the sunlight from fogging the film; (2) It was difficult to time the shutter to record full in-bore travel but close the shutter prior to muzzle flash; (3) Conventional metal rotating bands failed to obturate sufficiently allowing blow-by which obscured the light beam; (4) Film records required optical reading which is time consuming and cost ineffective. To overcome the ambient light and muzzle flash problems, a laser was substituted for the carbon arc lamp and a narrow band filter was placed in front of the camera. The 37mm, 90mm, and 105mm systems were studied with this instrument. The results were encouraging. Records of the complete in-bore travel were obtained with specially designed non-metallic rotating bands. But because of a shortage of funds and higher priorities of other projects this project has been dormant for several years.

B. CURRENT EFFORTS

New technology has made it possible to improve the technique for recording angular projectile motion. By using a continuous position sensing photodiode and electronic signal conditioning, the photographic film recording can be eliminated. The data can be recorded directly on magnetic tape along with pressure, force, displacement, strain, temperature, and other measurements made on a gun system; thus, all recorded data will have a common time scale. It is hoped that plastic rotating bands will improve obturation during the entire launch cycle, thus reducing the obscuration of the laser beam.

II. EQUIPMENT

A. THE OPTICAL SYSTEM:

The optical system as used at the BRL is shown in Figure 1. It represents a simple optical lever. A laser source is used in conjunction with a spatial filter, a large collimating mirror, and a photodiode for a detector.

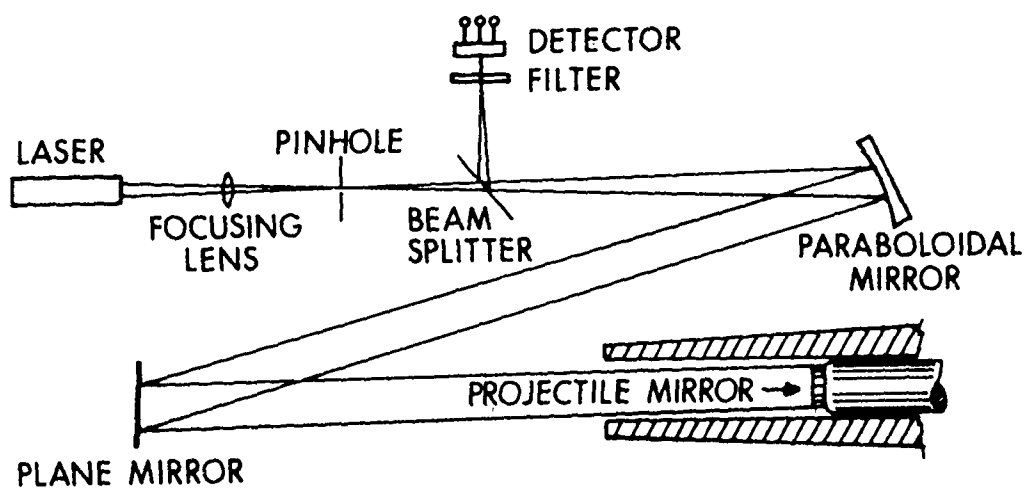


Figure 1. Layout of Optical System.

B. THE LASER

We have two lasers available: a He Ne laser with a 15mW output at a wavelength of 632.8nm, and an Argon laser with a total rated output of 2 W able to selectively emit any one of nine discrete wavelengths from 454.5nm to 514.5nm. The laser light source supplies us with a convenient, powerful source of useable light and the monochromatic nature of the beam allows us to use filters in front of the detector to screen the ambient light.

C. THE SPATIAL FILTER

The laser generates a beam which first passes through a spatial filter which smooths and diverges the beam. The spatial filter consists of a focusing lens and a pinhole. The pinhole is placed at the focal point of the lens. The diameter of the pinhole is determined by the focal length of the lens. The shorter the focal length the smaller the pinhole can be. If the pinhole is too large, the beam is not smoothed, and if the pinhole is too small it creates a diffraction pattern. A typical pinhole size is 100 μm with a 100mm lens.

D. THE BEAM SPLITTER

After the beam exits the spatial filter, it passes through a beam splitter, where it is divided into two linearly polarized beams. The beam which passes through the splitter is retained. The other beam is discarded. Originally a specially coated thick plate glass mirror and beam splitter device was used, but because of its thickness it suffered from internal reflections. Therefore,

a pellicle beam splitter is now employed. It is basically a very thin membrane and eliminates the double image caused by internal reflections. Pellicle beam splitters can be coated for various reflection to transmission ratios for specific wavelengths. For our purpose a 50/50 ratio is appropriate.

E. THE PARABOLOIDAL MIRROR

The main optical element of the lever is a 254mm diameter, front-surfaced, off-axis, paraboloidal mirror with a focal length of 1.22 m. The mirror is placed so that its focal point falls on the pinhole, thus collimating the laser beam. The diameter of the collimated beam depends on the focal length of the focusing lens. The shorter the focal length the larger the beam diameter. As shown in Eq. (1), the gain of the optical lever system is determined by the focal length of the paraboloidal mirror.

$$(1) \quad \frac{D}{\alpha} = \frac{\pi \ell}{1600}$$

where

D displacement on the detector in mm.

α angular projectile displacement in mils

ℓ focal length of the mirror in mm.

Eq (1) yields a 2.40 mm/mil gain with our mirror.

This large front-surfaced mirror is an off-axis paraboloid to allow the reflection of the light beam without introducing distortion. From this mirror the beam is directed to a front-surfaced plate mirror which is positioned along the gun axis, and directs the beam down the gun tube towards the projectile. The projectile has a mirror attached to its nose to initiate the beam's return path.

F. THE PHOTODIODE

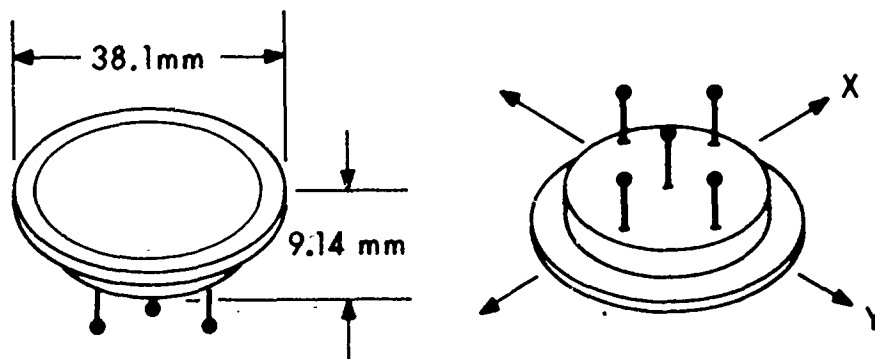
The information concerning angular motion of the projectile is contained in the angular deviations of the returning beam; however, no information about projectile displacement is contained in the beam due to its collimated nature. The paraboloidal mirror focuses the returning beam on the photodiode by means of the beam splitter. The diode is a continuous position sensing photodetector with an output proportional to the image position and intensity.

Figure 2 sketches the physical appearance of the diode and lists some of the specifications. The detector is sensitive to such a broad spectrum that it must be shielded from external light sources by an appropriate filter. Also the intensity of the incoming beam must be controlled to prevent damage to the detector. The diode can withstand 0.4 mW/mm^2 but operates more linearly at 0.2 mW/mm^2 .

III. DATA ACQUISITION AND REDUCTION

A. SIGNAL CONDITIONING

Figure 3 shows an equivalent circuit for the detector and the initial amplifier. The output current from each axis of the detector is the input to a sum and difference amplifier. The difference terms, X_d and Y_d , contain position and incident power information. The ratio of resistances varies with the image position, while the term I_s is determined by the total incident power. If the two sum outputs, X_s and Y_s , are added, the result is a term proportional to the total current. It is obvious from this that dividing the individual difference terms by the total current removes the dependence on intensity variations. The resulting two ratios, X_{out} and Y_{out} , are determined by position only.



POSITION SENSITIVITY _____ $15.7 \mu\text{A}/\text{mW}/\text{mm}$

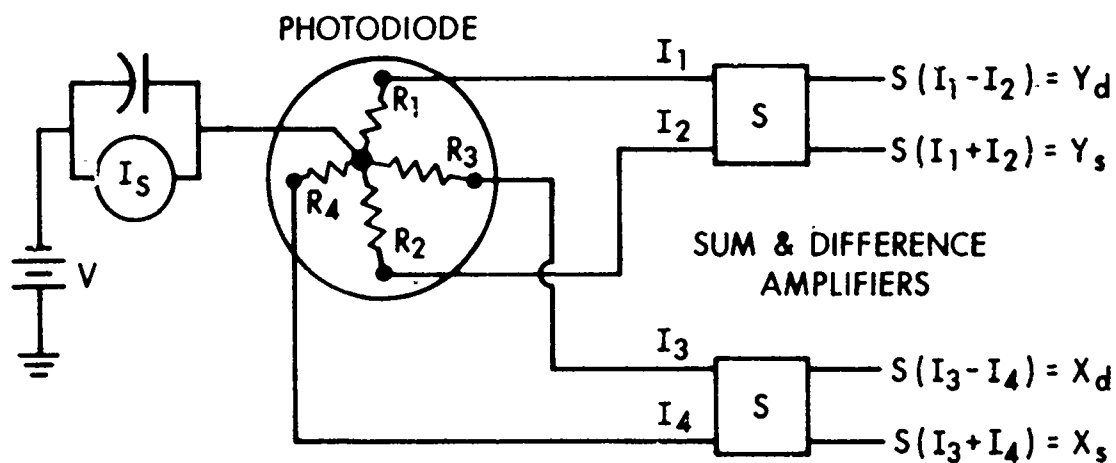
POSITION LINEARITY

1.5 mm from center _____ 1 %

75 % of distance from center to edge _____ 10 %

INTENSITY SENSITIVITY _____ $.25 \mu\text{A}/\mu\text{W}$

Figure 2. Photodiode used in Optical Lever System.



$$R_T = R_1 + R_2 + R_3 + R_4$$

$$I_1 = \frac{R_2 R_3 R_4}{R_T} I_S; \quad I_2 = \frac{R_1 R_2 R_3}{R_T} I_S$$

$$I_3 = \frac{R_1 R_2 R_4}{R_T} I_S; \quad I_4 = \frac{R_1 R_2 R_3}{R_T} I_S$$

$$X_{out} = \frac{I_3 - I_4}{I_S}$$

$$= \frac{X_d}{X_s + Y_s}$$

$$Y_{out} = \frac{I_1 - I_2}{I_S}$$

$$= \frac{Y_d}{X_s + Y_s}$$

Figure 3. Block Diagram of Detector and Sum and Difference Amplifier.

Figure 4 shows the results of varying the incident power level while maintaining a constant position. It is a plot of X_{out} versus $(X_s + Y_s)$, which is the total current from the diode and represents the intensity of the incident beam. The curve shows that large drops of intensity, greater than 75%, will cause a very small shift in the output, less than 10%.

B. CALIBRATION AND DATA REDUCTION

Extensive work has been completed to determine the best operating conditions for the diode and to provide a suitable technique for calibrating the output. It was determined that excessive power density can cause the output to drift. Figure 5 is a plot of the X_{out} vs. Y_{out} resulting from tracing a circle with a radius of 8 mm on the face of the detector with a laser beam of excessive power density. The drift is immediately apparent. By reducing the incident power density and shielding the diode from the ambient light, it was possible to eliminate the drift and to a large extent the noise too. The improved results can be seen in Figure 6. Shown in this plot are the results of tracing three circles on the detector with radii of 5, 10 and 15mm. Notice that the drift has disappeared; however, non-linearities are apparent in the larger circles.

It has been determined that the final outputs have a one-to-one relationship with the coordinates of the image position on the detector. The approach chosen for the data reduction is to fit a least squares circle to each set of data shown in Figure 6, subtract the circle, and perform a Fourier analysis on the residue. It is anticipated that the residue can be reduced to a cosine function with an amplitude controlled by the radial displacement of the incident beam and with a period of $\pi/2$. Once a mapping of the data is completed, an inverse transformation will be performed to predict the polar coordinates of the beam from the recorded data voltages.

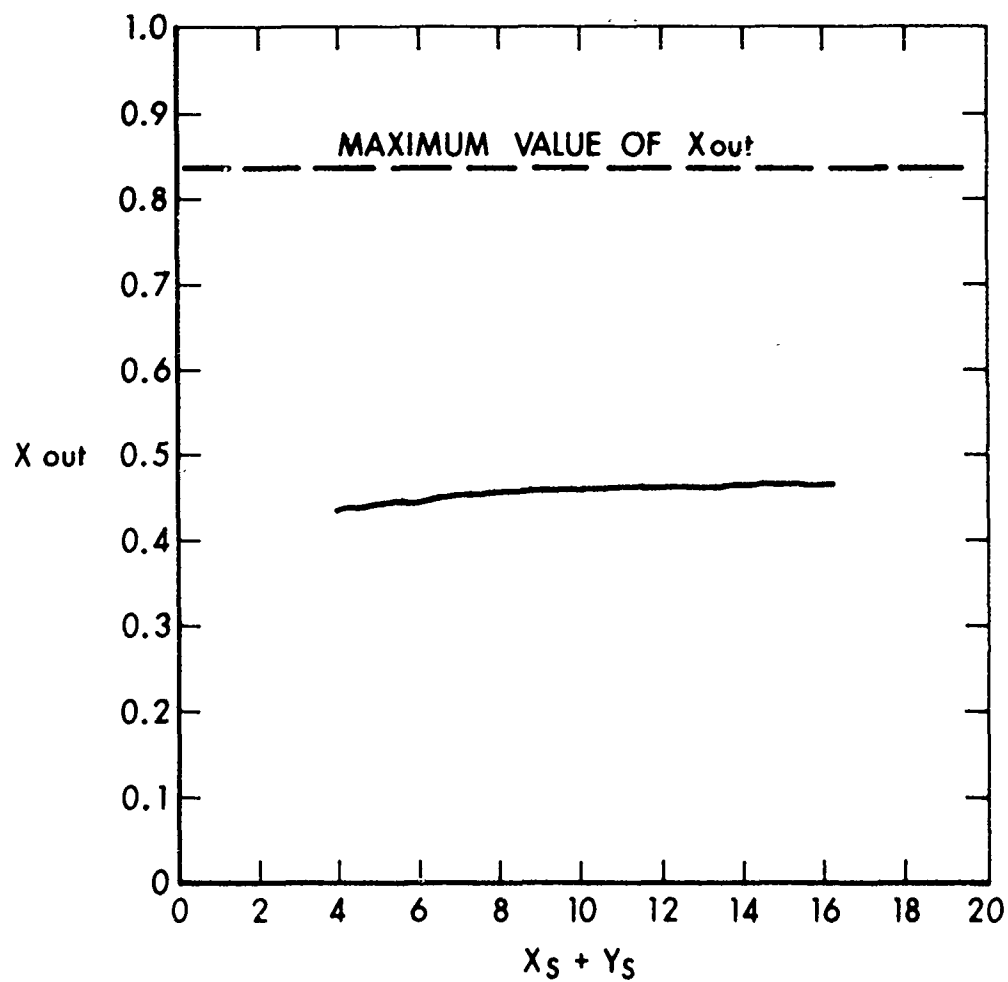


Figure 4. Intensity Sensitivity of Final Output.

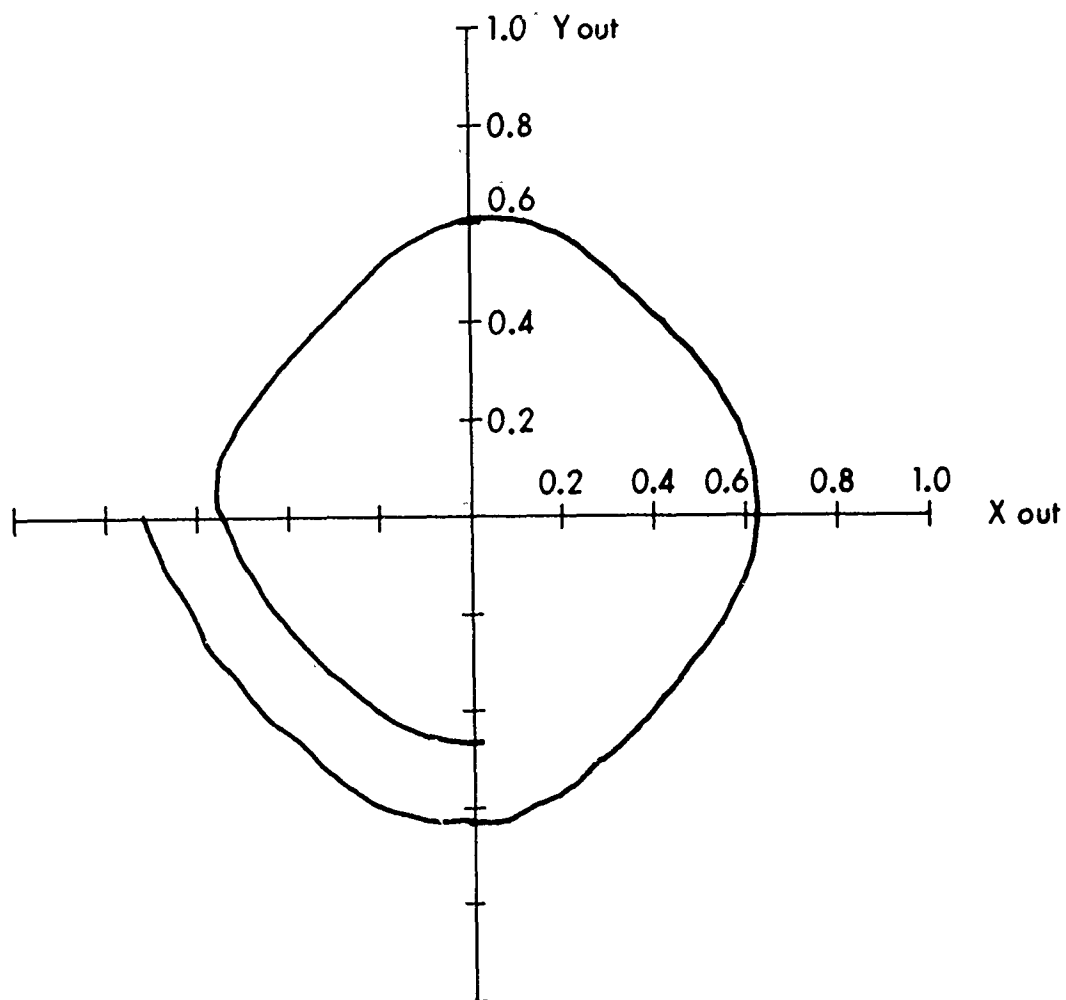


Figure 5. Result of Excessive Incident Power on Photodiode.

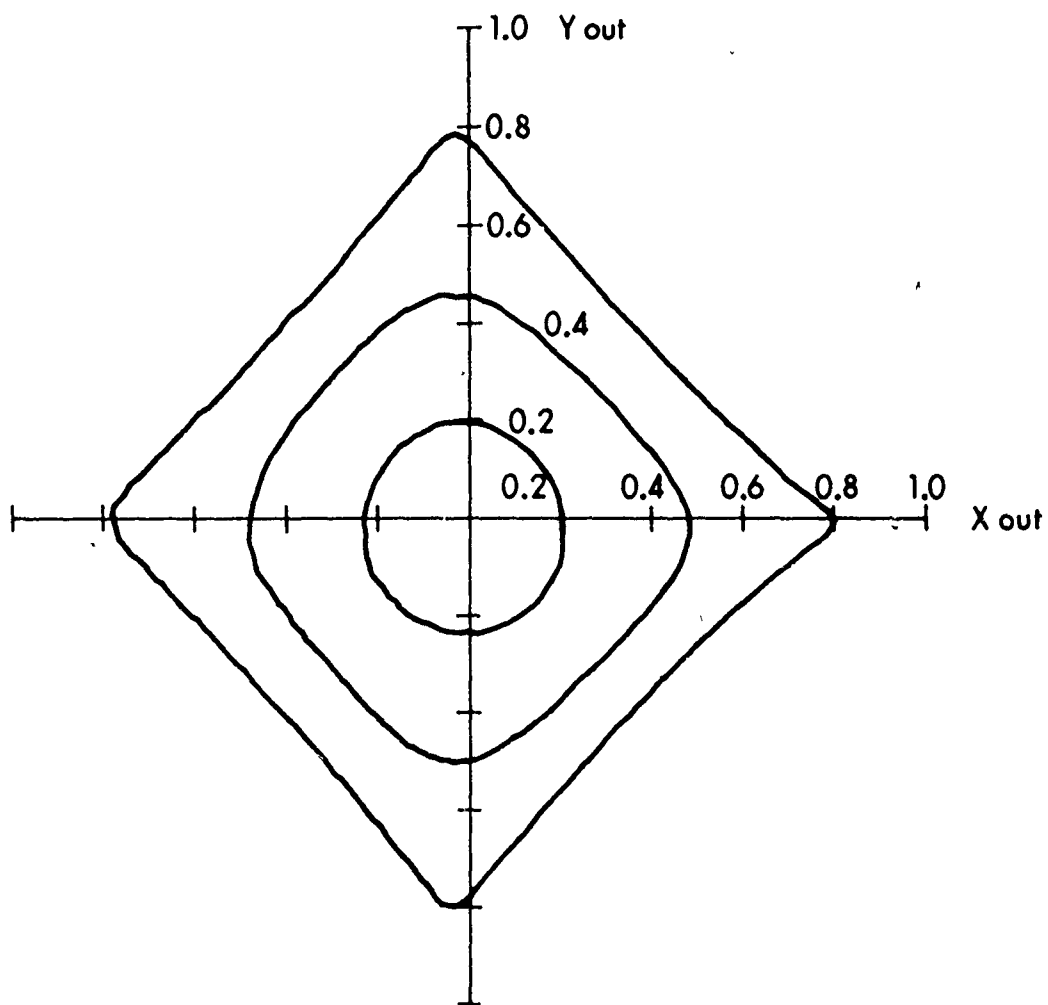


Figure 6. Plot of X_{out} and Y_{out} for a 5mm, 10mm and 15mm Circle Traced on Diode by Laser.

IV. RESULTS AND CURRENT EFFORT

Preliminary firing was done to show that indeed it is possible to make projectile in-bore measurements with an optical lever and photodiode detector instrumentation system. These firings were done with 37mm projectiles with conventional copper rotating bands. The results were encouraging, although obturation was somewhat of a problem. As mentioned in Section I, B, it is hoped that the use of plastic rotating bands will improve obturation and hence the obscuring and diffusion of the laser beam.

Once the calibration and the data reduction package are completed, it is felt that this system can provide analog measurements of transverse projectile in-bore motion of sufficient accuracy to evaluate computer code predictions and to investigate the dynamic traction history between projectile and tube. If this system is used in conjunction with an interferometer, the friction effects due to balloting can be evaluated. By taking advantage of the polarized nature of the light source, we hope to be able to retrieve information about in-bore projectile spin rate in a future effort. This would allow the evaluation of slippage of the rotating band and between a sabot and its subprojectile.

The same optical lever arm technique can be applied to the measurement of barrel motion. Barrel motion during the in-bore cycle must be known in order to correctly evaluate the in-bore motion of the projectile as these two are superimposed on any measurement made on the projectile. Accelerometers can also be used to determine barrel position during the firing cycle.

It is apparent that once the data reduction techniques are established that this instrumentation system will have many potential applications. There has been a continuing effort in the Propulsion Division of the Ballistic Research Laboratory to develop new instrumentation techniques for solving current and anticipated problems. The ability to measure the total in-bore projectile motion and the muzzle motion during the propulsion and launch cycle is an absolute requirement for studying system accuracy and the parameters that affect it.

STOCHASTIC OPTIMAL CONTROL OF
A HELICOPTER GUN TURRET

F.T. BROWN AND S.H. JOHNSON
Lehigh University
Bethlehem, Pennsylvania

TABLE OF CONTENTS

	<u>Page</u>
ABSTRACT	675
I. INTRODUCTION	676
II. SIMPLIFICATION OF THE MODEL	678
III. STOCHASTIC MODELING OF THE INPUT	680
IV. MEASUREMENT NOISE	684
V. COMPARISON OF THE SYSTEM TYPES	691
VI. RECOMMENDATIONS FOR FURTHER WORK	700
REFERENCES	703

Abstract

A preliminary comparison is made between a conventional feedback control, deterministic optimal control and stochastic optimal control for a helicopter gun turret. Stochastic command input and measurement noise is assumed in all cases, and the relevant variances and loss functions are compared. The conventional system with two states observed is found to be extremely sensitive to measurement noise, while the deterministic optimal controller with four measured states is found to be markedly less sensitive. Use of a particular Kalman filter further considerably reduces this sensitivity, while maintaining good response to the command disturbances. The advent of microprocessors should make such a system feasible, suggesting a deeper examination of the potential of stochastic optimal and sub-optimal control.

1. Introduction

This paper considers the control of a helicopter gun turret in response to gunner or other input.

The control of weapon systems in conventional helicopters and ground vehicles is based on simple classical feedback concepts. This has been appropriate, since implementation of modern optimal control theory with a limited number of measurement transducers would have required more complicated analog electronics than likely would have been cost effective. The advent of small and inexpensive microprocessors, however, portends a major change in the complexity which can be justified in controllers, suggesting a reexamination of the strategy used in the control of weapon systems.

Compensation for measurement errors is a key concept in stochastic optimal control theory. Such errors get amplified greatly in high-gain feedback loops, often causing a control variable to saturate and sometimes causing excessive noise at the output. The problem becomes more severe when some of the state variables are not measured directly. In practice, direct measurement of only a small proportion of the state variables can be justified, and the others must be fabricated by dynamic processing of the measured variables. A complete state vector must be deduced, nevertheless, for either deterministic or stochastic optimal control theory to

apply. Small measurement errors can be magnified many times in this deduction, especially if differentiation is involved. In addition, the model of the system needed in the processing inevitably contains errors which also tend to produce errors in the deduced state variables.

These errors are recognized by assuming direct contamination of the actual measurements by stochastic, usually white, noise. The Kalman filter idea then in effect weighs several successive measurements to secure a best estimate of the current state. Failure to introduce this noise can lead to serious problems in practice that would not likely show up in a simulation of the system that omits measurement noise and assumes a perfect model.

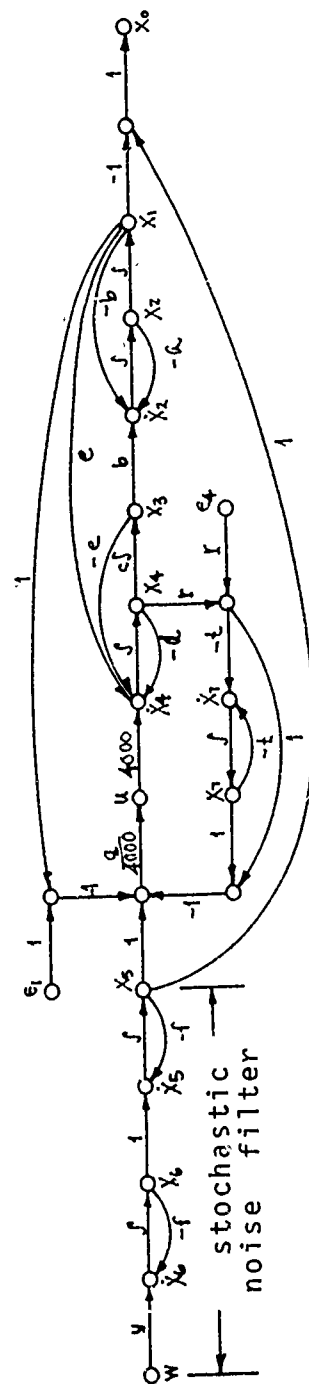
The relevant stochastic control theory also represents disturbances as having a stochastic nature (although deterministic inputs also can be used in a certain way). The spectrum of the stochastic input can be colored to represent the actual expected input, and the estimation and control logic is automatically modified in recognition of this spectrum. Theoretically, a deterministic input is incompatible with optimal control if the design is intended to be optimal for more than that particular input. Practically, stochastic inputs are at least as meaningful, and in the cases of wind gusts, for example, are likely to be more meaningful.

Loh [1] gives an eighth-order model of a conventional system which uses position and tachometer feedback. The latter involves a derivative-type filter for stability. This is then removed, leaving a seventh-order system, and an optimal feedback control is postulated using a quadratic performance index which weights the servo error, the command input and the servo drive voltage. A single control input is assumed, and the entire state vector is assumed to be measured without error. In Kasten et al. [2] the same system is considered, but the measurement of two of the state variables is replaced by a Luenberger observer, with little degradation of performance.

The introductory study presented herein comprises the following steps: simplification of the model, stochastic modeling of the input, insertion of measurement noise, comparison of the three system types, and recommendations for further work. The basic concepts for stochastic models and control are not referenced, since they are widely discussed in textbooks.

2. Simplification of the Model

The basic system model (not including a filter in the tachometer feedback path) used by Loh and Kasten et al. is of seventh order, with the eigenvalues spread over a bandwidth in excess of one-thousand to one. It seems reasonable to excise three very fast roots; to include them at an early stage gives a misleadingly complex control system. The model was thus simplified to fourth order, shown as part of the signal flow graph of Fig. 1. The (colored stochastic)



$$\begin{aligned} f &= 1.229 \\ y &= 2.72495 \\ q &= 1.605 \times 10^6 \\ r &= 9.7196 \times 10^{-5} \\ t &= 10 \end{aligned}$$

$$\begin{aligned} a &= 3.18471 \\ b &= 31847.1 \\ c &= 0.0016129 \\ d &= 7.68 \\ e &= 3.226 \times 10^6 \end{aligned}$$

- x_0 : output error
- x_1 : output position
- x_2 : output velocity
- x_3 : shaft position
- x_4 : motor velocity
- x_5 : desired output
- x_6 : variable internal to noise filter
- w : white noise input
- e_1 : position measurement noise
- e_t : tachometer measurement noise

FIG. 1 SIGNAL FLOW GRAPH OF REDUCED MODEL FOR CONVENTIONAL HELICOPTER GUN CONTROL

input is x_5 , the output is x_1 , and x_0 is the error. The frequency responses of the original and simplified systems are shown in Figs. 2 and 3, respectively.

3. Stochastic Modeling of the Input

A model for the stochastic input has been chosen by starting with the triple-ramp of Fig. 4a, which has the spectral content (Fourier transform) shown in Fig. 4b. This seems to represent the sort of motion the gunner might need, but of course the zeroes at $\omega\tau = n\pi$, $n = 1, 2, \dots$, are not realistic. A filter which gives roughly the same decay as ω increases, without these zeroes, is given by

$$H(s) = \frac{2f^3/2}{s^2 + 2fs + f^2} \quad ; \quad f = 1.229/\tau$$

The numerator is chosen so that when unity Gaussian white noise (autocorrelation $\delta(t)$) is inserted into the filter, using $\tau = 1$ second, the variance of the output is unity:

$$\text{variance of output} = \frac{1}{2\pi} \int_{-j\infty}^{j\infty} H(s)H(-s)ds = 1$$

A plot of the function $|H(j\omega)|$, scaled to match the zero-frequency value of the triple-ramp characteristic, is also shown in Fig. 4b. This is the square root of the power density spectrum. The resulting second-order filter is shown in Fig. 1, with w as its input and x_5 as its output.

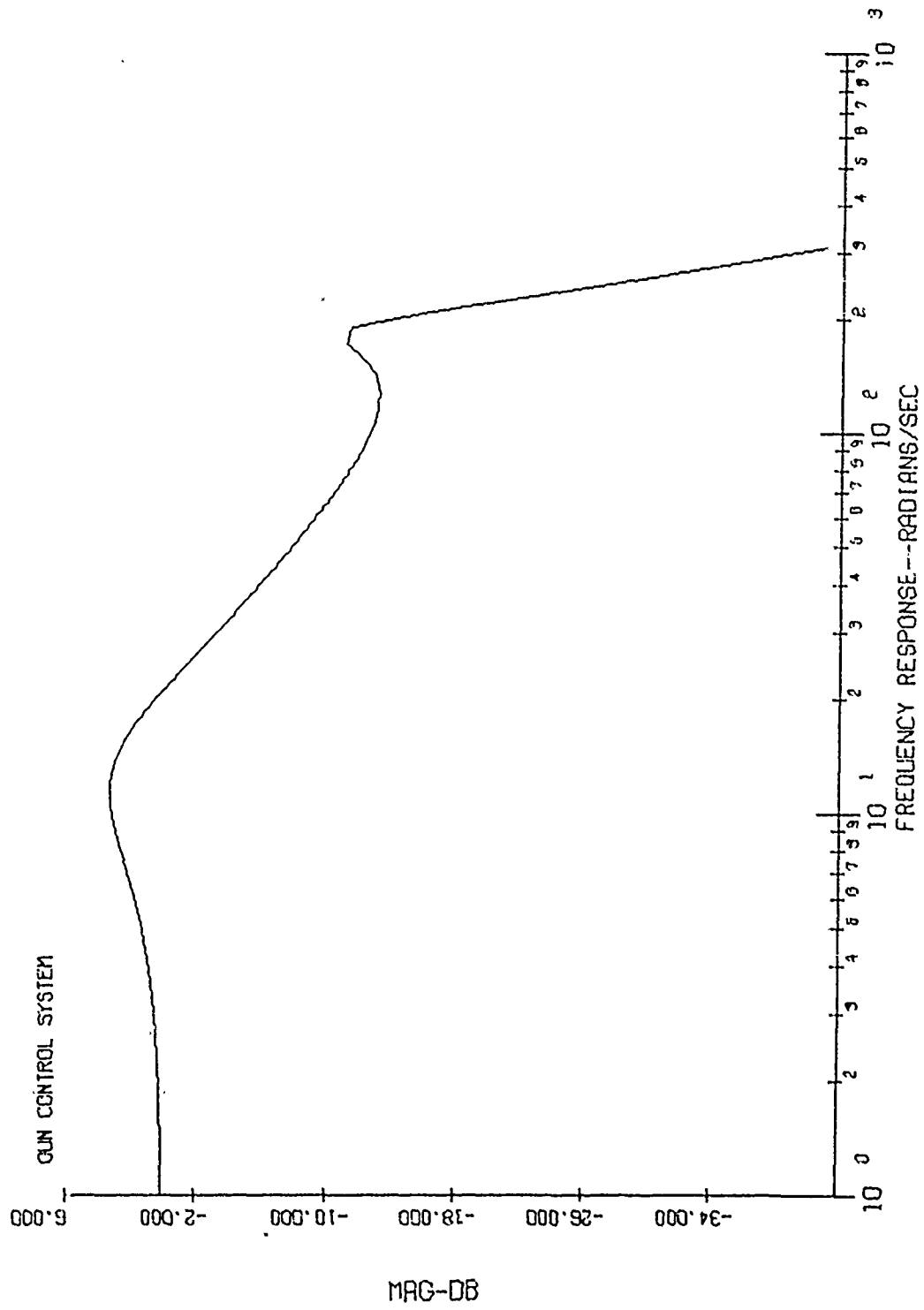


FIG. 2 GUN POSITION RESPONSE TO GUNNER COMMAND FOR SEVENTH-ORDER MODEL

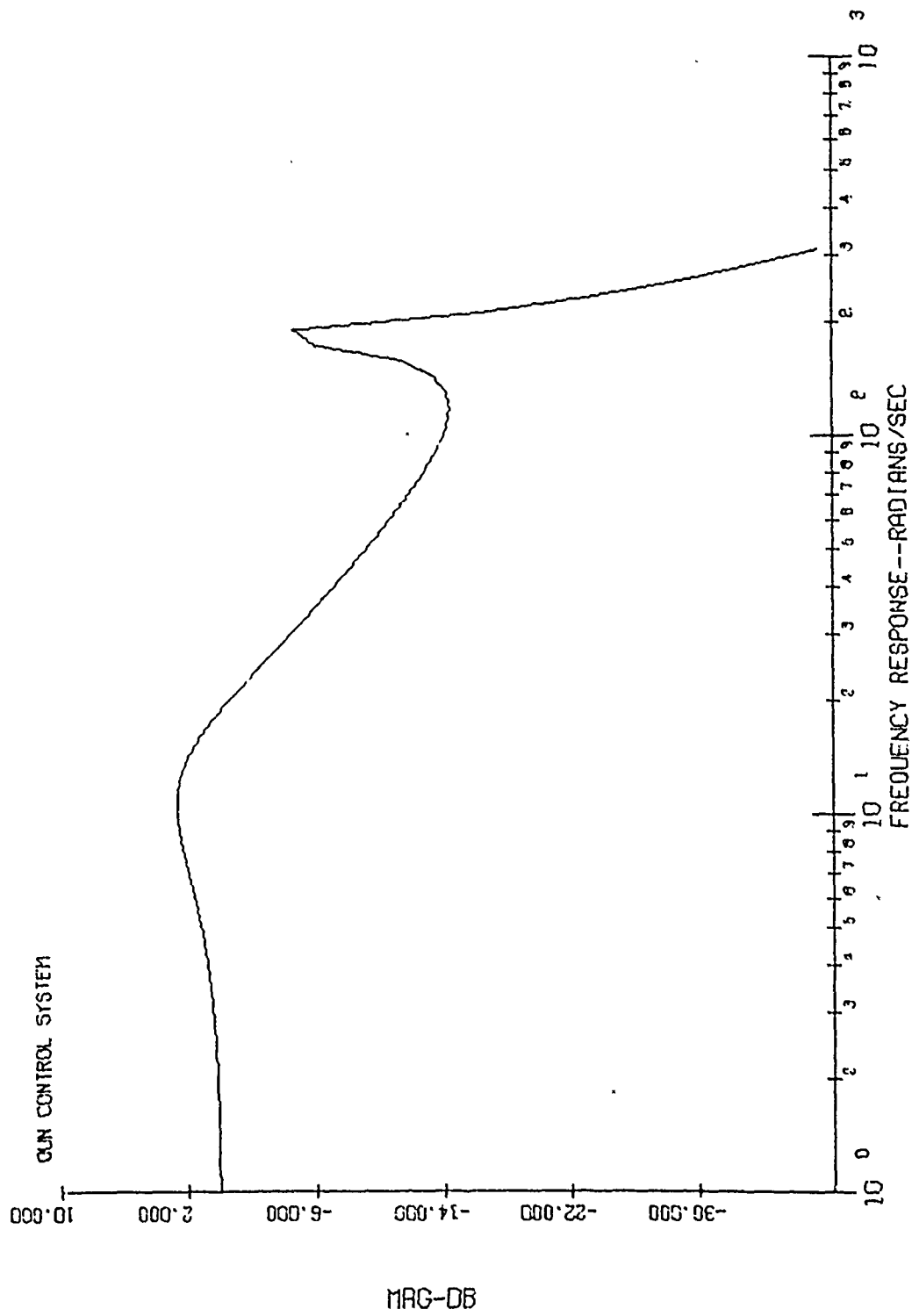
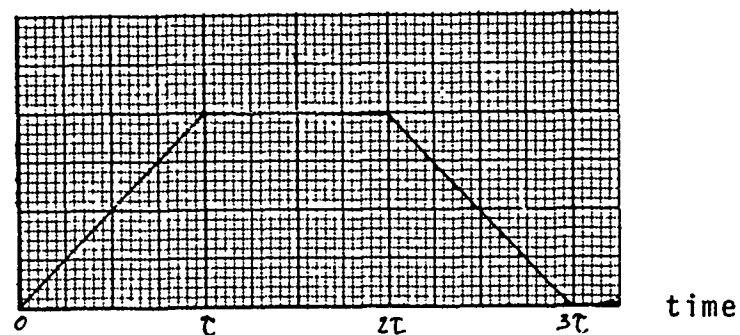
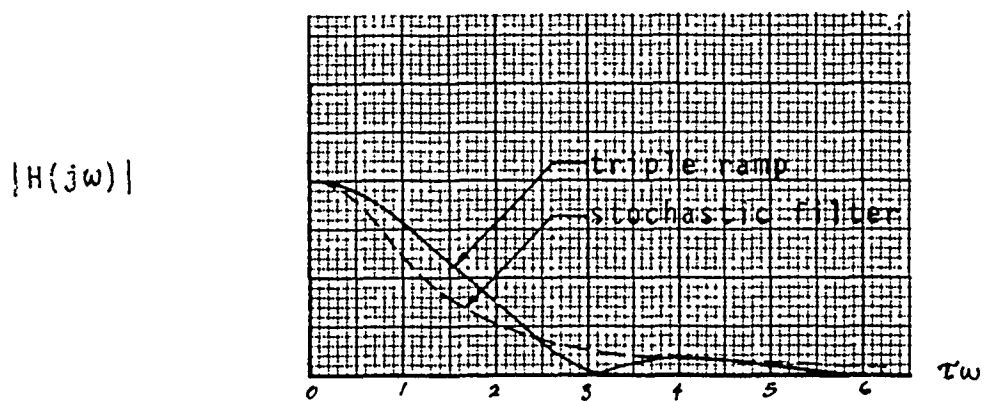


FIG. 3 GUN POSITION RESPONSE TO GUNNER COMMAND FOR FOURTH-ORDER MODEL



(a) triple-ramp



(b) frequency content (square root of power density spectrum)

FIG. 4

DEVELOPMENT OF FILTER FOR COLORED STOCHASTIC INPUT

Substitution of square-waves for the triple-ramp would give a first-order rather than a second-order filter, and perhaps should be used also. The $H(s)$ given above is used exclusively in what follows, nevertheless.

White noise which is very nearly Gaussian can be generated by superimposing just a few random numbers which are uniformly distributed over the same range. (The difference between the probability distribution for the sums of only four such numbers and the Gaussian distribution never exceeds 3.6% of the maximum value, for example.) A simulation of the conventional helicopter system (tenth order system, including two orders for the stochastic input filter and one order for the tachometer feedback) is shown in Fig. 5.

4. Measurement Noise

A white noise e_4 is superimposed on the tachometer signal, and a white noise e_1 in the position feedback, as shown in Fig. 1. Similar white noises are also superimposed on all the measurements of the other two systems. Since all inputs are independent, the variance of any variable is the sum of the variances produced by the individual inputs.

To make a comparison between the systems, it is necessary to choose the magnitudes of the white noise inputs. The tentative assumption made is that each measurement of x_1, \dots, x_4

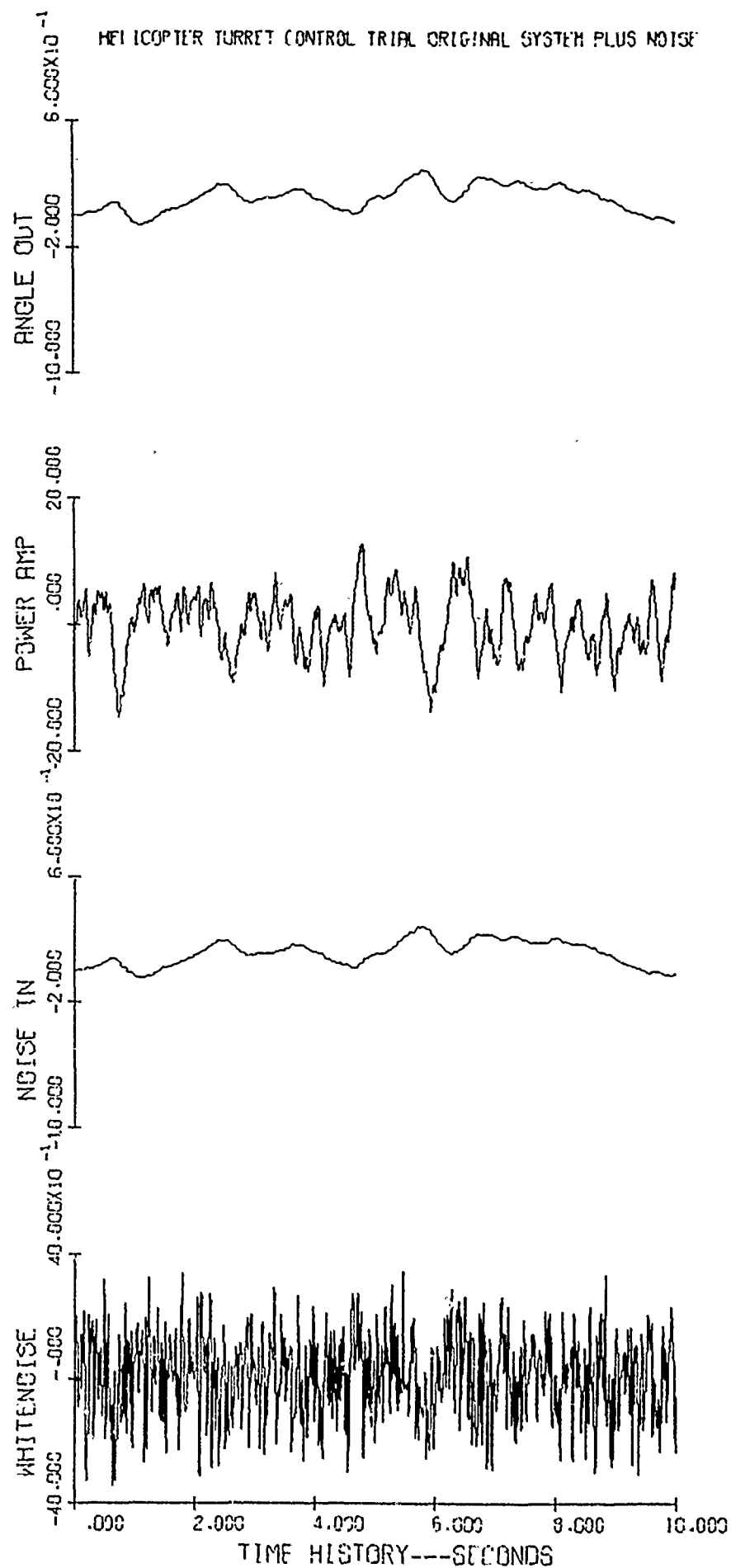


FIG. 5
685

is contaminated by a noise which has 1% of the variance of the measurement were there no noise present. (These noises then are not exceptionally small, since their standard deviations are 10% of those for the signals.)

The variance of white noise is infinity, but in fact the higher frequencies contribute little to any of the state variables, and especially the output which is of key interest, because of the filtering action of the system. A bandwidth of the system, b_0 , can be defined so that, for the system with x_5 or e_1 as the input and x_1 as the output, which has unity D.C. gain, the variance of the output response to the unbanded white noise input equals the variance of the white noise input over the bandwidth:

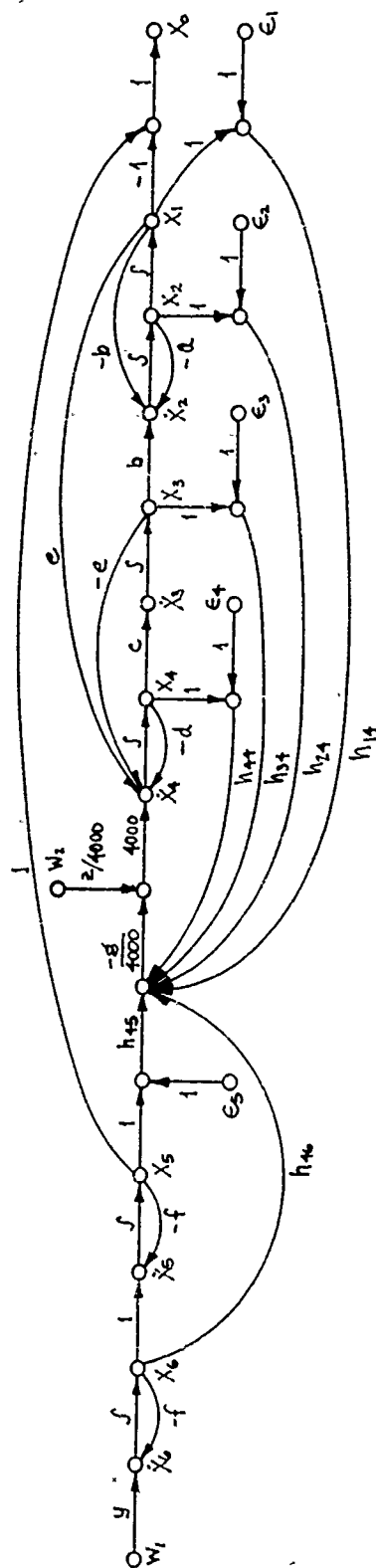
$$b_0 = \text{var}(x_1) \text{ for unity white noise input } e_1 = 18.54 \text{ s}^{-1}$$

The white noises e_4 and e_1 then are chosen to have the same variance, over the bandwidth b_0 , that x_4 and x_1 , respectively, have over the infinite bandwidth. These are given in the third column of Table 1.

The deterministic control system (but with stochastic inputs, of course) is shown in Fig. 6. Every state variable (x_1, x_2, x_3, x_4) and the input (x_5) is assumed to be measured; the sixth variable (x_6) is discussed below. The bandwidth of this system is 66.95 radians/sec., computed with the appropriate causalities inverted so the path h_{46} is included. The

index i of variable	Conventional System		Optimal Control Systems		
	Var (x_i) for unity input w_i	magnitude V_i of white noise e_i	Deterministic var (x_i) for unity input w_i	Both magnitude V_i of white noise e_i	Stochastic var (x_i) for unity white noise w_i
1	1.0166	5.483×10^{-4}	0.9979	1.4905×10^{-4}	0.9992
2	1.6975	-	1.5556	2.3235×10^{-4}	1.6553
3	1.0165	-	0.99774	1.4903×10^{-4}	0.9903
4	6.500×10^5	350.60	5.9153×10^5	88.354	6.0180×10^5
5	1.0000	-	1.0000	1.4936×10^{-6}	1.0000

Table 1 Variances of State Variables in Response to Command Input, and Resulting Assumed Measurement Noise



Additional coefficients to Fig. 5: $gh_{14} = 1.4524 \times 10^4$

$$gh_{44} = 16.594$$

$$gh_{24} = 1.5319 \times 10^3$$

$$gh_{45} = -1.5938 \times 10^5$$

$$gh_{34} = 1.6437 \times 10^5$$

$$gh_{46} = -1.4853 \times 10^4$$

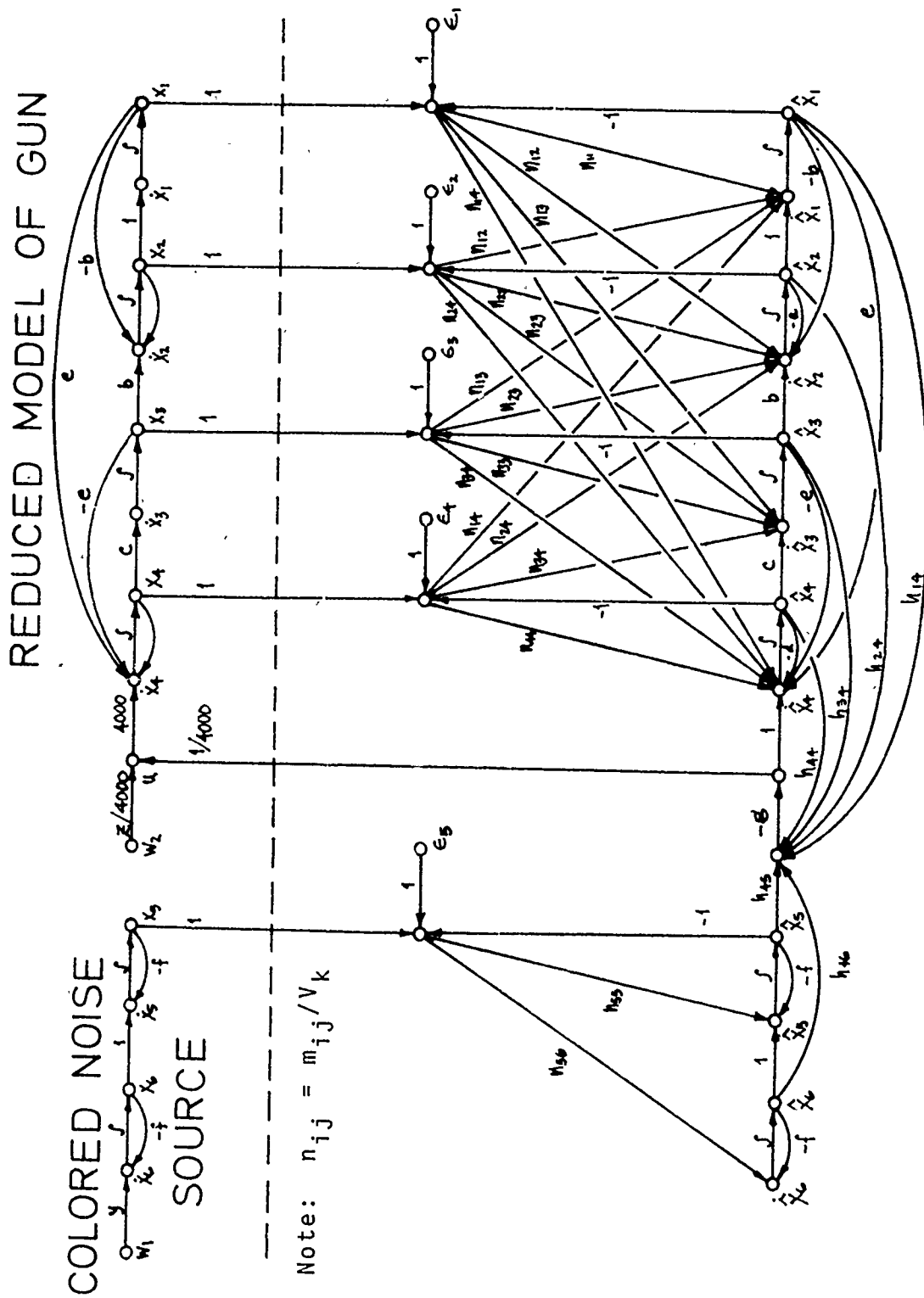
NOTE: The signal through h_{46} must be generated by an observer, not shown.

FIG. 6 DETERMINISTIC OPTIMAL CONTROL WITH STOCHASTIC INPUT

resulting amplitudes of the white measurement noises e_1, e_2, e_3, e_4 are shown in the fifth column of Table 1.

The stochastic optimal control system is shown in Fig. 7. The state variables (x_1, x_2, x_3, x_4) and the input (x_5) are assumed to be measured. The same values of the amplitudes of the white noises e_1, \dots, e_4 were used as deduced for the deterministic optimal control system. This seems reasonable in view of the similarity of the respective variances of x_1, \dots, x_5 , and precluded an iterative procedure. To derive the Kalman filter, some value for the amplitude of the white noise e_5 must also be assumed. In this special case the variance over the bandwidth of 66.95 s^{-1} was chosen at the very small value of 0.01% of the variance of x_5 ; the result is the bottom entry of the fifth column of Table 1.

The variances of x_0 and any of the state variables can be computed directly, without simulation, from the transfer functions between a white noise input and the output of interest. The transfer function of interest is substituted for $H(s)$ in the integral given in Section 3 above. General results are given for up to tenth-order systems by Newton et al, [3], and a Fortran algorithm is given by Aström [4], who also gives an equivalent algorithm for discrete-time systems. The transfer functions were computed in polynomial form from the state variable formulation using the NASA-Dryden program CONTROL presented by Edwards [5].



KALMAN FILTER AND CONTROLLER

FIGURE 7 SIGNAL FLOW GRAPH OF STOCHASTIC OPTIMAL CONTROL SYSTEM

5. Comparison of the System Types

Optimal control minimizes a loss function or performance index. The index used by Loh, when transformed to the reduced order system, gives virtually $\int (0.01u^2 + 20x_0^2)dt$. This is assumed herein, also. The relevant backward matrix Ricatti equation gives six relevant feedback coefficients: four from the state variables, one from the effective excitation of the system, x_5 , and one from inside the stochastic filter, x_6 . In a Kalman filter these six states are estimated, using a sixth order model with inputs from whichever of the variables x_1, \dots, x_5 (but certainly not x_6) are deemed measurable, despite contamination with measurement noise.

In the deterministic optimal system, the state x_6 would have to be fabricated, for example with a Luenberger observer. For the first of two schemes a perfect observation is assumed, which is theoretically possible if measurement noise is discounted. It should be recognized that this gives an unrealistic advantage to the system, however. For the second scheme, discussed below, a Kalman-type filter limited to the variables x_5 and x_6 is employed.

The stochastic optimal control system with complete Kalman filter is given by the vector equations

$$u = BG \hat{x}$$

$$\dot{\hat{x}} = K[c(x - \hat{x}) + e(t)] + A\hat{x} + u$$

$$\dot{x} = Ax + u + B_w w$$

$$K = MC^T V^{-1}$$

For the purposes of simulation this is better recast as

$$\frac{d}{dt} \begin{bmatrix} \tilde{x} \\ x \end{bmatrix} = \begin{bmatrix} \frac{A-BG}{0} & -\frac{BG}{A-KC} \end{bmatrix} \begin{bmatrix} \tilde{x} \\ x \end{bmatrix} + \begin{bmatrix} B_w^w \\ B_w^w - Ke \end{bmatrix}$$

$$\tilde{x} = x - \hat{x}$$

in which

$$A = \begin{bmatrix} 0 & 1 & 0 & 0 & 0 & 0 \\ -b & -a & b & 0 & 0 & 0 \\ 0 & 0 & 0 & c & 0 & 0 \\ e & 0 & -e & -d & 0 & 0 \\ 0 & 0 & 0 & 0 & -f & 1 \\ 0 & 0 & 0 & 0 & 0 & -f \end{bmatrix}$$

$$BG = g \begin{bmatrix} 0 & 0 & 0 & 0 & 0 & 0 \\ 0 & 0 & 0 & 0 & 0 & 0 \\ 0 & 0 & 0 & 0 & 0 & 0 \\ h_{14} & h_{24} & h_{34} & h_{44} & h_{45} & h_{46} \\ 0 & 0 & 0 & 0 & 0 & 0 \\ 0 & 0 & 0 & 0 & 0 & 0 \end{bmatrix}$$

$$KC = \begin{bmatrix} M_{11}/V_1 & M_{12}/V_2 & - & - & - & -M_{15}/V_5 & 0 \\ M_{12}/V_1 & & & & & & \\ - & - & - & - & - & & \\ - & - & - & - & - & & \\ - & - & - & - & - & & \\ M_{16}/V_1 & - & - & - & - & -M_{56}/V_5 & 0 \end{bmatrix}$$

$$B_w^t = [0 \ 0 \ 0 \ z \ 0 \ y] \quad ; \quad w^t = [w_1 \ w_2]; \quad z = 117.4$$

The non-controller part of the system differs from the usual textbook system in that it is divided into two parts, the input filter and the turret system proper. The turret system part is not excited by anything except the output of the controller, and is replicated in the Kalman filter.

For the moment assume w_2 is zero. If the system is started with $x = \hat{x}$, the ideal controller has $m_{ij} = 0$ for all $i \leq 4, j \leq 4$. This follows mathematically since then $x = \hat{x}$ for all time, and the measurement errors have no consequence since, in effect, no measurements are made anyway. If the system is started with $x \neq \hat{x}$, the ideal controller starts with m_{ij} equaling the covariance matrix of the initial state, and subsequently relaxes asymptotically toward zero.

The Kalman filter for the stochastic filter part of the system makes \hat{x}_5 reproduce x_5 increasingly well as V_5 is reduced and m_{55} , m_{66} and m_{56} increased. The limit of zero V_5 and infinite m_{55} , m_{66} and m_{56} gives $\hat{x}_5 = x_5$ and $\hat{x}_6 = x_6$. Since V_5 was neglected in evaluating the conventional and the first version of the deterministic optimal control system, and in view of the preceding paragraph, the ideal stochastic optimal control system gives the same variances for x_0 and u with measurement noise as the deterministic optimal control system gives without measurement noise. This ideal result compares very favorably, but of course is suspect for practical implementation of a real system.

A real system is of infinite order, and its characteristics vary with temperature, wear, etc. The model built into the Kalman filter is not exact, consequently, and its response inevitably differs somewhat from the system it attempts to represent. In addition, the real system is subjected to small disturbances which are not directly felt by the Kalman filter, causing additional filter divergence. The practical result of these differences is that the mathematically ideal behavior must be relaxed to permit measurements of the state vector to be felt by the Kalman filter, but not so much that the measurement noise has any more deleterious effect than necessary.

Carrying this out represents the art of the linear quadratic stochastic optimal control problem. Athans [6] gives a practical description of the trade-offs involved. The concept of system sensitivity becomes extremely important.

To demonstrate a simple technique we superimpose white noise onto the control variable u , as represented in Fig. 7 by w_2 . This noise could be thought of as a substitute for parameter errors, as well as its more direct interpretation. Following an approach similar to those for the other control systems, we let the variance of this noise, over the bandwidth $b_0 = 66.95$ rad/sec., equal 1% of the variance of u without this noise. Therefore, if w_2 is unity white noise,

$$\frac{z}{4000} = \sqrt{\frac{0.01 * 5.77}{66.95}} = 0.02936$$

The resulting steady-state values of the matrix M are

$$\begin{bmatrix} 8.2523 \cdot 10^{-5} & 6.2396 \cdot 10^{-5} & 8.2474 \cdot 10^{-5} & 3.8424 \cdot 10^{-5} & 0 & 0 \\ 6.2396 \cdot 10^{-5} & 2.8203 \cdot 10^{-3} & 6.3259 \cdot 10^{-5} & 5.1088 \cdot 10^{-1} & 0 & 0 \\ 8.2474 \cdot 10^{-5} & 6.3259 \cdot 10^{-5} & 8.2488 \cdot 10^{-5} & 3.8963 \cdot 10^{-2} & 0 & 0 \\ 3.8424 \cdot 10^{-2} & 5.1088 \cdot 10^{-1} & 3.8963 \cdot 10^{-2} & 4.4857 \cdot 10^{-2} & 0 & 0 \\ 0 & 0 & 0 & 0 & 9.6121 \cdot 10^{-5} & 3.2102 \cdot 10^{-3} \\ 0 & 0 & 0 & 0 & 3.2102 \cdot 10^{-3} & 2.1443 \cdot 10^{-1} \end{bmatrix}$$

The zero elements in the matrix result from the decoupling between the two parts of the system. The values for m_{35} , m_{56} and m_{66} follow from the value of V_5 discussed earlier, and cause the contributions to the variances of x_0 and u to increase from their ideal values.

The second scheme for the deterministic optimal controller employs that part of the Kalman filter which uses m_{55} , m_{56} , and m_{66} . Now, since e_5 can be incorporated, a meaningful comparison can be made with the stochastic optimal control system.

To compare the various systems objectively it is necessary to find the contributions to the variance of u from the relevant noises e_1, \dots, e_5 . This can be done in straightforward fashion for the stochastic optimal control system, but these contributions are infinite in other cases. To achieve meaningful results in these cases the noises are assumed to be band-limited with bandwidth b_0 , and the loops not touched by the path from the input to the output were not considered. This approximation is the same, for all except the response of the conventional system to e_4 , as 1% of the relevant variance x_1, \dots, x_4 found for the input w , multiplied by the square of the gain from the relevant noise input to the output, u . The path from

e_4 to u on the conventional system has some dynamics, and consequently was computed by integrating the appropriate integral of the form given in Section 3 over the finite limits $-b_0$ to $+b_0$.

The signal w_2 also is inserted in similar fashion in all cases, to permit a more realistic comparison.

The overall results for the three systems are compared in Table 2. The conventional system is seen to be quite unacceptable for the noise amplitudes assumed. The measurement of the output position is multiplied by so large a loop gain that the greatly amplified measurement noise saturates the actual power amplifier most of the time. The model neglects this saturation, and predicts a rather large output variance due to the noise. The noise e_4 in the tachometer measurement produces a contribution to the variance of u which would be modestly significant were it not greatly overshadowed by the effect of e_1 . Its effect on the variance of x_0 is almost negligible. These effects of e_4 are relatively small because the feedback gain is relatively small.

The first version of the deterministic optimal control system assumes perfect knowledge of x_6 , which is unrealistic. This system displays vastly less sensitivity to the measurement noise, both in the control and output error variables. This improvement presumably follows not so much from the use of the criterion for optimality as from the use of four instead

Input	Conventional with $e_5 = 0$		Deterministic Optimal with $e_5 = 0$		Deterministic Optimal with $e_5 \neq 0$ and observer		Stochastic Optimal* with $e_5 \neq 0$	
	Var (u)	var (x_0)	var(u)	var(x_0)	var(u)	var(x_0)	var(u)	var(x_0)
w_1	5.62	0.00149	5.77	695.00×10^{-6}	6.08	1923.9×10^{-6}	11.10	2234.2×10^{-6}
w_2	0.06	0.00000	0.06	2.40×10^{-6}	0.06	2.40×10^{-6}	0.058	7.8×10^{-6}
e_1	1636.74	0.01017	0.13	5.47×10^{-6}	0.13	5.47×10^{-6}	0.002	19.50×10^{-6}
e_2	-	-	0.002	0.10×10^{-6}	0.002	0.10×10^{-6}	0.003	9.06×10^{-6}
e_3	-	-	16.85	700.16×10^{-6}	16.85	700.16×10^{-6}	0.002	19.51×10^{-6}
e_4	1.32	0.00004	0.10	4.23×10^{-6}	0.10	4.23×10^{-6}	0.003	10.68×10^{-6}
e_5	-	-	-	-	1.27	23.27×10^{-6}	0.15	23.20×10^{-6}
sum	1643.74	0.01170	22.95	0.001407	24.49	0.002660	11.32	0.002324
Loss Function	16.437 16.67	0.2340	0.2291 0.2573	0.02815	0.2449 0.2981	0.05319	0.1132 0.1597	0.04548

*Note: The stochastic optimal system gives in the limit of $e_5 = 0$: $\text{var}(u) = 5.83$, $\text{var } x_0 = 6.974 \times 10^{-4}$,
Loss Function = 0.07225

TABLE 2 OVERALL COMPARISON OF SYSTEMS

of two measurements for feedback. The greatest source of noise on both the output error and the control variable is on the measurement of x_3 , a shaft angle. Note also that if measurement noise is neglected altogether, this system produces about half of the error variance as the conventional system, with about the same amplitude of the control variable.

The second version of the deterministic optimal control does not assume knowledge of x_6 , but uses x_5 contaminated by noise e_5 as the input to an optimal observer to give \hat{x}_5 and \hat{x}_6 as approximations of x_5 and x_6 , respectively. The performance of this more realistic model is consequently inferior to that of the first version, but is still greatly superior to the conventional system and is the proper basis of comparison for the stochastic optimal control system, which has an identical observer for \hat{x}_5 and \hat{x}_6 .

The stochastic optimal control system is seen to improve its performance, as defined by the loss function, by reducing and balancing the sensitivities of u and x_0 to the various measurement noises. It does this at the expense of a modest increase in the variance of x_0 when no noise is present.

An additional noise of significant magnitude could be inserted into the middle of the stochastic filter (at the \dot{x}_5 junction) to represent errors in the stochastic filter model itself. This would appropriately reduce the significance of \hat{x}_6 .

Stochastic optimal control appears to offer a significant potential for improvement in the precision of helicopter gun turrets and other weapons systems. But this sophisticated tool cannot reliably be applied in a disjoint manner; the uncertainties in the structure, parameters and the noise levels should be studied carefully, in concert with a sensitivity study of the system.

6. Recommendations for Further Work

The amplitudes of the noise in actual measurements and the spectral characteristics of real input disturbances should be examined much more carefully, and the calculations repeated in consequence. The system model then should be returned to seventh order, with no corresponding change in the controller, to assure that what becomes literally a sub-optimal controller does not produce serious filter divergence. A sensitivity study in which errors are assumed in the parameters of the system or the filter also is highly recommended, since an overly sensitive optimal control system can be distinctly inferior to a distinctly sub-optimal but insensitive control system.

Measurement of fewer than four state variables likely would be advantageous. It also may become advantageous to assume perfect measurement of one or more state variables, and consequently reduce the order of the Kalman filter. Asher and Reeves [7] give equations based on covariance analysis techniques which allow the evaluation of filters of reduced state.

Practical servomotors are rate-limited, and the amplifiers which drive them saturate. Linear control theory is forced to recognize these nonlinearities by penalizing large control signals so heavily that saturation rarely occurs. This is an artificial penalty, however; quicker response to small disturbances typically results from permitting saturation to occur frequently.

A suggested method for accommodating nonlinearities approximately into a stochastic optimization procedure is through the use of random-input describing functions (RIDF's). Taylor et al. [8] give a list of recent references. The general approach is discussed by Gelb [9] and by Atherton [10], who includes combination deterministic-random describing functions and discussions of alternate methods.

Microprocessor implementation of a Kalman-type filter operates in the discrete time mode, and use of discrete-time algorithms for the Kalman filter is more accurate than use of algorithms which simply approximate the continuous-time algorithms. Use of the Kalman pre-filter of Womble and Potter [11] also may permit a much longer Δt without excessive degradation of performance. The optimum Δt is a key question.

The overall results can be examined by simulations, including both deterministic and random disturbances. Some comparison with the measured behavior of an actual system is highly desirable.

The helicopter turret system interacts intimately with its surroundings, particularly for burst firing. Any comprehensive investigation must account for known or measurable periodic disturbances and, most importantly, the overall dynamics of the helicopter particularly in response to recoil forces.

Acknowledgements

This work was funded partly under Scientific Services Agreement DAAG 29-76-D-0100, D.O. No. 0252, with the Battelle Columbus Laboratories. Lehigh University provided the computer time.

References

1. N.K.Loh, "Optimal Control of a Helicopter Turret Control System", technical report, Div. of Information Eng., U. of Iowa, Iowa City, prepared for Gen. Th. J. Rodman Laboratory Rock Island Arsenal, Rock Island, Ill., AD A012 312, Jan. 1975.
2. R.E. Kasten, J. Murdock, R.B. Walljasper, A. Hauser and N.K. Loh, "Helicopter Turret Control with Inaccessible State Variables", presented at 7th Annual Pittsburgh Conference on Modeling and Simulation, 1976.
3. G.C. Newton, Jr., L.A. Gould, and J.F. Kaiser, Analytical Design of Linear Feedback Controls, J. Wiley, N.Y., 1957.
4. K.J. Astrom, Introduction to Stochastic Control Theory, Academic Press, N.Y., 1970.
5. J.W. Edwards, "A Fortran Program for the Analysis of Linear Continuous and Sampled-Data Systems", NASA Dryden Flight Research Center Document NASA TM X-56038, January, 1976.
6. M. Athans, "The Role and Use of the Stochastic Linear-Quadratic-Gaussian Problem in Control System Design", IEEE Transactions on Automatic Control, v AC-16 n 6 Dec. 1971 p. 529-552.
7. R.B. Asher and R. M. Reeves, "Performance Evaluation of Suboptimal Filters", IEEE Transactions of Aerospace and Electronic Systems, V. AES-11, N.3, May 1975, pp. 400-404.
8. J.H. Taylor, C.F. Price, J. Siegel, and A. Gelb, "Statistical Analysis of Nonlinear Stochastic Systems via CADET", paper presented at Winter Annual Meeting, ASME, Dec. 1976 with copies available from the Analytic Sciences Corp., Reading, Mass.
9. A. Gelb, (ed.), Applied Optimal Estimation, MIT Press, Cambridge, Mass., 1974.
10. D.P. Atherton, Nonlinear Control Engineering, Van Nostrand Reinhold, N.Y., 1975.
11. M.E. Womble and J.E. Potter, "A Prefiltering Version of the Kalman Filter with New Numerical Integration Formulas for Ricatti Equations", ibid, V. AC-20, N. 3, June 1975, pp. 378-381.

DISTRIBUTION

Copies

A. Department of Defense

Defense Documentation Center
ATTN: TIPDR
Cameron Station
Alexandria, VA 22314 12

B. Department of the Army

Commander
US Army Materiel Development and Readiness Command
ATTN: DRCRD-E 1
DRCRP-I 1
DRCQA-E 1
5001 Eisenhower Avenue
Alexandria, VA 22333

Commander
US Army Materiel Development and Readiness Command
Scientific and Technical Information Team - Europe
ATTN: DRXST-STL (Dr. Richard B. Griffin)
APO New York 09710 1

Commander
US Army Armament Materiel Readiness Command
ATTN: DRSAR-PPI-K 1
DRSAR-PPI-WW 1
DRSAR-RDP 1
DRSAR-SC 1
DRSAR-QAE 1
Rock Island, IL 61201

Director
US Army Materials and Mechanics Research Center
ATTN: DRXMR-M
Watertown, MA 02172 1

Director
US Army Maintenance Management Center
ATTN: DRXMD-A
Lexington, KY 40507 1

Commander US Army Electronics Command ATTN: DRSEL-PP/I/IM Fort Monmouth, NJ 07703	1
Commander US Army Missile Command ATTN: DRSMI-IIE DRSMI-PRT Redstone Arsenal, AL 35809	1 1
Commander US Army Tank-Automotive Command ATTN: DRSTA-RK DRSTA-RCM.1 Warren, MI 48090	1 1
Commander US Army Aviation Systems Command ATTN: DPSAV-ERE P. O. Box 209 St. Louis, MO 63166	1
Commander US Army Troop Support Command ATTN: DRSTS-PLC 4300 Goodfellow Blvd. St. Louis, MO 63120	1
Commander Ballistic Missile Defense Systems P. O. Box 1500 Huntsville, AL 35804	1
Project Manager Munition Production Base Mod Picatinny Arsenal Dover, NJ 07801	1
Commander Harry Diamond Laboratories ATTN: DRXDO-RCD 2800 Powder Mill Road Adelphi, MD 20783	1

Commander	
US Army Natick Research and Development Command	
ATTN: DRXNL-EQ	
Kansas Street	
Natick, MA 01762	1
Commander	
US Army Air Mobility R&D Labs	
ATTN: SAVDL-ST	
Fort Eustis, VA 23604	1
Commander	
Rock Island Arsenal	
ATTN: SARRI-PE	1
SARRI-RS (Mr. V. Long)	1
Rock Island, IL 61201	
Commander	
Watervliet Arsenal	
ATTN: SARWV-PPP-WP	1
SARWV-PPI-LAJ	1
SARWV-QA	1
Watervliet, NY 12189	
Commander	
Picatinny Arsenal	
ATTN: SARPA-MT-C	1
SARPA-QA-T-T	1
SARPA-C-C	1
Dover, NJ 07801	
Commander	
Frankford Arsenal	
ATTN: SARFA-T1000	1
SARFA-QA	1
SARFA-N5400	2
Bridge & Tacony Streets	
Philadelphia, PA 19137	
Commander	
Edgewood Arsenal	
ATTN: SAREA-QA	
Aberdeen Proving Ground, MD 21010	1

Director US Army Industrial Base Engineering Activity ATTN: DRXIB-MT Rock Island Arsenal Rock Island, IL 61201	2
Director USDARCOM Intern Training Center ATTN: DRXMC-ITC-PPE Red River Army Depot Texarkana, TX 75501	1
Commander US Army Tropic Test Center ATTN: STETC-MO-A (Technical Library) APO New York 09827	1
Commander Anniston Army Depot ATTN: DRXAN-DM Anniston, AL 36201	1
Commander Corpus Christi Army Depot ATTN: DRXAD-EFT Corpus Christi, TX 78419	1
Commander Fort Wingate Depot Activity ATTN: DRXFW-M Gallup, NM 87301	1
Commander Letterkenny Army Depot ATTN: DRXLE-M DRXLE-MM Chambersburg, PA 17201	1 1
Commander Lexington-Blue Grass Army Depot ATTN: DRXLX-SE-I Lexington, KY 40507	1

Commander New Cumberland Army Depot ATTN: DRSAR-ISS-A New Cumberland, PA 17070	1
Commander Pueblo Army Depot ATTN: DRXPU-ME DRXPU-SE Pueblo, CO 81001	1 1
Commander Red River Army Depot ATTN: DRXRR-MM Texarkana, TX 75501	1
Commander Sacramento Army Depot ATTN: DRXSA-MME-LB Sacramento, CA 95813	1
Commander Seneca Army Depot ATTN: DRXSE-SE Romulus, NY 14541	1
Commander Sharpe Army Depot ATTN: DRXSH-SO DRXSH-M Lathrop, CA 95330	1 1
Commander Sierra Army Depot ATTN: DRXSI-DQ Herlong, CA 96113	1
Commander Tobyhanna Army Depot ATTN: DRXTO-ME-B Tobyhanna, PA 18466	1

Commander	
Tooele Army Depot	
ATTN: DRXTE-SEN	1
DRXTE-EMD	1
Tooele, UT 84074	
Commander	
Badger Army Ammunition Plant	
Baraboo, WI 53913	1
Commander	
Holston Army Ammunition Plant	
Kingsport, TN 37660	1
Commander	
Indiana Army Ammunition Plant	
Charleston, IN 47111	1
Commander	
Iowa Army Ammunition Plant	
Burlington, IA 52602	1
Commander	
Joliet Army Ammunition Plant	
Joliet, IL 60434	1
Commander	
Lone Star Army Ammunition Plant	
Texarkana, TX 75501	1
Commander	
Louisiana Army Ammunition Plant	
P. O. Box 30058	
Shreveport, LA 71161	1
Commander	
Milan Army Ammunition Plant	
Milan, TN 38358	1
Commander	
Newport Army Ammunition Plant	
Newport, IN 47966	1
Commander	
Radford Army Ammunition Plant	
Radford, VI 24141	1

Commander Ravenna Army Ammunition Plant Ravenna, OH 44266	1
Commander Riverbank Army Ammunition Plant Riverbank, CA 95367	1
Commander Scranton Army Ammunition Plant Scranton, PA 18501	1
Commander Sunflower Army Ammunition Plant Lawrence, KS 66044	1
Commander Twin Cities Army Ammunition Plant New Brighton, MN 55112	1
Commander Volunteer Army Ammunition Plant ATTN: SARVO-T P. O. Box 6008 Chattanooga, TN 37401	1
C. <u>Department of the Navy</u>	
Officer in Charge US Navy Materiel Industrial Resources Office ATTN: Code 227 Philadelphia, PA 19112	1
D. <u>Department of the Air Force</u>	
Commander Air Force Materials Laboratory ATTN: LTE	1
LTM	1
LTN	1
Dayton, OH 45433	

E. Conference Participants with addresses

Director
US Army Air Mobility Laboratory
ATTN: SAVDL-AS (Mr. William L. Andre)
Ames Research Center 207-5
Moffett Field, CA 94035 1

Commander
US Army Armament Materiel Readiness Command
ATTN: DRSAR-ASI (Mr. George T. Balunis, Jr.)
Rock Island, IL 61201 1

Mr. C. M. Christensen
Code 523
Naval Ordnance Station
Indian Head, MD 20640 1

Mr. P. A. Cox
Southwest Research Institute
8500 Culebra Road
San Antonio, TX 78216 1

Mr. John Domen
Picatinny Arsenal
Bldg 62, ATTN: SARPA-QA-X
Dover, NJ 07801 1

Mr. Herman P. Gay
844 Aldino-Stepney Road
Aberdeen, MD 21001 1

SSgt Willie J. Hall, Jr.
465-76-5052
Development Center F/PR Division
Quantico, VA 22134 1

Mr. Michael Halter
Battelle-Northwest
3000 Area - EDL Bld.
Battelle Blvd.
Richland, WA 99352 1

Dr. William Holm
Radar Appl. Division
Engineering Experiment Station
Georgia Tech.
Atlanta, GA 30332 1

Mr. John C. Houston ARES, Inc. P. O. Box 459 Port Clinton, OH 43452	1
Mr. Robert Kasten Rock Island Arsenal ATTN: SARRI-EN Rock Island, IL 61201	1
Mr. Bertram Kramer Hughes Helicopters Centinela at Teale Street Culver City, CA 90230	1
Mr. John R. Masley Picatinny Arsenal Bldg 65, ATTN: SARPA-ND-C-C Dover, NJ 07801	1
Mr. William J. Pryor Picatinny Arsenal ATTN: SARPA-AD-E-A Dover, NJ 07801	1
Mr. George E. Reis Division 1331 Sandia Laboratories Albuquerque, NM 87115	1
Commander US Army Aviation Systems Command ATTN: DRSAV-EVW (Mr. Dan Sabo) 12th and Spruce Streets St. Louis, MO 63166	1
Dr. Martin Soifer S & D Dynamics, Inc. 755 New York Avenue Huntington, Long Island, NY 11743	1
Mr. Anthony J. Suchocki Chrysler Defense, Department 7111 C/MS 435-01-46 6000 E. 17 Mile Road Sterling Heights, MI 48078	1

Mr. Dean S. Williams
Ford Aerospace and Communications Cord
Ford Road, Room 24, Bldg 1
Newport Beach, CA 92663

1

Commander
Jefferson Proving Ground
ATTN: STEJP-TD (Dr. Norman Wykoff)
Madison, IN 47250

1

F. Conference Participants without addresses:

Mr. Paul Boggs
ARO, Durham, NC

1

Mr. Clive N. Bowden
RARDE, England

1

Mr. James Brown
Armor & Engr Board, Fort Knox

1

Mr. Harry J. Davis
Harry Diamond Laboratory

1

CW3 N. Goddard
MCDEC, Quantico

1

Mr. Roger H. Lapp
APL, John Hopkins University

1

Mr. Thomas Lewis
General Dynamics, Pomona

1

Mr. Victor Lindner
Picatinny Arsenal

1

Mr. William Rodgers
Naval Ordnance, Alexandria, VA

1

Mr. Joe Schmitz
Frankford Arsenal

1

Mr. T. Tsui
AMMRC, Lexington, MA

1

Mr. Leland A. Watermeier
BRL, Aberdeen, MD

1